Structure, Kinematics and Chemistry of the Milky Way Galaxy

Struktur, Kinematik und Chemie der Milchstrasse

Dissertation der Fakultät für Physik

der

Ludwig-Maximilians-Universisität München

vorgelegt von

Ralph Schönrich

aus München

München, den 21. Oktober 2011

STRUCTURE, KINEMATICS AND CHEMISTRY OF THE MILKY WAY GALAXY

STRUKTUR, KINEMATIK UND CHEMIE DER MILCHSTRASSE

Dissertation

an der
Ludwig–Maximilians–Universität (LMU) München

eingereicht von

Ralph Schönrich

geb. am 30. März 1982 in München

München, 21. Oktober 2011

Erstgutachter: Prof. Dr. S. White

Zweitgutachter: Prof. Dr. M. Asplund

Datum der mündlichen Prüfung: 9. Dezember 2011

Contents

List of Figures

List of Tables

Abstract

Ein analytisches Modell unserer Galaxie wird durch die Kopplung eines chemischen Evolutionsmodells mit analytischen Modellen der Kinematik unserer Galaxie entwickelt. Mit Hilfe dieses Modells wird die umfangreiche radiale Migration von Sternen in der galaktischen Scheibe nachgewiesen. Diese hat umfassende Konsequenzen für die Struktur und Geschichte der Scheibe, einschließlich der Ausbildung einer dicken Scheibe, ohne eine Kollision mit einer kleineren Galaxie voraussetzen zu müssen. Durch die Möglichkeit, die lokal gemessene Metallizitätsverteilung mit Hilfe von Sternen aus anderen Regionen der Scheibe aufzubauen, entfällt die Notwendigkeit starker Veränderungen in der chemischen Zusammensetzung unserer Galaxie in der jüngeren Vergangenheit. Im Gegenteil favorisiert das neue Modell einen nur sehr geringfügigen Anstieg der Metallizität, was in ausgezeichnetem Einklang mit den Beobachtungsdaten steht. Das Modell erklärt ferner auf natürliche Weise die bekannten Zusammenhänge zwischen Chemie und Kinematik in Sterndaten aus der Nachbarschaft unserer Sonne. Einige neue Befunde aus lokalen Beobachtungen werden gezeigt und mit den Modellerwartungen verglichen.

Mit Hilfe des Modells wurde ein grundlegender Fehler in der Bestimmung des Ruhestandards, bzw. der Geschwindigkeit unser Sonne relativ zur idealen Kreisbahn in unserer Galaxie gefunden. Zusammen mit der später erfolgten Messung der Rotationsgeschwindigkeit der Sonne um das Zentrum der Milchstraße konnten wir den galaktozentrischen Radius und die Rotationsgeschwindigkeit der Milchstraße am galaktozentrischen Radius der Sonne neu bestimmen. Diese zweite Messung wurde durch eine neue statistische Methode ermöglicht, die eine höhere Genauigkeit bei der statistischen Korrektur von Sterndistanzen erlaubt als die Ansätze der klassischen statistischen Astronomie. Die neue Methode war auch von großem Nutzen beim Nachweis, dass die jüngsten Behauptungen einer dualen Struktur des galaktischen Halos auf Distanzfehler und die ungerechtfertigte Beschreibung intrinsisch asymmetrischer Daten durch Gaußfunktionen zurückzuführen sind. Aus dem mathematischen Apparat für die Kinematik des Scheibenmodells wird eine einfache analytische Funktion zur Beschreibung der Geschwindigkeitsverteilung in der Scheibe hergeleitet, die bei gleicher Zahl freier Parameter eine physikalisch besser motivierte Alternative zu den häufig genutzten Gaußfunktionen bietet.

Abstract

An analytic model of our Galaxy is developed by coupling a chemical evolution model with analytic models of the kinematics of our Milky Way. With this model the presence of strong stellar radial migration in the Galactic disc is proven. This bears far-reaching consequences for the structure and history of our disc including the formation of a thick disc component. Hence there is no more need for a collision of the Milky Way with a smaller galaxy in the past to explain the existence of the thick disc. By building the locally observed metallicity distribution function with the help of stars from other regions of the Galactic disc the model does not require strong changes of the chemical composition in the near past. On the contrary the new model favours a relatively flat age-metallicity relationship in excellent agreement wih observations. The model explains in a very natural way the known links between chemistry and kinematics of Solar neighbourhood stars. Some new results from local observations are shown and compared to the model expectations.

With the help of the new model a systematic error was discovered in the classic determination of the Local Standard of Rest or respectively the velocity of the Sun relative to a circular orbit in the Galactic disc. Together with the later measurement of the total azimuthal speed of the Sun around the centre of the Milky Way we are able to determine the local galactocentric radius and the circular speed of the Milky Way at the local radius. The measurement of rotation from stars has been enabled by the creation of a new method that allows for a higher accuracy in correcting the average distance to asample of stars than the classic strategies of statistical astronomy. The new method was very useful in demonstrating that the recent claims of a dual structure of the galactic halo are the result of significant and systematic distance errors and the unjustified use of Gaussian functions to describe intrinsically asymmetric data. From the mathematical apparatus developed for the kinematics of our disc models we derived a simple analytic function describing the velocity distribution of disc stars that offers at the same number of free parameters a physically better motivated alternative to the commonly used Gaussian fits.

Chapter 1

Introduction

1.1   Preface

Work on the physics of our Milky Way sometimes resembles the job of a historian: piece together the heap of information that the true archaeologists of our Milky Way - observers and spectroscopists - provide and try to provide as simple as possible explanations that shatter some light of the wide variety of the data. Two simplifications could be done: With our new radial migration models the wealth of local spectroscopic and kinematic data of the Galactic disc could be explained without having to invoke any special violent merger that formed the Galactic thick disc while explaining the otherwise peculiar similarities between thick disc and inner disc. Second with our progress in understanding stellar distances, distance errors and their effect on kinematics we could not only re-institute stars to their role as a keystone in determining Galactic parameters, but also make our picture of the Galactic halo simpler by dismantling recent claims on a pronounced dual structure of the Galactic halo as a result of distance errors and insufficient analysis.

Soon in my research on the Galactic disc I had to notice that the theoretical modelling may be a well confined and rather foreseeable course of advance, but that without deep involvement in the actual data I would maybe make some observer happy whose data I use in blind trust, but would never hold a reasonable model of our Milky Way. Of course the result was not doing it better than the observers, but doing it better than without understanding of the traps and short-comes in observational data. This errand through Galactic astrophysics would have been a pain had not my supervisor turned out to be the epitome of patience bearing calmly and positively reacting to my weekly changes of interest and topics. The result is - as the reader may notice - a rather kaleidoscopic view on our Galaxy, that covers almost all their parts apart from the Galactic Bulge (which could perhaps also be covered in the context of our radial migration models, but that will be another, later story). This has the adverse effect that a general line of developing my thoughts and arguments cannot be found, although all of the presented work is connected to each other and none of these chapters and publications could exist without each other.

Among the presented work the unfortunately rather destructive piece on halo structure turned

out to be the most productive of them all - it forced me not only to create the analytic formula for disc kinematics that then triggered the shown improvement in adiabatic modelling that is key to development of an improved disc model in the near future, it is also the source of my idea to use stellar kinematics in a novel way and by these improved astrostatistics opened the way to obtaining Galactic parameters at high precision.

1.2 General remarks

Due to the broad scope of this work a complete introduction to the relevant physics cannot be given - it would have to cover the entire range of Galactic astrophysics, dynamics, stellar evolution, spectroscopy and much more. Instead I will present some rather simplistic explanations to central topics and refer the interested reader to Binney & Tremaine (2008) for stellar dynamics and kinematics, to Mo, van den Bosch & White (2010) for a view on Galactic evolution closer to cosmology, to Binney & Merrifield (1998) for questions of Galactic Astronomy, to Pagel (1997) for chemical evolution and to Trumpler & Weaver (1962) for an introduction to astrostatistics.

The field where stellar astrophysics and Galactic chemical evolution meet together is sometimes called Galactic archaeology. The stellar population hosts both the witnesses and the drivers of chemical evolution (for a related discussion, where the picture was drawn similarly I reference Schönrich, 2011a), i.e. the change of the chemical composition of the star forming gas by the products of stellar fusion and to a minor extent by spallation and radioactive decay. While the massive stars burn their nuclear fuel quickly and dispel it into the surrounding medium quickly, driving chemical evolution, their light-weight counterparts (around or below about a solar mass) live comparatively long with or longer than the age of our Galaxy. As the products of their fusion during the main sequence evolution (which would anyway be mostly limited to Helium and some changes to CNO abundances, i.e. elements involved in the Bethe-Weizsäcker cycle (Weizsäcker, 1937, 1938; Bethe, 1939), for stars above around $1 M_\odot$) do not pass through the mostly radiative interior of a star to its surface their surface metallicities reflect the composition of the interstellar medium from which they were born. So in principle the entire history of the Galaxy lies stretched on the sky before us, however, we need to perform the highly non-trivial task of decoding it, as their ages are uncertain and their birthplaces are unknown.

For this task a detailed theory of chemical evolution is very helpful to limit the range of possible developments that the chemistry in a galaxy can take and to link the observed trends to physical mechanisms. Fig. 1.1 delineates the main players in the chemical evolution process. The chemical evolution begins when enough gas has flown into the Galaxy to become unstable and trigger star formation. In contrast to elliptical galaxies, which contain mostly hot gas that does not support star formation, the Milky Way contains predominantly cool gas near its disc plane. This reservoir keeps up continuous star formation concentrated in its spiral arms as well as a small central ring near the centre and a ring of more intense star formation near $4\,\mathrm{kpc}$, probably triggered by the Galactic bar. The most massive stars from that star formation die after a couple of million years. As the iron core of the supernova progenitors in most cases collapses
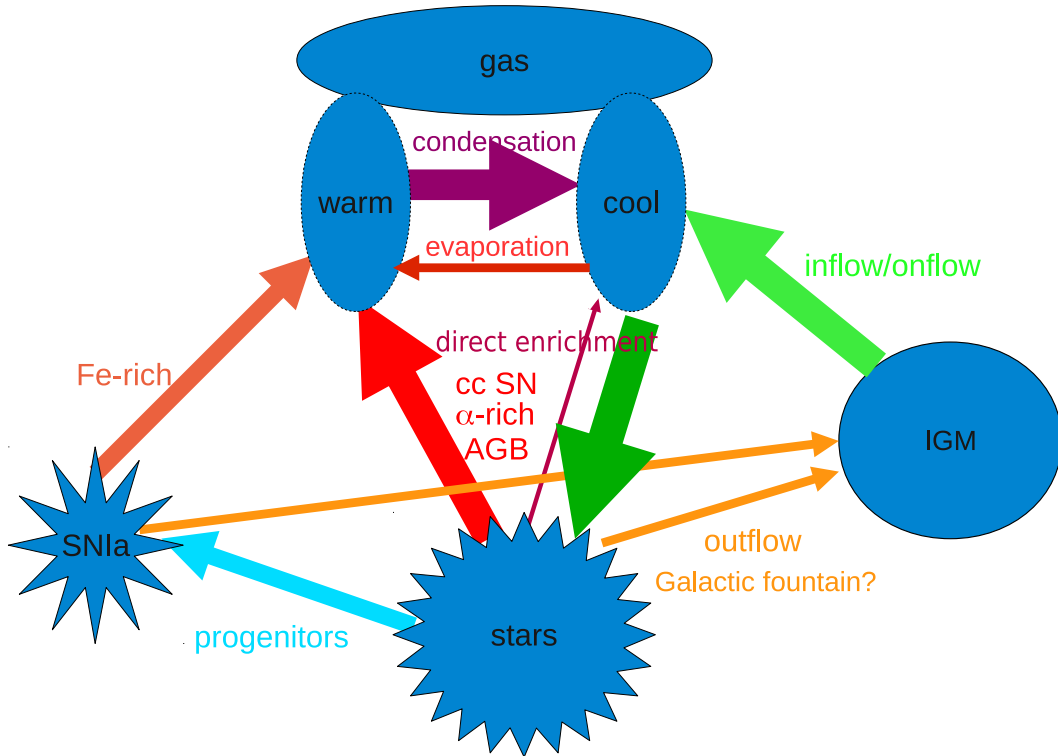
Figure 1.1: Sketch of processes in Galactic chemical evolution. "cc SN" is an abbreviation for the core collapse supernovae produced by massive stars and "AGB" indicates the elements freed in the final asymptotic giant branch stage of intermediate mass stars. Fe-rich indicates yields rich in iron, while α-rich classifies the yields of massive stars that are rich in α-elements like magnesium or calcium.

into a neutron star or black hole (see e.g. Janka et al., 2007), only the outer layers can be expelled and what is mixed up by turbulence and jets. Hence only a small amount of iron peak elements is given back to the interstellar medium, while those explosions set free a lot of CNO and α elements, i.e. elements whose nuclei are multiples of α particles derive from fusion before reaching the final stage of silicium burning. There exists a second channel of enrichment with heavy elements: Supernovae of type Ia (normally denoted SNe Ia) are thermonuclear explosions of a white dwarf that lead to the complete disruption of the body and as a considerable fraction of the mass is fused into iron they change the composition of the galactic interstellar medium considerably in favour of iron. Despite an ongoing debate about the exact timescales and if the dominant channel are mergers of two white dwarfs, white dwarfs reaching the Chandrasekhar

mass or sub-Chandrasekhar explosions triggered by a helium-flash (Sim et al., 2010; Fink et al., 2010), it is clear that the time necessary for the creation of a white dwarf from an intermediate mass star and the subsequent development require far more time than needed towards a core collapse supernova. This sets a natural clock that starts running with the first populations of stars born in a galaxy. At first the core collapse supernovae produce their yield in α elements and the $[\alpha/\text{Fe}]$ ratio begins to drop when the first SNe Ia are produced. This clock plays also a pivotal role as it was commonly believed that the bimodal behaviour of $[\alpha/\text{Fe}]$ ratios in local stellar samples indicated a hiatus in star formation probably connected to a cosmic catastrophe like a major merger of our Milky Way (see e.g. Brook et al., 2007) in the far past creating the thick disc as well. In Schönrich & Binney (2009a), or Chapter 2 we have shown that such a bimodal distribution even with a deep gap is the natural outcome of the logarithmic abundance scale acting together with radial migration of stars and the standard timing of SNe Ia making any hiatus in star formation obsolete for explaining the current observations.

Some words of caution have to be added to all this abundance timing: In its use we have to be always aware that we are not holding an absolute age, but an age relative to the first population born in the system. On its trend down in $[\alpha/\text{Fe}]$ there are also strong influences by the time line of star formation. A pronounced peak in star formation can increase the content of α elements and temporarily drive chemistry back to higher $[\alpha/\text{Fe}]$ ratios (cf. e.g. Colavitti et al, 2008). Even more caution has to be applied to absolute metallicities as time indicator. Fuelled by some simplistic chemical evolution models that neglected lock-up of processed material in the hot gas phase and other essential ingredients there has been spread that metallicities are a direct indicator for age. They are not. It is correct that in general a system will involve to higher abundances, but we have to acknowledge that the enrichment (see e.g. our galactic abundance gradient and the contrast to the intergalactic medium) is strongly inhomogeneous in space.

Chemical evolution bears also a lot of open questions. The lock-up of processed material in the hot gas phase and the transport of this material in the radial direction of a disc Galaxy are not understood. Similarly we know from isotope measurements in the Earth's crust and in meteorites that the solar system must have at its formation contained a relatively large amount of short-lived radioactive isotopes. This proves that there must be a significant direct enrichment of molecular clouds and protostellar systems by nearby supernovae (see e.g. Gounelle & Meibom, 2008). Still the absolute fraction of supernova yields dumped in the direct channel is neither sufficiently constrained by observations nor by theoretical argument. This is a sad situation as the early chemical enrichment of any system depends critically on this parameter.

1.3 Galactic structure

Despite the impressive reasoning by which Kant (1755) predicted not only the formation of stellar and Galactic systems from collapsing dust clouds and hence their disc shape as well as the fact that the then observed "nebulae" would turn out as remote stellar systems (termed "Welteninseln" by him) it took until the last century it became widely accepted that we are not in the centre of our

system (Shapley, 1918) and that there is a great abundance of other stellar systems outside our Galaxy (Curtis, 1920) and that we are not in the centre of our system as suggested by Herschel's (see Fig. 4 in Herschel, 1785) reddening and distance affected star counts, but live rather on the edge of our disc galaxy (Shapley, 1918). As most disc galaxies carry a more or less pronounced spiral pattern of enhanced star formation and molecular cloud density, they are commonly termed spiral galaxies.

In a very simplistic way the Milky way can be decomposed into three components: disc, bulge and halo. Like in all spiral galaxies, the disc of the Milky Way harbours almost all of the cold gas content in our Galaxy in a very thin layer (a scaleheight of about 10 pc or respectively 30 light years compared to a scale length of about 3 kpc). This gas condenses into the molecular clouds from which disc stars are formed till today. They constitute the thin stellar disc which at a comparable scale length to the gas attains a larger scale height of around 300 pc as stars gain random energy during their lifetimes and hence reach higher altitudes. While the average age increases drastically towards higher altitudes, the density slope gets shallower. Be it a separate entity or just a smooth transition, this can be well described by a second component (Gilmore & Reid, 1983) that locally (i.e. in the disc plane) makes up around 12% of the "thin" disc and has a scale height of around 900 pc (Ivezic et al., 2008).

In its centre our Galactic disc hosts a bar and a relatively small bulge. Many processes have been brought up for formation of this component. The fact that it attains around solar metallicity at still high $[\alpha/\text{Fe}]$ ratios (see Meléndez et al., 2008) indicates very dense and rapid star formation (the high $[\alpha/\text{Fe}]$ ratio indicates a short history of star formation that did not allow for SN Ia explosions to contribute significant amounts of iron to the metal enrichment and the high metallicity then demands rapid star formation to deliver the necessary amount of metals. Currently it is rather up to speculation what this entity constitutes. There is some indication (e.g. the relatively small mass estimates for the central black hole) that most of its mass is actually a pseudo bulge - older disc stars that have been taken to a bulge-like structure by secular processes. A major contributor might also have been a vigorous disc instability at the start of disc formation leading to the formation of giant clumps that by friction fall into the central regions (Aumer et al., 2010; Bournaud et al., 2009). The latter paper offered also a nice process that may contribute to thick disc formation. If preliminary results of Bulge studies hold true, a clumpy appearance of the metallicity distribution function for which some tentative indications have been found by (Bensby et al., 2011a; Hill et al., 2011) (the two-Gaussian fit done by Hill et al. may be considered irrelevant, as it is common knowledge that metallicity distributions of common chemical evolution models are intrinsically asymmetric) may be a first observational hint such a process.

The detailed origin of the Galactic halo, the extremely low density mass of stars surrounding our disc and bulge, is still unexplained. A lot of its mass is contributed by in-falling dwarf galaxies/satellites forced to spiral into the Galaxy by dynamical friction and getting disrupted in the tidal field of our Galaxy. The observational evidence so far is quickly summarised as: the Galactic halo is very metal poor with a quite broad metallicity distribution peaking somewhere around $[\text{Fe/H}] \sim -2$ to $[\text{Fe/H}] \sim -1.5$ (see e.g. Ryan & Norris, 1991; Schörck, 2009), i.e. at less then a tenth of the solar metal content, its populations are kinematically very hot with the

velocity ellipsoid elongated strongly in the radial direction at roughly a 2 : 1 axis ratio with the vertical and azimuthal components. With the globular clusters it hosts some of the oldest and still most enigmatic objects of the universe. Some globular clusters like ω Cen are believed to be cores of disrupted dwarf galaxies (Bekki & Freeman, 2003). Some may be remnants of mergers or chunks of in-falling gas that collapsed to stars during its infall into the Milky Way (the first to speculate about such a process again appears to have been Kant, 1755). Most of them display, contrary to what was believed until a couple of years ago, multiple populations visible both in spectroscopic metallicity distributions and photometry (see e.g. Bedin et al., 2004; Caretta et al., 2009; Lind et al., 2011; Marino et al., 2011). As globular clusters lose many of their members by core contractions and hence contribute a significant fraction of stars to the dispersed stellar population of the Galactic halo (see e.g. Martell & Grebel, 2010). Possible differences between the inner and the outer halo have always been central issues of research in this field. A priori it is clear that by the adiabatic contraction of the halo populations in the deepening gravitational potential of our Galaxy the outer halo should be on average a bit younger and probably contain a larger fraction of fresh debris from infalling satellites. Other studies, especially Carollo et al. (2007, 2010) claimed a strong retrograde motion for the outer halo and a lower metallicity for these objects from local halo star data. While other observational studies like Sesar et al. (2011) do not find a convincing metallicity gradient from in situ samples, we could show that all the signatures found by Carollo et al. (2007, 2010) can be traced back to distance biases and inadequate analysis of their data. This is presented in chapter 8 or respectively in Schönrich et al. (2011b).

Back to the structure of the Galactic disc: The main source of information about the structure, dynamics and history of the Disc is the combination between chemistry and kinematics of disc stars. Hence a deeper understanding of the chemical evolution of the Galactic disc is required. All of this is discussed in detail in the following chapters, but Fig. 1.2 sketches the most important processes. A central ingredient to this are the dynamics of the cold gas in the Disc. Most observational data apart from a few exceptions indicate present disc metallicity gradients of $d[\text{Fe/H}]/R \leq -0.05\,\text{dex}/\text{kpc}$, more than can be explained within chemical evolution models without radial flows, especially as we know from Casagrande et al. (2011) that the mean metallicity did not experience significant changes during the past few billion years. The most reasonable explanation for the persistent presence of a Galactic abundance gradient has been laid out by Goetz & Koeppen (1992) and Portinari & Chiosi (2000): A radial inflow through the Galactic disc can advect the yields of stars towards the central regions of the Galactic Disc, while the outer parts experience the inflow of "fresh", less enriched material. Flows of order $1\,\text{km}\,\text{s}^{-1}$ are entirely sufficient to drive this mechanism. The main drivers of this process are identified (see a discussion of possibilities in Lacey & Fall, 1985) and currently the most important factor seems to be the onfall of material with lower angular momentum onto the disc. At the same time Sancisi et al. (2008) find that there is demonstrably onflow of cold gas onto Galactic discs, but it is not sufficient to cover the needs of those systems for sustaining their high star formation rates. In this context Marinacci et al. (2011) delivered the welcome explanation that supernova explosions can push cold clouds out of the disc plane to higher altitudes where hot gas from the
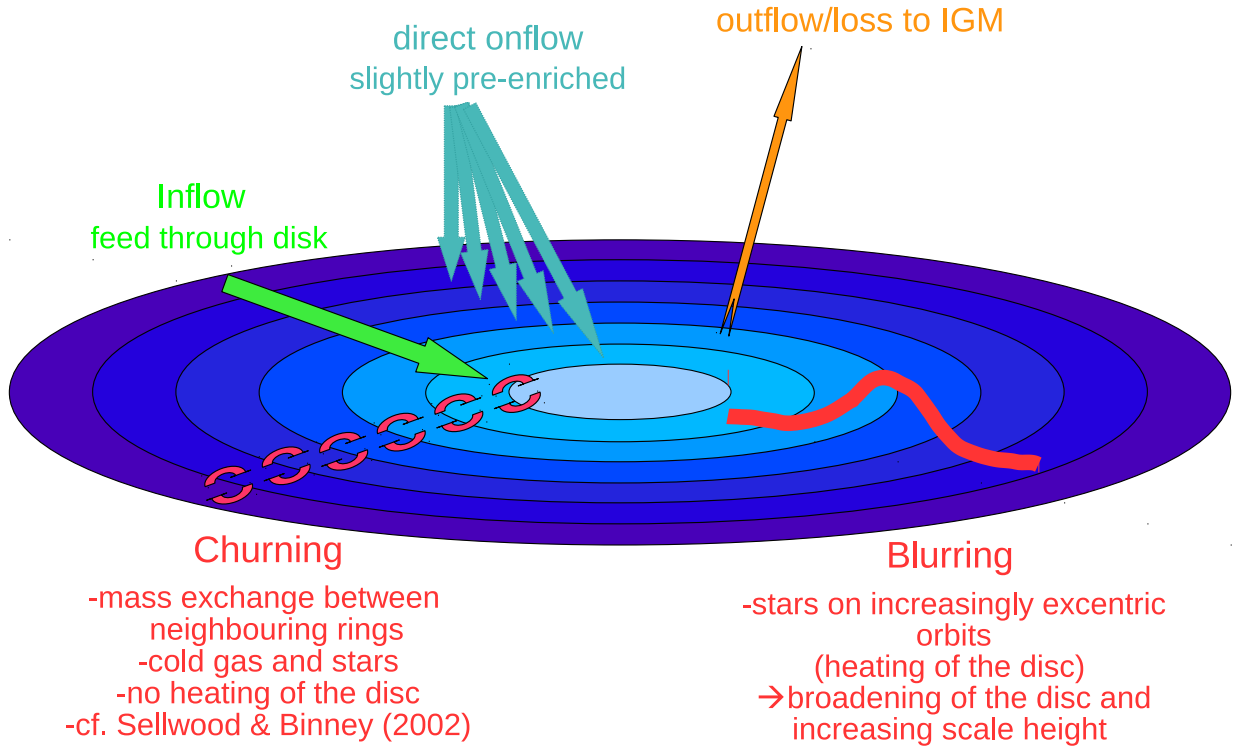
Figure 1.2: Sketch of gas flows and stellar migration in a typical disc galaxy. "IGM" abbreviates the intergalactic medium.

corona condenses on their thermally unstable boundaries. There is an interesting implication to this process: the hot coronal gas has a significantly lower angular momentum, lagging the local circular speed by roughly $75\,\mathrm{km\,s^{-1}}$. As we will demonstrate in an upcoming paper the radial abundance gradient as observed by Luck & Lambert (2011) is fully consistent with this angular momentum difference of the infalling gas driving the radial gas flow.

Once we have established a radial abundance gradient, the local metallicity distribution can be used to constrain disc dynamics. In Chapter 2, or respectively Schönrich & Binney (2009a) it has been shown that the shape of the local metallicity distribution function as observed in the Geneva-Copenhagen Survey (GCS, Holmberg et al., 2007; Casagrande et al., 2011) can only be explained when we allow for significantly more stars from other radii entering the solar neighbourhood than can be explained by orbital excursions due to the heating up of the populations ("blurring") alone. It is hence necessary to allow for an additional migration process that allows for stars changing their angular momentum significantly. The only such process is radial migration by

resonances with the potential perturbations from the Galactic bar and spiral pattern as described for the first time by Sellwood & Binney (2002). Stars participating in this process are expected not to experience any significant heating during their angular momentum change and we term this process "churning" in contrast to the aforementioned "blurring". Apart from the proof of radial migration/"churning" we discovered that the migration of inner disc populations with their hotter kinematics leads to a significant increase in the disc scale height in the outer disc regions and solar neighbourhood, explaining the larger scaleheight of the thick disc in addition to the already understood separation in chemistry without having to invoke any cosmic catastrophe. This analytical result was later confirmed by Loebman et al. (2011) on an N-body model. As a side result we also showed that this immigration of hotter stars into the solar neighbourhood resolves the old tension between theoretical expectations and observations on the disc heating function with time: By perturbations in the Galactic potential, mostly clouds, clusters and other density fluctuations, stars get scattered or in other words diffuse through phase space gaining random energy with time. Theoretically this can be approximated by a simple heating law like $\sigma_i \propto t + t_0{}^\beta$ where σ_i is the dispersion of a population in velocity component i, t is the age of the component, t_0 is a small offset giving the population a finite dispersion at birth and β is the time coefficient. Theoretically this relationship should display a time coefficient $\beta < 1/3$ while e.g. Aumer & Binney (2009) measured $\beta > 1/3$. This difference is readily displayed by increasing influence of inner disc stars on the solar neighbourhood with time as we show in Chapter 2.

These successes of radial migration motivated a detailed investigation into the links between kinematics and chemistry in our radial migration model performed in Chapter 3, focusing especially on the common selection schemes to separate suspected thick disc objects from thin disc objects. We proved on the basis of Toomre diagrams of the single components that no such selection could ever yield a clean result in terms of population separation, which explains the stragglers (low $[\alpha/\mathrm{Fe}]$ stars in the kinematically hot component and high $[\alpha/\mathrm{Fe}]$ stars in the kinematically cool, i.e. thin disc, selection). We have demonstrated that all the structure in the abundance plane observed in local studies is perfectly matched by our radial migration model without having to adapt a single further parameter. Also the observed abundance pattern was traced back to a very natural origin: Generally the thick disc displays a high $[\alpha/\mathrm{Fe}]$ enrichment up to quite high metallicities $[\mathrm{Fe/H}] \sim -0.4$ and then turns down towards lower $[\alpha/\mathrm{Fe}]$ enhancement meeting the thin disc ridge line around or slightly above solar ($[\mathrm{Fe/H}] = 0$) metallicity. The cradle of such a population must hence have experienced a far quicker enhancement or respectively star formation than the local population (that drops in $[\alpha/\mathrm{Fe}]$ at lower metallicities). In the simplest case this is just achieved when a quick metallicity increase is spurred by high star formation rates in a dense environment, exactly what is found in the early inner Galactic disc. In classical chemical evolution models this component had to be artificially created by driving up the local star formation rates by a manipulation of the Kennicutt law (the law connecting gas surface density to star formation efficiency) and a subsequent arbitrary break in star formation and the coefficient of the Kennicutt law. Apart from the very natural set-up of our thick disc formation, this is a very natural explanation for the finding of Meléndez et al. (2008); Bensby et al. (2011a) that the inner disc/bulge follow approximately the same trend in abundances as the

local thick disc.

Investigations into the structure of the model yielded a surprise for Galactic kinematics. At least since the work of Delhaye (1965) it was common knowledge that the Local Standard of Rest (LSR) could be determined via the Strömberg equation, or in other name asymmetric drift relation that states a linear relationship between the asymmetric drift (i.e. the velocity difference between the circular speed of the Galaxy and the azimuthal velocity component of a population in question) and its squared velocity dispersion. Intuitively this relationship is clear as a lack of angular momentum and hence kinetic energy in the azimuthal velocity component can be made up by random energy in the other components, formally it can be directly derived from the Jeans equations. Dissecting a sample into kinematically hot and cool objects, this linear relationship can in principle be measured and by extrapolation to zero asymmetric drift the LSR and the solar azimuthal velocity against this circular speed can be recovered. Until now an important aspect of the asymmetric drift relation has been overlooked throughout the history of its use: The relation contains the radial density gradient of a population. The gradient is remarkably stable for populations of different ages, but if we select a sample by metallicity, we select for inner and outer disc stars respectively. For moderately metal poor objects born in the outer disc, this gradient will even reverse leading in extreme cases up to a sign change in the asymmetric drift relation. And indeed the classic selection of stars involves metallicity: Having no other parameters at hand, stars were selected by their colour. This strategy uses the fact that blue stars have higher stellar masses, which makes them die young and hence the average age of a population of main sequence stars increases from blue to red until the red-most turn-off point that is set by the oldest stellar populations of our Galaxies, also called Parenago's discontinuity (Parenago, 1950), from where the dispersion should remain constant. However, as higher metallicity implies redder colours for stars of the same mass, the colour selection leads to metal-poor stars being preferentially in the young bins and metal-rich stars on the old, red side. This distorts the expected linear relationship and thus an unphysical linear relationship is faked on the red side. This novel view explains also the large systematic aberration observed for young stars from the slope defined by the linear relation and led to a correction of the standard value for the solar azimuthal velocity from $(5.25 \pm 0.54)\,\mathrm{km\,s^{-1}}$ to now $(12.24 \pm 0.47)\,\mathrm{km\,s^{-1}}$ with an assumed systematic uncertainty of $2\,\mathrm{km\,s^{-1}}$. Some observational data are presented that confirm the predictions made in this paper.

As mentioned above our tests on the alleged duality of the Galactic halo (Chapter 8) revealed that the claims of such a duality had no substance. While it is good news by itself that our Galaxy is not as complicated as it was suspected to do making its physics simpler and forcing less assumptions, this paper triggered a couple of further developments: For reliable comparisons of a theoretical model velocity distribution to the observations, several sources of error have to be respected, or technically their terms have to be folded onto the theoretical distribution to match the data. As a result of distance errors especially the azimuthal velocity distributions carry a highly asymmetric error term that mimics a second component when being neglected. Further the proper motion errors have to be correctly applied and distance errors enter the stage a second time by letting the other velocity components cross over into the component in question

(see Chapter 9). This folding is easily explained, but becomes painful when fitting complicated kinematic models to the observations. The alternative on the marketplace are the widely used Gaussian fits. However, their solutions are dynamically absurd and have nothing to do with the underlying physics, e.g. they neglect the intrinsic asymmetry of azimuthal velocity distributions in Galactic discs resulting in the need for artificial second or even third components. To solve this problem we created a simple analytic formula (presented in Chapter 6) that can of course not compete with a complete model, but does not demand more free parameters than the classical Gaussian fits and instead has physical motivations and interpretations for each used parameter, while it naturally covers the intrinsic asymmetry of velocity distributions and hence gives a true indication for allowed shapes and the need for further components.

In the course of this work we noticed an inconsistency in the classical approach of adiabatic models for the kinematics of our Galaxy: An inconsistency of classic adiabatic modelling was noted by Binney & McMillan (2011) in that with larger vertical energies adiabatic models give orbits an increasing inward bias. They approximated this bias by replacing the angular momentum aligned with the disc rotation axis (L_z) with the total angular momentum of the orbit in calculating its horizontal extent. Of course this correction pushes the orbit outwards as desired, but we found that a more natural explanation: The adiabatic approximation violates total energy conservation by changing the vertical energy of an orbit dependent on Galactocentric radius (the nearly adiabatic expansion of an orbit towards the outer Galaxy reduces vertical energy) and we demonstrated that this problem can be solved by the introduction of what we call the "adiabatic potential" in the horizontal term. This potential simply corrects the usual effective potential of horizontal motion by adding the energy difference in the vertical term, resulting in an outwards tilt of the effective potential. This copes naturally with the observation that a few stars in simulations at high vertical energies never reach their guiding centre radius (i.e. the orbit of a circular orbit with their L_z). In addition we show in Chapter 7 that the approximation by using the entire entire angular momentum of an orbit is by some coincidence valid near the solar neighbourhood, but does not generally hold in all potentials, while the adiabatic potential gives very promising results.

The second upshot of the halo paper was our work on distances, presented in Chapter 9. It uses the idea that distance errors induce specific correlations between velocities that vary over the sky. As an example think about a typical halo star (no motion in the azimuthal velocity direction) observed at an elevation of about 45 degrees in the direction of rotation of our Galaxy. As we are rotating with the Galactic disc beneath this star, it's Galactic latitude b will rise, while we see its light blue-shifted. Only when knowing its correct distance we will ascribe the right motion to this object. In case we overestimate its distance, the angular motion outweighs the line-of-sight velocity and consequently we will think that this object rises vertically into the sky. Vice versa - had it been placed behind our direction of motion, we would have - by our distance overestimate - have inferred it moving downwards. In short with a common sentence: With a systematic distance error we see "the skies falling". Exploiting this idea we developed a distance estimator that is more sensitive and robust than the classical strategies of statistical astronomy, i.e. the secular and the statistical parallax. This work also definitely revealed the fact

that the suspected subgiants/turn-off stars that were used by Carollo et al. (2007, 2010) and are still used by Beers et al. (2011) in the spectroscopic samples from the Sloan Digital Sky Survey (SDSS/SEGUE) are entirely unreliable, as they are dominated by contamination from dwarf and giant stars. We have also applied our distance estimator with great success to stellar distances in the RAVE survey. There it uncovered biases for a couple of different stellar categories and the results will soon be described elsewhere.

The novel distance estimator impacts our ability for using stellar samples in the determination of Galactic parameters, especially the solar Galactocentric radius and the circular speed of the Galaxy near the Sun. Since the invention of the Oort constants (Oort, 1927) this field has not made a lot of significant progress, especially as distances for stars outside the HIPPARCOS sphere, where we have geometric parallaxes, were too uncertain to allow high precision measurements. However, with our ability to assess the systematic distance scale this field lies suddenly open for exploration. First approaches are laid out in Chapter 10. In this work we discovered that the large geometric extension of the new big samples like SDSS and RAVE allows to measure the absolute rotation speed of a component from the systematic rotational streaming in the heliocentric radial velocities: Simply explained the stars on one side of the Galactic centre come towards us while they move away from us on the other side. Apart from a beautiful assessment of component rotation in our Galaxy that is fully independent of assumptions on the Solar motion itself, we can do more: By matching the measured rotation to the mean azimuthal motion of stars we can infer the total azimuthal velocity of the Sun and discounting for the already determined LSR motion of the Sun we can infer the local circular velocity of our Galaxy. As we can weigh the sample by its impact on the rotation estimator, we get a fully unbiased estimate of rotation that does not require any prior knowledge e.g. on the change of asymmetric drift with altitude above the plane. As a downside the inferred solar velocity depends on the assumed Solar Galactocentric radius. Adding the proper motion of Sgr A^* (Reid & Brunthaler, 2004) with which our relation intersects as second constraint we derive both the Solar Galactocentric radius and the solar velocity. As a second measurement we only have to use the fact that the derived circular velocity must be the same for all populations irrespective of their intrinsic rotation. Since our estimator is independent from the estimates of McMillan (2011), we can match our results (that are of comparable precision) to his and obtain the highest formal accuracy of Galactic parameters among the studies we are aware of with $R_0 = (8.24 \pm 0.09)\,\mathrm{km\,s^{-1}}$ and $v_{\phi,\odot} = (249 \pm 4)\,\mathrm{km\,s^{-1}}$.

Chapter 2

Chemical evolution with radial mixing[1]

2.1 Abstract

Models of the chemical evolution of our Galaxy are extended to include radial migration of stars and flow of gas through the disc. The models track the production of both iron and α elements. A model is chosen that provides an excellent fit to the metallicity distribution of stars in the Geneva–Copenhagen survey (GCS) of the solar neighbourhood, and a good fit to the local Hess diagram. The model provides a good fit to the distribution of GCS stars in the age–metallicity plane although this plane was not used in the fitting process. Although this model's star-formation rate is monotonic declining, its disc naturally splits into an α-enhanced thick disc and a normal thin disc. In particular the model's distribution of stars in the ([O/Fe],[Fe/H]) plane resembles that of Galactic stars in displaying a ridge line for each disc. The thin-disc's ridge line is entirely due to stellar migration and there is the characteristic variation of stellar angular momentum along it that has been noted by Haywood in survey data. Radial mixing of stellar populations with high σ_z from inner regions of the disc to the solar neighbourhood provides a natural explanation of why measurements yield a steeper increase of σ_z with age than predicted by theory. The metallicity gradient in the ISM is predicted to be steeper than in earlier models, but appears to be in good agreement with data for both our Galaxy and external galaxies. The models are inconsistent with a cutoff in the star-formation rate at low gas surface densities. The absolute magnitude of the disc is given as a function of time in several photometric bands, and radial colour profiles are plotted for representative times.

2.2 Introduction

Models of the chemical evolution of galaxies are key tools in the push to understand how galaxies formed and have evolved. Their application to our Galaxy is of particular importance both on

---

[1] This chapter was published as Schönrich & Binney (2009a). It was further done to a major part during my diploma thesis for which it was used. Text and content are identical to the journal paper apart from minor editing.

account of the wealth of observational data that they can be required to reproduce, and on account of the inherent interest in deciphering the history of our environment.

From the pioneering papers by van den Bergh (1962) and Schmidt (1963) it has generally been assumed that a galaxy such as the Milky Way can be divided into concentric cylindrical annuli, each of which evolves independently of the others (e.g. Pagel, 1997; Chiappini et al., 1997, 2001; Naab & Ostriker, 2006; Colavitti et al, 2008). The contents of any given cylinder are initially gaseous and of extremely low or zero metallicity. Over time stars form in the cylinder and the more massive ones die, returning a mixture of heavy elements to the remaining gas. The consequent increase in the metallicity of the gas and newly-formed stars is generally moderated by an inflow of gas from intergalactic space, and, less often, by an outflow of supernova-heated gas.

The cool, star-forming gas within any cylinder is assumed to be well mixed, so at any time it can be characterised by a metallicity $Z(r,t)$, where r is the cylinder's radius. Hence the stars formed within a given cylinder should have metallicities $Z(r,t_f)$ that are uniquely related to their time of formation, t_f. Observations do not substantiate this prediction; in fact Edvardsson et al. (1993) showed that solar-neighbourhood stars are widely distributed in the (t_f,Z) plane – for a detailed discussion see Haywood (2006) and Section 2.7.2.

The absence of an age-metallicity relation in the solar neighbourhood is naturally explained by radial migration of stars (Sellwood & Binney, 2002; Haywood, 2008; Roskar et al., 2008b). It has been recognised for many years that scattering by spiral structure and molecular clouds gradually heats the stellar disc, moving stars onto ever more eccentric and inclined orbits. Stars that are on eccentric orbits clearly contribute to different cylindrical annuli at different phases of their orbits, and thus tend to modify any radial gradient in the metallicities of newly formed stars. Moreover, scattering events also change the guiding centres of stellar orbits, so even a star on a circular orbit can be found at a different radius from that of its birth. In fact, Sellwood & Binney (2002) argued that the dominant effect of transient spiral structure is resonant scattering of stars across the structure's corotation resonance, so even a star that is still on a near-circular orbit may be far from its radius of birth. Roskar et al. (2008a) showed that in a cosmological simulation of galaxy formation that included both stars and gas, resonant scattering at corotation caused stars to move outwards and gas inwards, with the result that the stellar disc extended beyond the outer limit of star formation; the outer disc was entirely populated by stars that had formed much further in and yet were still on nearly circular orbits. This simulation confirmed the conjecture of Sellwood & Binney (2002) that gas would participate in resonant scattering alongside stars.

We distinguish two drivers of radial migration: when the angular momentum of a star is changed, whether by scattering at an orbital resonance or by non-resonant scattering by a molecular cloud, the star's guiding-centre radius changes and the star's entire orbit moves inwards or outwards depending on whether angular momentum is lost or gained. When a scattering event increases a star's epicycle amplitude without changing its angular momentum, the star contributes to the density over a wider range of radii. In a slight modification of the terminology introduced by Sellwood & Binney (2002), we say that changes in angular momentum cause "churning" while changes in epicycle amplitude lead to "blurring". This paper extends models of Galactic chemical

evolution to include the effects of churning and blurring.

Given the strength of the arguments that cold gas should participate in churning alongside stars, and that shocks induced by spiral structure cause gas to drift inwards, it is mandatory simultaneously to extend traditional chemical evolution models to include radial flows of gas within the disc. Lacey & Fall (1985) studied chemical evolution in the presence of a radial inflow of gas and demonstrated that a radial flow enhances the metallicity gradient within the disc. This enhancement plays an important role in our models, which differ from those of Lacey & Fall in that they include both radial gas flows and radial migration of stars. Moreover we can fit our models to observational data that is much richer than that available to Lacey & Fall (1985).

Our models are complementary to ab-initio models of galaxy formation such as those presented by Samland & Gerhard (2003) and Roskar et al. (2008b) in that they allow the solar neighbourhood to be resolved in greater detail, and because they are enormously less costly numerically, they permit parameter searches to be made that are not feasible with ab-initio models.

The paper is organized as follows. Section 2.3 presents the equations upon which the models are based. These consist of the rules that determine the rate of infall of fresh gas, the rate of star formation, details of the stellar evolution tracks and chemical yields that we have used and descriptions of how churning and blurring are implemented. Section 2.4 describes in some detail a "standard" model of the evolution of the Galactic disc. This covers its global properties but focuses on what would be seen in a survey of the solar neighbourhood. Section 2.5 presents the details of the selection function that is required to mimic the Geneva–Copenhagen sample (GCS) of solar-neighbourhood stars published by Nordström et al. (2004) and Holmberg et al. (2007), and explains how this sample has been used to constrain the model's parameters. Section 2.6 explains how the observable properties of the model depend on its parameters. Section 2.7 discusses the relation of the present models to earlier ones, and discusses the extent to which it is consistent with the analysis of solar-neighbourhood data by Haywood (2008). Section 2.8 sums up.

2.3   Governing equations

The simulation is advanced by a series of discrete timesteps of duration $30\,$Myr.

The disc is divided into 80 annuli of width $0.25\,$kpc and central radii that range from $0.125\,$kpc to $19.875\,$kpc. In each annulus there is both "cold" ($\sim 30\,$K) and "warm" ($\gtrsim 10^4\,$K) gas with specified abundances (Y, Z) of helium and heavy elements. The "warm gas" is not available for star formation and should be understood to include both inter-cloud gas within the plane and extraplanar gas, which probably contains a significant fraction of the Galaxy's ISM. Indeed, in NGC 891, a galaxy similar to the Milky Way, of order a third of HI is extraplanar (Oosterloo et al., 2007). In the Milky Way this gas would constitute the "intermediate-velocity clouds" that are observed at high and intermediate Galactic latitudes (Kalberla & Dedes, 2008).

Within the heavy elements we keep track of the abundances of O, C, Mg, Si, Ca and Fe. Each annulus has a stellar population for each elapsed timestep, and this population inherits the abun-

dances Y, Z, etc., of the local cold gas. At each stellar mass, the stellar lifetime is determined by the initial abundances, and at each age we know the luminosity and colours of such of its stars that are not yet dead. Each stellar population is at all times associated with the annulus of its birth; the migration of stars is taken into account as described below only when returning matter to the ISM or constructing an observational sample of stars.

2.3.1   Metallicity scale

The whole field of chemical modelling has been thrown into turmoil by the discovery that three-dimensional, non-equilibrium models of the solar atmosphere require the metal abundance of the Sun to be $Z_\odot = 0.012 - 0.014$ (Grevesse et al., 2007) rather than the traditional value ~ 0.019. This work suggests that the entire metallicity scale needs to be thoroughly reviewed: if the Sun's metallicity has to be revised downwards, then so will the metallicities of most nearby stars. Crucially there is the possibility that values for the metallicity of the ISM require revision: some values derive from measurements of the metallicities of short-lived stars such as B stars and require downward revision (e.g. Daflon & Cunha, 2004), while others are inferred from measurements of the strengths of interstellar emission lines, and are not evidently affected by changes in stellar metallicities. If the metallicity scale of stars were lowered while that of the ISM remained substantially unaltered, it would be exceedingly hard to construct a viable model of the chemical evolution of the solar neighbourhood. Moreover, both the stellar catalogue and most of the measurements of interstellar abundances with which we wish to compare our models are on the old metallicity scale, and unphysical anomalies will become rife as soon as one mixes values on the old scale with ones on the new. Therefore for consistency we use the old solar abundance $Z_\odot = 0.019$ and exclude from considerable metallicity values that are on the new scale.

2.3.2   Star-formation law

Stars form according to the Kennicutt (1998) law. Specifically, with the surface density of cold gas Σ_g measured in $M_\odot \, pc^{-2}$ and t in Myr, star formation increases the stellar surface density at a rate

$$\frac{d\Sigma_*}{dt} = 1.2 \times 10^{-4} \begin{cases} \Sigma_g^{1.4} & \text{for } \Sigma_g > \Sigma_{crit} \\ C\Sigma_g^4 & \text{otherwise} \end{cases}, \tag{2.1}$$

where the threshold for star formation, Σ_{crit} is a parameter of the model and $C = \Sigma_{crit}^{-2.6}$ ensures that the star-formation rate is a continuous function of surface density. The normalisation in equation (2.1) was chosen to yield the observed surface densities of gas and stars near the Sun. The stars are assumed to be distributed in initial mass over the range $(0.1, 100)\, M_\odot$ according to the Salpeter function, $dN/dM \propto M^{-2.35}$. The luminosities, effective temperatures, colours and lifetimes of these stars are taken by linear interpolation in (Y, Z) from the values given in the BASTI database (Cassisi et al., 2006).

2.3.3 Return of metals

The nucleosynthetic yields of individual metals are in many cases still subject to significant uncertainties (e.g. Thomas et al., 1998); in fact models of the chemical evolution of the solar neighbourhood have been used to constrain these yields (Francois et al., 2004).

For initial masses in the ranges $5 - 11 \, M_\odot$ and $35 - 100 \, M_\odot$ values of X, Y, Z, C and O were taken from Maeder (1992) using a non-linear interpolation scheme: the paper gives yields Y_{LZ} for a low metallicity ($Z = 10^{-4}$) and yields Y_{HZ} for a high metallicity ($Z = 0.02$). Guided by the metallicity-dependence of the sizes of CO cores reported by Portinari et al. (1998) we take

$$Y(Z) = (1 - \alpha)Y_{LZ} + \alpha Y_{HZ}, \tag{2.2}$$

where

$$\alpha = \begin{cases} 0 & \text{for } Z < 0.005 \\ 320(Z - 0.005) & \text{for } 0.005 < Z < 0.0075 \\ 0.8 + 16(Z - 0.0075) & \text{for } 0.0075 < Z < 0.02 \\ 1 & \text{for } Z > 0.02 \end{cases}. \tag{2.3}$$

The yields of elements other than X, Y, Z, C and O from stars with masses in this range were taken from the *ORFEO* database of Limongi & Chieffi (2008) with the mass cut set such that $0.05 \, M_\odot$ of ^{56}Ni is produced; this relatively low mass cut reproduces the Ca/Fe ratio measured in very metal-poor stars by Lai et al. (2008). Stars less massive than $10 \, M_\odot$ were assumed to produce no elements heavier than O. For stars with masses $< 5 \, M_\odot$, the yields were taken by linear interpolation from Marigo (2001).

For initial stellar masses in the range $11 - 35 \, M_\odot$ we used the metallicity-dependent yields of heavy elements from Chieffi & Limongi (2004) by linear interpolation on mass and metallicity, extrapolating up to $\alpha = 1.5$ or $Z = 0.03$ respectively. Chieffi & Limongi (2004) used a relatively high mass cut, which produced $0.1 \, M_\odot$ of ^{56}Ni. With our interpolation the average amount of ^{56}Ni produced is well within the expected range.

A fraction f_{eject} of the gas ejected by dying stars leaves the Galaxy; we tested models with $0 \leq f_{\text{eject}} \leq 0.05$ (Pagel, 1997). Increasing f_{eject} has the effect of reducing the final metallicity of the disc; in fact there is almost complete degeneracy between the values of f_{eject} and nucleosynthetic yields. In view of the evidence that star formation near the Galactic centre drives a Galactic wind (Bland-Hawthorn & Cohen, 2003), we set $f_{\text{eject}} = 0.15$ at $R < 3.5 \, \text{kpc}$ in models that use the accretion law (2.6) below. At all other radii we set $f_{\text{eject}} = 0.04$.

A fraction f_{direct} of the ejecta goes straight to the cold gas reservoir of the local annulus, and the balance goes to the annulus's warm-gas reservoir. Setting f_{direct} to values ~ 0.2 has a significant impact on the number of extremely metal-poor stars predicted near the Sun. However, such large values of f_{direct} are not well motivated physically, and in the models presented here $f_{\text{direct}} = 0.01$ has a negligible value.

In each timestep δt a fraction $\delta t / t_{\text{cool}}$ of the "warm" gas (which includes extraplanar gas) transfers to the cold-gas reservoir from which stars form. The parameter t_{cool} is determined by the

dynamics of extraplanar gas and the balance between radiative cooling and shock heating within the plane. Consequently, its value cannot be determined a priori from atomic physics. Increasing $t_{\rm cool}$ increases the mass of "warm" gas and delays the incorporation of freshly made metals into new stars, so the number of very metal-poor stars formed increases with $t_{\rm cool}$. Although of order a quarter of the neutral hydrogen of NGC 891 is extraplanar (Oosterloo et al., 2007), some of this gas will be formerly cold interstellar gas that has been shock accelerated by stellar ejecta. We do not model shock heating of cold gas, and replenish the warm-gas reservoir exclusively with stellar ejecta (from stars of every mass). Hence the warm-gas reservoir should be less massive than the sum of the extraplanar and warm in-plane bodies of gas in a galaxy like NGC 891. We have worked with values $t_{\rm cool} \gtrsim 1\,{\rm Gyr}$ that yield warm-gas fractions of order 10 percent. The results of the models are not sensitive to the value of $t_{\rm cool}$.

There is abundant evidence that pristine intergalactic gas disappeared from the intergalactic medium (IGM) long ago: quasar absorption-line studies reveal an early build up of heavy elements in the IGM (Pettini et al., 2003). While it is clear that the disc formed from material that had been enriched by pregalactic and halo stars, it is unclear what abundances this material had. We take the chemical composition of the pre-enriched gas to be that of the "warm" ISM after two timesteps, starting with $5 \times 10^8\,{\rm M}_\odot$ of pristine gas. In each of the following four timesteps, a further $1.25 \times 10^8\,{\rm M}_\odot$ of gas with this metallicity is added to the disc. The surface density of the added gas is proportional to

$$(1.0 - {\rm e}^{(R-19.8\,{\rm kpc})/11.8\,{\rm kpc}}){\rm e}^{-R/4\,{\rm kpc}}. \tag{2.4}$$

Thus the surface density is exponential with scalelength $4\,{\rm kpc}$ inside $\sim R_0$ but tapered to zero at the outer edge of the grid. The existence at the outset of a warm, pre-enriched component of the ISM is physically well motivated and proves the most effective way of producing the right number of metal-poor stars.

Type Ia supernovae are included by assuming that 7.5 per cent of the mass in white dwarfs formed by stars of initial mass 3.2 to 8.5 $\rm M_\odot$ ultimately explodes in type Ia supernovae. The yields were taken to be those of the W70 model in Iwamoto et al. (1999). It is believed that the progenitors of type Ia supernovae have lifetimes of order a Gyr (Förster et al., 2006) and we have taken the mass $M_{\rm WD}$ of the population that survives to time t from white-dwarf formation to satisfy

$$\frac{{\rm d}M_{\rm WD}}{{\rm d}t} = \begin{cases} 0 & \text{for } 0 < t \le 0.15\,{\rm Gyr} \\ -M_{\rm WD}/1.5\,{\rm Gyr} & \text{for } T > 0.15\,{\rm Gyr} \end{cases}. \tag{2.5}$$

The rate of type Ia SNe is constrained by the requirements that (i) [O/Fe] has to fall from ~ 0.6 for the oldest stars to around -0.1, and (ii) [Ca/Fe] should go from about ~ 0.3 to ~ 0. The full curve in Fig. 2.1 shows for the best-fitting model the mass-return rate as a function of time, while the green dashed curve shows the SFR at the solar radius.
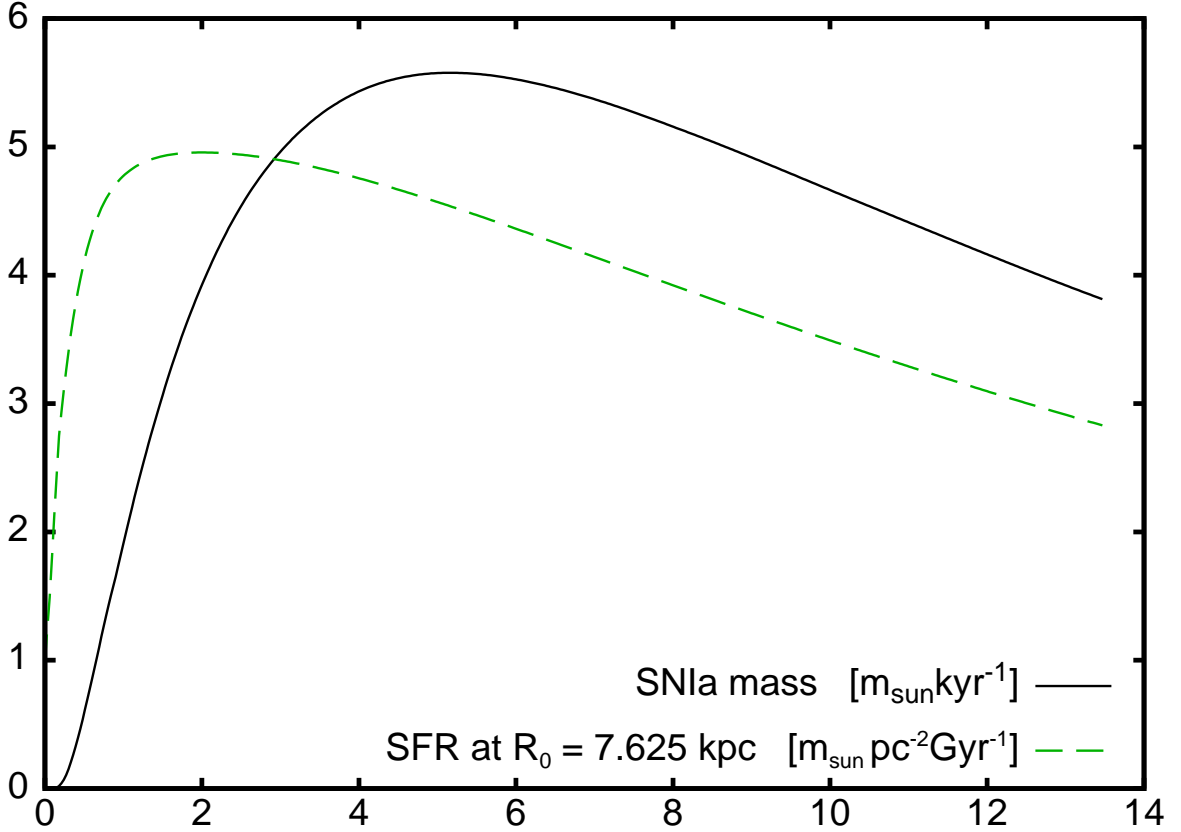
Figure 2.1: The rate of mass injection by SNIa in the standard model (solid black line) versus time. The broken green line gives the star formation rate in the solar annulus.

2.3.4 Inflow

It is generally agreed that viable models of galactic chemical evolution require the disc to be constantly fed with gas from intergalactic space; inflow resolves several serious problems, including (i) the appearance of too many low-metallicity stars near the Sun (the "G-dwarf problem", e.g. Pagel, 1997), (ii) excessive metallicity of the current ISM, (iii) an unrealistically low abundance of deuterium in the current ISM (Linsky et al., 2006). Moreover, both the short timescale for the current ISM to be consumed by star formation and direct manifestations of infalling gas (Sancisi et al., 2008) argue strongly for the existence of infall. Unfortunately, many aspects of infall are extremely uncertain. We find that the predictions of our models depend sensitively on how these uncertainties are resolved, so to the extent that other aspects of our models have sound foundations, they can usefully constrain the nature of infall.

In principle the rate and radial distribution of infall is determined by cosmology. For example, Naab & Ostriker (2006) infer it by assuming that the disc scale length grows in parallel with the cosmic scale, while Colavitti et al (2008) derive the global rate from N-body simulations. At this

stage we feel that cosmological simulations are beset by too many uncertainties to deliver even a secure global infall rate, never mind the radial distribution of infall. In particular the extent of angular-momentum exchange between baryons and dark matter is controversial, as are the extent to which gas is accreted from cold infall rather than a hot corona. Moreover, nothing is known with any confidence about the dynamics of the corona.

For want of clear inputs from cosmology we have sought a flexible parametrisation of infall. First we parametrise the global infall rate, and then the radial distribution of infall.

Infall rate

We have investigated two approaches to the determination of the infall rate. The first starts with a quantity of gas ($8 \times 10^9 \, M_\odot$) and feeds gas into it at a rate

$$\dot{M} = \frac{M_1}{b_1} e^{-t/b_1} + \frac{M_2}{b_2} e^{-t/b_2}. \tag{2.6}$$

Here $b_1 \simeq 0.3 \, \text{Gyr}$ is a short timescale that ensures that the star-formation rate peaks early on, while $b_2 \simeq 14 \, \text{Gyr}$ is a long timescale associated with sustained star formation in the thin disc. We adopt $M_1 \simeq 4.5 \times 10^9 \, M_\odot$ and choose M_2 such that after $12 \, \text{Gyr}$ the second exponential has delivered $2.6 \times 10^{10} \, M_\odot$.

In an alternative scheme, the gas mass within the disc is determined a priori and infall is assumed to be available to maintain the gas mass at its prescribed level. We have investigated schemes in which the gas mass declines exponentially with time, but focused on models in which it is held constant at $8.4 \times 10^9 \, M_\odot$; models in which the gas mass declines exponentially produce very similar results to models in which the infall rate declines exponentially.

Distribution of infall

We know even less about the radial distribution of the infalling gas than we do about the global infall rate. In fact our only constraint is that the stellar disc has an approximately exponential surface density now, and was probably exponential at earlier times too. Besides the star-formation law, the structure of the stellar disc depends on both the radial distribution of infall and gas flows within the disc, and a disc that is consistent with observations will not be formed if either the radial infall profile or the internal gas flow is fixed without regard to the other process. Consequently, the requirement that only observationally acceptable discs be produced requires one to develop a parametrisation that couples infall and flow in a possibly unphysical way. The scheme we have developed involves such an unphysical coupling – this is the price one pays for a scheme that allows one to explore as economically but fully as possible a range of infall profiles and internal flows that are consistent with the known radial structure of the disc.

We start from the assumption that the surface-density of gas is at all times exponential, $\Sigma_g(R) \propto e^{-R/R_d}$, where $R_d = 3.5 \, \text{kpc}$ is chosen such that with the star-formation law adopted above, the inner stellar disc acquires a scale length $R_* = R_d/1.4 = 2.5 \, \text{kpc}$ similar to that determined from

star counts (Robin et al., 2003; Juric et al., 2008). Our value for the scale length of the gas disc is in good agreement with the value measured by Kalberla & Dedes (2008): 3.75 kpc. Notice that we assume not only that the stellar disc is exponential, but that its scale length is unchanging. Hence we are assuming that the disc forms simultaneously at all radii, rather than "inside-out". The remarkably large age estimated for the solar neighbourhood (at $R = 3R_*$) suggests simultaneous formation (Aumer & Binney, 2009, and references therein). However, our work could be readily generalised to inside-out growth by making R_d a specified function of time (e.g. Naab & Ostriker, 2006), but we reserve this extension for a later paper.

Our scheme for parameterising infall and flow depends on two parameters, f_A and f_B and is easiest to explain by considering first the limiting cases in which one parameter vanishes.

Either of the algorithms of the last subsection specifies what the total gas mass should be at the start of a timestep: this is either the prescribed constant or, when equation (2.6) is used, it is the mass in the disc at the end of the previous timestep plus the amount that falls in during the most recent timestep. Hence the mass that should be in each annulus at the start of a timestep follows from the assumed exponential profile of the gas disc. Subtracting from this the mass that was present after the previous timestep, we calculate the need, i.e. the amount of gas that has to be added, of the ith annulus ΔM_i.

We fill annuli up with gas in sequence, starting with the innermost ring 0. When $f_B = 0$ ("Scheme A") this annulus receives $f_A \Delta M_0$ from the IGM, and grabs the balance, $(1 - f_A)\Delta M_0$, from annulus 1, where $f_A \simeq 0.2$ is a parameter of the model. Annulus 1 receives $f_A \Delta M_1$ from the IGM, and grabs the balance of its requirement, $(1 - f_A)(\Delta M_1 + \Delta M_0)$, from annulus 2. The updating of every annulus proceeds similarly, until the last annulus is reached, which covers its entire need from the IGM. The characteristic of this "Scheme A" is the development of a large flux of gas through the outer rings – an example is given by the full red curve in the upper panel of Fig. 2.2. This flux transports inwards metals synthesised in these rings and tends to deposit them at intermediate radii, where the inward flux is diminishing.

When $f_A = 0$ ("Scheme B") annulus 0 obtains $f_B \Delta M_0$ from the IGM and the rest from annulus 1. Annulus 1 now obtains $f_B[\Delta M_1 + (1 - f_B)\Delta M_0]$ from the IGM, and so on to the outermost ring, which is again entirely fed by the IGM. The short dashed blue curve in the upper panel of Fig. 2.2 shows a typical example of a mass flow through the disc with Scheme B. Whereas the flow generated by Scheme A (red curve) increases monotonically from the centre, the Scheme-B flow rises quickly with galactocentric distance R near the centre but then peaks at $R \simeq 5$ kpc. In the outer region in which the inflow is small, the metallicity forms a plateau. The extent of this plateau is controlled by f_B: the larger f_B, the smaller the radius at which the inflow rate peaks and the further in the metallicity plateau extends.

In either of these schemes a fixed fraction of each annulus's need is taken from the IGM, but the definition of "need" is different in the two schemes: in Scheme B it includes the gas that was taken from it by its inner neighbour, and in Scheme A it does not. In Scheme A only a fixed fraction of the local need is provided by the IGM, so the flow F_r in the disc continuously builds up through the disc. In Scheme B, by contrast, a part of the flow required in Scheme A is met by additional accretion. Consequently, if one wrote an equation for dF_r/dr, a term $-(f_B \Delta r)F_r$ would
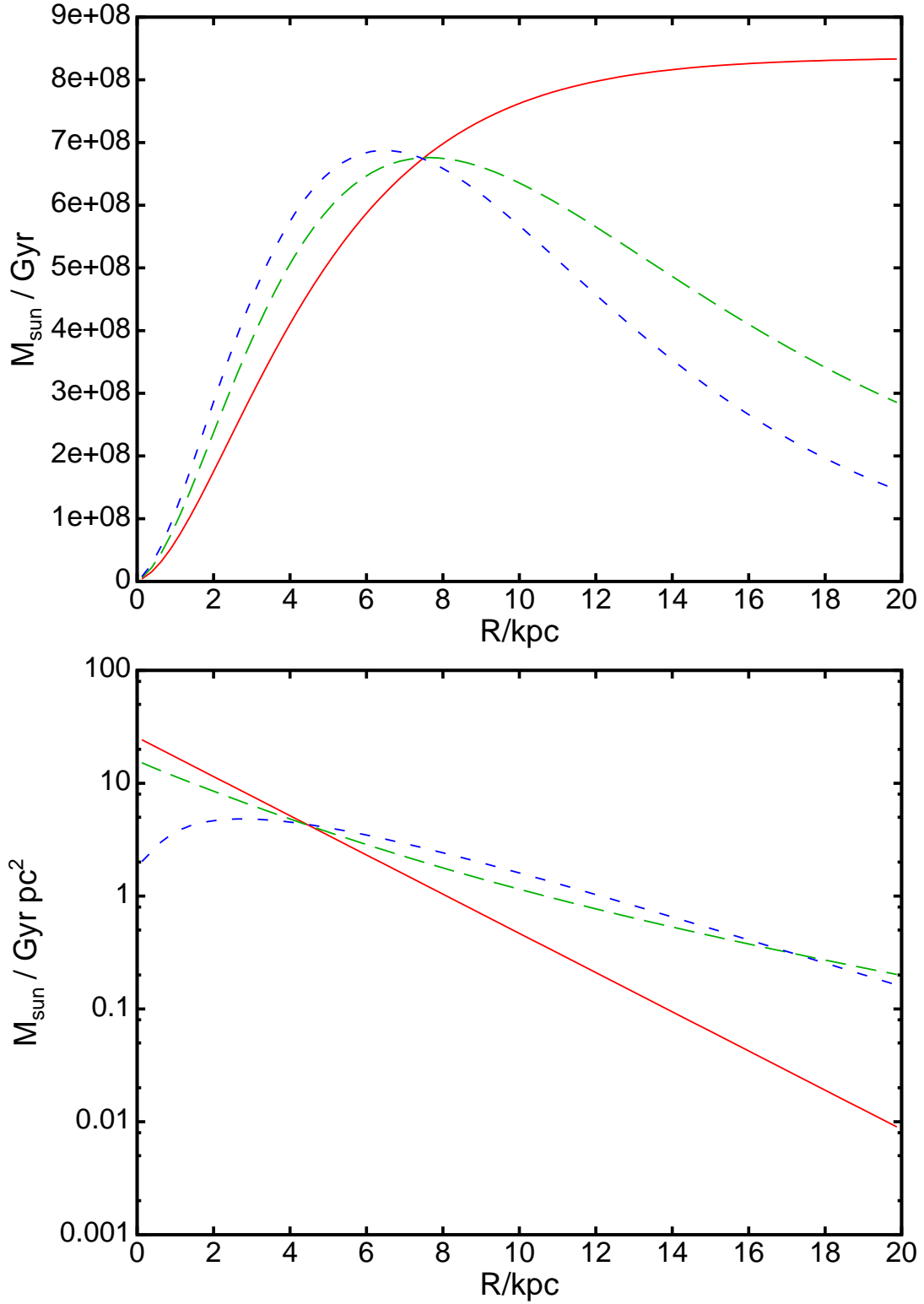
Figure 2.2: Upper panel: The rate of flow of gas over the circle of radius R induced by infall Scheme A with $f_A = 0.6$ (red curve), infall Scheme B with $f_B = 0.05$ (blue short dashed curve), and infall Scheme AB with $f_A = 0.35$ and $f_B = 0.025$ (green long dashed curve; the standard model). Lower panel: the corresponding rates of accretion from the IGM per unit area of the disc.

appear, where $\Delta r = 0.25\,\text{kpc}$ is the width of annuli, and this term drives exponential decay of F_r. Scheme A enhances the metallicity of the middle section of the disc and causes the metallicity gradient to be steepest towards the outside of the disc, Scheme B enhances the metallicity of the inner disc and flattens the gradient at large radii.

In Scheme A, if f_A is set too low, the flux of gas through the outer annuli becomes implausibly large in relation to the mass of gas that is in these annuli, and radial flow velocities $v_R \gtrsim 20\,\text{km}\,\text{s}^{-1}$ are predicted. In Scheme B f_B can be quite small because, although the flow of gas through the disc builds up more quickly at small radii, it peaks at a few kiloparsecs and then declines to small values in the outer disc. If either f_A or f_B is large, the flow through the disc becomes small and the metallicity of the solar neighbourhood becomes unrealistically large through the accumulation of metals created at the solar radius and beyond.

Satisfactory fits to the data can be obtained only when both f_A and f_B are non-zero In this "Scheme AB" annulus 0 receives a mass $(f_A + f_B)\Delta M_0$ from the IGM and grabs the balance $M_{01} = (1 - f_A - f_B)\Delta M_0$ from annulus 1. Annulus 1 receives a mass $f_A \Delta M_1 + f_B(\Delta M_1 + M_{01})$ from the IGM and grabs the balance of its requirement from annulus 2, and so on. Notice that the radial flow profile in Scheme AB is not simply the sum of the corresponding profiles for Schemes A and B used alone. The green curve in the upper panel of Fig. 2.2 shows the radial flow profile obtained with Scheme AB with the parameters of the standard model. In this model the radial velocity of disc gas currently rises roughly linearly from zero at the centre to $1.3\,\text{km}\,\text{s}^{-1}$ at the Sun. Beyond the Sun a plot of radial velocity versus radius gradually steepens to reach $5\,\text{km}\,\text{s}^{-1}$ at the edge of the disc.

For each accretion scheme, the lower panel of Fig. 2.2 shows the corresponding radial distribution of accretion from the IGM.

Metallicity of the IGM

We have to prescribe the metallicity and alpha-enhancement of gas taken from the IGM. It is far from clear how this should be done.

Quasar absorption line-studies reveal an early build up of heavy elements in the IGM (Pettini et al., 2003). Moreover, the handful of high-velocity clouds for which metallicities have been measured, have heavy-element abundances of order a tenth solar (van Woerden & Wakker, 2004). Finally, the metallicities of the most metal-poor thick-disc stars are similar to the metallicities of the most metal-rich halo stars, which suggests that the early disc was pre-enriched by pregalactic and halo stars. We assume that throughout the simulation accreted gas has metallicity $Z = 0.1 Z_\odot$. Given that the thick disc is alpha-enhanced (Venn et al., 2004), it is clear that when disc formation starts, infalling gas must be alpha-enhanced. It is natural that this enhancement should decline with time as Fe from type Ia SNe finds its way into the IGM. Indeed, in addition to gas that flows out in the Galactic wind (Bland-Hawthorn & Cohen, 2003), type Ia SNe in dwarf spheroidal galaxies will have contributed their Fe to the local IGM, and if the Magellanic Stream is made of gas torn from the SMC, it will have been enriched with Fe from SNe in the SMC. Thus we expect the metallicity and alpha enhancement of the IGM to be time dependent and governed by

the chemical-evolution histories of galaxies.

These considerations suggest making the α-enhancement of the IGM reflect that of an outer annulus of the Galaxy; the chemical evolution of this ring acts as a proxy for the combined chemical evolution of the many contributors to the chemical evolution of the IGM. If the IGM were assumed to mirror the outermost ring, its α-enhancement would remain extremely low because this annulus takes all its gas from the IGM, and passes what few heavy elements it synthesises inwards. Hence the IGM must mirror an outer annulus but not the outermost. In our models the α-enhancement of the IGM mirrors the annulus with radius $R = 12.125$ kpc. Since yields of α elements decline with increasing metallicity, the outer disc should be α-enhanced.

2.3.5   Churning

Transient spiral arms cause both stars and gas to be exchanged between annuli in the vicinity of the corotation resonance. Such exchanges automatically conserve both angular momentum and mass. Since these exchanges are driven by spiral structure, in which hot and extraplanar gas is not expected to participate, churning is confined to stars and cold gas. We restrict exchanges to adjacent rings but allow two exchanges per timestep, so within a timestep second-nearest neighbouring rings exchange mass.

Further studies of spiral structure in high-quality N-body simulations are required to determine how the probability of a star migrating varies across the disc. In the absence of such studies the following dimensional argument suggests what the answer might be. Consider the probability P_{ex} that in a characteristic dynamical time κ^{-1} (where κ is the local epicycle frequency) a star is involved in a resonant exchange across corotation. It is natural that a process dependent on gravitational self-energy in the disc should scale with the square of the surface density. Toomre's $Q = \sigma\kappa/\pi G\Sigma$, where σ is the radial velocity dispersion, is a dimensionless variable, so we conjecture that $P_{\text{ex}} \propto 1/Q^2$. Our grid is uniform in R whereas an exchange across corotation changes R by of order the most unstable wavelength $\lambda_{\text{crit}} = \sigma Q/\kappa$. The number of swaps between rings required to wander a distance λ_{crit} scales as λ_{crit}^2. Moreover, the number of ring-swaps in time κ^{-1} scales as κ^{-1}, so the ring-swap probability per timestep P_{ring} should be $\lambda_{\text{crit}}^2\kappa$ times P_{ex}. This argument yields $P_{\text{ring}} \propto \sigma^2/\kappa$. In realistic cases $\sigma^2 \propto \Sigma$ and $\kappa \propto R$, so $P_{\text{ring}} \propto \Sigma R \propto M$, the mass of a ring. This argument suggests that we take the probability p_{ij} that in a given half-timestep a star or gas cloud in the ith annulus is transferred to the jth annulus to be

$$p_{ij} = \begin{cases} k_{\text{ch}} M_j/M_{\text{max}} & \text{for } j = i \pm 1 \\ 0 & \text{otherwise} \end{cases}, \tag{2.7}$$

where M_j is the mass in cold gas and stars in the jth annulus and $M_{\text{max}} = \max_j(M_j)$. This rule ensures that the mass transferring outwards from the ith annulus is proportional to $M_i M_{i+1}$, and an equal mass transfers inwards, ensuring that angular momentum is conserved. The constant k_{ch} is the largest transition probability for any annulus in a given timestep. It is treated as a free parameter to be fitted to the data.
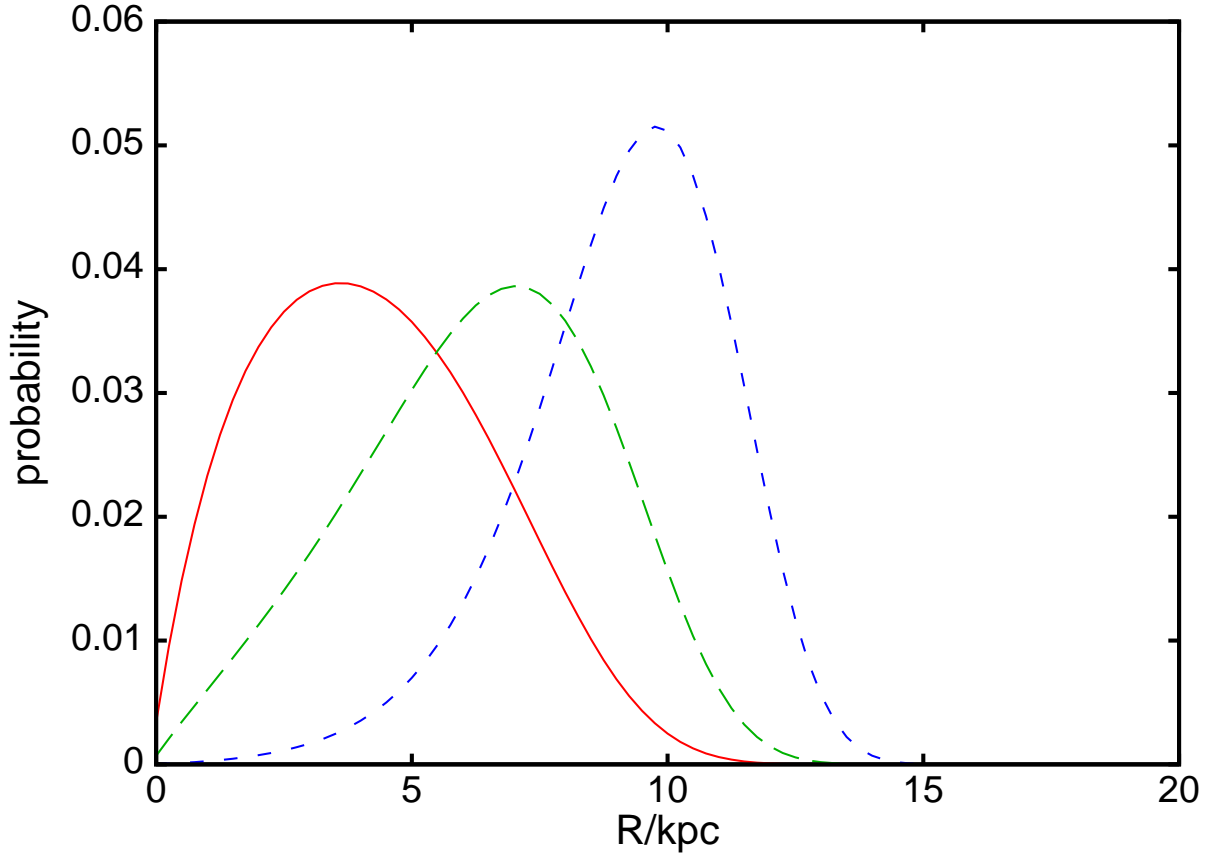
Figure 2.3: The radial distribution of the guiding centres of 12 Gyr-old stars that were born at 5 (red), 7.6 (green, long dashed) and 10 kpc (blue, short dashed) when the churning fraction $k_{ch} = 0.25$.

The procedure for distributing the metals released by a population of stars born in annulus i is as follows. The probability that a star born in annulus i at timestep m is found to be in annulus j at timestep n is equal to the ijth element of the product matrix $\mathbf{p}_m \mathbf{p}_{m+1} \times \cdots \mathbf{p}_n$. In practice we recompute $\mathbf{p}$ only each five timesteps and approximate $\mathbf{p}_m \times \cdots \mathbf{p}_{m+4}$ by $\mathbf{p}_m^5$. Fig. 2.3 shows the extent to which the guiding centres of stars are changed over the lifetime of the Galaxy when $k_{ch} = 0.25$.

2.3.6 Blurring

In addition to changing their guiding-centre radii through the churning process, stars oscillate around their guiding centres with steadily increasing amplitudes. Consequently, stars spend time away from their guiding-centre radii. For simplicity, we assume in this section that the circular speed v_c is independent of radius and that the vertical motion can be ignored because it decouples from motion in the plane.

The fraction of its time that the orbit with energy and angular momentum E, L spends in a radial interval $(R, R + dR)$ is

$$dp = \frac{dt}{T} = \frac{1}{T}\frac{dR}{v_R} = \frac{\Omega_R}{\pi}\frac{dR}{\sqrt{2(E - \Phi_{eff})}}, \tag{2.8}$$

where $T \equiv \pi/\Omega_R$ is the half period and $\Phi_{eff}(R, L) \equiv \Phi(R) + L^2/2R^2$ is the effective potential. We need to average this over all stars with given L. These stars have some distribution over the energy $E = \frac{1}{2}v_R^2 + \Phi_{eff}$. It is expedient to decompose E into the energy $\Phi_c(L) \equiv \Phi(R_c) + L^2/2R_c^2$ of the circular orbit (with radius R_c) of angular momentum L and the random energy $\mathscr{E} \equiv E - \Phi_c$. Following Shu (1969) we take the distribution function (DF) to be

$$f(\mathscr{E}, L) = \frac{F(L)}{\sigma^2}e^{-\mathscr{E}/\sigma^2}, \tag{2.9}$$

where $F(L)$ is a function to be determined. The DF (2.9) ensures that the radial velocity dispersion is approximately (but not exactly) σ. Normalizing f such that $\int dL\,dJ_R\,f = 1$, where $J_R(\mathscr{E})$ is the radial action, the probability that a randomly chosen star lies in $(R, R + dR)$ is $\int dL\,dJ_R\,f\,dp$. Recalling that $dL\,dJ_R = dL\,d\mathscr{E}/\Omega_R$ and substituting for f and dp, we find that the number of stars in the annulus is

$$\begin{aligned}
dn(R) &= \int dL\,dJ_R\,(f\,dp) \\
&= \frac{N dR}{\pi}\int dL\,\frac{F}{\sigma^2}\int_{\Phi_{eff} - \Phi_c}^{\infty} d\mathscr{E}\,\frac{e^{-\mathscr{E}/\sigma^2}}{\sqrt{2(\mathscr{E} + \Phi_c - \Phi_{eff})}} \\
&= \frac{N dR}{\sqrt{2}\pi}\int dL\,\frac{F}{\sigma^2}e^{[\Phi_c - \Phi_{eff}]/\sigma^2}\int_0^{\infty} dx\,\frac{e^{-x/\sigma^2}}{\sqrt{x}},
\end{aligned} \tag{2.10}$$

where N is the total number of stars in the system. The integral over x is simply $\sigma\int dt\,e^{-t}/\sqrt{t} = \sqrt{\pi}\sigma$. Thus we can conclude that the probability per unit area associated with a star of given L is

$$P(R) = \frac{dn}{N2\pi R dR} = \frac{K}{\sigma R}\exp\left[\frac{\Phi_c(L) - \Phi_{eff}(R, L)}{\sigma^2}\right], \tag{2.11}$$

where K is chosen such that $1 = 2\pi\int dR\,R P(R)$.

The parameter σ used in these formulae is actually smaller than the rms radial velocity dispersion, which is given by

$$\langle v_R^2\rangle = \frac{\sqrt{2\pi}}{R\Sigma}\int dL\,F\sigma\exp[(\Phi_c - \Phi_{eff})/\sigma^2], \tag{2.12}$$

where the stellar surface density is

$$\Sigma(R) = \frac{\sqrt{2\pi}}{R}\int dL\,\frac{F}{\sigma}\exp[(\Phi_c - \Phi_{eff})/\sigma^2]. \tag{2.13}$$

For specified radial dependencies of Σ and $\langle v_R^2 \rangle$, equations (2.12) and (2.13) can be used to determine the functions $F(L)$ and $\sigma(L)$ (Dehnen, 1999a). However, in the present application it is not $\Sigma(R)$ that we wish to specify, but the number of stars with guiding centres in each ring:

$$\frac{dN}{dR_c} = v_c N_{tot} \frac{dN}{dL} = v_c \int dJ_R\, f(L, J_R)$$
$$= \frac{v_c F N_{tot}}{\sigma^2} \int \frac{d\mathscr{E}}{\Omega_R}\, e^{-\mathscr{E}/\sigma^2}, \tag{2.14}$$

where N_{tot} is the total number of stars in the disc. We adapt the technique described by Dehnen (1999a) for determining $F(L)$ and $\sigma(L)$ from equations (2.12) and (2.13) to the determination of these quantities from equations (2.12) and (2.14). Specifically, we start from the values of $F(L)$ and $\sigma(L)$ that would hold in the epicycle approximation, when $\Omega_R = \kappa$ independent of $\mathscr{E}$ and

$$F(L) = \frac{\kappa}{v_c N_{tot}} \frac{dN}{dR_c}. \tag{2.15}$$

Then at each L we evaluate $\langle v_R^2 \rangle$ from (2.12) and multiply σ by the ratio of the desired value to the value just calculated. Then we re-evaluate F from (2.14) and repeat until convergence is obtained.

We now address the question of how $\langle v_R^2 \rangle$ should depend on radius. The scale heights h of galactic discs are found to be largely independent of radius (van der Kruit & Searle, 1982), and for $h \ll R$ (when the vertical dynamics can be considered one-dimensional) this finding implies that the vertical velocity dispersion scales with the surface density as $\Sigma^{1/2}$. If the ratio of the vertical and radial velocity dispersions $\sigma_z / \langle v_R^2 \rangle^{1/2}$ is independent of radius, as is often assumed (e.g. Kregel & van der Kruit, 2005), then $\langle v_R^2 \rangle \propto \Sigma \propto e^{-R/R_*}$. In the solar neighbourhood at $R \simeq 3R_*$ the oldest stars have $\sigma_R \gtrsim 40\,\mathrm{km\,s^{-1}}$, so this line of reasoning predicts that $\langle v_R^2 \rangle^{1/2} \gtrsim 180\,\mathrm{km\,s^{-1}}$ in the central regions, which is implausibly large.

Evidently these naive arguments based on complete decoupling of planar and vertical motions are inadequate for the old disc; we need a distribution function that treats the third integral properly. Pending the availability of such a DF we have adopted the assumption that $\langle v_R^2 \rangle \propto e^{-R/1.5R_*}$, which implies that at R_* the old disc has $\langle v_R^2 \rangle^{1/2} \simeq 85\,\mathrm{km\,s^{-1}}$, which is only slightly lower than the velocity dispersion in the Galactic bulge (Rich et al., 2007).

From Binney et al. (2000) we take the time dependence of $\sqrt{\langle v_R^2 \rangle}(R_0)$ at solar galactocentric distance R_0 to be

$$\sqrt{\langle v_R^2 \rangle}(R_0, t) = \max\left\{ 10, 38 \left(\frac{t + 0.038\,\mathrm{Gyr}}{10.038\,\mathrm{Gyr}} \right)^{0.33} \right\}\,\mathrm{km\,s^{-1}}, \tag{2.16}$$

which is consistent with the data of Holmberg et al. (2007).

Fig. 2.4 shows blurring distributions $P(R)$ from equation (2.11) for three radii (5, 7.6 and 10 kpc) and two values of $\langle v_R^2 \rangle^{1/2}$ at the Sun, namely $25\,\mathrm{km\,s^{-1}}$ and $40\,\mathrm{km\,s^{-1}}$.
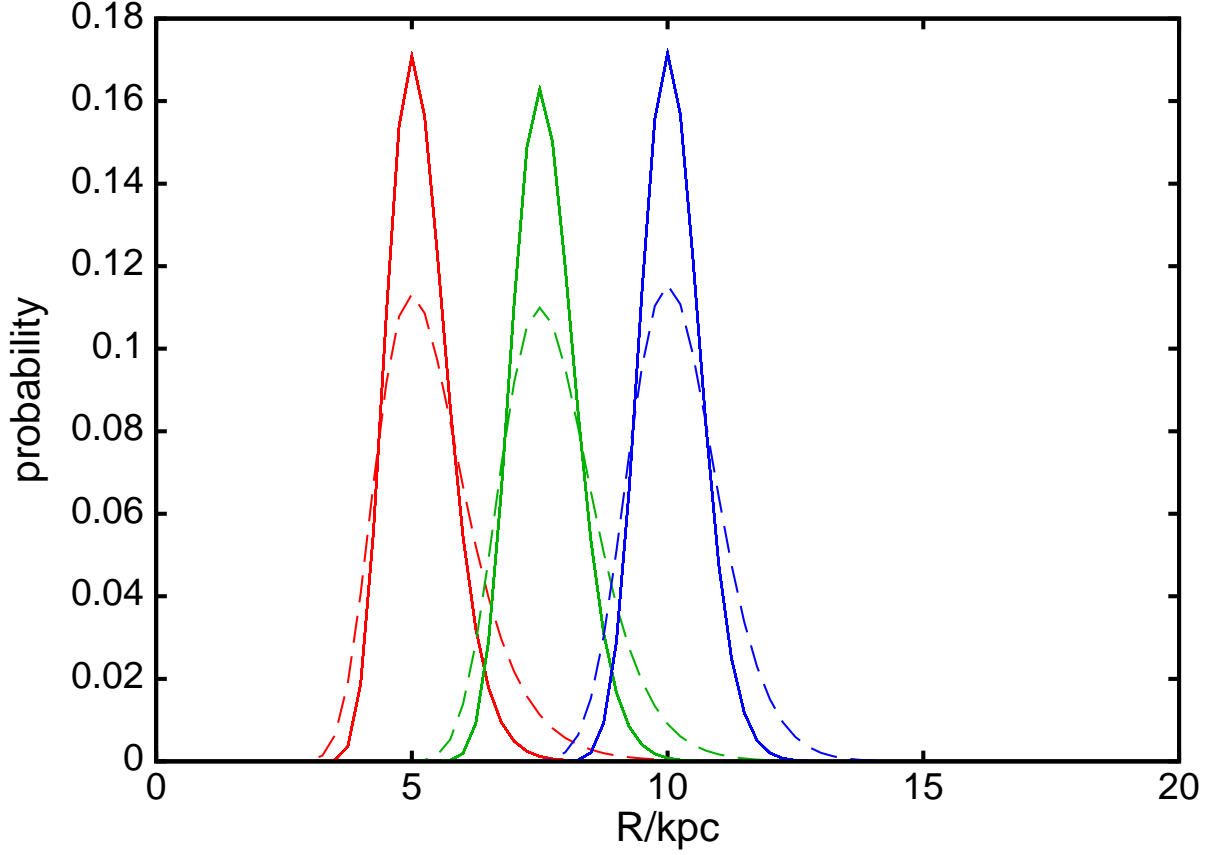
Figure 2.4: The radial distributions of stars with guiding centres at 5 (red), 7.6 (green) and 10 kpc (blue) when at the Sun $\langle v_R^2 \rangle^{1/2} = 25 \, \mathrm{km \, s^{-1}}$ (full curves) and $40 \, \mathrm{km \, s^{-1}}$ (dashed curves).

Note that scatterings by spiral arms and molecular clouds that heat the disc, also change the angular momentum of each star and therefore its guiding centre. Hence such scatterings contribute to both churning and blurring.

Since churning moves the guiding centres of the stars themselves we first apply the churning matrix and apply the blurring matrix afterwards.

2.3.7 Vertical structure

For comparison with observations of the solar neighbourhood we need to know the vertical distribution of stars near the Sun. We determine this by adopting a relationship between time and vertical velocity dispersion (Binney et al. , 2000)

$$\sigma_z(\tau) = \max \left\{ 4, 25 \left(\frac{\tau}{10 \, \mathrm{Gyr}} \right)^{0.33} \right\} \mathrm{km \, s^{-1}}. \tag{2.17}$$

Further assuming that stars of a given age form an isothermal population, their vertical density profile is

$$n(z) \propto e^{-\Phi(z)/\sigma_z^2}, \tag{2.18}$$

where $\Phi(z)$ is the difference in the gravitational potential between height z and the plane. This potential is calculated for a model similar to those presented by Dehnen & Binney (1998b) but with the thin and thick disc scaleheights taken to be 0.3 and 0.9 kpc, the total stellar surface density set to $35.5 \, M_\odot \, pc^{-2}$ with $3/4$ of the stellar mass in the thin disc, and the gas surface density set to $13.2 \, M_\odot \, pc^{-2}$ in conformity with Flynn et al. (2006) and Juric et al. (2008). The disc scalelength is taken to be $R_d = 2.5 \, kpc$ (Robin et al., 2003) and the dark halo density is set such that $v_c(R_0) = 220 \, km \, s^{-1}$.

2.4 The standard model

We now describe the properties of our standard model as a preliminary to explaining how these properties depend on the input assumptions and the values of the various parameters. In the standard model the accretion rate is given by equation (2.6); the values of the parameters for this model are given in Table 2.1.

The red dashed curve in Fig. 2.5 shows the current metallicity Z of the ISM as a function of radius. There is quite a steep outward decline in metallicity, the gradient in the vicinity of the Sun being of order $-0.11 \, dex \, kpc^{-1}$. The solid red curve shows that [O/H] falls less steeply with R than does [Z/H], having a gradient near the Sun $\sim -0.083 \, dex \, kpc^{-1}$. The shallower gradient in oxygen reflects our use of metallicity-dependent yields. Although shallower gradients are generally cited (e.g Rolleston et al., 2000) the data points in the figure are consistent with the model. The data derive from Shaver et al. (1983) who assumed $R_0 = 10 \, kpc$ and from Vilchez & Esteban (1996) and Rolleston et al. (2000), who assumed $R_0 = 8.5 \, kpc$. To plot these data on a consistent scale with $R_0 = 7.5 \, kpc$ we have when possible recalculated the Galactocentric distances from the heliocentric distances, taking the latter from Kharchenko et al. (2005) or Loktin & Beshenov (2003) when possible. For some of the points in Vilchez & Esteban (1996) and Rolleston et al. (2000) heliocentric distances were not available, so we simply reduced the cited Galactocentric distance by 1 kpc. The green line in Fig. 2.5 is the linear least-squares fit to the data; its slope is $-0.082 \, dex \, kpc^{-1}$. Our gradient in [O/H] lies within the range of frequently occurring values in Table 4 of Vila-Costas & Edmunds (1992), who assembled data for 30 disc galaxies.

The upper panel in Fig. 2.6 shows the evolution of Z for the cold ISM in a number of annuli – the solar annulus is coloured red. The smaller the radius of an annulus, the higher its curve lies in this plot because chemical evolution proceeds fastest and furthest at small radii. At small radii the metallicity of the cold ISM continues to increase throughout the life of the Galaxy, whereas at $R \gtrsim R_0 \, kpc$, Z peaks at a time that moves earlier and earlier as one moves out, and declines

Parameter	Meaning	Impact	Value
Σ_{crit}	Kennicutt's threshold surface density	limited impact	0
M_0	initial gas mass	affects only $N(Z)$ at [Z/H] < -0.7; from Hess diagram	$3.0 \times 10^9\,\mathrm{M}_\odot$
M_1	early infall mass	affects only $N(Z)$ at [Z/H] < -0.7; from Hess diagram	$4.5 \times 10^9\,\mathrm{M}_\odot$
M_2	long timescale infall mass to 12 Gyr	fixed by present mass	$2.9 \times 10^{10}\,\mathrm{M}_\odot$
b_1	early infall timescale	affects only $N(Z)$ at [Z/H] < -0.7; from Hess diagram	$0.3\,\mathrm{Gyr}$
b_2	long infall timescale	limited impact; estimated from Hess diagram and other work	$14\,\mathrm{Gyr}$
f_{A}	Scheme A fraction of gas from IGM	free parameter	0.36
f_{B}	Scheme B fraction of gas from IGM	free parameter fixed by local gradient	0.025
k_{ch}	churning amplitude	free parameter	0.35
t_0	delay before first type Ia SNe	taken from literature	$0.15\,\mathrm{Gyr}$
k^{-1}	timescale for decay of type Ia SNe	taken from literature	$1.5\,\mathrm{Gyr}$
f_{eject}	fraction of ejecta lost to Galaxy	small impact; mainly affects metallicity scale	$0.15 - 0.04$
f_{direct}	fraction of ejecta to cold ISM	small impact limited to [Z/H] < -0.7	0.01
t_{cool}	cooling time of warm gas	fixed by present mass of warm gas	$1.2\,\mathrm{Gyr}$
M_{warm}	initial warm gas mass	impact limited to $N(Z)$ at [Z/H] < -0.7	$5 \times 10^8\,\mathrm{M}_\odot$
Z_{IGM}	metallicity of the IGM	limited to $R > 12\,\mathrm{kpc}$; taken from literature	$0.1 Z_\odot$

Table 2.1: Parameters of the standard model. The infall rate is given by equation (2.6). The larger value of f_{eject} applies at $R < 3.5\,\mathrm{kpc}$.
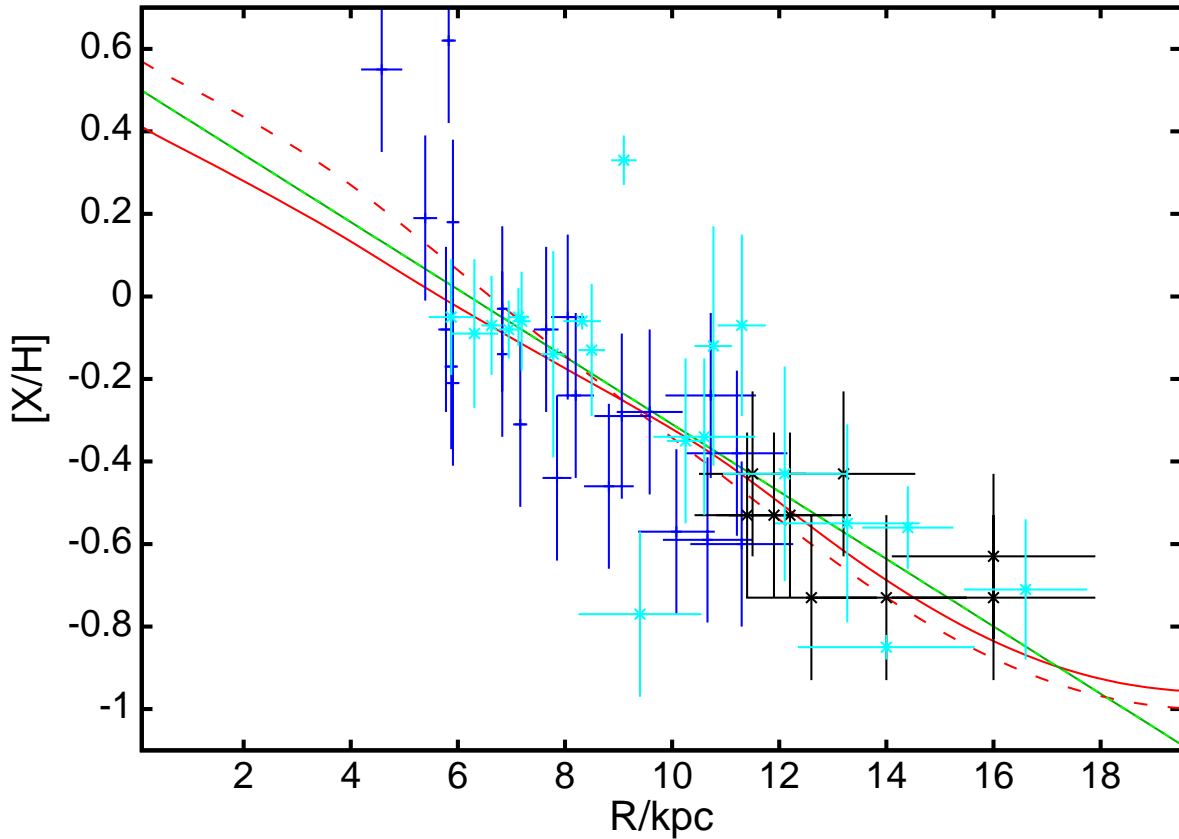
Figure 2.5: The metallicities of the current ISM in the standard model, [Z/H] (red dashed curve) and [O/H] (red full curve), as functions of Galactocentric radius. Also measurements of the metallicities of HII regions by Shaver et al. (1983) (dark blue), Vilchez & Esteban (1996) (black crosses) and Rolleston et al. (2000) (light blue crosses). The green line shows the linear least-squares fit to the measurements: it has a slope of $-0.082\,\mathrm{dex}\,\mathrm{kpc}^{-1}$. The data points have been updated and rescaled to $R_0 = 7.5\,\mathrm{kpc}$ as described in the text. Where necessary points have been shifted vertically by -8.93 to put them on the solar scale.

briefly before flattening out. This phenomenon reflects a combination of dilution by infalling metal-poor gas and the inward advection of metals by the flow through the disc.

The lower panel in Fig. 2.6 shows the corresponding present-day metallicity distribution of solar-neighbourhood stars. Although this is the distribution of stars currently in the solar annulus, it is clearly made up of a series of curves, one for each annulus in the model. The curves for interior annuli go from green to yellow as one goes forward in time, reflecting the fact that relatively recently formed stars are much less likely to have moved a large radial distance than older stars. Similarly, in the bottom part of the figure the colours go from blue to green to yellow as one moves towards the time axis, because then one is moving over curves for larger and larger radii, where both the star-formation rate and the probability of scattering in to the solar radius are
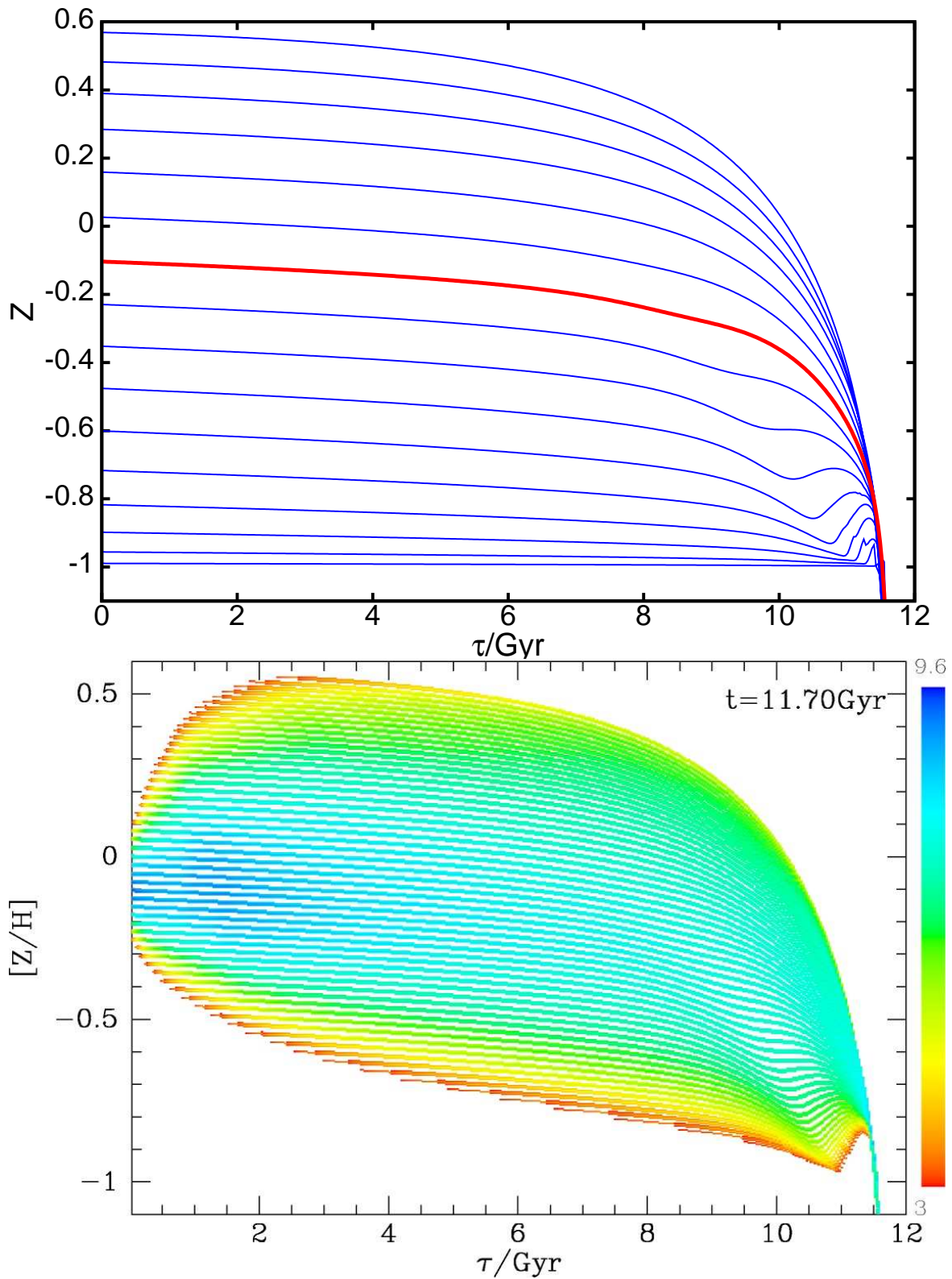
Figure 2.6: Upper panel: the metallicity of the cold ISM in each annulus as a function of lookback time showing each fifth ring. The curve for the solar annulus is red. Lower panel: the present density of solar-neighbourhood stars in the age-metallicity diagram. The colours encode the logarithm of the density of stars.
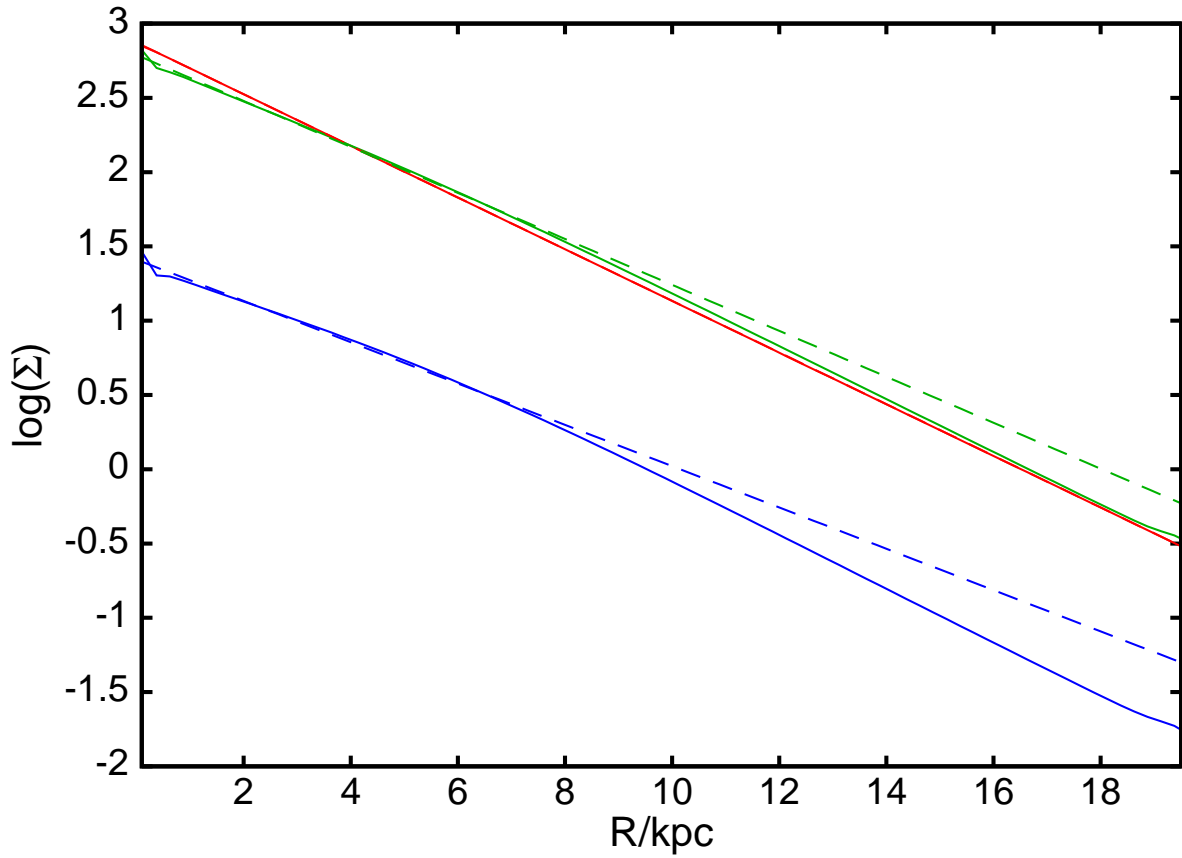
Figure 2.7: Full green curve: the surface density of the stellar disc at 11.7 Gyr. Broken green line: exponential fit to the inner part of this curve. Red curve: the surface density if stars remained where they were born. Blue curve: surface density contributed by stars born in the first 0.8 Gyr. Broken blue line: linear fit to this curve.

low. Hence, regardless of stellar age, most solar-neighbourhood stars have Z in a comparatively narrow range centred on $[Z/H] \simeq -0.1$.

The full green curve in Fig. 2.7 shows the surface density of the stellar disc at 11.7 Gyr, which is roughly exponential. The red line shows what the surface density would be if stars remained at their radii of birth. By construction this forms an exponential disc with a scalelength of 2.5 kpc. The broken green line shows that at $R < R_0$ the disc approximates an exponential with a larger scale length ~ 2.8 kpc. The blue curve shows the surface density contributed by stars formed in the first 0.8 Gyr, which will be α-enhanced. This distribution deviates more strongly from an exponential because radial migration is most important for old stars. Fitting an exponential to this curve at $R < R_0$ yields a scalelength 3.1 kpc.

Fig. 2.8 reveals that thin and thick disc components can be identified within this overall envelope: the upper panel shows that the vertical stellar density profile at the Sun is not exponential but can be fitted by a sum of two exponentials. There is significant latitude in these fits and the fraction
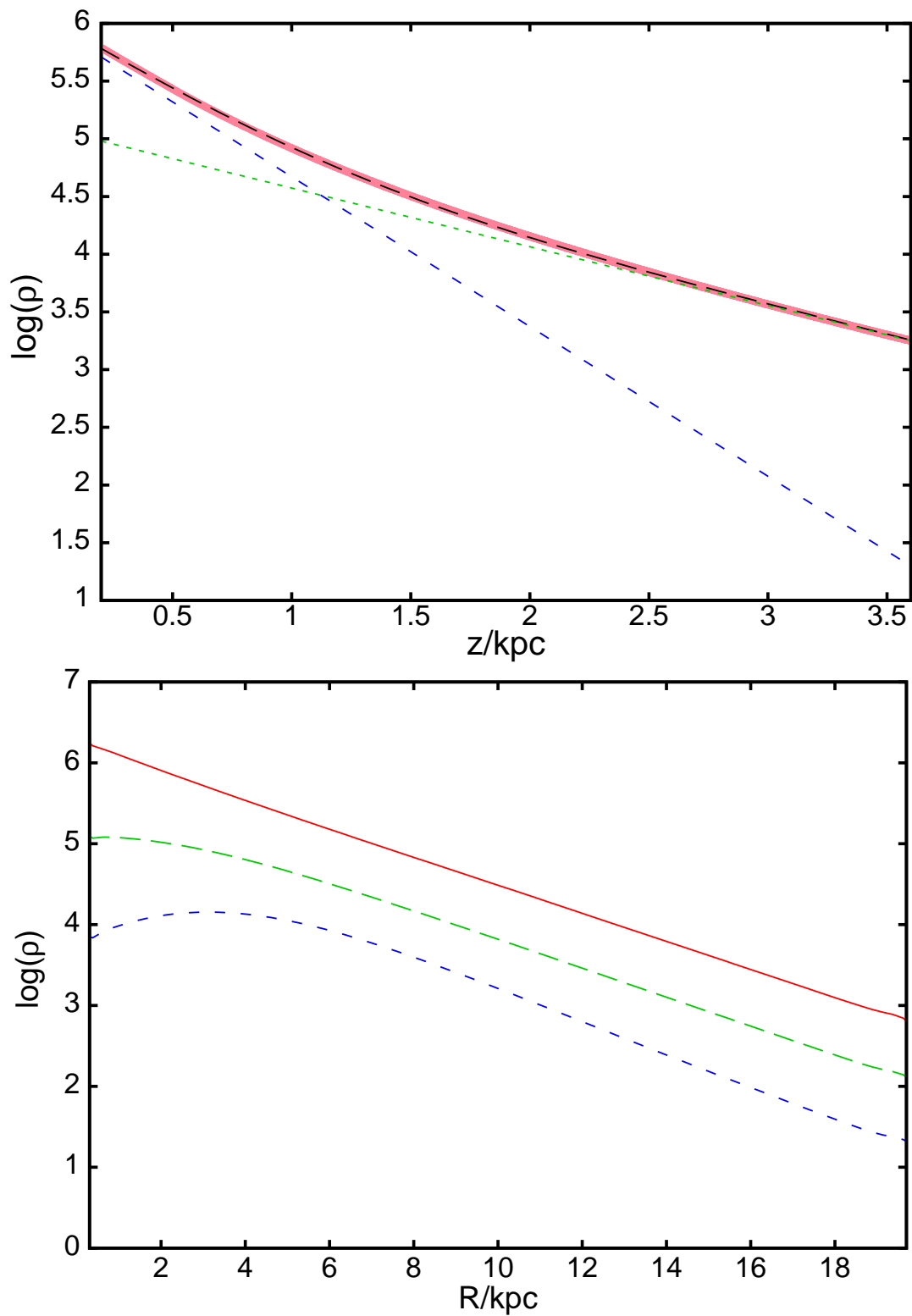
Figure 2.8: Upper panel: the volume density of stars at $R = 7.6\,\mathrm{kpc}$ as a function of height (red), a fit (black dashed) and its decomposition into thin and thick components. Lower panel: the volume density of stars at the current epoch at $z = 0$ (red), $z = 0.75\,\mathrm{kpc}$ (green dashed) and $z = 1.5\,\mathrm{kpc}$ (blue short dashed).
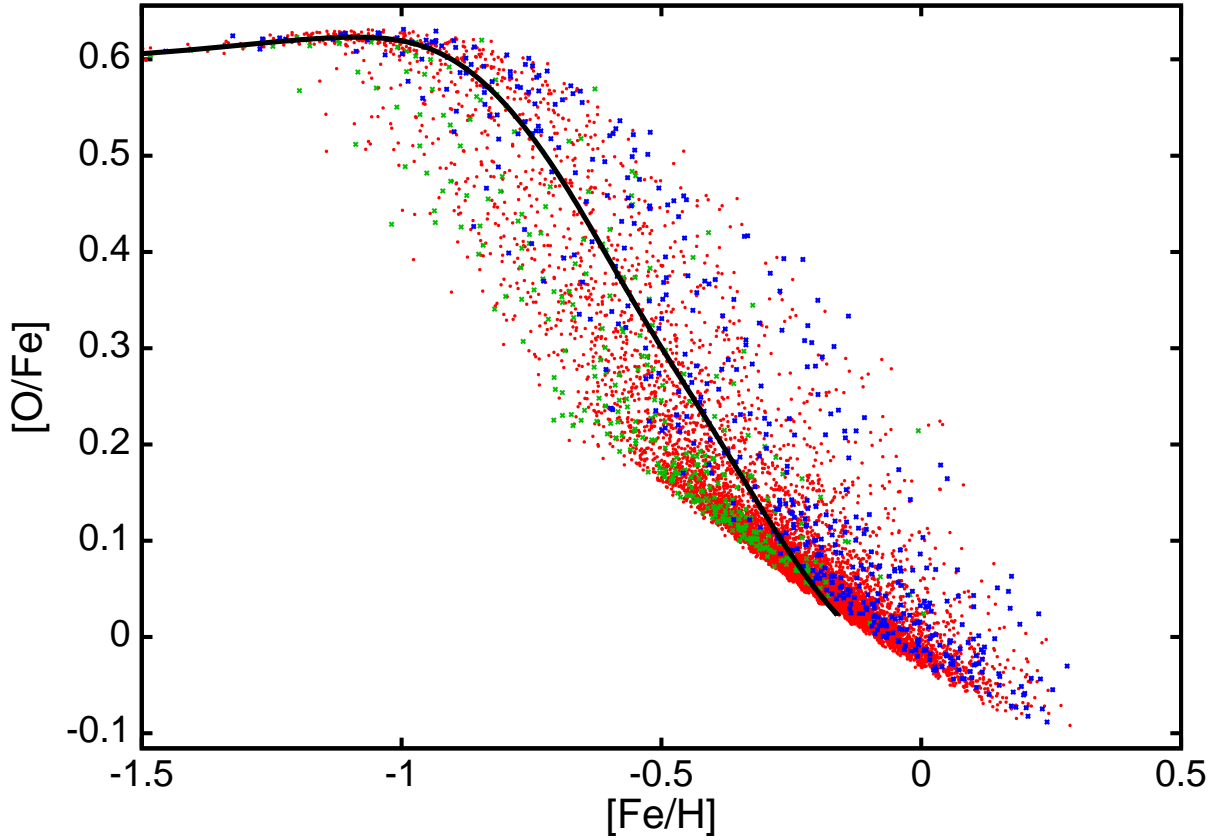
Figure 2.9: The predicted distribution of solar-neighbourhood stars in the ([Fe/H], [O/Fe]) plane. The sample is obtained by using the selection function of the GCS survey as described in Section 2.5 below. The colours of points depend on the star's azimuthal velocity: $v_\phi < 179\,\mathrm{km\,s^{-1}}$ blue; $179 < v_\phi/\mathrm{km\,s^{-1}} < 244$ red; $v_\phi > 244\,\mathrm{km\,s^{-1}}$ green. The black curve shows the trajectory of the solar annulus.

of stars that is assigned to each component varies with their scalelengths. For comparison with recent results of Juric et al. (2008) we present a fit with their value for the local thick disc fraction of 13 per cent. This yielded scaleheights of $h_1 = 335\,\mathrm{pc}$ and $h_2 = 853\,\mathrm{pc}$, very well in the range of their results. Note that the double-exponential density structure is *not* caused by any pecularity in star formation history, like a peak in early star formation, but is a consequence radial mixing combined with the given vertical force field. However, precise characterisation of the vertical structure must await dynamical models that employ a more accurate form of the third integral of galaxy dynamics.

The lower panel of Fig. 2.8 shows that at $z = 1.5\,\mathrm{kpc}$ (where the thick disc is dominant) the stellar distribution is less centrally concentrated than it is in the plane; if one were to fit an exponential profile to the stellar density at $z = 1.5\,\mathrm{kpc}$ for $R < 10\,\mathrm{kpc}$, the scalelength fitted would be larger than that appropriate in the plane. Just this effect is evident in Fig. 16 of Juric et al. (2008).

Fig. 2.9 shows the predicted distribution of solar-neighbourhood stars in the $([O/Fe], [Fe/H])$ plane when a sample is assembled using the GCS selection function described in Section 2.5 below. Two ridge-lines are evident: at top left of the figure a population starts that stays at $[O/Fe] \simeq 0.6$ until $[Fe/H] \simeq -0.75$ and then turns down towards $(0,0)$, while a second larger population starts at about $(-0.75, 0.25)$ and falls towards $(0.2, -0.05)$. This arrangement of points is very similar to that seen in Fig. 2 of Venn et al. (2004). The upper ridge-line is associated with the thick disc, and the lower ridge-line with the thin disc. In Section 2.9 we show that such bimodal distributions in [O/Fe] are a natural consequence of the standard assumptions about star-formation rates and metal enrichment that we have made. The structure is *not* a product of the double-exponential nature of the standard model's infall law; the model with a constant gas mass displays exactly the same structure. Breaks in the Galaxy's star-formation history (Chiappini et al., 1997) and accretion events (Bensby et al., 2005) have been hypothesised to account for the dichotomy between the thin and thick discs. Our models reproduce the dichotomy without a break or other catastrophic event in our model's star-formation history. When comparing Fig. 2.9 with similar plots for observational samples, it is important to bear in mind differences in selection functions: Fig. 2.9 is for a kinematically unbiased sample, while most similar observational plots are for samples that are kinematically biased in favour of "thick-disc" stars.

The full curve in Fig. 2.9 shows the trajectory of the solar-neighbourhood ISM. At low [Fe/H] this runs along the ridge line of the thick disc, and it finishes on the ridge line of the thin disc, but it is distinct from both ridge lines. The sharp distinction between this curve and the ridge line of the thin disc make it very clear that the latter is formed through the migration of stars into the solar neighbourhood, *not* through the chemical evolution of the solar neighbourhood itself. In many previous studies it has been assumed that the ridge line of the thin disc traces the historical evolution of the local ISM. Fig. 2.9 shows that this assumption could be wrong and that inferences regarding the past infall and star-formation rates that are based on this assumption are not to be trusted.

In Fig. 2.9 the points are colour coded by their angular momenta/guiding centres: blue points are for $v_\phi < 179 \, \mathrm{km \, s^{-1}}$ ($R_g < 0.81 R_0$), red points are for $179 \, \mathrm{km \, s^{-1}} \leq v_\phi \leq 244 \, \mathrm{km \, s^{-1}}$ and green points are for $v_\phi > 244 \, \mathrm{km \, s^{-1}}$ ($R_g > 1.1 R_0$). At the low-metallicity end of the thin-disc ridge line many points are green and few blue, while at the high-metallicity end the reverse is true. Thus low-metallicity thin-disc stars tend to have guiding centres $R_g > R_0$, while high metallicity stars have $R_g < R_0$. Haywood (2008) has noted the same metallicity-velocity correlations in samples of nearby stars. The thick disc contains stars from all three radial ranges, but stars with small R_g (blue) are most prominent at higher [Fe/H].

Fig. 2.10 shows the distribution of stars in the $([Z/H], v_\phi)$ plane: the upper panel is for the GCS stars and the lower panel is for the standard model. In both panels the highest density of stars lies near $(0, 220 \, \mathrm{km \, s^{-1}})$ and the upper edge of the distribution rises as one moves to lower metallicities. The metallicity gradient in the disc leads to the main cluster of stars sloping downwards to the right. A significant difference between the two panels is that in the upper panel there are more stars in the lower left region. This population is very much more prominent in Fig. 5 of Haywood (2008), where a band of points runs from small v_ϕ and [Z/H] up towards the
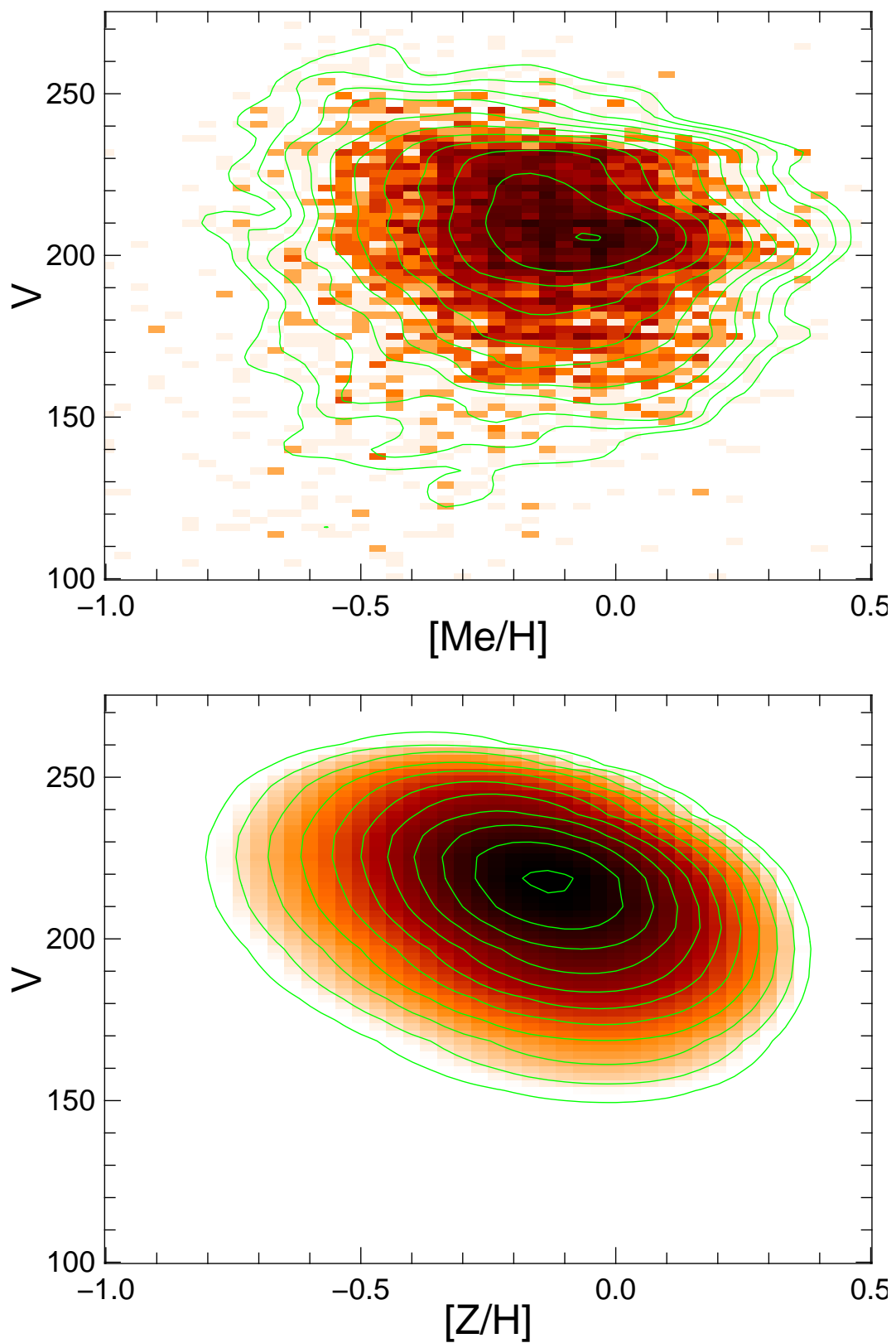
Figure 2.10: Upper panel: the distribution of GCS stars in the $([Z/H], v_\phi)$ plane. Lower panel: the prediction of the standard model. Colours and contours reflect the density on a logarithmic scale with a 0.2 dex spacing for contours.

main cluster. This band is made up of halo and thick-disc stars that are selected for in the samples from which Haywood drew data. The other difference between Haywood's Fig. 5 and the lower panel of Fig. 2.10 is that Haywood's main clump has a slightly less pronounced slope down to the right. It is likely that errors in the measurements of [Fe/H] have moderated this slope. The GCS distribution shown in the upper panel of Fig. 2.10 is (especially on the high metallicity side) dominated by overdensities around the rotational velocities of well-known stellar streams (e.g., the Hercules stream Dehnen, 1998). This pattern overlays the general downwards slope. The model accounts well for the steeper edge of the density distribution at high rotational velocities, which is the combined effect of lower inwards blurring and lower stellar densities from outer rings.

The top panel of Fig. 2.11 shows that the stellar metallicity distribution is less centrally concentrated than that of the cold ISM from which stars form. Three factors are responsible for this result. First, the mean metallicity of stars reflects the metallicity of the gas at earlier times, which was lower. This effect is most pronounced at the centre, where the metallicity of the ISM saturates later than further out. Second, radial mixing, which flattens abundance gradients, has a bigger impact on stars than gas because stars experience both churning and blurring. Third, the net inflow of gas steepens the abundance gradient in the gas. Holmberg et al. (2007) have estimated the stellar metallicity gradient from the GCS stars. When they select thin-disc stars they find $-0.09 \, \text{dex} \, \text{kpc}^{-1}$, but when one excludes stars with $[Z/H] < -0.7$ (which ensures halo objects are removed), one obtains $-0.11 \, \text{dex} \, \text{kpc}^{-1}$. The gradient of the dashed red line in Fig. 2.11 at $7.6 \, \text{kpc}$ is $0.10 \, \text{dex} \, \text{kpc}^{-1}$ in excellent agreement with the GCS data.

The lower panel of Fig. 2.11 shows the breadth of the metallicity distribution at three radii. These distributions have full-width at half maximum around $0.35 \, \text{dex}$ and are significantly offset to each other by $0.25 \, \text{dex}$.

Fig. 2.12 shows how α-enhancement varies in time and space, in stars and gas. Naturally, [O/Fe] declines with time in both the ISM and in the stellar population, and at a given time is higher in the stars than the gas. [O/Fe] generally increases outwards but at $12 \, \text{Gyr}$ in both stars and gas it attains a plateau at $R \gtrsim 10 \, \text{kpc}$, with $[\alpha/\text{H}] \sim 0.2$ in the gas. The existence of the plateau is a consequence of the rule that in the IGM [O/H] is the current value in the disc at $R \simeq 12 \, \text{kpc}$; gas with the given α-enhancement rains on the disc at $R \lesssim 20 \, \text{kpc}$, is enriched by supernovae of both types and a few gigayears later arrives at $R = 12 \, \text{kpc}$ with its original α-enhancement. This level is set by the metallicity-dependent yields we have employed.

Fig. 2.13 shows the B, R and I-band absolute magnitudes of the standard model as functions of time. The B-band luminosity rises quickly to a shallow peak around $5 \, \text{Gyr}$ and then commences a very slow decline. Emissions in the R-Band are almost constant at the present time, while I-band luminosities continue to rise throughout the Galaxy's life because additions to the stock of long-lived stars outweigh deaths of relatively short-lived and predominantly blue stars. In our model the Galaxy reaches an I-Band magnitude of around -22.7 which is exactly the result one would expect for a disc galaxy with a rotation velocity of $220 \, \text{km} \, \text{s}^{-1}$ (e.g. Pizagno et al., 2005) Fig. 2.14 shows the $U - B$ and $B - I$ colours of the disc at $t = 1.5$, 4.5, 8.4 and $12 \, \text{Gyr}$. As expected, the disc reddens at a declining rate throughout its life. There is at all times a significant
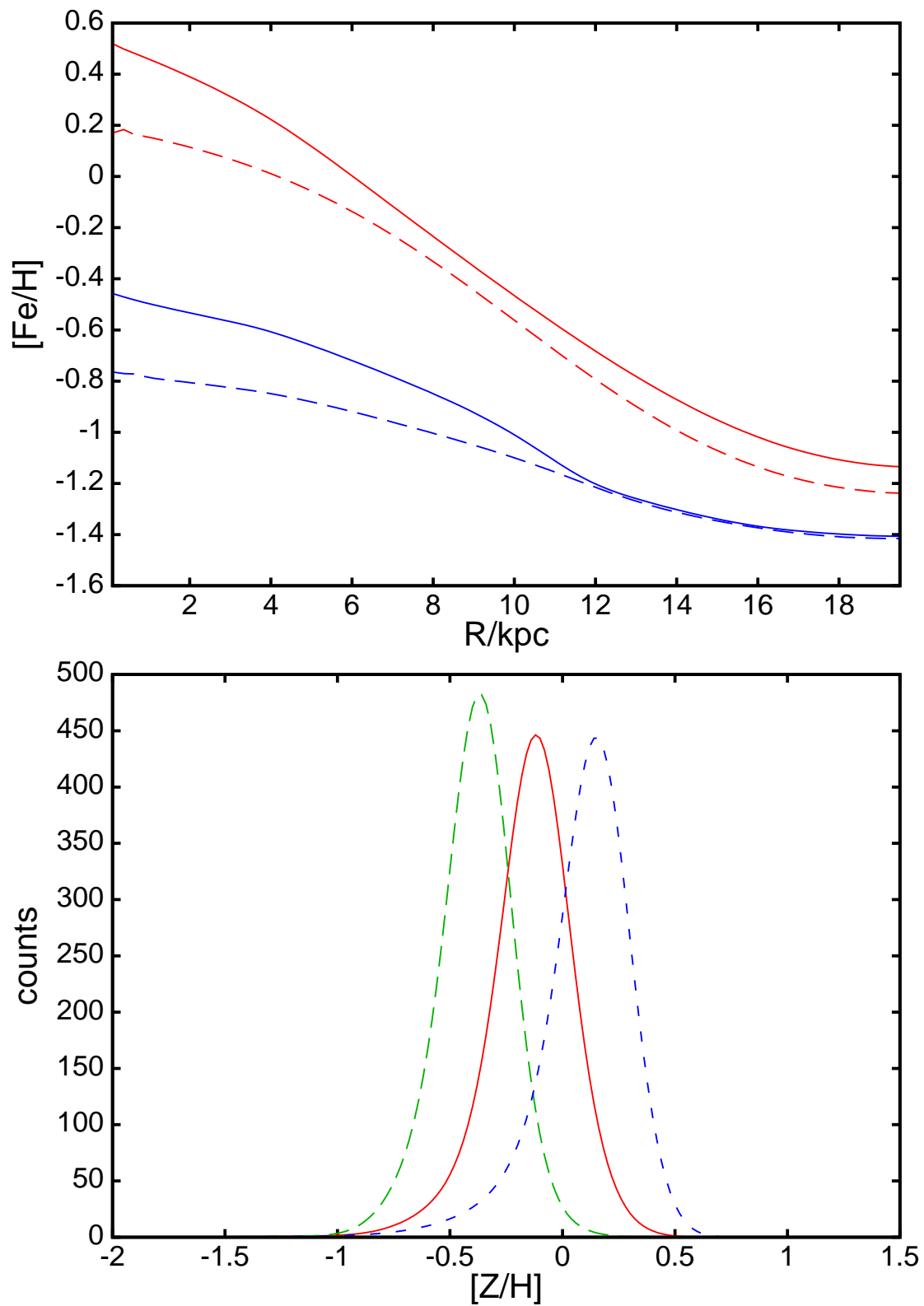
Figure 2.11: Upper panel: mean metallicities of stars (dashed) and cold ISM (full) as functions of R at the present time (red) and at 1.5 Gyrs (blue). Lower panel: the distributions over metallicity of stars currently at $R = 5$ kpc (blue), 7.6 kpc (red), and 10 kpc (green).
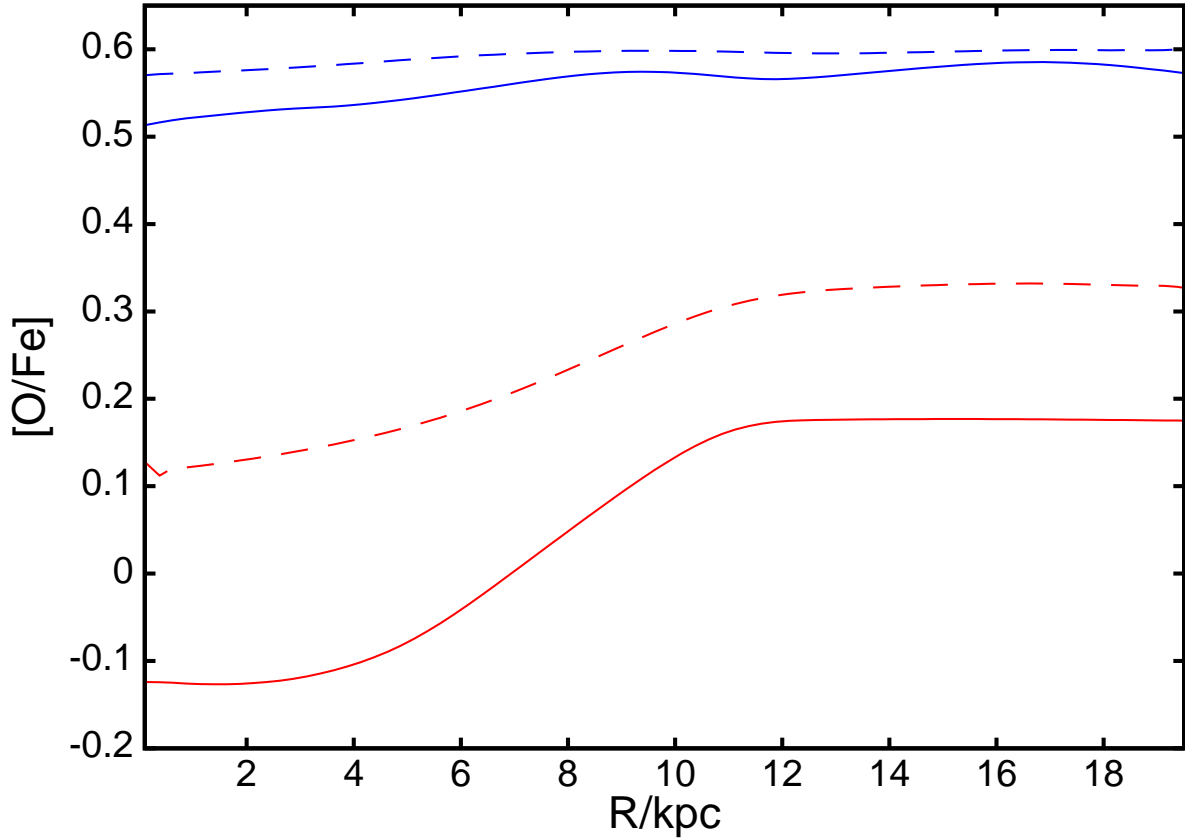
Figure 2.12: Full lines: [O/Fe] in the cold ISM after 1.5 Gyr (blue) and 12 Gyr (red). Dashed lines: Mean [O/Fe] of stars after 1.5 Gyr and 12 Gyr.

colour gradient between $R = 8$ and 16 kpc that make the disc's edge about 0.2 mag bluer in $B-I$ than its centre.

Fig. 2.15 shows that radial migration causes the dependence of velocity dispersion on time for stars that are currently in the solar neighbourhood to differ materially from the acceleration law (2.17) that determines the time dependence of σ_z for stars that are born at given radius. The outward migration of stars brings to the solar neighbourhood stars that carry with them the large velocity dispersions characteristic of their places of birth. The impact that these migrants have on σ_z for stars of a given age increases with age, so at high ages σ_z increases faster than equation (2.17) predicts. Least-squares fits of $\sigma_z \propto t^\beta$ to the red and green curves in Fig. 2.15 yield $\beta = 0.53$ and 0.44, respectively. Empirically the photometrically complete portion of the Hipparcos catalogue shows that the best power-law fits to the rate of increase of σ_z yield $\beta \simeq 0.45$ (Just & Jahreiss, 2007; Aumer & Binney, 2009). From a theoretical standpoint, this result has hitherto been puzzling because the largest exponent that can be obtained from the dynamics of star scattering is 1/3 (Binney & Lacey, 1988). Such studies treat the acceleration as a local process. Our result suggests that the conflict between theory and observation is attributable to
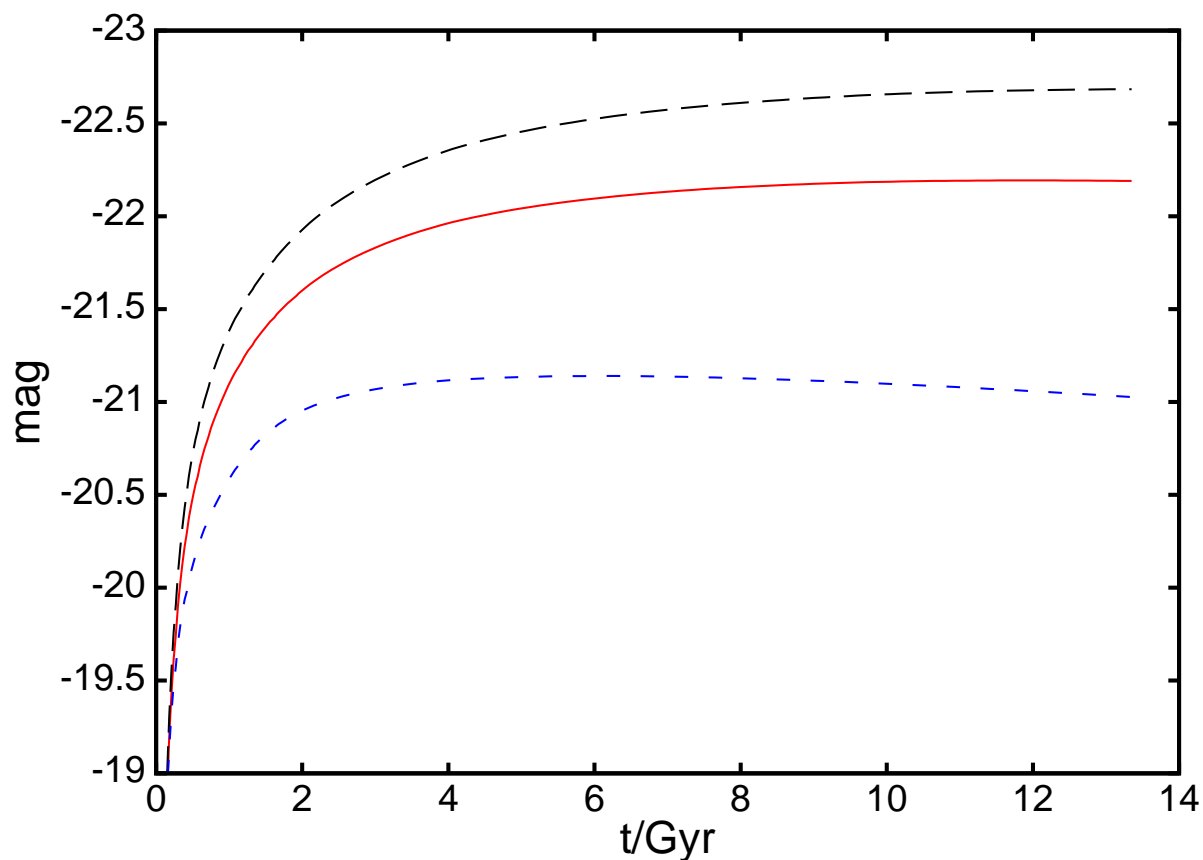
Figure 2.13: Absolute magnitudes in the *B* (blue short dashed), *R* (red) and *I* (black long dashed) bands as functions of time. No allowance has been made for obscuration.

violation of this assumption.

2.5 Fitting the model to the solar neighbourhood

A major constraint on the models is provided by comparing the model's predictions with samples of stars observed near the Sun. To make these comparisons, we have to reproduce the selection functions of such samples, which proves a non-trivial job.

The GCS is an important sample, and for each model we calculate the likelihood of this sample. Nordström et al. (2004) obtained Strömgren photometry and radial velocities for a magnitude-limited sample of 16 682 F and G dwarfs, nearly all of which have good Hipparcos parallaxes. From the photometry they estimated metallicities and ages. There has been some debate about the calibration of the metallicities and ages (Haywood, 2006; Holmberg et al., 2007; Haywood, 2008). Recently the re-calibrated data from Holmberg et al. (2007) became available and it is to these data that we have compared our models. We compare their metallicities ([Me/H]) to our
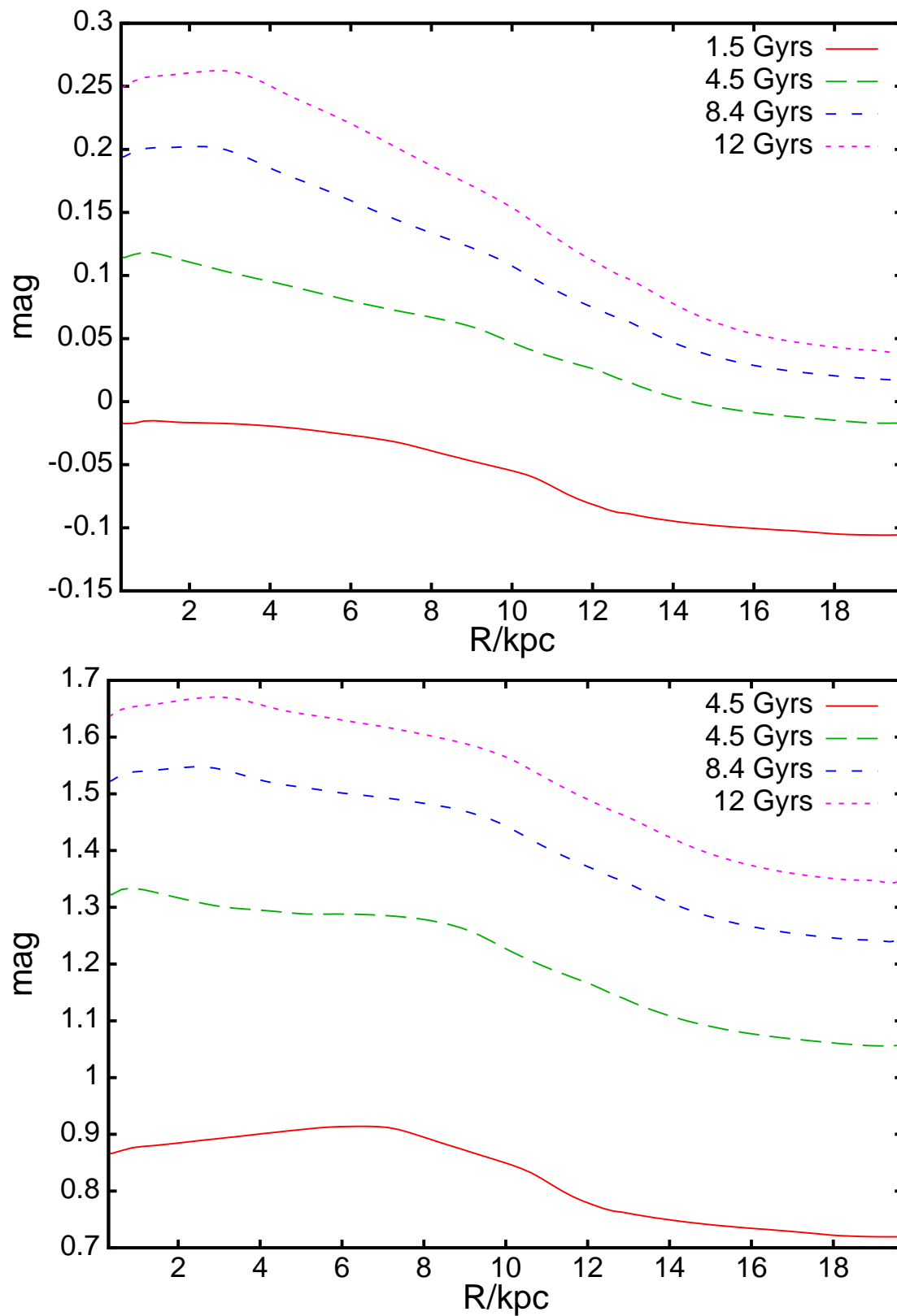
Figure 2.14: $U - B$ (upper panel) and $B - I$ (lower panel) as functions of radius at $t = 1.5$, 4.5, 8.4 and 12 Gyr. No allowance has been made for obscuration.
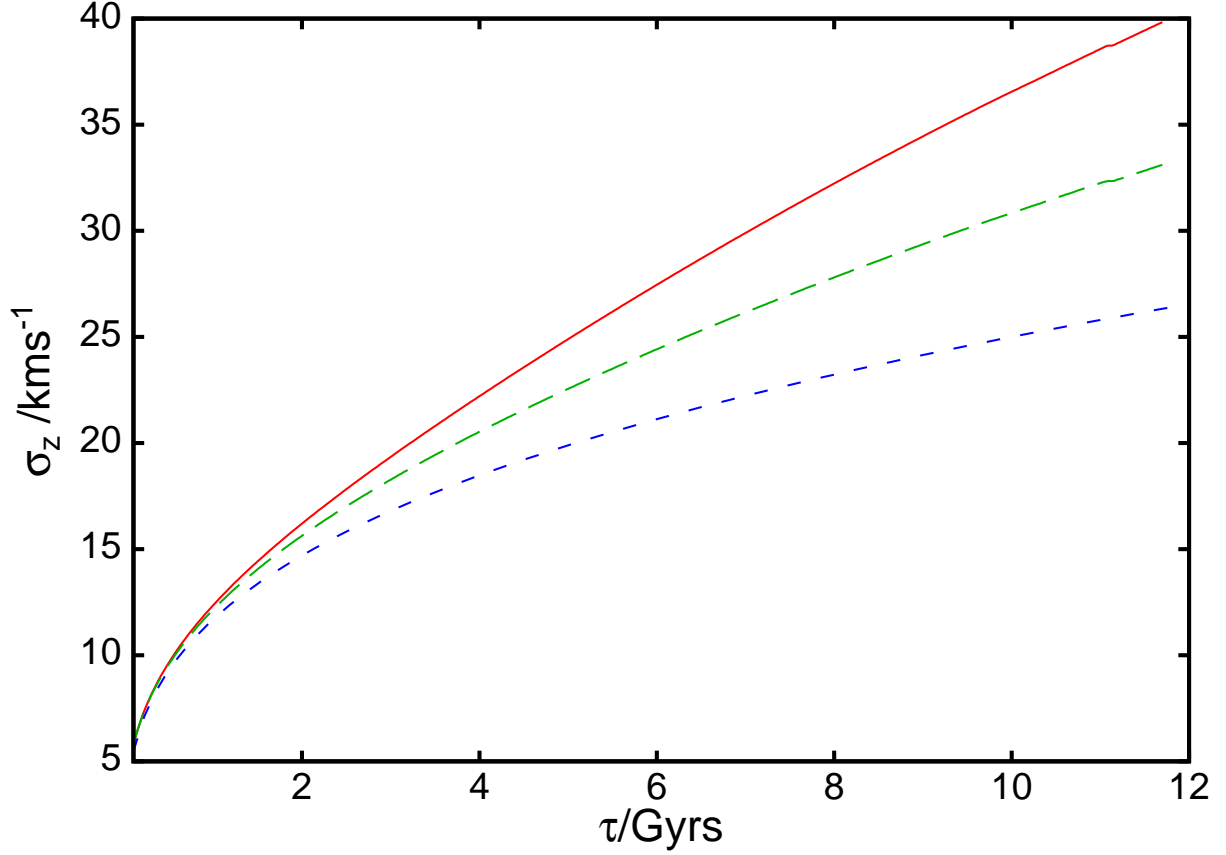
Figure 2.15: Velocity dispersion of solar-neighbourhood stars as a function of age. Red curve: σ_z for all stars in the solar annulus. Green (long dashed) curve: σ_z for stars within 100 pc of the Sun. Blue (short dashed) curve: σ_z for stars born in the solar annulus.

[Z/H] as it is not entirely obvious to what extent alpha enrichment enters into their measurements. Since assigning ages to individual stars is very difficult, we have concentrated on matching the distribution of stars in the (M_V, T_{eff}, Z) space from which ages are derived.

For each metallicity we construct a volume-limited stellar number density of stars in the (M_V, T_{eff}) plane by considering each annulus j, and calculating the fraction of each population in this annulus that will be in the solar neighbourhood. For given absolute magnitude, the probability that a star will enter the sample is

$$W(r_{\text{max}}) = \int_0^{r_{\text{max}}} dr\, r^2 \int d^2\Omega\, n(z), \tag{2.19}$$

where the space density of stars $n(z)$ is assumed to be plane parallel and given by equation (2.18). For the GCS selection function we use the approximate $b - y$ colour rules from Nordström et al. (2004) – a more sophisticated selection function could in principle be constructed, but it is not possible from the published data. At each colour, the appropriate selection function ϕ is

Table 2.2: Magnitudes defining the Geneva–Copenhagen selection function

$b - y$	$0.21 - 0.25$	< 0.344	< 0.38	< 0.42	> 0.42
v_1	7.7	7.8	7.8	7.8	8.2
v_2	8.9	8.9	9.3	9.3	9.9

characterised by two apparent magnitudes v_1 and v_2 listed in Table 2.2: ϕ declines linearly from unity at magnitudes brighter than v_1 to zero fainter than v_2. ϕ vanishes for $b - y$ bluer than 0.21. For $b - y$ redder than 0.38, ϕ is reduced by a factor 0.6.

The selection of Nordström et al. (2004) is designed to exclude red giant branch (RGB) stars from the data set. However, some of these stars are still in the sample, while the sample is biased against stars just below the giant branch. We take out of consideration the RGB itself and we downscale the theoretically expected population density near the starting point of the red giant branch by a factor of 4 to reconcile it with the data. Since the number of RGB-stars in the GCS is not large anyway, the loss of information is small. We also removed from the dataset three objects that are far too faint to be attributed to the main sequence. The theoretical distributions are convolved with a Gaussian of dispersion 0.1 dex in [Z/H] to allow for measurement errors.

Fig. 2.16 compares predicted (lower panel) and observed (upper panel) Hess diagrams for the GCS stars. As discussed by Holmberg et al. (2007), the ridge-line of the main sequence in the GCS data is significantly displaced from that predicted by isochrones. We have eliminated the effects of this offset on Fig. 2.16 in the simplest possible way, namely by decreasing all model values of $\log(T_{\mathrm{eff}})$ by the value, 0.015, that yields the closest agreement between the theoretical and observation main sequences. After this correction has been made, the agreement between the theoretical and observational Hess diagrams shown in Fig. 2.16 is convincing though not perfect. The original conception had been to determine the model's parameters by maximising the likelihood of the GCS stars in the model density in $(M_V, T_{\mathrm{eff}}, Z)$ space, but confidence in this plan was undermined by (i) the need for an arbitrary alignment of measured and theoretical values of T_{eff}, and (ii) the extent to which the likelihood of the data depends on the uncertain GCS selection function. Notwithstanding these reservations, we are encouraged that the standard model maximises the likelihood of the data at an age, ~ 11 Gyr, that agrees with other estimates of the age of the solar neighbourhood (Aumer & Binney, 2009, and references therein).

The full red curve in Fig. 2.17 shows the metallicity distribution of stars predicted by the standard model, and green points show the GCS data. The agreement is excellent. At the lowest metallicities theory predicts slightly too few stars, but the uncertainties in both the theory and the data are large in this limit and the theory does not include halo stars, so it should under-predict the data at $[Z/H] \lesssim -1$.
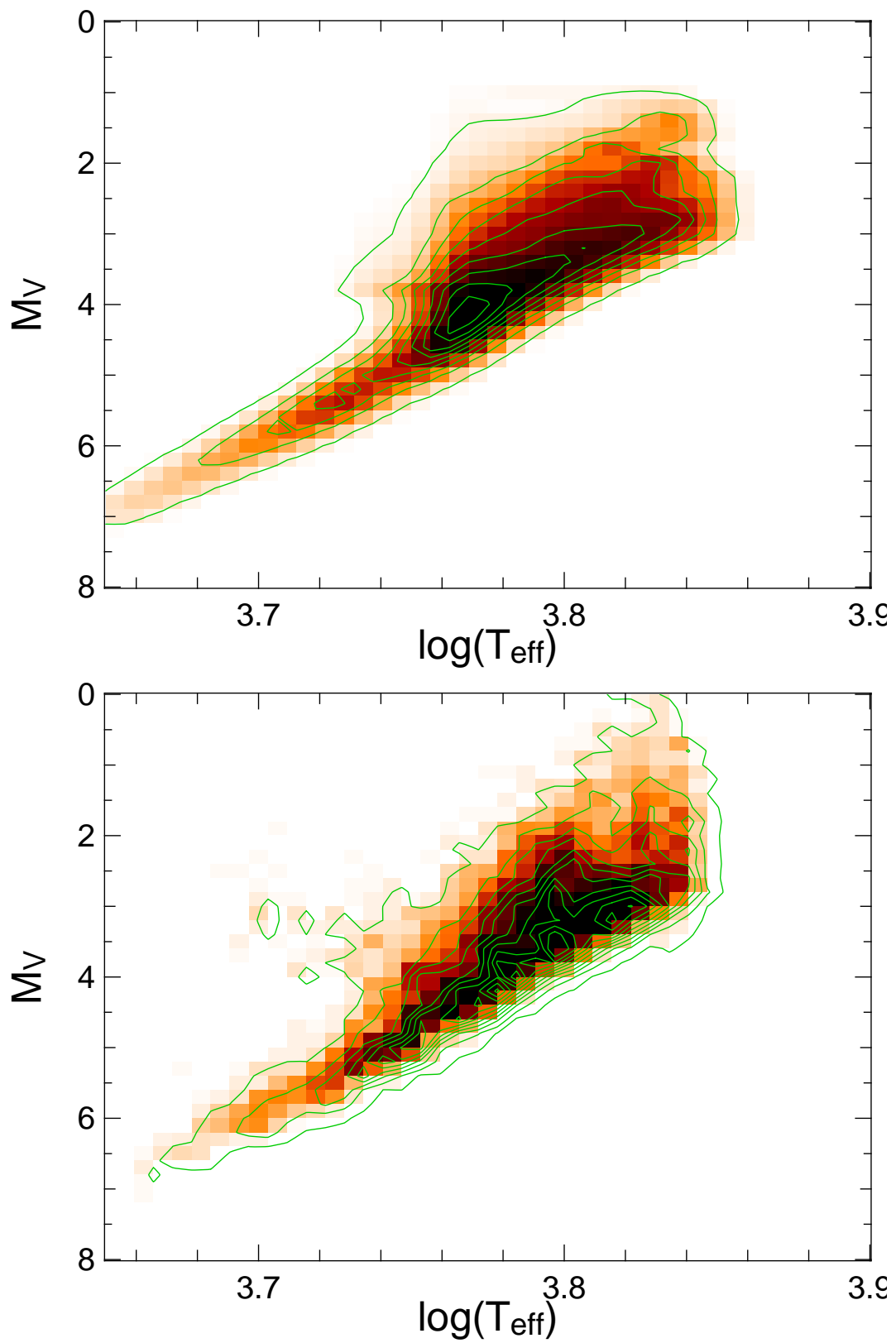
Figure 2.16: Comparison of the observed (upper) and predicted (lower) distributions of GCS stars in the (T_{eff}, M_V) plane. Contours have an equal spacing of 10 counts per bin, starting with 3.
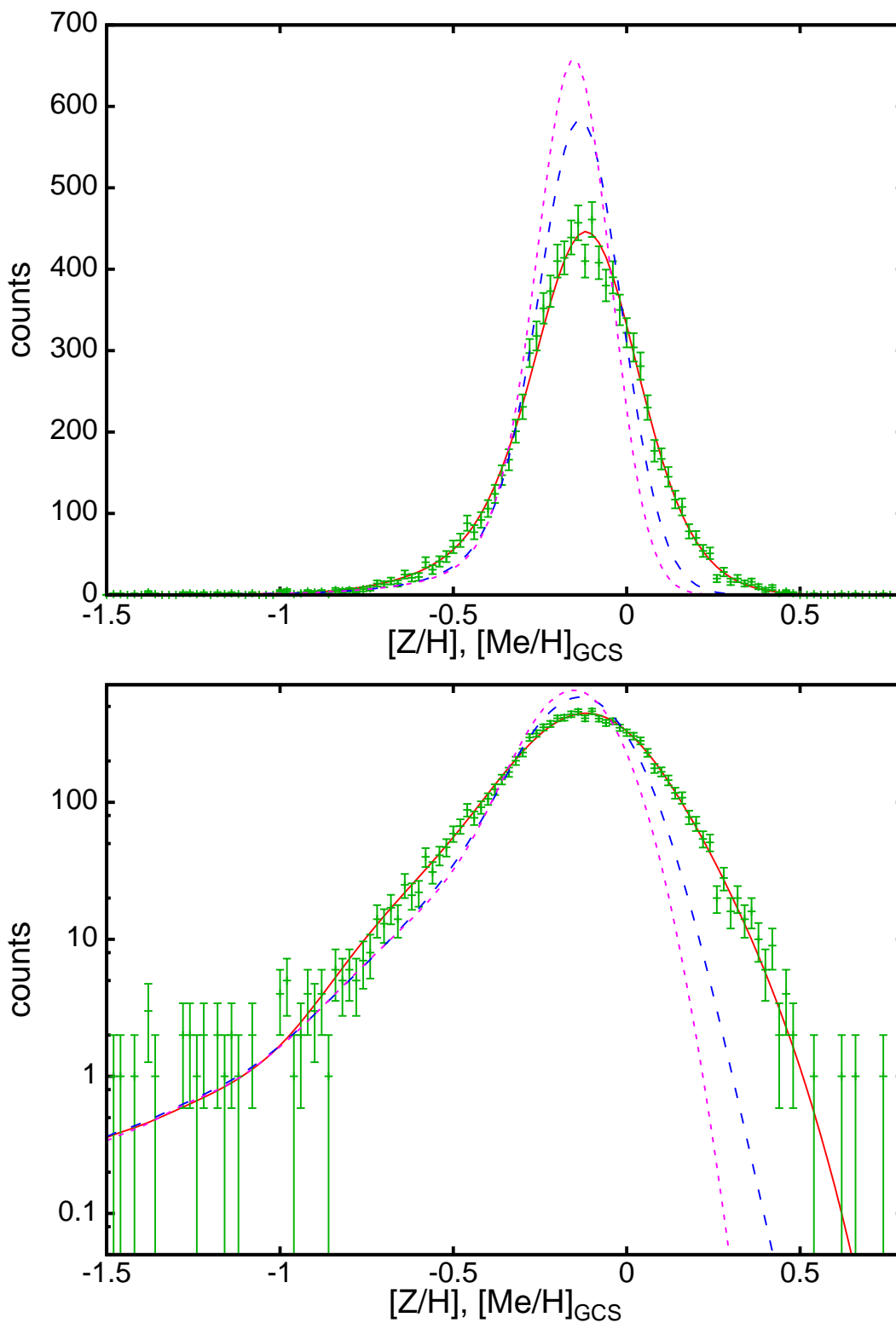
Figure 2.17: The metallicity distribution of GCS stars (green points) and the corresponding pre-diction of the standard model (full red curve). The broken blue curve shows the model that differs from the standard model only in the elimination of churning and radial gas flows. The broken pink curve shows the model with neither churning nor blurring. The lower panel shows the same data but with a logarithmic vertical scale to reveal structure in the wings of the distribution.

2.6   General trends

We now discuss aspects of how the observable properties of a model depend on its parameters, and what is required to achieve fits of the quality seen in Figs 2.5 and 2.17.

Table 2.1 lists the model's 16 parameters; the third column explains whether the parameter is fitted to the GCS data or taken from the literature, and indicates the sensitivity of models to that parameter. Five parameters ($M_0, M_1, b_1, f_{\text{direct}}, M_{\text{warm}}$) significantly affect only the distribution of stars at [Z/H] < −0.7. Six other parameters ($M_2, t_0, k^{-1}, t_{\text{cool}}, Z_{\text{IGM}}$) are fixed by observed properties of the Galaxy other than the solar-neighbourhood stellar distribution. The remaining five parameters are the critical surface density for star formation Σ_{crit}, the long infall timescale b_2, the accretion parameters f_A and f_B and the churning strength k_{ch}. We shall see that f_B is effectively set by the metallicity gradient in the gas, that b_2 is effective determined by the local Hess diagram, and that the value of Σ_{crit} is unimportant providing it is small (we have included this parameter only for consistency with earlier work; the models do not want it). Consequently the fit of the model to the data shown by the red curve and the green points in 2.17 is obtained by adjusting just f_A and k_{ch}.

The number of stars more metal poor than [Z/H] $\sim$ −1 depends sensitively on the thermal structure of the early ISM. Most previous studies (exceptions include Thomas et al., 1998; Samland & Gerhard, 2003) have used only one phase of the ISM. Introducing the warm component of the ISM delays the transfer of metals to the star-forming cold ISM by $\sim 1\,\text{Gyr}$, thus increasing the number of extremely metal-poor G dwarfs. Our first models initially had no warm gas, with the result that at early times the mass of warm gas was proportional to time and the metallicity of the cold gas rose quadratically with time. These models had an over-abundance of *very* metal-poor stars. These experiments led to the conclusion that pregalactic and halo stars endowed the disc with warm, metal-rich gas at the outset. Even at late times, the existence of the warm ISM delays the introduction of freshly-made metals into stars, and thus in concert with the gas flow through the disc steepens the metallicity gradient in the stellar disc; eliminating the warm component raises the metallicity of the solar neighbourhood and beyond by $\sim 0.1\,\text{dex}$.

The metallicity of infalling gas only affects the structure of the disc at $R \gtrsim 12\,\text{kpc}$. Lowering Z_{IGM} steepens the metallicity gradient at $R > R_0$.

It is instructive to consider the case in which blurring is included but churning is turned off by setting $k_{\text{ch}} = 0$ and radial flows are eliminated by ensuring that $f_A + f_B = 1$ so every ring's need is fully supplied from the IGM. The broken blue curve in Fig. 2.17 shows the present-day metallicity distribution that this model predicts for the GCS. The peak of the distribution is much narrower than in the standard model, and there is a striking deficiency of metal-rich stars. The broken pink curve shows the effect of also turning off blurring: the deficiency of metal-rich stars becomes even more striking but there is negligible change on the metal-poor side of the peak.

Reducing the current SFR by making the infall rate a more rapidly declining function of time shifts the peak of the distribution to higher metallicities by reducing the relative strength of recent inflow and thus the supply of fresh, metal-poor gas. The use of an IMF that is steeper in the low-mass region, as has been suggested by some studies, reduces the mass of metals that is locked

up in low-mass stars and increases the metal production by each generation. The metallicity in such a regime is accordingly higher, but the shape of the distribution does not change. Since changes in the IMF at the high-mass end, which is equally uncertain, can produce compensating variations in yields, loss rates, etc., we stayed with the traditional approach via the Salpeter IMF. In all interesting models the metallicity of the local ISM saturates early on. The saturation level depends on the pattern of gas flow through the disc, and on the current SFR relative to the mean rate in the past: the faster the decline in the SFR, the higher the current metallicity. Naturally the stars of the solar neighbourhood are on the average younger in models with a constant gas mass than in models in which the infall rate is declining according to equation (2.6). This relative youth is reflected in the structure of the local Hess diagram. We reject the model with constant gas mass because it assigns a significantly smaller likelihood to the Hess diagram of the GCS stars than does a model based on equation (2.6).

2.6.1   Selecting the standard model

All our models have quite strong metallicity gradients in both stars and gas (Figs 2.5 and 2.11). Since the metallicity of the central gas is enhanced by radial gas flow, and models with large f_B have larger central flows than models with large f_A and vice versa at large radii (Fig. 2.2), enhancing f_B steepens the metallicity gradient at small R and diminishes it at large R.

Eliminating churning and radial gas flows (by setting $k_{ch} = 0$, $f_A + f_B = 1$) dramatically reduces the metallicity gradient within both the stellar and gas discs: at the present epoch the gradient in the gas near the Sun falls from $-0.11 \, \mathrm{dex \, kpc^{-1}}$ to $-0.01 \, \mathrm{dex \, kpc^{-1}}$. Increasing the churning amplitude k_{ch} both increases the width of the peak in the predicted solar-neighbourhood metallicity distribution (Figs 2.11 and 2.17) and reduces the gradient in the mean metallicity of stars at $R \lesssim R_0$.

Fig. 2.18 shows how the likelihood of the GCS metallicity distribution plotted in Fig. 2.17 varies with f_A, f_B and k_{ch}. In the upper panel favoured models (with large symbols) lie along a line that slopes down and to the right. Along this line a decrease by 0.01 in f_B is compensated by an increase in f_A by ~ 0.08.

As one moves down the upper panel of Fig. 2.18, the steepness of the metallicity gradient near the Sun increases, and the models with $f_B = 0.015$ have local gradients steeper than $-0.12 \, \mathrm{dex \, kpc^{-1}}$, which may conflict with the data. Models higher up the panel have smaller local metallicity gradients and require larger values of k_{ch} to bring a sufficient variety of stars to the solar neighbourhood. Models to the right of the panel have smaller inward flows of gas, leading to local metallicities that rise faster in time and they match the GCS metallicity distribution at younger ages, especially if k_{ch} is large so metal-rich stars migrate to the Sun relatively rapidly. The structure of the local Hess diagram for either GCS stars (Fig. 2.16) or Hipparcos stars (Aumer & Binney, 2009) implies that the solar neighbourhood is not younger than 9 Gyr, so when the age is smaller than 9 Gyr the model is marked by a cross in Fig. 2.18. Models adjacent to the crosses do not violate the 9 Gyr limit but are nonetheless disfavoured because their local Hess diagrams yield relatively low likelihoods for the GCS sample.
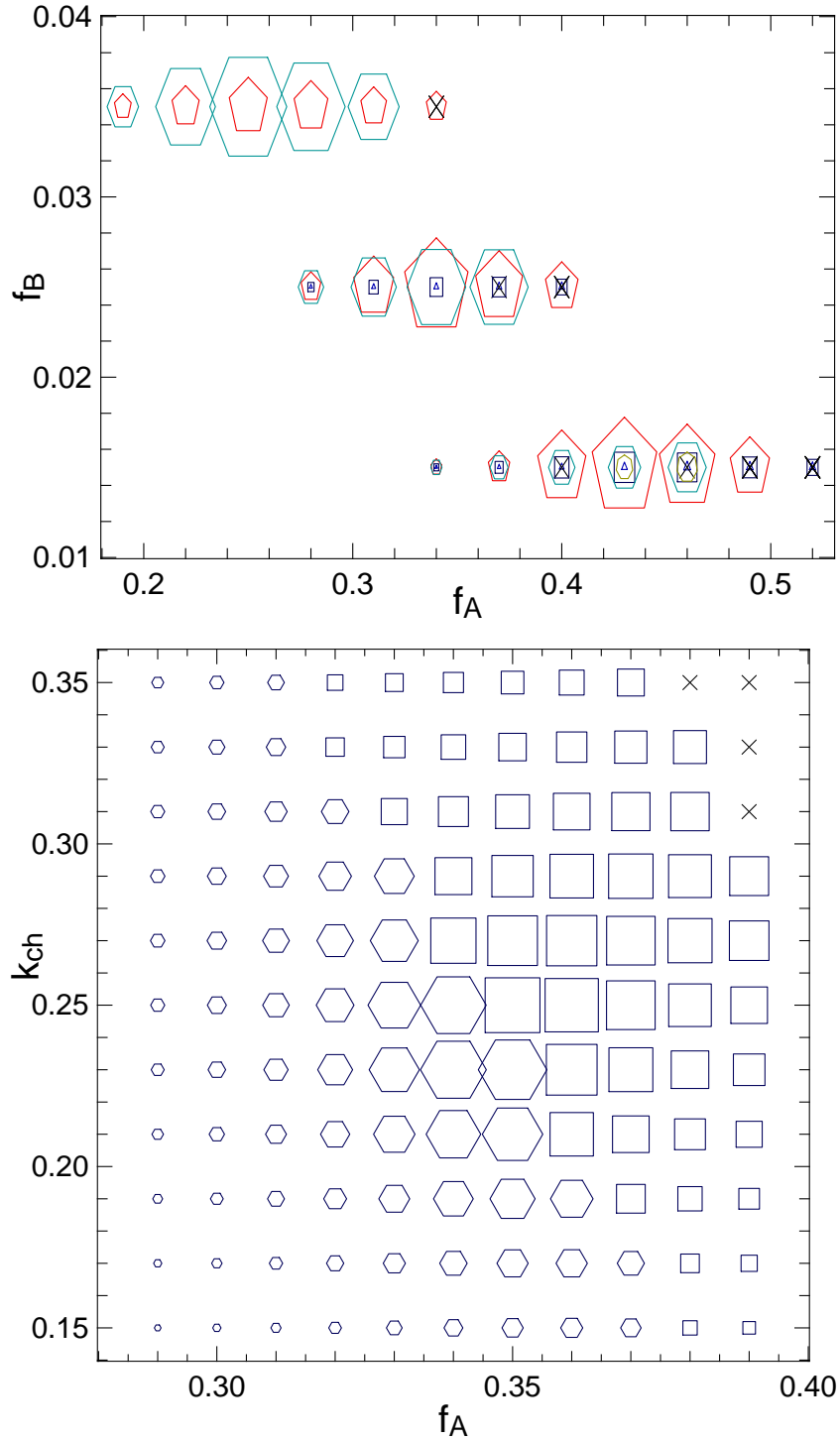
Figure 2.18: The likelihood of the GCS metallicity distribution in models with infall rates given by equation (2.6). Upper panel: the values of the infall parameters f_A and f_B are given by the locations of the symbols, and the value of k_{ch} is indicated by the number of sides of the polygon: 3, 4, 5, ... for $k_{ch} = 0.0, 0.1, 0.2, \ldots$. The size of the polygon increases linearly with the log likelihood of the data, models with ages smaller than $9 Gyr$ are marked with crosses. Lower panel: the likelihoods of models with $f_B = 0.025$ and varying (f_A, k_{ch}). In this panel the size of a symbol is a more sensitive function of likelihood than in the upper panel. Hexagons indicate models with best-fit ages higher than $12.6\,Gyr$, models with best-fit ages below $9.6\,Gyr$ are crossed.

Four factors make it difficult to confine narrowly the required value of k_{ch} within the part of Fig. 2.18 that has large symbols: (i) churning affects mainly the width of the metallicity distribution, which has less impact on the likelihood than the location of its peak; (ii) churning, which is strongest in the inner regions of the disc, tends to saturate near the centre in the sense that old stars become fully shuffled; (iii) the GCS sample is biased against old and highly dispersed populations of stars, so where churning has the strongest effect, the observational signature is weak; (iv) the required churning strength is sensitive to the local metallicity gradient which is not very well constrained by observations.

In our models there is no azimuthal variation in the metallicity of gas at a given radius, as is suggested by recent observations (see Nieva & Przybilla, 2008), which yield very small to negligible inhomogeneity of the ISM at a given radius. The effect of relaxing this assumption can be gauged by increasing the dispersion in the measured metallicities of a given population of stars: if there is intrinsic dispersion in the metallicity of the ISM in a given annulus, the measured metallicities of stars formed from it will reflect both this dispersion and measurement errors. The largest intrinsic dispersion in the metallicity of the ISM that would appear to be compatible with the data plotted in Fig. 2.5 is ~ 0.1 dex. When we combine this with measurement errors of 0.1 dex, we can obtain a fit to the GCS data of Fig. 2.17 that is only slightly worse than that provided by the standard model by lowering k_{ch} from 0.25 to ~ 0.1.

We have studied models with several values of the mass-loss parameter f_{eject} and concluded that up to the largest values studied ($f_{eject} = 0.15$ at $R < 3.5$ kpc and 0.05 elsewhere) f_{eject} does not have a large effect on the model's observable properties, and is anyway degenerate with the still uncertain nucleosynthetic yields. However, increasing f_{eject} makes it slightly easier to find an acceptable model, reflecting the fact that the yields we are using lie at the upper limit of the yields that are consistent with measured metallicities.

The upper panel of Fig. 2.19 shows the effect on the fit to the GCS metallicity distribution of using a non-zero value of the threshold gas density, Σ_{crit}, below which the SFR declines steeply. Raising Σ_{crit} from zero to $2.5 \, M_\odot \, pc^{-2}$ changes the model prediction from the red curve of the standard model to the blue curve; the distribution is now wider and peaks at lower metallicities. The pink dotted curve shows the result of maximising the likelihood of the data subject to the constraint $\Sigma_{crit} = 2.5 \, M_\odot \, pc^{-2}$. In this model f_A is increased (to 0.44) and k_{ch} is decreased (to 0.20) relative to the standard model. The new model provides a slightly worse fit to the GCS data than the standard model, but, as the lower panel reveals, there is a problem with using a non-zero value of Σ_{crit}: with minimal star-formation in the outer disc, the metallicity gradient of the ISM steepens near the edge of the star-forming regions, while further out the metallicity becomes constant at the intergalactic value. The data show no sign of this plateau, and are probably incompatible with a plateau as low as $[Z/H] = -1$. Values of $\Sigma_{crit} > 2.5 \, M_\odot \, pc^{-2}$ are incompatible with the data because they bring the edge of the star-forming disc too close to the Sun.

By considering the likelihoods of both the Hess diagram and the metallicity distribution of GCS stars, and our prejudices regarding the proper value of f_{eject}, we chose the model specified by Table 2.1 as the standard model. With this model the likelihood of the GCS metallicity peaks at
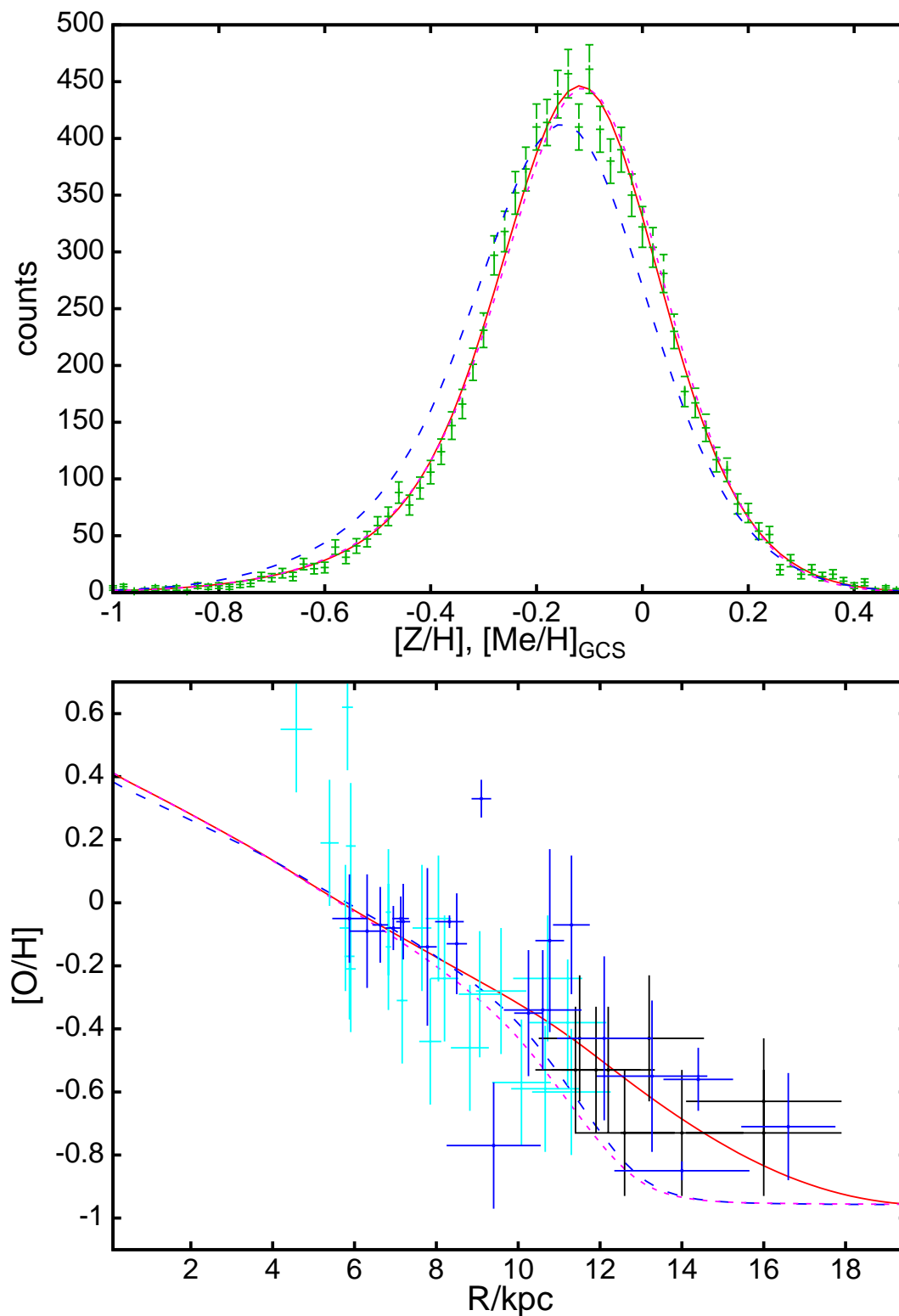
Figure 2.19: Upper panel: the data points are the GCS counts and the red curve is the standard model. The broken blue curve shows the effect on this model of raising Σ_{crit} from zero to $2.5\,\mathrm{M}_\odot\,\mathrm{pc}^{-2}$. The pink dotted curve shows that a good fit to the data can be obtained for this value of Σ_{crit}. Lower panel: measurements of the metallicity of the ISM and the predictions of the models shown above.

age 11.7 Gyr.

2.7 Relation to other work

Chemical evolution models of the Galaxy have a long history and a large literature. It would be inappropriate to attempt to review this literature in this section. Instead we highlight crucial differences with work that has most in common with ours, and relate our work to the analysis of the solar neighbourhood of Haywood (2008).

2.7.1 Comparison with earlier models

Some of the best known models of Galactic chemical evolution are those in Chiappini et al. (1997) and its successors Chiappini et al. (2001) and Colavitti et al (2008). In each case the disc is made up of annuli that exchange neither stars nor gas. Star-formation is driven by a Kennicutt law similar to equation (2.1). Chiappini et al. (1997) introduced a time-dependent infall rate that is superficially similar to (2.6) but differs from our infall rate in two important respects. First, the exponential with the longer time-constant is not turned on until 2 Gyr after the start of Galaxy formation with the consequence that star formation periodically ceases during the interval $1 \, \text{Gyr} < t < 2 \, \text{Gyr}$. Second, Chiappini et al. (1997) make the time constant b_2 a linearly increasing function of radius that vanishes at $R = 0.86 \, \text{kpc}$ (or $1.2 \, \text{kpc}$ in Chiappini et al., 2001), whereas here b_2 is constant. If we were to follow the prescription of Chiappini et al., our inner disc/bulge would become older, and a smaller churning rate would be required to bring stars more metal-rich than the local ISM to the solar neighbourhood. An outwards-increasing infall timescale enhances the metallicity gradient because metallicities are close to their equilibrium values, and these reflect the ratio of current to past SFRs.

Chiappini et al. (1997) adjusted their model's free parameters to optimise its fit to the G-dwarf metallicity distribution for stars in the solar annulus that was determined by Rocha-Pinto & Maciel (1996) from 287 stars that lie within 25 pc of the Sun. Fig. 2.20 illustrates the difference between the metallicity distributions of stars near the Sun and in the entire solar annulus: the full red curve shows the standard model's prediction for the metallicity distribution of GCS stars from Fig. 2.17, while the long-dashed green curve shows the corresponding distribution in the whole annulus. The distribution for the annulus is much broader than that for the GCS because stars with metallicities far from that of the local ISM are typically fast-moving and likely to be at high z. Rocha-Pinto & Maciel (1996) transformed their measured distribution for the local sphere to the modelled global distribution using correction factors estimated by Sommer-Larsen (1991), which depend on the local gravitational potential and the velocity distributions of stars of each metallicity. It is clearly more satisfactory to use internally generated values of these distributions to predict the metallicity distribution in the observed volume around the Sun than to infer the annular distribution from the measured one using external estimates of the velocity distributions. Moreover, the short-dashed blue curve in Fig. 2.20 shows the prediction of Chiappini et al. (1997)
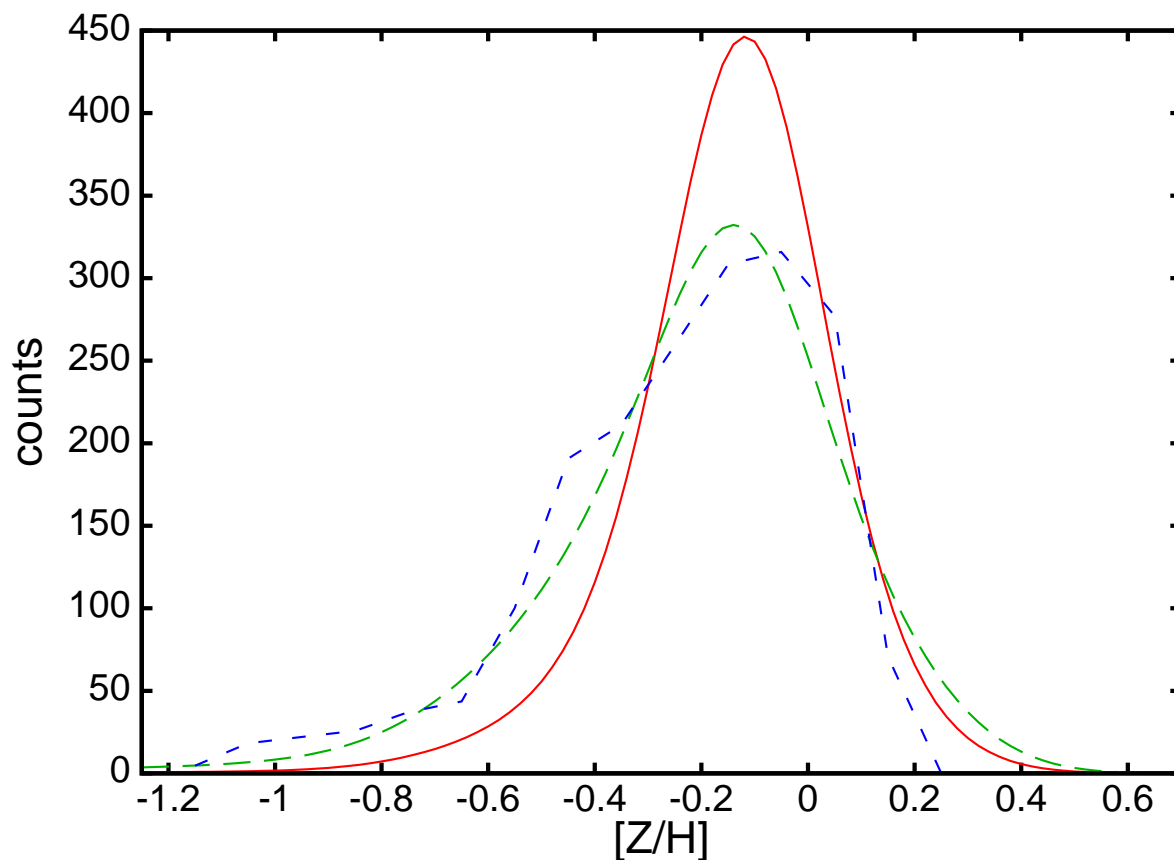
Figure 2.20: Full red curve: the metallicity distribution predicted by the standard model for the GCS stars. Long-dashed green curve: the prediction of the same model for the distribution of the whole solar annulus. Short-dashed blue curve: the prediction of Chiappini et al. (1997) for the solar annulus.

for the solar annulus. It declines much more steeply at high metallicities than the blue curve, predicting far too few metal-rich stars.

The scale of the discrepancy between the blue and the green curves illustrates that a model that provides an adequate fit to the data of Rocha-Pinto & Maciel (1996) is likely to be incompatible with the GCS stars. This discrepancy is partly due to problems with the calibration of the underlying dataset: Haywood (2002) and Twarog (2002) pointed out that the metallicity calibrations of Schuster & Nissen (1989) underlying those datasets severely underestimate the metallicities of metal-rich stars. This underestimation makes the decline in the number of stars at [Fe/H] > 0 steeper than it should be, and thus makes it easier for the data to be fitted by traditional models of chemical evolution, which predict a sharp cutoff at high [Fe/H]. Apart from its superior calibration, the GCS sample is 50 times larger than that used by Rocha-Pinto & Maciel (1996), so its statistical errors are much smaller and it is a more challenging distribution to fit.

In the models of Chiappini et al. (1997), star formation ceases entirely when the surface density

of gas falls below Σ_{crit}, while in our models Σ_{crit} merely marks an increase in the rate of decline of the SFR with decreasing gas density. While a cogent argument can be made for a rapid decline in the SFR at low gas densities, it is hard to justify a discontinuity in the rate. Chiappini et al. (2001) conclude that a non-negligible value of Σ_{crit} plays an essential role in fitting the data. In fact, they set $\Sigma_{\mathrm{crit}} = 7\,\mathrm{M}_\odot\,\mathrm{pc}^{-2}$, with the consequence that star formation in the solar neighbourhood was constantly stopping and starting, both during the first 2 Gyr and the last 4 Gyr of Galactic history (see their Fig. 4). Since the metallicity of the ISM declines when star formation has been switched off, this erratic behaviour broadens the stellar metallicity distribution. In our models the SFR is steady and in fact setting $\Sigma_{\mathrm{crit}} = 7\,\mathrm{M}_\odot\,\mathrm{pc}^{-2}$ would result in almost no stars forming at $R \gtrsim 10\,\mathrm{kpc}$ because the flow of gas through the disc would prevent the surface density building up to $7\,\mathrm{M}_\odot\,\mathrm{pc}^{-2}$. Hence in our models star-formation can occur at large radii only if Σ_{crit} is set to a small or vanishing value. An important difference between our models and those of Chiappini et al. (2001) is that in our models the SFR is a smooth function of time and the bimodality in $[\alpha/\mathrm{Fe}]$ is achieved without a dip in the star-formation rate.

Chiappini et al. (1997) give for the inner and outer parts of their models the radial gradients in the abundances of several elements. These gradients are largest in the inner regions, but even there they are much smaller than in our models: for example at 12 Gyr the inner gradients of [O/H] and [Fe/H] are -0.023 and $-0.027\,\mathrm{dex}\,\mathrm{kpc}^{-1}$ compared to values $\sim -0.08\,\mathrm{dex}\,\mathrm{kpc}^{-1}$ and $\sim -0.11\,\mathrm{dex}\,\mathrm{kpc}^{-1}$ obtained here. Our larger gradients are a direct consequence of the advection inwards of the products of nucleosynthesis. The GCS stars show a similar gradient in [Z/H]: Holmberg et al. (2007) derive a gradient of $-0.09\,\mathrm{dex}\,\mathrm{kpc}^{-1}$.

Colavitti et al (2008) used infall rates measured from simulations of clustering cold dark matter (CDM) in slightly updated models of Chiappini et al. (1997). No empirically determined infall rate gave such satisfactory results as the earlier double-exponential rate. The models were again compared to the metallicity distribution of Rocha-Pinto & Maciel (1996) and in most cases provided inadequate fits to the data. The empirically measured infall rates are very irregular in time, with the result that the model experiences powerful bursts of star formation. These lead to large excursions in the predicted plots of [O/Fe] versus [Fe/H] for which there is no evidence in the data. Moreover, studies of the past SFR in the disc show no signs of major bursts of star formation a few gigayears ago. The disappointing results of this study suggest that the rate at which gas joins the disc is not simply the ratio of masses of baryons and dark-matter times the dark-matter accretion rate. In fact, the wealth of evidence that the majority of baryons are still in the intergalactic medium (Persic & Salucci, 1992; Fukigita et al., 1998) is a clear indication that galaxies do not acquire gas as fast as this naive calculation suggests; rather gas is stored in the warm-hot intergalactic medium (WHIM) and from there accreted at a still uncertain rate. It seems unlikely that chemical evolution models will be successfully coupled to cosmological clustering simulations until we have understood the complex interface between the WHIM, cold infall and galactic fountains.

Naab & Ostriker (2006) determined the infall rate by assuming that the surface density of the disc is always exponential, but with a scale length that is proportional to v_{c}/H, where v_{c} is the Galaxy's circular speed (taken to be constant) and $H(t)$ is the Hubble parameter. The infall

rate at all times and places was fixed by assuming that the central surface density of the disc is constant at its current value. The model's observables were calculated by using the Kennicutt law (2.1) to convert gas to stars. A very simple approach to chemical evolution was employed, in which material does not move between annuli and only the overall metal content Z was followed. In these models the metallicity gradient in the ISM becomes less steep over time, and is now $\sim -0.04\,\mathrm{dex\,kpc^{-1}}$. Their model predicts for the solar neighbourhood fewer metal-rich stars and more metal-poor stars than are in the GCS.

In all these models, solar-neighbourhood stars should satisfy a well defined metallicity-age relation, and the G-dwarf metallicity distribution is simply the result of combining this relation with the SFR-age relation. As we have seen, the observed width of the local metallicity distribution is approximated by exploiting irregular time evolution of the metallicity of the local ISM (cf. also Portinari et al., 1998). As Fig. 2.9 illustrates, our models solve this problem in an entirely different way, and using a simpler history of star formation.

2.7.2 Haywood's analysis of the solar neighbourhood

Haywood (2006) and especially Haywood (2008) has critically re-examined the age-metallicity distribution of the GCS stars and concluded that the data are only consistent with the existence of a well defined age-metallicity relation for disc stars younger than $\sim 3\,\mathrm{Gyr}$; for such young stars the spread in [Fe/H] is consistent with the expected dispersion in the metallicity of interstellar gas at a given radius. At ages larger than $3\,\mathrm{Gyr}$ the width of the metallicity distribution is larger than can be accounted for by measurement errors and inhomogeneity of the ISM. In particular, there are stars with ages $\sim 5\,\mathrm{Gyr}$ that have [Fe/H] $= 0.5$, and stars with ages $< 7\,\mathrm{Gyr}$ that have [Fe/H] $= -0.5$. The older the age bracket that one examines, the wider the range of metallicities present. Our predicted age-metallicity distribution (Fig. 2.6) is in good agreement with that derived by Haywood (2008).

Haywood (2006) finds that when his revised ages are used for GCS stars, the metallicities of thick disc stars increase as their ages decrease. That is, these stars point to rapid self-enrichment of the thick disc. In fact, Haywood argues that the thick disc is not the relic of some captured satellite(s) but an integral part of the Galaxy's disc and has played a central role in the chemical evolution of the thin disc. Chemical evolution models should treat the disc as a whole, not just individual parts. Our results strongly underline this conclusion from a theoretical perspective. The metallicity-age plot shown in Fig. 1(b) of Haywood (2008) is satisfyingly similar to the lower panel of our Fig. 2.6: in both figures the stellar density is highest around ($\tau = 2\,\mathrm{Gyr}$, [Fe/H] $= -0.1$) and in this region the ridge line gradually drops to the right. At older ages the distributions become broader, being confined by [Fe/H] ~ 0.4 and -0.5. At ages greater than $10\,\mathrm{Gyr}$ both distributions reach down to [Fe/H] $= -1$. In fact the small differences between our figure and that of Haywood are readily accounted for by the substantial errors in measured stellar ages. This fit is remarkable because the model parameters were chosen without reference to measured stellar ages.

An argument sometimes advanced for a dichotomy between the thick and thin discs is the ex-

istence of two sequences in the $([\alpha/\text{Fe}], [\text{Fe/H}])$ plane (Fig. 2.9). This diagram suggests that the last thick-disc stars to form had higher abundances than the first thin-disc stars to form. To explain this finding in the context of a conventional chemical-evolution model, sudden dilution of the ISM by a massive gas-rich accretion is required (Bensby et al., 2005; Reddy et al., 2006). Against this proposal Haywood (2006) objects that the bulk of the oldest thin-disc stars have [Fe/H] $\simeq -0.2$ and there is no evidence that the most metal-poor thin-disc stars are particularly old. Our models show that the observed structure of the $([\alpha/\text{Fe}], [\text{Fe/H}])$ plane arises naturally when radial migration is allowed. Haywood (2008) examined the orbital parameters of stars of various metallicities and showed that local thin-disc stars with metallicities that overlap the metallicity range of the thick disc have higher angular momenta than more typical thin-disc stars. Similarly, he found that stars in the high-metallicity tail of the local metallicity distribution have low angular momenta. Even though churning could in principle eradicate the correlation between angular momentum and metallicity, our models reproduce these correlations (Figs 2.9 and 2.10) because blurring makes a sufficiently large contribution to bringing these chemically anomalous stars near the Sun.

Ivezic et al. (2008) also argue that in the SDSS data the kinematic properties of the thick disc evolve continuously with distance from the plane in a way that suggests that the thick disc joins continuously to the thin disc. By contrast, Veltz et al. (2008) argued for a clean break between the thin and thick discs on the basis of shallow local minima in the density of 2MASS stars $n(z)$ in seen at the Galactic poles as a function of photometric distance z. As Veltz et al. (2008) show, minima in $n(z)$ are not expected if the disc is a superposition of two exponential structures, but the minima yield a clean discontinuity in the distribution of velocity dispersions when multi-component isothermal distribution functions are used to model the data. The very unexpectedness of the minima makes the modelled break extremely clean. It will be interesting to see whether the distribution of measured radial velocities of stars in the RAVE survey substantiate these model velocity distributions.

2.8   Conclusions

It is now more than forty years since the theory of stellar evolution attained the level at which it became possible to model the chemical enrichment of the ISM. From the beginning of that endeavour measurements of the abundances of individual solar-neighbourhood stars have played a key role because a star preserves like a time capsule the state of the ISM at the remote epoch of its formation. Considerable theoretical and observational efforts have been devoted to probing the history of the Galaxy with this connection.

Half a century ago, Roman (1950, 1954) and others discovered the connection between the kinematics and chemistry of stars, yet curiously little has been done to include kinematics in models of chemical evolution. The general presumption has been that each annulus of the disc evolves independently of others, and the well-known correlations between chemistry and kinematics can be understood as arising through the stochastic acceleration of stars: older stars tend to have

larger random velocities and lower metallicities. No effort was made to develop greater diagnostic power by simultaneously modelling chemistry and kinematics.

The continued use of mutually independent annuli by modellers of chemical evolution is surprising given that it was from the outset recognised that many stars are on significantly non-circular orbits that each radial half-period cover more than a kiloparsec in radius. In fact, it has generally been assumed that the radial velocity dispersion within the disc rises as one moves inward to values that lead to radial excursions of several kiloparsecs (see Fig. 2.4). Moreover, observations have long indicated that galactic discs have significant metallicity gradients (e.g. Vila-Costas & Edmunds, 1992; de Jong, 1996), so radial migration of stars is bound to leave a signature on the metallicity distribution of solar-neighbourhood stars. We have called this aspect of radial migration "blurring".

The present study owes its impetus to the discovery by Sellwood & Binney (2002) that radial migration is a more potent process than mere blurring: the dominant effect of transient spiral arms is not to heat the stellar disc as had been supposed, but to cause stars either side of corotation to change places without moving to eccentric orbits ("churning"). Sellwood & Binney (2002) did not demonstrate that gas participates in churning, but they argued that it must on dynamical grounds, and Roskar et al. (2008a) found evidence that this was the case in their N-body–SPH simulations of galaxy formation. Since churning is an aspect of spiral structure that can *only* be probed through its impact on chemical evolution, we wanted chemical-evolution models that included churning, and logically it was natural to extend these models to include both blurring and radial gas flows.

An ingredient of our models that might be controversial is the introduction of radial gas flows. We have absolutely no reason to expect that the infall profile is exponential, so if discs are to be exponential this must be the result of flows through the discs redistributing mass within the disc. In fact, as gas streams through spiral arms it dissipates energy in shocks that is ultimately gravitational energy that becomes free as the gas surrenders angular momentum to the stars and drifts inwards. Hence at some level inward gas flows are mandatory (Lacey & Fall, 1985).

Unfortunately, the theory of galaxy formation has yet to advance to the point at which it can prescribe the spatial and temporal structure of gas accretion, so it is necessary to parametrise accretion in some way. The accretion process must be constrained to result in the formation of the observed stellar and gaseous discs. Our accretion Scheme AB satisfies this constraint for all values of the parameters, but it is inevitably acausal in that the formation mechanism is being driven by its known outcome. While its acausality is unattractive, Scheme AB is a flexible parametrisation that enables us to form exponential discs for a variety of different assumptions about the radial density of infalling gas, and the resulting radial profiles of infall and gas-flow (Fig. 2.2) are entirely plausible.

The impact that radial migration has on the local metallicity distribution obviously varies with the magnitude of the metallicity gradient in the ISM, which in turn depends on the gas flow within the disc and therefore the radial infall profile. For this reason the most important parameters of our models are f_A and f_B, which control the distribution of infalling gas.

The models provide good fits to the GCS counts of stars as functions of [Fe/H], M_V, T_{eff} and

stellar age, as well as reproducing the correlations between tangential velocity and abundance patterns that have been pointed out by Haywood (2008). These fits are achieved by churning, blurring and radial flows working together. They depend on the existence of an appreciable metallicity gradient in the ISM, which is established by the radial flow of gas, and they depend on radial mixing of stars by blurring and churning. The steeper the metallicity gradient in the gas, the smaller the effect of churning can be, but for any observationally consistent metallicity gradient, churning has a non-negligible role to play.

The models describe the coevolution of the thick and thin discs, and presume that thick-disc stars were formed in the Galaxy rather than accreted from outside. Given the simplicity of our assumptions, the extent to which a dichotomy between an α-enhanced thick disc and a solar-type thin disc automatically manifests itself in the models is remarkable. In particular, in the solar annulus the distributions of [O/H] at given [Fe/H] are bimodal in the range of [Fe/H] associated with the overlap of the two discs (Fig. 2.9), the vertical density profile can be represented at the sum of two exponentials, and at $R < R_0$ the radial density profile becomes flatter at lager distances from the plane (Fig. 2.8). None of these characteristics is dependent on our choice of a double exponential for the time dependence of infall: a model in which the gaseous mass, and therefore star-formation rate, is held constant also has these features. They are consequences of the $\sim 1\,\mathrm{Gyr}$ timescale of type Ia supernovae and the secular heating and churning of the disc.

The models assume that scattering of stars increases the velocity dispersion of a coeval population as $t^{1/3}$, but the models go on to predict that within the solar neighbourhood velocity dispersion increases as a higher power of age, roughly $t^{0.45}$ in agreement with what is found from Hipparcos stars with good parallaxes. This finding may reconcile scattering theory, which cannot readily explain an exponent in excess of $1/3$, with observations. The key point is that radial mixing brings to the solar neighbourhood stars born at small radii, where the velocity dispersion is undoubtedly large.

The nucleosynthetic yields from each generation of stars are still significantly uncertain. Our philosophy has been to use standard values from the literature rather than exploit uncertainties in the yields to tune the models to the data. The yields we are using are in the upper region of those that can provide adequate fits to the data, with the consequence that increasing the value of the mass-loss parameter f_{eject}, which is degenerate with the magnitude of the yields, makes it easier to fit the data. Our yields are surely not exactly right and consequently some of the properties the models derive from them will be in error. On account of these uncertainties we have suppressed the predictions of our code for the abundances of certain elements, most notably carbon.

The discovery that three-dimensional, non-equilibrium models of the solar atmosphere require the metal abundance of the Sun to be $Z_\odot = 0.012 - 0.014$ (Grevesse et al., 2007) poses a major problem for this field. A prerequisite for successful chemical modelling is a consistent metallicity scale for both stars and the ISM. At present the only consistent scale is the traditional one on which $Z_\odot = 0.019$, so this is the one we have used.

If a new scale were established on which all metallicities were significantly lower, viable models could be produced by lowering the yields. A straightforward way to do this would be to lower the maximum mass in the IMF: reducing this mass from $100\,\mathrm{M}_\odot$ to $50\,\mathrm{M}_\odot$ would reduce yields

by ~ 30 percent in line with the proposed reduction in $Z_\odot$. The oxygen yield would come down fastest, reducing [O/Fe] by $\sim 0.2\,\mathrm{dex}$.

Although we believe that this study represents a significant advance on all previous models of Galactic chemical evolution, it is highly imperfect. Some major weaknesses of our work are the following.

1. We have assumed that the probability of mass interchange between rings is proportional to the product of the rings' masses. This probability reflects the number and intensity of spiral feature with corotation at that radius, and should be a function of both mass and velocity dispersion. A further study of self-gravitating discs similar to that of Sellwood & Binney (2002) would be necessary to determine this function.

2. We have assumed that the vertical and radial motions of stars decouple. This assumption has a significant impact on both the relation between age and velocity dispersion in the so-lar neighbourhood and on the predicted vertical density profile in the solar annulus, which is interesting in itself and impacts on the selection function of GCS stars and thus on our choice of standard model. The assumption is unjustifiable for stars on eccentric orbits, which do play an important role in the model fits. Unfortunately, a sounder treatment is impossible until a better approximation to the third integral of Galactic dynamics is avail-able. It is our intention to resolve this problem through "torus modelling" (e.g. McMillan & Binney, 2008).

3. Our models include radial mixing of gas through churning and viscous inspiralling, but do not include radial redistribution of gas by the Galactic fountain (e.g. Benjamin & Danly, 1997). A significant body of evidence indicates that star formation drives neutral hydrogen to kiloparsec heights above the plane. NGC 891, which is not dissimilar to the Galaxy, has ~ 25 per cent of its neutral hydrogen more than $1\,\mathrm{kpc}$ from the plane (Oosterloo et al., 2007). This extraplanar gas must move over the plane on nearly ballistic trajectories, and in the absence of interaction with the corona (gas at the Galaxy's virial temperature $\sim 2 \times 10^6\,\mathrm{K}$), the gas must return to the plane further out than its point of ejection. However, observations suggest that neutral gas above the plane is actually flowing inward rather than outward, presumable as a result of interaction with the corona (Fraternali & Binney, 2008). The mass of extraplanar gas is so large and the timescale for its return to the plane so short that whichever way this gas flows, it has a considerable potential for radially redistributing metals. Extraplanar gas must be ejected from the disc by supernova-heated gas that is probably highly metal-rich. Some of this gas will be lost to the Galaxy as we have assumed, but some of it will return to the plane with infalling gas. Again there is potential here for significant radial redistribution of metals that has been ignored in the present study.

4. Our treatment of the inner Galaxy is unacceptably crude in that we have replaced the bar/bulge with a disc. Unfortunately introducing the bar opens a Pandora's box of com-plexities, and at the present time is probably only feasible in the context of a particle-based

model such as those of Samland & Gerhard (2003) and Roskar et al. (2008b). Our hope is that our imaginary central disc has a similar impact on the chemodynamical state of the local disc to the combined impact of the giant star-forming ring at $R \simeq 4\,\text{kpc}$, the gas-deficient region interior to this ring and the star-forming x_2 disc at $R \lesssim 200\,\text{pc}$.

From this list of shortcomings of our models it is clear that we are still far from a definitive account of the Galaxy's chemical evolution. We shall be satisfied if we have convinced the reader that the interplay between dynamics and chemistry is so tight at to be indissoluble. This fact is at one level inconvenient because it undermines the value of conclusions drawn from traditional models of chemical evolution. But at another level it represents an opportunity to learn more. The connection between the kinematics of stars and the compositions of stars and gas, which can be measured in great detail, involves three areas about which we are too ignorant: the distribution of dark matter within and around the Galaxy, the Galaxy's history of assembly, and the nature of the Local Group's IGM. By building dynamical models of the Galaxy that have chemical evolution built in to the basic structure, we should be able to make decisive progress with one of the major problems of contemporary astronomy.

2.9 Appendix: Origin of bimodal [O/Fe] distributions

We provide an analytic model of the development of the bimodal distributions of [O/Fe] evident in Fig. 2.9. We assume that star formation starts at $t = 0$ and that the SFR is $\propto e^{-Kt}$ for $t > 0$. Consistent with equation (2.5), we assume that a coeval group of stars formed at t' generates a rate of type Ia supernovae that vanishes for $t < t' + t_0$ and is subsequently $\propto e^{-k(t-t')}$. Then given that the rate of core-collapse SNe is proportional to the SFR, the rate of production of Fe is

$$\frac{\mathrm{d}M_{\text{Fe}}}{\mathrm{d}t} = \begin{cases} be^{-Kt} & \text{for } t < t_0 \\ be^{-Kt} + c\int_0^{t-t_0} \mathrm{d}t' \, e^{-Kt'} e^{-k(t-t')} & \text{for } t \geq t_0 \end{cases}, \tag{2.20}$$

where b and c are constants. Integrating this production rate, we obtain the iron mass at time $t > t_0$ as

$$M_{\text{Fe}}(t) = b\frac{1 - e^{-Kt'}}{K} \tag{2.21}$$
$$+ \frac{c}{k-K}\left(e^{-(k-K)t_0}\frac{e^{-Kt_0} - e^{-Kt}}{K} - \frac{e^{-kt_0} - e^{-kt}}{k}\right).$$

In the approximation that SNIa do not contribute α elements, and that the delay in the production of these elements by a stellar population is $\ll 1/k$, the mass of α elements is $M_\alpha = (1 - e^{-Kt})a/K$
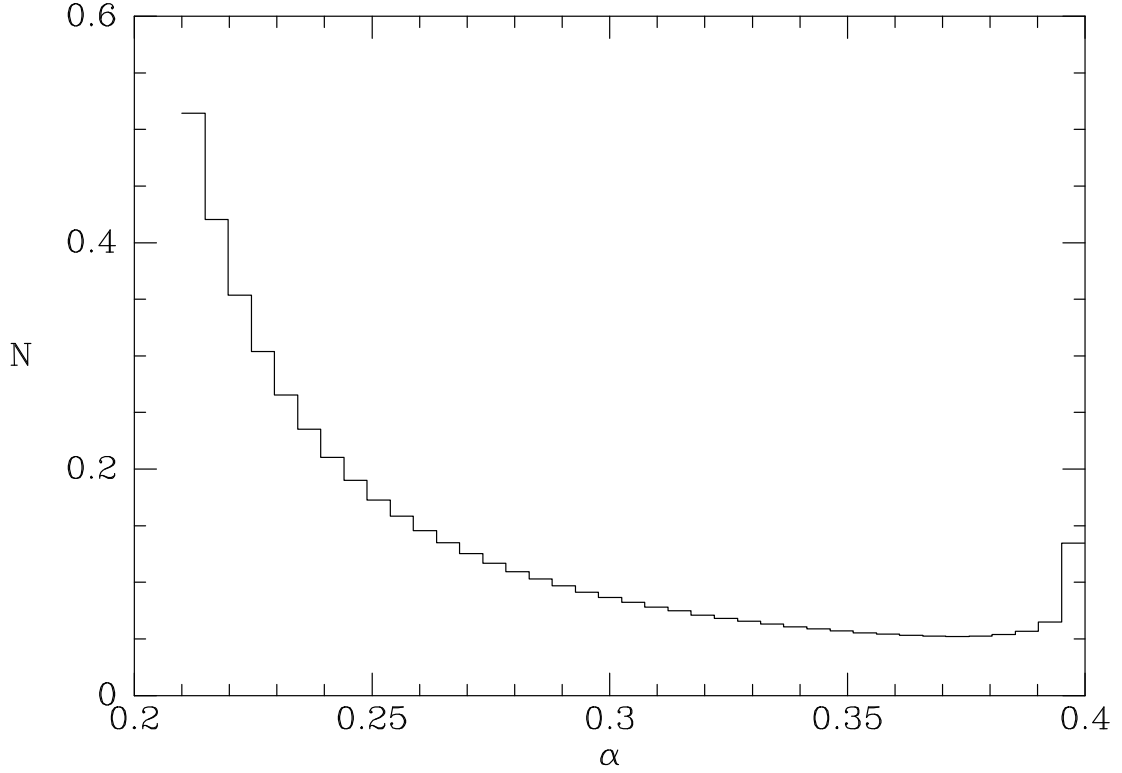
Figure 2.21: The distribution of α abundances predicted by equation (2.21).

where a is a constant. Then equation (2.21) predicts that $\alpha \equiv M_\alpha/M_{\mathrm{Fe}}$ equals a/b for $t \leq t_0$ and then drops rapidly towards its asymptotic value,

$$\alpha(\infty) = \frac{b}{K} + \frac{c}{Kk}\mathrm{e}^{-kt_0}. \tag{2.22}$$

Fig. 2.21 plots the distribution at $t = 13\,\mathrm{Gyr}$ of stars over α when the initial and asymptotic values of α are set to 0.4 and 0.2 and the other parameters are $K = 1/7\,\mathrm{Gyr}$, $k = 1/1.5\,\mathrm{Gyr}$ and $t_0 = 0.3\,\mathrm{Gyr}$, which allows $0.15\,\mathrm{Gyr}$ for white dwarfs to form and $0.15\,\mathrm{Gyr}$ for them to accrete prior to deflagrating.

Chapter 3

Origin and structure of the Galactic disc(s)[1]

3.1 Abstract

We examine the chemical and dynamical structure in the solar neighbourhood of a model Galaxy that is the endpoint of a simulation of the chemical evolution of the Milky Way in the presence of radial mixing of stars and gas. Although the simulation's star-formation rate declines monotonically from its unique peak and no merger or tidal event ever takes place, the model replicates all known properties of a thick disc, as well as matching special features of the local stellar population such as a metal-poor extension of the thin disc that has high rotational velocity. We divide the disc by chemistry and relate this dissection to observationally more convenient kinematic selection criteria. We conclude that the observed chemistry of the Galactic disc does not provide convincing evidence for a violent origin of the thick disc, as has been widely claimed.

3.2 Introduction

Our Galaxy's stellar disc was first divided into two components because the vertical density profile derived from star counts could be fitted by a superposition of two exponentials but not by a single exponential (Gilmore & Reid, 1983). Further investigations revealed a thick-disc component that was characterised by a high velocity dispersion, high α enrichment and a remarkably old age. Many authors consider the thick disc to be a relic of a turbulent era of Galactic history in which the thick disc formed from accreted satellites and/or a thin disc was violently heated by one or more merger events (for a discussion see e.g. Reddy et al., 2006). A violent origin of the thick disc is strongly supported by traditional models of chemical evolution (see e.g. Chiappini et al., 1997). These models require a period of rapid star formation early in the life of the disc, followed by a period in which star formation effectively ceased in which the interstellar medium

---

[1] Content and text of this chapter have almost identically been published as Schönrich & Binney (2009b).

could be enriched with iron by SNIa and the overall metallicity level could be brought down by accretion of metal-poor gas.

In an earlier paper (Schönrich & Binney, 2009a, hereafter SB09) we showed that when one allows for radial mixing, which is an unavoidable consequence of spiral structure (Sellwood & Binney, 2002; Roskar et al., 2008a), a two-component disc arises naturally in the simplest model, in which the star-formation rate (SFR) is a monotonically declining function of time from its global maximum. In this paper we examine in greater depth the contents of the model's solar neighbourhood, especially its characteristic stellar populations. We identify the solar-neighbourhood signatures of the thin and thick discs and analyse the relationship between the chemistry and kinematics of nearby stars. This exercise enables one to understand better the relationship between the underlying nature of the thin and thick discs and samples of stars that have been selected by kinematic, chemical or spatial criteria. A better understanding of this relationship is of considerable practical importance because substantial allocations of telescope time are currently committed to spectroscopic surveys (SEGUE, RAVE, HERMES, WFMOS, Gaia) that are designed to unravel the nature and history of the thick disc, and a clear picture will not emerge from these surveys without a secure understanding of selection effects.

The paper is structured as follows. In Section 2 we summarise the physics that underlies the model and analyse its prediction for the disposition of solar-neighbourhood stars in the $([Fe/H], [\alpha/Fe])$ plane. We identify the thin and thick discs within this plane, and show how the kinematics and ages of stars vary within the $([Fe/H], [\alpha/Fe])$ plane. The structures we identify seem to have all the properties expected of the Galaxy's thin and thick discs. In Section 3 we explore the extent to which stars can be successfully assigned to the thin and thick discs by kinematic selection. We show that this process cannot be clean. Finally in Section 4 we sum up and relate the characteristics of the features we have identified to the formation history of our model. Since the SFR in the model has been monotonically decreasing from its global maximum, and no merger or tidal event has ever occurred in it, we conclude that, contrary to widespread belief, features of the Galaxy, such as the overlap in [Fe/H] of the thin and thick discs do not in fact constitute convincing evidence for a violent origin of the thick disc.

3.3 The model

3.3.1 Physical inputs

The SB09 model is the endpoint of a simulation of chemical evolution within a disc in which the star-formation rate, which is controlled by the surface density of the ISM as in the Kennicutt (1998) law, declines monotonically with time from a unique global maximum. The gas disc always has an exponential surface density with scale length 3.5 kpc so that by the Kennicutt law the young stellar disc has an exponential surface density with scale length 2.5 kpc. The assumptions regarding the (universal) initial mass function, stellar lifetimes and yields are also taken from the literature. The only novel features are a radial flow of gas within the disc and radial migration of stars. The latter occurs both because over time stars change their angular momenta
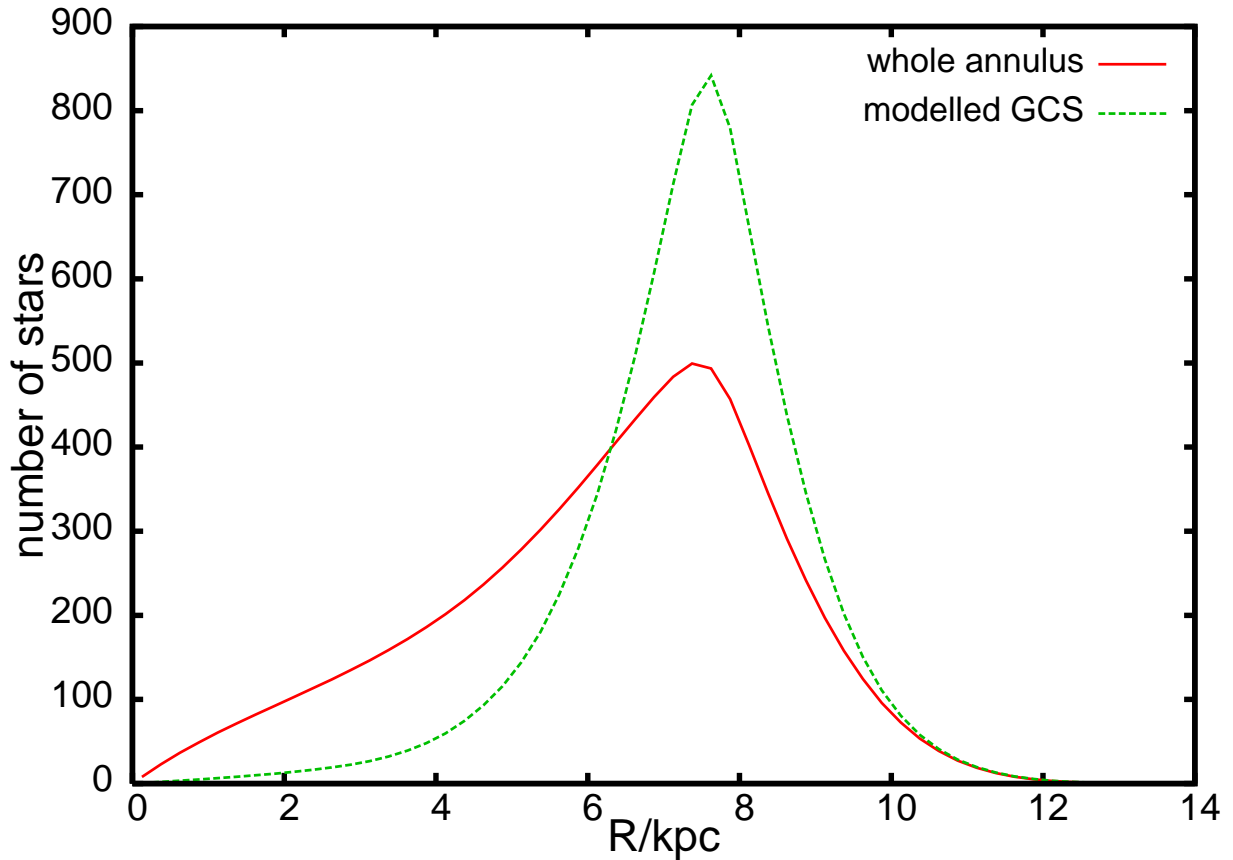
Figure 3.1: The distribution of birth radii of stars in the model GCS sample (green dashed line) and of all stars in the solar cylinder (solid red line).

("churning") and because they move on orbits that become increasingly eccentric and inclined to the Galactic plane ("blurring"). Traditional models of Galactic evolution have ignored these effects although it has always been evident that blurring occurs. The importance of churning was only realised when Sellwood & Binney (2002) found that even weak spiral structure in N-body simulations causes stars to shift their guiding centres by a kiloparsec and more in a single dynamical time. These motions, which arise when a star is at the corotation resonance with a spiral arm, do not heat the disc, so they come to light only when the angular momenta of individual stars are followed. In the model the extent of churning is governed by a parameter k_{ch} that could be determined from N-body models if we knew the past strength of spiral structure. SB09 determined k_{ch} by fitting the model to the distribution of solar-neighbourhood stars in [Fe/H]. The radial dependence of churning strength was taken to be proportional to the product of surface density and radius ΣR, following an argument based on disc instabilities.

The dashed green line in Fig. 3.1 shows the distribution of birth radii of stars in the model GCS sample. Because the GCS stars lie near the plane, the fraction of these stars that are young is higher than the fraction of young stars in the entire solar cylinder. This bias towards young stars
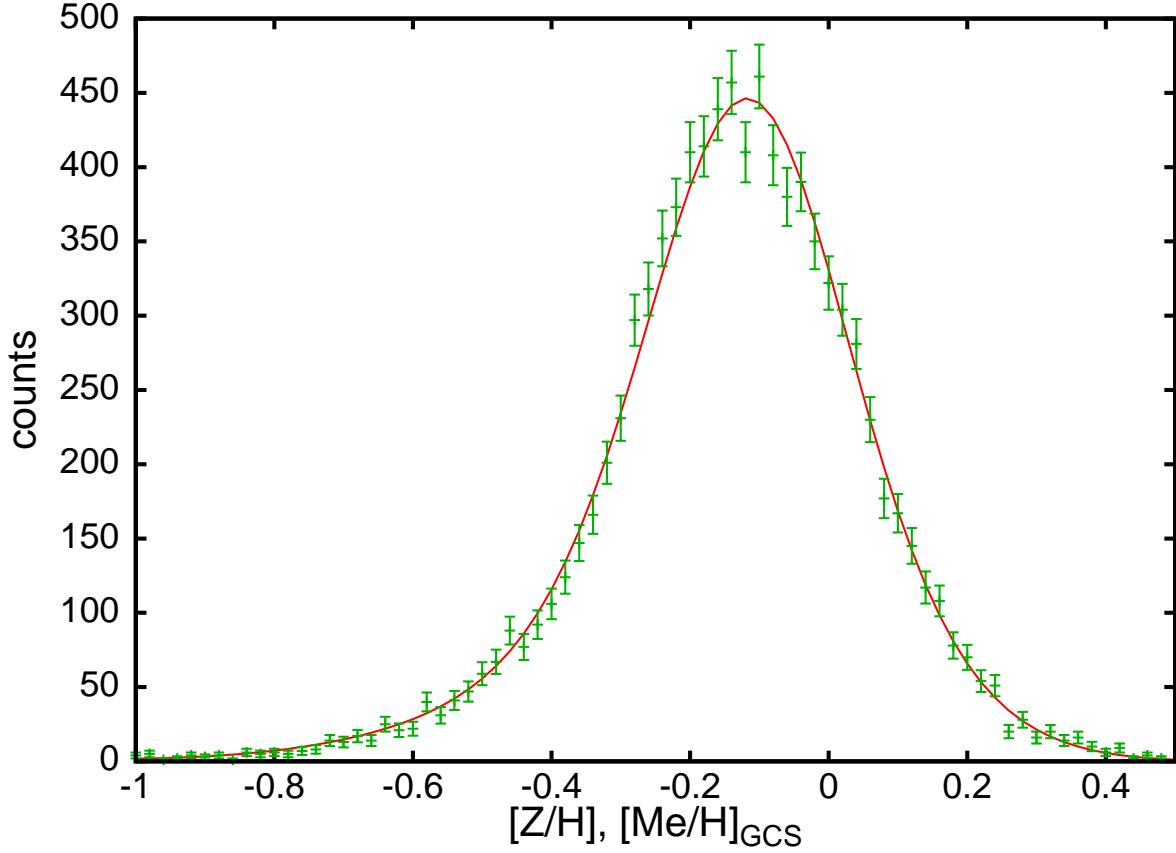
Figure 3.2: The metallicity distribution of solar-neighbourhood stars: data points from Holmberg et al. (2007); red curve the SB09 model. For the model total metal abundance is plotted horizontally, while for the data the plotted quantity is the photometric metallicity indicator given in Holmberg et al. (2007).

leads to the distribution of birth radii of GCS stars being narrower than the distribution of birth radii for all stars in the solar cylinder, which is show by the full red curve in Fig. 3.1. The difference between the two distributions is largest for stars born at $\lesssim 5\,\mathrm{kpc}$ because those inner disc stars have larger vertical velocity dispersions and therefore larger scaleheights.

Hot gas was assumed to be too far from the disc to take part in churning, while the cold gas and stars were assumed to be equally involved in this process. It is likely that these assumptions exaggerate the impact of churning on old stellar populations, which have high velocity dispersions, relative to its impact on young stellar populations. Since there is as yet no basis for quantifying the impact of velocity dispersion on churning rate, the model of Paper I avoids additional undetermined parameters by ignoring this possibility.

The flow of gas within the disc enables the surface density of star formation to be an exponential function of radius even though the rate at which accreted gas joins the disc does not necessarily vary exponentially with radius. The surface density of inflow of metal-poor gas and the flow of

gas within the disc are jointly controlled by two parameters, f_A and f_B, which substitute for a knowledge of the radial profile of cosmic infall. Attempts to obtain the latter from simulations (e.g., Colavitti et al, 2008) have not been successful, probably because much of the gas that joins the disc spends a significant time after infall in the warm-hot intergalactic medium (WHIM). Hence at the present time we must parametrise the infall in some way. SB09 found that f_B is effectively set by the measured oxygen gradient in the ISM, and f_A was fitted alongside k_{ch} to the local metallicity distribution of stars. Fig. 3.2 shows the fit that was obtained to data for $\sim 10\,000$ non-binary stars in the Geneva–Copenhagen survey (Nordström et al., 2004; Holmberg et al., 2007, hereafter GCS).

The random velocities of stars formed at a given radius are assumed to increase with age τ as $\tau^{1/3}$ in line with the predictions of both theory (Jenkins, 1992) and studies of the solar neighbourhood (Just & Jahreiss, 2007; Aumer & Binney, 2009). We have modified the Schönrich & Binney (2009a) model very slightly by increasing the $\langle v_R^2 \rangle^{1/2}$ of a 10 Gyr-old population of local stars from $38\,\mathrm{km\,s^{-1}}$ (cf Dehnen & Binney, 1998b) to $45\,\mathrm{km\,s^{-1}}$. This increase brings the $\langle v_R^2 \rangle^{1/2}$ for the entire GCS sample into line with the observed value. In concordance with observations (e.g. Lewis & Freeman, 1989) the square of the intrinsic velocity dispersion at a given age is assumed to scale with radius as $\mathrm{e}^{-R/1.5R_*}$, where $R_* = 2.5\,\mathrm{kpc}$ is the scale-length of the stellar disc, so $\langle v_R^2 \rangle^{1/2} \simeq 90\,\mathrm{km\,s^{-1}}$ at $R = R_*$. The square of the vertical velocity dispersion component is assumed to show a slightly steeper rise (implying approximately constant scaleheight) being proportional to e^{-R/R_*}.

3.3.2   Predictions of the model

The merit of the SB09 model is that it tracks the kinematics of stars in addition to their chemistry. Observations always have a kinematic bias of some kind, either because they are restricted to stars that lie near the Sun and therefore the plane, a region favoured by stars with small vertical velocity dispersions, or (as in Juric et al., 2008; Ivezic et al., 2008) because they focus on faint stars that are far from the plane, or because an explicit high-velocity criterion is applied in order to reduce contamination of a thick-disc sample by thin-disc stars. A model that includes both chemistry and kinematics is essential for the interpretation of a kinematically selected study.

The SB09 model makes predictions for the global structure of the Galaxy's stellar and gas discs, but in this paper we focus on the solar neighbourhood, and especially the stars that happen to lie within 100 pc of the Sun. This volume is of particular interest because within it G-dwarfs are bright enough to have good Hipparcos parallaxes, measured radial velocities, and in a few cases medium-to-high resolution spectra from which detailed chemical abundance patterns can be extracted. The GCS provides space velocities, surface gravities and metallicities for this volume, and detailed abundance analyses have been carried out for much smaller subsets of stars (Fuhrmann, 1998; Bensby et al., 2003; Venn et al., 2004; Bensby et al., 2005; Gilli et al., 2006; Reddy et al., 2006). Because the GCS sample is essentially magnitude limited, it is not representative of the volume typically simulated by models of chemical evolution, namely a cylindrical annulus around the disc. In particular, thick-disc stars are under-represented within
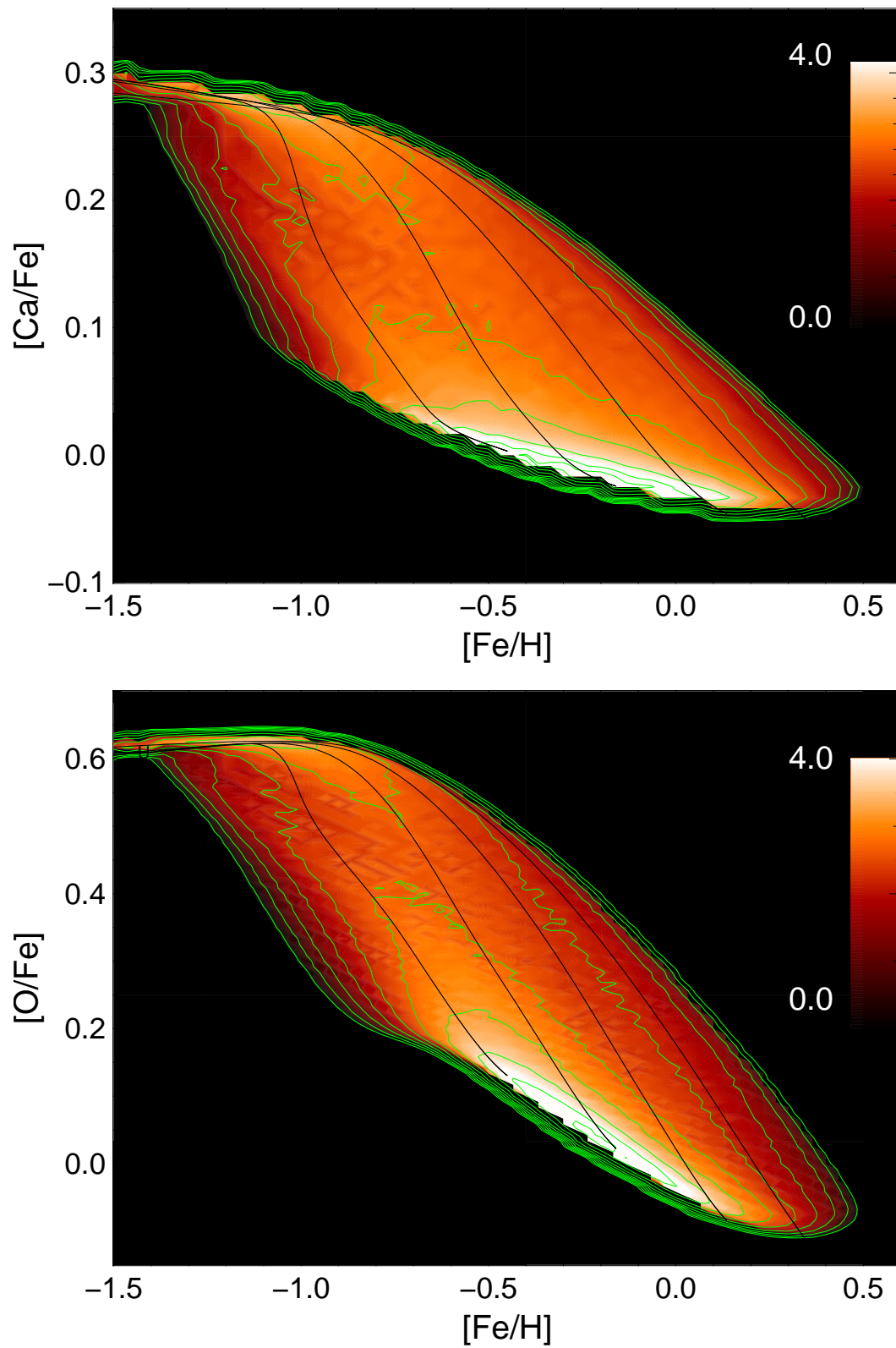
Figure 3.3: Logarithmic stellar densities for a simulated GCS stellar sample in the ([Ca/Fe], [Fe/H]) (top) and ([O/Fe], [Fe/H]) planes. Contours have a 0.5 dex spacing. Black lines track the development of the cold ISM in annuli of radii of (from right to left) 2.5, 5.0, 7.5 and 10 kpc.

the GCS relative to a cylindrical annulus. The SB09 model provides an arena in which the impact of this bias can be assessed.

Fig. 3.3 shows the densities of simulated GCS stars in the $([Fe/H], [Ca/Fe])$ (upper) and $([Fe/H], [O/Fe])$ planes. Trajectories of the cold ISM at galactocentric radii of $10, 7.5, 5, 2.5 \, \mathrm{kpc}$ (from left to right) are indicated by black lines. The ISM starts at early times with low metallicity and high α enhancement at the top left of each panel. As the gas is enriched with metals, each trajectory moves to the right. With the onset of SNIa, the composition of stellar yields shifts towards iron, so $[\alpha/Fe]$ decreases and the trajectories move downwards. Eventually the ISM approaches a steady state in which additional enrichment is balanced by the infall of fresh metal-poor material from the IGM. Since the delay of SNIa-enrichment is assumed to be independent of environment, the time at which trajectories first move downward is independent of radius. By the fact that the timescale of SNIa-enrichment does not vary with radius either, the ISM trajectories tend to be nearly aligned. Thus the point of turndown is at higher metallicities (further to the right) for populations closer to the Galactic centre, where the ISM is enriched faster by more intense star formation relative to the present gas mass.

The colours and green contours in Fig. 3.3 show the density of stars within each plane. In each panel two ridges of high density are apparent – one at high $[\alpha/Fe]$, which we call the metal-poor thick disc and one at low $[\alpha/Fe]$, which is associated with the thin disc. Crucially, the thin-disc ridge runs at a large angle to the black trajectories of the ISM. Thus the thin-disc ridge in no sense traces the chemical history of the thin disc; instead it reflects the spread in radii of birth of local stars, which gives rise to a spread in [Fe/H] by virtue of the metallicity gradient within the ISM (which is larger in the SB09 model than in traditional models of chemical evolution). In a similar manner the thick-disk ridge follows the evolution of all rings at low metallicities, but stretches significantly to higher [Fe/H] than the point at which the solar annulus leaves it.

The depression in the stellar density between the ridges in Fig. 3.3 is a consequence of the rapid downward motion of all trajectories after the onset of SNIa, and of the ISM approaching a steady state as it enters the thin-disc ridge line; relatively few stars are formed at intermediate values of $[\alpha/Fe]$. Variations in the timescales of enrichment will change the depth of the depression – for example, a shorter timescale for the decay of SNIa progenitors will cause trajectories to move downwards faster, leading to fewer stars in the intermediate region. Our models use a prescription for SNIa that is standard for models of chemical evolution, with no SNIa until $0.15 \, \mathrm{Gyr}$ after star formation, and then an exponential decay in the rate of SNIa with time constant $1.5 \, \mathrm{Gyr}$. Mannucci et al. (2006) suggest that $\sim$half SNIa explode promptly (within $0.1 \, \mathrm{Gyr}$ of star formation) and the rest explode at a rate that declines exponentially with time constant $3 \, \mathrm{Gyr}$. The existence of prompt SNIa would not materially affect our work as long as a significant fraction of SNIa are in the population with a long time constant, since the prompt SNIa will lower the alpha-enhancement level of the thick disc component, but not affect the evolution between the two density ridges in the abundance plane. Förster et al. (2006) showed that timescales are very weakly constrained by SNIa counts due to uncertainties in the star-formation histories.

Since both Ca and O are α-elements, the distributions in the upper and lower panels of Fig. 3.3 are qualitatively similar, and O will be the only α-element explicitly discussed below.
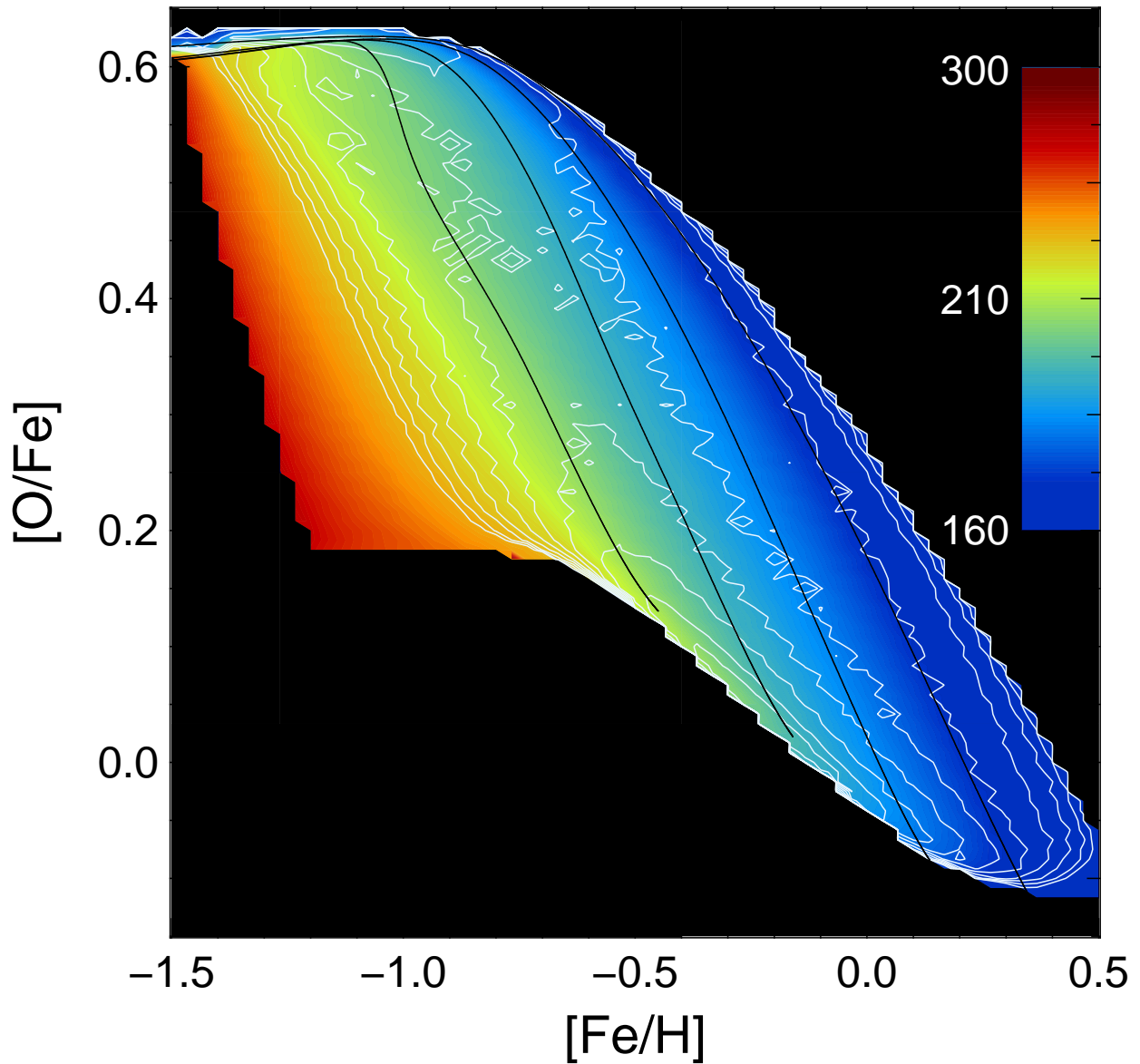
Figure 3.4: The structure of a simulated sample of GCS stars in the ([Fe/H], [O/Fe]) plane. Contours spaced by 1 dex give the density of stars in this plane, while colour codes the average rotational velocity of the stars found at the point in question – the local circular speed is assumed to be 220 km s^{-1}. Black lines give the trajectories of the cold ISM during the model Galaxy's evolution for galactocentric distances of (from left to right) 10, 7.5, 5, 2.5 kpc.

As Haywood (2008) has pointed out, the principal tracers of radial mixing are the large dispersion in the metallicities of stars in the solar neighbourhood and the strong increase in this dispersion with age, which is caused by immigration of high-metallicity stars from inwards and low-metallicity stars from outwards. In fact, as SB09 demonstrated, it is impossible to fit the shape of the local metallicity distribution under plausible assumptions without radial mixing.

As well as generating a large dispersion in the metallicities of old stars, radial migration has a big impact on the interdependence of kinematics and chemistry. This impact is illustrated by Fig. 3.4, which is another plot of the $([Fe/H], [O/Fe])$ plane, but now with colour indicating the mean rotation velocity of stars at each point – blue indicates low rotation velocities and red large ones. We see that at any given value of $[\alpha/Fe]$, there is a tight correlation between $[Fe/H]$ and rotation velocity in the sense that high $[Fe/H]$ implies low rotation velocity because stars with high $[Fe/H]$ are migrants from small radii and tend to be deficient in angular momentum, while stars with low $[Fe/H]$ are migrants from large radii. The black lines that show the trajectories of the ISM almost constitute contours of constant mean rotation velocity, but there is a barely perceptible tendency for the rotation velocity to decrease as one moves up along a black line.

While the correlation between $[Fe/H]$ and rotation velocity seen in Fig. 3.4 is qualitative consistent with stars being scattered to more eccentric orbits while retaining their angular momenta ("blurring"), quantitatively changes in angular momentum ("churning") play a big role in structuring Fig. 3.4. While churning does occasionally move the guiding-centre radius of a star from $R_g < R_0$ to $R_g > R_0$ and thus increase the mean rotation speed at large $[Fe/H]$, the dominant effect of churning is to move guiding centres from $R_g \ll R_0$ to $R_g < R_0$ such that a *very* metal-rich star is found in the solar neighbourhood at a relatively low rotation velocity. To illustrate the impact of churning quantitatively, if angular momentum were conserved, the population born 5 kpc from the Galactic centre would have $v_\phi \sim 150\,\mathrm{km\,s^{-1}}$, while stars born at 10 kpc would have $v_\phi \sim 300\,\mathrm{km\,s^{-1}}$. In the simulated sample, the mean speeds associated with these radii of birth are actually $200\,\mathrm{km\,s^{-1}}$ and $240\,\mathrm{km\,s^{-1}}$.

Churning substantially increases the chemical heterogeneity of the stars that one finds near the Sun with a given V velocity: if high-α, high-$[Fe/H]$ stars were brought to the Sun only by blurring, then all stars with a given V and therefor angular momentum would have identical chemistry. By changing the angular momenta of stars, churning ensures that stars of a given chemical composition are seen near the Sun over the whole range in V.

In Fig. 3.4 the density of stars is indicated by white contours, which are spaced by 1 dex. The very top edge of the populated region is shaded blue, indicating low rotation velocities. Thus the highest-α stars form a structure with a large asymmetric drift. This fact reflects the large velocity dispersion of these stars, and the increased opportunity for migration enjoyed by this old population. Note that in this region of the diagram the colour rapidly changes to red as one moves downwards. Hence there is also a population of high-α stars that have large rotation velocities. These are typically slightly less old stars that formed outside the solar radius. The thin-disc ridge line at low α enhancement ranges from the strongly trailing at high metallicities to high rotational velocities and slight α enhancement at low $[Fe/H]$, as found observationally by Haywood (2008).
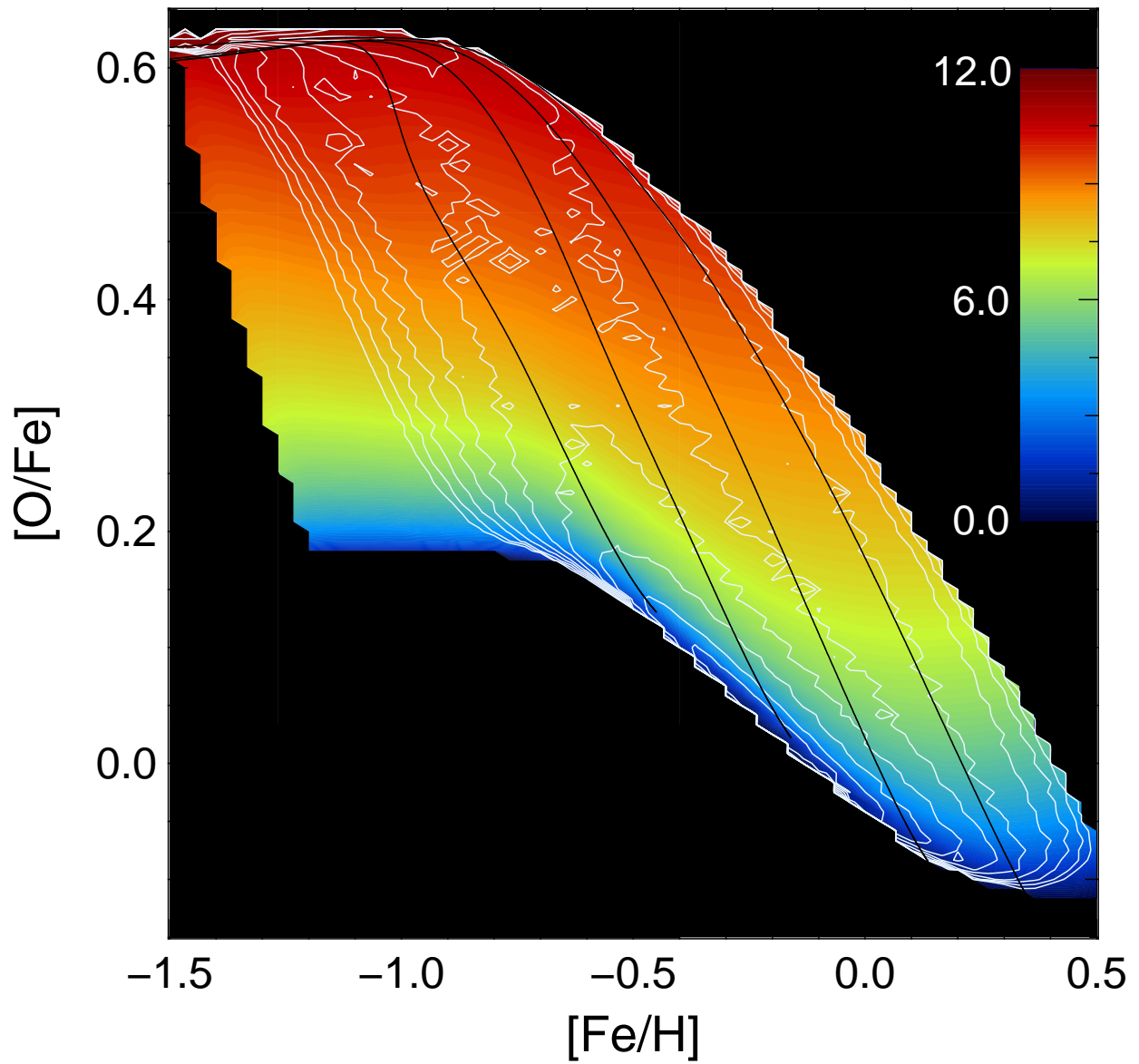
Figure 3.5: Same as Fig. 3.4 with colour coding for age and 0.5 dex spacing for density contours.

In Fig. 3.5 the contours show stellar density in increments of 0.5 dex and colours encode the mean age of stars, with blue implying youth. Naturally the oldest stars are high up, in the region of high $[\alpha/\text{Fe}]$. Right at the top, lines of constant age run almost horizontally. As one descends the diagram, lines of constant age slope more steeply down to the right as a result of the more rapid decline in $[\alpha/\text{Fe}]$ at small radii. The youngest stars both from outer and from inner rings have yet to reach the solar neighbourhood in significant numbers, so in Fig. 3.5 several white contours are crossed as one moves along the thin-disc ridge from the location of the solar-radius ISM.

In Fig. 3.6 both colours and contours ($10 \, \text{km s}^{-1}$ spacing) show the velocity dispersion σ_U of stars of a given chemical composition. The structure of the figure is the product of two mechanisms: (i) The velocity dispersion of stars born at any given radius scales with the third power of age, so older stars have larger velocity dispersions than younger stars born at the same locations. Consequently, in the figure velocity dispersion tends to increase from bottom to top. (ii) Velocity dispersion increases inwards, so stars that have reached the solar neighbourhood from small radii of birth have larger velocity dispersions than stars that have reached us from large radii. When this fact is combined with the fact that for any given date of birth more metal-rich stars are born at smaller radii, a steep rise in σ_U from left to right arises in Fig. 3.6. This plot suggests that we should include the region of high velocity dispersion along the upper right part of the populated region in the thick disc.

Since the single populations have – according to their ages and places of birth – different vertical dispersions, the older populations and those coming from inner radii will have higher scale heights and so reduced weights in a local sample. However, these populations dominate the composition high above the Galactic plane. The upper panel of Fig. 3.7 depicts the iron abundance distributions of the stars at different heights above the plane. Both tails of the distribution are strengthened as one moves away from the plane. The growth in the proportion of metal-rich stars with $|z|$ is at first unexpected, but is a natural consequence of the higher vertical velocity dispersion of stars in the inner disc. Notwithstanding the growth of the metal-rich wing of the metallicity distribution, the mean metallicity falls with increasing $|z|$ by more than 0.2 dex, while the dispersion increases from below 0.3 dex to 0.5 dex. We expect the model, however, to underestimate the vertical metallicity gradient on account of our assumption that a star inherits the velocity dispersion of the galactocentric radius at which it was born. A better model would take account of the actual migration paths of stars – how long each star spent with its guiding centre at each radius. It would predict smaller scale heights for populations of stars born in the inner disc. Thus the model might predict too high a fraction of high-metallicity stars to high altitudes.

The metallicity distribution at high altitudes depends on the weakly constrained early evolution of the disc and on details of mixing, so comparisons with observational data would provide valuable constraints on these less secure aspects of the model. Unfortunately, such comparisons are not feasible at present. In particular, we cannot compare with the SDSS data of Ivezic et al. (2008) because their metallicity determination breaks down above $[\text{Fe/H}] \sim -0.5$ dex. The model however has a constant mean rotational velocity in the metallicity range probed by the SDSS survey, in line with the data of Ivezic et al. (2008).
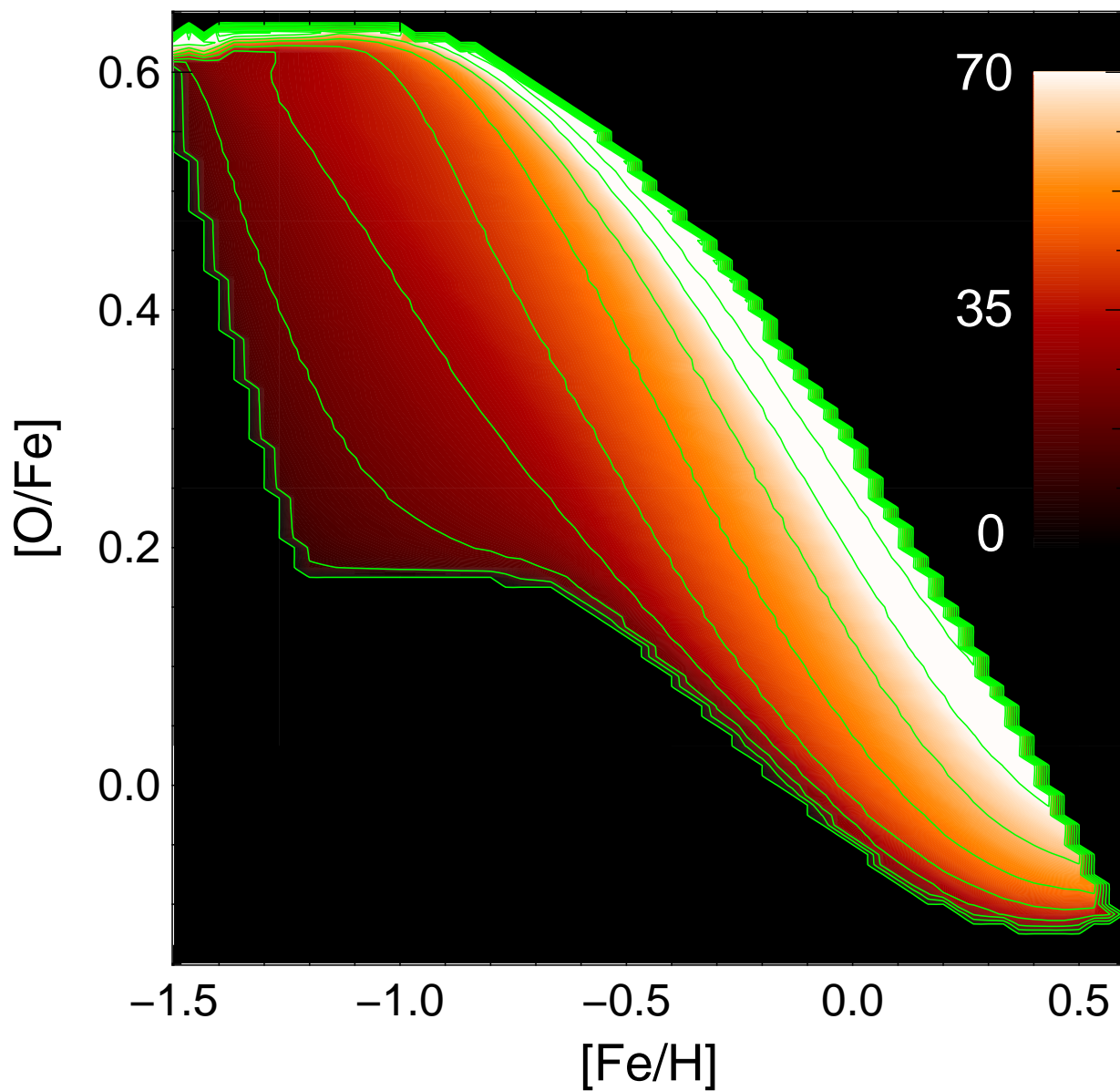
Figure 3.6: Velocity dispersions (in $\mathrm{km\,s^{-1}}$) as functions of position in the $([\mathrm{Fe/H}], [\mathrm{O/Fe}])$ plane. The graph is derived for a solar-neighbourhood sample by measuring the velocity dispersions of the populations with a specific chemical fingerprint. Two effects act on the velocity dispersion: The dependence on age mostly induces a top-down gradient following the evolution lines of the ISM. In the perpendicular direction (left-right) velocity dispersion increases with decreasing galactocentric radius. The low dispersion of the Galactic thin disc is visible on the lower left side, girded by a high dispersion band running from top left to bottom right.
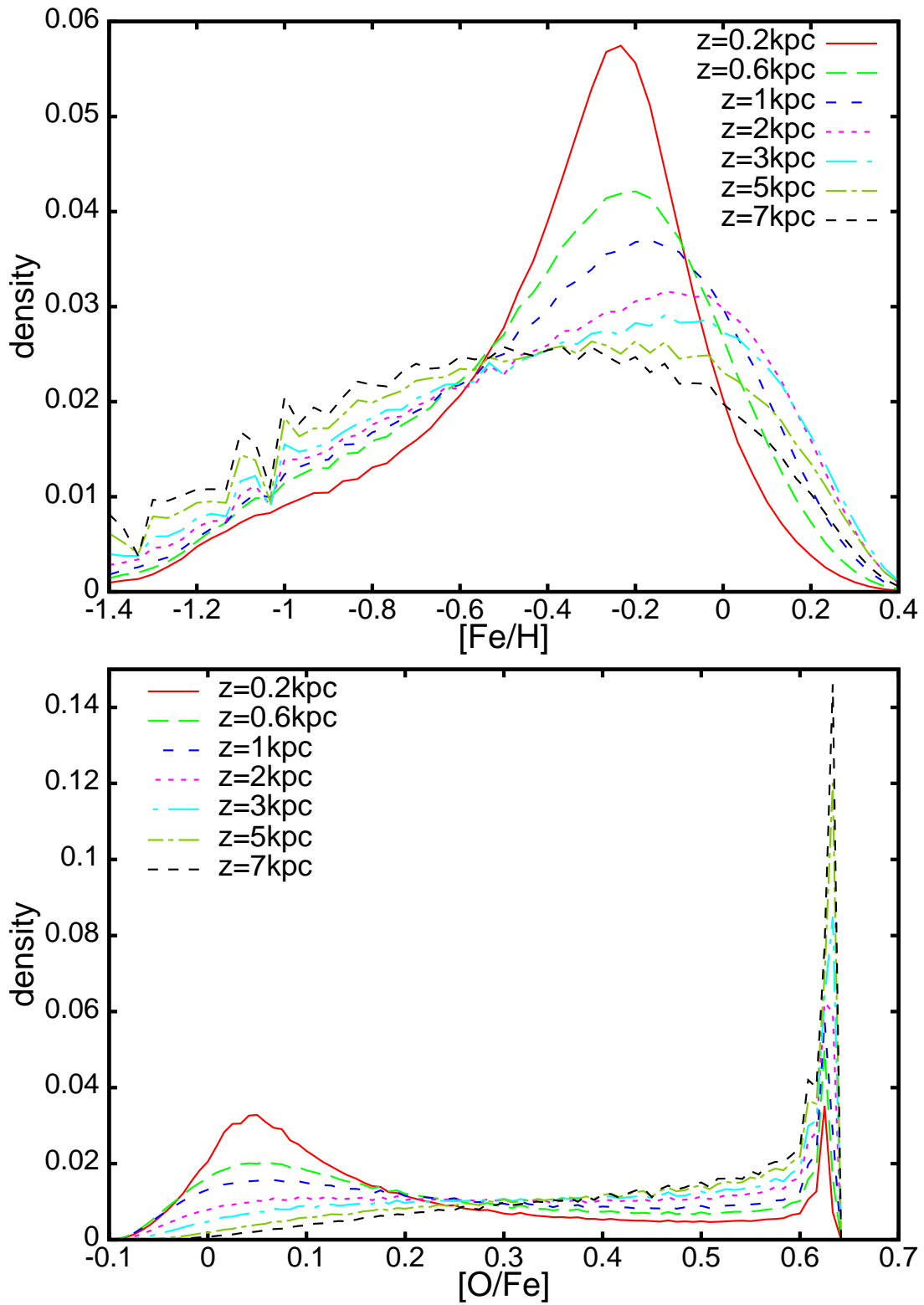
Figure 3.7: The model's stellar metallicity distributions at different heights above the plane at R_0. Here we avoided implying a specific selection function by using the mass of a specific population to determine its weight in the distribution. The diagrams are unsmoothed and the scatter comes from the radial (0.25 kpc) and temporal (30 Myr) resolution of the model. Upper panel: distributions of iron abundance. Lower panel: distributions of relative oxygen abundances.

The lower panel of Fig. 3.7 shows the [O/Fe] distributions at different heights. It reveals the bimodal structure that motivates the division of the disc into two. The exact shape of the two peaks as well as the number of stars in between depend on assumptions about gas enrichment and the behaviour of SNIa, but the bimodality of the distribution is a fundamental prediction of the model, as was shown in the appendix of SB09. The increasing bias to high ages as $|z|$ increases is reflected in the growing strength of the high [O/Fe] peak relative to the low [O/Fe] peak associated with the thin disc.

3.3.3   The disc divided

There are principally two strategies by which the disc has classically been dissected: by kinematics and by chemistry. We caution that different selection procedures do yield intrinsically different samples and that in general these are not equivalent. We shall see that these selection differences, which account for the spread by almost an order of magnitude in estimates of the relative local densities of the thick and thin discs, are readily understood in the context of our model. In each scheme criteria are set that define both thin and thick disc components, while stars that meet neither criterion are here assigned to an "intermediate population". We turn first to chemical selection and then in the light of this assess the quality and effects of kinematical criteria.

The dots and crosses in the upper panel of Fig. 3.8 show a realisation of a GCS-like sample of stars in the model. The ridge of the thin disc is evident, as is a ridge of metal-poor thick-disc stars at $[Fe/H] \lesssim -0.65$ and $[O/Fe] \sim 0.6$. We consider the thin disc to consist of all stars that lie within the black lines around this ridge. Less clear is the extent of the thick disc at $[Fe/H] \gtrsim -0.6$. Guidance is provided by plotting in green the locations of those stars in the realisation that satisfy the kinematic selection criteria of Bensby et al. (2003) to belong to the thick disc. A few of these stars lie in the region reserved for the thin disc; this phenomenon illustrates the inability of any kinematic selection criteria to separate cleanly the thin and thick discs – see §3.4 below. In light of the distribution of green crosses in Fig. 3.8, we define the thick disc to consist of all stars that lie either above the horizontal line at $[O/Fe] = 0.56$ or to the right of the sloping line, which has the equation

$$[O/Fe] = 0.56 - 0.55([Fe/H] + 0.8) . \qquad (3.1)$$

The lower panel of Fig. 3.8 shows the chemical compositions of stars in three large observational programs. These studies used different selection criteria – Bensby et al. (2005) kinematically selected for thick-disc stars, while Gilli et al. (2006) studied stars with planets, so their stars are all metal-rich.
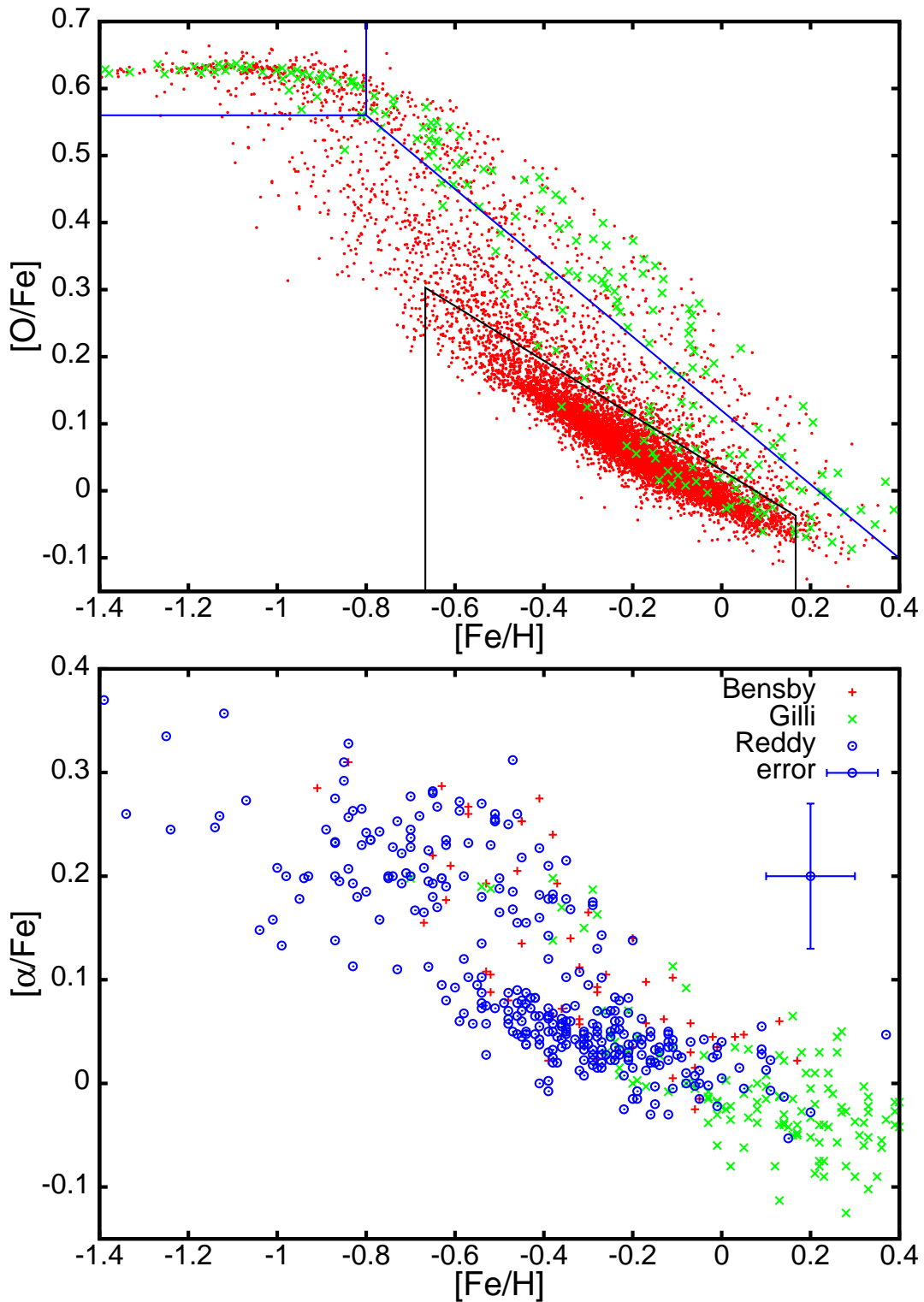
Figure 3.8: Upper panel: a scatter plot for a GCS-like measurement of solar-neighbourhood stars in the ([Fe/H], [O/Fe]) plane. Red dots mark positions of stars, while green crosses mark stars that are selected to the thick disc via the kinematic selection scheme. Lines mark possible criteria to dissect the data with a chemical classification scheme in the ([Fe/H], [O/Fe]) plane. Lower panel: the locations in the ([Fe/H], [α/Fe]) plane of stars with spectroscopically determined chemical compositions from Bensby (2005), Gilli (2006) and Reddy (2006).
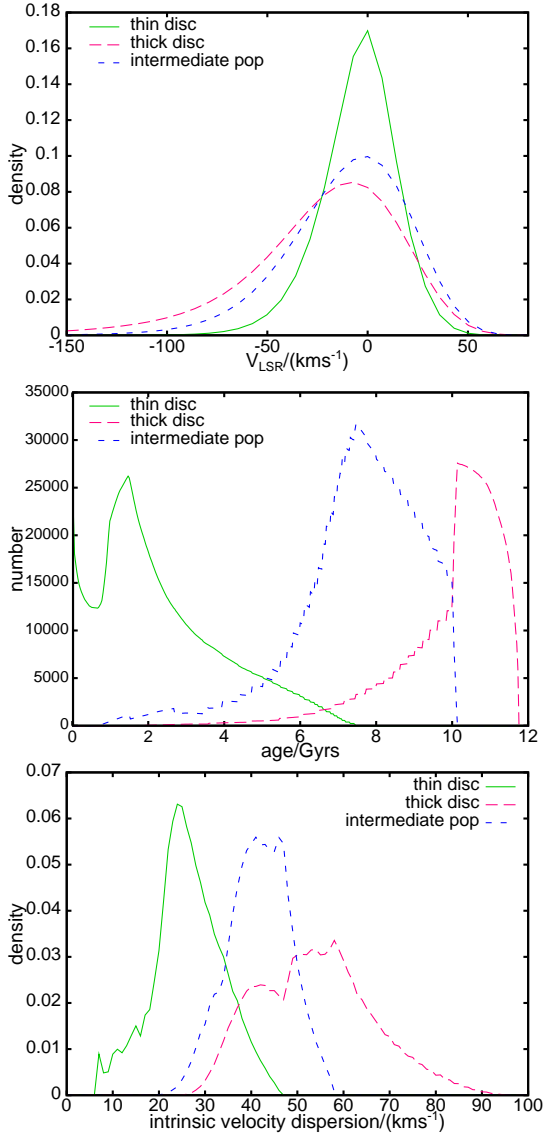
Figure 3.9: The top two panels show the distribution of stars from the three chemically selected populations in *V* velocity and age. The bottom diagram shows the distribution of stars by the velocity-dispersion parameter of the cohort to which they belong – see the description in text. The populations are the thin disc (green), the intermediate population (blue) and the thick disc (red). The curve showing the age distribution of the thin disc has been scaled down by a factor of 10 relative to the curves for the other two components. In the other panels each curve is separately normalised to unity. The steps in the age distribution are artifacts arising from the model's radial resolution (0.25 kpc); a step is produced as an individual ring passes over the selection criterion.
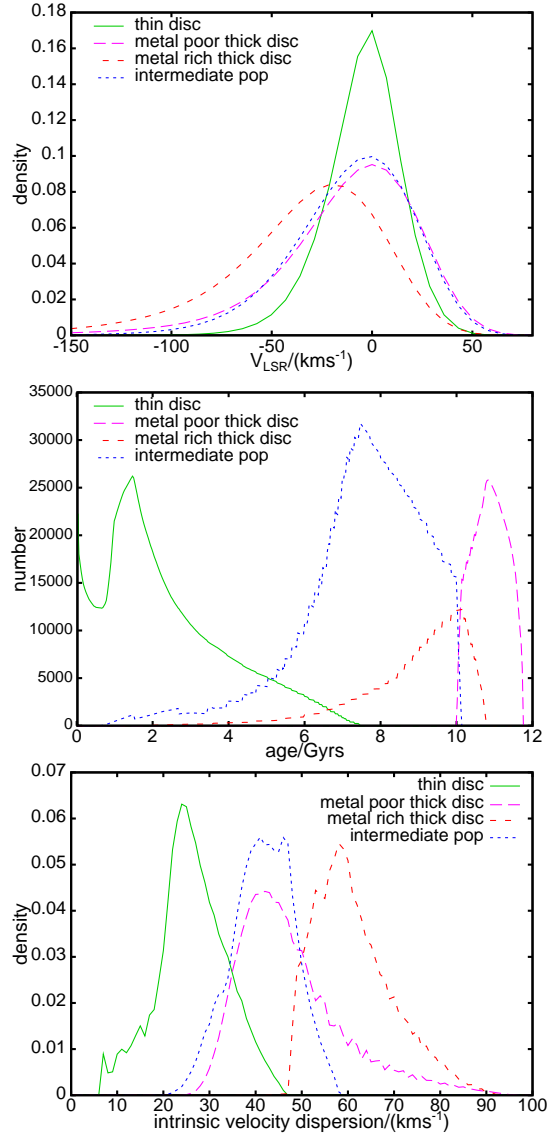
Figure 3.10: As Fig. 3.9 but with the thick disc split into its metal-weak (purple) and -rich (red) parts, the latter being defined to comprise [Fe/H] > -0.8.

The top and centre panels of Fig. 3.9 show the distributions of rotation velocity (top) and age (centre) within the thin disc (green), the thick disc (red) and the intermediate population (blue) when the local stellar population is divided in this way. In the top panel the thick disc stands out for the extent to which its V-distribution extends to low V. However, its peak lags circular rotation by only $\sim 10\,\mathrm{km\,s^{-1}}$ because it has a significant extension to $V > 0$. On account of its long tail, the average asymmetric drift of the thick disc is $\sim 22.5\,\mathrm{km\,s^{-1}}$, which is slower than that of the thin disc by $\sim 18\,\mathrm{km\,s^{-1}}$. The intermediate population is much more symmetrically distributed in V and, like the V-distribution of the thin disc, peaks near $V = 0$ with an average drift of $\sim 10\,\mathrm{km\,s^{-1}}$. Note that these velocities are relative to the local standard of rest (LSR), rather than the Sun, which is rotating faster than the LSR by $\sim 5\,\mathrm{km\,s^{-1}}$ (cf. Dehnen & Binney, 1998b). Hence relative to the Sun, the asymmetric drift of the thin disc is $\sim 10\,\mathrm{km\,s^{-1}}$.

Haywood (2008) showed that the population with moderate α enhancement is a superposition of stars that either combine lower metallicity (at fixed $[\alpha/\mathrm{Fe}]$) with fast rotation, or higher metallicity with lower rotation. The former sub-group bear a clear outer-disc signature, while the latter sub-group one associates with the thick disc by virtue of their slow rotation. Higher metallicities at given $[\alpha/\mathrm{Fe}]$ point to a flatter trajectory in the $([\alpha/\mathrm{Fe}], [\mathrm{Fe/H}])$ plane of the relevant ISM, i.e. to faster metal-enrichment before SNIa started to explode. Such fast enrichment is to be expected in the dense inner disc. Thus the structure found by Haywood (2008) is an inevitable consequence of chemical evolution in the presence of radial mixing.

The middle panel of Fig. 3.9 shows that essentially all thick-disc stars are older than $6\,\mathrm{Gyr}$. Most stars of the intermediate population are also this old, but whereas the modal age of the thick disc exceeds $10\,\mathrm{Gyr}$, no stars in the intermediate population are older than $10\,\mathrm{Gyr}$. The sharp rise in the number of thick-disc stars at $\sim 10\,\mathrm{Gyr}$, just where the number of stars in the intermediate population plummets, is very striking. The purple curve in the central panel of Fig. 3.10 clarifies the cause of this feature by showing the age distribution of stars that have $[\mathrm{O/Fe}] > 0.56$ (the horizontal boundary in Fig. 3.8) and $[\mathrm{Fe/H}] < -0.8$. We see that all these metal-poor, highly α-enhanced stars are older than $10\,\mathrm{Gyr}$, so the significance of a $10\,\mathrm{Gyr}$ age is that older stars formed before SNIa started to enrich the ISM with iron. The purple curve in the top panel of Fig. 3.10 shows that the modal rotation velocity of these high-α stars is not far from circular. That is, the metal-poor thick disc has a smaller asymmetric drift than the portion of the thick disc that lies to the right of the division line in Fig. 3.8 (red curves in Fig. 3.10), which we henceforth refer to as the metal-rich thick disc because all its stars have $[\mathrm{Fe/H}] > -0.8$. This metal rich portion has an average asymmetric drift of $\sim 35\,\mathrm{km\,s^{-1}}$, which is $30\,\mathrm{km\,s^{-1}}$ below the mean rotation velocity of the thin disc.

The green curve in the central panel of Fig. 3.9 shows that all thin-disc stars are younger than $7\,\mathrm{Gyr}$ and the rate of their formation appears to rise rapidly towards a peak at $\sim 1.5\,\mathrm{Gyr}$. In reality the SFR in the disc was monotonically declining throughout this period, so this apparent rise is entirely a selection effect. Several factors contribute to the detailed shape of the thin-disc age distribution in Fig. 3.9, including the restriction of the sample to a volume near the Galactic plane (which disfavours old stars) and the brightening of stars as they begin to turn off the main sequence (which accounts for the peak at $\sim 1.5\,\mathrm{Gyr}$).

The bottom panels of Figs. 3.9 and 3.10 show decompositions of each population into isothermal cohorts. A decomposition is possible because in the model each cohort of stars (stars formed at a given time and place) has a steadily increasing velocity dispersion. The plotted decompositions show the distribution of the current velocity dispersions for the cohorts that make up each population, weighted by the fractional contribution of the cohort to the population.

In Fig. 3.9 the isothermal decompositions of the thin disc (green) and intermediate population (blue) are similar except that the distribution for the intermediate population is shifted to the right by $\sim 20 \, \mathrm{km \, s^{-1}}$. The isothermal decomposition of the thick disc is bimodal. The purple curve in the bottom panel of Fig. 3.10 shows that the peak of this curve around $40 \, \mathrm{km \, s^{-1}}$ is associated with the metal-poor thick disc. So within our model the bulk of the metal-poor thick disc has smaller velocity dispersions than are found in the metal-rich thick disc. This chimes with the higher characteristic V velocities of the metal-poor thick disc in indicating that it is cooler and faster rotating than the metal-rich thick disc. The tail to high dispersions in the decomposition of the thick disc is contributed by a small number of very old stars that were formed at small radii, where the velocity dispersion is currently large.

By fitting the model's vertical density profile with the sum of two exponentials in $|z|$, SB09 concluded that in the model a fraction $f_{\mathrm{thick}} \sim 0.13$ of solar-neighbourhood stars belong to the thick disc; it followed that of order one third of the entire disc mass is contributed by the thick disc. These numbers were in good agreement with the conclusions that Juric et al. (2008) and Ivezic et al. (2008) drew from SDSS counts of stars $\gtrsim 1 \, \mathrm{kpc}$ from the plane. Using the present chemical decomposition into thin and thick discs, we find $f_{\mathrm{thick}} \sim 0.14$. In principle this number does not have to agree with the value obtained from the density profile. It does agree well because at $|z| \gtrsim 1 \, \mathrm{kpc}$ the disc is dominated by stars that have thick-disc chemistry (Fig. 3.7).

Fig. 3.11 shows the vertical density profiles of the thin disc (green), thick disc (red) and the entire disc (blue). Fits of exponentials to the density profiles yield scale heights of $268 \, \mathrm{pc}$ for the thin disc and and $822 \, \mathrm{pc}$ for the thick disc. The two components of the latter have scale heights $690 \, \mathrm{pc}$ for the metal-poor thick disc and $890 \, \mathrm{pc}$ for the metal-rich component. All components show more or less exponential profiles. The metal-poor thick disc has the strongest deviations from an exponential due to its being a mix of very old stars from all over the disc with radically different intrinsic velocity dispersions. When a sum of exponentials is fitted to the measured vertical profile of the Galactic disc, good fits can be obtained with quite a wide range of scale heights on account of a correlation between the scale heights of the two discs and their normalisations. The fits above to our individual discs are within the range of observationally acceptable scale heights (e.g., Juric et al., 2008), consistent with the thick disc identified by Juric et al. being close to what we have identified in the model using totally different criteria.

3.3.4 Inside-out formation?

For simplicity the SB09 model does not accelerate the formation of the disc at small radii relative to large radii, as is required by the popular "inside-out" model of disc formation. If the model were adjusted to include inside-out formation, the main change would be to the metal-poor thin
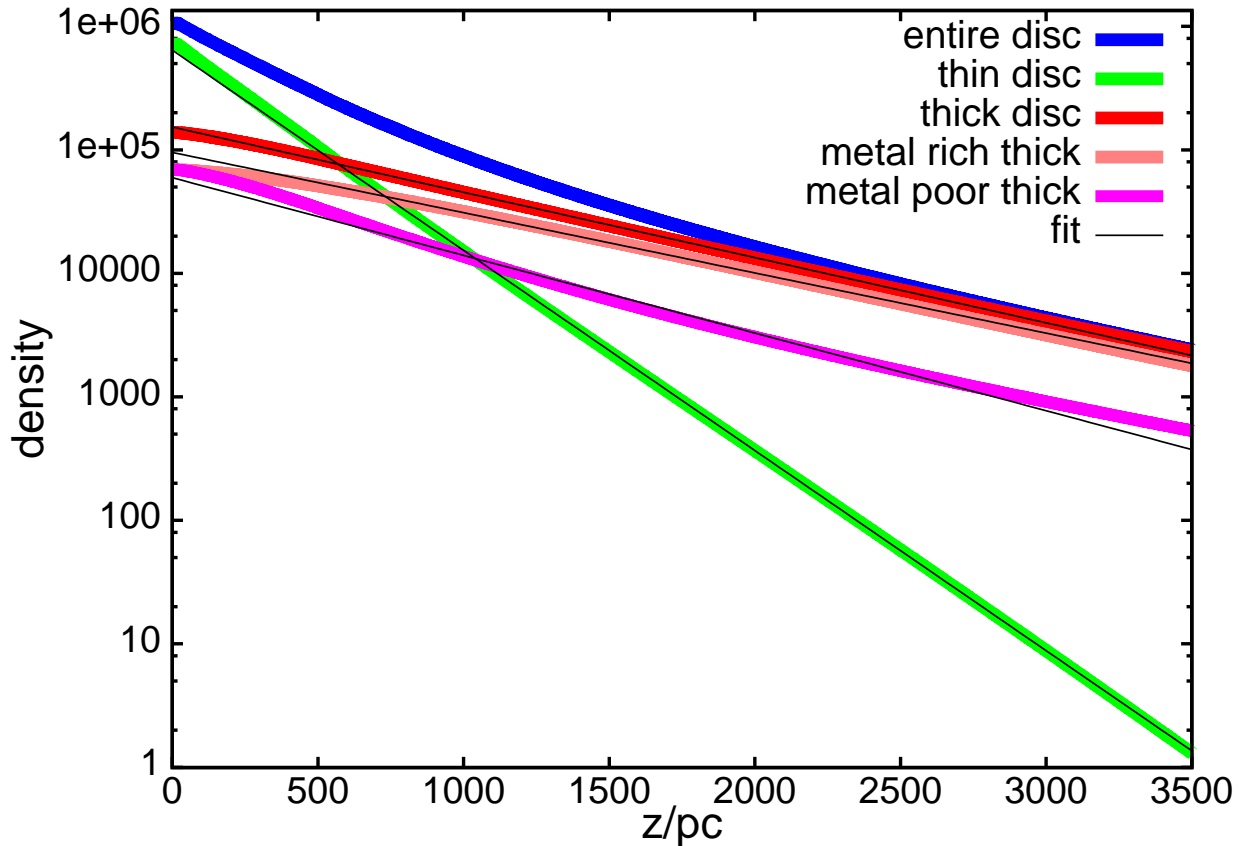
Figure 3.11: The vertical density profiles of the total disc (blue), thin disc (green), thick disc (red), the metal poor thick disc component (purple) and the metal rich thick disc (orange). The thick disc partition at z=0 is 14%, scale heights of the single components are (measured between $z = 400\,$pc and $z = 3000\,$pc): $h_{thin} = 270\,$pc, $h_{thick} = 820\,$pc, $h_{poorthick} = 690\,$pc and $h_{richthick} = 890\,$pc.

disc, which would lose parts of its high-V wing. Hence the inside-out scenario could be put in doubt by demonstrating that the V distribution of the high-α stars extends significantly to $V > 0$, and that many high-V stars have ages in excess of $10\,$Gyr. Further inside-out formation could give rise to some alpha enhanced, relatively metal-poor stars younger than $\sim 10\,$Gyr by the later onset of star formation in outer rings. Neither the thin disc nor the metal-rich thick disc would be strongly affected by the introduction of inside-out formation.

3.4   Kinematic division of the disc

Because it is much easier to measure the velocity of a star than to determine its chemical composition (particularly its α-enhancement), nearly all analyses select stars kinematically. Our model

provides an arena in which we can examine the extent to which kinematically selected samples of each component will be contaminated with stars from other components.

Samples of local stars such as those of Venn et al. (2004) and Bensby et al. (2005) are kinematically divided into thin and thick-disc stars with the aid of model distribution functions for each component: as described in Bensby et al. (2003), each star is assigned to the component whose DF is largest at the star's velocity. Both DFs are of the type introduced by Schwarzschild (1907), namely

$$f(U,V,W) = k f_i \exp\left(-\frac{U^2}{2\sigma_U^2} - \frac{(V - V_{\mathrm{asym}})^2}{2\sigma_V^2} - \frac{W^2}{2\sigma_W^2}\right) \tag{3.2}$$

where all components are with respect to the Local Standard of Rest, $k = (2\pi)^{-3/2}(\sigma_U \sigma_V \sigma_W)^{-1}$ is the standard normalisation constant, f_i is the relative weight of the population. The dispersions σ_i assumed for the thick disc are larger than those assumed for the thin disc, so high-velocity stars tend to be assigned to the thick disc. Because V_{asymm} is assumed to be $\sim 30\,\mathrm{km\,s}^{-1}$ larger for the thick disc than the thin, stars with lagging rotation velocities and therefore guiding centres at $R < R_0$ also tend to be assigned to the thick disc. This effect is reinforced by the fact that the dispersions must increase inwards, so stars with guiding centers well inside R_0 are also likely to be high-velocity stars. Consequently the "thick disc" stars in Venn et al. (2004) and Bensby et al. (2005) tend to belong to the inner disc. In the context of our model this fact explains why Bensby et al. (2003) found a long tail of "thick disc" stars that have higher [Fe/H] at a given $[\alpha/\mathrm{Fe}]$ than the "thin-disc" stars.

We examine the effectiveness of kinematic selection in two ways. First, in each panel of Fig. 3.12, we plot the distribution in a Toomre diagram of each of the components that we have identified chemically. Subsequently, in Figs 3.14–3.16 we examine the distributions in the $([\alpha/\mathrm{Fe}], [\mathrm{Fe/H}])$ plane of model stars that have been kinematically identified as belonging to the thin or thick disc.
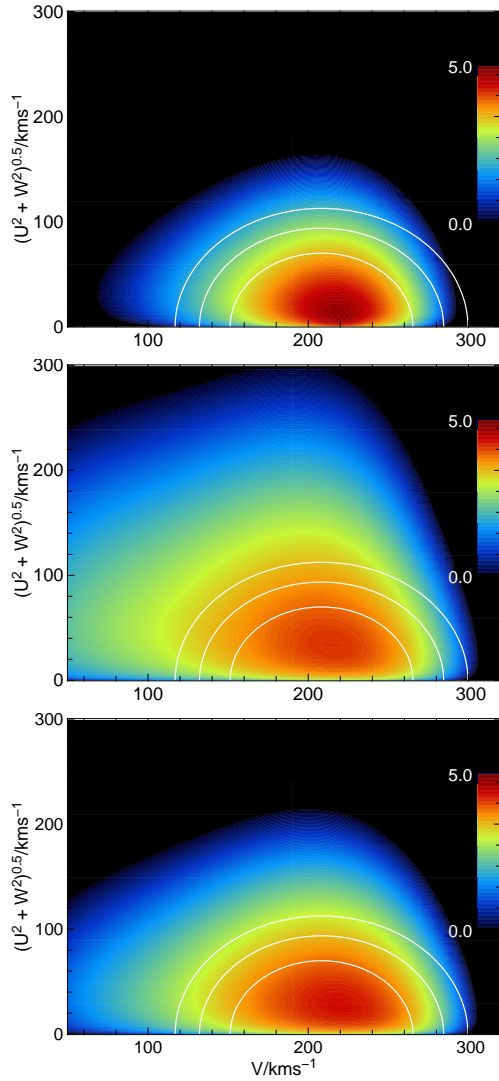
Figure 3.12: From top to bottom Toomre diagrams for the chemically selected thin-disc, thick-disc and intermediate populations within the model's solar-neighbourhood. Colour encodes the density of stars and ranges over 5 orders of magnitude. Shown in white are curves on which the probability of star belonging to the thick disc by the criteria of Bensby et al. (2003) is constant given $W = 0.55U$; on these curves from inwards out the thick-disc probability is $0.1, 1.0$ and 10.0 times the thin-probability. Inside the inner curve stars were deemed to belong to the thin disc, and outside the outer curve they were assigned to the thick disc.
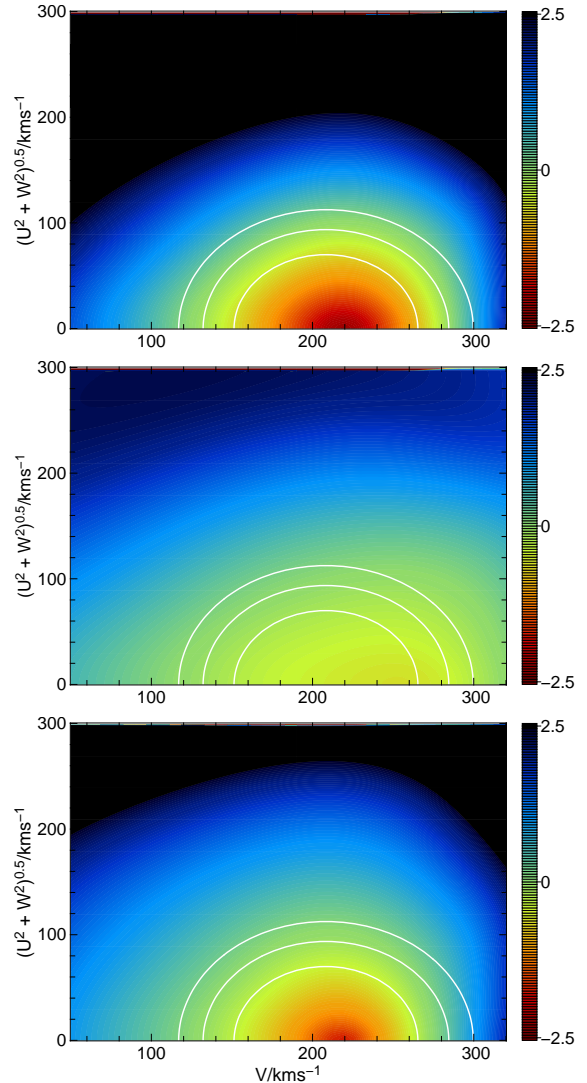
Figure 3.13: From top to bottom the ratio of thick by thin disc, thick disc by intermediate disc, and intermediate disc by thin disc stars at each point in the Toomre diagram when metal poor and metal rich thick disc are combined. Colours show the log of the ratio with values in the range $(-2.5, 2.5)$. White contours are the same as in Fig. 3.12.

Fig. 3.12 shows the Toomre diagrams for the thin, thick and intermediate components, respectively. In Fig. 3.12 all densities are separately normalised to unity, while Fig. 3.13 shows the density ratios of components in the Toomre diagram. The extensive overlap of the chemically-selected populations in the Toomre diagram is striking, but a natural consequence of the approximately Gaussian nature of the distribution functions of each component, which implies that the density of thick-disc stars peaks at velocities close to the LSR, which is where the thin disc is dominant. Consequently, no kinematic selection of stars from a particular chemical component can be very clean. This point is underlined by the white curves in Figs. 3.12 and 3.13, which are such that Bensby et al. (2003) classified stars with[2] $W = 0.55U$ as thick-disc if they lay outside the outermost white curve and thin-disc if they lay inside the innermost curve. The top panel in Fig. 3.12 shows that this criterion does exclude most thin-disc stars from a thick-disc sample. However, the upper two panels of Fig. 3.13 imply substantial contamination of the thick disc: in these panels red indicates a region where most stars are not thick disc stars, yet at lower right red extends significantly beyond the outermost white curve in both panels. From Fig. 3.12 it is evident that a slightly cleaner kinematic separation could be obtained if a non-Gaussian distribution function were used in place of (3.2), but the main problem with kinematic selection is the extensive overlap of the components in velocity space.

From the centre panel of Fig. 3.12 we see that a large fraction of the thick disc is also excluded from a kinematically selected sample of thick-disc stars, and many of the excluded stars will be assigned to the thin disc because they lie within the region reserved for the thin disc.

Fig. 3.14 shows the probabilities used by Bensby et al. (2003) for a star to be assigned to the thin (upper panel) and thick (lower panel) discs. The probability of being assigned to the thin disc is large in a broad swath that runs from $[O/Fe] = 0.6$ and $[Fe/H] = -1.2$ down to the lower edge of the populated region of the diagram, and then on to solar $[Fe/H]$ and above. Thus the kinematically selected thin disc includes high-α stars in contrast to our chemically selected thin disc. Kinematic selection does not confine the thin disc to stars near the ridge-line of the chemical thin disc because the low velocity dispersions and high rotation velocities characteristic of large radii cause most stars formed at large radii to be kinematically assigned to the thin disc. Stars in the more metal-rich flank of the chemical thin-disc ridge tend to be assigned partly to the intermediate population, or even (for the highest metallicities/innermost rings of origin) to the thick disc.

In Fig. 3.14 the probability of a star being assigned to the thick disc is high along the sloping upper edge of the populated region of the $([Fe/H], [\alpha/Fe])$ plane. Consequently, the Bensby et al. (2003) kinematic criterion for being a member of the thick disc does pick stars that belong to the thick disc by our chemical definition. However, the density of stars actually assigned to the thick disc by the kinematic criterion, which is shown in Fig. 3.15, extends below the sloping dashed line in Fig. 3.8 because the density of stars assigned to the thick-disc is the product of the assignment probability plotted in Fig. 3.14 and the density of stars in the $([Fe/H], [\alpha/Fe])$

---

[2] For general values of W/U the Bensby et al. (2003) kinematic selection criterion, which is three-dimensional, cannot be plotted in a Toomre diagram because the latter is two-dimensional. Hence we choose the approximate ratio of the dispersion components for our graphs.
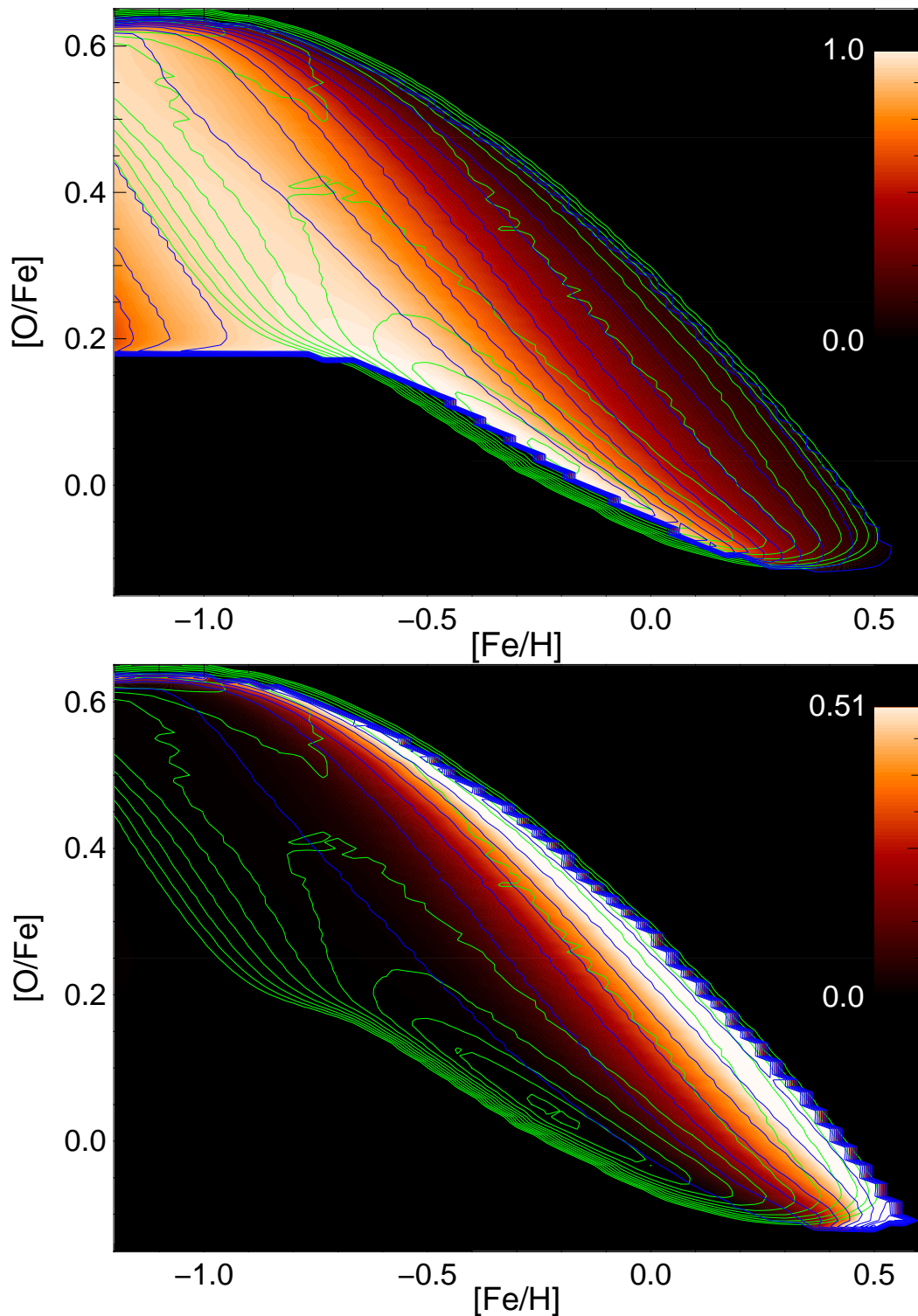
Figure 3.14: Selection probabilities using the kinematic selection function of equation (3.2) for the thin (upper panel) and thick disc (lower panel). Blue contours give lines of same selection probability for a star at a certain chemical composition with levels running from 0.01 to 0.91 with a 0.1 spacing for the thin disc and from 0.01 to 0.61 with a 0.05 spacing for the thick disc. Colours encode the selection probability and the green contours show lines of the model's entire disc population density at a 0.5 dex spacing.
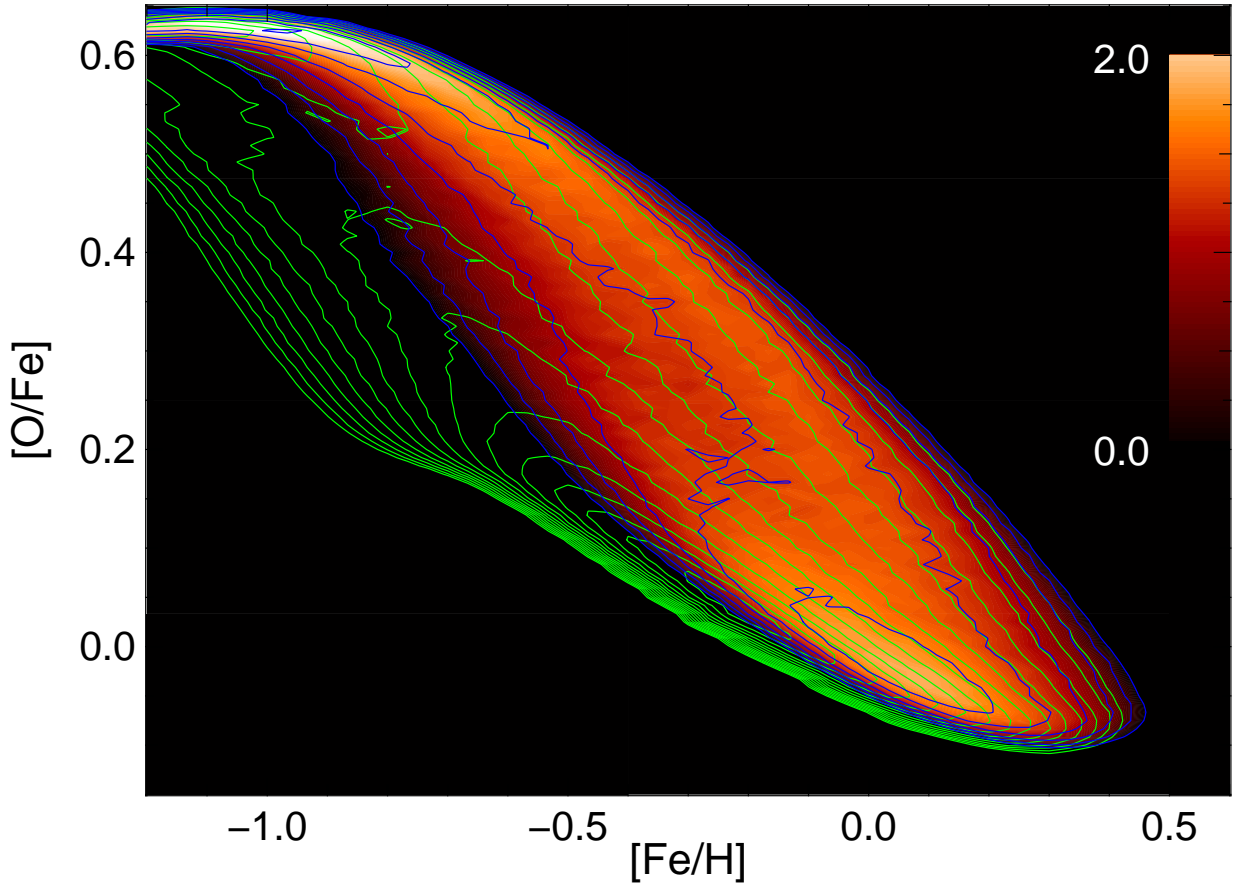
Figure 3.15: Green lines show the density contours in the ([Fe/H], [O/Fe]) plane of the entire disc population with a 0.3 dex spacing. Colours and blue contours show the absolute density of stars selected kinematically according to equation (3.2) to the thick disc with 0.3 dex contour spacing.

plane, which declines steeply as the edge of the populated region is approached. In fact the ridge of kinematically-selected thick-disc stars leaves the upper edge of the populated region at the α-enhancement turnoff and then runs downwards parallel to the thin-disc ridge at an offset of $\simeq 0.3$ dex in [Fe/H], just as reported by Bensby et al. (2003) and Venn et al. (2004). Moreover, the zone of thick-disc stars merges with the thin-disc population at [Fe/H] $\simeq 0$, which was one of the main findings of Bensby et al. (2003).

The upper panel of Fig. 3.16 shows the age distributions of the kinematically-selected components, and should be compared with the middle panel of Fig. 3.9. When kinematically selected, the thin disc has a long tail of very old stars. Conversely, the age distributions of the thick disc and especially the intermediate population extend to much younger ages when these components are kinematically selected. It is inevitable that a kinematically selected thin disc will contain old stars that properly belong to either the thick disc or the intermediate population because stars
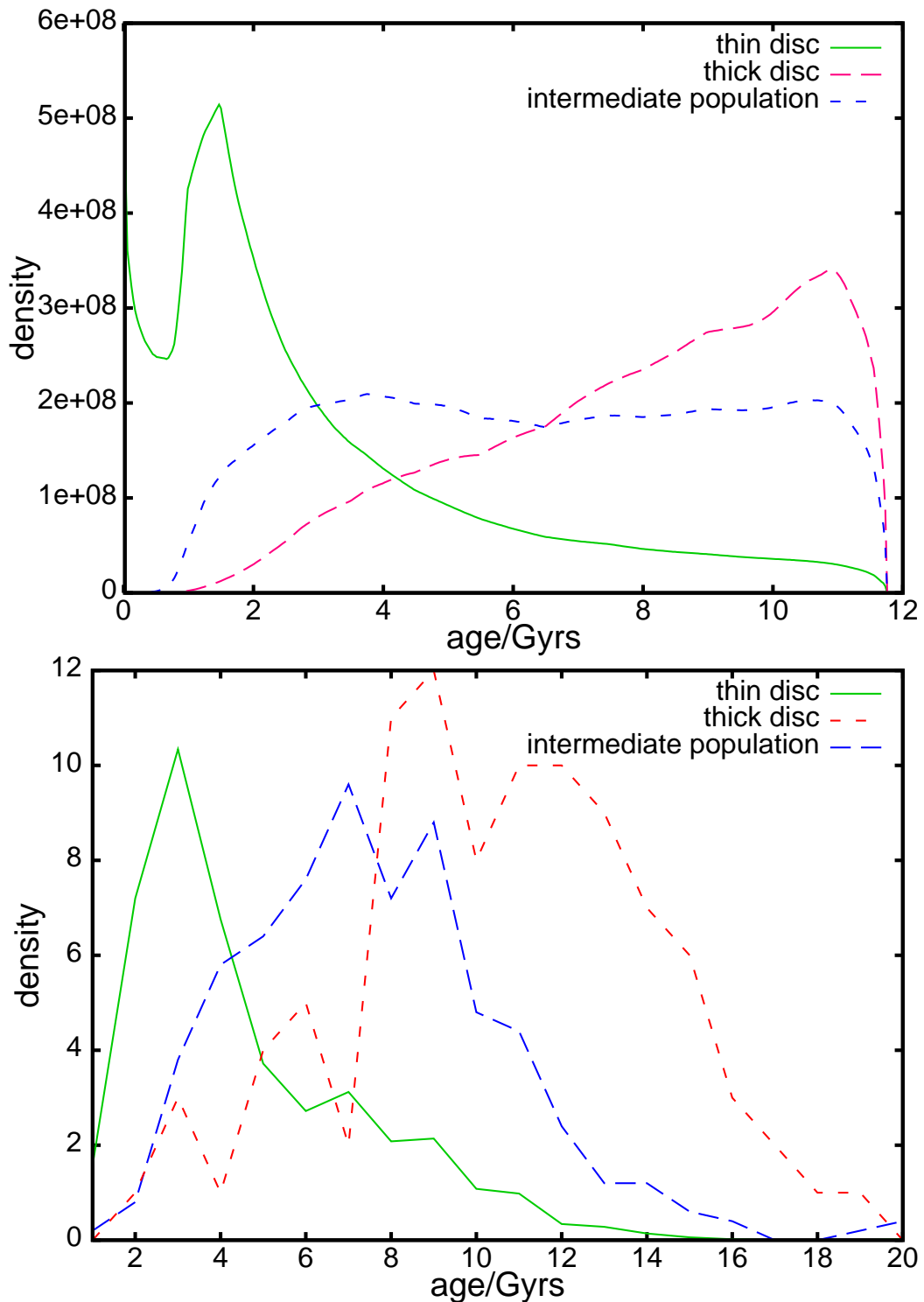
Figure 3.16: Upper panel: model age distributions for the three kinematically selected components in the model. As in Figures 3.9 and 3.10 the curve for thin disc has been lowered by a factor of 50 and that for the intermediate population by a factor 5 relative to the curve for the thick disc. Lower panel: the distribution of measured ages of GCS stars given by Haywood (2008) with stars kinematically assigned to components using the Bensby (2003) criteria. Stars with age younger than 0.5 Gyr are not taken into consideration due to high errors. When the ages published by Holmberg et al. (2007) are used, the lower panel does not change significantly.

with small velocities relative to the LSR must be assigned to the thin disc, yet any plausible distribution function for the thick disc will be significantly non-zero at such velocities. The assignment of young stars to the intermediate population reflects the red colour in the lower right corner of the centre panel of Fig. 3.13 that was discussed above.

The lower panel of Fig. 3.16 shows histograms of the ages of GCS stars in Haywood (2008) when stars are assigned to components using the kinematic criteria of Bensby et al. (2003) – the corresponding histograms of the ages given by Holmberg et al. (2007) is very similar. Clearly the histograms are badly distorted by errors in the ages, which scatter stars to unrealistically large ages, so the horizontal scale of the lower panel is nearly twice that of the upper panel. None the less, the lower panel seems to be as consistent with the upper panel as the large errors permit.

The numbers of model stars in the solar neighbourhood that are kinematically assigned to the three components analysed in the upper panel of Fig. 3.16 is thin : intermediate : thick $= 1 :$ $0.099 : 0.0239$. The same ratios for the observational sample analysed in the lower panel of Fig. 3.16 are $1 : 0.085 : 0.029$ in satisfactory agreement with the model's prediction, but the agreement is actually better than this comparison suggests, when one accounts for the difference between the selection functions used to select the observed stars in the lower panel of Fig. 3.16. If we use the GCS sample without binaries, which our selection function was designed for, the ratios are changed to $1 : 0.095 : 0.029$. When we further remove likely halo stars, the observational thick disc fraction shrinks to ~ 0.025. Indeed, the fraction of the local column of thick-disc stars that resides near the Sun is sensitive to the distribution of W velocities. The latter is not tightly constrained because one of the least satisfactory aspects of the model is the absence of dynamical coupling between horizontal and vertical motions, which obliges one to make an arbitrary assumption about the variation with random velocity in the shape of the velocity ellipsoid. It is worth noting that the model probably has more metal-rich stars high above the Sun than it should have as a consequence of our assumption that high-velocity stars are as susceptible to churning as low-velocity stars.

3.5 Conclusions

The thick disc is the Proteus of Galactic physics: depending on which questions you ask it changes its shape. Although it has been identified both by its extended vertical density profile and its distinct kinematics, it is most usefully characterised chemically, not least because chemical composition is a permanent feature of a star, whereas distance from the plane and peculiar velocity are ever-changing properties. Moreover, chemical composition is intimately connected to the time and place of the star's birth.

The determination of the chemical composition of large numbers of old main-sequence stars is feasible only for samples of nearby stars. Unfortunately, the nearby stars constitute a strongly biased sample of the whole Galactic disc. It is absolutely essential to interpret the statistics of the solar neighbourhood in the context of these biases. We have used our model Galaxy to explore these biases, and in particular the relationship between the components one obtains by

assigning stars to them on the basis of their kinematics or their chemistry. A very straightforward conclusion is that kinematic selection inevitably mis-allocates many stars, both adding old stars to the thin disc and young stars to the thick disc.

We have shown that our model provides a consistent interpretation of observations of the solar neighbourhood in which components are identified as regions of the ([Fe/H], [α/Fe]) plane. Thin-disc stars lie in a narrow ridge of high density between [Fe/H] ~ -0.65 and [Fe/H] ~ 0.15 that forms part of the lower edge of the populated part of the ([Fe/H], [α/Fe]) plane. The metal-rich thick disc occupies a broader swath of the ([Fe/H], [α/Fe]) plane that runs parallel to the downward-sloping ridge of the thin disc and ~ 0.3 in [O/Fe] higher. The metal-rich thick disc extends in [Fe/H] from ~ -0.9 to well above 0, where it merges with the thin disc. At its low-metallicity high-α end, the metal-rich thick disc touches the metal-poor thick disc, in which [O/Fe] $\simeq 0.63 \pm 0.5$ and [Fe/H] goes at least down to ~ -1.4. There is an "intermediate population" of stars that in the ([Fe/H], [α/Fe]) plane lie between the thin and thick discs, but the density of such stars in the ([Fe/H], [α/Fe]) plane is relatively low. Thus the two discs are well defined structures.

Thin-disc stars are all younger than 7 Gyr and are on fairly circular orbits. Their values of [Fe/H] and rotation velocity V are correlated in the sense that higher V implies lower [Fe/H]. The stars of the metal-rich thick disc are nearly all older than 8 Gyr. Most are on significantly non-circular orbits with guiding centres inside R_0 and a significant number have $V < -100 \, \mathrm{km \, s^{-1}}$. Specifically, the metal-rich thick disc can be considered to be a superposition of isothermal components with radial velocity dispersions between 50 and 80 km s^{-1}, strongly peaked around 60 km s^{-1}. The metal-poor thick disc consists exclusively of stars older than 10 Gyr. Its stars have on average more angular momentum and smaller velocity dispersions than the stars of the metal-rich thick disc. Among the population of strongly α-enhanced stars there is (cf. Fig. 3.4) an extremely strong negative correlation between α and V.

Meléndez et al. (2008) remarked that the thick disc has similar properties to the Galactic bulge. This conclusion is natural in the context of our model, in which the metal-rich thick disc is made up of stars that have migrated to the Sun from the inner disc, where rapid early star formation enriched the ISM to significant metallicities before SNIa began to lower [α/Fe]. It is to be expected that many of the stars that formed alongside the thick-disc stars of the solar neighbourhood are now bulge stars.

Perhaps the most uncertain aspect of the modelling is our assumption that a star's probability of being "churned" to a different angular momentum is independent of the star's random velocity. Since Sellwood & Binney (2002) did not investigate the dependence of churning probability on random velocity, our assumption could be significantly in error, and it is not implausible that stars with large random velocities have low churning probabilities. In this case the thick disc would be less radially mixed than our model predicts. We will shortly investigate the dependence of churning probability on random velocity.

Given our model's success in synthesising studies of the Galactic disc into a coherent picture, it is useful as it stands regardless of the theoretical considerations that motivated its construction. However, it was not made by searching an extensive parameter space for a model that would fit

the studies described here. Rather it was made by building a code that combined standard chemical evolution modelling with a model of dynamical evolution that reflects the understanding of how spiral structure works that Sellwood & Binney (2002) gained from N-body models and analytical dynamics. Its two free parameters were determined from the model's fit to the metallicity gradient in the ISM and to the metallicity distribution of the GCS stars given in Nordström et al. (2004) and Holmberg et al. (2007). Hence we consider the model's ability to reproduce the data sets of Fuhrmann (1998), Bensby et al. (2003, 2005), Venn et al. (2004) Reddy et al. (2006), Haywood (2008), Juric et al. (2008) and Ivezic et al. (2008) is remarkable and suggests that it has a sound physical basis.

The key respect in which the model goes beyond traditional models of chemical evolution is its inclusion of radial migration by stars and inward flow by gas. Inward flow of gas is important for the model's success because it establishes a much steeper metallicity gradient than traditional models produce. The radial migration of stars is absolutely key, because it structures the thick disc. Moreover it explains the significant spread in [Fe/H] within the local thin disc, and the correlation that Haywood (2008) identified between [Fe/H] and V.

The discovery that the thick disc overlaps the thin disc in [Fe/H] presented a challenge to conventional models of chemical evolution because it implies that there are thick disc stars that have both $[\alpha/\text{Fe}]$ and [Fe/H] higher than in some thin-disc stars. The lower values of $[\alpha/\text{Fe}]$ in the thin-disc stars imply earlier times of birth, so how come [Fe/H] is lower? The conventional response to this challenge it to suppose that some violent event led to a suspension of star formation in the disc, and that during this hiatus a massive injection of metal-poor gas lowered [Fe/H] in the ISM (Chiappini et al., 1997, 2001). An objection to this scenario is that many other galaxies have thick discs with similar properties to ours (Yoachim & Dalcanton, 2006), so thick-disc formation should not require special circumstances. We do not press this argument but would strongly make the point that a model of chemical evolution that includes only *essential* physics and has a single, early, maximum in the star-formation rate and a monotonically rising value of [Fe/H] at each radius automatically produces a thick disc with just the properties observed locally. In fact an α-enhanced thick disc forms because the speed at which [Fe/H] rises declines as one moves outwards, so the value attained by [Fe/H] when SNIa start to lower $[\alpha/\text{Fe}]$ increases inwards. Spiral structure and the Galactic bar scatter α-enhanced stars formed at small radii onto more eccentric and more inclined orbits and even scatters some of them onto orbits of sufficiently high angular momentum that they are found in the solar neighbourhood. Readers who want to believe in a violent origin of the thick disc may continue to do so. But they should be aware that the simplest model of the chemo-dynamical evolution of the disc that includes all relevant physics reproduces the data. Hence there is absolutely no *evidence* that the thick disc has a violent origin.

Acknowledgements

Chapter 4

Local Kinematics and the Local Standard of Rest[1]

4.1 Abstract

We re-examine the stellar kinematics of the Solar neighbourhood in terms of the velocity $v_\odot$ of the Sun with respect to the local standard of rest. We show that the classical determination of its component $V_\odot$ in the direction of Galactic rotation via Strömberg's relation is undermined by the metallicity gradient in the disc, which introduces a correlation between the colour of a group of stars and the radial gradients of its properties. Comparing the local stellar kinematics to a chemodynamical model which accounts for these effects, we obtain $(U, V, W)_\odot = (11.1^{+0.69}_{-0.75}, 12.24^{+0.47}_{-0.47}, 7.25^{+0.37}_{-0.36})\,\mathrm{km\,s}^{-1}$, with additional systematic uncertainties $\sim (1, 2, 0.5)\,\mathrm{km\,s}^{-1}$. In particular, $V_\odot$ is $7\,\mathrm{km\,s}^{-1}$ larger than previously estimated. The new values of $(U, V, W)_\odot$ are extremely insensitive to the metallicity gradient within the disc.

4.2 Introduction

The Sun's velocity $v_\odot$ with respect to the Local Standard of Rest (LSR)[2] is required to transform any observed heliocentric velocity to a local galactic frame. Since this transformation is often necessary for scientific interpretation of observed velocities in terms of Galactic structure, the determination of $v_\odot$ is a fundamental task of Galactic astronomy. The radial and vertical components $U_\odot$ and $W_\odot$ of $v_\odot$ are straightforwardly obtained from the mean heliocentric velocities of several different groups of Solar-neighbourhood stars: $U_\odot$ and $W_\odot$ are simply the negative radial

---

[1] Content and text of this chapter have been published almost identically in Schönrich, Binney & Dehnen (2010). A more popular description and explanation can be found in Schönrich (2010).

[2] The LSR is the rest frame at the location of the Sun of a star that would be on a circular orbit in the gravitational potential one would obtain by azimuthally averaging away non-axisymmetric features in the actual Galactic potential.

and vertical components of these means[3].

The component $V_\odot$ of $v_\odot$ in the direction of Galactic rotation is much harder to determine, because the mean lag with respect to the LSR, the asymmetric drift v_a, depends on the velocity dispersion σ of the respective stellar population. The classical solution to this problem exploits the empirical linear relation between the negative mean heliocentric azimuthal velocity of any stellar sample $\overline{v}_s = v_a + V_\odot$ and its σ^2 (Strömberg, 1946). Hence, a straight-line fit yields $V_\odot$ as the value of $\overline{v}_s$ for a hypothetical population of stars on circular orbits, for which $\sigma = 0$.

The theoretical underpinning of this method is the asymmetric drift relation (see Binney & Tremaine, 2008, eq. 4.228)

$$\overline{v}_s - V_\odot = v_a \simeq \frac{\overline{v_R^2}}{2v_c} \left[\frac{\sigma_\phi^2}{\overline{v_R^2}} - 1 - \frac{\partial \ln(v\overline{v_R^2})}{\partial \ln R} - \frac{R}{\overline{v_R^2}} \frac{\partial(\overline{v_R v_z})}{\partial z} \right],$$ (4.1)

where R is Galactocentric cylindrical radius, z the height above the plane, v_c the circular speed, and ν the number density of stars, while a bar indicates a ν-weighted local mean. The equation applies separately to each relaxed stellar population, for example to M stars or G stars. The idea behind the classical determination of $V_\odot$ is that the square bracket in equation (4.1) takes essentially identical values for each stellar population, with the consequence that a plot of $\overline{v}_s$ against $\overline{v_R^2}$ should be linear.

Dehnen & Binney (1998, hereafter DB98) applied this method to a sample of $\sim 15\,000$ main-sequence stars from the Hipparcos catalogue and their value of $V_\odot = (5.25 \pm 0.62)\,\mathrm{km\,s^{-1}}$ has been widely used. Recent re-determinations using an improved reduction of the Hipparcos data (van Leeuwen, 2007) confirm the DB98 value though with reduced error bars (van Leeuwen, 2007; Aumer & Binney, 2009).

However, two recent studies call the DB98 value for $V_\odot$ into question. Binney (2010, hereafter B10) fitted distribution-function models (a) to velocity distributions inferred by Ivezic et al. (2008) from proper motions and photometric distances of stars in the Sloan Digital Sky Survey, and (b) to the space velocities of F and G in the Geneva-Copenhagen Survey (GCS, Nordström et al., 2004). The GCS stars are a subset of the Hipparcos stars (analysed by DB98) for which radial velocities have been obtained. B10 was able to obtain satisfactory fits to these data only if $V_\odot$ was larger than the DB98 value by $\sim 6\,\mathrm{km\,s^{-1}}$, about ten times the formal error on $V_\odot$. Another body of evidence against the DB98 value for $V_\odot$ originates from radio-frequency astrometry of masers in regions of massive-star formation (Rygl et al., 2010; Reid et al., 2009a). If the DB98 value for $V_\odot$ is correct, these sources systematically lag circular rotation by $\sim 17\,\mathrm{km\,s^{-1}}$ (Reid et al., 2009a). Such a high systematic lag is unexpected for young stars and McMillan & Binney

---

[3] According to the above definition, the LSR's radial and vertical motion w.r.t. the Galactic centre vanish. Therefore, the determination of $U_\odot$ and $W_\odot$ from such means implicitly assumes that the Solar neighbourhood as a whole does not move radially or vertically w.r.t. the Galaxy. That such motions are at most small is suggested by the proper motion of Sgr A* (Reid & Brunthaler, 2004) and the mean radial velocity of the stars orbiting it (e.g. Reid et al., 2007). Moreover, such motions should also obey an asymmetric-drift like relation (see below), i.e. the mean velocities depend systematically on velocity dispersion, which is not observed.

(2010) argued that a more plausible interpretation of the data is obtained if $V_\odot$ exceeds the DB98 value by $\sim 6\,\mathrm{km\,s}^{-1}$.

This paper does two things: (i) it explains why the approach to the determination of $V_\odot$ by DB98 and subsequent studies is misleading, and (ii) it determines $V_\odot$ from similar data but a different methodology. Both these tasks are accomplished with the help of a particular chemo-dynamical model of the Galaxy, that of Schönrich & Binney (2009a, hereafter SB09a), but the points that we make are general ones and the role played by the SB09 model is essentially illustrative. In Section 4.3 we show that a metallicity gradient in the disc gives rise to distributions of mean azimuthal velocity and velocity dispersion within the colour-magnitude plane that are much more complex than one naively expects, and we show that these distributions invalidate the methodology of DB98. In Section 4.4 we re-estimate $V_\odot$ by fitting the entire velocity distribution of the GCS stars to the distribution predicted by the SB09 model without reference to the Strömberg relation.

4.3   Kinematics in colour and magnitude

DB98 divided their sample of Hipparcos main-sequence stars into populations with different velocity dispersions by binning in $B-V$ colour because colour is correlated with age and therefore with velocity dispersion. To examine the relation between colour, mean rotation velocity and velocity dispersion for stars near the Sun, we employ the SB09a model of the Galactic Disc. This model describes the chemodynamical evolution of the thin and thick Galactic discs and is a refinement of models pioneered by van den Bergh (1962) and Schmidt (1963). The disc is divided into 80 annuli, within each of which the chemical composition of the ISM evolves in response to the ejection of material by dying stars, while stars form continuously with the current composition of the ISM. The new features of the model are (a) stochastic stellar accelerations accounting for heating processes; (b) radial stellar migration accounting for both non-circular orbits and guiding-centre shifts caused by stochastic resonant scattering off spiral arms (Sellwood & Binney, 2002); and (c) transfer of gas between annuli, both as result of resonant scattering by spiral arms and as a result of a secular tendency of gas to spiral inwards through the disc. Surprisingly, the model contains both thin and thick discs that are consistent with the available observational constraints (Schönrich & Binney, 2009b).

Fig. 4.1 shows the model kinematics in the colour-magnitude diagram. Each point in colour-magnitude space defines a separate sub-population whose asymmetric drift $v_a \equiv v_c - \overline{v}_\varphi$ and radial velocity dispersion are plotted via colour coding, such that dynamically cold and warm populations are shown with blue and red shades, respectively. The region in the colour-magnitude diagram shown in this figure corresponds to the cuts used by DB98 to define their sample.

Our naive expectation is that as we proceed down the main sequence from its blue end towards the main-sequence turnoff at $B-V \sim 0.6$, we encounter successively older stars with lower mean rotation velocities and higher velocity dispersions, so in both panels of Fig. 4.1 the shading should become redder as we move from left to right along the main sequence. The pattern
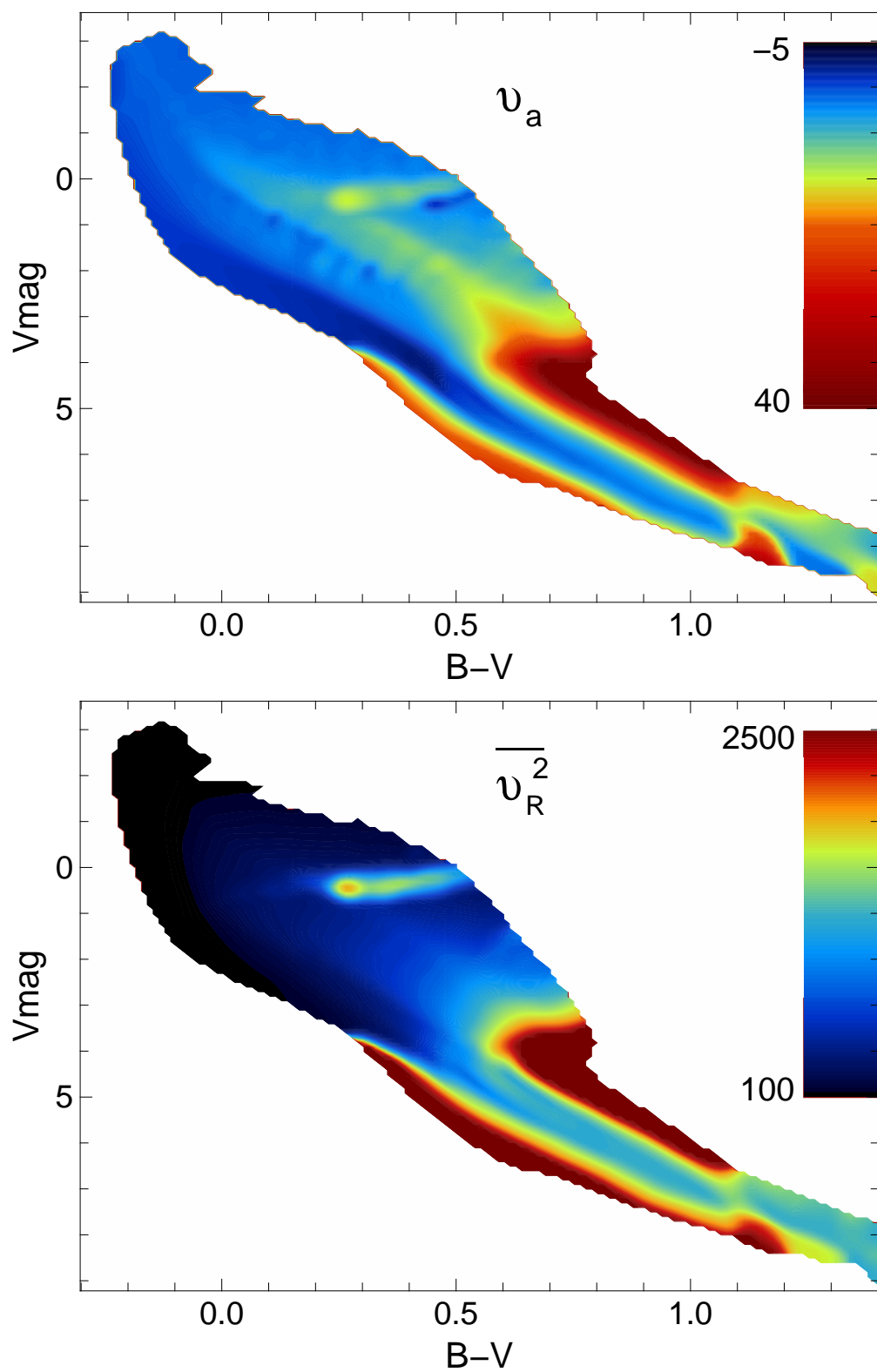
Figure 4.1: The variation with colour and magnitude of the asymmetric drift v_a (top) and radial velocity dispersion (bottom) in the SB09a model of the Solar neighbourhood. Shown is the range of colours and magnitudes used by DB98 to generate their main-sequence sample. Note that the number density of stars is highly non-uniform across the region shown.
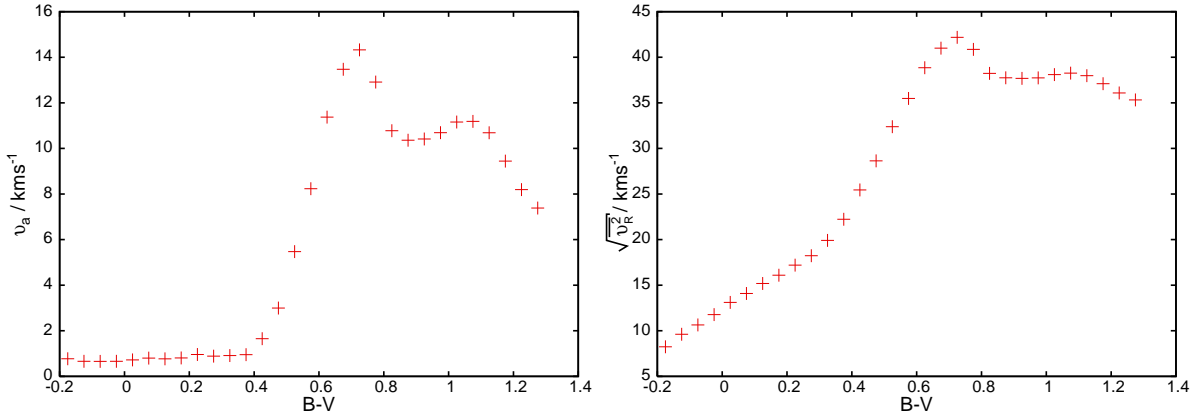
Figure 4.2: The asymmetric drift (top) and radial velocity dispersion (bottom) for stellar samples of given $B-V$ colour drawn from the model thus simulating the effects of the Hipparcos and DB98 selection criteria.

actually found in Fig. 4.1 is more complex. Most notably, there is a pronounced velocity gradient *across* the lower main sequence. In the range $0.6 < B-V < 1$ the lower edge of the main sequence is dynamically warm (orange in Fig. 4.1) on account of subdwarfs, which are metal-poor and therefore old with large velocity dispersions and low mean rotation rates. The number of these subdwarfs is small, however, so they will not have a significant impact on a sample binned by colour alone. More significant is the orange shading on the upper edge of the lower main sequence, which reflects the metallicity gradient within the disc: as metallicity increases, the main sequence shifts to the right, so in the upper panel the orange upper edge of the main sequence implies that the more metal-rich stars of the Solar neighbourhood are rotating more slowly because they formed at $R < R_0$. To the left of $B-V \simeq 0.5$ this trend is weakened by contributions from old, sometimes metal-poor populations whose isochrones move up through this region. Still the more metal-rich main-sequence stars with smaller guiding centre radii give rise to slightly higher dispersions and asymmetric drifts to the red side of the main sequence.

The upper panel of Fig. 4.1 shows that in the crucial colour range $0.4 < B-V < 0.6$, the asymmetric drift is a complex function of colour and absolute magnitude because in this region stars of widely differing ages and metallicities are found as a result of old, metal-poor isochrones intersecting younger, metal-rich isochrones.

The horizontal branch is clearly visible on both panels of Fig. 4.1 as an almost horizontal feature just below $M_V = 0$. It is less pronounced in the upper panel because the blue end of the horizontal branch contains metal-poor stars, which tend to have large guiding-centre radii and therefore low υ_a even at large $\overline{\upsilon_R^2}$.

Fig. 4.2 shows the asymmetric drift υ_a and velocity dispersion $\overline{\upsilon_R^2}$ obtained when stars are binned by colour alone. The lower panel can be compared with corresponding observational plots in DB98 and Aumer & Binney (2009). The model reproduces the structure of the data very well – in particular, the steepening in the slope around $B-V = 0.4$ and the flatness redwards of
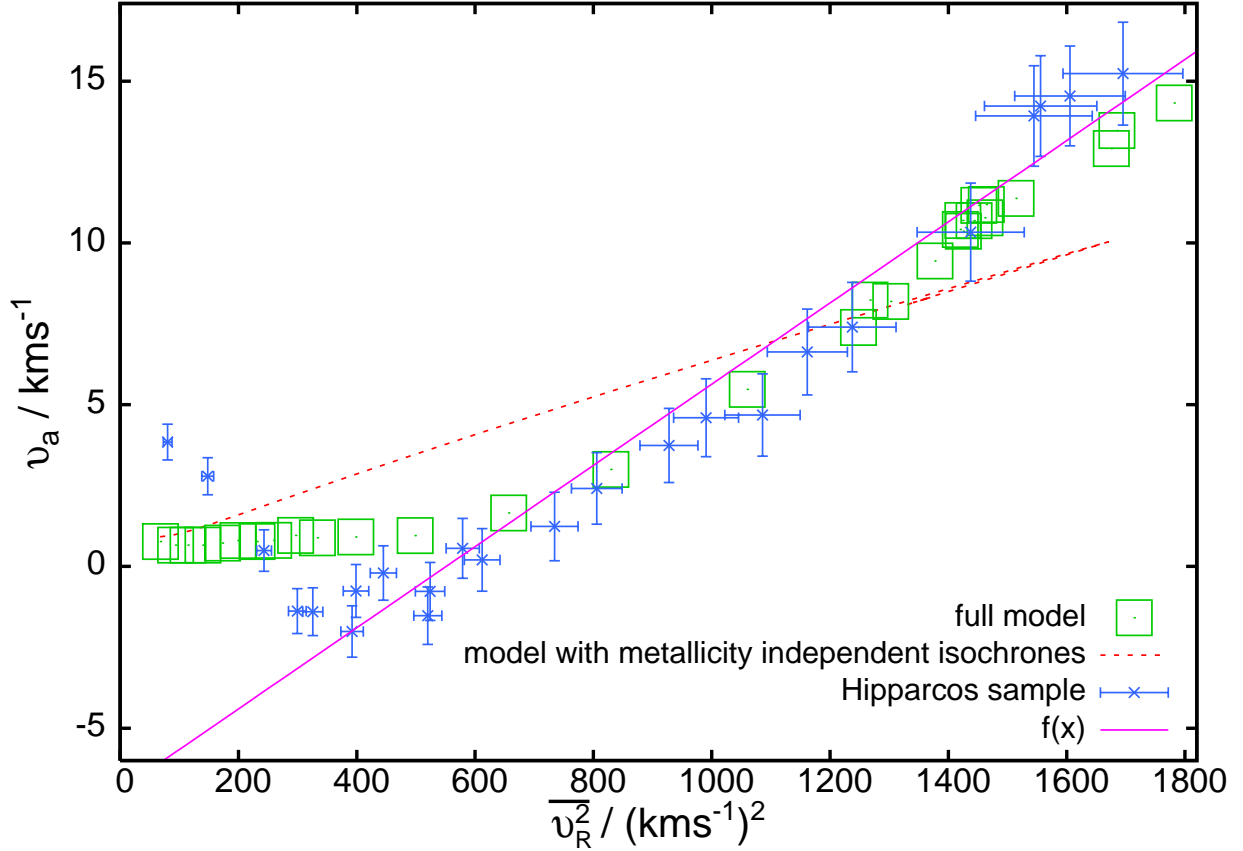
Figure 4.3: Green squares: the asymmetric drift for synthetic stellar sub-samples defined by $B-V$ colour plotted against their radial velocity dispersion squared for the SB09a model. The red dots: the same relation obtained from a model with only one chemical composition (solar). Blue data points: the values of Aumer & Binney (2009) shifted by $11\,\mathrm{km\,s^{-1}}$ and with the radial velocity dispersion increased by 7%. Purple line: a linear fit to the Hipparcos points in the range of $\overline{\upsilon_R^2}$ used by DB98.

$B-V = 0.6$. The peak in velocity dispersion seen in the lower panel of Fig. 4.2 is much less evident in Fig. 2 of Aumer & Binney (2009) but can be traced in their σ_R and σ_z data. Note that the rise with $B-V$ in $\overline{\upsilon_R^2}$ for $B-V < 0.4$ is not accompanied by any change in υ_a. This unexpected phenomenon arises because at these colours the contribution of old metal-poor stars is increasing with $B-V$, and because we see many of these stars near pericentre, they have small asymmetric drifts despite their large random velocities.

Since at its bright end the Hipparcos sample is close to being volume limited, the relative number of horizontal-branch stars is small and the complex structure above the main sequence in Fig. 4.1 has no significant effect in Fig. 4.2.

In Fig. 4.3, the squares show the resulting plot of the asymmetric drift υ_a against velocity dispersion squared for the synthetic samples of Fig. 4.2; they do not lie on a straight line. The red dots

show the plot one obtains if all stars are assigned solar metallicity. These dots *do* lie on a good approximation to a straight line.[4] The effect of re-assigning stars with large guiding-centre radii from solar metallicity to their true, low metallicities is to move them from redder to bluer bins. Since these stars have small or even negative values of υ_a on account of the metallicity gradient in the disc, the transfer reduces υ_a for the young, bluer bins and increases it in the old, redder bins. Consequently, the transfer morphs the near-straight line of the red points into the curve defined by the green squares.

DB98 estimated $V_\odot$ by fitting a straight line to the observational analogue of Fig. 4.3, which is a plot of the solar velocity relative to a colour-selected group of stars versus the squared velocity dispersion of that group. The blue data points in Fig. 4.3 show such data for the Hipparcos sample in the re-analysis of Aumer & Binney (2009) after subtracting $11\,\mathrm{km\,s^{-1}}$ from each value of solar velocity. We see that for $\overline{\upsilon_R^2} \gtrsim 600\,[\mathrm{km\,s^{-1}}]^2$ the Hipparcos data define the same straight line as the green crosses from the model. This straight line intercepts the υ_a axis at $\sim -7\,\mathrm{km\,s^{-1}}$ rather than 0, causing $V_\odot$ to be underestimated by this amount. For $\overline{\upsilon_R^2} \lesssim 400\,[\mathrm{km\,s^{-1}}]^2$ the Hipparcos data points in Fig. 4.3 deviate from this straight line, but DB98 ignored samples with very low velocity dispersion on the grounds that such samples may not be in dynamical equilibrium. Indeed, both dissolving star clusters and the non-axisymmetric gravitational potentials of spiral arms are liable to distort the kinematics of stellar samples with low random velocities such that equation (4.1) does not hold.

The failure of the synthetic samples to follow a straight line in Fig. 4.3 implies that the square bracket in the asymmetric drift relation (4.1) does depend on colour: it varies by a factor ~ 4 in the colour range $0.4 < B - V < 0.6$ as demonstrated in Fig. 4.4. A significant contribution to the value of the bracket comes from the first derivative term, which is smallest for metal-poor populations because their densities ν decline more slowly outwards on account of the metallicity gradient in the disc. Physically, including metal-poor, thin-disc stars decreases υ_a because such stars typically visit the Solar neighbourhood at pericentre, where they have $\upsilon_\phi > v_c$.

4.4   determining the Solar motion from the Velocity distribution

In view of the argument just presented, that the classical procedure cannot yield a reliable value of $v_\odot$, we now estimate $v_\odot$ by fitting the observed distributions of heliocentric velocities to the velocity distribution of the SB09a model. That is, we seek the offset $-v_\odot$ from the circular velocity at which the model velocity distributions provide the best match to the distribution of observed heliocentric velocities. B10 used an analogous procedure to argue that $V_\odot \simeq 11\,\mathrm{km\,s^{-1}}$; however, the model distributions he used were obtained from analytic distribution functions rather from a model of the Galaxy's chemical evolution. By using velocity distributions that reflect much

---

[4] The slight deviation from a straight line of the model without metallicities is an effect of the approximations in SB09a and leads to a small underestimation of the real metallicity bias by the model.
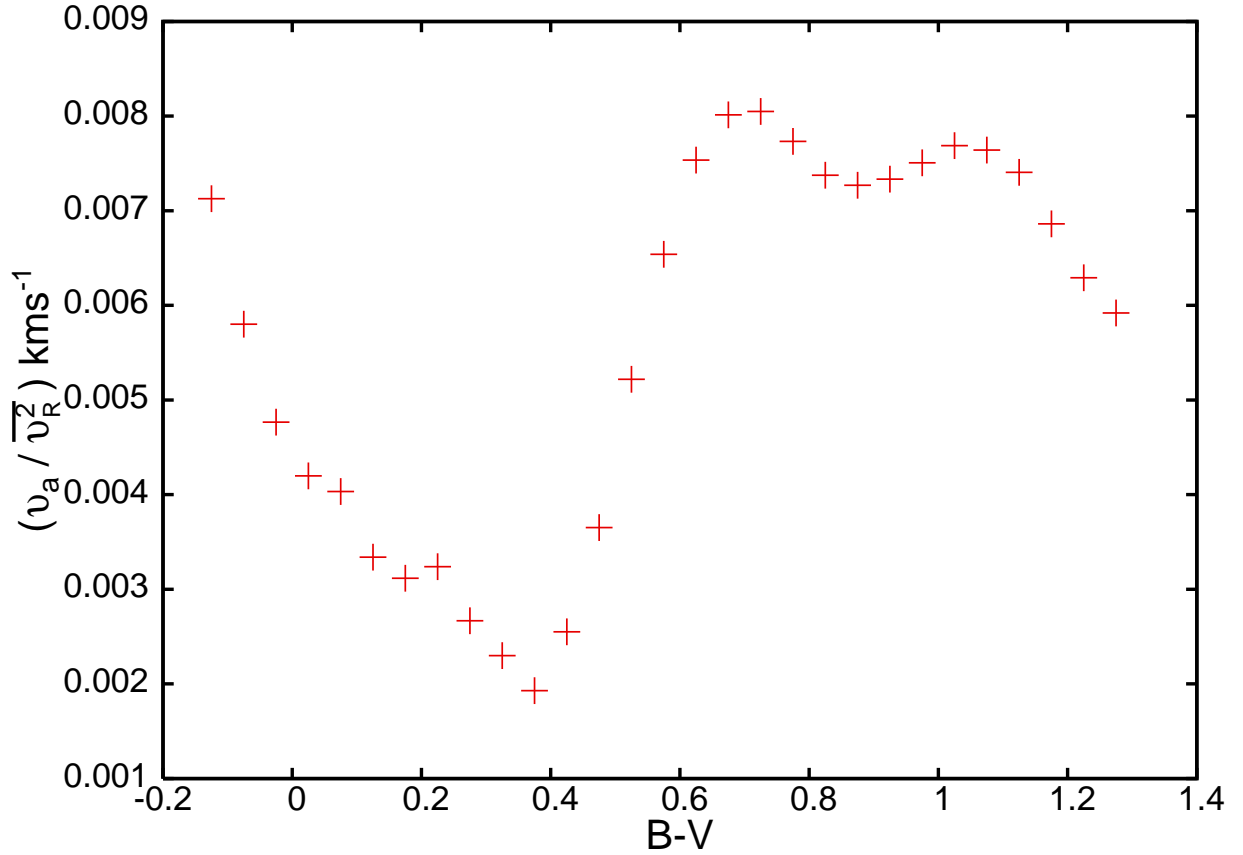
Figure 4.4: Asymmetric drift velocity divided by squared velocity dispersion for synthetic colour-selected samples using the SB09a model. This ratio should be proportional to the square bracket in equation (4.1).

prior information about the chemodynamical history of the Galaxy in place of simple analytic functions, we hope to achieve a closer fit to the observed velocity distributions and therefore determine the requisite offset $-v_\odot$ with greater precision.

In Fig. 4.5 the points with (Poisson) error bars are for a subsample of GCS stars for which Holmberg et al. (2007, 2009) give reliable metallicities; thirty likely halo stars have been removed by requiring $[\text{Fe/H}] > -1.2$. This criterion is slightly stricter than that used in SB09b for the determination of the in-plane dispersion parameter (σ_R of a 10 Gyr old local population), such that we now use a marginally smaller value, $43 \, \text{km s}^{-1}$, while lowering the vertical dispersion parameter to $23 \, \text{km s}^{-1}$. The curves in Fig. 4.5 show the model distributions when offset by $-v_\odot = (11.10^{+0.69}_{-0.75}, 12.24^{+0.47}_{-0.47}, 7.25^{+0.37}_{-0.36}) \, \text{km s}^{-1}$ – we used cubic splines to interpolate between individual data points provided by the model in the V component and determined the offset by maximising the likelihood of the data given the model. We used only five parameters for all three distributions: the two dispersion parameters and the three components of Solar motion, yet the fit is of good quality. The small fluctuations of the data around the model V and to a lesser extent U
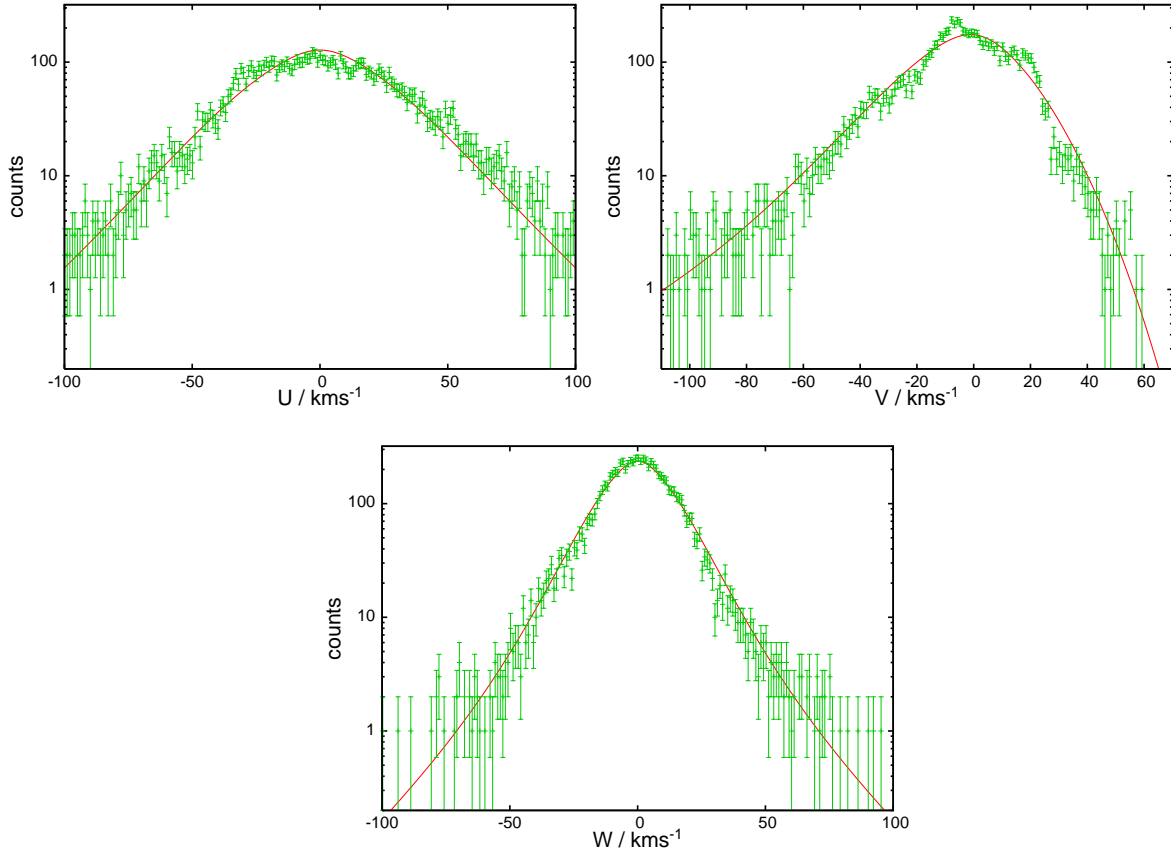
Figure 4.5: Curves: The model distributions predicted by the SB09a model in the *U*, *V* and *W* components of velocity (from top left to bottom). Data points with Poisson error bars: the observed distributions of the GCS stars shifted by our estimate of $v_\odot$ to optimise the fit of the data.

distributions are readily accounted for by the well known stellar moving groups (Dehnen, 1998), likely caused by the dynamical influence of the Galactic bar and spiral structure (Dehnen, 1999b; De Simone et al., 2004; Antoja et al., 2009; Minchev et al., 2009).

A significant advantage of determining $v_\odot$ from the entire sample, as in this section, rather than from subsamples as done in the past, is the robustness of the result to changes in the modelled metallicity gradient. In fact, eliminating the model's metallicity gradient changes $V_\odot$ by less than $0.1\,\mathrm{km\,s^{-1}}$.

One should note that the quoted errors on the components of $v_\odot$ are purely formal. Sources of additional systematic error include the possible presence of halo stars in the sample, the dynamical approximations used in constructing the model, and the effects of stellar streams, which have a big impact on the observed distribution of stars near the circular velocity but are completely excluded from the model. Fortunately the likelihood of the data used here is not particularly

sensitive to the fit of the data to the model around the peak density. In view of these uncertainties we roughly estimate systematic errors of $\sim (1, 2, 0.5)\,\mathrm{km\,s^{-1}}$, assuming that U and W are mostly affected by distortions by streams and V showing even more structure and having an additional uncertainty from the modelling. This is in perfect agreement with previous estimates as regards $W_\odot$ and slightly higher in $U_\odot$ compared to the DB98 value, which can be traced back of the larger influence of the Hercules stream at $\sim -30\,\mathrm{km\,s^{-1}}$ (lowering the estimate) on their statistics. However, it differs significantly from the value for $V_\odot \simeq 5.2 \pm 0.5\,\mathrm{km\,s^{-1}}$ obtained by the classical technique (DB98, Aumer & Binney, 2009). Our value for $V_\odot$ is in good agreement with $V_\odot \simeq 11\,\mathrm{km\,s^{-1}}$ proposed by B09. Given the residual uncertainties of $v_\odot$, it is questionable whether the standard practice of "correcting" observed (heliocentric) velocities for the Solar motion is useful, at least the adopted value should be explicitly provided.

4.5 Conclusions

The metallicity gradient in the Galactic disc causes a systematic shift in the kinematics especially near the turnoff region. By the relationship between the colour and metallicity of a star, the more metal-rich populations, with on average lower angular momentum and thus higher asymmetric drifts, are displaced relative to their metal-poor counterparts, which have lower asymmetric drifts. When stars are binned by colour, the metallicity gradient in the Galactic disc prevents the relationship between mean rotation speed and squared velocity dispersion taking the linear form predicted by a naive application of the Strömberg relation. This breakdown in the conventionally assumed linearity invalidates the traditional technique for determining the Sun's velocity with respect to the LSR, which involves a linear extrapolation to zero velocity dispersion of the empirical relation between the mean velocity and squared velocity dispersion. Moreover the SB09a model predicts that a treacherous linear relationship underestimating the solar azimuthal motion by $\sim 7\,\mathrm{km\,s^{-1}}$ will be mimicked redwards of the onset of the turnoff region, coinciding well with the behaviour observed in the Hipparcos data.

The Sun's velocity with respect to the LSR may be alternatively determined from the velocity offset that optimises a model fit to the observed velocity distribution. Using the velocity distribution predicted by the SB09a model of the chemodynamical evolution of the Galaxy, we find $v_\odot = (11.1^{+0.69}_{-0.75}, 12.24^{+0.47}_{-0.47}, 7.25^{+0.37}_{-0.36})\,\mathrm{km\,s^{-1}}$ and roughly estimate the systematic uncertainties as $\sim (1, 2, 0.5)\,\mathrm{km\,s^{-1}}$. The radial and vertical components of this value of $v_\odot$ agree with earlier estimates, but the V component is larger than the widely used value of DB98 by $\sim 7\,\mathrm{km\,s^{-1}}$. This is in nice concordance with the model expectations for the systematic error arising from naively using the Strömberg relation and in good agreement with the value obtained by B09 using a similar method but with a less sophisticated distribution function. Curiously it agrees well with the result $V_\odot \sim 10 - 13\,\mathrm{km\,s^{-1}}$ obtained by Delhaye (1965) using the classical method with pre-Hipparcos data.

In this paper we have relied heavily on the SB09a model, so the question arises of how vulnerable our argument is to the model's shortcomings. Our critique of the classical approach to the

determination of $v_\odot$ is secure so long as the disc has significant age and/or metallicity gradients. It is beyond question that such gradients exist, so the classical technique is certainly unreliable. Our proposed value of $V_\odot$ is essentially independent of the assumed metallicity gradient, but does have some sensitivity to the dynamical approximations used in making the SB09a model – plausible variations of how one handles the secular acceleration of stars lead to changes in the estimated value of $V_\odot$ by 0.5 to $1\,\mathrm{km\,s^{-1}}$. Modest reassurance that the error of our value of $V_\odot$ is less than $2\,\mathrm{km\,s^{-1}}$ is furnished by the fact that B10 favoured the same value using a distribution function that takes no account of the age and metallicity gradients in the disc. Consequently, our result is probably not sensitive to the assumptions about star formation and chemical evolution made by SB09a. However, as we develop more elaborate models of the Galaxy which fit a wider range of data, in particular more distant stars, we anticipate further small revisions in the value of $V_\odot$.

Acknowledgements

Chapter 5

Observations and Applications

5.1 Abstract

This chapter collects some of the observational tests and their discussions on implications for the model as well as a short description of Bayesian models for getting spectroscopic parameters that resulted from our work on Bayesian age determinations. The trend of azimuthal velocities against metallicities in the thin disc is discussed, showing that a shallow slope is a sign for stronger radial mixing, while a steep slope would be a consequence of missing migration. We demonstrate that mixing appears to be stronger than originally derived from the Schönrich & Binney (2009a) model. This can be traced back to the rather high radial metallicity gradient used for calibration. We show that eccentricity distributions should be disfavoured as an indicator for the history of the disc. Further we show observational evidence for migration in the metallicity plane of the new GCS as well as the confirmation for the predicted kinematic structures in the colour magnitude diagram of the Hipparcos data. We conclude by a short determination of the Solar birthplace.

5.2 About the trend in azimuthal velocities

Triggered by the findings in Chapter 3 some research has been undertaken to discover some of the features that had been predicted in the abundance plane. One of the most interesting features is a trend in mean azimuthal velocity of stars with increasing metallicity for objects belonging chemically to the thin disc. While the Schönrich & Binney (2009a) model cannot make a firm prediction about such trends for the high $[\alpha/\text{Fe}]$ stars that formed at early epochs, where it is not constrained yet what the radial abundance gradient and the radial behaviour of star formation really looked like, it makes very firm predictions about the trend with metallicity for the younger, low $[\alpha/\text{Fe}]$ stars: Those objects should show a significant downtrend of mean azimuthal velocity with metallicity, deriving from the radial abundance gradient of the young stars. With radial migration those objects then become shuffled around in angular momentum,

but the populations should still contain some residual information on where they were born: as stars from the inner Galaxy get scattered to larger angular momenta from where they can visit the solar neighbourhood, the metal-rich population is preferentially concentrated towards the inner Galactocentric radii, while the metal-poor outer disc populations are preferentially at large angular momentum. The explanation in Schönrich & Binney (2009b) focused on the fact that radial migration is largely responsible for us being able to find those migrated objects in large numbers at all, but unfortunately evoked the widespread misconception that radial migration is responsible for this gradient. This is not true, because in truth radial migration weakens the observed trend as can be made clear by considering two extreme cases: Assume a young disc radial abundance gradient of $-0.06\,\mathrm{dex/kpc}$ (see Luck & Lambert, 2011). In the first extreme case we assume that stars only get blurred, i.e. they do not change their angular momentum. Holding gradient and metallicity constant, we can write this as:

$$[\mathrm{Fe/H}](R) = [\mathrm{Fe/H}]_0 + \frac{d[\mathrm{Fe/H}]}{dR}(R - R_0) \tag{5.1}$$

where R_0 and $[\mathrm{Fe/H}]_0$ denote the Solar Galactocentric radius and the local metallicity. Assuming a disc with constant rotation velocity of $V_c = 233\,\mathrm{km\,s^{-1}}$ we can then replace the galactocentric radius R using angular momentum conservation and resolve the linear relationship for the local azimuthal velocity V:

$$V_\phi([\mathrm{Fe/H}]) = V_c \left(1 + \frac{[\mathrm{Fe/H}] - [\mathrm{Fe/H}]_0}{R_0} \frac{dR}{d[\mathrm{Fe/H}]}\right) \tag{5.2}$$

and we obtain for the slope in V_ϕ (on the quite meagre baseline in metallicity that would be observable.

$$\frac{dV_\phi}{d[\mathrm{Fe/H}]} = \frac{V_c dR}{R_0 d[\mathrm{Fe/H}]} = -474\,\mathrm{km\,s^{-1}/dex} \tag{5.3}$$

and for the values used in Schönrich & Binney (2009a) the result would be about $dV_\phi/d[\mathrm{Fe/H}] \sim -300\,\mathrm{km\,s^{-1}/dex}$, largely due to the steeper metallicity gradient assumed there. Measurement errors in metallicity would blur out the baseline and reduce the measured gradient, but this will not remove the stark contrast to what is observed in the data, as well as contributions from age-dependent evolution of the Galactic disc can hardly remove all difference on the super-solar metallicities. Radial migration with its redistribution in angular momentum, however, does a huge change to this relation: If we assume the other extreme case of complete radial mixing, the gradient will vanish, as the distribution of populations does not depend any more on where the stars have been born. So we see that in general radial migration reduces the gradient and is both detectable by the expansion of the baseline in metallicity and by the reduced gradient. The presence of a weak velocity-metallicity correlation in data confirms that there is considerable radial migration, but the mixing is not complete.

Let us examine those trends a bit on a real data set. From the model of Schönrich & Binney (2009a) we expect that the thick disc velocities are likely to destroy or remove any trend in the
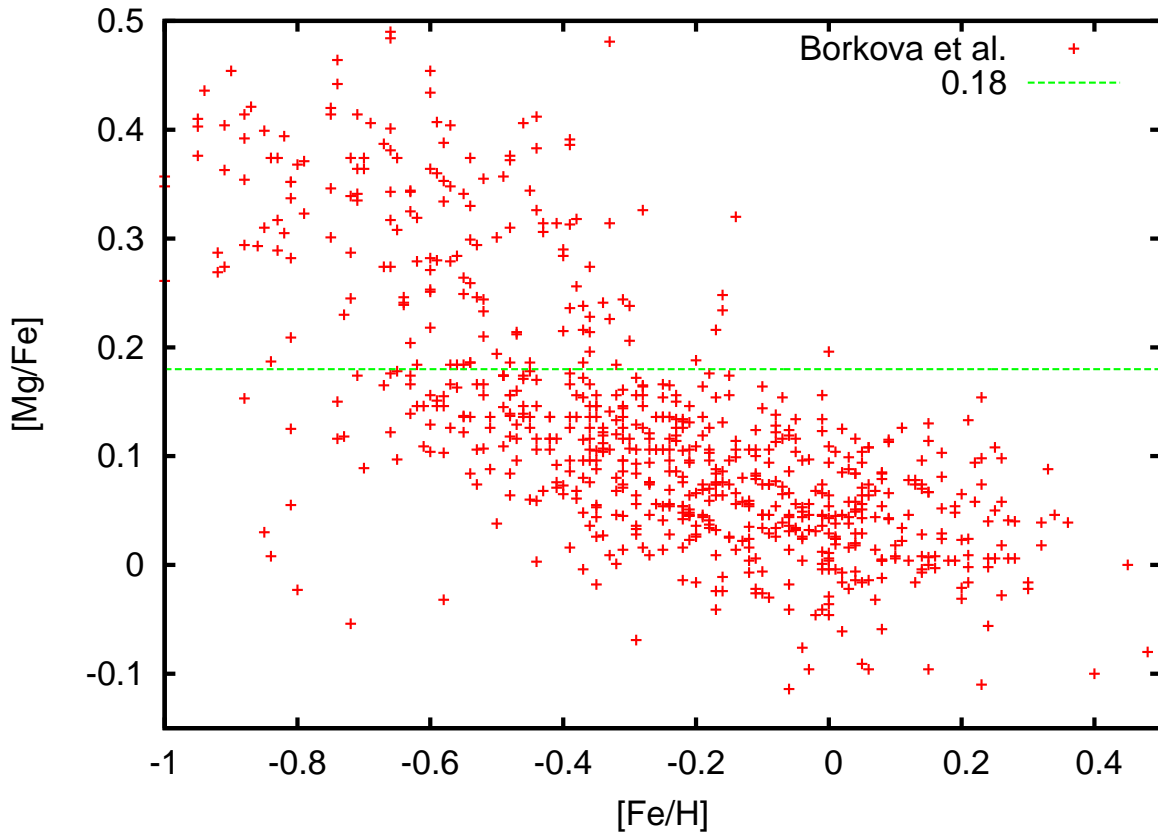
Figure 5.1: The metallicity plane in [Mg/Fe] versus [Fe/H] of the Borkova et al. sample. The depopulated region in the data advises a cut somewhere between [Mg/Fe] = 0.14 and [Mg/Fe] = 0.18 where we set the cut.

mean azimuthal velocities with mean metallicities. In the model they cancel out at intermediate metallicities, because the downtrend for the younger low [α/Fe] stars is compensated for by the increasing number of high asymmetric drift, high [α/Fe] stars of the chemical thick disc towards lower metallicities. In the lower metallicity regime ([Fe/H] < −1.0) we even encounter a mildly positive slope in the model, because of some peculiarities in early disc formation that will be discussed in an upcoming paper. In this light it is essential to get a clean cut in the metallicity plane, removing the high [α/Fe] population. The following exercise was first presented at the IAU assembly, but concerning the need for re-interpretation it seems appropriate to show it again. Fig. 5.1 shows the metallicity plane as defined by [Mg/Fe] as alpha element against [Fe/H] in the Borkova & Marsakov (2005) sample. This sample is a homogenised compilation of high resolution spectroscopic data from different major studies of local stars, like the Bensby et al. sample (Bensby et al., 2005), the Fuhrmann sample (Fuhrmann, 2004) or the Reddy et al. sample (Reddy et al., 2003, 2006). One should keep in mind a major caveat against over-interpretation of any data we use here: Almost all local high resolution data have strong kinematic selection

biases for increasing or decreasing the number of selected thin/thick disc stars. It should also be kept in mind that because of the strong correlations between single velocity components and also (as laid out in Chapter 3) between metallicities and kinematics, any such sample is uncontrollably biased both in metallicities and in velocity space. Yet it seems interesting to at least look at the trends. As advocated by the depopulated region at intermediate [Mg/Fe] we cut the sample to keep only objects with [Mg/Fe] < 0.18, to get a chemical thin disc selection. In light of the observational errors there might be some residual contamination, which seems to be confirmed when we measure the gradient of metallicity against angular momentum: Since the local azimuthal velocities can be translated directly into the angular momentum of those stars and let us this way estimate the stellar guiding centre radii, a local sample can be used as a good indicator of the radial abundance gradient. For our cut we estimate $d[\text{Fe/H}]/dR = -0.04\,\text{dex}/\text{kpc}$ a value that rises up to $-0.1\,\text{dex}/\text{kpc}$ depending on how much of the low angular momentum regime we remove from the sample and how far down in [Mg/Fe] we move the cut (the radial gradient increases mildly for stricter selections which indicates that we are tossing out some residual old stars). Interestingly this gradient is a bit higher than in the Luck & Lambert (2011) data, but this should not be taken too seriously in the light of the diverse biases in our sample.

The trend of mean heliocentric V velocity against metallicity in the low [Mg/Fe] subsample is examined in Fig. 5.2. A linear fit (green line) yields a highly significant slope of $dV_\phi/d[\text{Fe/H}] = (-31.5 \pm 4.2)\,\text{km}\,\text{s}^{-1}/\text{dex}$ and is plotted onto the data. The observed trend is a bit higher than what was found by Lee et al. (2011) - this can most likely be traced down to the larger $[\alpha/\text{Fe}]$ errors of the SEGUE (Yanny et al., 2009) sample with its low resolution spectra that likely results in larger contamination of the low $[\alpha/\text{Fe}]$ part with high $[\alpha/\text{Fe}]$ stars. Surprisingly our finding is not consistent with the result of Navarro et al. (2011) on essentially the same data. The same result as with the linear fit is seen from the binned means, where we divided the sample into 0.1 dex wide subsets. At the same time we plot the dispersions for each bin (purple line). We can compare this with the qualitative predictions of the different chemical evolution models: In classical chemical evolution models (e.g. Chiappini et al., 2001) the thin disc density ridge is created by the local population running along this ridge from low to high metallicities. This implies a significant age trend in metallicity and hence via the age-metallicity relation the most metal poor stars should show the highest velocity dispersions with a clear downtrend towards the metal rich objects. This is not observed, while the data are consistent with the behaviour in the radial migration models that would favour a rather flat behaviour of dispersions with metallicity. Similarly the mean V velocity trend is hard to explain in the classical framework, but straight forward in the framework of radial migration models. Yet there is a little problem: The trend of V velocities with metallicity is considerably higher in the model (predicting up to $50\,\text{km}\,\text{s}^{-1}/\text{dex}$) than it is in the data.

When we look at the above implications of the velocity gradient on metallicities, it becomes clear what went wrong in Schönrich & Binney (2009a). When we set the radial abundance gradient in the model, we had to rely on older abundance gradient data that now seem to have indicated a too steep abundance gradient. At least it is significantly steeper than the value derived by Luck
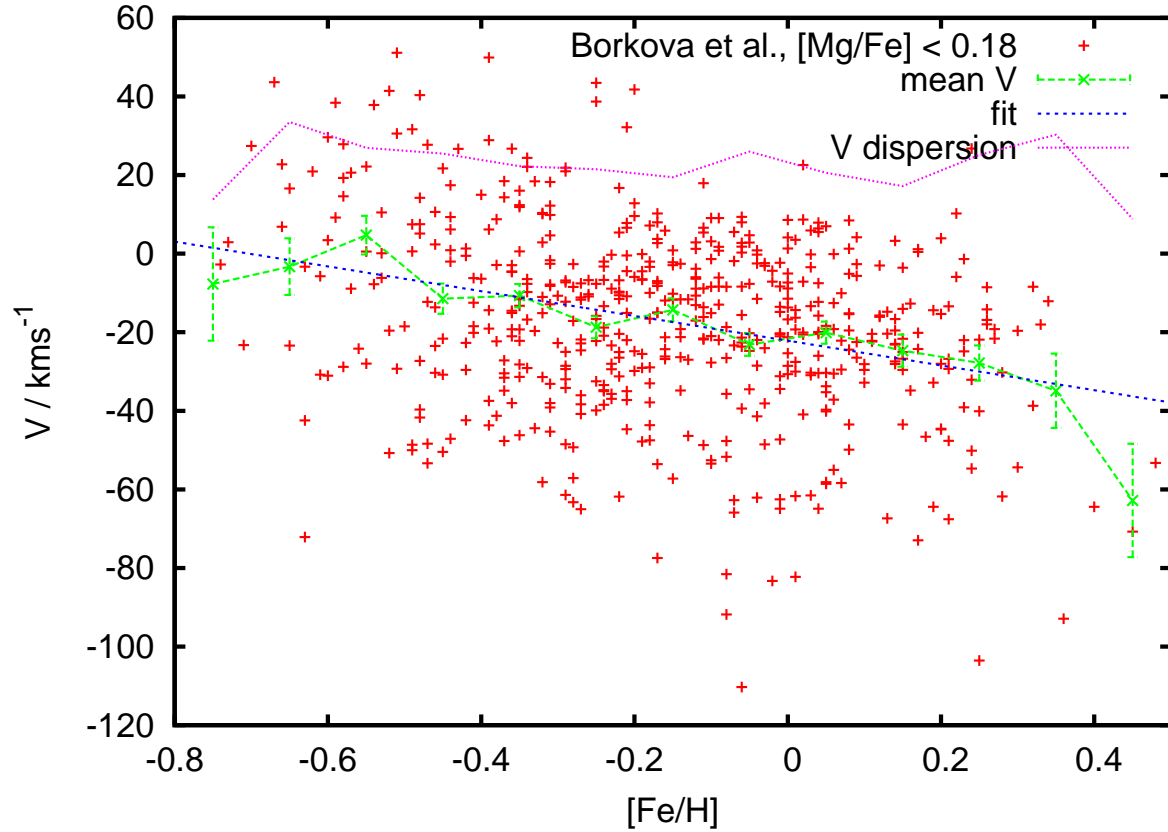
Figure 5.2: Kinematics versus metallicities in the Borkova dataset in the subsample of stars with [Mg/Fe] < 0.18 (red data points). The blue line gives the linear fit of the sample compared to the binned heliocentric mean velocities shown in green. The purple line shows the velocity dispersions.

& Lambert (2011). The overestimated gradient places one of the main findings of the first paper on firm grounds, namely that radial migration is necessary for explaining the local metallicity distribution. Yet, it appears that with the too steep gradient we underestimated the need for stellar radial migration: The lower the gradient is the farther stars need to migrate to yield the same width of the metallicity distribution. Strengthened migration should then result in a shallower slope of velocities with metallicity. As a side effect the stronger migration would result in a locally stronger and larger scale-height thick disc. The standard model from Schönrich & Binney (2009a) was already rather on the upper edge on how strong the thick disc may be. Again things fit together as on the decision between vertical energy and vertical action as conserved quantity Schönrich & Binney (2009a) decided for vertical energy. Solway et al. (in prep) and also the recent paper of Bird et al. (2011) showed that vertical action is rather conserved than vertical energy. This will deliver some reduction in thick disc scale heights that can balance the stronger thick disc arising from increased radial migration. An impediment to modelling has so far been
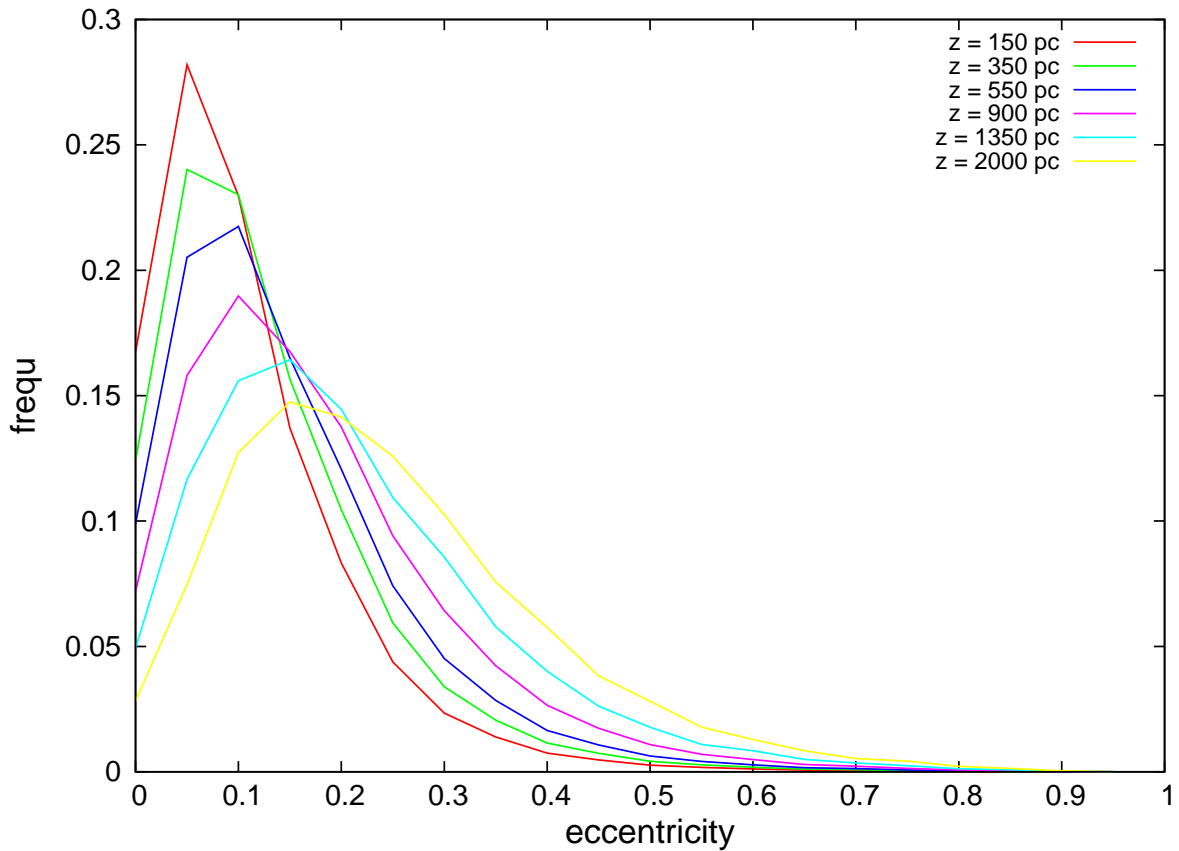
Figure 5.3: The eccentricity distribution from Schönrich & Binney (2009a) at different altitudes above the plane at Solar Galactocentric radius. We used simple population masses, i.e. no selection function was applied.

that despite its advantages the classic adiabatic approximation and also adiabatic modelling of stellar populations as put forward in Binney (2010) violate total energy conservation. After we found a simple solution to this problem in Schönrich & Binney (2011) by introduction of the adiabatic potential that corrects the horizontal potential for the lost energy (which results in pushing the high vertical energy orbits back to the outer disc compensating locally for some of the difference between isothermal approximations and the adiabatic approximation), we are currently running a recalibration of the model for getting a more definitive answer.

5.2.1   About eccentricity distributions

In recent studies starting with Sales et al. (2009) and e.g. later Lee et al. (2011) the comparison of eccentricity distributions has become a frequently used tool to assess possible scenarios for the history of the Galactic disc. Fig. 5.3 shows the eccentricity distribution from the Schönrich & Binney (2009a) model without change of any parameter and applying no selection function,

i.e. using the population masses as weight. The result looks quite similar to Lee et al. (2011), yet we do not want to book this as a win, as we would like to advocate against the use of eccentricity distributions for several reasons: First of all it is counter-intuitive to quench all the ample information we have into a single quantity that only gives a distorted picture on important things like the angular momentum distribution of the disc. As a minor other point there needs to be performed a real propagation of distance, proper motion and line-of-sight velocity errors that to date does not appear to have been fully performed (this would be a very time-consuming exercise, because in contrast to simple velocity space the errors have to be calculated on the orbital model from which the eccentricities must be derived). More important the derived eccentricity values depend on the assumed potential, which governs the orbit extension of a star derived from its estimated position and velocity. The Achilles heel of the method that comparisons of eccentricities utilise a different potential for the calculation of orbits than the theoretical models they compare to, has in most cases been neglected. One may of course argue that eccentricities express the general circularity of orbits in the different approaches. To some part this is true, but there a far more vigorous problem: The heating in models and even principle heating mechanisms are very weakly constrained (see e.g. the discussion in Aumer & Binney, 2009). Locally the eccentricities are quite directly related to azimuthal velocities in that high asymmetric drifts or respectively low rotational velocities imply large eccentricities. So we see the large uncertainty in the expected eccentricities by looking at the major changes in Fig. 6.2 that are induced by moderate variation in the assumed parameters of the disc. For example heating up the inner disc of the Galaxy a bit more, which is covered either by heating from a bar or respectively simply in the uncertainties intrinsic to molecular clouds as source of random energy, the number of high eccentricity visitors from the inner disc largely increases. This would in the one-dimensional comparison be nearly indistinguishable from high eccentricity stars contributed e.g. by a minor merger in the outer regions of the disc. Summed up we see that a large range of eccentricity distributions can be explained just by uncertainty in heating and potential, but moreover the sole use of eccentricity distributions hides a lot of valuable information.

5.3 The metallicity plane as seen by the new GCS

In their recalibration of the Geneva-Copenhagen Survey (hereafter GCS, Nordström et al., 2004; Holmberg et al., 2007) Casagrande et al. (2011) were able to derive tentative $[\alpha/\text{Fe}]$ estimates from Strömgren photometry. This opened new perspectives to test the predictions of the Schönrich & Binney (2009a) model on the GCS that is now the largest unbiased sample with some indication of $[\alpha/\text{Fe}]$ abundances and highly reliable kinematics. As a recalibration of the model is still ongoing we have to limit ourselves to a qualitative discussion where we show the main structures in the metallicity plane of the Geneva-Copenhagen Survey, but postpone a real quantitative examination. All details on he derivation of parameters can be found in Casagrande et al. (2011) and will not be discussed here.

Fig. 5.4 gives an overview of the metallicity plane in the "good subsample", i.e. stars with
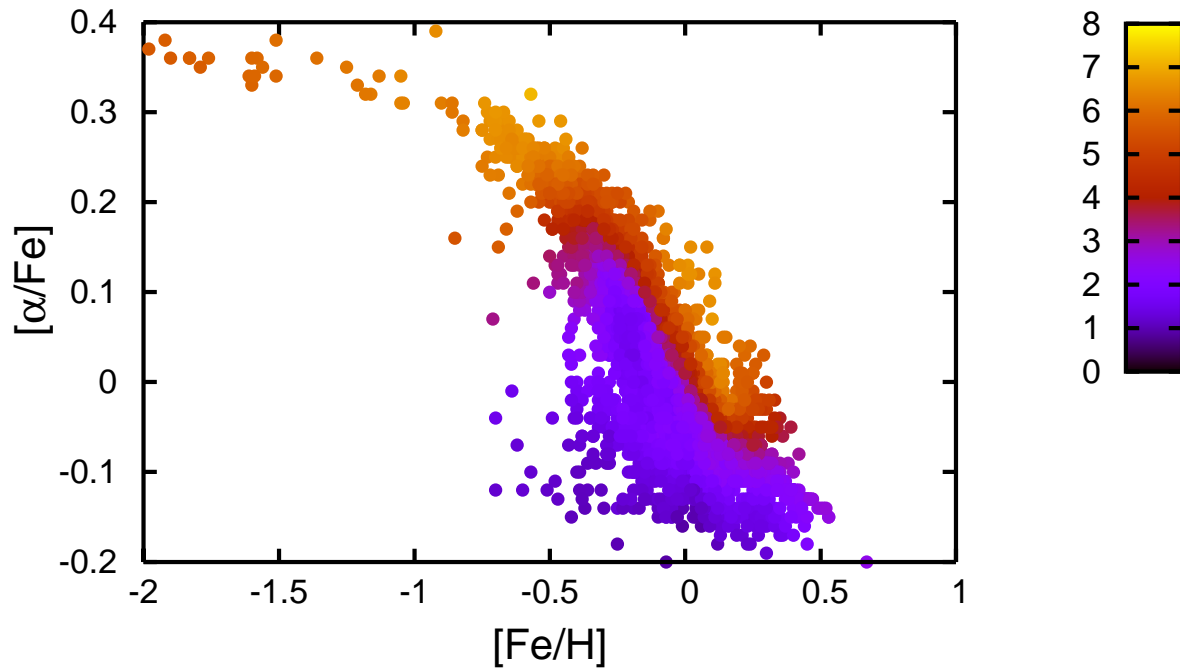
Figure 5.4: Average age in the metallicity plane ($[\alpha/\text{Fe}]$ versus [Fe/H] of the GCS. The colour codes the mean age determinations in Gyrs.

infrared photometry available, so that the stars have good parameters and especially a sensible $[\alpha/\text{Fe}]$ estimate. For getting the mean ages, we searched for each star in the plane its hundred closest neighbours and evaluated the mean age from the age expectation values using BASTI (Pietrinferni et al., 2004) isochrones. The age determinations are described in more detail Casagrande et al. (2011). Although the plane covers the main features we see some weaknesses. At first the age determinations are quenched down to a maximum of 8 Gyr. This is mostly caused by stars with very uncertain age determination (e.g. when they lie on the red part of the main sequence) that then are assigned mean ages of about 6 Gyr. Yet the expected features are in place: The high $[\alpha/\text{Fe}]$ stars are very old in contrast to the low $[\alpha/\text{Fe}]$ stars that are very young. In the low $[\alpha/\text{Fe}]$ part there does not appear to reside a strong dependence of age on metallicity, which is much in favour of radial migration models that can allow for the stars on the thin disc ridge line to be relatively young without significant trend. Classical chemical evolution models would require older ages on the metal poor side compared to the metal rich side, because the model has to evolve from metal poor to metal rich slowlier than radial migration models, where the width of the thin disc ridge line is formed by immigrants from other parts of the disc. As a word of caution the ages are the weakest constraint, because it is not clear if the isochrones show a robust metallicity dependent reddening, which can produce wrong age trends against metallicity. Rather than a constraint on chemical evolution models this plot is a consistency check for the $[\alpha/\text{Fe}]$ estimates, although they are of course far from perfect: It is clearly visible that there is no real gap
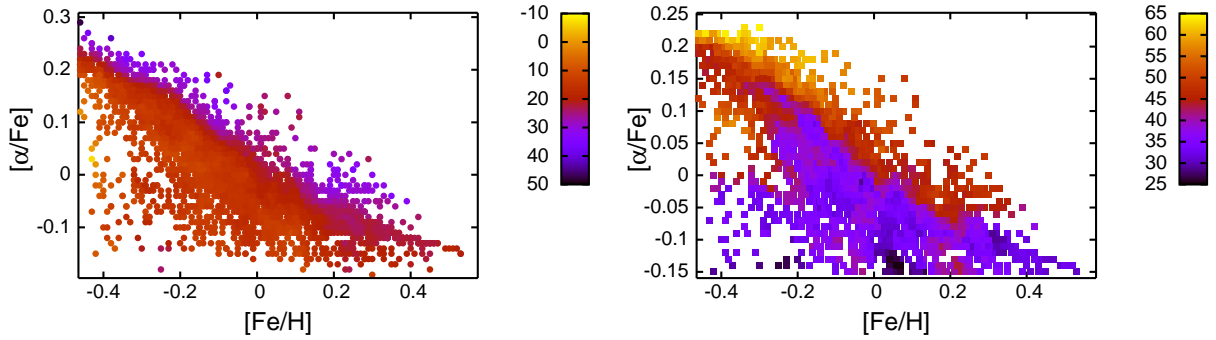
Figure 5.5: Left panel: Average asymmetric drift (in $\mathrm{km\,s}^{-1}$) in the metallicity plane ($[\alpha/\mathrm{Fe}]$ versus [Fe/H] of the GCS. Right panel: Average velocity dispersion (in $\mathrm{km\,s}^{-1}$).

in densities between the thick and thin disc components, which is a consequence of the $[\alpha/\mathrm{Fe}]$ determination uncertainties. Was the error in the determinations larger than expected, we would not see the clear distinction in ages along the plot. On the side of ages it is also worth mentioning that Bensby et al. (2007) find the lowest ages near solar metallicity with both metal-poor and metal-rich stars tend to be slightly older, which would be very reasonable in the framework of radial migration, where those objects require a little bit of time to reach the solar neighbourhood. The results of Fig. 5.5 confirm very nicely our findings from Section 5.2. On the low $[\alpha/\mathrm{Fe}]$ side we find a region of almost constant velocity dispersions $\sqrt{S^2}$ in [Fe/H], which is in stark contrast to what would be predicted in the framework of classical chemical evolution models, but is very well in the range of the expectations from Schönrich & Binney (2009b). The region of high velocity dispersions wraps nicely around the thin disc at the edge of high $[\alpha/\mathrm{Fe}]$, high [Fe/H] values, i.e. we can clearly identify the high metallicity tail of the thick disc as suggested by the studies of Bensby et al. (e.g. Bensby et al., 2003, 2005). The expansion of the high dispersion regime towards lower $[\alpha/\mathrm{Fe}]$ values for the most metal poor stars is caused by a very low number of extreme objects and might be a contamination by relatively metal-rich halo objects. The left panel of Fig. 5.5 also confirms that the trends that we have seen in the Borkova & Marsakov (2005) sample were not a result of kinematic biases. At all $[\alpha/\mathrm{Fe}]$ values (apart from the highest $[\alpha/\mathrm{Fe}]$, where the thick disc ridge line bends to the left) we see a robust downtrend of mean azimuthal velocity with increasing metallicity.

5.4 A hot spot in kinematics

The most exciting result from the new GCS is shown in Fig. 5.6. Radial migration models predict that on the metal rich low $[\alpha/\mathrm{Fe}]$ side of the metallicity plane we should see young populations that have quite low velocity dispersions, but that have migrated just far enough outwards so that they can be seen in local samples at high asymmetric drift. In terms of the asymmetric drift relation discussed in the previous chapter this means that they have a very strong radial density
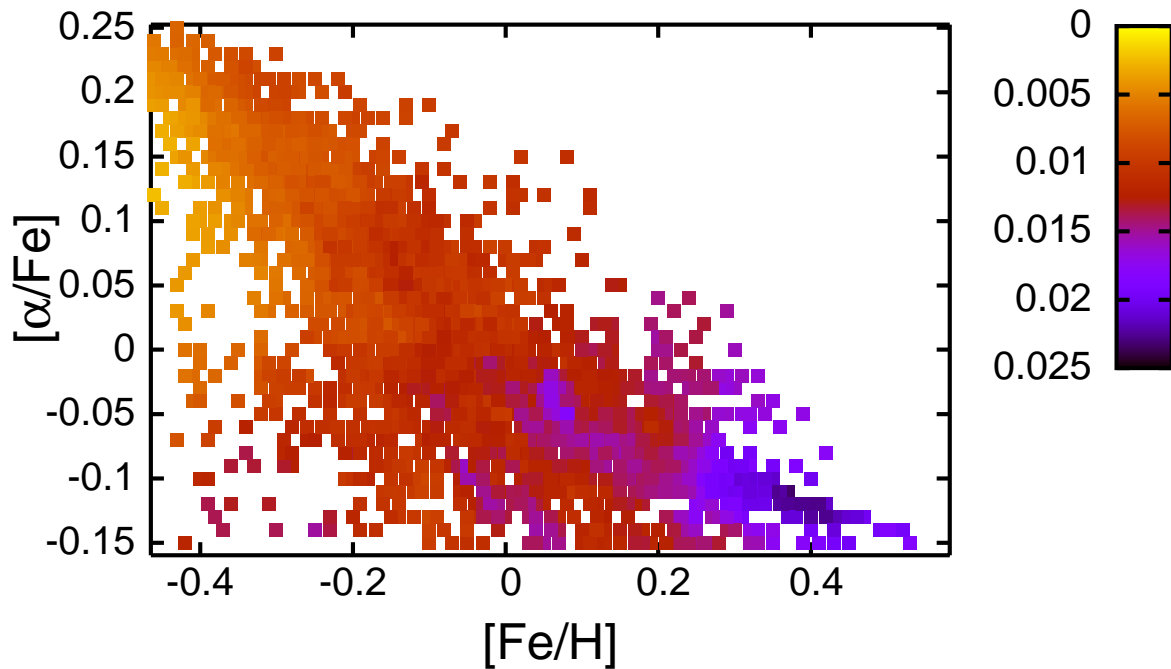
Figure 5.6: Left panel: Average asymmetric drift (in $\mathrm{km\,s^{-1}}$) divided by the average velocity dispersion in the metallicity plane ($[\alpha/\mathrm{Fe}]$ versus $[\mathrm{Fe/H}]$ of the GCS.

gradient in the solar neighbourhood and should thus have a very low asymmetric drift to dispersion ratio. And indeed this "hot spot" can be spotted Fig. 5.6, where we plot the mean difference to the suspected circular velocity divided by the squared velocity dispersion of the population: The stars with high $[\mathrm{Fe/H}]$ and low $[\alpha/\mathrm{Fe}]$ values show an extreme ratio of asymmetric drift to velocity dispersion. The same could already be guessed from the Borkova et al. sample, where the asymmetric drift increases with metallicity, while the dispersion does not experience notable change, however, with the new GCS we have this result free of a possible kinematic bias. As it should be expected the stark contrast between high and low metallicity populations gets reduced towards higher $[\alpha/\mathrm{Fe}]$ values, although we cannot very well disentangle how much of this might be a consequence of the uncertainty in $[\alpha/\mathrm{Fe}]$ estimates. This inhomogeneity is also a welcome confirmation to the prediction from Chapter 4 that local populations have highly different constants in the asymmetric drift relation.

Despite the importance for the determination of the Local Standard of Rest, the predictions from Chapter 4 stayed essentially untested so far. However, after having seen the trends in the metallicity plane we can already be sure that we will see strong signals when we examine the colour-magnitude diagram. Fig. 5.7 shows the kinematics in the colour-magnitude diagram of the Aumer & Binney (2009) subsample of the Hipparcos data (van Leeuwen, 2007), that was kindly provided by M. Aumer. For each star we took the closest 150 neighbours in a mildly elongated ellipse oriented parallel to the main sequence. This proved to be the best compromise between
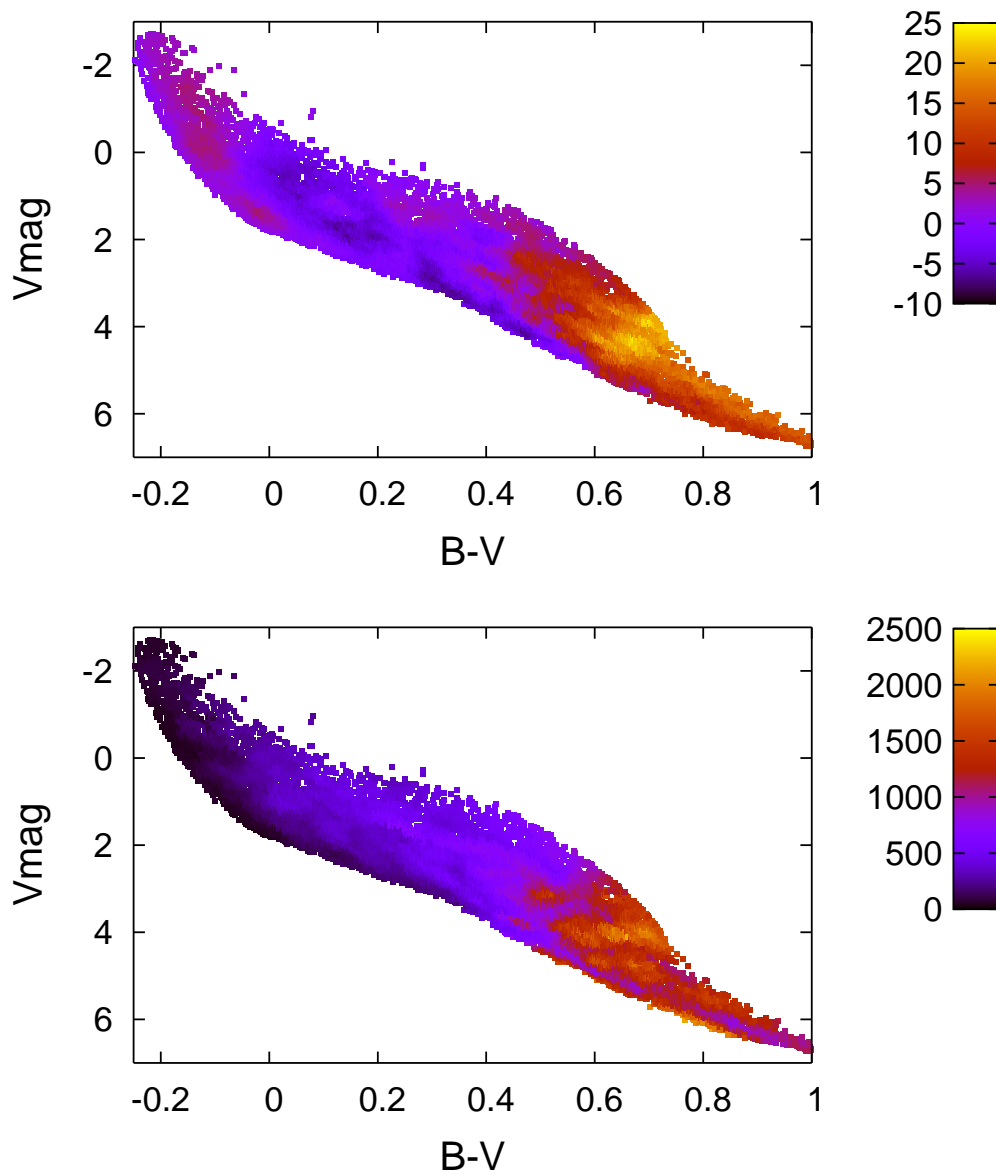
Figure 5.7: Kinematics on the colour-magnitude diagram of the Hipparcos data (absolute *V* magnitude against *B* − *V* colour). Upper panel shows the mean asymmetric drift, lower panel the squared velocity dispersion in the radial velocity component of stars. Like in the GCS we took the closest 150 of each star as sample.

additional blurring of our data that are already affected by the parallax and hence magnitude errors of Hipparcos as well as photometry errors and scatter in the results by too small subsample sizes. In the top panel we display the mean asymmetric drift and in the bottom panel the mean U velocity dispersion. The similarity of the results to the equivalent plots in Chapter 4 is surprising. As predicted from the Schönrich & Binney (2009a) model we do not see at all a uniform increase of asymmetric drift and dispersion towards redder colours, but there is a lot of fine structure. In the lower panel we can even see the relatively cool main sequence of lower metallicity disc stars quenched between the hotter high metallicity stars and the sub-dwarfs (visible towards the red at $B - V > 0.45$). The fainter/bluer objects with higher dispersion are the sub-dwarfs, while on the red side we encounter the metal-rich stars. We can as well see the kinematically hot spot of the older high metallicity turn-off accompanied by relatively high asymmetric drift values (at the "knee" in the plot around $B - V \sim 0.65$). This hot region can be held responsible for the mild overshooting that was encountered by Aumer & Binney (2009) in their pure colour binning near Parenago's discontinuity in some velocity components and that is also featured in the predictions of Schönrich, Binney & Dehnen (2010). The peak asymmetric drifts and dispersions stay a little bit behind what might at first glance be expected from the models, but we have to take into account that the extreme velocities appearing in the models also come in very low number densities so that they are buried in the error tails (with typical Hipparcos parallaxes the absolute magnitude has a notable error) of their neighbouring populations. In light of these difficulties it is already surprising that we can detect the cooler main sequence part between its hot counterparts. Interestingly we can even see the negative asymmetric drift values or respectively high azimuthal velocity values of the metal poor populations on the blue side of the turn-off region. Similarly the "hot valley" of slightly lower angular momentum/kinematically hotter stars located red-wards of the main sequence rising towards higher luminosities shows a tentative imprint to these data.

As the non-constant coefficient in the Strömberg equation or respectively asymmetric drift relation basically describes the radial density gradient of a population, it is not useless as one might conclude from the failure in the determination of the Solar velocity, but it is a valuable indicator to identify subpopulations in a sample. In Fig. 5.8 we see on the luminous blue end of the Hipparcos sample a young population with high asymmetric drift to dispersion ratio that follows nicely a very metal-rich young isochrone. To its red side we see a population that obviously comes from outer radii and hence we can now clearly see the reason for the pronounced wiggles that were found on a pure colour selection by Dehnen & Binney (1998b) and later by Aumer & Binney (2009): they are simply young open clusters dominating the blue end of the colour magnitude diagram with substructure. Red-wards of $B - V \sim 0.3$ (as can be expected from the source terms losing importance in the Jeans equations as stellar ages increase) we see a very well mixed sample. But again the expected structures are confirmed: From blue to red (or respectively from faint to bright) across the main sequence the ratio of asymmetric drift to squared radial velocity dispersion increases as the radial density gradient steepens for the more metal rich inner disc populations.

Although all these results look stunningly similar to the theoretical predictions we would like to put some words of caution: Especially inside-out formation can be a second reason apart from
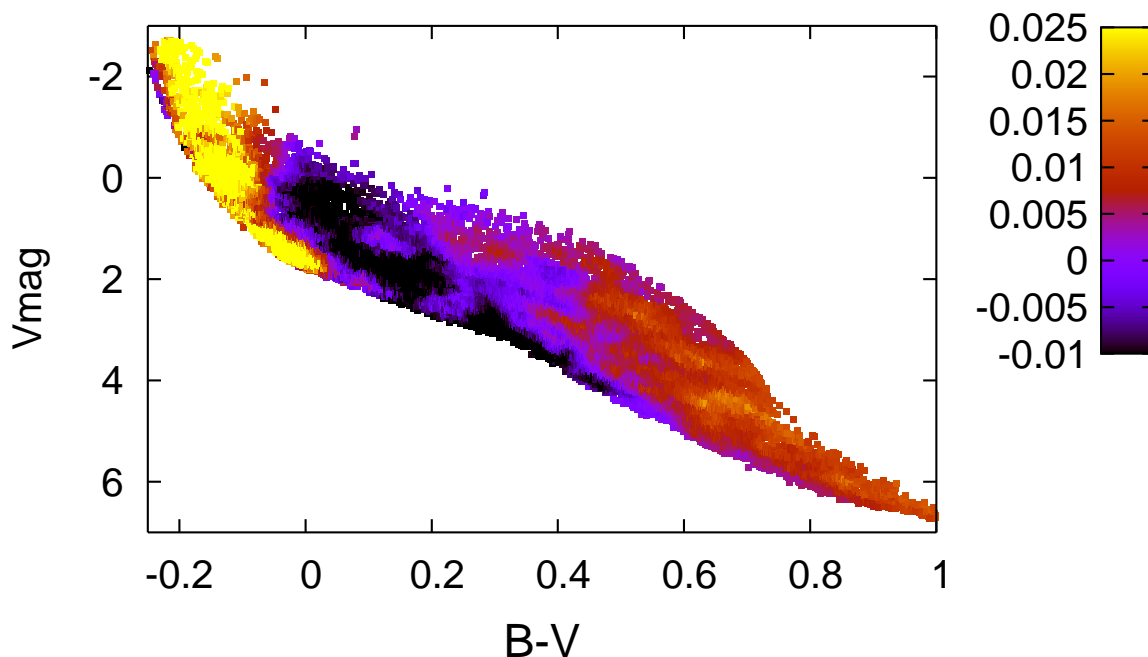
Figure 5.8: The coefficient of the Strömberg equation, in our case dividing the asymmetric drift by the squared radial velocity dispersion.

the metallicity gradient that can be held responsible for the observed structure, so a definitive interpretation will require deeper and more quantitative analysis than the presented as well as detailed and improved models on the theoretical side.

5.5   A Bayesian method for spectroscopy

5.5.1   Introduction

This work is a further development from the Bayesian age determination that I developed for the recalibration of the GCS (Casagrande et al., 2011). Having all those algorithms already at hand we decided that it would be a pity to let the machinery stay unused and developed it towards an area where it can help improve the uncertain parameter determinations: low resolution spectroscopy. With the advent of large spectroscopic surveys, spectroscopic analysis has at least partly experienced a shift from analytic craftsmanship in resolving the spectroscopic jigsaw by hand and experience to the development of large automatic pipelines that are required to cope with the huge amount of data. Many of these surveys, particularly RAVE (Steinmetz et al., 2005), SDSS/SEGUE (Yanny et al., 2009) and LAMOST work in a regime of low to intermediate resolution spectroscopy with mostly moderate signal to noise ratios, where the determination of

stellar parameters is uncertain. Although a lot of work has been invested into the development of the RAVE (e.g. Zwitter et al., 2008) and SEGUE (e.g. Lee et al., 2008a,b) another development in stellar astrophysics that would naturally fit into these automatic knowledge machines has been left out.

Following the use of probabilistic schemes or respectively Bayesian analysis in other fields of astrophysics, those methods were pioneered by Jørgensen & Lindegren (2005) and Pont & Eyer (2004) for stellar astrophysics in order to gain more reliable age estimates to especially the Geneva-Copenhagen Survey (Nordström et al., 2004) that are particularly devoid of biases arising from naive age analysis like the terminal age bias: Stars on short-lived stages in stellar evolution, i.e. rare objects are unphysically overrepresented in the analysis results, if no proper weighting function (or respectively the wrong one, as no weighting means a constant weight) has been applied to the isochrones. A good description of Bayesian analysis to fix also other parameters like the absolute magnitude (and hence distance modulus) can be found in Burnett & Binney (2010).

In the following draft we aim to develop a probabilistic scheme to directly exploit our a priori knowledge in combination with spectroscopic analysis and photometric parameter calibrations, especially via the infrared-flux-method (IRFM Casagrande et al., 2010).

5.5.2 Probabilistic Approach

General Approach

Spectroscopists usually quote on their analysis the best-fit parameters on their quantities plus some error margin. Yet this is only a subset of the information that can actually drawn from their analysis - it would only be if the errors on the stellar parameters were not correlated, i.e. if $Cov(\mathrm{T_{eff}}, [\mathrm{Fe/H}]) = 0$. This is by far not true - the errors are highly correlated by the underlying physics. The stellar effective surface temperature $\mathrm{T_{eff}}$ and also surface gravity $\log(g)$ do affect the ionisation equilibria, the atomic level populations, etc., and hence spectral line strengths and inferred elemental abundances. Hence the metallicity estimate will be a function on those two variables, while it affects their values by itself. The strong correlation between estimated temperature and metallicity is found everywhere in literature and can e.g. be guessed from figs. 6 and 7 in Zwitter et al. (2008), or fig. 12 in Siebert et al. (2011). So the quantity handling all the available information are not the single best-fit values, but the multidimensional probability distribution of the stellar parameter estimates on the given spectrum:

$$P_{sp}([\mathrm{Fe/H}], \mathrm{T_{eff}}, \log(g), [\alpha/\mathrm{Fe}], X_{\mathrm{sp}}) \tag{5.4}$$

where X_{sp} sums up all the spectral parameters not listed in this course, e.g. micro-turbulence - if not a $3D$ model atmosphere is run (see a discussion of advanced spectroscopic analysis in Asplund, 2005b), that does not require this parameter - , rotational velocity of the star, reddening, etc.

Yet, as discussed by Asplund (2005a) in view of the IRFM, spectroscopy is not the only thing we know: We also have photometric information about the examined objects, with Hipparcos

and Gaia knowledge about their parallaxes and hence distances, strong constraints by stellar evolution and a priori knowledge on stellar parameters, i.e. expectations about the IMF or stellar ages. The latter become particularly important for surveys with low to intermediate spectral resolution and for large samples as a quality control. So what needs to be done and unfortunately has not been undertaken before is the design of a scheme to optimally combine those different sources of information. Let's first go to stellar evolution and some a priori knowledge: Stellar evolution models give very firm constraints on the possible loci of stars in parameter space: In simple models their parameters are a simple function of their initial mass, metallicity and age:

$$(T_{eff}, \log(g), C) = f'(M_i, [Fe/H], [\alpha/Fe], \tau), \tag{5.5}$$

where C denotes the full information by the absolute magnitude and colours of stars. This relation provides in theory a very accurate mean of discarding major parts of the parameter space of spectroscopic results.

As has been shown by various sources (e.g. Chieffi et al., 1991; Chaboyer et al., 1992), the different metallicity indicators can moreover be replaced by an effective [Me/H] without significant accuracy. In an ideal world stellar evolution would hence give us a three-dimensional region in parameter space, where stars can reside, which before the isochrone turnoff with its age dependence even collapses into a two-dimensional sheet. In reality those predictions are affected uncertainties in atmosphere models, in the modelling of the stellar interior (see e.g. Magic et al., 2010) and in a couple of initial parameters (Charlot et al., 1996), particularly the initial helium problem particularly on the metal poor side (Casagrande et al., 2007). This should be accounted for by broadening the above relation. In a simple way speaking in the formalism of Burnett & Binney (2010) this can be achieved by augmenting the observable errors a bit. In this case it will be advisable to work with variable errors: While stellar models are very precise on the upper main sequence, their reliability deteriorates towards the coolest and evolved objects, i.e. M dwarf and the giant branches.

Using the mapping given by stellar evolution models, we can write down the probability distribution:

$$P(T_{eff}, \log(g), C) = G'(\sigma) \circ$$
$$\circ \int f'(M_i, [Fe/H], [\alpha/Fe], \tau)$$
$$\cdot P_p(\tau, M_i, [Fe/H], [\alpha/Fe], X) dM_i d[Fe/H] d[\alpha/Fe] dX \tag{5.6}$$

where $P_p(\tau, M_i, [Fe/H], [\alpha/Fe], X)$ sums up our a priori information on these quantities and the result gets convolved with $G'(\sigma)$, taken as described above to be some Gaussian broadening according to the error vector $\sigma = (\sigma_{T_{eff}}, \sigma_{\log(g)}, \sigma_C)$. In case we want to accommodate a Galactic model, one would need to further work in the distance distribution and the distance modulus for the sample.

On the left hand side we must now attain the parameter space that we need for compatibility with the spectroscopic results (i.e. we need a probability distribution in the same dimensions):

Replace the function f' by an extension of f' that is equivalent with f' on $(T_{eff}, \log(g), C)$ space and is an identity mapping on the other parameters (and do so in parallel with G'):

$$P([Fe/H], [\alpha/Fe], T_{eff}, \log(g), M_i, \tau, C, X) = G(\sigma) \circ$$
$$\circ \int f(M_i, [Fe/H], [\alpha/Fe], \tau)$$
$$\cdot P_p(\tau, M_i, [Fe/H], [\alpha/Fe], X) dM_i d[Fe/H] d[\alpha/Fe] dX \qquad (5.7)$$

This entity looks evil, but it is not. We can gain it by a simple weighted (via our priors) integral over the isochrones and any condition we impose upon our parameter set can be gained by multiplying the corresponding probability function onto P and then (like in Burnett & Binney, 2010) normalising the sum to one, after we have integrated out all dimensions we do not like. So we can get the probability distribution in our favourite parameter space:

$$P_i([Fe/H], [\alpha/Fe], T_{eff}, \log(g)) =$$
$$\int P([Fe/H], [\alpha/Fe], T_{eff}, \log(g), M_i, \tau, C, X) dM_i d\tau dC dX \qquad (5.8)$$

Once this is established, we can combine the spectroscopic information with the stellar evolution and a priori knowledge by a simple multiplication:

$$P' = P_{sp} P_i \qquad (5.9)$$

Isochrone sets and priors

To get some rudimentary grip on the uncertainties in stellar models we make use of two independent data sets: A dense grid drawn from the web interface of the Padova isochrones (Bertelli et al., 2008, 2009) and a dense grid of BASTI isochrones (Pietrinferni et al., 2004, 2006, 2009) that was kindly provided by S. Cassisi for our own probabilistic age determinations in Casagrande et al. (2011). The Padova sample consists of isochrone data sets at 56 metallicities ranging from $Z = 0.0001$ to $Z = 0.07$. Their solar metallicity is at the Grevesse & Sauval (1998) estimate of $Z_\odot = 0.017$, while the price they have to pay for the closer proximity to recent estimates (Asplund et al., 2009) is a rather low solar ($Y_\odot = 0.26$) and hence at a standard $\Delta Y/\Delta Z$ too low primordial helium abundance compared to standard Big Bang Nucleosynthesis (Steigman, 2010) (another point might be their lack of diffusion, which acts in the same direction). In the query we hence had to limit $Y > 0.23$, where their grid ends. We applied a dense age spacing of 0.01 dex or respectively 2.3%. The BASTI isochrones still use the (Grevesse & Noels, 1993) solar metallicity and we apply their standard helium abundances. We have 20 metallicity bins from $Z = 0.0001$ to $Z = 0.04$ and an age spacing of at maximum 100 Myr.
As initial mass function we apply the Salpeter (1955) IMF, with the usual exponent $\alpha = 2.35$, any other IMF of desire can be readily implemented and tested for.
It would be tempting to use a more specific age prior or even age-metallicity relation, but this would raise concerns about that results might be influenced by prejudices on the age of stellar components. Many studies make firm conclusions that the oldest populations in the Galaxy exceed 10 Gyr in age (cf. Aumer & Binney, 2009; Schönrich & Binney, 2009a). Hence we use a simple flat age distribution between 0 and 14 Gyr as a prior.

Photometric calibration

The isochrones are a splendid tool to cut out unphysical parameter space. Yet if using isochrone colours we would inherit the vulnerabilities and uncertainties of model atmospheres and synthetic colours. It can thus be appropriate and currently appears the more reliable way to ignore the colour information on the isochrones and exploit it instead by well-calibrated empirical relations. These are delivered by the infrared-flux method (IRFM, Blackwell & Shallis, 1977; Casagrande et al., 2010). In addition the remaining colour information can be scanned for information on reddening, metallicity, alpha enhancement or in some cases gravity. Photometric calibrations are a vastly used tool and if parameters apart from T_{eff} are required, narrow band filter systems like Strömgren or Washington photometry contain the best information. Yet some tentative estimates can be derived from broad band photometry as well. Overall, photometric methods deliver a third probability distribution $P_{ph}(T_{eff}, \log(g), [Fe/H], [\alpha/Fe])$. Again this can be combined with the two other sources to the final probability distribution

$$P_f = P_{sp}P_iP_{ph}, \tag{5.10}$$

from which our improved parameter estimates can be drawn. The photometrically derived temperatures are generally of a quality excelling that of spectroscopic ones in their scatter and their zero points: It was shown in previous studies (Casagrande et al., 2011) that photometric temperatures from the IRFM are (apart from the most metal poor objects) in sound agreement with stellar evolution models.

5.5.3 Photometric method of getting temperatures

Photometry can be a powerful method to derive stellar parameters (Bessel, 2005). In fact, each colour convolve the information enclosed by a stellar spectrum over the considered filter transmission curve. Selecting filters over regions of a spectrum primarily sensitive to certain physical parameters, it is thus possible to derive the latter to a certain accuracy (see e.g. Asensio Ramos & Allende Prieto, 2010, for a generalisation of this idea). A typical example is provided by the intermediate band Strömgren system, through the m_1 and c_1 indices. Those are designed to measure the depression owing to metal lines around $4100\,\text{Å}$ and the Balmer discontinuity, respectively, making the two indices ideal estimators of metallicity and surface gravity in late type stars. In contrast, focusing on spectral region relatively unaffected by line blanketing can give important information on T_{eff}, as e.g. the $b-y$ index (to remain on the Strömgren system). However, broad-band colours are usually more useful to estimate T_{eff}; notice though that colours per se are not analytically related to the stellar effective temperature, metallicity or other physical parameters. Relations linking stars of known physical parameters to their colour indices must be constructed. Those can be obtained e.g. from synthetic colours and the underlying T_{eff} of the models used, but the resulting calibration is very vulnerable to the uncertainties in the adopted theoretical fluxes. Similarly, colour-temperature calibrations obtained employing spectroscopic T_{eff} intrinsically carry the uncertainties which plague spectroscopic T_{eff} estimates. To
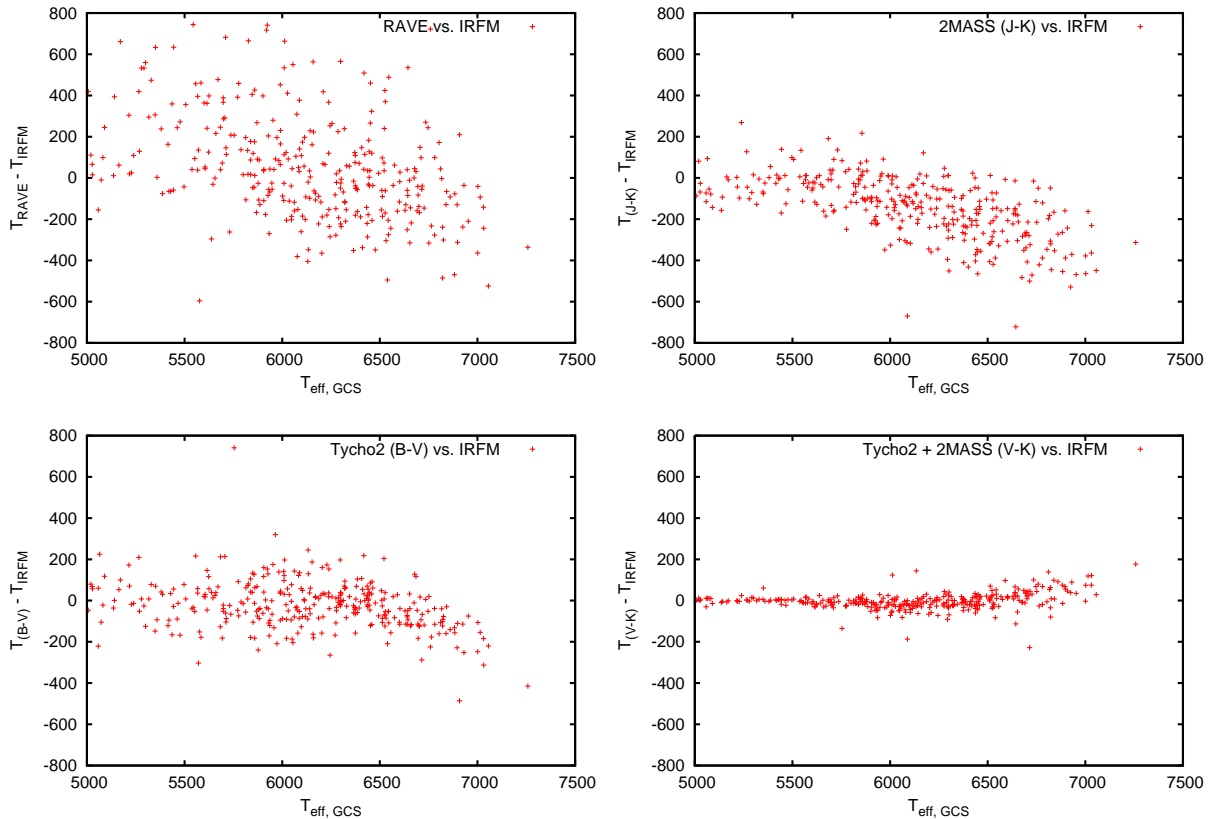
Figure 5.9: Differences in temperatures between IRFM derived temperatures and RAVE (top left) as well as three colour calibrations in different colour bands. It can clearly be seen that even on pure infrared colours (for obvious reasons they lose accuracy on hot stars) the colour calibration gives some value added with the best information contained of course in a combination of infrared and visible. Good visible photometry would hence boost the reliability of temperatures in RAVE. The slight trends at higher temperatures in the colour calibrations derive from the use of unchanged, old relationships that are not yet calibrated in that temperature range for this sample and can hence be removed from the sample.

this respect, only few methods are really empirical. One resorts on stars with measured angular diameters θ, where the effective temperature can be derived from the fundamental relation $F_{Bol} = \left(\frac{\theta}{2}\right)^2 \sigma T_{\mathrm{eff}}^4$. However θ can be measured only for nearby stars, thus limiting the calibration to solar metallicity stars. In addition, nearby stars are so bright to be saturated in most of the recent systems (such as e.g. 2MASS or SDSS), which are instead heavily used for the purpose of Galactic investigations. The IRFM provides another empirical way of determining T_{eff}, using multiband optical and infrared photometry to recover the bolometric F_{Bol} and infrared F_{IR} flux of each star and using the analytical relation linking T_{eff} to the ratio $\frac{F_{Bol}}{F_{IR}}$. Taking into account

photometric zero point uncertainties and random photometric errors, reliable estimates on the uncertainties on the derived T_{eff} can also be obtained. Improved reddening estimates would be beneficial, e.g. via known calibrations using $H\beta$ photometry (e.g. Karatas & Schuster 2010). A comparison on a GCS star sample between RAVE, the IRFM and single colour calibrations can be seen in Fig. 5.9. We will soon see if our method can really improve on the stellar parameters compared the standard pipeline results.

5.6   The Origin of the Sun

At least since the paper of Wielen et al. (1996) the birthplace of the Sun as been an open question in astrophysics. As the Sun was believed to be more metal-rich than the Solar Neighbourhood it was believed that the Sun was born considerably inside the current solar radius. The common line of argument is as follows: Assume that the composition of the interstellar medium, i.e. absolute value and radial gradient, has not changed significantly changed during the lifetime of the Sun, measure the offset between the Solar metallicity and the local interstellar medium, divide by the radial abundance gradient and you get an estimate for the birthplace of the Sun, in the case of Wielen et al. (1996) with an adopted radial metallicity gradient of $d[\text{Fe/H}]/dR = (-0.09 \pm 0.02)\,\text{dex}/\text{kpc}$ and a metallicity difference of $\Delta[\text{Fe/H}] = (0.17 \pm 0.04)\,\text{dex}$ this resulted in placing the birthplace of the Sun $(1.9 \pm 0.9)\,\text{kpc}$ inwards of our current position. Other estimates for the Solar cradle have recently been attempted from the dynamics of the Solar system (e.g. Kaib et al., 2011, claim that the Sun must have travelled even to the inner regions of the Galaxy). While such a peculiar trajectory is of course possible in the framework of radial migration though not necessarily likely (and this low likelihood has not been fully accounted for in this study), this kind of estimates depends critically on the initial state of the solar planetary system, possible interactions in the denser environment of the open cluster giving birth to the Sun, the initial state of the Oort cloud and also on assumptions about the number of lower mass bodies or respectively the low mass IMF in the Galaxy as well as it is deeply affected by small number statistics, we consider this approach to be rather speculative. Hence we concentrate in the following on the arguments from chemistry.

With the recalibration of the Geneva-Copenhagen Survey (Casagrande et al., 2011) the mean metallicity of the Solar Neighbourhood has been considerably shifted up by around $0.1\,\text{dex}$ mostly due to an upwards shift in the temperature scale by about $100K$ that came about by the use of the infrared flux method (Casagrande et al., 2010) and also brought the main sequence location of the new GCS into concordance with stellar models. When estimating the solar birth radius this shift moves the birthplace of the Sun outwards by more than one kpc and hence while we found proof for radial migration from the metallicity distribution of the solar neighbourhood, the original precedent made on the origin of the Sun is getting lost.

To estimate the past state of the local interstellar medium it is not sufficient to simply gather all stars that have approximately the age of the Sun and search for their mean metallicity: As the solar neighbourhood is subject to immigration from other radii both by blurring and by churning,

the local composition is changed considerably apart from that uncertainties of ages can lead to significant contamination by old objects. We can directly see the immigration effect from the top panel of Fig. 16 in Casagrande et al. (2011). There the metallicity distribution of the older (see esp. the intermediate age stars) populations widens considerably and we see a longer tail especially to the high metallicity side, that is readily explained as more stars being brought outwards by radial migration due to the higher migration rates in the inner disc and by the same reason that gives rise to increasing asymmetric drift with age: Stellar densities inside the solar annulus are higher, the effective potential is flatter towards larger Galactocentric radii, and further those stars are kinematically hotter so that they travel outwards in larger numbers than stars from the outer regions of our Galaxy visit the inner regions. This gives rise to a considerable bias that prevents us at current stage from estimating the composition of the solar neighbourhood via the data, apart from saying that obviously there cannot have taken place major changes. From the youngest population where this contamination is weakest, we can estimate a local metallicity of around $[\text{Fe/H}] = (-0.08 \pm 0.05)\,\text{dex}$, where we added a minor systematic error for undiscovered selection effects an uncertainties in the setting of the original metallicity scale. This value might be challenged with the argument that there is still some residual abundance scatter among the youngest stars in the Geneva-Copenhagen Survey and that a young star selection may also be prone to a positive metallicity bias evoked by the blue limit of the GCS. Yet, there is some confirmation from high resolution data: While Luck & Lambert (2011) have a higher absolute metallicity in the Solar neighbourhood, but Nieva & Przybilla (2008) find, based on the abundance scale of Asplund et al. (2009) a difference of $[\text{Fe/H}] = (-0.1 \pm 0.06)\,\text{dex}$ and for the two reliable α elements they give $[\text{Mg/H}] = (-0.08 \pm 0.06)\,\text{dex}$ and $[\text{Si/H}] = (-0.05 \pm 0.05)\,\text{dex}$. Albeit tiny, this difference between the α elements and $[\text{Fe/H}]$ is assuring as it coincides well with a small residual trend in Schönrich & Binney (2009b) that the $[\alpha/\text{Fe}]$ ratios still fall slightly by of order $0.03\,\text{dex}$ during the lifetime of the Sun.

Taking all this together we use in the following a metallicity difference $[\text{Me/H}] = (-0.07 \pm 0.06)\,\text{dex}$, a more elaborate study will have to await the model recalibration on the new GCS data.

How do we get the past state of the ISM? Currently the only viable strategy seems to be asking our chemical evolution models. The bitter truth is, however, that their results depend to some extent on the development of radial flows and star formation rates. If we assume a smooth behaviour for the past Gyrs, we can from the Schönrich & Binney (2009a) model roughly estimate that the metallicities have increased by about $0.05\,\text{dex}$ during the lifetime of the Sun with an unknown systematic error (that depends on the development of radial flows, detailed changes of the star formation rates, etc.). Taking this result together with an abundance gradient of $d[\text{Me/H}]/dR = (-0.06 \pm 0.01)\,\text{dex/kpc}$ from Luck & Lambert (2011), where we cautiously allow for a systematic uncertainty of around $0.01\,\text{dex/kpc}$ the best current estimate for the birthplace of the Sun can be put to around $\Delta R = 2.0^{+1.5}_{-1.2}\,\text{kpc}$ or with our new estimates for the current radius R_0 the Sun should have been born around $R = 6.2\,\text{kpc}$. As the lower abundance gradient balances the lower metallicity different a bit, our result is remarkably similar to Wielen et al. (1996). We would like to note that the Sun is a bit more unusual than it appears from its value.

By its high rotational velocity that we know from Chapter 4 the guiding centre radius of the Sun is placed $(0.43 \pm 0.10)\,\mathrm{kpc}$ outside R_0, so that the Sun is one of the rather rare outer disc visitors to the Solar Neighbourhood and the estimate for the total radial migration experienced by the Sun increases to more than $2\,\mathrm{kpc}$, with a formal lower limit slightly above $1\,\mathrm{kpc}$. This means that the Sun is still a clear case for radial migration. It will be interesting to see if we can get a substantially better estimate on the solar origin with the help of the re-calibrated model.

Chapter 6

A new formula for fitting the azimuthal component of disc kinematics[1]

6.1 Abstract

In a disc galaxy the distribution of azimuthal components of velocity is very skew. In the past this skewness has been modelled by superposed Gaussians. We use dynamical arguments to derive an analytic formula that can be fitted to observed velocity distributions, and validate it by fits to the velocities derived from a dynamically rigorous model, and to a sample of local stars with accurate space velocities. Our formula is much easier to use than a full distribution function. It has fewer parameters than a multi-Gaussian fit, and the best-fitting model parameters give insight into the underlying disc dynamics. In particular, once the azimuthal velocities of a sample have been successfully fitted, the apparatus provides a prediction for the corresponding distribution of radial velocities v_R. An effective formula like ours is invaluable when fitting to data for stars at some distance from the Sun because it enables one to make proper allowance for the errors in distance and proper motion when determining the underlying disc kinematics. The derivation of our formula elucidates the way the horizontal and vertical motions are closely intertwined, and makes it evident that no stellar population can have a scale height and vertical velocity dispersions that are simultaneously independent of radius. We show that the oscillation of a star perpendicular to the Galactic plane modifies the effective potential in which the star moves radially in such a way that the more vertical energy a star has, the larger is the mean radius of its orbit.

6.2 Introduction

Currently considerable effort is being invested in surveys of the solar neighbourhood. Fifteen years ago the study of nearby stars was revived by the Hipparcos mission, which pioneered

---

[1] Content and text of this paper have been published in nearly identical form as Schönrich & Binney (2011).

space astrometry. Hipparcos put ground-based astrometry onto a more secure foundation, so now useful proper motions are available for tens of millions of stars. In the last decade the proper motions have been complemented by photometric surveys, both in the infrared and to fainter magnitudes at optical wavelengths. Finally, the RAVE (Steinmetz et al., 2005) and SEGUE (see York et al., 2000; Yanny et al., 2009) surveys have measured nearly a million line-of-sight velocities.

As a result of these major observational programmes, it is becoming possible to determine the velocity distribution within the disc of our Galaxy, not only at the location of the Sun, but also at significant distances, especially at higher Galactic latitudes. Naturally one wants to quantify the velocity distribution observed at some location $\mathbf{x}$ in the Galaxy in an efficient way. Conventionally one does this by imagining that the density of stars in velocity space forms a "velocity ellipsoid" – a triaxial ellipsoidal region of over-density in velocity space. If the Galaxy were axisymmetric (which is a reasonable first approximation), we would expect that in the Galactic plane the principal axes of the the velocity ellipsoid would be aligned with the coordinate directions of cylindrical polar coordinates, (R, z, ϕ). As one moves above the plane, two of the principal axes of the velocity ellipsoid are expected to tip slightly with respect to the $\hat{\mathbf{R}}$ and $\hat{\mathbf{z}}$ directions. Let the components of velocity parallel to these principal axes be denoted v_1 and v_2, where $v_1 \to v_R$ and $v_2 \to v_z$ as $z \to 0$. The third axis is expected to remain aligned with the $\hat{\phi}$ direction.

The distributions of the v_1 and v_2 components of velocity are expected to be roughly Gaussian with vanishing means and to be to good approximation aligned with the Galactic polar coordinates (minor vertex deviations as found in the solar neighbourhood by Dehnen, 1998, will not be discussed here). Consequently, they can be characterised by their standard deviations σ_1 and σ_2. The distribution of the v_ϕ components peaks at a value of v_ϕ that is slightly smaller than the circular speed v_c. However, it is not at all well modelled by a Gaussian, because it is very skew, with many more stars at $v_\phi = v_c - v$ than at $v_c + v$, causing the population to have non-zero asymmetric drift. Notwithstanding this skewness that was already known to Gustav Strömberg (Strömberg, 1927), v_ϕ distributions have traditionally been characterised by a mean and a standard deviation. Since a single Gaussian fits the data very poorly, the observed distribution is frequently modelled by a superposition of two Gaussians: then the overall distribution is characterised by two means, two dispersions and the ratio of the numbers of stars accounted for by each Gaussian, a total of five shape parameters.

The purpose of this note is to introduce a new representation of v_ϕ distributions that is more effective in the sense that it fits typical data more accurately with fewer and physically more meaningful parameters. Moreover, the new representation has a dynamical basis, so it is able to connect the skewness of the v_ϕ distributions to the standard deviations in v_1 and v_2. With the new representation, a single free shape parameter suffices to describe the distribution in v_ϕ for the whole population of stars in the solar cylinder, and two parameters are sufficient to fit the distribution in v_ϕ of stars that have a given distance from the plane. The formula predicts in a natural way both the magnitude of the asymmetric drift and the offset of the modal azimuthal velocity from the circular velocity, neither of which is achieved by multiple Gaussians.

The paper is organised as follows. In Section 6.3 we derive an approximation to the v_ϕ distribution in an annulus in the Galactic disc that can be used as standard for extragalactic measurements. As most samples of the Galaxy are centred on certain Galactic altitudes $|z|$, in Section 6.4 we use the adiabatic approximation (Binney, 2010) to take into account the vertical motions of stars. In 6.4.1 we derive a formula that accounts for the variation in the v_ϕ distribution with $|z|$ and test it against the velocity distributions of more elaborate models. In Section 6.4.2 we derive a formula for the way in which the in-plane motion of a star depends on the extent of its excursions perpendicular to the plane. The outcome is a small correction to the v_ϕ distribution derived in Section 6.4.1. In Section 6.4.3 we give formulae from which the distributions of v_R and v_z follow once the distribution in v_ϕ has been fitted. In Section 6.5.1 we show that our formulae provide good fits to the disc model of Binney & McMillan (2011; hereafter BM11), which has a rigorous dynamical basis. In Section 6.5.2 we demonstrate the practical application of the formula by fitting data from the Geneva-Copenhagen Survey. Section 6.6 sums up and looks to the future.

6.3 Velocity distribution as a 2D problem

There are three reasons for the asymmetry of the distribution of v_ϕ components of nearby stars: stars at low v_ϕ are approaching apocentre, so they have guiding-centre radii R_g smaller than the solar radius, R_0. As one moves inwards through the disc, not only does the density of stars increase rapidly on account of the exponential increase in the surface density $\Sigma(R) \propto \exp(-R/R_d)$, but the random velocities of stars also increase, so a greater fraction of all stars are on eccentric orbits that carry them far from their guiding-centre radius R_g. Moreover, the effective potential in which a star oscillates around R_g rises much more steeply at $R < R_g$ than it does at $R > R_g$, so stars spend more time beyond R_g than they do interior to it. In fact, as a population of stars heats up over its lifetime, the asymmetry of the effective potential causes the population to expand spatially, and by conservation of angular momentum its mean rotation rate diminishes. For all these reasons, there are many more visitors reaching R_0 with guiding centres at $R_0 - \Delta$ than at $R_0 + \Delta$. A functional form for $n(v_\phi)$ that is successful in fitting observed distributions will reflect these facts.

Following Shu (1969) we decompose the energy of a disc star into three parts. If the star were on a circular orbit with angular momentum L_z, it would have energy

$$E_c(L_z) = \Phi_{\text{eff}}(R_g, L_z), \tag{6.1}$$

where with the Galactic potential in the plane $\Phi(R)$

$$\Phi_{\text{eff}}(R, L_z) \equiv \frac{L_z^2}{2R^2} + \Phi(R) \tag{6.2}$$

and the guiding-centre radius $R_g(L_z)$ solves the equation $R_g v_c(R_g) = L_z$, with $v_c(R)$ the circular speed. In addition to this energy, the star has two smaller energies, namely the energy E_z of

vertical motion and the energy E_R of random motion within the plane. We postpone discussion of E_z and focus for now on stars with $E_z = 0$, which move in the plane. We have

$$
\begin{aligned}
E_R &= \tfrac{1}{2}v_R^2 + \Phi_{\mathrm{eff}}(R, L_z) - \Phi_{\mathrm{eff}}(R_{\mathrm{g}}, L_z) \\
&= \tfrac{1}{2}v_R^2 + \Delta\Phi_{\mathrm{eff}}(R, L_z)
\end{aligned}
\tag{6.3}
$$

where

$$
\Delta\Phi_{\mathrm{eff}}(R, L_z) \equiv \Phi_{\mathrm{eff}}(R, L_z) - \Phi_{\mathrm{eff}}(R_{\mathrm{g}}, L_z).
\tag{6.4}
$$

Suppose that the disc's distribution function (DF) is (Shu, 1969)

$$
f(E_R, L_z) = \frac{F}{\sigma^2}\mathrm{e}^{-E_R/\sigma^2},
\tag{6.5}
$$

where $F(R_{\mathrm{g}})$ is a function that determines the surface density of the young disc and $\sigma(R_{\mathrm{g}})$ is a function that determines how the radial velocity dispersion. On account of the tendency noted above for a population to expand radially as it heats up, if $F(R_{\mathrm{g}})$ is the same for both cool and hot populations, the hotter populations will have slightly larger radial scale-lengths than the cool ones. Note that σ gives the intrinsic dispersion of stars at their guiding centre radius R_{g}. The dispersion $\langle v_R^2\rangle^{1/2}$ actually measured at some radius R will have contributions from all populations that reach this radius and turns out to be ~ 10 per cent higher than the value of σ for the stars that have $R_{\mathrm{g}} = R$ on account of the presence of stars that have guiding centres at $R_{\mathrm{g}} < R$. Schönrich & Binney (2009a) show that the probability per unit area that a star with angular momentum L_z will be found at R is

$$
P(R|L_z) = \frac{K}{\sigma R}\exp\left[-\frac{\Delta\Phi_{\mathrm{eff}}(R, L_z)}{\sigma^2}\right],
\tag{6.6}
$$

where $K(R_{\mathrm{g}})$ is chosen such that $1 = 2\pi\int \mathrm{d}R\,R\,P$.

Let $n(v_\phi, R)\,\mathrm{d}v_\phi$ be the number per unit area of stars at R with v_ϕ in $(v_\phi, v_\phi + \mathrm{d}v_\phi)$. Then

$$
n(v_\phi, R)\,\mathrm{d}v_\phi = N(L_z)\,\mathrm{d}L_z\,P(R|L_z) = N(L_z)P(R|L_z)R\mathrm{d}v_\phi,
\tag{6.7}
$$

where $N(L_z)\,\mathrm{d}L_z$ is the number of stars in the disc with L_z in $(L_z, L_z + \mathrm{d}L_z)$. In a cold disc, the number of stars with angular momenta in $(L_z, L_z + \mathrm{d}L_z)$, is simply the mass in the corresponding annulus, $2\pi\Sigma(R_{\mathrm{g}})R_{\mathrm{g}}\,\mathrm{d}R_{\mathrm{g}}$. Hence under the neglect of the mild radial expansion noted above of a population as its dispersion increases, an exponential disc with surface density

$$
\Sigma(R) = \Sigma_0\mathrm{e}^{-(R-R_0)/R_{\mathrm{d}}},
\tag{6.8}
$$

where Σ_0 is the local surface density and R_{d} is the radial scale-length of the disc, has

$$
N(L_z) \simeq \frac{2\pi\Sigma_0 R_{\mathrm{g}}}{v_{\mathrm{c}}}\,\mathrm{e}^{-(R_{\mathrm{g}}-R_0)/R_{\mathrm{d}}},
\tag{6.9}
$$

where we have assumed a constant circular speed, so $dL_z = v_c dR_g$. Combining equations (6.6), (6.7) and (6.9), we have

$$n(v_\phi, R) = \frac{2\pi \Sigma_0 R_g}{v_c} e^{-(R_g - R_0)/R_d} \frac{K}{\sigma} \exp\left[-\frac{\Delta \Phi_{\text{eff}}(R, L_z)}{\sigma^2}\right]. \tag{6.10}$$

Our assumption of constant v_c allows us to evaluate $K(R_g)$, because then

$$-\Delta \Phi_{\text{eff}}(R, L_z) = \tfrac{1}{2} L_z^2 (R_g^{-2} - R^{-2}) + v_c^2 \ln(R_g/R), \tag{6.11}$$

so the normalisation condition $1 = 2\pi \int dR \, R P$ reads

$$\begin{aligned}
\frac{\sigma}{2\pi K} &= \int dR \exp\left[-\frac{\Delta \Phi_{\text{eff}}(R, L_z)}{\sigma^2}\right] \\
&= \int dR \exp\left[c \left(2\ln R_g/R + 1 - R_g^2/R^2\right)\right] \\
&= g(c) R_g,
\end{aligned} \tag{6.12}$$

where

$$c(R_g) \equiv \frac{v_c^2}{2\sigma^2(R_g)}, \tag{6.13}$$

and

$$g(c) \equiv \frac{e^c (c - \tfrac{3}{2})!}{2 c^{(c-1/2)}}. \tag{6.14}$$

So

$$\begin{aligned}
n(v_\phi, R) &= \frac{\Sigma_0}{v_c g(c)} \exp\left[-\frac{\Delta \Phi_{\text{eff}}}{\sigma^2} - \frac{R_g - R_0}{R_d}\right] \\
&= \frac{\Sigma_0}{v_c g(c)} \exp\left[c \left(2\ln \frac{R_g}{R} + 1 - \frac{R_g^2}{R^2}\right) - \frac{R_g - R_0}{R_d}\right].
\end{aligned} \tag{6.15}$$

As here we are aiming at velocity distributions and not stellar densities at a certain position, we will henceforth use the normalised velocity distribution at a fixed radius R

$$n(v_\phi | R) = \frac{\mathcal{N}}{g(c)} \exp\left[c \left(2\ln \frac{R_g}{R} + 1 - \frac{R_g^2}{R^2}\right) - \frac{R_g - R_0}{R_d}\right], \tag{6.16}$$

where $\mathcal{N}$ normalises the integral of n in v_ϕ to unity.

Note that on the right side of eq. (6.16) the dependence on v_ϕ is carried by the instances of $R_g = R v_\phi / v_c$ and by $c(R_g)$.

From equation (6.6) we expect K (which has the units of a frequency) to be constant when $\sigma \ll v_c$, and indeed from an asymptotic expansion of equation (6.12) for large c we obtain
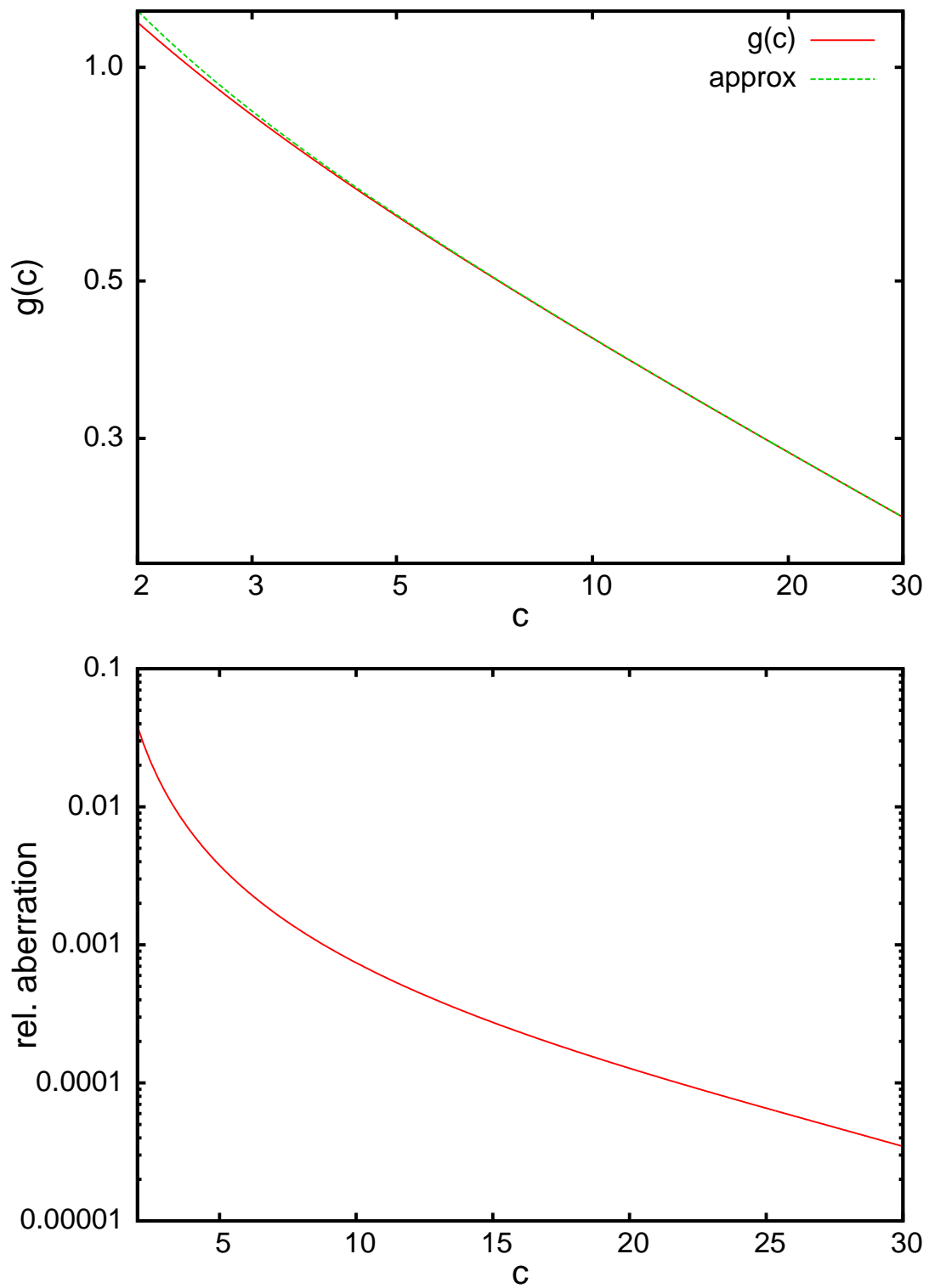
Figure 6.1: Upper panel: The function $g(c)$ defined by eq. (6.14) with solid red line and the approximation of eq. (6.17) shown by a dashed green line. Lower panel: the relative difference between the approximation and the underlying formula.

$g(c) \propto c^{-1/2} \propto \sigma$ and $K = v_{\rm c}/(2\pi^{3/2}R_g)$. Fig. 6.1 shows that $g(c)$ satisfies this expectation throughout the entire parameter range of interest. For ($c > 25$), the direct computation of $g(c)$ becomes impractical so that apart from the advantage of a numerically less costly formula a reasonable approximation must be found. The dashed green line in Fig. 6.1 demonstrates that for $c > 2$ this is achieved to high precision by

$$g(c) \simeq \sqrt{\frac{\pi}{2(c-0.913)}}. \tag{6.17}$$

Alternatively $g(c)$ can be stringently approximated using eq. (8.327) of Gradshteyn & Ryzhik (1980), but our term appears to be the best compromise of simplicity and accuracy throughout the interesting part of the parameter range. For σ we adopt the radial dependence

$$\sigma(R_{\rm g}) = \sigma_0 e^{-(R_{\rm g}-R_0)/R_\sigma}. \tag{6.18}$$

Above we have restricted ourselves to stars with $E_z = 0$. However, to the extent that the motion in R of a star is unaffected by its motion perpendicular to the plane, the distribution we have derived will apply to the population formed by all stars that now lie in the solar cylinder (the region restricted in radius to $R \simeq R_0$ but unrestricted in z). From our formulae we have that the shape of this velocity distribution is controlled by four parameters: the galactocentric radius of the measurement R_0, the scale-length $R_{\rm d}$ of the young disc, the local velocity dispersion σ_0, and the scale-length R_σ on which the velocity dispersion varies. The first two parameters are generally well-known and for fits of the solar neighbourhood can be set to $R_0 = 8\,{\rm kpc}$ and $R_{\rm d} = 2.5\,{\rm kpc}$. The value of R_σ is less clear and will be discussed below.

The dependence of $n(v_\phi|R_0)$ on σ_0 and R_σ is shown in Fig. 6.2. In the upper panel we hold the dispersion scale-length constant at $7.5\,{\rm kpc}$ and show the velocity distributions for local dispersion values of $\sigma_0 = 20,25,30,40,50\,{\rm km\,s^{-1}}$. As σ_0 increases, the distribution becomes wider and the low-velocity tail rises much faster than does the high-velocity tail, corresponding to an increasing asymmetric drift. Simultaneously, the peak slowly shifts to lower velocities. The lower panel shows the velocity distributions for fixed $\sigma_0 = 30\,{\rm km\,s^{-1}}$, but different scale-lengths of the velocity dispersion, $R_\sigma = 10, 7.5, 5, 4\,{\rm kpc}$. Smaller values of R_σ imply higher dispersion in the inner regions of the Galaxy and lower dispersion in the outskirts. Thus for small R_σ stars from the inner disc can more easily reach the R_0 compared to their counterparts with larger R_g so the azimuthal velocity distribution is more skewed and develops a strong low-velocity tail. In the most extreme case, $R_\sigma = 4\,{\rm kpc}$, the model breaks down, as $\langle v_R^2 \rangle^{1/2}$ approaches v_c in the inner regions. Notice that as R_σ falls, the mode of the velocity distribution shifts to higher v_ϕ even as the tail at high v_ϕ becomes weaker. This effect reflects the fact that stars with large random velocities spread their contributions to the velocity distribution over many radii, while stars with small random velocities localise their contributions. Consequently, when R_σ is small, the width in R over which stars contribute to v_ϕ narrows strongly as $R_{\rm g}$ increases, which puts stars with $R_{\rm g} \simeq R_0$ strongly in control of the mode of the local v_ϕ distribution.
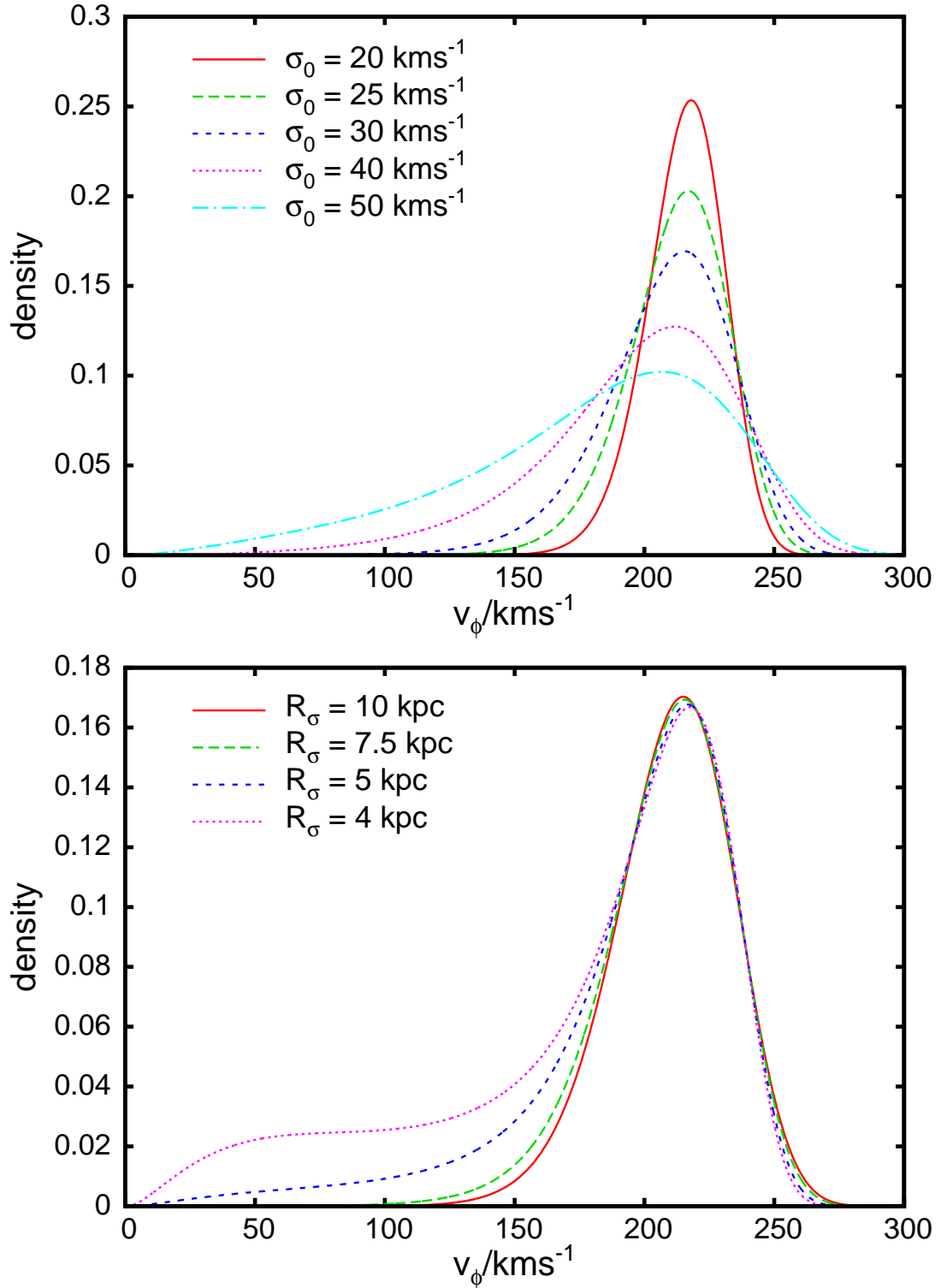
Figure 6.2: The behaviour of eq. (6.16) for different local dispersions (upper panel) and different scale-lengths on which the dispersion varies (lower panel). The radius of observation is $R = 8\,\mathrm{kpc}$ at a young-disc scale-length $R_\mathrm{d} = 2.5\,\mathrm{kpc}$. In the upper panel we set the scale-length of the velocity dispersion to $R_\sigma = 3R_\mathrm{d} = 7.5\,\mathrm{kpc}$ and show results for local dispersions $\sigma_0 = 20, 25, 30, 40, 50\,\mathrm{km\,s^{-1}}$, while we use $\sigma_0 = 30\,\mathrm{km\,s^{-1}}$ in the lower panel.

6.4 The velocity distribution as a function of distance from the plane

In the previous section we set $E_z = 0$ to obtain results that are approximately valid for the distribution of stars in v_ϕ regardless of their distance from the plane. In practice we can determine the velocity distributions of the stars that lie in various more-or-less narrow ranges in z. We must now consider how these distributions will vary with z and differ from the aggregate distribution determined above. In the following we do so using a number of quite crude physical approximations. These approximations give useful physical insight into why the distribution in v_ϕ varies with $|z|$ as it does, but ultimately the value of our final fitting formula does not depend on the correctness of the arguments used to motivate it.

6.4.1 Weights of different populations as functions of z

The key idea is that within the solar cylinder there coexist many populations, one for each value of R_g. Indeed the chemical compositions and ages of stars vary systematically with R_g (see e.g. Luck & Lambert, 2011; Bensby et al., 2011a; Schönrich, Binney & Dehnen, 2010, for observations and a short discussion of consequences for studies of kinematics). Moreover, the smaller a population's value of R_g, the larger will be its mean value of E_z and therefore the larger will be its vertical scale-height h at radius R; here $h(R_g, R)$ is the distance that at radius R provides the best fit to the vertical density profile of the population through

$$n_{R_g}(R, z) \propto \frac{1}{h} e^{-|z|/h}. \tag{6.19}$$

Note that with this formula we are not asserting that the real vertical density profile is exponential, but simply identifying the characteristic vertical extent of the population. We now investigate how the vertical extent of the population increases with R because the vertical restoring force, which scales like $\Sigma(R)$, decreases outwards.

BM11 show that a very good approximation to the vertical dynamics of a population of stars can be obtained by assuming that the vertical action

$$J_z \equiv \frac{1}{2\pi} \oint dz \, v_z \tag{6.20}$$

of the population's stars is adiabatically invariant as the stars oscillate in radius. We use this adiabatic approximation (AA) to estimate the ratio $h(R_g, R)/h(R_g, R_g)$.

J_z can be evaluated analytically only for a vertical force K_z that is proportional to $z^{\alpha-1}$ and to the local surface density of the disc Σ, so we assume these dependencies in order to gain an analytic model – in reality K_z has a much more complex dependence on z, which does not yield an analytic expression for $E_z(J_z)$. Then the vertical action is

$$J_z = \frac{2^{3/2}}{\pi} \int_0^{z_m} dz \, \sqrt{E_z - k \Sigma z^\alpha}, \tag{6.21}$$

where k is a constant and

$$z_m = (E_z/k\Sigma)^{1/\alpha} \tag{6.22}$$

is the height at which the radical vanishes. In terms of the variable $\theta = z/z_m$ we have

$$J_z = \frac{2^{3/2}}{\pi}(k\Sigma)^{1/2} z_m^{1+\alpha/2} \int_0^1 d\theta \sqrt{1 - \theta^\alpha}. \tag{6.23}$$

With the AA, it now follows that

$$z_m \propto \Sigma^{-1/(2+\alpha)}. \tag{6.24}$$

The scale-height $h(R_g, R)$ of the population will scale like z_m, so

$$\frac{h(R_g, R)}{h(R_g, R_g)} = \left(\frac{\Sigma(R)}{\Sigma(R_g)}\right)^{-1/(2+\alpha)} = \exp\left(\frac{R - R_g}{(2+\alpha)R_d}\right). \tag{6.25}$$

Photometry of edge-on spiral galaxies shows that the overall scale-height varies very little with radius (van der Kruit & Searle, 1982). Since the velocity dispersion at radius R will be dominated by the population that has $R_g = R$, we assume that

$$h_0 \equiv h(R, R) \tag{6.26}$$

is independent of R. Hence

$$\frac{h(R_g, R)}{h(R, R)} = \exp\left(\frac{R - R_g}{(2+\alpha)R_d}\right). \tag{6.27}$$

For stars that make only small-amplitude vertical oscillations, $K_z \propto z$ so $\alpha = 2$. If the amplitude of a star's oscillations significantly exceeds the local disc scale-height (but is none the less small compared to R), a better approximation is that the disc is razor thin, so $K_z \simeq$ constant and $\alpha = 1$. For amplitudes not small compared to the disc's scale-length, a yet smaller value of α is appropriate. In the fits described below we assumed that α decreases with z according to

$$\alpha(z) = \begin{cases} 2 - 1.5z/1.5\,\mathrm{kpc} & \text{for } z \leq 1.5\,\mathrm{kpc} \\ 0.5 & \text{otherwise} \end{cases}. \tag{6.28}$$

These choices are educated guesses that produce useful results.

Let the ratio of the contributions to the distribution in v_ϕ at height z of the population with guiding-centre radius R_g and the local population be given by the factor $f(z, R_g - R)$. Then from equation (6.15) the distribution of v_ϕ at altitude z above the plane is

$$n(v_\phi|R, z) = \frac{\mathcal{N}}{g(c)} \exp\left[\frac{-(R_g - R_0)}{R_d}\right] \exp\left[-\frac{\Delta\Phi_{\mathrm{eff}}}{\sigma^2}\right] f(z, R_g - R), \tag{6.29}$$
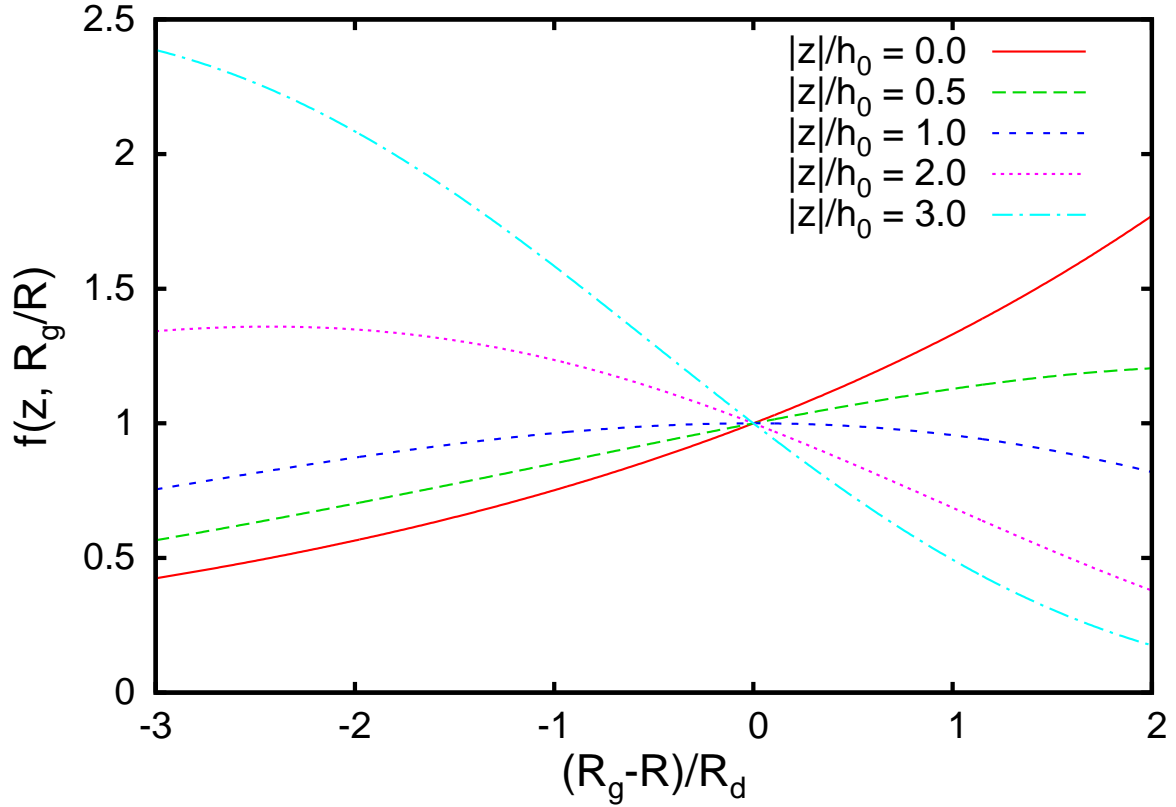
Figure 6.3: The relative contributions given by eq. (6.30) of the populations with guiding-centre radius R_g measured at galactocentric radius R to the velocity distribution at various values of $|z|$. We use $\alpha = 1.5$, $h_0 = 300\,\text{pc}$ and $R_d = 2.5\,\text{kpc}$.

where $\mathcal{N}$ is a new normalisation constant.

By equation (6.19), the factor f will scale as

$$
\begin{aligned}
f(z, R_g - R) &= \frac{n_{R_g}(z)}{n_R(z)} \\
&= \frac{h(R, R)}{h(R_g, R)} \exp\left[\frac{|z|}{h_0}\left(1 - \frac{h(R, R)}{h(R_g, R)}\right)\right] \\
&= \exp\left(\frac{R_g - R}{(2 + \alpha)R_d}\right) \exp\left\{\frac{|z|}{h_0}\left(1 - \exp\left(\frac{R_g - R}{(2 + \alpha)R_d}\right)\right)\right\},
\end{aligned}
\tag{6.30}
$$

where in the second step we have used the definition (6.26). Fig. 6.3 shows, for five values of z, how f varies with R_g at $R = R_0$. At $z = 0$, f is an increasing function of R_g because at large R_g stars typically have small E_z and therefore are more numerous in the plane than in the solar cylinder as a whole. At $z = 1\,\text{kpc}$, by contrast, f falls with increasing R_g because high above the

plane a sample is richer in stars with small R_g, and therefore large E_z, than is the solar cylinder as a whole. The formula attains a maximum, where the local scale-height of a population equals the altitude. Since by definition $f(z, R_g - R_0)$ gives the enhancement of stars with guiding-centre radius R_g relative to local stars, all lines intersect at ($f = 1$, $R_g = R_0$) irrespective of the chosen altitude.

6.4.2 Impact of the AA on the radial motion

The AA predicts that any star's value of E_z varies as it moves radially. Since the star is moving in a time-independent potential, its total energy is constant. It follows that changes in E_z must be compensated by changes in its energy of motion parallel to the plane. Since L_z is a true invariant, the energy $\Phi_{\rm eff}(R_g, L_z)$ associated with the underlying circular orbit is unchanged, so changes in E_z must be compensated by changes in the radial energy E_R. Hence (6.3) becomes

$$\tfrac{1}{2}v_R^2 + \Delta\Phi_{\rm eff}(R, L_z) + \Delta E_z = {\rm constant}, \tag{6.31}$$

where

$$\Delta E_z(J_z, R, R_g) \equiv E_z(J_z, R) - E_z(J_z, R_g): \tag{6.32}$$

takes into account the decrease in a star's vertical energy as it moves outwards: by conservation of energy, this energy must be transferred to the radial motion. One way of thinking about this energy transfer is to imagine that the star moves at constant energy in an effective potential

$$\Delta\Phi_{\rm ad}(R, L_z) \equiv \Delta\Phi_{\rm eff}(R, L_z) + \Delta E_z(J_z, R, R_g), \tag{6.33}$$

which might be called the "adiabatic potential" since it is the effective potential for radial motion that follows from adiabatic invariance of the vertical motion. At $R > R_g$ $\Delta\Phi_{\rm ad}$ increases with R less rapidly than the standard effective potential $\Delta\Phi_{\rm eff}$, so stars can reach larger radii than they could if E_z were constant. BM11 simulated this effect by simply increasing L_z to $L_z + J_z$. With the power-law forms of the vertical potential that we introduced above, we can obtain the dependence of E_z on Σ. From equations (6.22) and (6.23) we find

$$E_z \propto \Sigma^{2/2+\alpha}, \tag{6.34}$$

so

$$\Delta E_z(J_z, R, R_g) = E_z(J_z, R)\left[1 - \exp\left(\frac{2(R - R_g)}{(2 + \alpha)R_d}\right)\right]. \tag{6.35}$$

Our plan is to use ΔE_z to modify our expression (6.10) for $n(v_\phi | R, z)$, which has no dependence on v_z and therefore does not specify a value of J_z or E_z. Therefore in equation (6.35) we now replace $E_z(J_z, R)$ by an estimate $\overline{E_z}$ of the typical vertical energy of the stars that are encountered
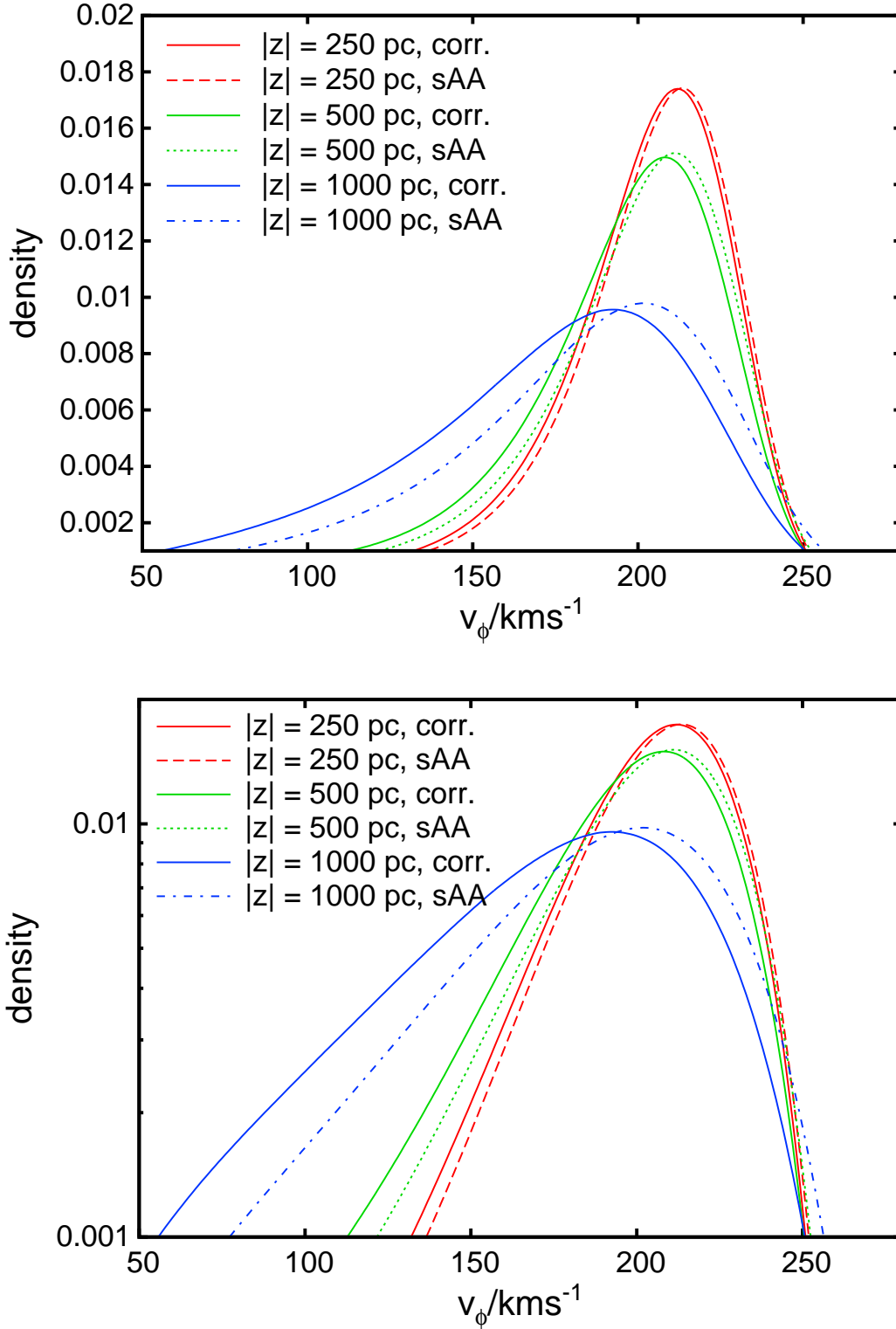
Figure 6.4: Demonstration of the effect on velocity distributions above the Sun of adding ΔE_z to the effective potential to allow for the tendency of vertical energy to shift orbits outwards. The velocity distributions are derived from fits to the models discussed in Section 6.5.1. Full curves show the full corrections with E_z ("corr"), dashed lines give the same models with the simple adiabatic approximation ("sAA") ignoring energy conservation.

at (R,z) with angular momentum $L_z = Rv_\phi$. Equation (6.47) in Section 6.7 is an expression for $\overline{E_z}$ in terms of $h(R_g, R)$ and the vertical component of the gravitational potential.

Our next step is essentially to replace $\Delta\Phi_{\text{eff}}$ by $\Delta\Phi_{\text{ad}}$ in equation (6.29) but before we do this we have to recall that the prefactor $g(c)$ arose from normalising the radial probability density $P(R|L_z)$ as given by equation (6.6). For consistency in this formula we must now replace $\Delta\Phi_{\text{eff}}$ by $\Delta\Phi_{\text{ad}}$, with the consequence that the normalising integral is no longer analytic. Therefore our final formula for the distribution of v_ϕ at a given point in the Galaxy must be written

$$n(v_\phi|R,z) = \mathcal{N}\,e^{-(R_g-R_0)/R_d}\,\frac{2\pi R_g K}{\sigma}$$
$$\times \exp\left[-\frac{\Delta\Phi_{\text{ad}}}{\sigma^2}\right]f(z,R_g-R), \tag{6.36}$$

where $K(c, E_z, R_g)$ is the numerically-determined result of normalising the revised form of $P(R|L_z)$ [cf eq. (6.12)], $\mathcal{N}$ normalises the distribution in v_ϕ and f is defined by equation (6.30). Fig. 6.4 illustrates the effect that the inclusion of ΔE_z in the effective potential has on $n(v_\phi|R,z)$ by showing for $R = R_0$ and several values of z the velocity distributions predicted with (full curves) and without (dotted curves) ΔE_z. Including ΔE_z moves all velocity distributions to lower v_ϕ, particularly on the left side. The magnitude of the shift increases with z because at low z, $n(v_\phi|R,z)$ is dominated by orbits with small E_z and therefore small ΔE_z.

Far from the plane ($z \sim 2\,\text{kpc}$) equation (6.36) breaks down because the physical assumptions on which it depends fail. A problem that must be encountered at some height is that the vertical frequency becomes comparable to the horizontal frequency, so the assumption of adiabatic invariance of J_z fails – the coupling between the horizontal and vertical motions becomes strong and complex. However, BM11 did not encounter problems with the AA below $\sim z = 2\,\text{kpc}$. The failure we encounter here probably arises from equation (6.47) for $\overline{E_z}$, so we below explore the effect of limiting the energy transfer by placing an uper limit on the value of $\overline{E_z}$ to less than $(50\,\text{km}\,\text{s}^{-1})^2$.

6.4.3 Velocity moments

From the formulae we have in hand we can calculate a variety of moments. Suppose the stellar population of the disc were a superposition of populations that have DFs of the form

$$f(E_R, L_z, E_z) \propto e^{-E_R/\sigma^2}e^{-E_z/\sigma_z^2}, \tag{6.37}$$

where the dependence on E_z is inspired by equation (6.19). Then since this DF is a Gaussian in v_R, we would have $\langle v_R^2\rangle = \sigma^2$. To each value of R_g and therefore v_ϕ we could ascribe a fixed value for $\langle v_R^2\rangle = \sigma^2$, where in general lower v_ϕ are connected to higher $\langle v_R^2\rangle = \sigma^2$. Hence the velocity dispersion of the entire disc could be obtained from the weighted average

$$\langle v_R^2\rangle(R,z) = \int dv_\phi\, n(v_\phi|R,z)\sigma^2(Rv_\phi/v_c). \tag{6.38}$$

Similarly the asymmetric drift would be

$$v_a(R,z) = v_c - \int dv_\phi\, n(v_\phi|R,z)v_\phi. \tag{6.39}$$

From the work of Section 6.4.2 we know that E_R is not strictly a constant of the motion on account of the transfer of energy between the radial and vertical motions, so these formulae are only approximate. We shall see that they are nevertheless useful.

The DF (6.37) is also a Gaussian in v_z so naively we have $\langle v_z^2 \rangle = \sigma_z^2$ for the population formed by stars of a given value of L_z. However, when calculating $\langle v_z^2 \rangle$ for the entire disc it is essential to bear in mind the radial variation of E_z implied by adiabatic invariance of J_z (eq. 6.34). In effect this variation of E_z causes σ_z to vary with radius even at fixed L_z. Hence an approximate expression for the vertical velocity dispersion of the entire disc is

$$\langle v_z^2 \rangle (R,z) = \int dv_\phi\, n(v_\phi|R,z)\sigma_z^{2}(R_0 v_\phi/v_c)\left(\frac{\Sigma_0}{\Sigma(R)}\right)^{2/2+\alpha}. \tag{6.40}$$

6.5 Applications

6.5.1 Comparison with torus models

To evaluate the performance of the above equations we fit the velocity distributions of the torus model of BM11. The DF of this model is

$$f(J_r,L_z,J_z) = f_{\sigma_r}(J_r,L_z) \times \frac{\nu}{2\pi\sigma_z^2}\, e^{-\nu J_z/\sigma_z^2}, \tag{6.41}$$

where

$$f_{\sigma_r}(J_r,L_z) \equiv \left.\frac{\Omega\Sigma}{\pi\sigma_r^2\kappa}\right|_{R_c}[1+\tanh(L_z/L_0)]e^{-\kappa J_r/\sigma_r^2}. \tag{6.42}$$

Here $\Omega(L_z)$ is the circular frequency for angular momentum L_z, $\kappa(L_z)$ is the radial epicycle frequency and $\nu(L_z)$ is its vertical counterpart and $\Sigma(R_g)$ is given by equation (6.8). The factor $1+\tanh(L_z/L_0)$ in equation (6.42) is there to effectively eliminate stars on counter-rotating orbits and the value of L_0 is unimportant provided it is small compared to the angular momentum of the Sun. In equations (6.41) and (6.42) the functions $\sigma_z(L_z)$ and $\sigma_r(L_z)$ control the vertical and radial velocity dispersions. The observed insensitivity to radius of the scale-heights of extragalactic discs motivates the choices

$$\sigma_r(L_z) = \sigma_{r0}\, e^{q(R_0-R_c)/R_d}$$
$$\sigma_z(L_z) = \sigma_{z0}\, e^{q(R_0-R_c)/R_d}, \tag{6.43}$$

where $q = 0.45$ and σ_{r0} and σ_{z0} are approximately equal to the radial and vertical velocity dispersions at the Sun. BM11 take the DF of the entire disc to be the sum of a DF of the form (6.41)

Table 6.1: Parameters of the torus model's DF.

Disc	$R_{\rm d}/{\rm kpc}$	$\sigma_{r0}/{\rm km\,s}^{-1}$	$\sigma_{z0}/{\rm km\,s}^{-1}$	$L_0/{\rm kpc\,km\,s}^{-1}$
Thin	2.4	27	20	10
Thick	2.5	48	44	10

Table 6.2: Parameters of the potential employed

Component	$\Sigma(R_0)/{\rm M}_\odot\,{\rm pc}^{-2}$	$R_{\rm d}/{\rm kpc}$	$h/{\rm kpc}$	$R_{\rm m}/{\rm kpc}$
Thin	36.42	2.4	0.36	0
Thick	4.05	2.4	1	0
Gas	8.36	4.8	0.04	4

Component	$\rho/{\rm M}_\odot\,{\rm pc}^{-3}$	q	γ	β	$r_0/{\rm kpc}$	$r_t/{\rm kpc}$
Bulge	0.7561	0.6	1.8	1.8	1	1.9
Halo	1.263	0.8	-2	2.207	1.09	1000

z	σ_0	R_σ	h_0	$\langle v_R^2\rangle^{1/2}$	$\langle v_R^2\rangle^{1/2}_{\rm BM11}$	χ^2
0	27.07	5.30	—	30.9	33.4	0.000095
250	27.56	5.39	229.8	32.3	35.2	0.000134
500	29.23	5.70	170.4	36.4	40.4	0.000265
750	33.30	6.25	190.4	44.1	48.4	0.000338
1000	38.93	6.86	247.7	53.9	55.1	0.000063
1250	40.85	6.90	281.3	60.0	58.7	0.000079
1500	42.21	7.29	294.5	62.4	60.7	0.000034
1750	44.45	8.26	284.7	63.7	61.8	0.000113
2000	49.27	10.90	271.5	64.8	63.1	0.000363

Table 6.3: Values of the parameters for the fits shown in Fig. 6.5, which employ the simple adiabatic approximation. z denotes the distance from the plane in parsecs, R_σ the scale-length of radial velocity dispersion, h_0 the local scale-height. We fixed the circular speed $v_c = 216.25\,{\rm km\,s}^{-1}$ and disc scale-length $R_{\rm d} = 2.4\,{\rm kpc}$ to the values used by BM11. For a further comparison we give the rms radial velocity from eq. (6.38) and the value of the corresponding parameter $\sigma_{R,{\rm BM11}}$ of the torus model. All fits and their χ^2 values were derived for $60\,{\rm km\,s}^{-1} < v_\phi < 260\,{\rm km\,s}^{-1}$. Note that the χ^2 values are not sensible per se, but a mere description of the relative fit quality, as there are no proper errors on the theoretical distributions underlying the fit.
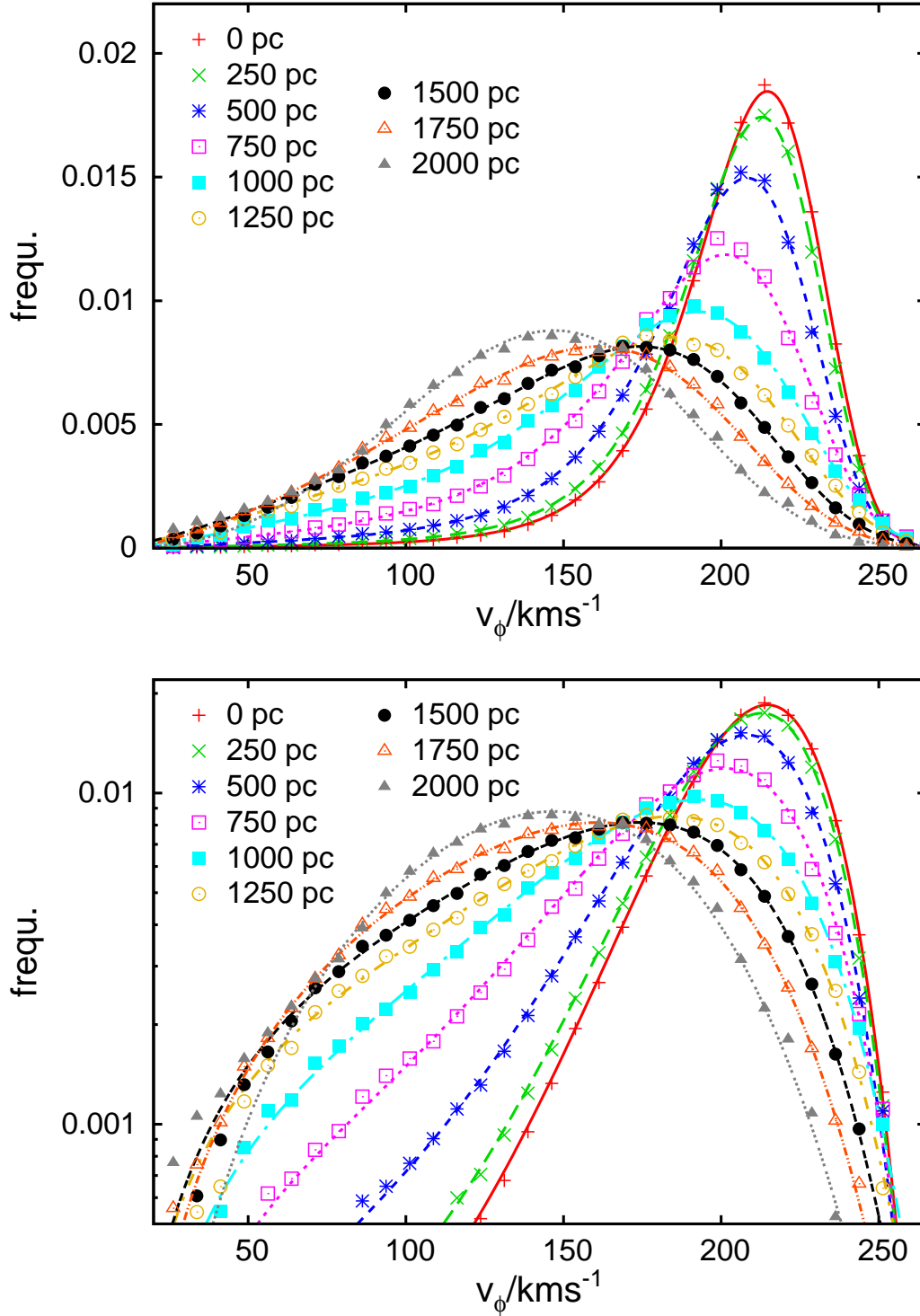
Figure 6.5: Fitting velocity distributions of a torus model from BM11 at different altitudes using eq. (6.29). Points show values from the torus model and the curves show our fits to these points. The scale-length of the disc was fixed at the BM11 value of $R_d = 2.4\,$kpc, the parameter α used to estimate the adiabatic invariant was set via equation (6.28).

for the thin disc, and a similar DF for the thick disc, the normalisations being chosen so that at the Sun the surface density of thick-disc stars is 23 per cent of the total stellar surface density. Table 6.1 lists the parameters of each component of the DF.

BM11 took the gravitational potential to be that of Model 2 in Dehnen & Binney (1998a) modified to have thin- and thick-disc scale-heights of 360 pc and 1 kpc (Table 6.2). In this model the disc contributes 60 per cent of the gravitational force on the Sun, with dark matter contributing most of the remaining force.

Distribution in v_ϕ

The points in Fig. 6.5 show the v_ϕ distributions of the BM11 model at R_0 and heights up to 2 kpc, while the curves show the fits to these points that we obtain from equation (6.36) when we approximate $\Delta\Phi_{\mathrm{ad}}$ with $\Delta\Phi_{\mathrm{eff}}$. We take α from equation (6.28) and at each location (R_0, z) we fit the given v_ϕ distribution independently by adjusting the parameters σ_0, R_σ and h_0. Table 6.3 gives the parameter values obtained from the fits and also the radial velocity dispersions that the fits yield through equation (6.38) and the true radial velocity dispersion within the model. Notice that the parameter σ_0 rises from $27\,\mathrm{km\,s^{-1}}$ at the plane to $48\,\mathrm{km\,s^{-1}}$ at $z \sim 2\,\mathrm{kpc}$ and that these values coincide with the values of the corresponding parameters in the DFs of the thin and thick discs, respectively. Fig. 6.6 and Table 6.4 show the fits obtained to the same data when $\Delta\Phi_{\mathrm{ad}}$ in equation (6.36) is evaluated from equation (6.33) with ΔE_z replaced by $\overline{E_z}$ from equation (6.47). In both Figs. 6.5 and 6.6 the quality of the fits is excellent, so the inclusion of ΔE_z improves the optimum fit only marginally. However, inclusion of ΔE_z does change the optimum value of h_0 significantly and in the sense of bringing it closer to the true scale-height of the model disc, which increases from small values very close to the plane, where the gas disc dominates the gravitational potential, through 300 pc at $z \sim 300\,\mathrm{pc}$, where the thin disc accounts for the majority of stars, to $\sim 1\,\mathrm{kpc}$ at large heights, where the thick disc is dominant. Note that far from the plane the dominant population's scale-height h_0 is significantly smaller than the locally measured scale-height of the disc because the population is dominated by stars with $R_{\mathrm{g}} < R$, which by equation (6.25) have $h(R_{\mathrm{g}}, R) > h_0$. Even so, when ΔE_z is omitted, the fitted values of h_0 are unexpectedly small. Including ΔE_z increases h_0 at all heights, while limiting the values of $\overline{E_z}$ employed to less than $(50\,\mathrm{km\,s^{-1}})^2$ yields intermediate values of h_0, which are not far from constant as we would wish. The reason adding ΔE_z to the effective potential increases h_0 is that ΔE_z increases the contribution to the velocity distribution at R_0 of stars with small values of R_{g} and therefore v_ϕ and thus reduces the need to suppress the contribution of the population with $R_{\mathrm{g}} \simeq R_0$, which dominates the peak of the v_ϕ distribution, relative to the stars that form the prominent left wing of the distribution. The other improvement effected by including ΔE_z is to lower $\langle v_R^2 \rangle^{1/2}$ slightly and thus bring it closer to its true value at high altitudes. When there is no upper limit on the values of $\overline{E_z}$ used in the calculation of ΔE_z, this lowering of $\langle v_R^2 \rangle^{1/2}$ becomes excessive above $z \simeq 2\,\mathrm{kpc}$ because at such altitudes the vertical energy becomes comparable to the radial energy.

Irrespective of whether ΔE_z is used, the scale-length R_σ exhibits a continuous rise in the fits,

z	σ_0	R_σ	h_0	$\langle v_R^2 \rangle^{1/2}$	$\langle v_R^2 \rangle^{1/2}_{\mathrm{BM11}}$	χ^2
0	27.06	5.31	50.5	30.9	33.4	0.000097
250	27.46	5.48	347.2	32.1	35.2	0.000310
500	29.65	5.61	323.4	37.1	40.4	0.000267
750	33.99	6.14	326.8	45.4	48.4	0.000338
1000	39.81	6.79	438.7	55.4	55.1	0.000060
1250	41.99	6.81	533.2	62.3	58.7	0.000085
1500	43.08	7.40	564.1	63.6	60.7	0.000040
1750	43.83	8.50	496.4	62.3	61.8	0.000117
2000	43.94	10.70	416.2	58.3	63.1	0.000234
0	27.06	5.31	50.5	30.9	33.4	0.000097
250	27.46	5.48	347.2	32.1	35.2	0.000310
500	29.65	5.61	323.4	37.1	40.4	0.000269
750	33.99	6.14	326.8	45.4	48.4	0.000338
1000	39.88	6.74	391.0	55.7	55.1	0.000062
1250	41.74	6.79	401.8	61.9	58.7	0.000081
1500	42.72	7.28	390.7	63.4	60.7	0.000035
1750	43.69	8.13	345.8	63.1	61.8	0.000105
2000	45.87	10.18	301.9	61.7	63.1	0.000230

Table 6.4: Fit parameters when the vertical energy correction ΔE_z is included. The upper half applies the unlimited correction and its fits are presented in Fig. 6.6. The lower half includes an upper limit $\Delta E_z \simeq \overline{E_z} = (50\,\mathrm{km\,s^{-1}})^2$ that produces comparable fits, but prevents a breakdown of the horizontal dispersion starting around $z = 2\,\mathrm{kpc}$. Fits were taken with the same fixed parameters and in identical range as the fits described in Table 6.3, but this time with non-zero ΔE_z.

moving away from the value $R_\mathrm{d}/0.45$ of the corresponding parameter of the torus model. R_σ comes closer to $R_\mathrm{d}/0.45$ the lower α is chosen at higher altitudes.

Distributions in v_R

As we remarked in Section 6.4.3, the DF (6.37) is such that stars of given L_z have a Gaussian distribution in v_R. Consequently, the distribution in v_R of all stars found at a given distance from the plane should in this picture be a weighted sum of Gaussian distributions with the weights implicit in equation (6.38). Fig. 6.7 compares this prediction (lines) at several altitudes z with the corresponding distributions from the torus models (data points). The overall agreement between the data points and the predictions of the formula is remarkable when one bears in mind that the curves have not been obtained by fitting to the data points. At low altitudes (red and green) the formula predicts a distribution that is slightly too sharply peaked and deficient in the wings.
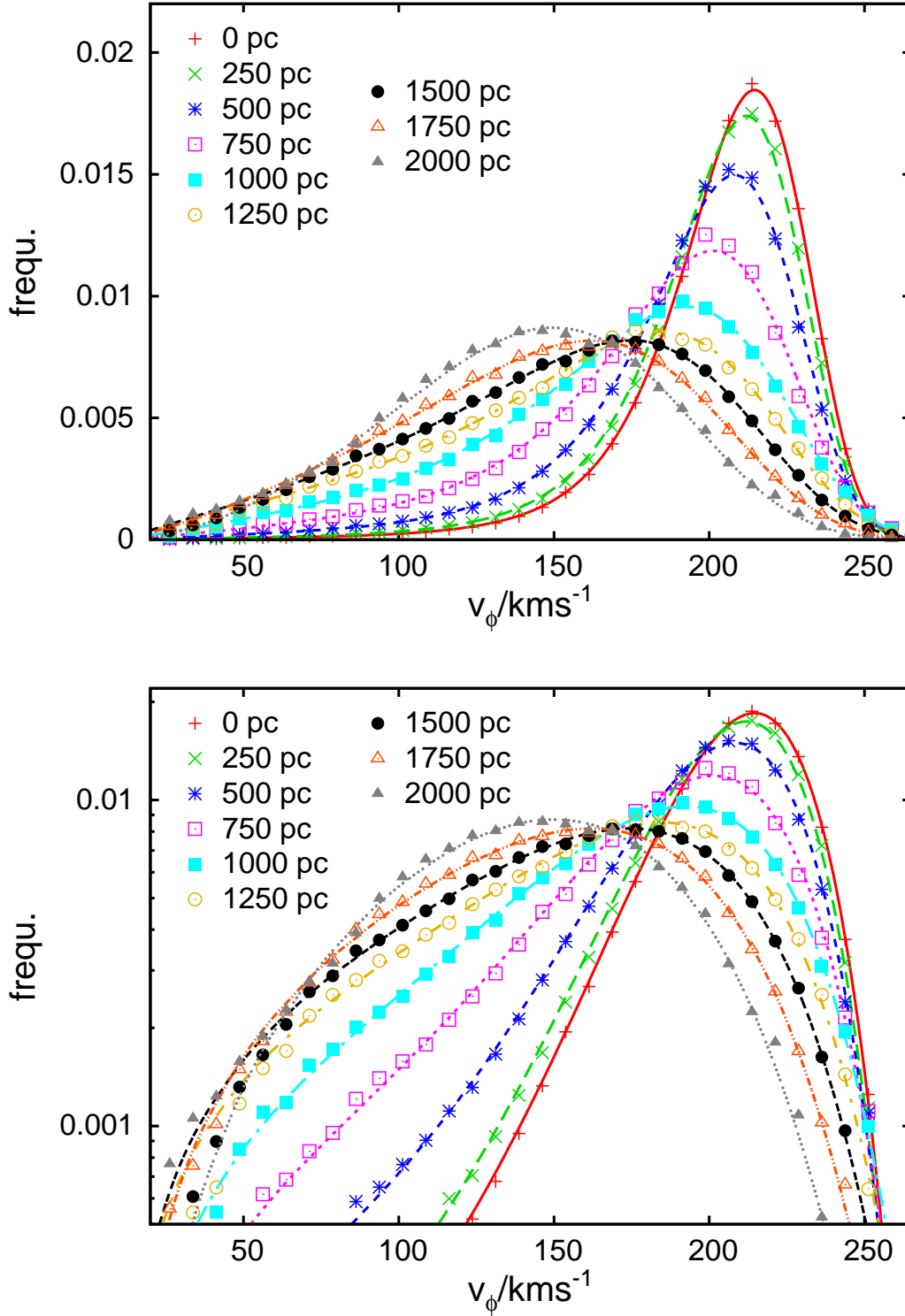
Figure 6.6: Fitting the velocity distributions of BM11 at different altitudes using eq. (6.36). The scale-length of the disc was fixed at their value of $R_{\rm d} = 2.4$ kpc and the parameter α was assumed to be the function of z specified by eq. (6.28).
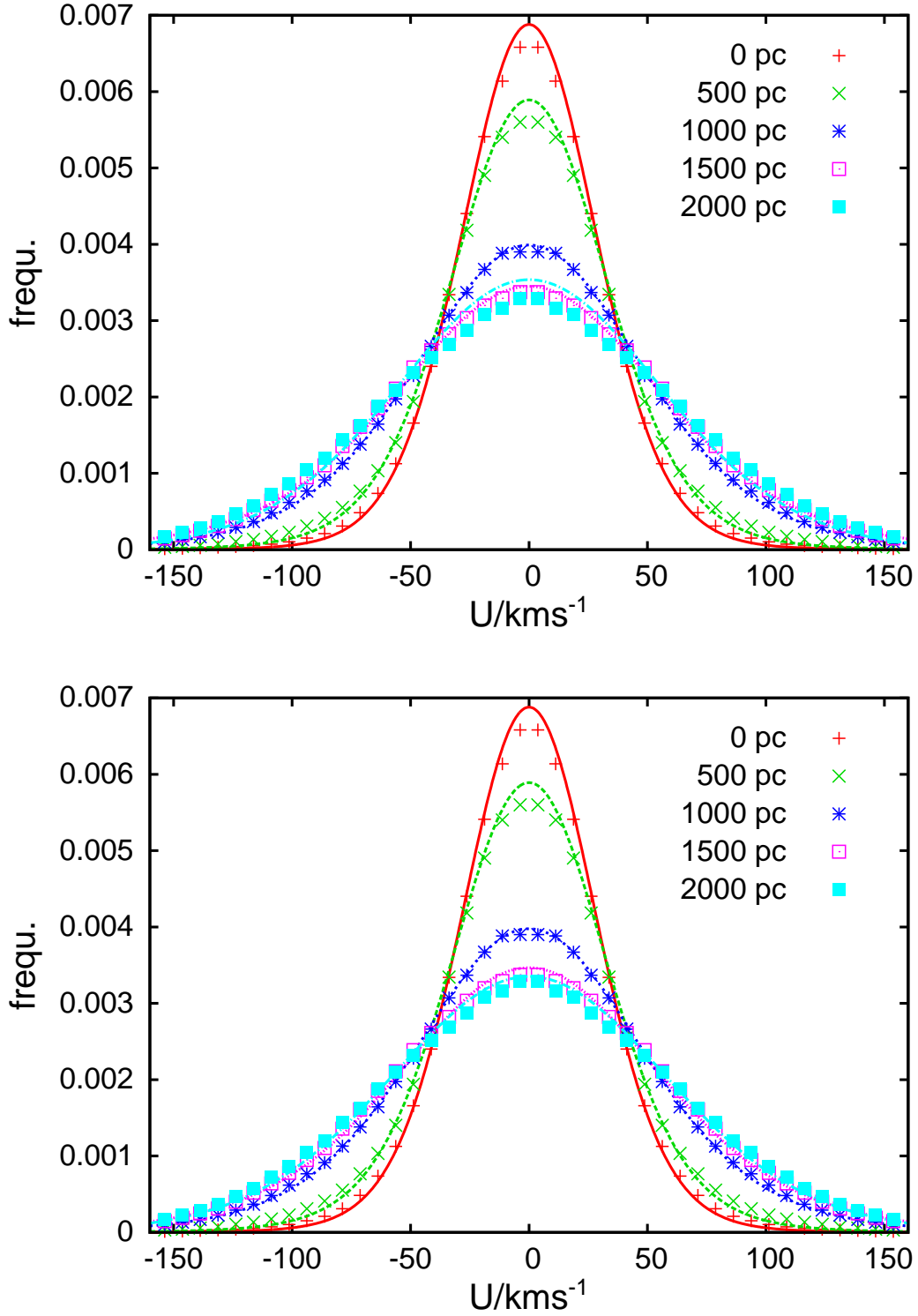
Figure 6.7: v_R velocity distributions from the models with non-zero ΔE_z (lines) compared to the torus models (data points) at different altitudes z. The upper panel is for when $\overline{E_z}$ is unlimited and the lower panel is for when $\overline{E_z} < (50\,\mathrm{km\,s}^{-1})^2$.

Around $\sim 1\,\mathrm{kpc}$ from the plane the fit is near perfect. The agreement between the curve for $2\,\mathrm{kpc}$ and the data points at $|v_R| < 50\,\mathrm{km\,s}^{-1}$ is much better in the lower panel than the upper panel, vindicating the use of the correction provided by ΔE_z.

6.5.2 Application to the Geneva-Copenhagen Survey

We have fitted the full formula (6.36) at an altitude of $z = 40\,\mathrm{pc}$ to the velocity distribution of the Geneva-Copenhagen Survey (GCS) of F and G stars (Nordström et al., 2004; Holmberg et al., 2009). As sample we selected the full $13\,520$ objects that have measured space velocities. We adopted $v_{\mathrm{c}} = 220\,\mathrm{km\,s}^{-1}$ and assumed that the Sun's velocity with respect to the Local Standard of Rest is $12.24\,\mathrm{km\,s}^{-1}$ (Schönrich, Binney & Dehnen, 2010), so $232.24\,\mathrm{km\,s}^{-1}$ was added to the published heliocentric v_ϕ velocities. Given that the sample lies near to the mid-plane, where $\alpha = 2$ would apply, we adopted $\alpha = 1.5$, and we also set the local scale-height to $h_0 = 200\,\mathrm{pc}$: when α and h_0 are allowed to vary when fitting to the data, they prove to be strongly correlated in the sense that low values of α enhance the contribution of populations with smaller R_{g} and thus favour larger values of h_0 for balance. However, the differences between the residuals of the various best fits are not statistically significant.

Fig. 6.8 shows two typical fits performed on the region $150 < v_\phi/\mathrm{km\,s}^{-1} < 250$, which demonstrate how nicely and naturally the formula reproduces the non-Gaussianity of the azimuthal velocity distribution. The fits are for scale-lengths $R_\sigma = 7.5\,\mathrm{kpc}$ (blue dashed line) and $R_\sigma = 5\,\mathrm{kpc}$ (red solid line). The shorter scale-length provides the better fit at low v_ϕ and the worse fit to the high-velocity tail. The shorter length scale also yields the smaller value of the velocity-dispersion parameter, $\sigma_0 = 22.90 \pm 0.45\,\mathrm{km\,s}^{-1}$ versus $\sigma_0 = 24.57 \pm 0.48\,\mathrm{km\,s}^{-1}$. In the plane the core of the velocity distribution is dominated by the youngest part of the thin disc, while the wings of the distribution will be dominated by the thick disc, and as we proceed from the core to the wings of the distribution stars of ever increasing age will grow in importance. Hence the true distribution in $v_< < phi$ reflects the entire star-formation history of the Galaxy and we cannot expect to obtain a perfect fit to it by adjusting a single velocity-dispersion parameter, σ_0. Moreover, the statistics of the GCS catalogue to some extent reflect the complex selection biases involved in the catalogue's formation, and we have made no attempt to replicate these biases. Neglect of these complexities is presumably why our fit is less good than that obtained by Schönrich, Binney & Dehnen (2010). The presence of kinematically hotter objects is confirmed by the estimated value for σ_0 drifting to higher values when we expand the velocity interval on which we perform the fits. A couple of thin-disc scale-heights above the plane the population will be more homogeneous, being dominated by the thick disc, and it should be possible to obtain better fits by adjusting σ_0.

Interestingly, on testing for a systematic shift in v_ϕ the formula recovered to $2\,\mathrm{km\,s}^{-1}$ the expected local standard of rest both from the GCS data and from the velocity distributions of the torus models at low altitudes. At higher altitudes the performance deteriorates due to the higher uncertainties. We found that for local stars ΔE_z does not play a significant role, although it gives a bias of order $1\,\mathrm{km\,s}^{-1}$. In a forthcoming re-determination of the local standard of rest we will
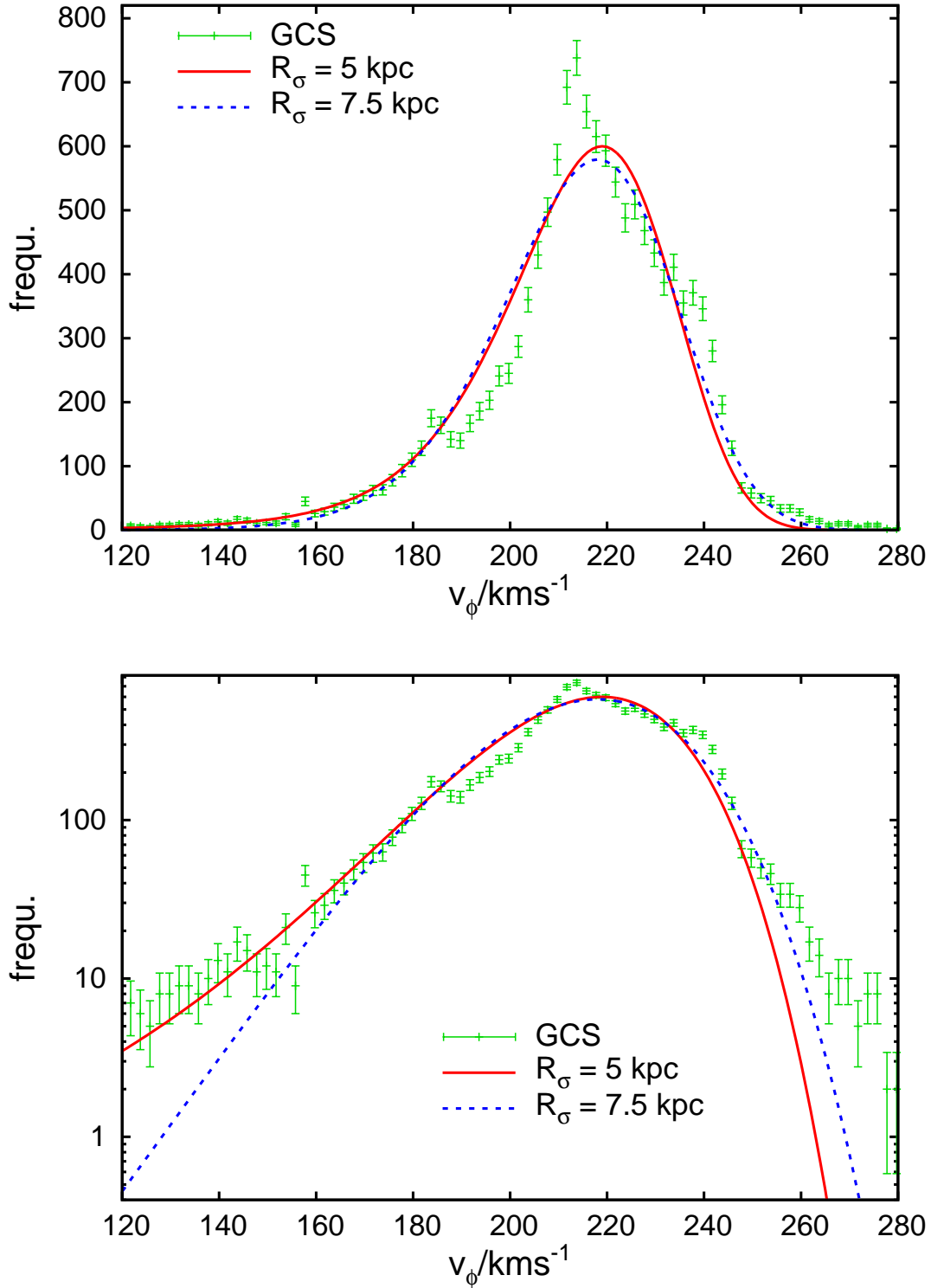
Figure 6.8: Fitting the GCS velocity distribution with a two-parameter fit, using only a normalization constant and the local dispersion σ_0. The lower panel shows the fit on a logarithmic scale to show the wings, while the upper panel presents the linear scale. We separately fit σ_0 for dispersion scale-length $R_\sigma = 7.5\,\text{kpc}$ (blue dashed line) and $R_\sigma = 5\,\text{kpc}$ (red solid line).

take this effect into account.

Fig. 6.9 compares the GCS data with the v_R distributions that follow from the fits to v_ϕ. It is clear that the formula under-estimates the width of the v_R distribution. In Section 6.5.1 we found that in the case of the torus model at small $|z|$, the fitted v_R distribution was somewhat narrower than the true one even though the v_ϕ distribution was very closely fitted. Correspondingly, in the case of the GCS data, the failure of the fit to the v_ϕ to adequately populate populate the wings of the distribution is mirrored in the fit to the v_R distribution in Fig. 6.9 being least satisfactory in the wings.

6.6   Conclusions

The distribution of azimuthal velocities in the disc of a galaxy like ours is very skew and varies systematically with distance from the plane. Naturally one wants to be able to quantify such a distribution in an effective way. The traditional approach of fitting it with a superposition of Gaussians (e.g. Bensby et al., 2003; Ivezic et al., 2008; McConnachie et al., 2006) is unsatisfactory, both because there is no physical reasoning behind the use of a Gaussian when the distribution is not dominated by measurement error, and because when a superposition of Gaussians is used, the parameters of the fit are neither unique nor physically informative.

Our formula is based on the approximation that the vertical actions of stars are invariant as stars oscillate radially. We have refined this approximation by considering anew the impact that vertical motion has on the radial oscillations, which BM11 found to be a significant effect. Our treatment of this effect, being based on overall energy conservation, is conceptually much sounder than that of BM11 and promises to play a valuable role in the interpretation of stellar velocities with rigorous dynamical models. However, we find that the power of our formula is only marginally improved by our more rigorous treatment of how vertical motion affects the radial oscillations.

Ultimately, our formula is just a fitting formula rather than a dynamical theory, even though we have derived it from dynamical considerations. Something the derivation highlights is how closely the horizontal and vertical motions of stars are intertwined, notwithstanding the adiabatic invariance of actions. Because both the vertical and horizontal random velocities of stars increase with age, as one moves away from the plane the mix of stars one sees fundamentally changes in the sense of increasing age and decreasing radius of birth. The cleanest way to model this phenomenon is by means of a DF like those presented by Binney (2010), but a couple of computationally challenging steps are required to extract observationally testable velocity distribution such as $n(v_\phi)$ from a DF: first a connection has to be established between ordinary phase-space coordinates and the isolating integrals upon which the DF depends, and then one has to marginalise over two velocities. Evaluation of our formula is trivial by comparison.

Our derivation makes it plain that no population of stars can simultaneously have scale-height and velocity dispersion that are both independent of radius: the sub-population formed by stars that have a narrow range of angular momenta must inevitably increase in scale-height and decrease in
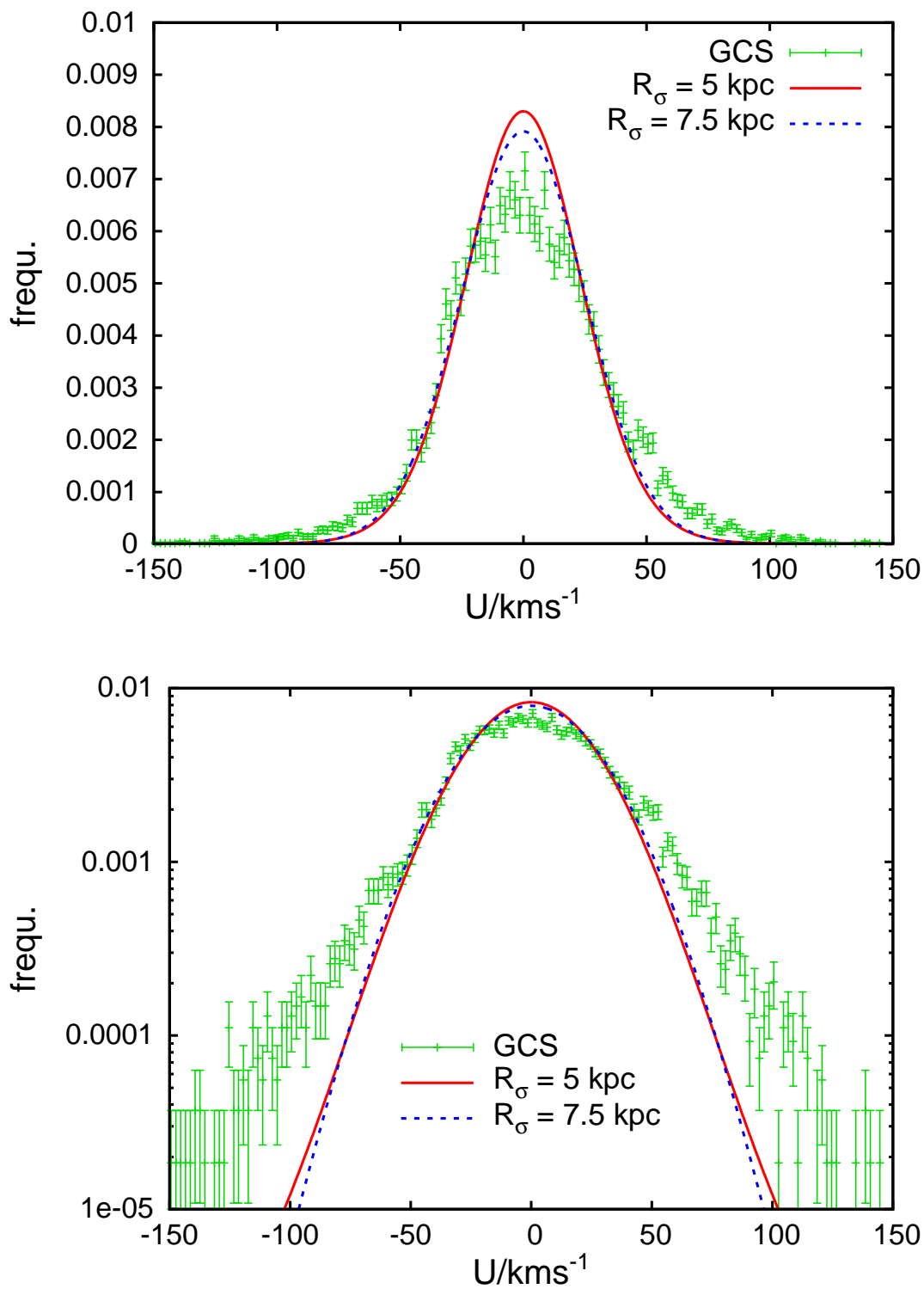
Figure 6.9: Derived v_R velocity distributions at the parameters of Fig.6.8 versus data.

vertical velocity dispersion with increasing R, and if stars of larger angular momenta are added in to hold constant the scale-height, they will have to have an even smaller vertical velocity dispersion, so the vertical dispersion of the entire population will decline steeply outwards. Given this situation, it is unwise to seek to define the thick disc in terms of a given scale-height and velocity dispersion, as some recent papers have done.

We validated our fitting formula by using it to fit the distributions of v_ϕ components at several distances from the plane in a model with a well-defined DF that included both thin and thick discs. Excellent fits were obtained. The values of the fitting parameters varied slightly with the level of sophistication of the model employed, but were broadly in agreement with the values we would expect given the underlying DF, especially when the most sophisticated approximations were used. This exercise implies that physical significance can be attached to the values of parameters derived from fits to real data. Each fit to a v_ϕ distribution implies a model of the corresponding v_R distribution. In our tests these models turned out to be very useful although showing a slight tendency to be too narrow at small $|z|$.

We fitted the formula to the v_ϕ velocities of GCS stars and obtained good but not perfect fits for plausible values of the parameters. The blemishes in these fits will arise from three causes: (i) the well known presence of pronounced clumping of stars in the (U, V) plane (Dehnen, 1998), (ii) the need to model subtle selection effects in the GCS sample, and (iii) our formula is derived from an isothermal DF and must encounter difficulty fitting data drawn from a system that is a superposition of systems with very disparate dynamical temperatures. Hence in part the difficulties encountered in fitting the GCS data may reflect the importance at the extremes of the v_ϕ distribution of the thick disc and/or stellar halo. With a larger body of data, or data taken further from the plane, it might be profitable to fit the data to a sum of two or more instances of our formula. Our fit to the v_ϕ components yields a model of the v_R components that is rather too narrow, in agreement with our work with the model based on a DF.

Our formula could be used to fit the line-of-sight velocity distributions (LOSVDs) of galaxies in which individual stars are not resolved (e.g. Bacon et al., 2001). Since our formula has been derived on the assumption that the circular speed is independent of radius, it might fail to produce a satisfactory fit to the velocity distribution of stars in a galaxy with a distinctly non-flat rotation curve. The physical basis of our formula breaks down at distances from the plane of order 2 kpc, so failure to fit data for stars at higher altitudes might have no physical significance.

We derived our formula by adapting to the three-dimensional world the planar DF of Shu (1969). It would be interesting to adapt in a similar way the planar DF of Dehnen (1999b), which Dehnen has argued is in certain respects superior to the Shu DF. Unfortunately, the adaptation of a planar DF is a non-trivial exercise on account of the intertwining of the radial and vertical motions mentioned above. Therefore in this paper we have confined ourselves to the Shu DF, which proves to provide a very useful point of departure.

Data for stars that lie at significant distances from the plane are now becoming available (Ivezic et al., 2008; Siebert et al., 2011). The measured space velocities of such stars contain significant errors arising from a combination of errors in proper-motion and distance. It is essential to take proper account of these errors when inferring the true kinematics of the underlying populations.

Our formula provides the natural way to do this: one fits the data to the result of folding the formula with appropriate distance and proper-motion errors. Schönrich, Asplund & Casagrande (2011a) use this methodology to extract in an elegant way the information contained within the measured distribution of azimuthal velocities of stars that have quite large random velocities. We will shortly present similar analyses of samples that include a higher proportion of disc stars.

Acknowledgements

6.7   Appendix: Estimating the typical vertical energy

In this section we estimate the typical value $\overline{E_z}(R_g)$ of the vertical energy $E_z(J_z, R)$ of the stars that we encounter with specified angular momentum $L_z = Rv_\phi$ at a given location (R, z). Let σ_z be the vertical velocity dispersion at (R, z). then

$$\overline{E_z}(R_g) \simeq \tfrac{1}{2}\sigma_z^2(R_g) + \Phi_z(z). \tag{6.44}$$

Regarding σ_z, we have that to an excellent approximation the vertical Jeans equation reads (Binney & Tremaine, 2008, eq. 4.271)

$$\frac{\mathrm{d}\left(\rho\sigma_z^2\right)}{\mathrm{d}z} = -\rho\frac{\mathrm{d}\Phi_z}{\mathrm{d}z}. \tag{6.45}$$

Neglecting the derivative of $\ln\sigma_z^2$ relative to that of $\ln\rho$ this yields

$$\sigma_z^2 = h\frac{\mathrm{d}\Phi_z}{\mathrm{d}z}, \tag{6.46}$$

where $h \equiv -(\mathrm{d}\ln\rho/\mathrm{d}z)^{-1}$ is the local scale-height of the population. As we saw from equation 6.27 the local scale-height decreases towards lower guiding centre radii, if we assume all populations to have at their guiding centre radius a constant scale-height. Hence finally we adopt:

$$\overline{E_z}(R_g) = \tfrac{1}{2}h(R_g, R)\frac{\mathrm{d}\Phi_z}{\mathrm{d}z}\bigg|_z + \Phi_z(z). \tag{6.47}$$

Equation (6.47) involves the potential and its derivative at altitude z. We obtain these from a simple mass model with a razor thin gas layer that at the solar radius has surface density

$12\,M_{\odot}\,pc^{-2}$ and three exponential stellar components. In each such component the mass per unit surface area within distance z of the plane is

$$\Sigma_i(z) = \Sigma_{i,0}\left(1 - e^{-z/h_i}\right). \tag{6.48}$$

The three components represent the thin disc, the thick disc and the halo with parameters

$$(\Sigma_{1,0}, \Sigma_{2,0}, \Sigma_{3,0}) = (30, 10, 70)\,M_{\odot}\,pc^{-2} \tag{6.49}$$

and

$$(h_1, h_2, h_3) = (300, 1000, 4000)\,pc. \tag{6.50}$$

The halo contribution was chosen to match the local vertical potential from the adopted Dehnen potential, which was used for the torus models to which we compare our formalism – the modifications required for a different radius or disc mass are simple. We approximate the contribution $\Phi_i(z)$ to the potential from the ith component by assuming that the component is an infinite plane-parallel sheet. Then

$$\Phi_i(z) = 2\pi G\Sigma_{i,0}\left[z + h_i\left(e^{-z/h_i} - 1\right)\right]. \tag{6.51}$$

Chapter 7

Application of the formula to study kinematics and changes to the adiabatic approximation

7.1 Abstract

In this little chapter the necessity for a change in the adiabatic correction is shortly discussed, followed by a comparison of the two possible solutions: A change in the adopted angular momentum of a star and the use of the adiabatic potential. We find the adiabatic potential more robust and show that by pushing the orbits further out there is a significant increase of the asymmetric drift at larger altitudes, where the vertical energy and its change with galactocentric radius are larger. In the second part we lay out our error analysis for kinematic data and show an application to the SEGUE sample.

7.2 Consequences of the new adiabatic potential for the adiabatic approximation

7.2.1 correcting the adiabatic correction

In the previous chapter we motivated the need for changing the horizontal potential when using the adiabatic approximation. The need for this change is obvious as the adiabatic approximation reduces the vertical energy of stars total energy conservation is violated in the classical adiabatic approximation. To correct for this we suggested in the previous chapter to let the balance go over to the horizontal term:

$$\Phi_{\mathrm{ad}}(R, L_z) = \frac{L_z^2}{2R^2} + \Phi(R) - \Delta E_z(\alpha, v_z^2, R),$$

(7.1)

where L_z is the angular momentum parallel to the rotation axis, $\Delta E_z(\alpha, v_z^2, R)$ is the relative change of vertical energy in the orbit relative to its guiding centre radius. We call this term the adiabatic potential as it describes the horizontal motion of the adiabatic approximation with energy conservation. Binney & McMillan (2011) suggested in contrary that the orbits of their stars can be very well described, if the vertical motion that pushes orbits outwards is accounted for by using in the effective potential the entire angular momentum instead of its projection onto the rotation axis. As of these two suggestions the energy conservation arguments is on firm grounds, this raises the question why and under which conditions the angular momentum approximation can be a sensible solution.

For the assumed vertical potential that follows a power law and is approximately proportional to the surface density of the disk $\Sigma(R)$ we obtained in Equation (6.35):

$$\Delta E_z = E_{z,g} \left(1 - \exp\left(-\frac{R - R_g}{R_d} \frac{2}{2 + \alpha} \right) \right). \tag{7.2}$$

This term delivers the aforementioned outwards tilt of the effective potential that pushes out the inner boundary of the orbit and allows it to travel further out. We can now directly check the suggestion of Binney & McMillan (2011) for the assumed power law potential approximating the contribution by E_z to the effective potential with a term in $1/R^2$:

$$E_z \sim -E_z \frac{R_g^2}{R^2} \frac{1}{2 + \alpha} \frac{R_g}{R_d} \tag{7.3}$$

If we now replace E_z by the vertical velocity squared near guiding centre radius, we have simply

$$E_z \frac{R_g^2}{R^2} \sim \frac{L_\phi^2}{2R^2} \tag{7.4}$$

and so our formula is a simple adding of angular momenta in the effective potential, if $\frac{1}{2+\alpha} \frac{R_g}{R_d} \sim 1$, which happens to be the case near the region $R_g \sim 2.5 R_d$. However, this only matches the first derivative. Already the second derivative of the approximation does not match its parent formula. We check our assumptions for a naive potential in Fig. 7.1. As underlying potential we use an unrealistic but handy potential with a constant circular rotation speed $V_c = 220\,\text{km}\,\text{s}^{-1}$ and a razor thin disc vertical potential with an exponentially declining mass surface density of scale length 2.5 kpc and a local mass surface density of $40\,\text{M}_\odot\,\text{pc}^{-2}$. This potential is, however, useful for tests, as we know the power law index to be precisely $\alpha = 1$, eliminating uncertainty on the right choice of this parameter. The upper panel shows an orbit starting from $R = 8\,\text{kpc}, z = 0\,\text{pc}$ with initial velocities $(v_R, v_\phi, v_z) = (35, 220, 20)\,\text{km}\,\text{s}^{-1}$, the lower panel displays an orbit with the same initial kinematics, but starting from $R = 3\,\text{kpc}, z = 0\,\text{pc}$. On the vertical axis we plot changes in the horizontal energy term $E_h = E_{kin,h} + \Phi_{eff}$, where E_h is the assumed measure for horizontal energy, $E_{kin,h}$ is the kinetic energy in radial direction and Φ_{eff} are the three possible assumptions for the effective potential. For the blue curves we take the classical effective potential derived
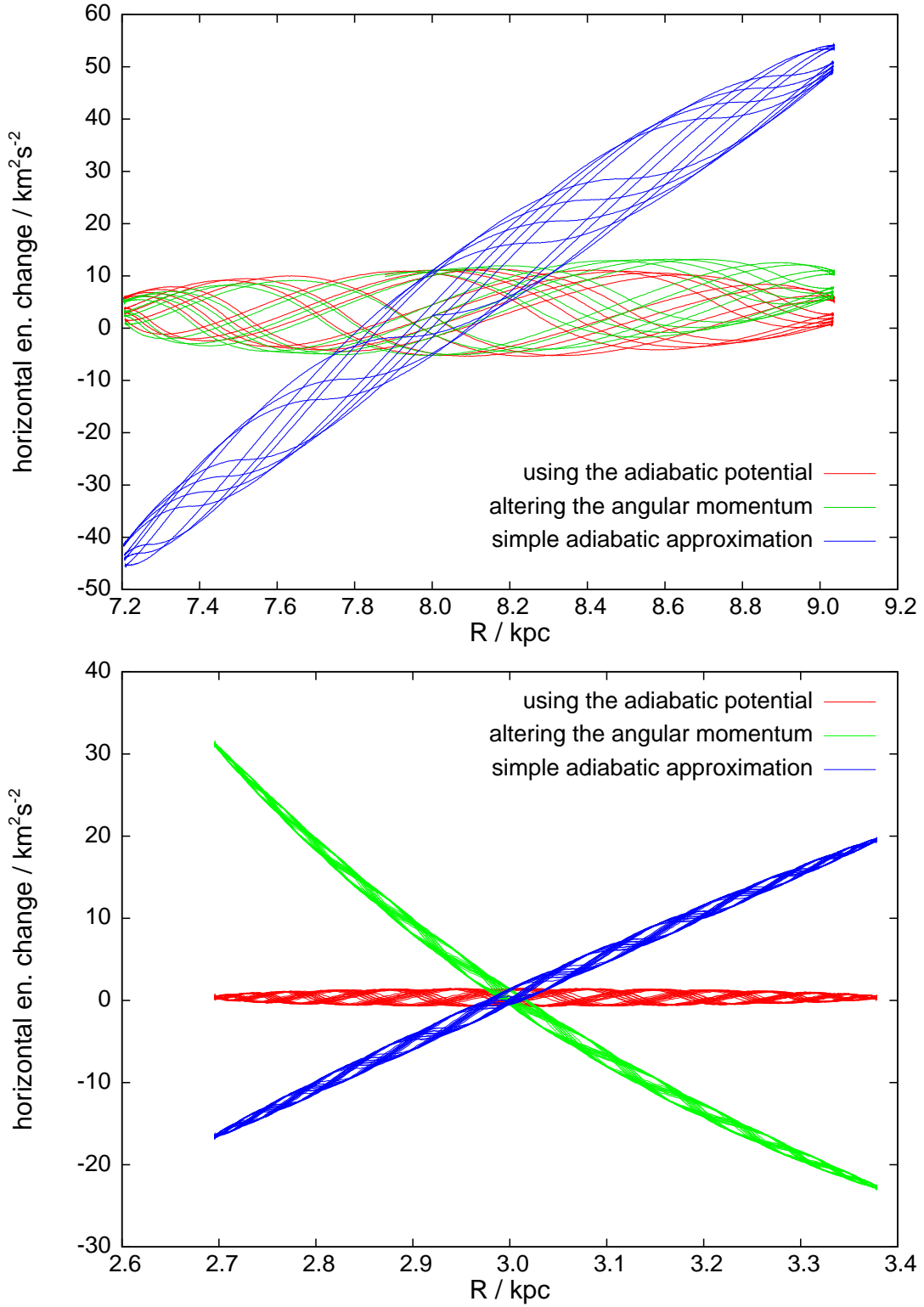
Figure 7.1: Testing the adiabatic approximation for two orbits in an idealised potential. The lines display the horizontal energy part $E_h = E_{kin,h} + \Phi_{eff}$ for different assumptions: The blue line shows the classical adiabatic approximation, the green has the angular momentum term corrected according to Binney & McMillan (2011), while the blue line contains the correction for vertical energy from eq.7.2.

just from the vertical angular momentum and the potential in the disc plane. Consistent with our expectations this leads to a drift in the overall horizontal energy along galactocentric radius R, with E_h rising towards larger radii, as the simple adiabatic approximation neglects the energy transfer from the vertical term. The red curves give the energy E_h measured with the adiabatic potential, i.e. balancing the expected vertical energy changes in the horizontal term. As we hoped, this term is (apart from the minor phase dependent oscillations around the mean value that arise from our approximation to split the motion into horizontal and vertical parts instead of calculating the orbit or using the real actions) completely flat in R for both plots, which implies that the horizontal motion is correctly described by the adiabatic potential. The green curves give the angular momentum approximation by Binney & McMillan (2011). For the adiabatic index $\alpha = 1$ of our chosen potential, our simple calculation suggests that the approximation attains its optimal value at $R_g = 3R_d = 7.5\,\text{kpc}$, so E_h should bend very slightly upwards for $R_g = 8\,\text{kpc}$ in the upper plot, as it really does, and bend strongly downwards due to severe over-correction of the energies for $R_g = 3\,\text{kpc}$ in the lower plot, which it fulfils as well.

To demonstrate how important this kind of effects is for a correct assessment of Galactic kinematics, Fig. 7.2 shows the asymmetric drift in the kinematic model of Binney (2010) with his thin and thick disc distribution function against altitude. For this we use the best-fit potential of McMillan (2011). With the continuous red line we plot the mean rotational velocities calculated with our adiabatic potential. These are significantly below the values from the original approach without vertical energy correction (dashed blue line). The difference is nearly negligible in the disc plane, where vertical energies are small and grows towards larger altitudes that require large vertical energies that push the stars from the inner disc outwards. As a side effect this relation mildly decreases the importance of the thick disc in the inner parts of the Galaxy from where the thick disc orbits are pushed away and increases its relative importance in the intermediate and outer parts as orbits are taken to regions where they feel less vertical restoring force and as we have a more numerous population of energetic inner disc stars.

As a last point we would like to mention a speciality of the adiabatic potential: As vertical energy tilts the effective potential outwards, the potential minimum shifts to larger radii. Stars with large vertical energy and slow radial motion can hence be on orbits that never cross their guiding centre radius as defined by the classic effective potential. We encountered those peculiar objects in N-body simulations (Solway et al. in prep.) and hope to find them also in real data once we can derive more precise kinematics.

7.3   Application to SEGUE

Lastly we apply the fitting formula to data release 8 of Sloan Digital Sky Survey (SDSS, York et al., 2000) for stars that were observed spectroscopically with the SEGUE Survey (Yanny et al., 2009). Stellar parameters for the stars were estimated using the SEGUE Stellar Parameters Pipeline (SSPP, Lee et al., 2008a,b; Allende Prieto et al., 2008). In contrast to the Geneva-Copenhagen-Survey, which combined radial velocity measurements with the Hipparcos paral-
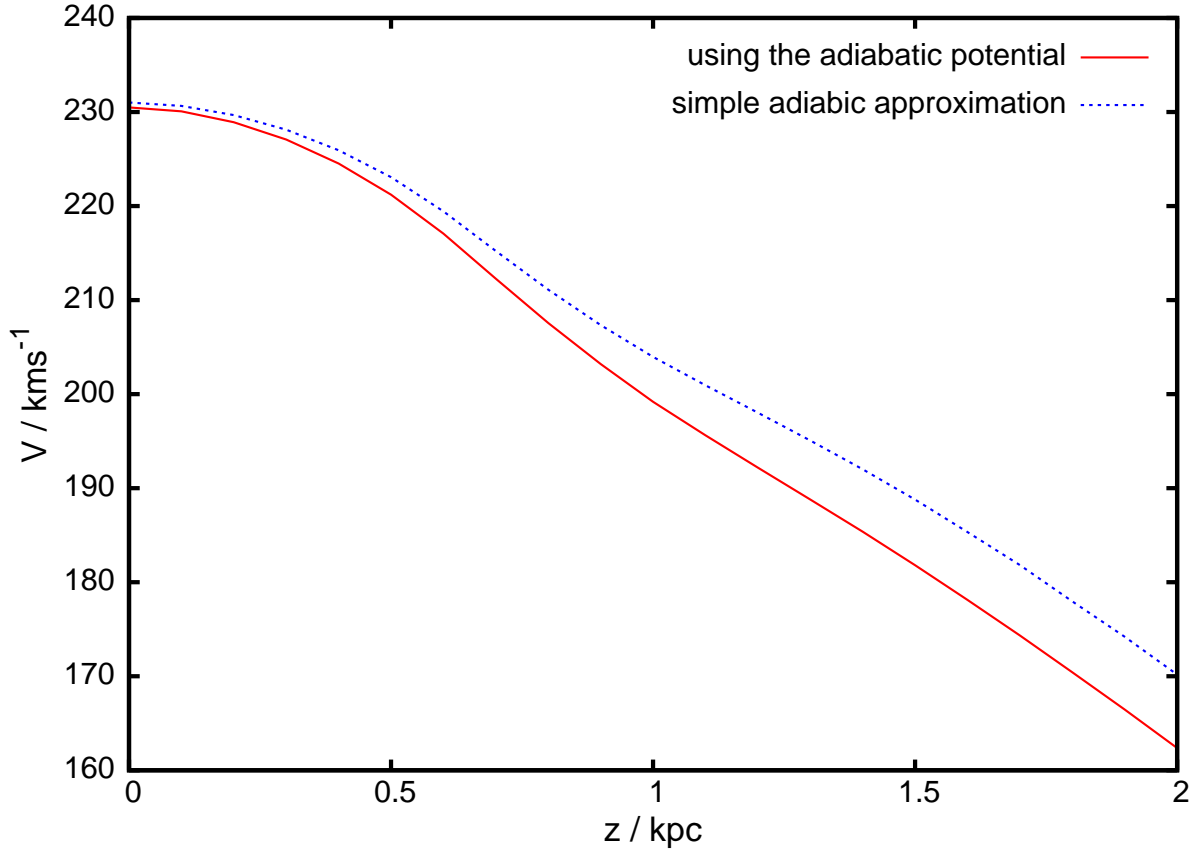
Figure 7.2: Comparison of the mean rotational velocities against altitude above the plane with and without the correction of the adiabatic potential. We used an adaption of the formalism of Binney (2010), using the potential from McMillan (2011).

altitude/pc	$0-400$	$400-800$	$800-1200$	$1200-1700$	$1700-2300$	$z > 2300$
num. stars	1002	7243	7630	5601	3637	3217
mean z/pc	433	595	985	1423	1971	2808
$\ln(P)$	-80.10	-195.23	-93.64	-88.22	-88.35	-87.1
1 - p-level	0.999	1	0.734	0.194	0.606	0.672
σ_0	32.6	31.6	34.1	37.75	40.59	39.42
h_0	432.8	594.6	856.1	691.7	651.3	472.7
adopted α	1.38	1.08	0.72	0.28	-0.27	-1
$\overline{\langle v_R^2 \rangle}$	32.02	35.44	39.60	45.89	52.41	55.0
$\langle v_R^2 \rangle_{data}$	42.63	45.79	49.12	55.25	60.39	68.3

Table 7.1: Fit parameters and observers at different altitudes in the SEGUE DR8 sample. Dispersion values are from stars with $|U| < 200\,\mathrm{km\,s^{-1}}$ and $|W| < 80\,\mathrm{km\,s^{-1}}$.
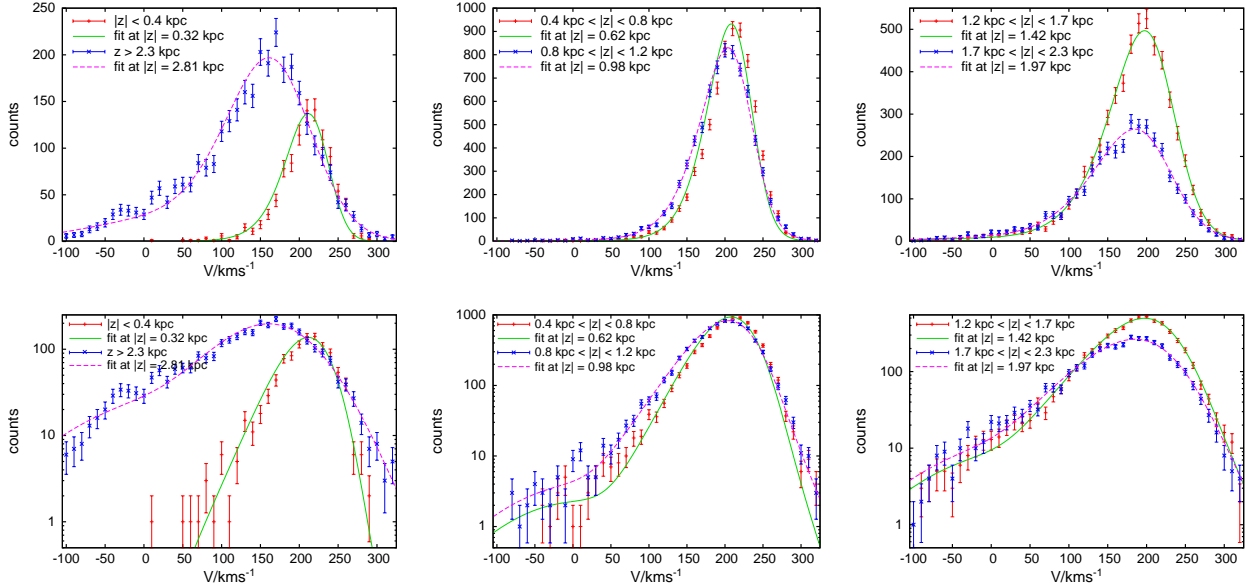
Figure 7.3: Velocity distributions from SEGUE DR8 versus the fits with parameters from table 7.1 at different altitude bins. Error bars give the Poisson noise, but do not account for systematic or velocity errors.

laxes and proper motions, SEGUE only contains line-of-sight velocities, proper motions and stellar parameters. The survey is far deeper and covers a larger volume reaching higher altitudes, but due to the larger distance proper motion errors translate into larger velocity errors. As there are no parallaxes, distances are highly uncertain and every study of kinematics is complicated by non-Gaussian errors arising from the distance uncertainties. As a first approach we adopt the main sequence calibration of Ivezic et al. (2008) (Eq. A7 in their Appendix) to obtain photometric parallaxes for stars with gravities $\log(g) > 4.1$ determined in the SSPP. An alternative that would reduce the loss of available objects would be to use the method of Burnett & Binney (2010), however, we have sufficient numbers of stars so that we can afford to limit the risk of systematic mis-selections by restricting the sample to main sequence stars with a tight surface gravity cut. The selection of stars, distance determination and derivation of kinematics are done as in Schönrich, Asplund & Casagrande (2011a) (see esp. their appendix). In contrast to Schönrich, Asplund & Casagrande (2011a) we do not make use of the calibration sample, but use instead all objects that fulfil the target selection criteria of the categories: F turnoff, low metallicity, K dwarf, F/G dwarfs, M sub-dwarfs, G dwarfs in SEGUE1 and of the categories: MS turnoff, Low metallicity for SEGUE2. This gives 191522 unique entries among which 28830 pass our quality criteria plus a cut for $0.2 < (g-i)_0 < 0.7$ (to remove red and very blue stars), have [Fe/H] > 1.0, are considered to be within 4 kpc distance and satisfy the surface gravity cut $\log(g) > 4.1$.

With the distances space velocities of stars are readily calculated in the heliocentric coordinate

system, where we adopt again the proper motion of the Sun from Schönrich, Binney & Dehnen (2010), a standard rotation velocity of $220 \, \text{km} \, \text{s}^{-1}$ and a galactocentric radius of $R = 8 \, \text{kpc}$. Velocities were transformed into the local coordinate systems at the stars' supposed position. The necessity for the latter transformation is given by the extension of the sample and reduces the systematic drift in radial velocities.

For our tentative fits we cut the sample into six altitude regions and performed separate fits. At each altitude we fit the sum of a simple Gaussian halo component and a disc component with the presented analytical function including the adiabatic correction and re-correction. As there are very few halo stars in this sample, it contains insufficient information for a determination of the halo velocity distribution and hence we use the values from Schönrich, Asplund & Casagrande (2011a) fixing the halo velocity distribution at Galactic rest with an azimuthal velocity dispersion of $70 \, \text{km} \, \text{s}^{-1}$. Its normalisation is the only free fitting parameter applied to this component. As errors are relatively large, information inherent in the velocity distribution is limited and so we fix the disc scale length at $R_d = 2.5 \, \text{kpc}$, the adiabatic correction to $\alpha = 1.7 - 0.01 |z| / \text{pc}$. As we presented in Schönrich, Asplund & Casagrande (2011a) very reasonable fits without the vertical energy re-correction, we this time show results making use of it.

Due to the large uncertainties of distances and proper motions an elaborate error analysis is essential to get at least a rough picture on the real distribution of velocities underlying the observed distribution. We identify three sources of errors in the distribution: The "direct" errors from proper motions and the radial velocity determinations, the uncertainties in distance determinations directly stretching the V velocities and velocity "cross-overs" (cf. Schoenrich et al. in prep.) from the other velocity components by distance errors.

The first category is easily accounted for: At each altitude we performed an error propagation of the line-of-sight velocity errors and proper motion errors onto the velocity components. This error propagation delivers the error distribution from proper motion errors as a sum of Gaussians (for different error amplitudes), which is then folded onto the theoretical distribution. We can write this error function caused by the proper motion errors as:

$$err_{pm}(\Delta V) = N_{err,pm} \sum_i g_i(\Delta V, \sigma_{V,i}, 0) \tag{7.5}$$

where the sum runs over all stars going into the distribution and $g_i((\Delta V, \sigma_V, 0)$ is the unbiased Gaussian error of with $\sigma_{V,i}$ for star i. We thus estimate the width of the error for a single star to be the square root of the sum of the squared proper motion errors and squared radial velocity errors on the velocity component in question, which are derived by inserting the errors instead of their observables into the terms connecting the velocity components to the observables. The normalisation $N_{err,pm}$ just ensures that $err_{pm}(v)$ has weight 1:

$$\int err_{pm}(\Delta V) d(\Delta V) = 1 \tag{7.6}$$

The second major source of errors is the uncertainty of distances, leading to a second error distribution $err_d(v)$. Apart from the systematic uncertainties in the choice of the locus of isochrones,

there is a small observational scatter in the measured observed magnitudes as well as a larger scatter in the assumed absolute magnitudes, which directly affects the distance modulus estimate. This error derives from errors in [Fe/H], in the alpha enhancement, in the observed colour and in the reddening that affects both the inferred magnitude and dereddened colour of the star. In this case we assume a global error of 0.25 mag, which is applicable as the vast majority of objects is sufficiently out of the plane to have relatively similar reddening uncertainties and the decreasing uncertainty by influence of metallicity on the isochrones with decreasing metallicity is partly balanced by an increased intrinsic scatter in the parameter determinations. As described in Schönrich, Asplund & Casagrande (2011a) the distance error from a Gaussian distance modulus error is highly non-Gaussian, but has a prolonged tail towards larger distances. We obtain the distance error distribution by transforming the Gaussian distance modulus error into relative distance space. For the azimuthal velocity V we calculate the average part of the squared V velocity component in the sample that is carried by proper motions, $\overline{\zeta_V}$. As the sample is rather high up in the sky and additionally concentrates away from the the apex and antapex of a circular orbit, the average proper motion partition on V approaches 1 (cf. also Schönrich, Asplund & Casagrande, 2011a). The distance error distribution translates into a map of the observed V velocity distribution onto itself that we to zeroth order approximate as:

$$V \rightarrow V + (V - V_\odot)\overline{\zeta_V}\frac{\Delta s}{s} \tag{7.7}$$

where $\Delta s/s$ is the relative distance mis-estimate, and $(V - V_\odot)$ is the stellar velocity in a heliocentric frame. This is not the only term. Additionally there will be small crossovers from the U and V velocities, that give a minor error term to the V velocities, which should again be shaped as a sum of Gaussians. We approximate this by a single Gaussian error term $err_{cv}(V) = g(\Delta V, 7\,\mathrm{km\,s^{-1}}, 0)$ ($7\,\mathrm{km\,s^{-1}}$ would correspond to a $70\,\mathrm{km\,s^{-1}}$ velocity dispersion at a conversion factor of 0.5 and an effective distance error of 20%. This has also the pleasant effect to waive a tiny numerical instability that happens by the integration of err_d at the solar velocity $V_\odot$. The entire error calculation is done by first folding err_pm, then err_d and finally err_{cv} onto the data:

$$f_{obs} = err_{cv} \circ err_d \circ err_{pm} \circ f \tag{7.8}$$

where f is the theoretical velocity distribution and f_{obs} is its estimated observational representation. The folding with the error functions is numerically described with matrices mapping the velocity space onto itself to keep the calculation budget at a reasonable value. Due to their different positions in the sky we treat the halo and disc components separately and take all stars with $V < 50\,\mathrm{km\,s^{-1}}$ for assessing the halo errors and all stars with $V > 80\,\mathrm{km\,s^{-1}}$ as basis for an assessment of the disc velocity errors. We checked that this analytic approach is equivalent to the results of a Monte Carlo scattering of the stars in distances and the observables. Numerically (to speed up the calculations) the error propagation was solved by a transition matrix in V velocity at $1\,\mathrm{km\,s^{-1}}$ resolution.

Table 7.1 shows fitting parameters and observables for the data sets at different altitudes binned in $10\,\mathrm{km\,s^{-1}}$ intervals. Fits were performed in the azimuthal velocity range $-250\,\mathrm{km\,s^{-1}} \leq V \leq$

$280\,\mathrm{km\,s^{-1}}$, the left limit fully covering the halo velocity distribution to get the right normalisation, the right limit near the upper edge of the theoretical velocity distribution and thus placed inwards of the high velocity edge of the observed distribution to reduce the influence of mere measurement error on the fits.

For the fits we used four free parameters, namely the normalisation of disc and halo, the local horizontal dispersion σ_0 and the local scale height h_0. The p-levels given are taken in the disc component region and hence they are a bit below what could be attained if the fit was performed on that range exclusively. Yet it can be seen, that in the two lowest bins the fit does not yield a proper result, mostly by the fitting function being $3-5\,\mathrm{km\,s^{-1}}$ shifted against the observations. This can have three reasons: First it is an indication that a mixture of more than one disc component could be required in this region (indeed by introducing another disc component the result can be improved). Second we expect large and partly systematic distance errors in the formula we used. This can to some extent shift the peak towards solar velocity (distance underestimates) and lead to a wrong shape in the distribution. And third the adiabatic re-correction for vertical energy could exaggerate the effect, offsetting the distribution too much towards the low velocity side.

At the altitude bins above $800\,\mathrm{pc}$ the fits are of very good quality, indicated also by p-levels that exclude any significant deviation from the model prediction. The local scale height differs a bit from the expected values, yet it's value is uncertain and depends on the assumption for the vertical energy correction.

In an upcoming study we will make use of our improved distances to get a better characterisation of both SEGUE and RAVE data and will publish the above in the revised framework.

7.4   Effects of magnitude induced fractional distance errors

Here we show that when distances are estimated photometrically, the pdf of the fractional distance over-errors will have an enhanced tail towards distance over-estimates ($f > 0$). Let $\Delta_M = DM - DM_0$ be the difference between the estimated distance modulus DM of a star and its true value DM_0, and let the pdf of Δ_M be $P_M(\Delta_M)$. Then the pdf of f, $P_f(f)$, is

$$P_f(f) = P_M(\Delta_M(f))\frac{\mathrm{d}\Delta_M}{\mathrm{d}f}. \tag{7.9}$$

Since $\Delta_M = 5\log(1+f)$ and $\mathrm{d}\log x/\mathrm{d}x = 1/(x\ln 10)$, we obtain

$$P_f(f) = \frac{5}{\ln 10}\frac{P_M(\Delta_M)}{1+f}. \tag{7.10}$$

Setting $P_M \propto e^{-\Delta_M^2/2\sigma_M^2}$ this becomes

$$P_f(f) = \frac{5}{\sqrt{2\pi}\sigma_M \ln 10}\frac{1}{1+f}\exp\left(-\frac{[(5\log(1+f)]^2}{2\sigma_M^2}\right). \tag{7.11}$$
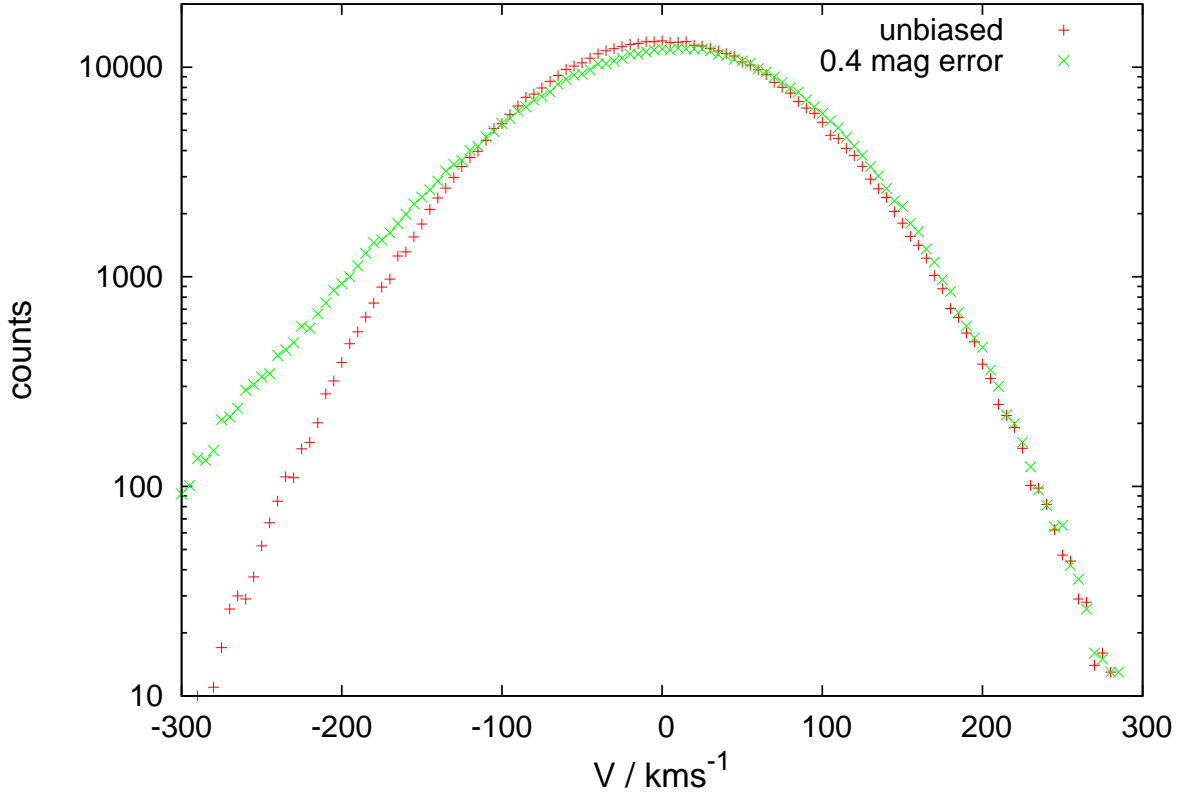
Figure 7.4: The red curve displays the Gaussian V velocity distribution of a mock halo sample of 500 000 objects. The green curve shows the same sample, but with a 0.4 mag Gaussian magnitude error applied.

This pdf has its maximum at $f < 0$ and a long tail at $f > 0$. The larger σ_M is, the further the peak is displaced to the left of the origin, yet the more strongly positive the pdf's expectation value becomes.

In Fig. 7.4 we demonstrate an important consequence of this skewness of the pdf by scattering the distance moduli of 500 000 halo stars by a Gaussian that has a dispersion of 0.4 mag. The parameters of the halo model are the same as those used to generate Fig. 9.5. The red points show the true distribution of V velocities in the sample, while the green points show the distribution of V velocities that follow from the distance moduli. On account of the magnitude errors, more stars are placed at $V \simeq -v_c$ than at $v \simeq v_c$, and if one is unaware of the bias caused by unbiased errors in distance modulus, one would infer that the halo is in the mean counter-rotating. We will see in the following Chapter that this effect can have far-reaching complications for our understanding of Galactic structure.

Chapter 8

On the alleged duality of the Galactic halo[1]

8.1 Abstract

We examine the kinematics of the Galactic halo based on SDSS/SEGUE data by Carollo et al. We find that their claims of a counter-rotating halo are the result of substantial biases in distance estimates (of the order of 50 per cent): the claimed retrograde component, which makes up only a tiny fraction of the entire sample, prone to contaminations, is identified as the tail of distance overestimates. The strong overestimates also result in a lift in the vertical velocity component, which explains the large altitudes those objects were claimed to reach. Errors are worst for the lowest metallicity stars, which explains the metal-poor nature of the artificial component. We also argue that measurement errors were not properly accounted for and that the use of Gaussian fitting on intrinsically non-Gaussian Galactic components invokes the identification of components that are distorted or even artificial. Our evaluation of the data leads to a revision of the estimated velocity ellipsoids and does not yield any reliable evidence for a counter-rotating halo component. If a distinct counterrotating halo component exists it must be far weaker than claimed by Carollo et al. Finally we note that their revised analysis presented in Beers et al. does not alleviate our main concerns.

8.2 Introduction

Galactic haloes are an excellent testbed for cosmology and galactic dynamics. Their exploration can constrain the early assembly of galaxies as well as the dynamics of accretion of smaller galaxies. Our Milky Way offers an ideal case for those investigations, as we can directly obtain the detailed parameters like kinematics, elemental abundances and physical properties of single stars surrounding us. New material is still being accreted into the Galactic halo, as the numerous streams and newly discovered dwarf galaxies confirm (see e.g. Ibata et al., 1995; Klement et

---

[1] Content and text of this chapter have been published identically as Schönrich, Asplund & Casagrande (2011a). Minor editing has been applied.

al., 2006; Belokurov et al., 2007). As metallicity gradients go in lockstep with star formation, young accreted objects may be more metal-poor than old stars from the inner Galaxy and thus metallicity can not be simply used as a cosmic clock. This would also make it plausible that a later accreted halo component could indeed be on average younger and more metal poor than the older parts. The formation of at least parts of the halo by accretion (combined with later adiabatic contraction) could give rise to differences between early more turbulent accretion/collapse processes and later accretion, which might leave an imprint in differences between the inner and outer halo (see e.g. Cooper et al., 2010). Another possible source of discrepancies between inner and outer halo is dynamical friction, which could be more efficient for prograde than for retrograde infall (Quinn & Goodman, 1986; Byrd et al., 1986). This could give rise to a different rotational signature for accreted material in the outer Galactic halo compared to the inner regions (Murante et al., 2010).

Historically (and as well today), halo stars have been extremely difficult to identify, particularly in local samples, e.g. demonstrated by the historic argument between Oort and Strömberg (Oort, 1926; Strömberg, 1927). Like it is practically impossible to get a clean selection into thin and thick Galactic disc based on kinematics (Schönrich & Binney, 2009b), we face the analogous problem between thick disc and the prograde stars of the halo. Wrong assumptions about the kinematics of the Galactic disc will thus affect results on the halo component. Soon after the existence of the Galactic halo was established (Schwarzschild, 1952; Eggen et al., 1962), the central question was raised if the stars of the inner and the outer halo had the same properties or if gradients or even breaks in metallicities or kinematics existed with galactocentric radius. Two main strategies to identify and examine halo stars have been used in the past: either stars in the solar neighbourhood are studied, classified according to their kinematics and then conclusions about the structure further away are drawn by extrapolation (e.g. Sommer-Larsen & Zhen, 1990), or the surveys concentrate on bright objects in the outer halo regions, such as RR Lyrae variables or globular clusters (e.g. Sandage, 1970). The second alternative allows to directly map the spatial structure by those standard candles with good distance information (e.g. Saha, 1985). This strategy implies selection biases: for example the position and presence of RR Lyrae stars on the horizontal branch are correlated with metallicity and age, while it is not known if the formation of globular clusters is representative also for all halo field stars.

Claims of differences between the inner and outer Galactic halo are almost as old as the discovery of the halo itself. After van den Bergh (1967) discussed differences in metallicity and the second parameter between the haloes of the Milky Way and those of its neighbouring galaxies (M31, M33), Searle & Zinn (1978) found that Galactic clusters in the outer regions showed a larger scatter in the ratio of blue to red horizontal branch stars than inner halo globular clusters, which they interpreted as a signature of an age spread. Preston et al. (1991) found a similar difference in field BHB stars.[2] Differences in kinematics have also been suggested between inner and outer halo globular clusters (Zinn, 1993), although precision and reliability of estimates in this

---

[2] While it is clear that age is one parameter which will cause an older globular cluster to be bluer than a younger one at the same metallicity, whether this is the dominant cause of differences in horizontal branch morphology is still debated (see, for example, Dotter et al. (2010) and VandenBerg (2000) for opposing views.)

respect are limited by the small number of available globular clusters. Various claims of an asymmetry in the halo azimuthal velocity distribution with an extended tail to retrograde orbits have been made (e.g. Norris & Ryan, 1989). Majewski (1992) even found the entire halo to be on average counterrotating, could, however, not find any significant velocity gradient. Ryan (1992) pointed out that measurements of kinematics based on proper motions were particularly vulnerable to distance errors and showed that overestimated distances for halo stars can lead to false identifications of counter-rotating stars.

In this paper we will revisit the recent claim by Carollo et al. (2007) (hereafter C07) and Carollo et al. (2010) (hereafter C10) that the Galactic halo consists of two components: a more metal-poor counterrotating component with larger scaleheights, distinct from a slightly prograde component and starts dominating the halo at high altitudes in their analysis.[3] In particular we will carefully re-examine their distance estimation procedure; we will focus on C10 as this paper deviates from its precursor mostly by the larger sample size. To avoid relying on any of the uncertain available distance calibrations, we apply in parallel both the C10 distances and two native SDSS main sequence distance calibrations, checking results additionally with an isochrone method. In Section 8.3 we outline those methods, discuss the SDSS/SEGUE data used for this purpose and describe how the sample cleaning was performed.

Thereafter (Section 8.4) we discuss the underlying assumptions and the reliability of gravity estimates used to sort stars into different sequences as well as the actual assumptions for absolute magnitudes by C07 and C10. We will show that their claim to have distances precise to $10 - 20\%$ is unsupported and that the C10 sample contains a class of stars with significant distance overestimates by being sorted into unphysical positions in the colour magnitude diagram. In Section 8.5 we present statistical proofs of distance biases in the sample and in Section 8.6 we discuss the implications of different distance schemes on kinematics and the inner-outer halo dissection.

8.3   The calibration sample of SDSS and the Carollo dataset

All the data used in this paper come from the Sloan Digital Sky Survey (SDSS, York et al., 2000), and consist of spectroscopic observations of stars from both SDSS-I and II and from the SDSS-II/SEGUE survey (Yanny et al., 2009). Stellar parameters for the stars were estimated using the SEGUE Stellar Parameters Pipeline (SSPP, Lee et al., 2008a,b; Allende Prieto et al., 2008).

---

[3] This dominance of a retrograde component in the outer halo has recently been contested by Deason et al. (2010) although they find a retrograde motion for metal-poor ([Fe/H] < -2) and prograde ([Fe/H] > -2) for metal-rich stars using a BHB sample in the outer Galactic halo. In our view, this issue needs to be further investigated, as they assume constant g band magnitudes for the horizontal branch in a region affected by the blue tail, which spans of order $2\,\mathrm{mag}$ in g band luminosity. If a considerable fraction of the halo giants is in the blue tail, their colour and temperature cuts remove a large part of this tail, but still leave *BHB* members spanning ~ 0.7 magnitudes, as we tested it on SDSS photometry of metal-poor globular clusters known to have such a strong blue tail ($M3$, $M13$, $M15$ and $M92$) and the BASTI isochrones.

For this study we use the calibration star sample from SDSS public data release 7 (DR7).[4] As the colour transformations and distances used in C07 and C10 are not part of the public data releases, we draw this information from the sample used by C10, which is a cleaned version of DR7 and which was kindly provided on our request.

The calibration star sample comprises two datasets, namely the photometric calibration star sample and the reddening calibration star sample. Querying the DR7 catalogue for these stars produces a total of 42841 entries, but many refer to identical objects, so that the actual number of unique objects in the database is 33023. The interested reader is referred to Section 8.9 where we describe how the cleaning of the sample from questionable objects has been performed that cuts down the sample to 28844 stars.

Throughout the paper we make use of two different classes of distance determinations (see Section 8.9 for details): On the one hand the distances used by C07 and C10 and on the other hand two derivations adopted from Ivezic et al. (2008). When using the distances by C07 and C10 we examine the effects of their different sequences by both using their entire sample ("Carollo all") and using exclusively their dwarf stars ("Carollo dwarfs"). For the native SDSS calibrations we restrict ourselves to the dwarf stars, imposing in general a gravity limit of $log(g) > 4.1$ to reduce the impact of giant and subgiant contamination). We there use two different schemes: An adopted main sequence derivation, where we increase distances defined via their Eq. (A2) and (A3) by accounting for alpha enhancement and additionally decreasing the adopted absolute magnitudes of all stars by 0.1 mag, hereafter termed the adopted main sequence calibration, short "IvzMS"). Second the calibration favoured by Ivezic et al. (2008) using Eq. (A7) from their appendix, which is steepened towards the isochrones in order to account for age dependent effects, hereafter called the age dependent calibration (short: "IvzA7"). We would like to point out that we believe neither distance calibration to deliver the full truth, yet they are currently the most commonly used schemes and can give hints on the intrinsic uncertainties of all methods. To have an additional test we cross-checked and confirmed our findings with distances derived directly from using 12.5 Gyr BASTI isochrones (Pietrinferni et al., 2004, 2006); some details are provided in the Section 8.9.

C10 applied two different geometric cuts. The first was a distance cut at an estimated distance of 4 kpc, limiting the errors on velocities caused by proper motion errors. The second was a cut that removed stars differing from the Sun by more than 1.5 kpc in galactocentric radius (i.e. outside 7.0 kpc $\leq R_G \leq 10$ kpc with their value of $R_\odot = 8.5$ kpc for the Sun). The latter cut was reasoned in C10 by the use of their applied orbit model, which was adopted from Chiba & Beers (2000) using a Stäckel-type potential from Sommer-Larsen & Zhen (1990). As we do not make use of this orbit calculation, in this work we do not apply the second cut, which removes of order one third of the available stars.

Due to the magnitude ranges in the SEGUE survey the distance cuts imposed by C10 and C07 remove almost all giants from the sample, a minor fraction of subgiants and very few dwarf stars. The effects of both selections depend strongly on the adopted distances and thus the absolute

---

[4] http://casjobs.sdss.org/dr7/en/
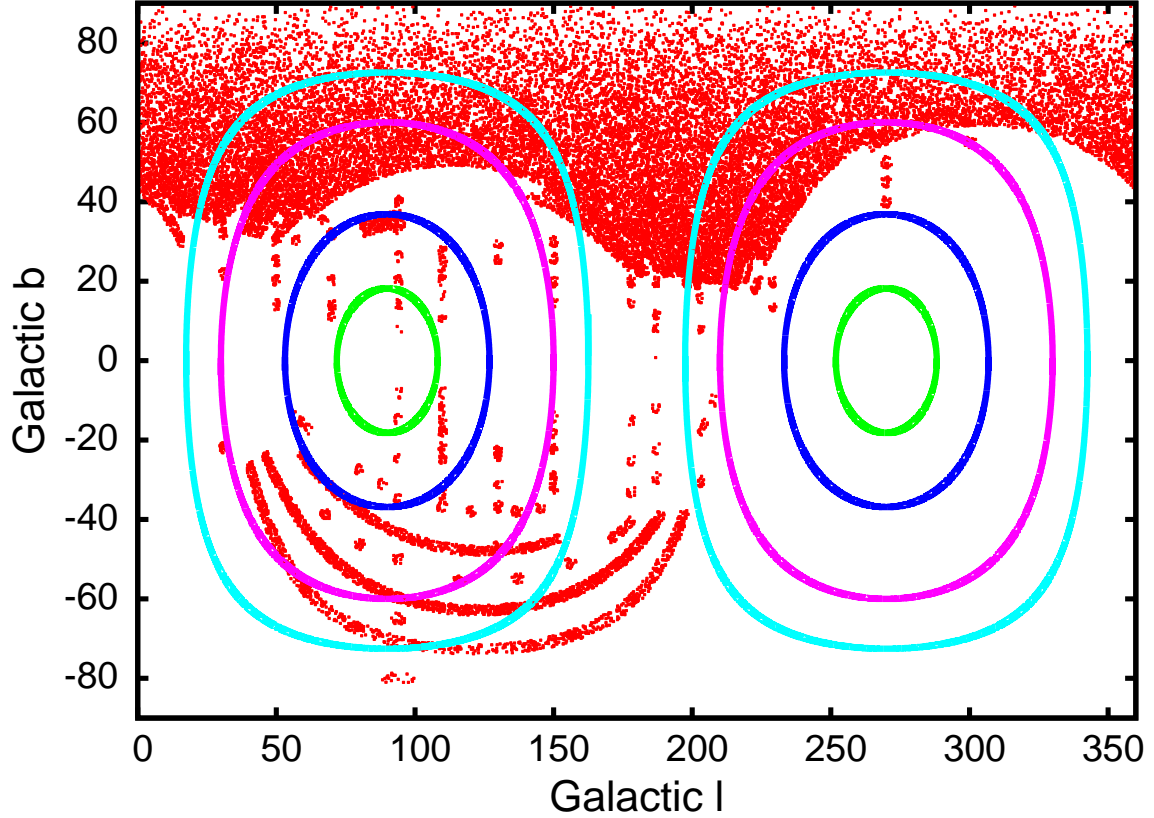
Figure 8.1: The distribution of all reliable stars in the calibration sample, fulfilling the temperature range limit and with acceptable kinematic information. To demonstrate the weak line-of-sight motion support of azimuthal velocities we plot the 0.95 (innermost lenses, green), 0.8, 0.5 and 0.3 (outermost lenses, light blue), contours of the angle term η_V in Eq.(8.7) that quantifies the relative support by the direct line-of-sight velocity measurements. This demonstrates the vulnerability of V velocities in this sample to distance errors as they cannot be found directly from line of sight velocities.

magnitudes of the stars. Applying the C10 distances to the sample, 21600 stars remain within the distance limit of 4 kpc, of which 14763 have surface gravities $\log(g) > 4.0$ and are thus classified as dwarf stars. With the adopted main sequence calibration 15808 stars with $\log(g) > 4.0$ are found in the sample, which gives a first hint to the more stretched distance scale by C10.

Metallicities are taken from the DR7 pipeline adopted values (Lee et al., 2008a,b). For a discussion of the different metallicity scales of DR7 and C10 the reader is referred to the Section 8.9. There we also describe in more detail how kinematics are derived from distances, radial velocities and proper motions.

8.4 Assessing the distance calibrations

The core assumptions in C10 are those about stellar distances. They claim that by using the log(g) estimates from the SEGUE stellar parameter pipeline stars can be reliably sorted into clean sequences, i.e. main sequence, turn-off and subgiant/giant. The attraction of this idea, laid out in Beers et al. (2000), is that it seems to reduce the distance errors to simple uncertainties in colour and metallicity on well-determined sequences. However, as we will see below, things are more complicated.

8.4.1 Effects of distance errors

Selecting a star into the wrong position in the colour-magnitude diagram results in a faulty estimate of its absolute magnitude and thus an erroneous distance. As they are the most common population we would naively expect the largest contamination to be main sequence stars mistakenly addressed as turn-off stars. These will be assumed to be far brighter than they are, hence their distance will be overestimated, bringing many of them, especially halo stars, falsely into the retrograde tail of the velocity distribution. This effect happens via the translation of proper motions into velocities and thus prevails for samples that have low support by radial velocities (cf. Section 8.9.1 of Section 8.9). Fig. 8.1 depicts the locations of stars (red dots) in Galactic longitude (x-axis) and latitude (y-axis). The SDSS/SEGUE sample is (due to the location of the telescope in the northern hemisphere and the strategy to avoid the high extinction in the Galactic plane) largely concentrated away from the plane and towards the Galactic North Pole. Consequently it has almost no points at directions that would have high support of azimuthal velocities by the direct line-of-sight velocity measurements. The contours in the plot encircle the regions of high line-of-sight velocity support of V_h in the sky.[5] Within the ellipses, the fraction η_V (Eq.(8.7) in Section 8.9) of the line-of-sight velocity going into the heliocentric azimuthal velocity V_h is larger than 0.95 (smallest lenses), 0.8, 0.5 and 0.3 (largest lenses). They demonstrate how heavily any analysis of the azimuthal velocities has to rely on the transverse velocity component and thus proper motions and distance estimates.

The effect of distance errors in this process is easily understood: Think of driving a car past a field that has a rabbit sitting on it. As the speed of the car is known, the fact that the rabbit rests on the lawn can be derived by the car driver from its apparent angular speed - if the distance is right. If the natural size of the rabbit is overestimated, so will be its distance and to explain its angular motion one wrongly infers that it moves opposite to the car's direction of motion. And vice versa a distance underestimate drags the estimated rabbit velocity towards that of the car, i.e. it is wrongly inferred that the rabbit moves in the same direction as the car does. As the Sun moves with a velocity of more than $200\,\mathrm{km\,s^{-1}}$ around the Galactic centre, for this sample a 10% distance overestimate implies that an average halo star in the sample will be wrongly pushed

---

[5] Throughout the paper we distinguish between the velocities in the solar rest frame and coordinate system (U_h, V_h, W_h) and velocities in the Galactic rest frame and Galactic cylindric coordinate system (U, V, W). For a short discussion of those we refer to Section 8.9.
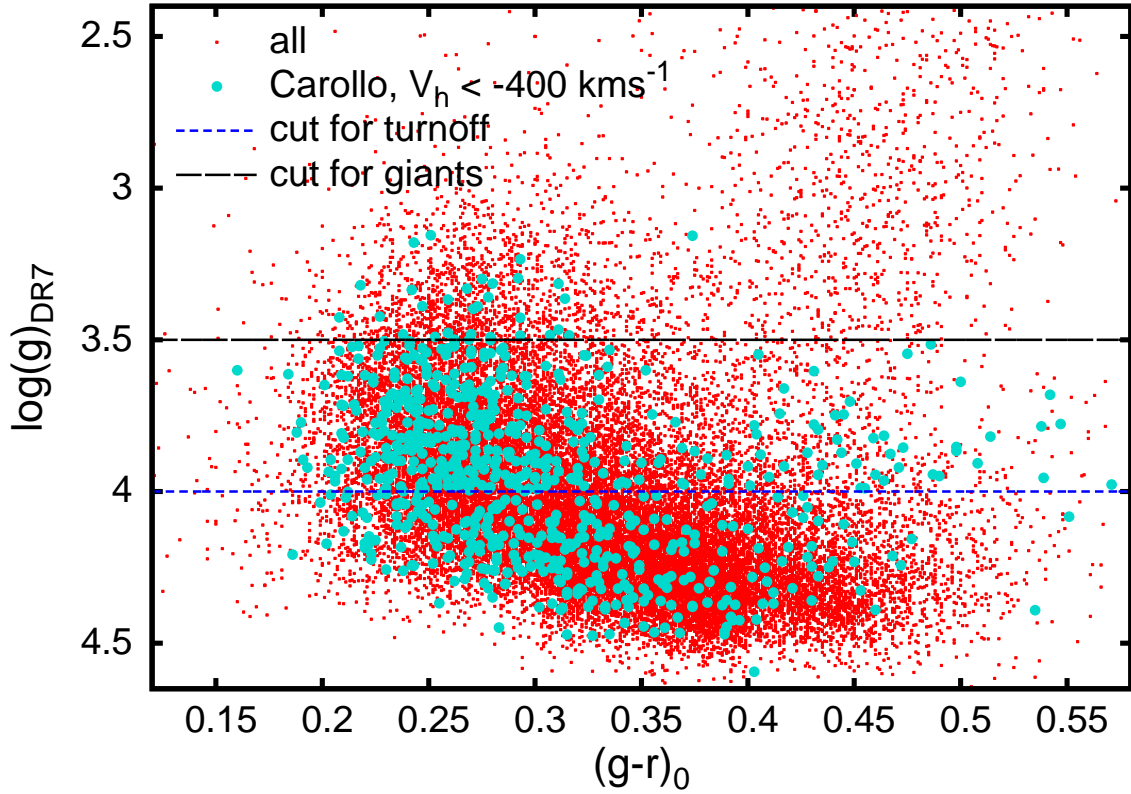
Figure 8.2: The distribution of the "well behaved" stars in the calibration sample (red crosses, without distance cut to make the giants visible) in the dereddened colour-gravity (DR7 pipeline) plane. Horizontal lines mark the cuts adopted by Carollo et al. between the dwarf, turn-off and subgiant/giant regions. Stars that have likely membership in their counter-rotating halo, i.e. with $V_h < -400 \, \mathrm{km \, s^{-1}}$ and fulfilling $d < 4 \, \mathrm{kpc}$ are marked with blue points.

by $\sim 20 \, \mathrm{km \, s^{-1}}$ into retrograde motion, and a larger distance error will entail a proportionately larger retrograde motion.

It should also be mentioned that azimuthal velocities are subject to an error similar to the Lutz-Kelker (1973) bias: Even if there is no net bias on estimated absolute magnitudes and thus of distances, a symmetric magnitude error distribution will cause an asymmetric distribution of estimated distances with a longer tail in the overestimates. As these directly translate to the transverse velocities one will with any magnitude based distance scheme encounter asymmetric velocity errors that give rise to an extended counterrotating tail in the measured halo azimuthal velocity distribution. This may also be related to the asymmetry found by Norris & Ryan (1989).

8.4.2 Gravities

Fig. 8.2 shows the positions of all cleaned sample stars in the colour - log(g) plane (red points). The horizontal lines show the selection regions in log(g) used by C10. Stars with log(g) > 4.0 are classified as main sequence stars. Those with log(g) < 3.5 are assumed to be subgiants or giants, while the intermediate objects are classified into their "turn-off" branch. The blue dots mark the objects in the C10 sample that have heliocentric azimuthal velocities, V_h, smaller than $-400 \, \mathrm{km \, s^{-1}}$, i.e. they are on highly retrograde orbits and should be in the majority counter-rotating halo objects according to C10. There can be minor differences between the gravities directly from DR7 and their sample, as we we use the best determined values when their are double or multiple entries for a star, while their log(g) values (which we do not have access to) are probably averaged.

The plot reveals one crucial problem with those criteria: although it may be expected that some distinct branches of stars are present, they are not reflected by the SEGUE measurements. While the upper giant branch is apparent, we cannot make out a substantial decrease of densities between the main sequence and subgiant regions. Measurement errors prevail, especially in the turn-off region, and veto against a clean selection of the components.

One possibility is that the measurement errors on log(g) are so large that it is not possible to use the log(g) measurements to classify stars into these three categories. Also the true main sequence is inclined in gravity versus colour. In this perspective the constant (colour and metallicity independent) gravity cuts applied by C07 and C10 do not appear well founded. If one aims to select a pure dwarf sample, the tightening of the constant cut relative to the inclined main sequence, is, however, beneficial in reducing the turn-off-contamination.

The accuracy of the DR7 log(g) values is discussed by Lee et al. (2008b), who show estimated surface gravities for open and globular cluster stars observed by SEGUE for the purpose of calibration of the survey. As demonstrated by Lee et al. (2008b) (see their Fig. 15 ff.) the low spectral resolution results in a significant scatter in log(g) values: some turn-off stars have log(g) < 3.5, and significant numbers of stars with log(g) measurements in the region assigned by Carollo et al. to the turn-off (3.5 < log(g) < 4) are clearly either subgiants or main sequence stars. Thus we have to expect a significant number of main sequence objects in the turn-off band of the Carollo et al. (2007, 2010) samples.

The consequent bias in distance estimation discussed above will give an artificially enhanced fraction of retrograde halo stars residing in the turn-off/subgiant regime. Although Fig. 8.2 should play this effect down with the red points being drawn from the main sample without distance cuts (to keep the red giant branch visible), while the blue circles satisfy $d < 4 \, \mathrm{kpc}$ in addition to the velocity cut, this crowding of the counterrotating halo stars into the designated turn-off region is still prominent. The distance cut is responsible for the missing enhancement in the giants.

Carollo et al. also find that their outer counterrotating halo members display significantly lower metallicities than the average of the inner halo. Could this be related to problems with distance estimation as well? It would not be unreasonable to expect the accuracy of the log(g) estimates

to decrease for the stars of lowest metallicity, increasing by this the fraction of fake turn-off stars and subgiants, since the stellar lines become weaker. In fact, Ma et al. (in prep.) find this effect. A better understanding of why the "counter-rotating" component of Carollo et al. has lower metallicity can be achieved from Fig. 8.3. In its top panel we plot the gravities against the metallicity, again with red points for the entire sample and with blue circles for the strongly retrograde stars. Stars with lower metallicities in the sample get on average assigned lower gravities. This could arise from the fact that determining gravities gets more difficult on the lowest metallicity side. The inclination of the sample in the metallicity-gravity plane favours distance overestimates for metal poor stars, thus lowering the average metallicity of the "counter-rotating" component. This shift in classification of stars is demonstrated in the middle panel of Fig. 8.3: Almost all identified subgiants are metal-poor, while the average metallicity rises towards the higher surface gravity categories. The bottom panel shows the ratio of the number of turn-off to main sequence stars, ρ, against metallicity. One might argue that the pronounced rise of ρ towards lower metallicities be caused by the intrinsic rarity of metal-poor objects. As the sample is dominated by magnitude cuts, the different ratios could, however, just be explained by different geometry of the subpopulations, which indeed puts stars with higher scaleheights (e.g. halo) to more remote positions than those with low scaleheights (e.g. disc). Since the C10 sample extends by definition less than 4 kpc away from the plane it is hardly possible to explain how ρ can rise by a factor of ~ 3 from $[Fe/H]_{DR7} \sim -1.5$ to $[Fe/H]_{DR7} \sim -2.5$ as the large scaleheight of the halo should veto against relative density variations of the halo populations by this amount.
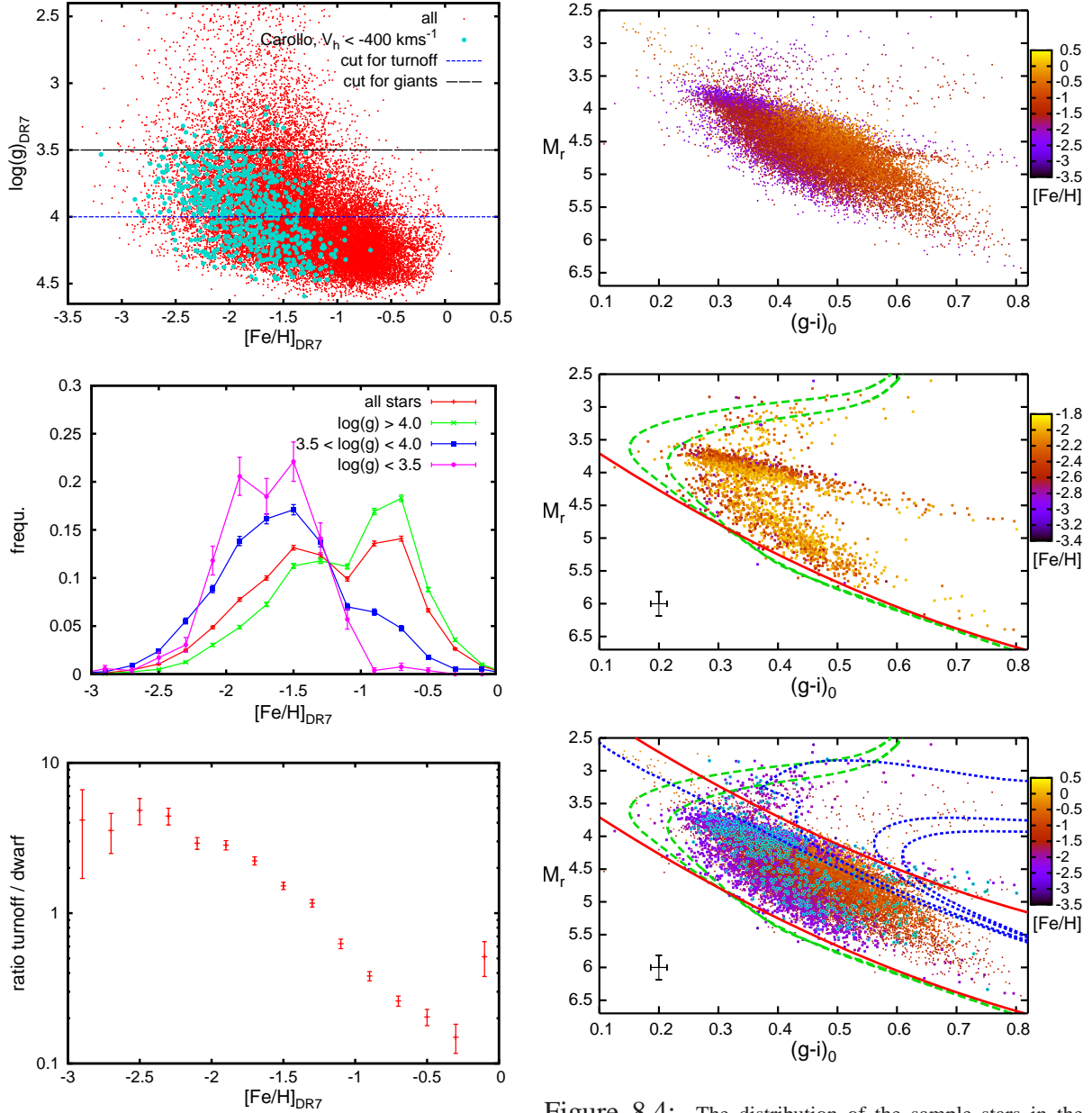
Figure 8.3: Top panel: The distribution of the cleaned "all star" sample in the metallicity- surface gravity plane. Horizontal lines mark the cuts adopted by Carollo et al. between the dwarf, "turn-off" and subgiant/giant regions. Stars in the C10 subsample displaying a clear membership to what might be a counter-rotating halo, i.e. with $V_h < -400.0\,\mathrm{km\,s^{-1}}$ are marked with blue points. Middle: Metallicity distributions for the different gravity classes used by Carollo et al., showing how low metallicies dominate the "turn-off" and "subgiant" stars. Bottom panel: Ratio of identified "turn-off" stars to dwarf stars as function of $[Fe/H]_{DR7}$ using the gravity cuts by Carollo et al. Even between $[Fe/H]_{DR7} \sim -1.5$ and $[Fe/H]_{DR7} \sim -2.5$ there is a strong uptrend.
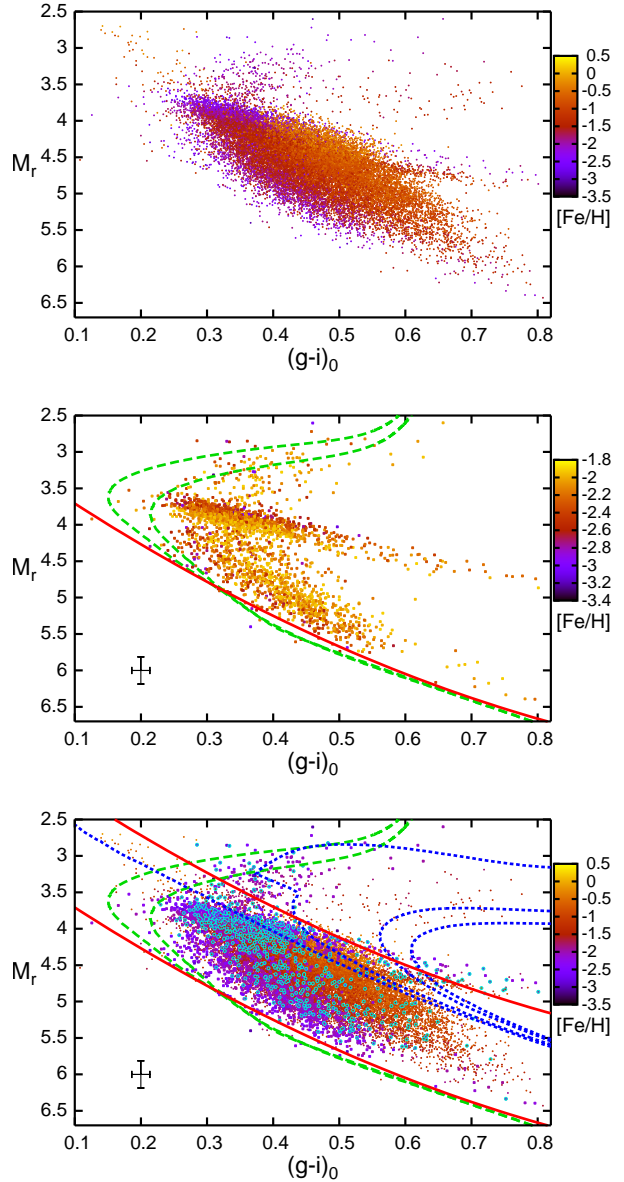
Figure 8.4: The distribution of the sample stars in the $(g-i)_0, M_r$ plane with tiny crosses. Colours give the metallicity $[Fe/H]_{Car}$ according to the colour bar on the right. The top panel contains all stars in the C10 sample that pass our quality cuts, while the middle panel exclusively contains stars with $[Fe/H]_{DR7} < -1.9$. For comparison we give the BASTI (Pietrinferni et al. 2004, 2006) alpha enhanced isochrones at $[Fe/H] = -2.14$ of ages 10 and 12.5 Gyrs (green lines) and the Ivezić et al.(2008) absolute magnitude calibration at the same iron abundance (red line). In the bottom panel the metal-poor stars have been enhanced in size and stars with $V_h < -400\,\mathrm{km\,s^{-1}}$ derived with C10 distances are marked by light blue circles. Red lines show the adopted main sequence calibration (IvzMS) at $[Fe/H] = -2.14$ and $[Fe/H] = 0$. Dark blue lines show the BASTI isochrones at solar metallicities for 1, 4, 10 and 12.5 Gyrs, green lines same as in the middle panel. The crosses mark the typical photometric errors and uncertainties in the isochrones.

8.4.3   Absolute magnitudes

Having discussed the surface gravity estimates it is time to turn towards the actual assumptions on absolute magnitudes of stars from which the distances are inferred. The claim by C10 to reach an accuracy of "$10-20\%$" in distance estimates is predicated on the ability to cleanly select stars according to their spectroscopically determined gravity into several branches. If such a selection was feasible, it would indeed limit the uncertainties to those caused by metallicity, reddening and photometric errors. The reader should bear in mind that the low relative density of the outer halo component found by Carollo et al. implies that even a contamination on the 1% level (i.e. 200 out of ~ 20000 stars) can alter the results.

The sorting into different branches via the formalism of Beers et al. (2000) can be seen in the top panel of Fig. 8.4. The plot shows all stars in the C10 sample in the $(g-i)_0, M_r$ plane that do not have warning flags. The absolute magnitudes were derived directly from the C10 distances using the distance modulus via

$$M_r = r_0 - 5\log_{10}(\frac{d_{Car}}{0.01\,\text{kpc}}) \tag{8.1}$$

where M_r is the derived absolute magnitude, r_0 is the reddening corrected apparent magnitude from the DR7 database and d_{Car} the distance given by Carollo et al. and derived from the Beers et al. (2000) sequences.

The three branches, into which the sample stars are selected, can be identified in the figure. Lower metallicity stars are brighter and bluer, but the latter shift dominates. Thus the main sequence gets fainter at the same colour. As the metallicity spread of especially the main sequence in the top panel of Fig. 8.4 partially obscures the underlying sequences, we restricted the sample to $[Fe/H]_{DR7} < -1.9$ in the middle panel. For comparison we plot the adopted main sequence calibration at $[Fe/H] \sim -2.14$ and the alpha enhanced Basti isochrones (Pietrinferni et al., 2004, 2006) for SDSS colours (cf. Marconi et al., 2006) at $[Fe/H] = -2.14$ at ages 10 and 12.5 Gyrs. The main sequence and the giant branch are apparent and between them lies a strong sequence sloping down from $(0.2, 3.8)$ to about $(0.8, 4.8)$. The stars in this band are termed turn-off stars by Carollo et al. as they comprise everything that has gravities $3.5 < \log(g) < 4$. As we can see from the bottom panel, this artificial turn-off sequence comprises the majority of heavily counter-rotating stars (green dots). The reader might ask why we do not see a large number of stars as false identifications in the brightest subgiant branch. As already discussed above the absolute magnitude difference to those stars is, however, so large that by the distance limits most stars sorted into the subgiant and giant branches will be dropped from the sample, as they are deemed to be more than 4 kpc away. This conclusion is verified by the subgiant branch getting much more populated when the distance cut is removed (cf. Fig 2).

In stellar evolution there exists no unique turn-off branch. Instead there is just a region where stars leave the main sequence and move up to the subgiant branch, and which depends on metallicity and age of the population. Thus the artificial sequence we face here can only be thought of as a compromise for stars in the broad region between main sequence and subgiant branch that intends to describe the average luminosity of these objects. In this perspective, the claim
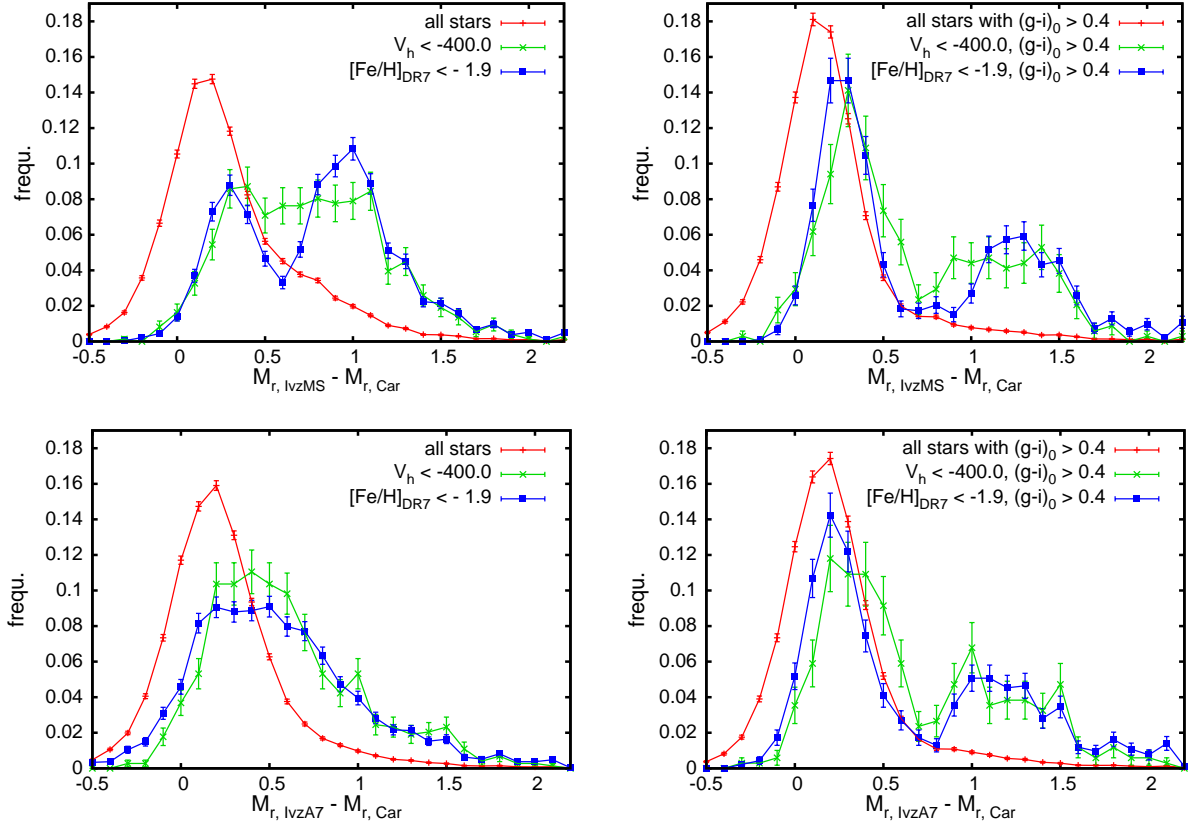
Figure 8.5: The distribution of absolute magnitude differences between the Carollo et al. calibration and the other metallicity-dependent colour-magnitude calibrations. In the top row we show the results for the adopted main sequence calibration ("IvzMS"), while in the bottom row we compare to the age-dependent calibration by Ivezić et al. (2008) ("IvzA7"). On the left we show the entire colour range, while we plot only redder objects with $(g - i)_0 > 0.4$ on the right. In the entire sample (red bars) the main sequence by Carollo et al. is brighter by ~ 0.15 mag than in the native SDSS calibrations. The offset gets larger for the counter-rotating (green crosses) and metal-poor (blue squares) stars; note that the Carollo et al. turn-off sequence is very prominent with an offset of about 1 magnitude.

by Carollo et al. to achieve $10 - 20\%$ accuracy in distances is ruled out in this transition region as it intrinsically spans more than one magnitude (at fixed metallicity and colour), i.e a distance uncertainty of more than 50%. Because this "turn-off" branch is constructed to be a compromise between subgiants and main sequence, the gap between the subgiant branch (moving up towards lower metallicity) and the main sequence (moving down, as the colour effect dominates) widens with decreasing metallicity. This aggravates the effects of misassignments on estimated distances for lower metallicity objects.

The worst problem with the "turn-off" stars appears in comparison with stellar models. Com-

parison of the adopted positions of metal-poor stars in the colour-magnitude diagram with the isochrones at 10 and 12.5 Gyrs reveals that most objects in the artificial "turn-off" branch reside on the red side of the low metallicity turn-off region. Some of the selected "turn-off" stars are even on the red side of what could be achieved at solar metallicity. In fact the overwhelming majority of strongly retrograde stars is actually claimed to be in a region where according to our knowledge of astrophysics no star of reasonable ages can reside.

8.4.4   Colour transformation and main sequence comparison

It should be mentioned that the distances used in C07 and C10 were derived using the $B - V$ colour calibration and thus the colour transformation of Lee et al. (2008a) had to be performed to apply them to SDSS colours. Fortunately there are now good isochrones (e.g. BASTI isochrones, Pietrinferni et al., 2004), fiducials (An et al., 2008) and photometry in SDSS colours readily available, making such a colour transformation to translate SDSS colours to the former $B - V$ calibration by Beers et al. (2000) unnecessary. The colour transformation may explain some of the scatter and systematic shifts presented in Fig. 8.5 that shows the comparisons of the absolute magnitudes from C10 to the native SDSS calibrations. The latter is depicted by red lines in Fig. 8.4 at [Fe/H] $= -2.14$ and [Fe/H] $= 0$. Both isochrones and the two main sequence approximations are fainter than the adopted C10 absolute magnitudes, especially at lower metallicities. This can be seen from the middle panel of Fig. 8.4 and from Fig. 8.5, which depicts the distribution of differences in absolute magnitudes of C10 towards those derived via the adopted main sequence calibration (top panels) and those derived via the Ivezic et al. (2008) age-dependent relation (bottom panels) for all stars (red), metal poor objects with [Fe/H] < -1.9 (blue) and for the "counter-rotating" stars with $V_h < -400\,\mathrm{km\,s^{-1}}$ (green crosses and errorbars). Errorbars depict the Poisson noise. On the right side of Fig. 8.5 we show the same quantities, but exclusively for redder stars with $(g - i)_0 > 0.4$ where the sequences of Beers et al. (2000) have a larger separation, and which also excludes the expected turn-off region (cf. the isochrones in Fig. 8.4) for the very metal-poor stars. Apart from the observational scatter, the peaks arising from the main sequence $\Delta_M \sim 0.3$ and from the "turn-off branch" around $\Delta_M \sim 1.0$ are washed out for the whole population, as the sequences shift with metallicity and the main sequence dominates. However, the generally higher intrinsic brightness under the Carollo et al. assumptions is clearly seen in both distance descriptions. On the blue end the age-dependent formulation by Ivezic et al. (2008) is a bit brighter than the adopted main sequence calibration and makes the peak of the "turn-off sequence" in the metal poor and counterrotating subsamples of C10 merge with the main sequence at blue colours, yet the large offset remains.

For stars that are claimed by C10 to have heliocentric velocities $V_h < -400\,\mathrm{km\,s^{-1}}$ and thus make up the bulk of what they identify as a counter-rotating halo the two peaks of main sequence and turn-off stars are separated, as the metallicities of these stars are more narrowly distributed . For comparison we show the result of selecting only stars that have $[Fe/H]_{DR7} < -1.9$ (blue squares in Fig. 8.5). These distributions look very similar apart from the counter-rotating stars being more inclined to the bright side. Also regard the increased importance of the turn-off band for
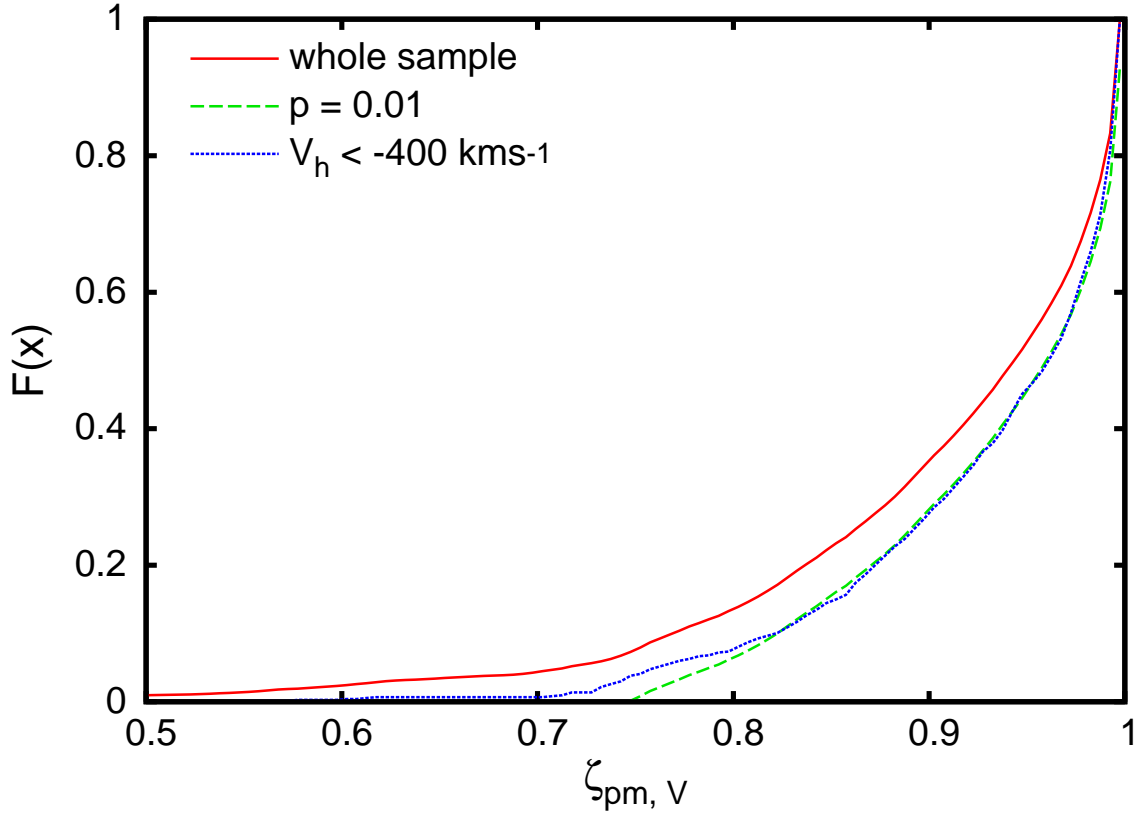
Figure 8.6: The cumulative distribution of stars on the part of V_h that is covered by proper motions and not radial velocity measurements. The stars with $V_h < -400\,\mathrm{km\,s^{-1}}$ are drawn with a purple line while the overall sample distribution is drawn with a red line. Beneath is the 0.01 significance level of a Kolmogorov-Smirnov test.

those populations.

In summary there are two main drivers of overestimated distances in Carollo et al. compared to the native SDSS distance calibrations: The main sequence of C10 for metal-poor stars is brighter than in the other calibrations and the number of stars in the turn-off and subgiant/giant branches is increased by a large factor for metal-poor stars; most of the designated "turn-off" stars by C10 reside in positions in the colour-magnitude plane that would require unreasonable ages. We thus conjecture that the "counter-rotating" halo as presented by C10 is due to distance uncertainties and the selection of stars into unphysical stellar branches an artifact.

8.5   Signatures of misselection

8.5.1   Geometric distribution anomaly

Even if the biases in distance assignments were not obvious there are still ways to detect them. As erroneous distance estimates mostly act on the part of motion perpendicular to the line of sight, populations with distance errors will be preferentially found in regions of the sky perpendicular to the velocity component in question, or in other words, if stars end up in one component by misselection this should should show up as a bias in sample geometry. Such a bias will not be aligned directly with the Galactic coordinates, but with the part of the biased velocity component covered by proper motion. This is obvious as the largest errors should happen where the uncertainty in the motion is largest, i.e. where the proper motion and distance estimates have the largest impact. For these statistics we make use of the squared angle terms connecting the proper motion to the azimuthal velocity (from now called the "proper motion partition"). We take from eq.(8.6) in Section 8.9 the angle terms that connect V_h to the proper motions $\dot{l}$ and $\dot{b}$, square them and add them together:

$$\zeta_{pm,V} = \sin^2(l)\sin^2(b) + \cos^2(l). \tag{8.2}$$

Fig. 8.6 shows the cumulative distribution of stars over the proper motion partition for V_h (red line). The C10 sample is (as the entire SEGUE survey) concentrated towards positions where the azimuthal velocity is mostly covered by proper motions as it is mostly oriented towards high Galactic latitudes. Yet the counter-rotating subsample (purple line) is even more concentrated towards the high proper motion contributions. The average value for $\zeta_{pm,V}$ rises from 0.909 for all stars to 0.933 for the subsample with $V_h < -400.0$. In other words, the fraction covered by robust radial velocities drops from 0.091 to 0.067. In a Kolmogorov-Smirnov test the probability for equality of the two distributions is well below the 1% level and thus equality is strongly rejected. Again the high values for $\zeta_{pm,V}$ show how vulnerable the sample azimuthal velocities are to any distance errors.

This is of course not a proof of the bias, but a strong indication. Against this argumentation one could raise the objection that stars at low metallicities are located more polewards, as the halo to disc ratio in the sample rises (higher altitudes are reached) and so metal-poor / halo stars show a different spatial distribution. Indeed for lower metallicities the sample distribution shifts polewards reducing the difference, which remains present in all cases, but can become insignificant due to the shrinking sample numbers.

8.5.2   Linear error analysis and velocity crossterms

A robust approach to prove and quantify the distance errors is presented in Fig. 8.7, which shows the W_h velocities against $\sin(l)\sin(b)\cos(b)$ for all stars that should be part of the counter-rotating halo, i.e. have $V_h < -400\,\mathrm{km\,s^{-1}}$. The strong uptrend cannot be any stream, which would show up as a narrower band. It appears that the entire halo experiences a lift in W velocity, which
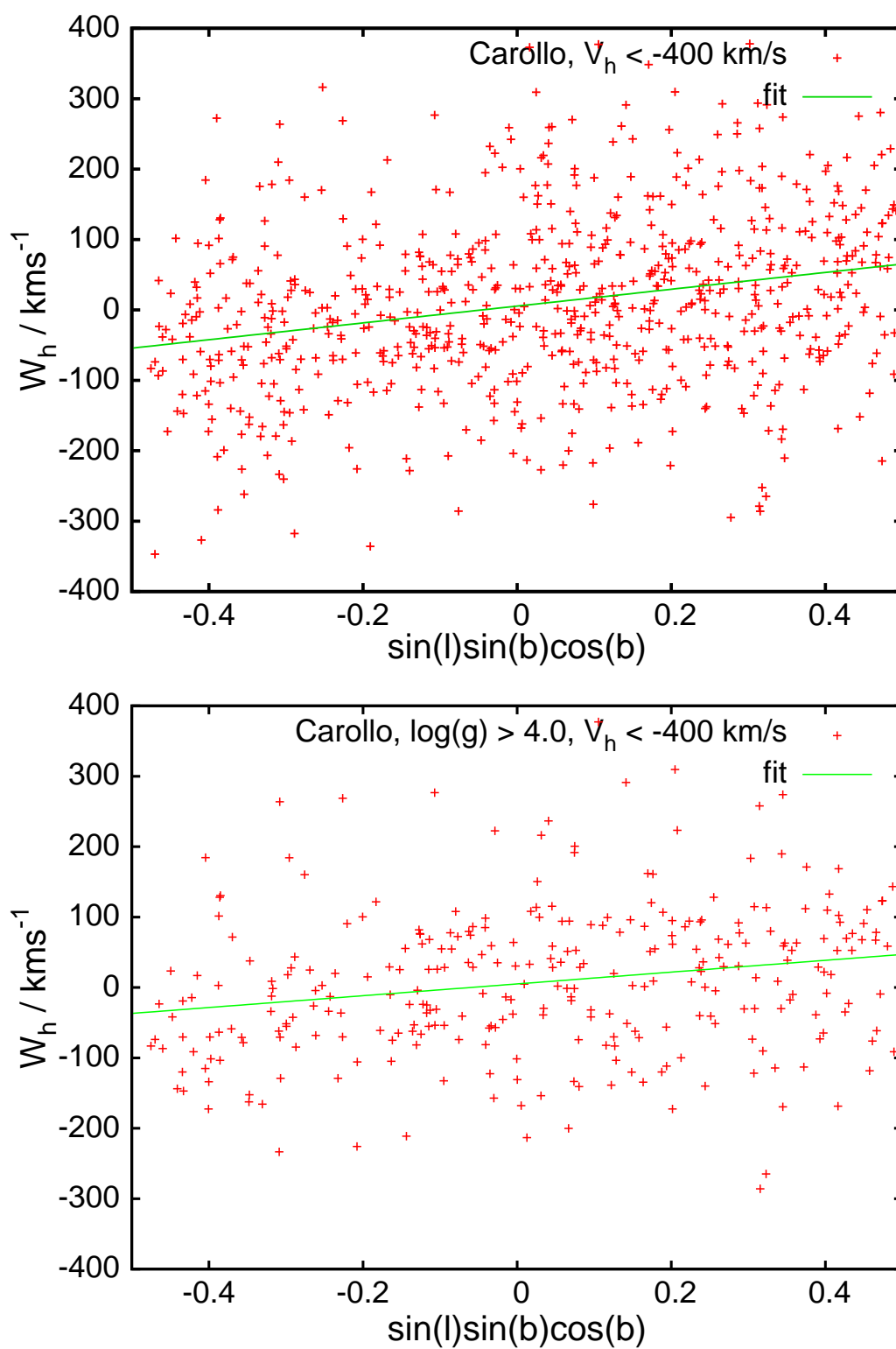
Figure 8.7: The counter-rotating stars display an intense trend in average W_h velocity over the angle combination that describes the connection of the azimuthal and vertical velocity components via distance errors.

has its origin in the distance errors of the C10 analysis. By wrongly assessing distances the relative motion of stars in the azimuthal direction mixes over the proper motions into the vertical component depending on this angle term. To illustrate this effect think of a star that is seen at $b = 45^o$, $l = 90^o$ and has $U_h = 0$, $V_h = -500\,\mathrm{km\,s^{-1}}$, $W_h = 0$. Due to the geometry of the setup the star will have a significant proper motion in b. With a wrong distance estimate the relative impact of line-of-sight velocity and proper motion changes and the star is assigned a non-zero W velocity. A more detailed description is found in Schönrich et al. (in prep.). The fitting line has a slope of $119.5 \pm 16.5\,\mathrm{km\,s^{-1}}$, i.e. the trend is significant at a level of more than 7σ. We can thus state that a significant distance error that is expected from the discussions above is here quantitatively demonstrated. Since the alleged counterrotating halo stars in this subsample (with a cut at $V_h < -400\,\mathrm{km\,s^{-1}}$) have on average $\overline{V_h} \sim -470\,\mathrm{km\,s^{-1}}$, we arrive at a distance bias of roughly 40% for the counter-rotating stars, which translates into a magnitude error of around 0.7 mag. It should be mentioned that errors might even be higher: Selecting more strongly retrograde stars the trend estimate gets even higher.

Restricting the sample of stars with $V_h < -400\,\mathrm{km\,s^{-1}}$ further to dwarfs ($\log(g) > 4.0$) and thus removing the largest identified source of distance errors, the numbers of stars in the sample drop by the selection dramatically from 735 stars to 299. The removal of the low gravity stars also gives fewer outliers in the velocity distribution. Only one object has $|W| > 400\,\mathrm{km\,s^{-1}}$. The lower panel of Fig. 8.7 shows the remaining stars together with an equivalent linear fit. Again the trend is highly significant, though now more moderate with $83.8 \pm 22.5\,\mathrm{km\,s^{-1}}$. The σ_W in the sample is already down from $129\,\mathrm{km\,s^{-1}}$ to $110\,\mathrm{km\,s^{-1}}$. The more moderate trend corresponds to an error of about 25%. It also fits well into the picture that the distance overestimate for the full sample is larger than for the dwarfs, when we remove the spurious "turn-off" branch. This bias has the effect that the distance overestimates do not only increase the W velocity directly, but also give rise to an additional contribution to the W velocity dispersion by turning a part of the large heliocentric azimuthal motion of halo stars into a fake vertical term. We will call this behaviour "velocity crossovers". This effect is even more important in the original analysis by C07 and C10, as they restrict their sample in galactocentric radius, thus increasing the weight around $l = 90°$ and $l = 270°$, where $\sin(l)$ is largest.

8.6 Velocity distribution

How do the described biases and different distance derivations affect the velocity distribution and what might remain of the alleged counter-rotating component halo when we reduce the distance biases that spuriously inflate it? Fig. 8.8 shows the velocity distributions under different cuts and distance approximation both on a linear scale and on a logarithmic scale that reveals the wings of the distributions. Error bars give the Poisson noise, but neglect any other sources of error. The velocity distributions of the halo and the Galactic disc can be made out in both plots. The long tail of the counter-rotating halo is clearly visible for the C10 sample (red circles). As already noted above, a restriction to dwarf stars (green crosses) diminishes the counter-rotating tail (around
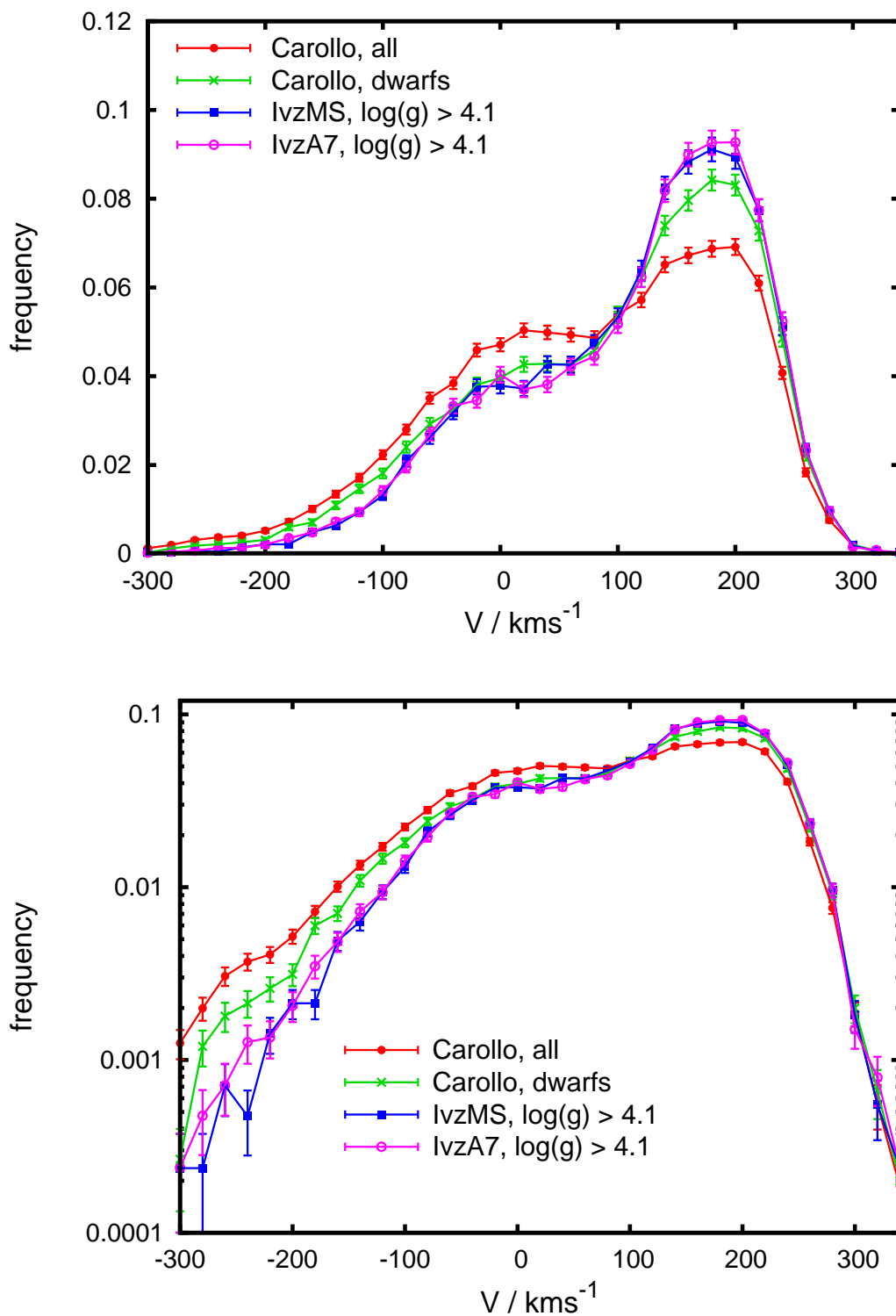
Figure 8.8: Velocity distributions for stars in the calibration sample. To make them comparable at the different sample sizes, all distributions were normalized to unity (i.e. divided by the total number of stars in each subsample). Error bars show again Poisson errors.

$V < -170 \, \mathrm{km \, s^{-1}}$, which corresponds to $V_h < -400 \, \mathrm{km \, s^{-1}}$). The blue filled squares show what we obtain with the adopted main sequence calibration, and the purple empty circles depict the age-dependent distance calibration by Ivezic et al. (2008). With both native SDSS distance calibrations the sample displays a clean downtrend to the low velocity side corresponding to a V velocity dispersion of around $70 - 80 \, \mathrm{km \, s^{-1}}$.

One might argue that the two native SDSS calibrations lead to some contamination by giants that are treated as dwarfs and thus provoke the opposite effect of underestimating distances. To reduce the contamination by evolved stars we use a gravity cut of $\log(g) > 4.1$ in the following discussions, which mostly helps to reduce the density saddle between the disc and halo component, where halo stars with severe distance underestimates tend to assemble. However, the left tail of the halo distribution does not change significantly on a tightening or loosening of the gravity cut. In the following discussions we will always use the slightly tightened condition $\log(g) > 4.1$, but we checked that all of our conclusions are valid regardless of the specific choice of the gravity cut. The absence of a significant excessive tail for dwarf stars can in our view only be explained by the fact that strongly counter-rotating halo dwarfs are at the best an extremely rare population. It is highly implausible that the counter-rotating halo consists exclusively of subgiants and giants.

8.6.1   Kinematics versus metallicities

The reason why Carollo et al. (2007, 2010) get a transition between their inner and outer halo from a local sample is the increasing scaleheight of their populations with lower metallicity, which is linked to the increasing velocity dispersion perpendicular to the plane. According to our above discussion of kinematic fingerprints of distance errors, at least the increase of vertical dispersion by velocity crossovers (Section 8.5.2) due to distance overestimates should disappear when cutting away the unphysical turn-off stars and further when switching from C10 dwarf distances to the native SDSS calibrations. This is indeed observed in Fig. 8.9: It shows the values of vertical velocity dispersion against metallicity for different subsamples together with Poisson errors. The full C10 sample (red circles) harbours a prominent uptrend towards lower metallicity, which is at odds with the earlier result from Chiba & Beers (2000). This uptrend almost vanishes in their dwarf subsample (green crosses). Both when using the adopted main sequence calibration (blue filled squares) and when using the Ivezic et al. (2008) age-dependent distance estimates (purple empty squares), we see no significant trend with metallicity any more; this finding is robust against changes in the gravity cut. To guide the eye we plot a horizontal line at $85 \, \mathrm{km \, s^{-1}}$. There is a suggestion of a subtle increase below $[Fe/H]_{DR7} < -1.8$, yet numbers are too small to allow for a judgement. A source of uncertainty is the degree of possible giant contamination. It likely rises towards the metal-poor side, which may result in a reduction of measured dispersions. On the other hand the radial velocity support for the vertical velocity component is very high due to the polewards orientation of the sample. So the decrease effected by distance underestimates is relatively weak. Underestimating distances takes a further moderated effect on vertical dispersions: While a distance overestimate both increases the measured vertical disper-
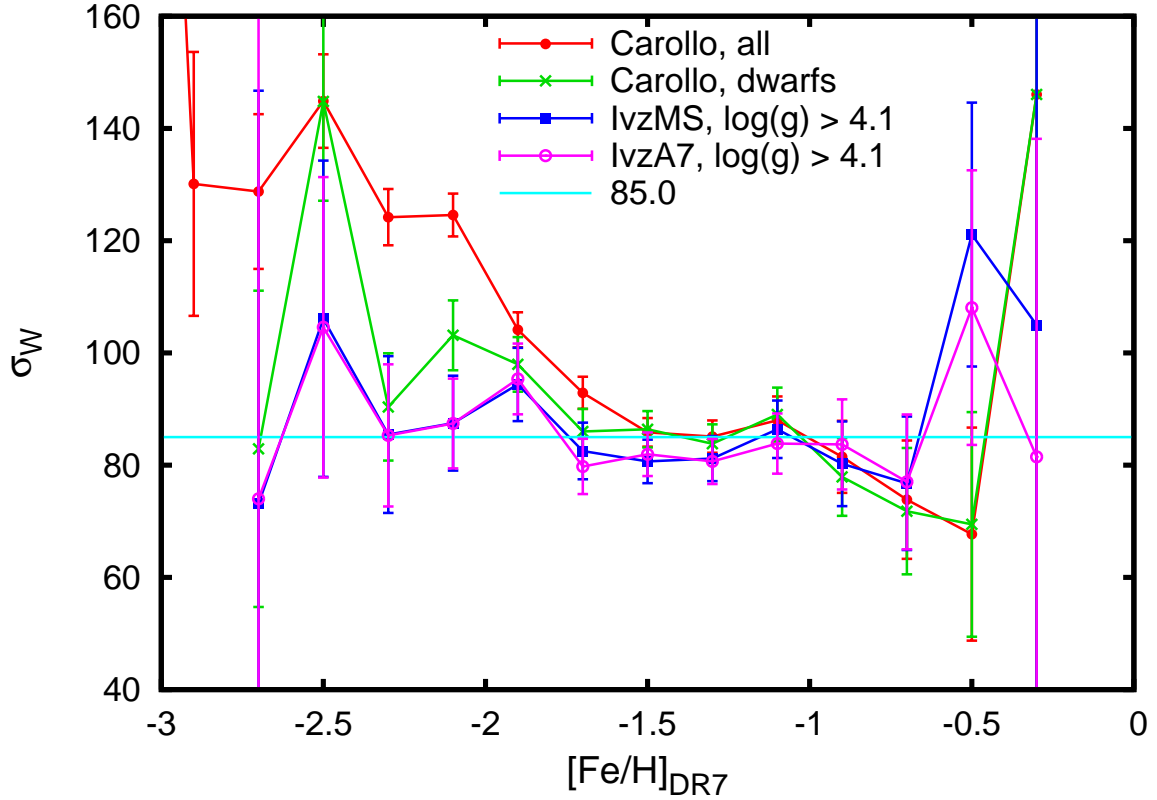
Figure 8.9: Vertical velocity dispersions against metallicity for different halo subsamples and distance calibrations. In all samples we cut away all prograde stars to eliminate most of the disc contamination. While the Carollo et al. full sample (red line) shows a vigorous uptrend towards the lowest metallicities, this trend almost vanishes in their dwarf star subsample (green line), while using the two native SDSS calibrations no significant trend is detectable.

sion by direct overestimate of the proper motion part, and a lift via the velocity cross-overs, on distance underestimates the effects have opposite signs, thus to some part balancing each other. Another way to look at the problem is to plot metallicity distributions as a function of the kinetic energies (by stellar mass) of stars. In Fig. 8.10 we show the separations in entire kinetic energy (v^2, left column) and in vertical kinetic energy (W^2, middle column). In the rightmost column we show the vertical kinetic energy, but for retrograde stars ($V < -10\,\mathrm{km\,s^{-1}}$). As the rotation velocity of disc stars adds to the kinetic energy the disc has its strongest dominance of course not in the lowest energy bin, but at $180^2(\mathrm{km\,s^{-1}})^2 < v^2 < 270^2(\mathrm{km\,s^{-1}})^2$, as most disc stars are on quite circular orbits with an entire velocity close to the circular rotation speed of the Galaxy. The prominent shift especially in the left tail and also peak of the metallicity distributions in the original C10 distance prescription for the full sample (top row) can be seen in both the total and vertical energy separation. However, this already diminishes, when we plot the subsample of
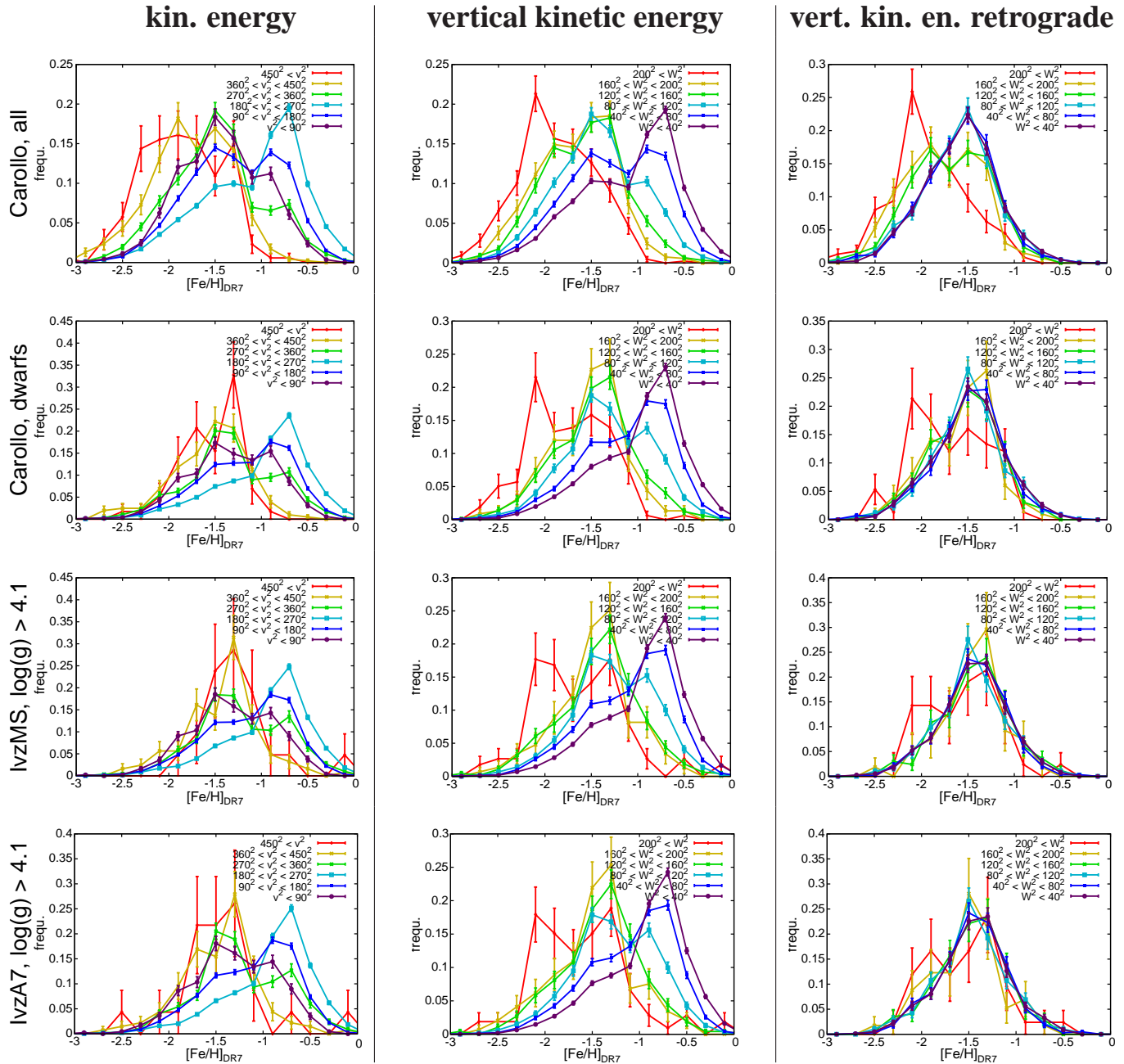
Figure 8.10: Metallicity distributions at different values for kinetic energy in the different distance prescriptions. From top to bottom we show the entire C10 sample, the dwarf stars from C10, the adopted main sequence calibration and the Ivezić et al.(2008) age-dependent calibration. The left column displays a separation by the entire kinetic energy, while the centre column makes only use of the vertical velocity W. The right column shows the distributions using the vertical energy part for retrograde stars ($V < -10\,\mathrm{km\,s^{-1}}$) to reduce the disc contamination. Velocities are taken in $\mathrm{km\,s^{-1}}$. Error bars indicate the Poisson errors.

the C10 dwarf stars with $\log(g) > 4.0$ (second row). No convincing outer halo signature can be found in either of the native SDSS calibrations (bottom row). At the highest vertical energies a single spike at [Fe/H] ~ -2.2 sticks out. At first glance this could be taken as a hint for an outer halo. However, in this interpretation it should be mirrored by the entire energy distribution, which is not the case. We are tempted to identify this feature at least partly with a prominent metal-poor stellar stream described by Helmi et al. (1999) and Kepley et al. (2007), which we expect exactly at these very high vertical energies. This stream can as well serve as explanation for the subtle and insignificant increase of vertical velocity dispersions at $[Fe/H]_{DR7} < -1.8$ that was seen in Fig. 8.9.

There appears also a slight general drift towards lower metallicity at the highest energies, which can be mainly seen in the vertical term. Caution should be exercised, however, due to the varying presence of the Galactic disc (most prominent at the lowest vertical kinetic energies and at total energies corresponding to the rotation speed), which then impacts on the normalization of the halo component and fools the eye because the apparent halo peak can be shifted by the wing of the disc distribution. A quite robust approach is removing all prograde stars from the sample to minimize disc contamination. As this biases kinematics, the overall energy distributions are altered, but the vertical energies (right hand column) should not be affected. In Fig. 8.10, the entire C10 sample shows a clear signature of lower metallicities in the higher vertical energy bins. When removing the contested turn-off stars (i.e. plotting dwarfs, centre row) no trend apart from the discussed spike can be detected regardless of the applied distance determination.

In summary it can be stated that also in terms of metallicity versus energy the sample has no reliable outer halo signature, neither when using the native SDSS calibrations nor when using the C10 dwarf subsample.

8.6.2 Component fit

Fig. 8.11 shows fits to the azimuthal velocity distribution (green data points) for the the four different subsamples and distance calibrations we use. Both columns show the same data, the left column on a linear scale, the right column on a logarithmic scale to examine both centres and wings of the distributions. We apply a simple Gaussian halo and a single non-Gaussian disc component. All fits were done for $-250\,\mathrm{km\,s}^{-1} < V < 280\,\mathrm{km\,s}^{-1}$, a limit that stays out of the regions dominated by noise, but reaches on the retrograde side still well into the region where any suspected retrograde halo component would be influential. To account for the observational errors, we folded the underlying distributions with a sum of Gaussians (with a spacing of $1\,\mathrm{km\,s}^{-1}$), of which the relative weights were derived globally for each component from error propagation on the single objects (stars with $V > 50\,\mathrm{km\,s}^{-1}$ attributed to the disc, objects with $V < 10\,\mathrm{km\,s}^{-1}$ to the halo) concerning proper motion and radial velocity errors. This treatment is a bit crude and we suspect that it underestimates errors on the left wing of the distribution and overestimates them on the right wing, which we identify as the most likely reason for the overshooting of the model against the data at $V > 270\,\mathrm{km\,s}^{-1}$. In a second step we folded with another Gaussian magnitude error of $0.25\,\mathrm{mag}$ to account for uncertainties in the intrinsic brightness and thus dis-
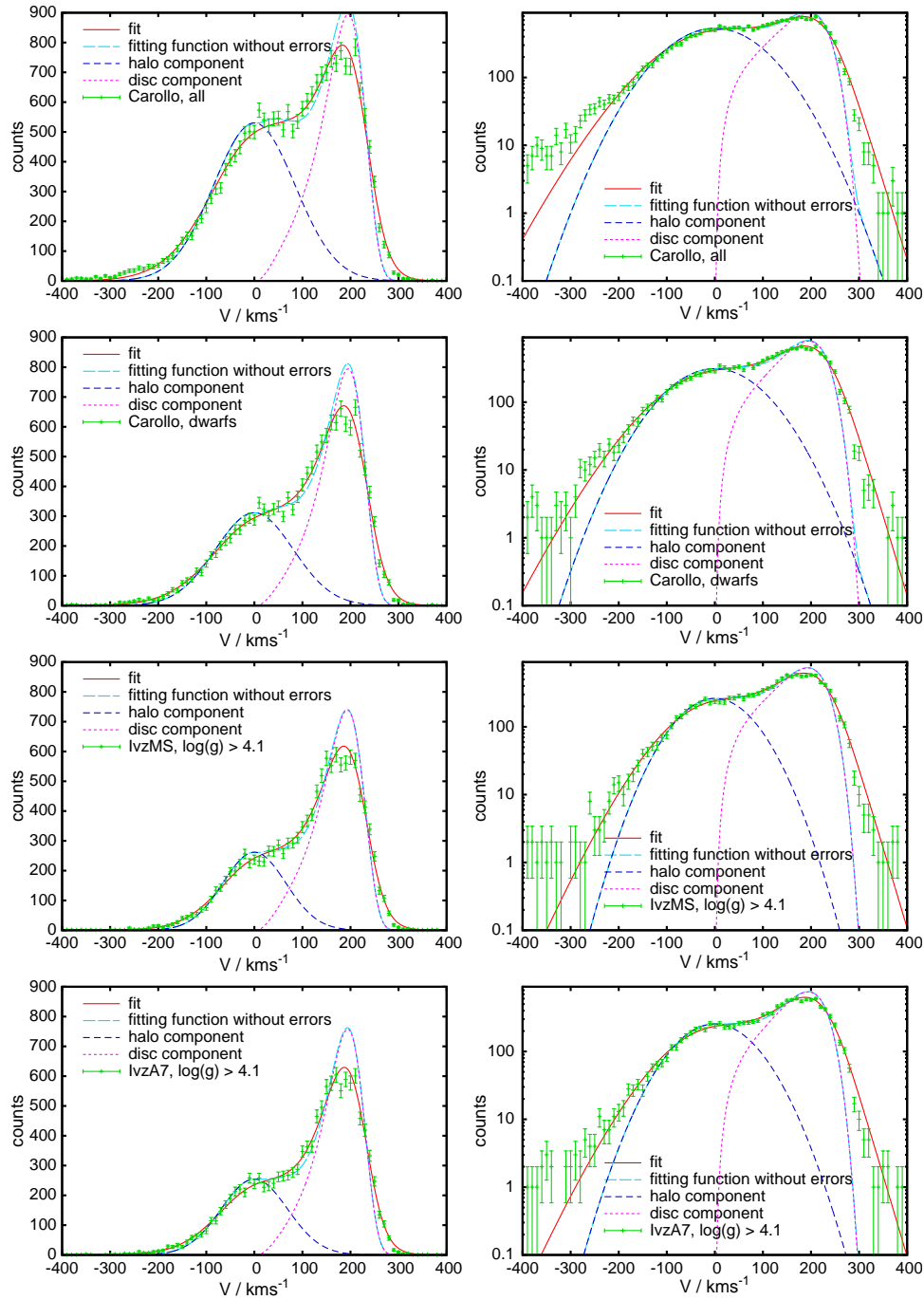
Figure 8.11: Velocity distributions for stars (light blue, with Poisson errors) in the calibration sample for different selections and distance prescriptions: From top to bottom: The entire C10 sample, the C10 dwarf stars with $\log(g) > 4.0$, the dwarfs with $\log(g) > 4.1$ using the adopted main sequence calibration distances and the age-dependent formula from Ivezić Ž et al. (2008). To show both distribution centre and wings we contrast the linear scale (left) with logarithmic plots of the distributions (right). All distributions are fitted by a simple model (red line) with a Gaussian halo and a single (non-Gaussian) disc component. We did an error propagation from the values given in DR7 which is – together with a magnitude error of 0.25 mag - folded onto the original distribution (light blue). The error broadens the peaks and thus lowers the maximum count rates especially of the disc peak. The dark blue line shows the underlying Gaussian halo component and the purple curve the analytic disc component.

tance of the stars and thereafter a third Gaussian of $7\,\mathrm{km\,s^{-1}}$ to account for velocity crossovers via the distance uncertainties.

For the disc component we make use of the analytic formula of Schönrich & Binney (in prep.). The underlying assumption is that of an isothermal sheet through the Galaxy with increasing velocity dispersions towards the centre, i.e. the stellar populations at each galactocentric radius are given a specific vertical and horizontal energy dispersion. For those populations their likelihood to be in the solar annulus and their local scaleheight can be estimated assuming a simple potential with constant rotation speed. We used a solar galactocentric radius $R_0 = 8.0\,\mathrm{kpc}$, a circular rotation speed of $v_c = 220\,\mathrm{km\,s^{-1}}$, a disc scalelength of $R_d = 2.5\,\mathrm{kpc}$, a scalelength for the vertical dispersion of $R_{\sigma_z} = 5.0\,\mathrm{kpc}$ and for the horizontal dispersion as $R_\sigma = 7.5\,\mathrm{kpc}$. The adiabatic correction index (index dependent on the shape of the potential that describes the change of vertical energy along orbits that are extended over different galactocentric radii) was set to 0.5. As we are using the adiabatic correction without a recorrection for energy conservation, the disc local scale height gets moderately underestimated, an effect that we partially cope with by setting the adiabatic correction index to 0.5, slightly below the expected value for the upper disc. To simplify the calculation we summed up disc contributions at equal parts at altitudes $z = 400, 700, 900, 1100, 1400, 1800, 2400\,\mathrm{pc}$. The Gaussian halo component was set at rest ($V = 0$). The five free parameters of the fit were disc and halo normalization ($N_h = 530, N_d = 16691$ for the entire C10 sample, $N_d = 14403, N_h = 312$ for the C10 dwarfs, $N_d = 13031, N_h = 262$ for the adopted main sequence calibration, $N_d = 13254, N_h = 255$ for the age-dependent calibration), halo azimuthal velocity dispersion ($84.7, 80.9, 65.4, 68.9\,\mathrm{km\,s^{-1}}$), disc local horizontal dispersion ($\sigma_0 = 43.2, 41.4, 41.5, 40.1\,\mathrm{km\,s^{-1}}$), and local scaleheight ($h_0 = 571, 499, 466, 439\,\mathrm{km\,s^{-1}}$). As seen in Fig. 8.11, apart from a weakness on the high velocity side, which presumably derives from the use of a global observational scatter that could overestimate the uncertainty for disc stars, the two-component approximation gives decent fits (red lines) to the velocity distributions for the dwarf samples. The relative halo normalization varies between the different datasets as the most metal-poor stars are more likely to be classified into the turn-off or subgiant bands.

Of most interest for this discussion is the shape of the (retrograde) halo velocity distribution. For the entire C10 distance sample (left column) we can clearly identify the bump that encouraged C07 and C10 to fit a separate velocity peak starting from around $-200\,\mathrm{km\,s^{-1}}$. This anomaly becomes especially apparent in the logarithmic plot and is confirmed by Poisson loglikelihood values ruling out equality of the theoretical (simple Gaussian halo) and observed distributions at highest significance.

We point out that even this strong anomaly in the fit alone would not be a sufficient justification for a second physical component, especially not for a retrograde component. There is no reason to firmly believe that the Milky Way halo or its possible components should have a strictly Gaussian velocity structure; the disc certainly can not be adequately described by Gaussian fits (a discussion of this can be found in Strömberg, 1927) and similarly the halo might have a more complex velocity distribution. The only way to cleanly identify a retrograde velocity distortion on the Galactic halo from kinematics would be to prove a difference to the prograde halo tail. As this is, however, impossible at the required accuracy due to the disc contamination, we conclude

that without a clean halo-disc separation any attempt to use the azimuthal velocity distribution for proving a retrograde halo component is unreliable.

Besides its doubtful significance for indicating a separate component, the extended retrograde tail anyway diminishes when we turn to the dwarf samples, which do not contain the at least partly unphysical turn-off stars: restricting the C10 sample to their dwarf stars (centre column of Fig. 8.11) the bump below $-200\,\mathrm{km\,s^{-1}}$ disappears. There is a weak surplus of stars between $-220\,\mathrm{km\,s^{-1}}$ and $-280\,\mathrm{km\,s^{-1}}$, which could, however, just be a statistical fluctuation. This is confirmed by statistics, which have the p-level (measured under the assumption of Poisson errors) for equality of the fit and the measured distribution at 0.55 for $-250\,\mathrm{km\,s^{-1}} \leq V \leq 20\,\mathrm{km\,s^{-1}}$ (and 0.20 when we extend the range to $-300\,\mathrm{km\,s^{-1}} \leq V \leq 20\,\mathrm{km\,s^{-1}}$) meaning that when drawing realisations from the given theoretical distribution, about 55% of the samples would be more different from the theoretical distribution than the current one. Regarding our imperfect treatment of distance errors the quality of the fit is rather surprising. Using the main sequence distance calibration the distribution gets even more contracted due to the shorter distances. Apart from the slight surplus of stars left of $V \sim -320\,\mathrm{km\,s^{-1}}$, which just appear to be some sample contamination (indeed a distance test on the 100 objects with lowest V velocities still reveals a 2σ distance overestimate) and the single bin with 8 stars around $V = -260\,\mathrm{km\,s^{-1}}$ no anomaly is traceable any more, confirmed by statistics. Using the age-dependent calibration from Ivezic et al. (2008) the picture is similar. The fit looks even better down to $V \sim -300\,\mathrm{km\,s^{-1}}$ beyond which there is a weak surplus of about a dozen objects between $V = -400\,\mathrm{km\,s^{-1}}$ and $V = -300\,\mathrm{km\,s^{-1}}$. This can be attributed to misassignement of stars between the catalogues for proper motions and a probable non-Gaussian far tail of the proper motion error distribution.

It can also be argued that an attempt to fit the disc velocity distribution via a Gaussian fit increase the need for a spurious second halo component, especially as the large (unavoidable) velocity errors limit the information on the real shapes of the underlying velocity distributions: as the disc velocity distribution is naturally skewed towards lower velocities, a Gaussian fit will drop too steeply towards low rotation velocities. This invokes a second Gaussian for the disc (thin-thick discs), which will in most cases show the same problem again, forcing the halo component a little bit up into the prograde regime. This again increases the need for the creation of an artificial retrograde halo component. In this case we avoided this problem by using a more physical fitting formula for the Galactic disc, yet there was still noticeable influence by the disc fit onto the parameters of the simple Gaussian halo component.

Overall we can state that any striking excess of highly retrograde stars disappears from the distribution when we limit the sample to the more reliable dwarf stars. There is a good agreement between fits and data for the dwarf samples, apart from a misfit at high velocities and a slight surplus at the lowest velocities against a Gaussian fit, which, however, rather looks like imperfect error handling or a probable contamination of the sample with misidentifications in between the different catalogues delivering the proper motions or a non-Gaussianity in their contamination. Replacing the questionable Gaussian analysis for the disc by a more physically motivated formula and by applying an error propagation we have shown that neither a second halo nor a second or even third disc component are required for explaining the azimuthal velocity distribution.

8.6.3   Velocity dispersions

Using the adopted main sequence approximation and restricting the sample to 2020 retrograde stars ($V < -10\,\mathrm{km\,s}^{-1}$) we can give a tentative estimate for the halo kinematics of $\sigma_U \sim 157 \pm 10\,\mathrm{km\,s}^{-1}$ and $\sigma_W \sim 75 \pm 8\,\mathrm{km\,s}^{-1}$. The latter is close to the azimuthal velocity dispersion of $\sigma_V \sim 70\,\mathrm{km\,s}^{-1}$ from the last section. In these values we accounted for the errors reported in the SEGUE pipeline plus a dispersion of roughly estimated 15% in the distances. These act to reduce the derived velocity dispersions from the actually measured ones. Those values are considerably smaller in V and W than what was given by C10 partly due to the spurious crossover into W velocities having diminished. We point out that these values agree well with the results of Kepley et al. (2007) and Smith et al. (2009). Although we use the same sample with the same distance scale as Smith et al. (2009) we cannot confirm their quoted errors of $2\,\mathrm{km\,s}^{-1}$, since the systematic uncertainties by the distances within the Ivezic et al. (2008) method and sample cleaning are currently too large to assess dispersions on a scale better than 5%.

8.7   Conclusions

We have described how errors in distance estimates result in an apparent systematic retrograde motion of the Galactic halo, an effect to which the SEGUE/SDSS sample is especially prone by its strong poleward orientation. The general problem of distance biases similarly applies to any study that makes use of proper motion-based estimates. We find that the distance derivation of Carollo et al. (2007) and Carollo et al. (2010) is flawed by sorting stars into unphysical positions in the colour-magnitude diagram: objects are placed between the subgiant and dwarf sequences in positions that would require stellar ages in excess of the age of the universe. Despite the elegance of the general idea to sort stars into known sequences according to their estimated gravities, the method itself and the used gravity cuts are not well supported by measurements. Moreover there is no "turn-off"-sequence, but turn-off stars are populating a region that spans of order 1 magnitude in luminosity. In this light the statement by C10 to have distances precise to about $10 - 20\%$ is an unsupported claim.

From the distances kindly provided by Carollo et al. we calculated back to their assumed absolute magnitudes and found systematic differences of ~ 0.2 to $0.3\,\mathrm{mag}$ and a large scatter for metal-poor main sequence stars towards the adopted main sequence calibration as well as towards the age-dependent calibration by Ivezic et al. (2008), also far to the red side of the suspected turn-off region. The adopted main sequence calibration is only slightly fainter than the theoretical BASTI isochrones.

We have shown in Section 8.4.3 that the claim by C07 and C10 to have found a counter-rotating extended tail of the halo is largely caused by unphysical assumptions about locations of stars in the colour-magnitude diagram, by magnitude uncertainties in the turn-off stars and by the use of a too bright main sequence calibration. The correctness of this tail can be ruled out by statistical tests, as described in Section 8.5. The tail diminishes when we limit the C10 sample to dwarf stars and disappears when we make use of the better founded Ivezic et al. (2008) calibrations,

which are consistent with fiducials and isochrones. In Section 8.6.2 we demonstrated that the halo distribution for the dwarf samples regardless of the applied distance determination can be fit by a simple Gaussian component.

We have also shown that in the DR7 pipeline stars with lower metallicities are shifted towards lower gravities, considerably increasing their fraction among the thought-to-be turn-off stars. Further the magnitude difference for their main sequence stars against the Ivezic et al. (2008) main sequence calibration grows towards lower metallicities. The stronger prevalence of distance errors at the metal-poor end of the metallicity distribution will thus give any spurious counter-rotating tail members a biased metallicity distribution.

Finally we have shown that the claim of C10 that the counter-rotating component members reach to higher altitudes can as well be traced back to distance determinations: the dispersion of the vertical velocity component is significantly increased by their distance errors, though due to the polewards sample orientation this effect would at first order be smaller than for the other velocities. As shown in Section (8.5) simultaneously the W velocities of the halo stars with distance overestimates are artificially increased by of order $50 \, \mathrm{km \, s^{-1}}$ via spurious velocity cross-over terms from the heliocentric azimuthal velocities in the derivation. The effect is strongest for the most strongly retrograde objects (they have the largest heliocentric V_h) and is aggravated by their selection for stars in galactocentric radius $7 \, \mathrm{kpc} < R < 10 \, \mathrm{kpc}$. This colludes with their metallicity dependent distance bias (see above) to produce their findings of decreasing metallicities at high altitudes. There is a slight excess of more metal-poor stars in a single velocity bin at high vertical velocities, which is not mirrored by the behaviour at high total kinetic energies. We argue that this is most likely a reflection of a well-known local stream that has been identified by Helmi et al. (1999) and Kepley et al. (2007).

Another source of error is the modelling of especially the Galactic disc azimuthal velocity distribution by Gaussian components. It was shown by Strömberg (1927) that Gaussian modelling of the Galactic disc lead to unphysical results and the identification of spurious components on the low rotation side because of the extented tail. As the skewed V velocity distribution enforces in most cases the introduction of a second Gaussian component, that - being a mere artifact by wrong assumptions - can then be misinterpreted as physical reality, Gaussian modelling of the Galactic disc in a combined disc and halo sample can wrongly force the halo component into the prograde regime to compensate for the two steeply falling disc terms. Consequently this then creates the need for inference of a retrograde component to compensate for the bias.

We also argue that magnitude based distance assessment schemes introduce a velocity bias that resembles the Lutz-Kelker bias: If the error in absolute magnitudes follows a Gaussian distribution, the distance error distribution will thus form an extended tail that grows stronger with increasing dispersions. Via the proper motion part in the determination of space velocities, which is proportional to the estimated distance, measured velocities develop extended tails away from the solar motion. For the V velocity distribution of especially the halo this gives the halo an asymmetric velocity distribution with a longer tail in the retrograde regime, a process that can explain the moderate asymmetries found e.g. by Norris & Ryan (1989).

Finally we note that it is by no means imperative that the halo have a Gaussian velocity distribu-

tion. In this light it is rather surprising that our simple Gaussian halo component can fit the data so well. Even if there were deviations from Gaussianity this would alone be no convincing sign for a separate component. A more convincing indication would be a proven difference between the prograde and the retrograde tail of the halo azimuthal velocity distribution, but disentangling this from disc contamination on the prograde side will be difficult.

Recently Carollo and collaborators submitted a rebuttal paper (Beers et al., 2011) claiming that our analysis presented here be wrong. Instead of discussing all our arguments their revised analysis relies on two central claims: They state that the distance scale adopted by us is wrong and that there is an asymmetric halo azimuthal velocity distribution for their metal-poor stars, neither of which we concur with.

Concerning the distance issue we stress that our conclusions are valid for the Carollo et al. (2007, 2010) and both Ivezic et al. (2008) distance calibrations; our work does not rely on a single distance scale in contrast to claims made by Beers et al. (2011). Beers et al. criticize us for adopting the incorrect main sequence calibration of Ivezic et al. (2008) but failed to note that we actually stretched this calibration in the same direction of their preferred one by increasing the luminosities by 0.1 magnitudes and accounting for alpha-enhancement by increasing the measured metallicities by 0.2 dex (Sect. 2). Importantly, we have also made use of their preferred Ivezic et al. (2008) calibration (here denoted IvzA7) and find no significant differences (e.g. Fig. 11). Finally, we have made use of direct isochrone distances, which fully corroborates our findings.

As for the azimuthal velocity distribution of the most metal-poor stars, we re-emphasize that any magnitude-based distance scheme invokes a bias in the inferred distances and thus an asymmetric azimuthal velocity distribution by definition; this effect is akin to the well-known Lutz-Kelker (1973) bias and is illustrated in Fig. 8.11. In view of a large magnitude scatter (which their metal-poor stars clearly have, see their Fig. 5) a Gaussian fit is inappropriate due to the missing error handling. In this light it is not surprising that their new revised parameters are quite different from their original results (e.g. for $z_{max} > 5\,\text{kpc}$ their outer halo mean velocity rose from $-128\,\text{km}\,\text{s}^{-1}$ (cf. Table 1 in C10) to -59 ± 20 km/s). Finally, we argue that moving a considerable fraction of the wrongly identified turnoff stars up to the subgiant/giant branch as done by Beers et al. will make the distance overestimate for misidentified dwarfs among them even more severe.

In summary our criticism of the C07, C10 works remains in full: our in-depth re-analysis of their data with different distance calibrations and a proper error handling reveal no convincing evidence for a dual halo.

The systematic distance uncertainties make it dangerous to draw a definitive conclusion for the strength or existence of a possible counter-rotating halo component. All current distance calibrations have problems and need improvement before a method along the lines used by C07 and C10 can be attempted. We would like to stress that we do not and would not want to rely on either of them. Two central conclusions can, however, be drawn without having to trust any of the different distance calibrations: Even on the C10 or C07 sample using their distances, no reliable detection of any non-Gaussianity in the halo, be it a counter-rotating halo or not, is possible on the examined data set in any of the dwarf samples. If a separate component gets detected on a

larger sample in the future, it should be significantly weaker than what was claimed by C10.

8.8   Acknowledgements

8.9   Appendix: Details on sample selection and treatment

8.9.1   Kinematics and geometry

We use up-to-date values for the basic constants of our Galaxy. The rotation speed is assumed to be $220 \, \mathrm{km \, s^{-1}}$ in concordance with recent results of Koposov et al. (2010). We apply the recent determinations of solar motion relative to the local standard of rest from Schönrich, Binney & Dehnen (2010), which is $v_\odot = (11.1^{+0.69}_{-0.75}, 12.24^{+0.47}_{-0.47}, 7.25^{+0.37}_{-0.36}) \, \mathrm{km \, s^{-1}}$ with additional systematic uncertainties of $\sim (1,2,0.5) \, \mathrm{km \, s^{-1}}$. Neither the Galactic rotation rate nor the solar galactocentric radius $R_\odot$ are very well determined, but the angular motion of Sagittarius A^* is (Reid & Brunthaler, 2004). The galactocentric radius of $R_\odot = 8.5 \, \mathrm{kpc}$ assumed in C10 is inconsistent with their assumption for the rotation speed. We adopt $R_\odot = 8.0 \, \mathrm{kpc}$, which is in concordance with most measurements, and coincides with the most recent trigonometric parallax determination for Sagittarius B2 (Reid et al., 2009b).

8.9.2   Distance calibrations and metallicities

For adopted distances in SDSS colours two alternatives exist: The Ivezic et al. (2008) calibration (see Appendix therein) or the Beers (2000) calibration. A third possibility would be using the isochrones directly, which would allow for a statistical implementation of the subgiants and also allow for natural shape changes: however, their handling is beyond the scope of this work. The Ivezic et al. (2008) main sequence calibration uses the formula:

$$M_r(g-r, [\mathrm{Fe/H}]) = \tag{8.3}$$

$$= 1.65 + 6.29(g-i)_0 - 2.30(g-i)_0^2 - 1.11[\mathrm{Fe/H}] - 0.18[\mathrm{Fe/H}]^2 \tag{8.4}$$

where M_r is the adopted absolute magnitude and $(g-i)_0$ is the dereddened SDSS colour index. A short assessment of this formula reveals that it fits the zero age main sequence relatively well in the required colour range at low metallicity. Apart from the shortcome that the subgiants are not considered, the metallicity dependence is not well matched at the high metallicity end. Further the colour dependence is not perfect at the level of precision required for distances and there

are no crossterms between metallicity and colour, i.e. there is no implementation of metallicity-dependent shape changes. Thus this relation has to be used with caution. A comparison with the BASTI isochrones reveals that the Ivezic et al. (2008) calibration at low metallicities is slightly fainter than the isochrones without alpha enhancement. To correct for alpha enhancement we slightly increase the metallicity of all metal-poor stars (with $[Fe/H]_{DR7} < -1.0$) by 0.2 dex and let this correction go linearly to zero between $[Fe/H]_{DR7} = -1.0$ and $[Fe/H]_{DR7} = 0$. In addition we increase all luminosities by 0.1 mag to reconcile the calibration better with the main sequence of M92 according to the fiducials by An et al. (2008), to avoid any suspicion to have buried the counter-rotating tail by a too faint calibration, and as we detected a minor distance underestimate in our statistics without this shift. Further the calibration is now just slightly brighter than the isochrones as seen in Fig. 8.4, which is a desired effect at those metallicities, as there are indications that metal-poor isochrones could underestimate the luminosities (or equivalently overestimate the effective temperatures) of lower main sequence stars (Casagrande et al., 2007). To account for age effects Ivezic et al. (2008) also suggested an "age-dependent" calibration, which rises more steeply towards the blue side (Eq. A7 in their appendix). To meet concerns of our referee we show all relevant statistics also in the light of this other calibration. This calibration is steeper in colour than the main sequence calibration, i.e. it is brighter at blue colours and fainter at red colours, following an intention to cope with the steepening of isochrones near the turn-off. However, the steepening of isochrones only applies near the turn-off, while this relation is globally inclined against the main sequence of the isochrones as well as against the main sequence calibration. As this relation thus does not follow the blueward shift of the turn-off towards lower metallicity, a relative overestimate is expected for the distances of the blue stars at lowest metallicity. Vice versa the distances to metal rich turn-off stars might be underestimated. We tested all our results for the C10 dwarf sample and also for cutting in colour and different gravity selections to delineate the impact by the turn-off region. As can be seen from the central panel in Fig. 8.4 the difference between the adopted main sequence calibration and the C10 magnitudes persists also to the red side of the turn-off region and is also present for the Ivezic et al. (2008) age-dependent relation.

As an even fourth distance determination we made use of the BASTI isochrones (Pietrinferni et al., 2004, 2006). To accomplish that we account again for alpha enhancement with the same prescriptions as for our adopted main sequence relation. For each star we choose the closest 12.5 Gyr isochrone in metallicity from a dense grid kindly provided by S. Cassisi for our age determinations in Casagrande et al. (2011). On this isochrone we choose the r-band magnitude from (g-i) on the main sequence. When the turn-off is to the red of the stellar position, we extrapolate from the turn-off point of the isochrone following the shape of the Ivezic et al. (2008) main sequence relation. So these stars are placed at an extrapolated turn-off point. As one can easily see from Fig. 8.12 in the central statistics there are no significant changes towards the other main sequence calibrations. We confirmed that no real difference was detectable.

C10 used a slightly different metallicity scale from DR7, which was reasoned to balance out a possible metallicity overestimate on the lowest metallicity end:

$$[Fe/H]_{Car} = -0.186 + 0.765[Fe/H]_{DR7} - 0.068[Fe/H]_{DR7}^2 \qquad (8.5)$$
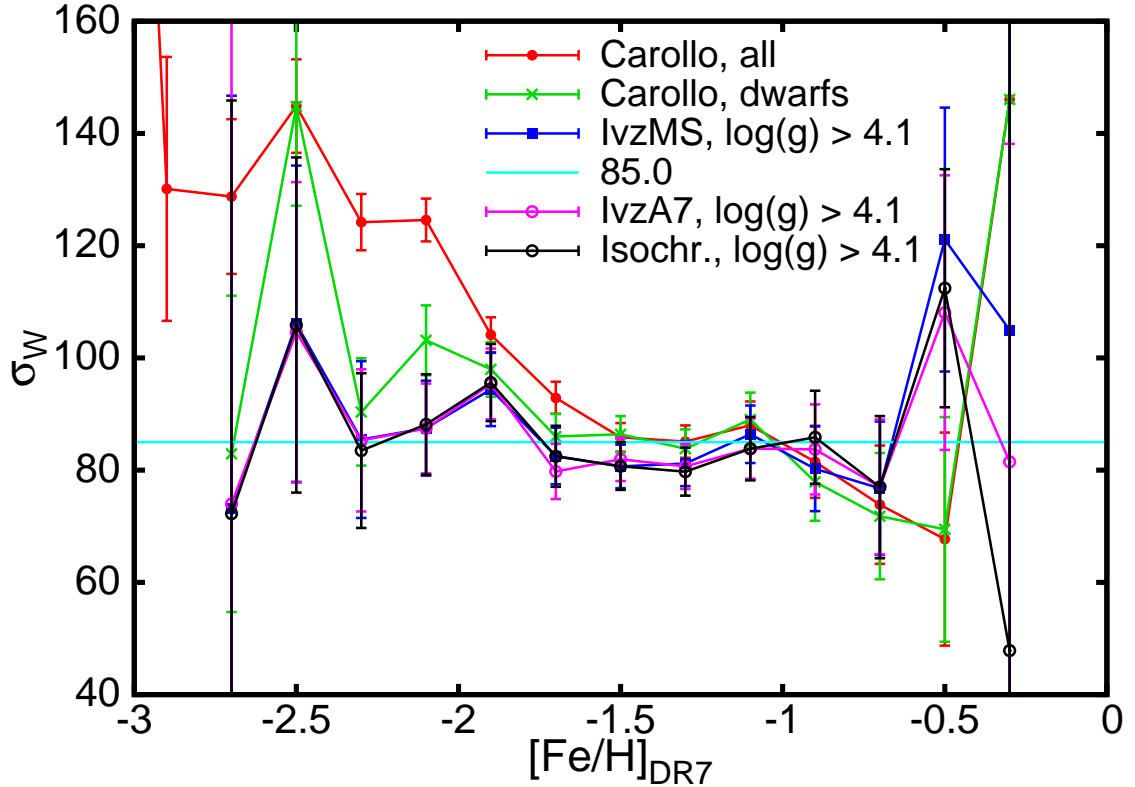
Figure 8.12: Vertical dispersions vs. metallicity revisited. The lines are the same as in Fig. 8.9. Additionally we plot in black the same derived via direct isochrone determination of distances.

We argue that their claimed overestimate at low metallicities most likely reflects the impossibility of the pipeline to cope with the faint metal lines in this region, getting lost in the low resolution and low signal-to-noise ratios. This effect is quite similar to the loss of accuracy e.g. in Strömgren photometric metallicities. The formula has the dissatisfactory effect of aggravating the well-known bias of the DR7 pipeline to underestimate the metal content of metal-rich stars. This can be seen by comparison of local stars from the Geneva-Copenhagen Survey (Nordström et al., 2004) with high vertical energy, to the metallicity distribution of the SEGUE disc stars. Similarly the ugriz metallicity calibration fails to reproduce metallicities already slightly below solar metallicity as can be seen from Fig. 11 in Árnadóttir et al. (2010). The latter problem is not of major importance for the halo, but applying the formula by Carollo et al. would exacerbate metallicity-induced errors on the disc population. We estimate that distances are only weakly affected by this correction on the low metallicity side (i.e. mostly for halo stars) as the sensitivity of stellar atmospheres to the logarithmic metallicity scale gets lower. This can be seen in VandenBerg et al. (2010) or for comparison in fig. 13 of Casagrande et al. (2010).

We use the DR7 metllicities throughout the paper and do not apply the correction from (8.5), but

checked that our findings are not significantly affected by switching the distance scale.

8.9.3 Deriving space velocities

The dataset contains information on magnitudes, colours, the distances, stellar parameters, radial velocities and proper motions. We can thus derive the velocities in the solar/local coordinate system by:

$$U_h = -d\sin(l)\dot{l} - d\cos(l)\sin(b)\dot{b} + \cos(b)\cos(l)v_{\parallel}$$
$$V_h = d\cos(l)\dot{l} - d\sin(l)\sin(b)\dot{b} + \cos(b)\sin(l)v_{\parallel} \qquad (8.6)$$
$$W_h = d\cos(b)\dot{b} + \sin(b)v_{\parallel}$$

where l, b are Galactic longitude and latitude, $\dot{l}, \dot{b}$ are the proper motion components in l and b and d is the assumed distance to the stars. Of special interest is the degree of support of the measurement by radial motions, which are independent of distance biases and have smaller errors. Neglecting the geometrical extension of the sample, the quantity of interest is thus the term connecting the azimuthal velocity in the heliocentric frame V_h to the line-of-sight velocity $v_{\parallel}$:

$$\eta_V = |\cos(b)\sin(l)| \qquad (8.7)$$

The term η_V is 1 where the V_h velocity is measured directly from the line-of-sight velocity $v_{\parallel}$ i.e. at $b = 0$ and $l = 90°, 270°$, its contours on the sample are depicted in Fig. 8.1.

Due to the extension of the sample to a radius of more than $3\,\mathrm{kpc}$ projected on the Galactic plane a small angle approximation cannot be reliably taken. Using the Galactic rest frame velocities in heliocentric coordinate $U_a = U_h + U_\odot, V_a = V_h + V_G + V_\odot, W_a = W_h + W_\odot$ (where V_G is the Galactic rotation speed, $V_\odot, U_\odot$ and $W_\odot$ are the components of solar motion relative to the local standard of rest) the correction from the local coordinate system can be done via the Galactic angle

$$\alpha = \arctan(\frac{d\sin(l)\cos(b)}{R_\odot - d\cos(l)\cos(b)}) \qquad (8.8)$$

between the line sun-centre to the line star-centre:

$$U = U_a\cos\alpha - V_a\sin\alpha$$
$$V = V_a\cos\alpha + U_a\sin\alpha - V_G \qquad (8.9)$$
$$W = W_a$$

Throughout the paper blank letters U, V, W denote the corrected velocities in a Galactic reference frame, which are useful for assessing kinematics, U_h, V_h, W_h denote the velocities in the rest frame of the Sun and heliocentric coordinates, which are the native setting for exploring kinematic biases.

8.9.4   Sample cleaning

The DR7 calibration sample contains 42841 spectra. The steps for cleaning the sample and the subsequent reduction of numbers are listed in Table 8.1; subsamples used in this work and the plots are set in bold font. However, a considerable fraction of these entries is double, i.e. stars whose spectra have been taken several times, some for observational reasons as to improve the signal to noise, some as they were both listed among the photometric calibration stars and the reddening calibration stars. Therefore it is necessary to clean DR7 samples by identifying any measurements that are within 1.5 arcsec of each other in both right ascension and declination or are within an angular distance of 3 arcsec and have a g band magnitude difference below 0.1 mag. We chose the entry that gives full information on proper motions and the latest measurement in case both contain it. This leaves 33023 unique calibration stars in our DR7 sample. The C10 sample was already cleaned by them and has the 4 kpc distance cut (according to their distances) applied, but not the cut in galactocentric radius (which we do not apply either). Hence the number of unique stars in the C10 sample is only slightly reduced when we demand a cross-match by stellar position on our DR7 table for being less then 2.5 arcsec apart both in right ascension and declination. There are some stars dropping out because of a missing cross-match and there were 52 candidate double entries with identical position in the C10 sample. Among those objects some are ~ 0.3 mag fainter than their second entry and the corresponding entry in DR7. In total we found 41 stars which are ~ 0.3 mag fainter in apparent magnitude than their counterparts in DR7. We checked that none of these differences has a significant impact on the results.

We also removed from the sample the stars with signal to noise ratio $S/N < 10$ and those which are flagged by the SSPP for spectral abnormalities, for colour mismatches or for being a suspected or proven white dwarf, as well as those with particularly unreliable radial velocity measurements or SSPP parameters. We thus cleaned the C10 sample from ~ 1700 flagged stars. Superficial tests did not show any obvious problems caused by those stars. Following C10, we also excluded all stars without determined proper motions and "clean" the sample according to Munn et al. (2004) requiring that both σ_{RA} and $\sigma_{DEC} < 350$ mas, with an additional requirement of those stars to have quoted errors in each proper motion component of < 5 mas yr^{-1}. We checked on the C10 sample that 224 objects in their sample not passing this cut did not cause any noticeable biases. The full cleaning gives a final DR7 sample of 28844 stars, which we will use when plotting "all" stars in DR7. In plots of the full C10 sample we use its counterpart of 21600 stars that already fulfills at their distances the condition of having all distances smaller or equal to 4 kpc.

condition	DR7	Carollo et al. (2010)
original sample entries	42841	—
cleaned sample by C10	—	23647
unique & cross-matched	33023	23553
unflagged	29655	21828
$S/N > 10$	29638	21825
$4500 \leq T_{\mathrm{eff}} \leq 7000$	29601	21823
$[Fe/H]_{DR7}, v_{\parallel}$ fine	29584	21819
prop. motion fine	**28844**[a]	21600
$\log(g) > 4.0$	17365	15023
$\log(g) > 4.1$	13880	12120
$d_{Ivz} < 4\,\mathrm{kpc}, \log(g) > 4.0$	15808	14763
$d_{Ivz} < 4\,\mathrm{kpc}, \log(g) > 4.1$	**12678**[b]	11894
$d_{Car} < 4\,\mathrm{kpc}$	—	**21600**[c]
$d_{Car} < 4\,\mathrm{kpc}, \log(g) > 4.0$	—	**15023**[d]

Table 8.1: Numbers of stars at different cuts in the two samples. The quality cuts are applied cumulatively from the first row until the horizontal line. Below the horizontal line we show selected subsamples with gravity and distance cuts. The cuts down to the quality cut in proper motion are applied successively. Below the horizontal line we show the effects of differnt distance estimations and cuts on the number of remaining stars.
Subsamples used in the paper: [a] "all star sample", [b] "Ivezic dwarfs", [c] Carollo all, [d] Carollo dwarfs.

Chapter 9

The detection and treatment of distance errors in kinematic analyses of stars[1]

9.1 Abstract

We present a new method for detecting and correcting systematic errors in the distances to stars when both proper motions and line-of-sight velocities are available. The method, which is applicable for samples of 200 or more stars that have a significant extension on the sky, exploits correlations between the measured U, V and W velocity components that are introduced by distance errors. We deliver a formalism to describe and interpret the specific imprints of distance errors including spurious velocity correlations and shifts of mean motion in a sample. We take into account correlations introduced by measurement errors, Galactic rotation and changes in the orientation of the velocity ellipsoid with position in the Galaxy. Tests on pseudodata show that the method is more robust and sensitive than traditional approaches to this problem. We investigate approaches to characterising the probability distribution of distance errors, in addition to the mean distance error, which is the main theme of the paper. Stars with the most over-estimated distances bias our estimate of the overall distance scale, leading to the corrected distances being slightly too small. We give a formula that can be used to correct for this effect. We apply the method to samples of stars from the SEGUE survey, exploring optimal gravity cuts, sample contamination, and correcting the used distance relations.

9.2 Introduction

Studies of stellar kinematics in the Milky Way are of enormous importance as they hold the key both to measuring the gravitational field of the Galaxy and to unravelling the Galaxy's history and manner of formation. Consequently considerable resources have been, and are being, devoted to measuring the velocities of stars.

---

[1] The content and text of this chapter are being published in nearly identical form as Schönrich et al. (2011b).

Two different techniques have to be used to measure the three components of velocity with respect to the Sun: the component $v_\parallel$ along the line of sight to the star is measured spectroscopically, while the component $\mathbf{v}_\perp$ transverse to the line of sight is determined by combining the measured proper motion $\bar{}$ with an estimate of the distance s to the star. Over the next decade enormous numbers of distances will be obtained from parallaxes measured by the Gaia satellite, but currently the great majority of distance estimates have been obtained by comparing an estimate of the star's absolute magnitude with its apparent magnitude. This process is liable to systematic error in several ways. Giants can be mistaken for subgiants or even dwarfs of the same colour (or vice versa) and assumed ages severely influence the adopted luminosities in the turn-off region even for well classified stars. Also, the adopted metallicities may be biased as discussed by Lee et al. (2008a) and as demonstrated by the shifts in metallicity scale between Nordström et al. (2004), Holmberg et al. (2007) and Casagrande et al. (2011). An erroneous metallicity will lead to the wrong isochrone being used to infer the luminosity, and an erroneous luminosity and distance will follow. Further problems are that synthetic colours can be wrong (cf. the discussion in Percival & Salaris, 2009) and that stellar-evolution models can predict different luminosities for given metallicity and effective temperatures; there is evidence that they make the main sequences of metal-poor objects too faint (the "helium problem", e.g. discussed in Casagrande et al., 2007). Finally, erroneous extinctions may be adopted. Since the problems just enumerated can readily accumulate to systematic distance biases in excess of 20 per cent, some way of independently calibrating the distance scale is invaluable.

Here we present a method for calibrating distances that exploits correlations between the measured U, V, W components of velocity that are introduced by systematic distance errors, and is applicable to any survey that provides proper motions and line-of-sight velocities over a wide area of the sky.

The idea that the typical distance to objects in a sample can be constrained by proper motions is well known in astronomy – for a useful recent review see Popowski & Gould (1998). The method of secular parallaxes determines the mean parallax of a population by combining proper motions and the known mean motion of the population with respect to the Sun (e.g. Trumpler & Weaver, 1962; Binney & Merrifield, 1998, §2.2.3), while the method of statistical parallaxes estimates the mean parallax by combining proper motions with line-of-sight velocities (e.g. Binney & Merrifield, 1998, §2.2.4). Our method has points in common with both the above methods in that it hinges on comparing proper motions with line-of-sight velocities but also exploits the mean motion of the stars with respect to the Sun. It is much less vulnerable than classical methods to questionable assumptions regarding the shape of the velocity ellipsoid and/or the nature of mean velocity field (see esp. the discussion in Trumpler & Weaver, 1962). By examining the way correlations between components of space velocity vary with position on the sky, we dispense with the need for prior knowledge of the mean velocity field. All we require is knowledge of the formal errors of the observables and, if the sample is sufficiently non-local, reasonable assumptions about the orientation of the velocity ellipsoid at relevant points in the Galaxy.

Section 9.3 lays out the basic theory for the case in which distances are all in error by a common factor. Section 9.4 extends the theory to the realistic case in which distance errors contain a

random component. Section 9.5 applies the method to data from the Sloan surveys. Section 9.6 sums up.

9.3   The mean distance error

We are concerned with the case in which calibration errors in the distance scale cause all distances have a fractional error f, so the assumed distance s' to a star is related to the true distance s by

$$s' = (1+f)s. \tag{9.1}$$

Consequently the assumed tangential velocity $\mathbf{v}'_\perp$ is related to the true tangential velocity $\mathbf{v}_\perp$ by

$$\mathbf{v}'_\perp = (1+f)\mathbf{v}_\perp. \tag{9.2}$$

The velocity component $v_\parallel$ along the line of sight is of course unaffected by distance errors. From $v_\parallel$ and the proper motions $(\mu_b = \dot{b}, \mu_l = \cos b\,\dot{l})$ parallel to each Galactic coordinate we infer the velocity components (U,V,W) in the Cartesian coordinate system in which the Sun is at rest at the origin. In this system the U axis points to the Galactic centre, the V axis points in the direction of Galactic rotation, and the W axis points to the north Galactic pole. The relevant transformation is

$$\begin{pmatrix} U_0 \\ V_0 \\ W_0 \end{pmatrix} = \mathbf{M} \begin{pmatrix} s\mu_b \\ s\mu_l \\ v_\parallel \end{pmatrix}, \tag{9.3}$$

where the orthogonal matrix

$$\mathbf{M} \equiv \begin{pmatrix} -\sin b\cos l & -\sin l & \cos b\cos l \\ -\sin b\sin l & \cos l & \cos b\sin l \\ \cos b & 0 & \sin b \end{pmatrix}. \tag{9.4}$$

The velocity components inferred from distances that have fractional error f are

$$\begin{pmatrix} U \\ V \\ W \end{pmatrix} = \mathbf{M}(\mathbf{I}+f\mathbf{P}) \begin{pmatrix} s\mu_b \\ s\mu_l \\ v_\parallel \end{pmatrix}, \tag{9.5}$$

where $\mathbf{I}$ is the identity matrix and

$$\mathbf{P} \equiv \begin{pmatrix} 1 & 0 & 0 \\ 0 & 1 & 0 \\ 0 & 0 & 0 \end{pmatrix}. \tag{9.6}$$

Table 9.1: Explicit expression for the matrix $\mathbf{T}$ through which distance errors introduce correlations between the apparent components of velocity, and an expression for the relation between the errors in (U, V, W) and in $(\mu, v_\parallel)$.

$$\mathbf{T} = \mathbf{MPM}^T = \begin{pmatrix} 1 - \cos^2 b \cos^2 l & -\frac{1}{2}\cos^2 b \sin 2l & -\frac{1}{2}\sin 2b \cos l \\ -\frac{1}{2}\cos^2 b \sin 2l & 1 - \cos^2 b \sin^2 l & -\frac{1}{2}\sin 2b \sin l \\ -\frac{1}{2}\sin 2b \cos l & -\frac{1}{2}\sin 2b \sin l & \cos^2 b \end{pmatrix}$$

$$\begin{pmatrix} e_U \\ e_V \\ e_W \end{pmatrix} = \mathbf{M}(\mathbf{I} + f\mathbf{P}) \begin{pmatrix} s\varepsilon_b \\ s\varepsilon_l \\ \varepsilon_\parallel \end{pmatrix} = \begin{pmatrix} -\sin b \cos l (1+f)s\varepsilon_b - \sin l (1+f)s\varepsilon_l + \cos b \cos l \varepsilon_\parallel \\ -\sin b \sin l (1+f)s\varepsilon_b + \cos l (1+f)s\varepsilon_l + \cos b \sin l \varepsilon_\parallel \\ \cos b (1+f)s\varepsilon_b + \sin b \varepsilon_\parallel \end{pmatrix}$$

Hence the true and measured Galactocentric components of velocity are related by

$$\begin{pmatrix} U \\ V \\ W \end{pmatrix} = \mathbf{M}(\mathbf{I} + f\mathbf{P})\mathbf{M}^T \begin{pmatrix} U_0 \\ V_0 \\ W_0 \end{pmatrix} = (\mathbf{I} + f\mathbf{T}) \begin{pmatrix} U_0 \\ V_0 \\ W_0 \end{pmatrix}, \tag{9.7}$$

where

$$\mathbf{T} \equiv \mathbf{MPM}^T. \tag{9.8}$$

Table 9.1 gives an explicit expression for $\mathbf{T}$, which has direction-dependent off-diagonal elements. Consequently, when $f \neq 0$ the inferred value of W has linear dependencies on U_0 and V_0 with coefficients that are known functions of Galactic position times f. By detecting these patterns of bias, we can measure the amount f by which distances have been over-estimated.

The phenomenon we exploit can be understood by an example. Consider a star at a Galactic longitude $l = 0$ and latitude $b = 45°$. Suppose the star's only non-zero component of velocity (in the Sun's rest frame) is $U_0 > 0$. This motion generates both a proper motion $\mu_b < 0$ and a line-of-sight velocity $v_\parallel$ away from us. If we over-estimate the star's distance, the tangential velocity, which lies in the (U, W) plane, will be over-estimated, and we will infer a negative value for W instead of zero. By the same token, a star with over-estimated distance that had $U_0 < 0$ would have $W > 0$. In the southern Galactic hemisphere signs reverse and a star with over-estimated distance at $b = -45°$ with $U_0 > 0$ will be wrongly assigned a positive value of W. Hence a systematic tendency to misjudge distances can be detected by looking for correlations between velocity components that vary over the sky in given ways.

The Sun moves in the direction of Galactic rotation faster than the circular speed and all Galactic components are subject to at least some asymmetric drift, so $\langle V_0 \rangle < 0$ for most groups of stars, especially halo stars. Consequently, the clearest signals of an erroneous distance scale are usually correlations between the measured values of U and V and between W and V.

9.3.1   A naive Approach

Equations (9.7) yield

$$\begin{aligned}
U &= (1+fT_{UU})U_0 + fT_{UV}V_0 + fT_{UW}W_0 \\
V &= (1+fT_{VV})V_0 + fT_{VU}U_0 + fT_{VW}W_0 \\
W &= (1+fT_{WW})W_0 + fT_{WU}U_0 + T_{WV}V_0.
\end{aligned} \tag{9.9}$$

Suppose for each hemisphere $b > 0$ and $b < 0$ we bin stars in l and in $V \simeq V_0$. Then for each bin we could average the first and third equations, obtaining for each bin two equations

$$\begin{aligned}
\langle U \rangle &= \langle (1+fT_{UU})U_0 \rangle + f\langle T_{UV}V_0 \rangle + f\langle T_{UW}W_0 \rangle \\
\langle W \rangle &= \langle (1+fT_{WW})W_0 \rangle + f\langle T_{WU}U_0 \rangle + f\langle T_{WV}V_0 \rangle.
\end{aligned} \tag{9.10}$$

We expect the population of stars under study, taken as a whole, to be moving neither radially nor vertically, so at any (b,l) the mean values of U_0 and W_0 should be the reflex of the solar motion, $(U_\odot, W_\odot)$. With this assumption in the U equation we may set

$$\begin{aligned}
\langle (1+fT_{UU})U_0 \rangle &= -(1+f\langle T_{UU} \rangle)U_\odot \\
\langle T_{UW}W_0 \rangle &= -\langle T_{UW} \rangle W_\odot,
\end{aligned} \tag{9.11}$$

and similar relations can be used in the W equation. Finally we make f the only unknown in equations (9.10) by assuming, in a first approximation, that $V_0 = V$. On account of Poisson noise, the sample values of quantities such as $\langle T_{UW}W_0 \rangle$ will differ from our adopted value, $-\langle T_{UW} \rangle W_\odot$, so the equations will not be exactly satisfied, but we can seek the values of f that minimise the quantities

$$\begin{aligned}
S'_U &\equiv \sum_{\text{bins}} \Big[\langle U \rangle + (1+f\langle T_{UU} \rangle)U_\odot \\
&\qquad\qquad -f\langle T_{UV}V \rangle + f\langle T_{UW} \rangle W_\odot \Big]^2 \\
S'_W &\equiv \sum_{\text{bins}} \Big[\langle W \rangle + (1+f\langle T_{WW} \rangle)W_\odot \\
&\qquad\qquad +f\langle T_{WU} \rangle U_\odot - f\langle T_{WV}V \rangle \Big]^2.
\end{aligned} \tag{9.12}$$

After determining the optimum value of f, this value can be used to correct the distances and the velocities derived from them, and a new value of f is then obtained, enabling the distances to be corrected a second time, and so on until convergence has been reached.

The scheme just described is straightforward conceptually and does work, but suffers a significant loss of information from the need to bin the data and to replace the measured values of U and W by $-U_\odot$ and $-W_\odot$. Therefore the results shown in this paper are obtained by a different scheme that is described in the next subsection.

9.3.2 A more effective approach

Our method is based on the principle that the true value of U or W can be decomposed into a mean velocity field of known form with components $\overline{U}$ and $\overline{W}$, plus a random variable δU or δW that has zero mean, so $U_0 = \overline{U} + \delta U$, etc. In this subsection we make the assumption that the mean velocity field may be approximated by the reflex of the solar motion, so $\overline{U} = -U_\odot$ etc. In Section 9.3.5 we will lift this restriction to allow for Galactic rotation. Also we argue that in the second or third terms on the right of equations (9.9) we may replace V_0 by V on the ground that the inferred value is close to the true value and the presence in these terms of an explicit factor f implies that the error made by replacing V_0 by V is $O(f^2)$. The same argument enables us to replace U_0 by U and W_0 by W in these terms. With these replacements the first and third of equations (9.9) become

$$U = -U_\odot + fx + (1 + fT_{UU})\delta U$$
$$W = -W_\odot + fy + (1 + fT_{WW})\delta W, \tag{9.13}$$

where

$$x \equiv -T_{UU}U_\odot + T_{UV}V + T_{UW}W$$
$$y \equiv -T_{WW}W_\odot + T_{WU}U + T_{WV}V. \tag{9.14}$$

We now eliminate reliance on prior knowledge of the solar motion by subtracting from each of equations (9.13) its expectation value, and have

$$U - \langle U \rangle = f(x - \langle x \rangle) + (1 + fT_{UU})\delta U$$
$$W - \langle W \rangle = f(y - \langle y \rangle) + (1 + fT_{WW})\delta W, \tag{9.15}$$

We determine the optimum value of f by forming the sample sums[2]

$$\sum_i [U_i - \langle U \rangle - f(x_i - \langle x \rangle)]x_i = \sum_i (1 + fT_{UUi})\delta U_i x_i \tag{9.16}$$
$$\sum_i [W_i - \langle W \rangle - f(y_i - \langle y \rangle)]y_i = \sum_i (1 + fT_{WWi})\delta W_i y_i.$$

The right side of the first equation would vanish if δU were uncorrelated with x but it *is* correlated because x depends on V and W, which in turn depend on $U_0 = -U_\odot + \delta U$. In fact one easily shows that

$$\langle (1 + fT_{UU})\delta Ux \rangle = f\langle (1 + fT_{UU})(T_{UV}^2 + T_{UW}^2)\delta U^2 \rangle. \tag{9.17}$$

---

[2] The accuracy with which f is determined can be slightly increased by weighting each term in the sums in eqs.(9.16) by the inverse of the expected standard deviation of the noise term or by using Huber-White standard errors (White, 1980).

Table 9.2: Parameters of the mock disc and halo samples used in tests. All velocities are in $\mathrm{km\,s}^{-1}$

Component	σ_U	σ_V	σ_W	$\bar{v}_\phi$
Disc	55	45	35	180
Halo	150	75	75	0

Since we are working to O(f) only, we neglect the second term in the first bracket on the right and use the resulting expression in equation (9.16) to solve for f. We find

$$f = \frac{\mathrm{Cov}(U,x)}{\mathrm{Var}(x) + \langle T_{UV}^2 + T_{UW}^2 \rangle \sigma_U^2},\tag{9.18}$$

where $\sigma_U^2 \equiv \langle \delta U^2 \rangle$ and we have identified sample means with expectation values. Analogously, from the second of equations (9.16) we have

$$f = \frac{\mathrm{Cov}(W,y)}{\mathrm{Var}(y) + \langle T_{WV}^2 + T_{WU}^2 \rangle \sigma_W^2}.\tag{9.19}$$

As with the naive scheme, we proceed iteratively, successively correcting the distances according to the value of f yielded by the current distances, until f becomes negligible. The precise values of the denominators in our expressions for f are not important because we rescale distances until $f \propto \mathrm{Cov}(U,x) = 0$ or $f \propto \mathrm{Cov}(W,y) = 0$. This circumstance is fortunate as only an approximate values of σ_U and σ_W may be available. Note that equations (9.18) and (9.19) make no reference to the solar motion so that in contrast to the secular parallax they require only information about the shape, but not the average value of the mean velocity field.

In the following, when using equation (9.18) we shall call U the "target variable" and x the "explaining variable", while when we use equation (9.19), W will be the target variable and y the explaining variable.

The reader may wonder why we do not obtain a third estimate of f from the V equation of the set (9.9). The problem is that we cannot write $V_0 = -V_\odot + \delta V$ by analogy with our treatment of U and W, because most stellar groups have mean azimuthal velocities smaller than that of the Sun, and in fact the mean azimuthal velocity of a group will vary with location.

The quantities $\sum_i U_i x_i$ and $\sum_i W_i y_i$ implicit in the right sides of equations (9.18) and (9.19) contain cross-terms such as $\sum_i U_i V_i$ and $\sum_i U_i W_i$. As explained above, usually the V cross-terms contain the largest amount of information regarding f, except when V lies near zero, when the W cross-terms provide the strongest constraints on f. W is the target velocity of choice both because it has the lowest velocity dispersion, and because it is least affected by streaming motions, which are largely confined to the UV plane (Dehnen, 1998).
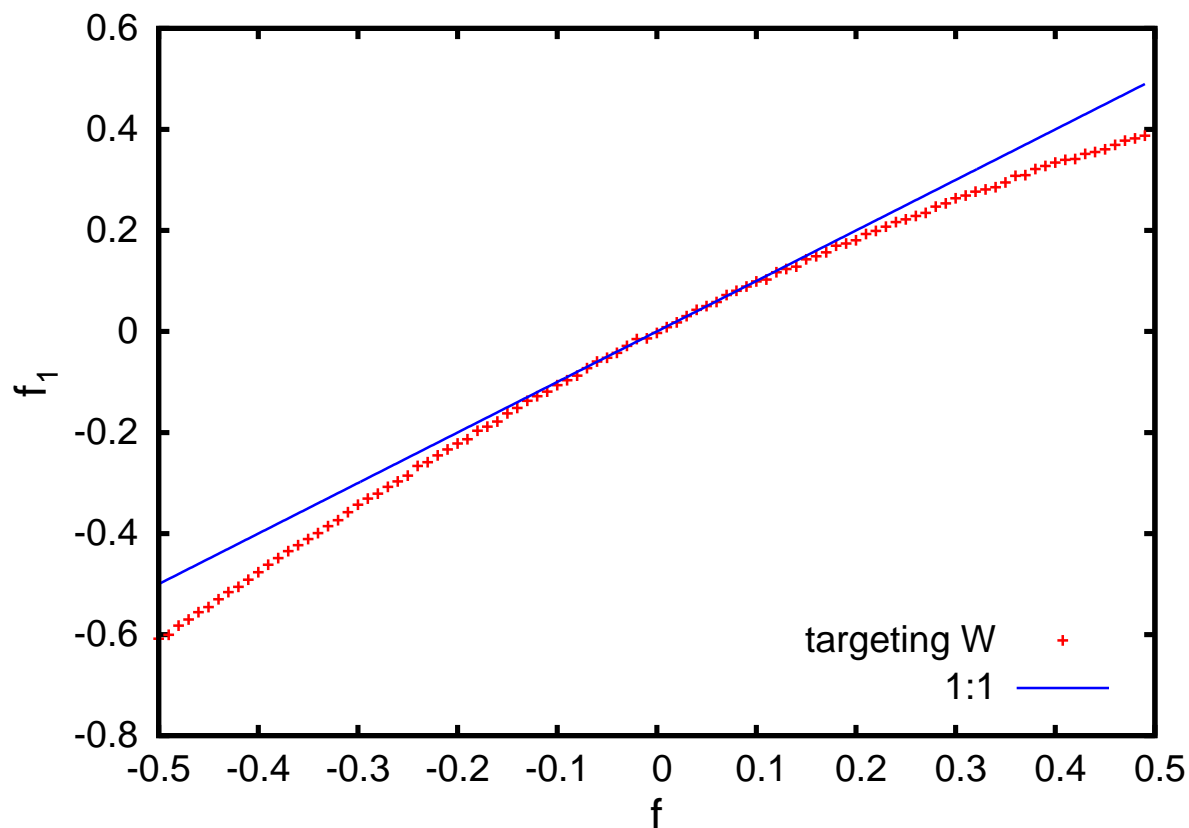
Figure 9.1: Value of the fractional distance error f from equation (9.19) versus value of f bias in a mock sample of $450\,000$ disc and $50\,000$ halo stars. The blue line has unit slope.

9.3.3 Tests

In this section we test the effectiveness of the scheme derived in the last subsection by deriving pseudo-data from a model Galaxy, and analysing them in the presence of systematic distance errors. We have conducted such tests using a model obtained by adding gas and star formation to a halo formed in simulations of the cosmological clustering of collisionless particles. The results of these tests were entirely satisfactory, but we do not report them here for two reasons: (a) considerable space would be required to describe the Galaxy model with sufficient precision and the model is in any case not entirely realistic, and (b) the model provides a rather limited number of particles in the vicinity of the Sun, so the statistical precision of the tests is inferior to that of the tests we will present. These use data obtained from a Galaxy model that is highly idealised, but which has the flexibility to produce data that include or exclude whatever features in the data might affect the performance of our method.

Our idealised Galaxy model has a non-rotating halo and a rotating disc. The velocity ellipsoids of both components are triaxial Gaussians: Table 9.2 gives the values of the dispersions. The

mean rotation velocity of the disc is taken to be $180\,\mathrm{km\,s^{-1}}$ and the circular speed is $220\,\mathrm{km\,s^{-1}}$. The sampled stars are distributed uniformly in distance between $0.5\,\mathrm{kpc}$ and $4\,\mathrm{kpc}$, and uniformly in Galactic longitude and latitude, which gives the sample a strong poleward bias that resembles the bias encountered in real samples better than an isotropically distributed sample would. The solar motion is in addition offset by the local standard of rest velocity vector as determined by Schönrich, Binney & Dehnen (2010).

The crosses in Fig. 9.1 show the value of f recovered from equation (9.19) on the first iteration, f_1, versus the preset fractional distance over-estimate f applied to the sample. Each cross shows an independent realisation of the pseudodata, which contained $450\,000$ disc and $50\,000$ halo stars. The crosses fall on a curve that passes through $(0,0)$ as we would hope. The straight line through the origin with unit slope is also plotted and we see that for $|f| \lesssim 0.2$ the slope of the curve is close to unity, so convergence of the iterative procedure is rapid. However, the key point is that the curve passes through the origin and has no point of inflection. So long as these conditions are satisfied, the iterative scheme will converge on the correct distance scale regardless of the slope or curvature of the curve.

Fig. 9.2 demonstrates that the method works well even in the absence of solar motion by showing results analogous to those of Fig. 9.1 for a sample of stars that has no net motion with respect to the Sun and an isotropic velocity distribution around the solar motion, i.e. without any systematic offset. The minor difference between the estimators on U and W derives from second-order effects in f by the polewards bias in the sample geometry. Note that a simple linear regression of W on y from equation (9.13) would give the right zero point and so finally an unbiased distance estimate, but due to the lack of correction factors to the denominator $\mathrm{Var}(x)$ would give a slope that is a factor 2 too large and hence a bad convergence behaviour in the iteration.

9.3.4 Impact of random errors

We now consider the impact on our technique of random measurement errors. If we measured U, V and W directly, random errors would have no impact because they would simply inflate the scatter in these variables that is inherent in stars having random velocities. Unfortunately, we do not measure U,V,W directly but calculate them from the measured values of μ_b, μ_l and $v_{\parallel}$. Consequently the error in say μ_l introduces correlated errors into both U and V. Since our technique consists precisely in attributing correlations between U and x (which depends on V) to a non-zero value of f, we must consider the contribution of the errors to the correlations between U and x or W and y if we are to estimate f correctly.

Our key assumption is that the errors in $\mu_b\,\mu_l$ and $v_{\parallel}$ are statistically independent, have vanishing mean, and have finite and approximately known variances. Let $\varepsilon_b, \varepsilon_l, \varepsilon_{\parallel}$ be the errors in the proper motions and line-of-sight velocity. Then the random errors in U,V,W are

$$\begin{pmatrix} e_U \\ e_V \\ e_W \end{pmatrix} = \mathbf{M}(\mathbf{I}+f\mathbf{P}) \begin{pmatrix} s\varepsilon_b \\ s\varepsilon_l \\ \varepsilon_{\parallel} \end{pmatrix}. \tag{9.20}$$
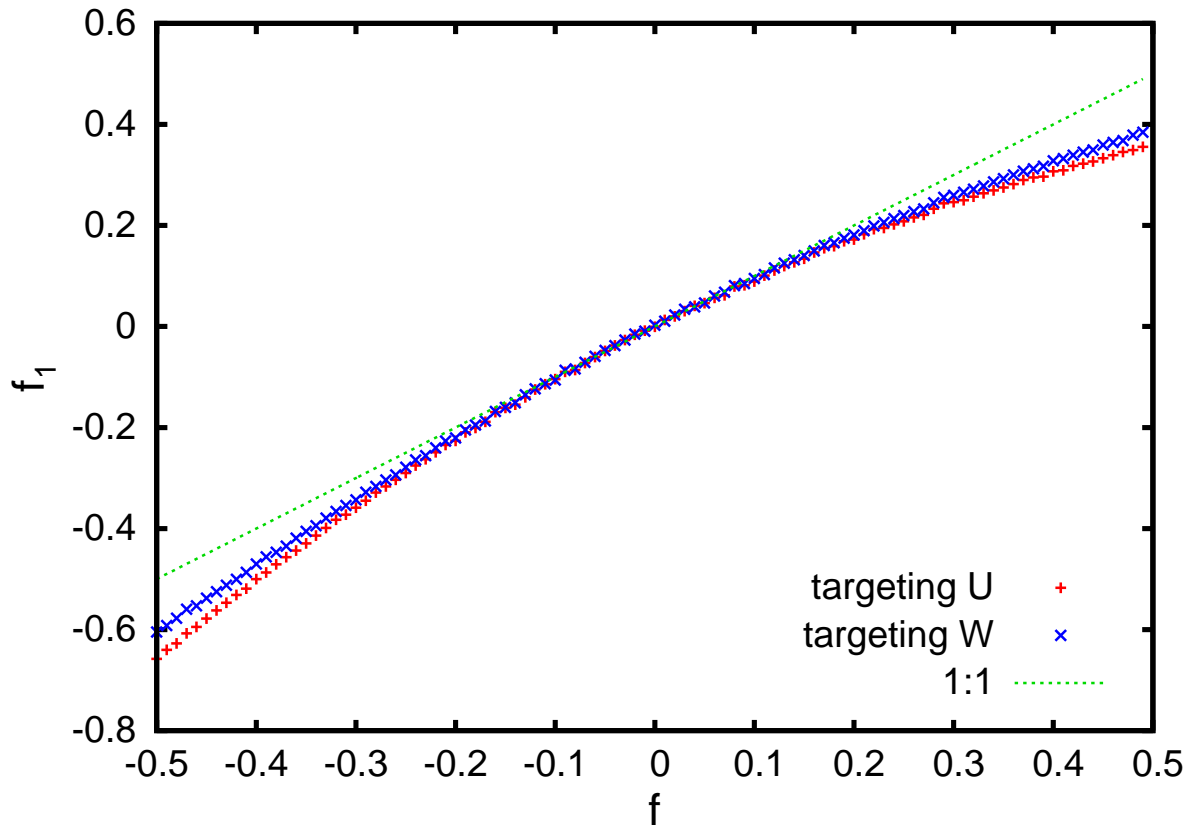
Figure 9.2: Value of the fractional distance error f from equation (9.18) or (9.19) versus the input value of f for samples of 500 000 stars with an isotropic velocity distribution and no solar motion. The line of unit slope is also shown.

Table 9.1 gives an explicit expression for the right side of this equation.

Consider now the correlation, between a target variable, say W, and the explaining variable y. Let $W = W' + e_W$ and $y = y' + e_y$, where the primed variables are the components without the error and e_W, e_y are their errors derived from equation (9.20)

$$\langle Wy \rangle = \langle W'y' \rangle + \langle e_W e_y \rangle + \langle W'e_y \rangle + \langle e_W y' \rangle. \tag{9.21}$$

Given that the errors are unbiased, the correlations such as $\langle W'e_y \rangle$ between the true velocities and the errors vanish. Consequently the changes in f that the errors introduce through equation (9.19) is

$$e_f = \frac{\langle e_W e_y \rangle}{\langle y^2 \rangle + \langle T_{WU}^2 + T_{WV}^2 \rangle \sigma_W^2}$$

$$- f \frac{\langle e_y^2 \rangle}{\langle y^2 \rangle + \langle T_{WU}^2 + T_{WV}^2 \rangle \sigma_W^2}. \tag{9.22}$$
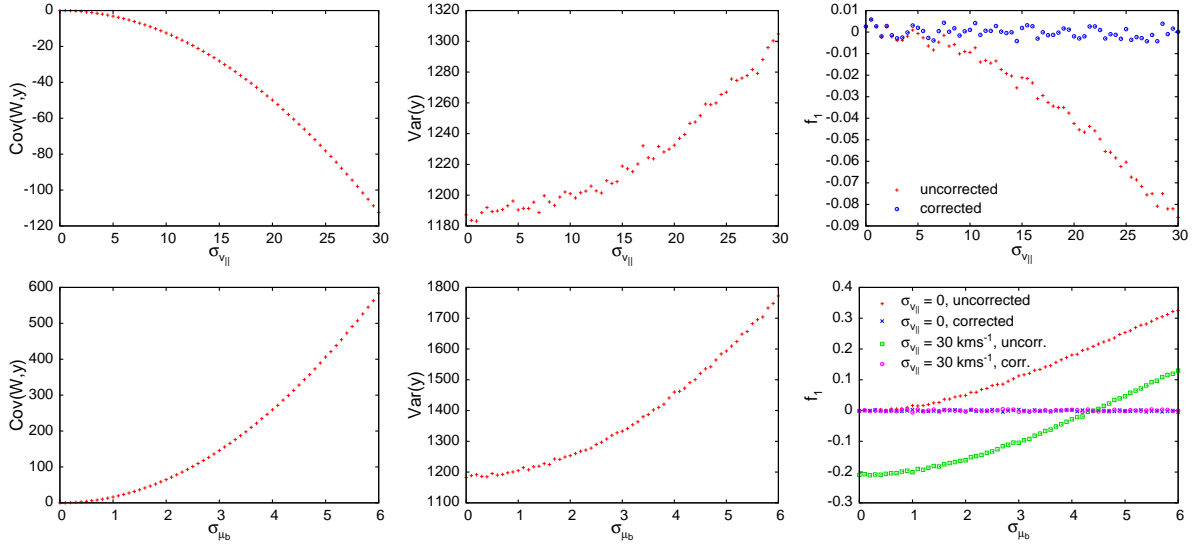
Figure 9.3: Tests of the effects of random measurement errors in a mock sample of $500\,000$ stars, among which are $50\,000$ halo stars. The left and centre panels show how the values of $\text{Cov}(W, y)$ and $\text{Var}(y)$ are affected by measurement errors, while the right panels show the values of f_1 using equation(9.19) with and without the correction terms for these samples. In the upper row the proper motions are error free and the horizontal axis gives the error in $v_\parallel$, while in the lower panel $v_\parallel$ is error free (red and green crosses) and the horizontal axis gives the error in proper motions. In the bottom right panel we added the case of a fixed radial velocity error of $30\,\text{km}\,\text{s}^{-1}$ (green squares and purple circles) to demonstrate the simple superposition of the error correlation terms on the covariance.

The second term on the right side is smaller than the first, and as we iterate towards $f = 0$ it vanishes altogether. Hence we neglect it. With this term neglected, we can obtain the error-corrected value of f simply by subtracting $\langle e_W e_y \rangle$ from the measured value of $\langle Wy \rangle$ before inserting its value into equation (9.19).

We now calculate the error-error correlations. We have from equations (9.14)

$$\langle e_U e_x \rangle = T_{UV} \langle e_U e_V \rangle + T_{UW} \langle e_U e_W \rangle$$
$$\langle e_W e_y \rangle = T_{WU} \langle e_W e_U \rangle + T_{WV} \langle e_W e_V \rangle. \tag{9.23}$$

When we use Table 9.1 to express the errors in terms of the (uncorrelated) errors in the observables, we find

$$\langle e_U e_V \rangle = \tfrac{1}{2} \sin 2l [(1+f)^2 s^2 (\sin^2 b \varepsilon_b^2 - \varepsilon_l^2) + \cos^2 b \varepsilon_\parallel^2]$$
$$\langle e_U e_W \rangle = -\tfrac{1}{2} \sin 2b \cos l [(1+f)^2 s^2 \varepsilon_b^2 - \varepsilon_\parallel^2] \tag{9.24}$$
$$\langle e_W e_V \rangle = -\tfrac{1}{2} \sin 2b \sin l [(1+f)^2 s^2 \varepsilon_b^2 - \varepsilon_\parallel^2].$$

From the definition of f we see that these terms exclusively depend on the measured distance $s' = (1+f)s$, so we can correct for proper-motion errors before determining f. Finally using the explicit form of $\mathbf{T}$ from Table 9.1 we obtain our correction terms:

$$\langle e_U e_x \rangle = -\tfrac{1}{4}\{\cos^2 b \sin^2 2l \,[(s'^2(\sin^2 b \varepsilon_b^2 - \varepsilon_l^2) + \cos^2 b \varepsilon_\parallel^2]$$
$$\qquad - \sin^2 2b \cos^2 l \,[s'^2 \varepsilon_b^2 - \varepsilon_\parallel^2])\} \qquad (9.25)$$
$$\langle e_W e_y \rangle = \tfrac{1}{4}\sin^2 2b \{s'^2 \varepsilon_b^2 - \varepsilon_\parallel^2\}.$$

The left panels in Fig. 9.3 show $\langle e_W e_y \rangle$ as a function of the errors in the line-of-sight velocities (upper panel) and the errors in proper motions (lower panel). (In the upper panels the proper-motion data are error-free, while in the lower panels the line-of-sight velocities are error-free.) All points are determined from realisations of a Monte-Carlo sample of 450 000 disc stars and 50 000 halo stars sampled from the model described by Table 9.2. The agreement between the analytic formula and the Monte-Carlo results is perfect. On account of the large distances of most of the stars, the proper-motion errors produce substantially greater values of $\langle e_W e_y \rangle$ than do the errors in $v_\parallel$ (which will be negligible for most present-day samples). The right panels of Fig. 9.3 show the shifts in f_1 (red crosses) that arise from the correlations plotted on the left. The uncorrected values of f_1 exhibit a quadratic behaviour for small errors as can be expected from equation (9.25), while for larger errors growth in the denominator on the right of equation (9.19) abates the growth in $|f_1|$. The blue crosses show the values for f_1 obtained when we correct our estimate according to equation (9.25). The green squares in the bottom right panel depict the case when we vary σ_{μ_b} at a fixed line-of-sight velocity error $\sigma_{v_\parallel} = 30\,\mathrm{km\,s}^{-1}$. This demonstrates that the error effects can be added linearly and our formalism gives a perfect account of them (purple circles). We also checked that as predicted σ_{μ_l} does not affect our distance estimate when targeting W.

The largest uncertainty in the corrections given by equations (9.25) lies in the assessment of the measurement errors. The model data used above include remote disc stars, which have errors that are larger than will often be encountered in practice. So this test suggests that it should be possible to correct for the effects of measurement errors in most samples.

9.3.5 Rotation of the velocity ellipsoid

Regardless of a star's location, we have been decomposing its velocity into Cartesian components in the frame that is aligned with the Sun-centre line. Since this frame is not aligned with the principal axes of the velocity ellipsoid at the location of a distant star, we anticipate non-vanishing values of $\langle UV \rangle$, etc., even in the absence of distance errors. We now address this issue.

Let the components of velocity of any star along the principal axes of its local velocity ellipsoid be (U_g, V_g, W_g). Then with the angles α and β defined as shown in Fig. 9.4, the angle α between the projection onto the plane of the velocity ellipsoid's long axis and the Sun-centre line is given
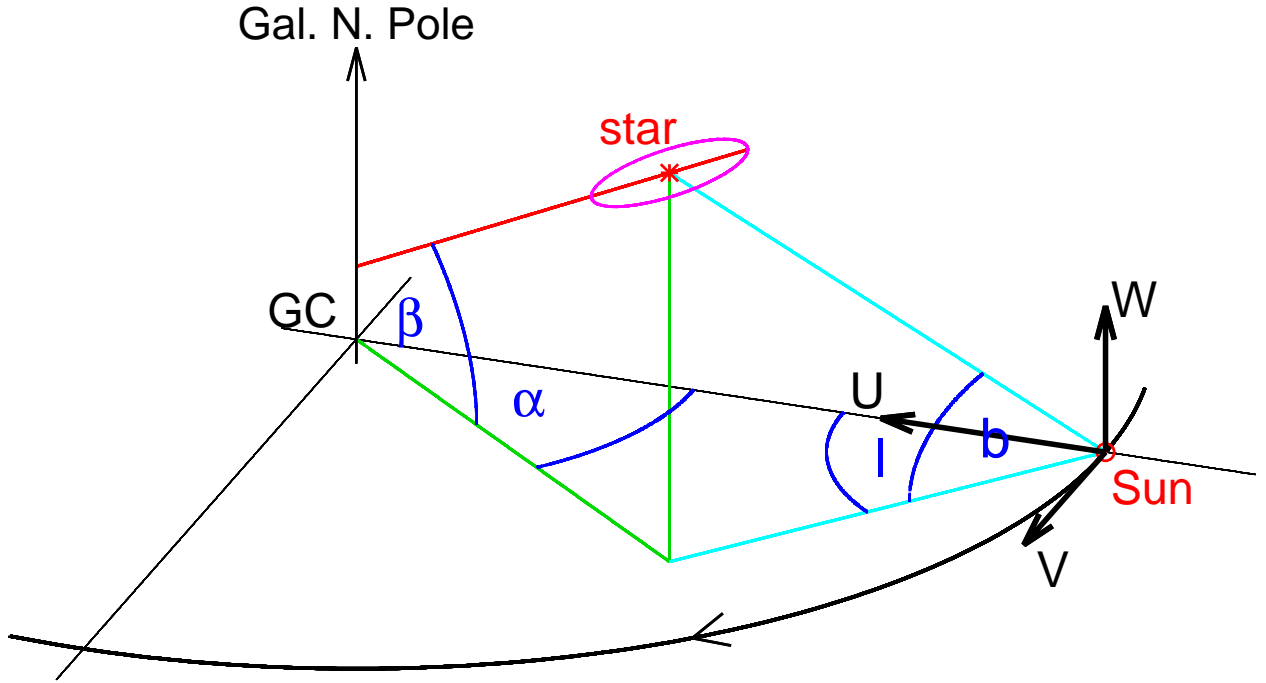
Figure 9.4: The definition of Galactic coordinates, heliocentric velocities and the angles α and β. GC signifies the Galactic Centre. The purple ellipse depicts the direction of the radially oriented main axis of the velocity ellipsoid (along U_g), which defines β.

by

$$\alpha = \arctan\left(\frac{s\sin l\cos b}{R_0 - s\cos l\cos b}\right), \tag{9.26}$$

and the heliocentric velocity components (U,V,W) are given by

$$\begin{pmatrix} U + U_\odot \\ V + V_\odot \\ W + W_\odot \end{pmatrix} = \mathbf{R}(\alpha,\beta) \begin{pmatrix} U_\mathrm{g} \\ V_\mathrm{g} \\ W_\mathrm{g} \end{pmatrix}, \tag{9.27}$$

where

$$\mathbf{R}(\alpha,\beta) \equiv \begin{pmatrix} \cos\alpha\cos\beta & \sin\alpha & \cos\alpha\sin\beta \\ -\sin\alpha\cos\beta & \cos\alpha & -\sin\alpha\sin\beta \\ -\sin\beta & 0 & \cos\beta \end{pmatrix}. \tag{9.28}$$

Both observation (Siebert et al., 2011) and theory (Binney & McMillan, 2011) suggest that α and β will take values close to the Galactocentric azimuth ϕ and latitude $\frac{1}{2}\pi - \theta$ of the location in question. In our tests we will assume that these relations are exact.

Correlations from mean streaming

A major contribution to the velocity components U and V comes from the azimuthal streaming of stars, which we take to have magnitude $\bar{v}_\phi(R,z)$. This motion invalidates our assumption above that $U = -U_\odot + \delta U$. Instead we now have $U = -U_\odot + \overline{U} + \delta U$, where $\overline{U}$ is the U component of the velocity field given by $\bar{v}_\phi$ at the star's location. Specifically we have

$$\overline{U}(s,l,b) = \bar{v}_\phi \sin\alpha, \tag{9.29}$$

where there is dependence on (s,l,b) both through α and through the (generally unknown) dependence of $\bar{v}_\phi$ on (R,z). Unfortunately, both T_{UV} and $\overline{U}$ are odd functions of l, so correlations contributed by distance errors can be interpreted as due to differential rotation and vice versa. On account of this fact, W, to which $\bar{v}_\phi$ does not contribute, is a more useful target velocity than U. However, it is nonetheless worthwhile to consider how U can be targeted. The first of equations (9.13) now becomes

$$U = -U_\odot + \bar{v}_\phi \sin\alpha + fx' + (1 + fT_{UU})\delta U. \tag{9.30}$$

To determine f from these equations we assume that

$$\bar{v}_\phi = \Theta g(R,z), \tag{9.31}$$

where $g(R,z)$ is a function that describes the way in which $\bar{v}_\phi$ varies with position and $\Theta \equiv \bar{v}_\phi(R_0,0)$ is the local streaming velocity of the population under study. In the simplest case we assume that g has no dependence on R, and we estimate its dependence on z from the data, using the current distance scale. Once g has been chosen, and a preliminary value for Θ adopted, we can determine the value of x for each star. We primed x in equation (9.30) because x contains the mean motion in U, so we have to split off the rotation term:

$$x' = x + T_{UU}\Theta g(R,z)\sin\alpha. \tag{9.32}$$

The distance error f causes the measured α' to deviate from the true value α, but we can correct for this effect by Taylor-expanding $\alpha'(f)$:

$$\sin\alpha = \sin\alpha' - f\cos^3\alpha' \frac{s'R_0 \sin l \cos b}{(R_0 - s'\cos l \cos b)^2} + \mathrm{O}(f^2). \tag{9.33}$$

Then

$$U = -U_\odot + \Theta\rho + fx + f\Theta k + (1 + fT_{UU})\delta U, \tag{9.34}$$

where

$$\rho \equiv g(R,z)\sin\alpha'$$

$$k \equiv T_{UU}\rho + \cos^3\alpha' \frac{s'R_0\sin l\cos b}{(R_0 - s'\cos l\cos b)^2}. \tag{9.35}$$

Now we can proceed identically to the derivation of equation (9.18): we first subtract from equation (9.34) its expectation value to obtain

$$U - \langle U\rangle - \Theta(\rho - \langle\rho\rangle) - f(x - \langle x\rangle)$$
$$- f\Theta(k - \langle k\rangle) = (1 + fT_{UU})\delta U, \tag{9.36}$$

and then we multiply x_i and ρ_i and sum over our sample. Introducing the abbreviation $s_{a,b} \equiv \mathrm{Cov}(a,b)$, this gives two equations for the unknowns f and Θ:

$$s_{Ux} - \Theta s_{\rho x} - f s_{xx} - \Theta f s_{kx} = f\langle T_{UV}^2 + T_{UW}^2\rangle\sigma_U^2$$
$$s_{U\rho} - \Theta s_{\rho\rho} - f s_{\rho x} - \Theta f s_{k\rho} = 0 \tag{9.37}$$

Inserting Θ from the second equation into the first and dropping all terms of order f^2 we obtain our estimator

$$f = \frac{s_{Ux}s_{\rho\rho} - s_{\rho x}s_{U\rho}}{s_{xx}s_{\rho\rho} - s_{\rho x}^2 + s_{kx}s_{U\rho} - s_{Ux}s_{k\rho} + t^2\sigma_U^2 s_{\rho\rho}} \tag{9.38}$$

where $t^2 \equiv \langle T_{UV}^2 + T_{UW}^2\rangle$. For a quick calculation the third and fourth term in the denominator can be neglected as they are in general small and only affect the slope. Again we solve these equations iteratively, at each iteration updating the distances and recalculating for each star x, α and g.

Correlations from random velocities

In the heliocentric frame the random component $\delta U \equiv U_0 + U_\odot - \overline{U}$ is correlated with $\delta V \equiv V_0 + V_\odot - \overline{V}$ because the velocity ellipsoid at the star's location is not aligned with that at the Sun's location, so the rotation matrix $\mathbf{R}(\alpha,\beta)$ of equation (9.28) is non-trivial. Consequently, when we calculate $\langle UT_{UV}V\rangle$ in the course of evaluating $\langle Ux\rangle$, the correlation will be larger than the one we want by $\langle\delta UT_{UV}\delta V\rangle$. We now determine the magnitude of this correlation so we can subtract it from the correlations we obtain from the data prior to determining f. Bearing in mind that $\langle\delta U_\mathrm{g}\delta V_\mathrm{g}\rangle = 0$, we have

$$\langle\delta UT_{UV}\delta V\rangle = \langle(\delta U_\mathrm{g}\cos\alpha\cos\beta + \delta V_\mathrm{g}\sin\alpha + \delta W_\mathrm{g}\cos\alpha\sin\beta)$$
$$\times T_{UV}(-\delta U_\mathrm{g}\sin\alpha\cos\beta + \delta V_\mathrm{g}\cos\alpha - \delta W_\mathrm{g}\sin\alpha\sin\beta)\rangle \tag{9.39}$$
$$= \tfrac{1}{4}\langle\cos^2 b\sin 2l\sin 2\alpha(\cos^2\beta\sigma_U^2 - \sigma_V^2 + \sin^2\beta\sigma_W^2)\rangle$$

Similar calculations yield the additional correlations

$$\langle\delta UT_{UW}\delta W\rangle = \tfrac{1}{4}\langle\sin 2\beta\sin 2b\cos l\cos\alpha(\sigma_U^2 - \sigma_W^2)\rangle \tag{9.40}$$
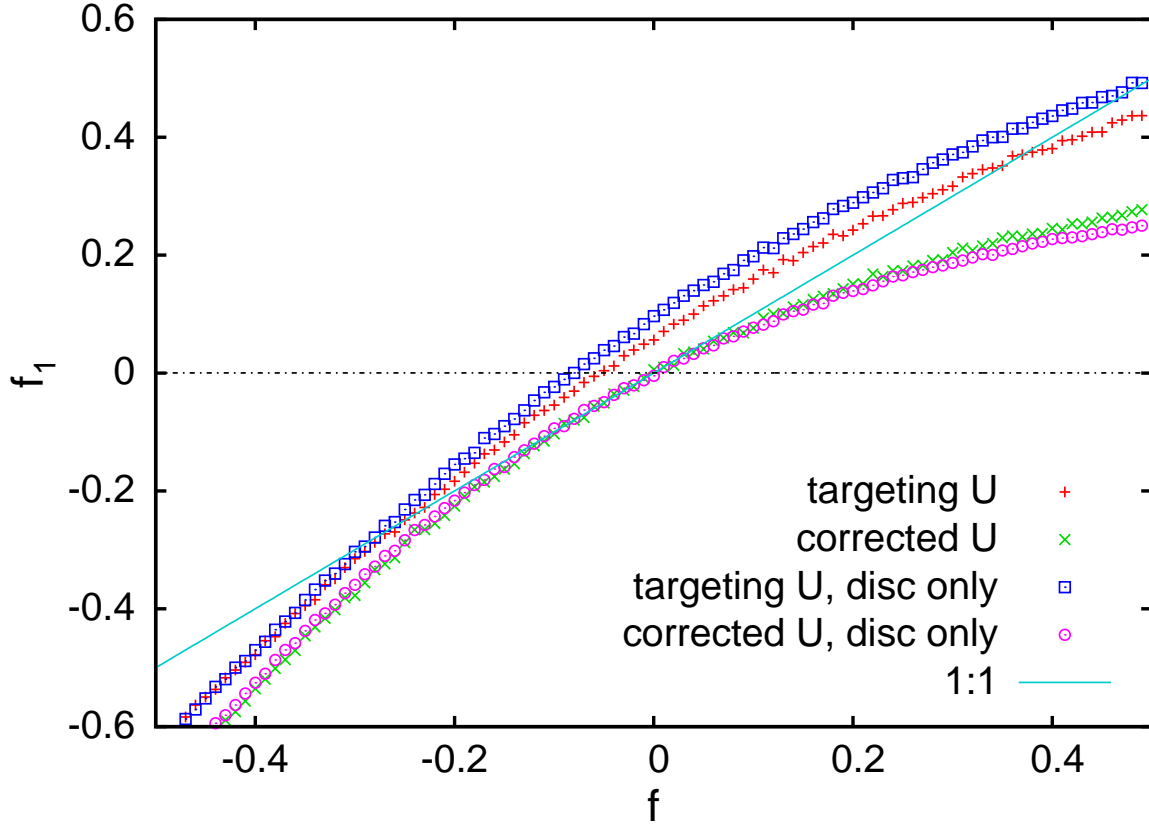
Figure 9.5: The effect of including the corrections for rotation of the velocity ellipsoid. Two samples are used: one has just 500 000 disc stars and the another has 450 000 disc plus 50 000 halo stars. Both samples are strongly affected by rotation of the velocity ellipsoid, yet the correction successfully shifts the points so they pass through the origin. As expected, the sample with a halo contribution is less strongly affected.

and

$$\langle \delta V T_{VW} \delta W \rangle = \tfrac{1}{4} \langle \sin 2b \sin l \sin \alpha \sin 2\beta (\sigma_W^2 - \sigma_U^2) \rangle \tag{9.41}$$

The red and blue points in Fig. 9.5 show what happens if one ignores the impact of azimuthal streaming and rotation of the velocity ellipsoids when determining f by plotting on the vertical axis the value of f that is recovered from equation (9.18) against the input value of f. The red points do not pass through the origin, so the estimated value of f is non-zero even when the distances are, in fact, correct. The green and blue points show that when the formulae above are used to subtract the contributions to the measured correlations from velocity-ellipsoid rotation, the points pass through the origin as we require. The mock data used in these tests consisted of 450 000 disc stars and 50 000 stars belonging to a non-rotating halo in one case and a pure disc sample of 500000 objects in the other case. For one test case only the disc stars were used, while

all the stars were used in the other case.

9.3.6 Components with extreme velocities

Samples of halo stars generally have large mean V velocities relative to the Sun. So long as we are confident that the sample means of U_0 and W_0 are far smaller than that of V, we can greatly simplify the analysis of the sample. While some samples of high-velocity stars may show a degree of radial streaming on account of the Hercules star stream, the only indication of streaming in the vertical direction is a very small correlation between V and W that was detected in the Hipparcos proper motions by Dehnen (1998), and interpreted by him as the signature of the Galactic warp. We proceed under the assumption that $\langle U_0 \rangle = -U_\odot$ and $\langle W_0 \rangle = -W_\odot$.

At each point on the sky we imagine taking the sample mean of the third of equations (9.9) to obtain

$$\langle W \rangle + (1 + f T_{WW}) W_\odot + f T_{WU} U_\odot = f T_{WV} \langle V_0 \rangle \tag{9.42}$$

On the left we neglect terms of order f and redetermine f as the value which gives the least-squares fit between the functions of sky coordinates $\langle W \rangle + W_\odot$ and $T_{WV} \langle V_0 \rangle \simeq T_{WV} \langle V \rangle$. The formal error in the recovered value is

$$\varepsilon_f = \frac{1}{\sqrt{N}} \frac{\sigma_W}{\langle V \rangle \sigma_{T_{WV}}}, \tag{9.43}$$

where N is the number of bins on the sky. For a typical sample $\sigma_{T_{WV}} \sim 0.2$, and for halo stars we have $\langle V \rangle \sim 250\,\mathrm{km\,s^{-1}}$ and $\sigma_W \sim 100\,\mathrm{km\,s^{-1}}$, so $\varepsilon_f \sim 2/\sqrt{N}$, which gives an error in f $\varepsilon_f \simeq 6.3\%$ for a sample of 1000 objects. We can reduce this error by using the corresponding equation for $\langle U \rangle$ – the reduction is by a factor slightly smaller than $\sqrt{2}$ because $\sigma_U > \sigma_W$.

If initially our distance scale is significantly in error, our first values of $\langle V \rangle$ will be wrong. The magnitude of the problem is given by the first term on the right of the second of equations (9.9):

$$\langle V_0 \rangle \simeq \frac{\langle V \rangle}{1 + f \langle T_{VV} \rangle}, \tag{9.44}$$

where the angle brackets around T_{VV} imply the average over the surveyed region of the sky. Eliminating $\langle V_0 \rangle$ between equations (9.42) and (9.44), we obtain

$$\langle W \rangle + W_\odot \simeq \frac{f}{1 + f \langle T_{VV} \rangle} T_{WV} \langle V \rangle. \tag{9.45}$$

It is now straightforward to determine f from the mean slope x of the correlation between $\langle W \rangle + W_\odot$ and $T_{WV} \langle V \rangle$:

$$f = \frac{x}{1 - x \langle T_{VV} \rangle}. \tag{9.46}$$
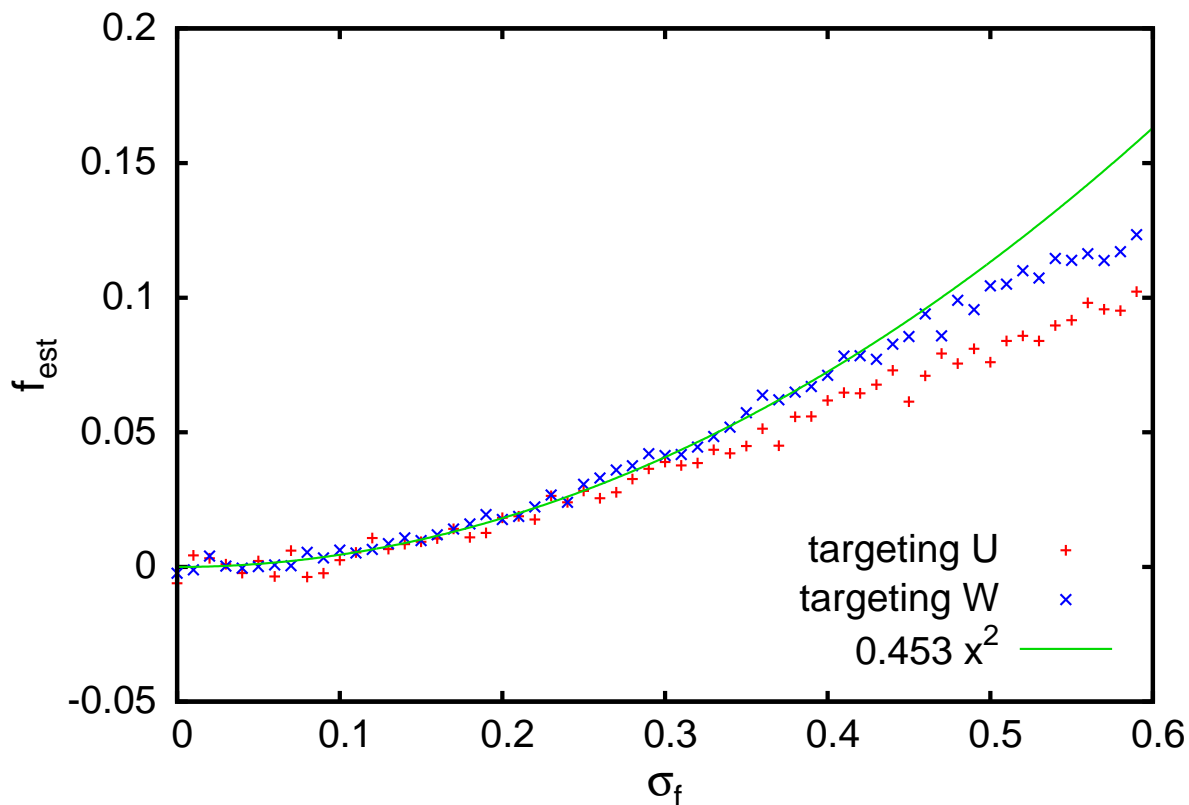
Figure 9.6: The effect of an unbiased Gaussian distribution of distance errors in a sample of 450 000 disc and 50 000 halo stars. For comparison we plot the fits via U and W for the corrected fitting formulae. At larger standard errors of the distances, the average distance estimate diverges quadratically. For W we show the fitting line $0.453\sigma_f^2$ obtained for $0.0 < \sigma_f < 0.4$. Beyond this point the error loses Gaussianity because we have to cut the Gaussian distribution in order to avoid negative distances.

This simple-minded approach to the determination of f uses the available information less efficiently than the technique described in Section 9.3.2, but it is a good way of detecting a systematic distance error and its sign prior to iteratively correcting the distance scale. This is the approach that led Schönrich, Asplund & Casagrande (2011a) to suggest that the distances to low-metallicity stars in the SEGUE dataset were being systematically over-estimated.

9.4 Scatter in the distance errors

To this point we have assumed that the distances to all stars contain the same fractional error, f. In reality any systematic offset will be combined with random scatter, and we now consider

whether in these circumstances the factor f that we recover from the whole population will equal the average of the f factors of the stars. In other words, does our procedure provide an unbiased estimate of f?

9.4.1   The bias in f

In fact it is not hard to see from equation (9.18) that we must anticipate a tendency to over-estimate the mean value of f: stars with $f > 0$ will be ascribed the largest velocities and will thus tend to dominate the sums implicit in $\langle Wy \rangle$ and $\langle y^2 \rangle$. From the perspective that equations (9.13) describe linear relations between U and x or W and y, stars with over-estimated distances will dominate the ends of the line and influence more strongly our estimate of the line's slope f than stars with under-estimated distances, which will cluster near the middle of the line.

Fig. 9.6 shows this effect in samples of 450 000 disc and 50 000 halo stars in which the input distances have errors f that have zero mean but the dispersion σ_f that is given by the horizontal axis. The vertical axis gives the recovered value of f. To both cases we apply the corrections described in subsections 9.3.4 and 9.3.5. The expected tendency for f to be over-estimated in the presence of significant scatter in the input f values manifests itself in the parabolic shape of the curves formed by the corrected results.

We can recover this behaviour analytically as follows. We assume that the stars with a given fractional distance error f' occur everywhere on the sky, so we can form the sky-average $\langle Wy \rangle_{f'}$ over just this group of stars. Defining

$$n^2 \equiv (T_{WV}^2 + T_{WU}^2)\sigma_W^2, \tag{9.47}$$

the inferred fractional distance error of the population is

$$
\begin{aligned}
f &= \frac{\int df' P_f(f') \langle Wy \rangle_{f'}}{\int df' P_f(f') \langle y^2 + n^2 \rangle_{f'}} \\
&= \frac{\int df' P_f(f') f' \langle y^2 \rangle_{f'}}{\int df' P_f(f') \langle y^2 + n^2 \rangle_{f'}},
\end{aligned}
\tag{9.48}
$$

where $P_f(f')$ is the probability density function (pdf) of f'. Now we we decompose $\langle y^2 \rangle$ into the part $\langle y^2 \rangle_\perp$ that derives from tangential velocities and the part $\langle y^2 \rangle_\parallel$ that derives from line-of-sight velocities. Since the inferred tangential velocities scale like $1 + f$ we then have

$$f = \frac{\int df' P_f(f') f' [(1+f')^2 \langle y^2 \rangle_{f'\perp} + \langle y^2 \rangle_{f'\parallel}]}{\int df' P_f(f') [(1+f')^2 \langle y^2 + n^2 \rangle_{f'\perp} + \langle y^2 + n^2 \rangle_{f'\parallel}]} \tag{9.49}$$

Setting $P_f \propto e^{-f^2/2\sigma_f^2}$ and neglecting the variation of $\langle y^2 \rangle_{f'}$ with f', this yields

$$f \simeq \frac{2\sigma_f^2}{1 + \sigma_f^2 + \langle n^2 \rangle_\perp / \langle y^2 \rangle_\perp + \langle y^2 + n^2 \rangle_\parallel / \langle y^2 \rangle_\perp}. \tag{9.50}$$

The parabolic variation of the recovered value of f with the width σ_f of the scatter in individual f-values is now manifest.

Actually, the assumption above of a Gaussian distribution of fractional distance errors is not fully realistic. In fact, the $P_f(f)$ has a long tail at $f > 0$. Stars in this tail will have seriously over-estimated tangential velocities, and Schönrich, Asplund & Casagrande (2011a) argue that as a consequence a halo sample that in reality has no net rotation can be interpreted as consisting of two populations, one of which is counter-rotating.

9.4.2 The second moment of the error distribution

We can obtain information about the breadth of the distribution of distance errors in an approach largely similar to the classical statistic parallax: we compare the square of the speed v with the squares of the line-of-sight velocity $v_\parallel$. For the measurement of the ith star, we have

$$v_i^2 = v_{\parallel,i}^2 + F_i^2 v_{\perp,i,0}^2, \tag{9.51}$$

where $F_i \equiv 1 + f_i$. Summing over the N stars in the sample, we obtain

$$
\begin{aligned}
\frac{\overline{v^2}}{\overline{v_\parallel^2}} &= 1 + \frac{\sum F_i^2 v_{\perp,i0}^2}{N\overline{v_\parallel^2}} \\
&= 1 + \frac{\overline{F^2}\sum v_{\perp,i0}^2 + \sum(F_i^2 - \overline{F^2})v_{\perp,i0}^2}{N\overline{v_\parallel^2}} \\
&= 1 + \overline{F^2}\frac{\overline{v_{\perp0}^2}}{\overline{v_\parallel^2}} + \frac{1}{\overline{v_\parallel^2}}\mathrm{Cov}\left(F^2, \overline{v_{\perp0}^2}\right).
\end{aligned}
\tag{9.52}
$$

If the distance errors are statistically independent of velocities, the covariance vanishes. Further, if either the velocity distribution is isotropic or the sample is uniformly distributed on the sky so $v_\perp$ and $v_\parallel$ sample equally all three principal axes of the velocity ellipsoid, then $\overline{v_{\perp0}^2} = 2\overline{v_\parallel^2}$ and equation (9.52) yields

$$\overline{F^2} = \tfrac{1}{2}\left(\frac{\overline{v^2}}{\overline{v_\parallel^2}} - 1\right) \qquad \text{(isotropy)}. \tag{9.53}$$

If the velocity distribution is anisotropic and the sky coverage is non-uniform, this formula will under-estimate $\overline{F^2}$ when the sample points towards the longest axis of the velocity ellipsoid and over-estimate it in the contrary case.

Classical statistical parallaxes are obtained under the assumption of isotropic velocity dispersion, which is the circumstance in which equation (9.53) is most likely to hold, and clearly this equation is closely related to the classical formula for a statistical parallax. The main difference is that is yields the second rather than the first moment of F.

The covariance in equation (9.52) is non-vanishing when the distance errors are not statistically independent of the velocities, for example, because distances are more likely to be under-estimated when looking into the plane than when looking to a Galactic pole.

In practice the scope for reliable application of equation (9.52) is limited since few samples are uniformly distributed on the sky and have securely known values of the covariance term.

A more effective way to determine the scatter in f exploits the idea introduced at the start of this Section that stars with over-estimated distances tend to have large values of $|x|$ and $|y|$, while stars with under-estimated distances have small values of $|x|$ and $|y|$. Consequently, if in equations (9.18) or (9.19) we restrict the sum to stars with small (resp. large) x^2 or y^2 we will probe the smallest (resp. largest) values of f within the sample. By combining these estimates of f with the numbers of stars associated with each range of values of x^2 or y^2, we can construct the probability distribution $P(f)$ of the overall sample.

Whichever approach we adopt to determine the scatter in f, we should take into account the errors in proper motions. In the first approach they increase $\overline{v_\perp^2}$ and $\overline{v^2}$, in the second approach they push stars to large vales of x^2 and y^2 and thus affect the distance estimator. Fortunately, in relatively nearby samples the impact of errors in proper motions is limited.

9.5   Implementation

In this section we explain which of the several formulae we have given for the fractional distance error f we recommend, and in what order they should be used. Then we illustrate the procedure by applying it to a sample of stars from the Sloan Extension for Galactic Understanding and Exploration (SEGUE, Yanny et al., 2009) and a sample from Data Release 8 of the Sloan Digital Sky Survey (Eisenstein et al., 2011; Aihara et al., 2011).

In any real data set there are likely to be stars with implausibly large heliocentric velocities, and the first step should be to discard those stars. We discard stars for with extreme galactocentric velocities, i.e. $|U|, |V| > 800\,\mathrm{km\,s^{-1}}$ or $|W| > 400\,\mathrm{km\,s^{-1}}$. Then we bin the stars by some quantity of interest, such as surface gravity, metallicity or value of v_ϕ, and for each bin use equation (9.19) iteratively to determine f for that group. The values of $\langle Wy \rangle$ used in this equation are the raw values from the data minus the corrections $\langle e_W e_y \rangle$ from equations (9.25) and the corrections for rotation of the velocity ellipsoid from equations (9.40) and (9.41). Once this stage in the analysis has been completed, the distances of stars have been corrected for the most important errors in the original data, and we may assume that any residual systematic errors are small.

9.5.1   Used samples

We will make use of two subsamples from the SEGUE survey. Our main sample consists of a raw dataset of 224 019 stars from the eighths Sloan data release (DR8, Aihara et al., 2011). As we want the maximum number of stars we can get and not a specific subset and do not fear metallicity biases in the sample, we use all stars with clean photometry from target selection schemes that
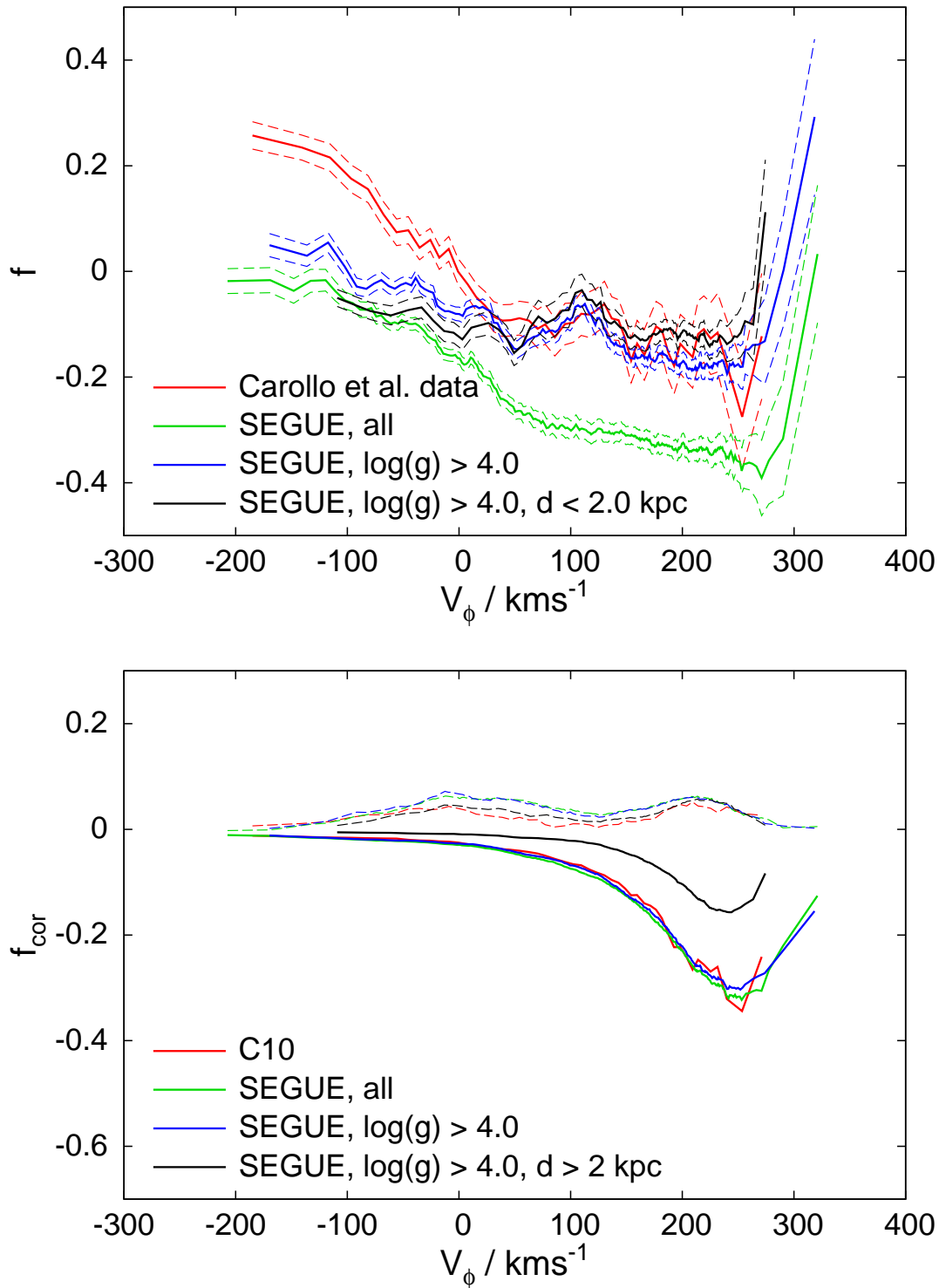
Figure 9.7: Values of *f* for the sample of ∼ 20000 main-sequence stars in the sample of Carollo et al. (2010) (red curve) and three different selections on our SEGUE sample. A mask with a width of at least 1600 stars and at least $25\,\mathrm{km\,s^{-1}}$ width was moved over the sample in steps of 200 stars. The dotted lines delimit the formal 1σ error bands associated with these estimates. In the lower panel we plot the distance corrections from proper motions (negative, solid lines) and the velocity ellipsoid turn (positive, dashed lines) as defined in eq. 9.40.

do not include any direct kinematic (i.e. proper motion or line-of-sight velocity) bias. To ensure decent quality of the used kinematics, we follow Munn et al. (2004) in requiring a match in the proper motion identifications ($match = 1$), a good position determination $\sigma_{RA}, \sigma_{DEC} < 350\,$mas. To ensure sensible stellar parameters, we require an average signal-to-noise ratio larger than 10. Further we require the formal errors on the proper motions to be moderate: $\sigma_{\mu_b}, \sigma_{\mu_l} < 4\,$mas yr^{-1}. We exclude any star that lacks a metallicity or a proper motion or is flagged as having an unusual spectrum (Lee et al., 2008a) unless the flag indicates carbon enhancement. To eliminate a handful of objects with colours far outside the normal calibration ranges we require $0 < (g-i)_0 < 1$. Only stars that would be within 4 kpc in the first guess distance determination and pass our criteria for not being velocity outliers are used. When adopting the Ivezic et al. (2008) (A7) main-sequence distance calibration a total of 119 577 stars pass these cuts. Velocities are derived as in Schönrich, Asplund & Casagrande (2011a) with an adopted solar galactocentric radius of $R_0 = 8\,$kpc, a circular speed of 220 km s^{-1} and the solar motion relative to the local standard of rest from Schönrich, Binney & Dehnen (2010). For this work we make use of the dereddened Sloan photometric colours provided in the catalogue.

The sample of Carollo et al. (2010), which comprises $\sim 30\,000$ calibration stars from SEGUE, constitutes our second sample. Its parameters derive from an earlier version (DR7, Abazajan et al., 2009) of the SEGUE parameter pipeline, but are consistent with the new data release. While their sample is no more than a mere subset of our larger sample, their sample suffers from distance over-estimates (as shown by Schönrich, Asplund & Casagrande, 2011a) whose re-detection illustrates the potential of the method presented here.

9.5.2   Mapping the samples in azimuthal velocity

Fig. 9.7 shows the results of binning the main-sequence stars of four subsamples of SEGUE stars by azimuthal velocity v_ϕ (with the Sun at $v_\phi = 232\,$km s^{-1}). The upper panel shows values of f, while the lower panel shows the corrections used to obtain these f-values.

The full lines in the bottom panel of Fig. 9.7 show the corrections to f that are required to account for proper-motion errors – the impact of errors in $v_\parallel$ is negligible and not plotted. Proper-motion errors tend to increase the recovered value of f, so they require a negative correction to f. Their importance peaks around solar velocity because they contribute a roughly constant term to $\mathrm{Cov}(W,y)$, while the typical heliocentric velocities of stars, which provide our signal, shrink as v_ϕ tends to the Sun's value both because of the diminishing offset in the rotational component and because the velocity dispersion of disc stars diminishes as v_ϕ approaches the circular speed. The dashed lines in the bottom panel of Fig. 9.7 show the corrections to f that are required to account for the rotation of the velocity ellipsoid. These curves have two peaks because there is a similar competition between decreasing heliocentric velocities and decreasing size of the velocity ellipsoid that drives the correction term.

The full red curve in the upper panel of Fig. 9.7 shows the values of f yielded by equation (9.19) when distances from Carollo at al. are used for their "main-sequence" stars; the dashed red curves show the error bounds on f. We see that f is significantly greater than zero for $v_\phi < 0$, the region

of retrograde rotation, implying the presence of significant distance over-estimates. At $v_\phi > 0$, f drops slightly below zero. The full green curve shows the corresponding values of f for the full SEGUE sample when distances are obtained from the Ivezic et al. (2008) (A7) main-sequence relation. Since the samples are now much larger, the formal error bounds are tighter than in the case of the Carollo et al. sample. Now at $v_\phi > 0$, f is decidedly negative (~ -0.3) implying the presence of significant distance under-estimates. The f-value of a sample is an *average* distance correction, so a given value of f could imply that all stars have the corresponding distance mis-estimate, or that a fraction of the stars have a larger mis-estimate while the bulk of the stars have good distances. The blue full curve in the upper panel of Fig. 9.7 shows the values of f obtained when the all-star sample is restricted to dwarfs by imposing the restriction $\log g > 4$: with this cut the distances are under-estimated by only ~ 10 per cent because the gravity cut eliminates most sub-giants and giants from the sample. The black line shows the same "dwarf" star sample with the additional restriction for the primary distance estimate to be $d' \leq 2\,\text{kpc}$. This cut removes mostly relatively blue stars that have a tendency to be on the blue side of the turn-off point. And as we can see from the black line in the lower panel the impact of proper motion errors is greatly reduced as these are proportional to the square of the estimated distance.

In light of this finding we conclude that the deep trough in the green curve for the all-star sample arises because that sample is severely contaminated by subgiants and giants. We can probe the extent of the contamination by dissecting a sample in velocity space because, as we saw in Section 9.4.1, stars with over-estimated distances assemble at extreme velocities, while stars with under-estimated distances are dragged towards the solar motion. This is why the curves of the two contaminated samples (the Carollo et al. sample and the all-star sample) slope steeply downward from left to right in the upper panel of Fig. 9.7. The slope of the curve for the cleaner sample produced by the gravity cut is much smaller. We can even in analogy interpret the minor difference between the black and the blue curves: by the general inclination of the main sequence, the distance cut preferentially removes relatively bright blue stars from the sample that have a larger spread in estimated distances.

The sudden rise of f at super-solar v_ϕ has a different cause. These stars are few in number and have small heliocentric velocities, and, as the lower panel of Fig. 9.7 shows, their f-values are strongly affected by assumed proper-motion errors. It is likely that our probably false assumption of a constant proper-motion error has biased the f-values for these stars. By contrast, the f-values of stars with v_ϕ substantially smaller than the solar value are insensitive to the handling of proper-motion errors.

While valuable insights can be obtained by examining f as a function of velocity, a word of caution about such dissection is in order. No cut or selection should directly affect the target variable (here W), and cuts on the explaining variable can introduce artifacts that should be explored with mock data. For example cutting in the heliocentric V velocity instead of v_ϕ introduces a velocity-dependent error in f of order ~ 5 per cent. In this case the bias arises from the rotation of the velocity ellipsoid, which from selection in V creates a bias in U, which in turn evokes biases in W through the vertical tilt of the ellipsoid.
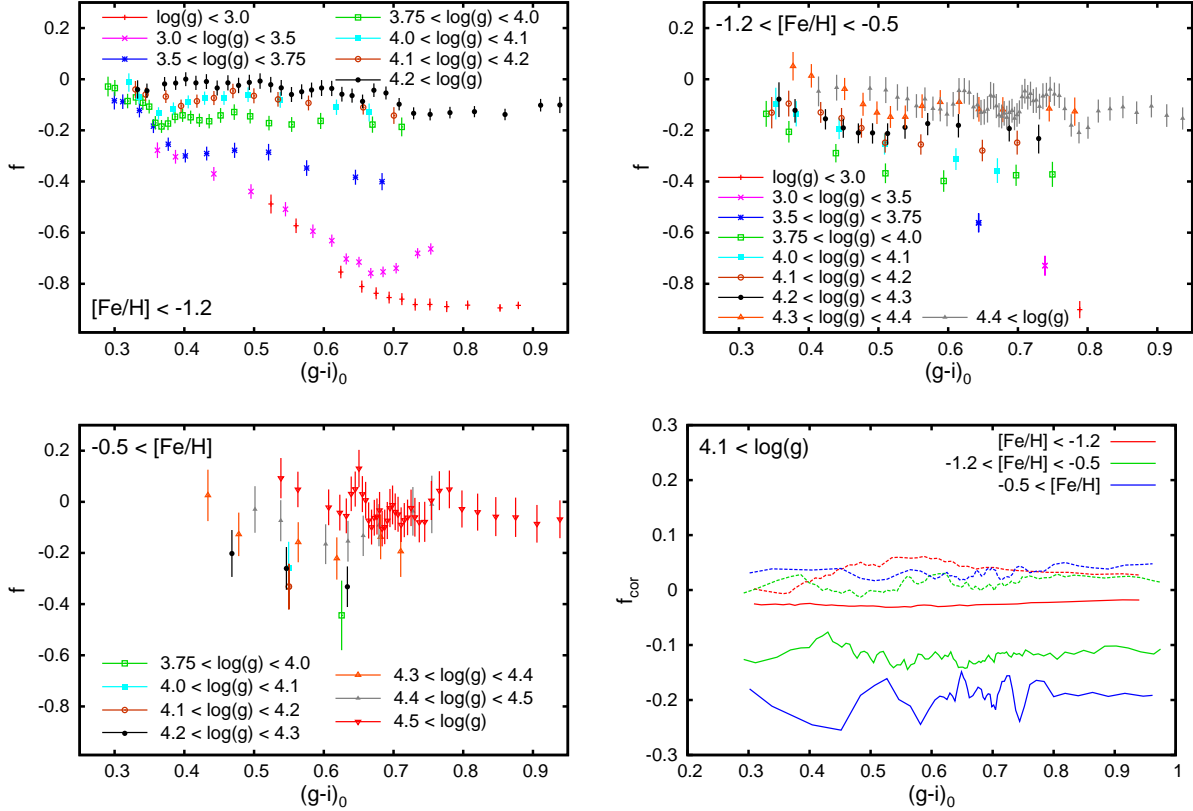
Figure 9.8: An evaluation of the performance of gravities in SEGUE DR8 and the performance of the Ivezic (2008) A7 calibration against metallicity and colour. Each of the first three panels shows results for stars in a restricted range of metallicity. Each metallicity group was then divided by surface gravity and $g - i$ colour and f determined for that group from equation (9.19). We move a 1200 stars wide mask over the sample in steps of 400 objects, so that every third data point is fully independent. Error bars give the formal error plus a 30% error on the systematic corrections. The bottom right panel shows the corrections made to the f-values of high-gravity stars of various metallicities for proper motions (solid lines) and the turn of the velocity ellipsoid (dashed lines).

9.5.3 Dissecting the main sample in gravity

By partitioning a sample in gravity we can explore the extent to which a sample contains stars at different evolutionary stages since they should fall into different bins in gravity. In the following we use only the A7 calibration of Ivezic et al. (2008).

The first three panels of Fig. 9.8 show results obtained by splitting the $\sim 120\,000$ stars into three ranges of metallicity, with boundaries at [Fe/H] $= -1.2$ and -0.5 and then within each metallicity group splitting the stars in $\log g$, and finally binning them in colour. Each colour bin has ≥ 1200 stars (the ones at the edges carry ≥ 800 and ≥ 400 objects), and from one bin to

the next 400 stars are dropped, so every third data point is independent. Points are plotted at the average colour of the stars in the bin. Most giant stars in this sample have low measured metallicities so the low-gravity bins are only well-populated for the most metal-poor stars. The error bars indicate the formal errors on f plus an error of 30% in the corrections to f for proper-motion errors and rotation of the velocity ellipsoid.

Since the distances employed assume that every star is on the main sequence, giants have severe distance under-estimates (negative f). In the top two panels of Fig. 9.8 one can assess the colour at which stars move up from the subgiant branch to the giant branch – the precision with which this colour can be determined is increased if the sample is not divided by gravity or metallicity. The distance under-estimates indicated by Fig. 9.8 are similar to those we would expect a priori, but the agreement is imperfect because the giants in this sample are very remote, so proper-motion errors have a big impact on kinematically determined distances.

In the literature SEGUE stars with gravities within $3.0 < \log g < 3.5$ are considered subgiants (see e.g. Carollo et al., 2010). Stars with $3.5 < \log g < 4.0$ were classified as turn-off stars until it was shown by Schönrich, Asplund & Casagrande (2011a) that this practice sorts stars into unphysical positions in the colour-gravity plane (at the relevant low metallicities, the turn-off region should end bluewards of $(g-i)_0 < 0.4$). More recent studies (Beers et al., 2011; Carollo et al., 2011) classify the stars with $3.5 < \log g < 3.75$ as subgiants and the higher-gravity objects as main-sequence stars. However, the purple and blue points in the upper two panels of Fig. 9.8 show that it cannot be the case that all stars with $\log g < 3.75$ are subgiants, both because at $(g-i)_0 > 0.4$ the f-values of the stars with $3.5 < \log g < 3.75$ are significantly less negative than those of stars with $\log g < 3.5$, and because the f-values of the high-gravity sub-sample are no smaller than ~ -0.3. This corresponds to their being more luminous than main-sequence stars of the same colour by less than a magnitude, whereas, depending on metallicity, already at $(g-i)_0 \sim 0.4$ subgiants should be more luminous than main-sequence stars by more than 1.5 magnitudes. We conclude that no reliable selection for subgiants is feasible with the current gravities: in general there is a contamination by dwarf stars (with the well-known effects of distance overestimates mimicking kinematically hot retrograde populations) and at least on the red side we have to expect some contamination by giants.

The main-sequence relation appears to describe relatively well the distances of stars with measured $\log g > 3.75$. Yet, especially in the top right panel of Fig. 9.8 we see that for all metallicity subsamples, f tends to increase bluewards. This phenomenon arises because the colour-luminosity relation we have used is inclined relative to the theoretical zero-age main sequence and assigns quite high luminosities and consequently large distances to blue stars relative to their red counterparts.

Fig. 9.8 enables us to choose the lower limit on gravity that will most effectively minimise contamination of the final sample by stars that are not dwarfs. This limit appears to rise from about $\log g \sim 4.1$ at the lowest metallicities to $\log g \sim 4.4$ at the highest metallicities. Some part of the trend may also be connected to the redward shift of the turn-off with metallicity. However, this conclusion should not be blindly transferred to catalogues other than DR8 because in this parameter derivation measured gravity is likely correlated with metallicity, so we may

to some extent see mapping errors in assumed luminosity that arise from errors in metallicity. Fig. 9.8 also enables us to detect the redward shift with increasing [Fe/H] in the turn-off colour as the colour at which the dark-blue points of lower-gravity stars become clearly separated from the black points of dwarf stars. Also, blueward of the turn-off we expect an increased spread in values of f within the highest-gravity bins, as the SEGUE stellar parameter pipeline retains some residual information on how high above the main sequence a star is placed in gravity.

The bottom-right panel of Fig. 9.8 shows the corrections to f required by proper-motion errors (solid lines) and rotation of the velocity ellipsoid (dashed lines). The impact of proper-motion errors on the most metal-weak stars is small because these stars are in the halo and have large heliocentric velocities. Rotation of the velocity ellipsoid has similar impact on stars of all metallicities because these stars are distributed through broadly the same volume and a higher velocity dispersion both inflates the correction and the signal in f. For this plot velocity errors were calculated by measuring the dispersions in each subsample and then assuming constant velocity dispersions in the lowest metallicity bin and in the other metallicity bins an increase of the dispersion by 15 per cent for each kiloparsec in $|z|$ and assuming that $\langle U^2 \rangle^{1/2} \propto \exp(-R/R_\sigma)$ with $R_\sigma = 7.5\,\text{kpc}$. This correction term is small and minor changes in how it is derived will not alter our results.

9.6   Conclusions

Systematic distance errors give rise to correlations between the measured components (U,V,W) of heliocentric velocities. Similar correlations arise from three other sources: (i) measurement errors in the proper motions, (ii) Galactic streaming motions and (iii) dependence of the orientation of the local velocity ellipsoid on position in the Galaxy. However, each of these sources of correlation between (U,V,W) has a different and known pattern of variation over the sky, so provided the data come from a wide-area survey, we can disentangle their effects. We have described an iterative procedure by which the distances to stars are rescaled until correlations between (U,V,W) are fully accounted for by effects (i) – (iii) above, and the contribution from systematic distance errors vanishes.

The procedure works best when the group of stars under study has a large net motion with respect to the Sun. This net motion is often dominated by azimuthal streaming, since the Sun has more angular momentum than a circular orbit, while nearby thick-disc and halo stars tend to have substantially less angular momentum. When azimuthal streaming is dominant, the simpler formulae of Section 9.3.6 apply. For stars in the thin disc that have similar angular momentum to that of the Sun the other velocity components usually still carry sufficient information to assess distances.

In principle we can determine distance errors by using either U, V or W as a "target" variable, with the "explaining" variable being composed of the other components of velocity and the sky coordinates. In practice V should not be used as a target variable as the systematic variation of V velocities with position in the Galaxy would invoke spurious correlations with the angle terms

connecting it to the explaining velocity components. W is the target variable of choice both because it has the smallest velocity dispersion and because it is least affected by the complexities of differential rotation. U is mainly useful as a target variable for its ability to determine the mean rotation rate of a population once the distance scale has been corrected by exploiting W. We will discuss an application to this rotation term in a forthcoming paper.

There are some restrictions on the applicability of the method that should borne in mind when using it. The proper motions need to be unbiased and their errors should have finite and approximately known variances. These conditions seem to be satisfied by data from the SDSS (Dong et al., 2011). If the sample is non-local we need to estimate the extent of rotation of the velocity ellipsoid within the sampled region. Such an estimate can be obtained from the sample itself, but with some residual uncertainty arising from proper-motion errors that particularly affect remote stars.

Streams and a warp will induce unwanted correlations but the likelihood of these giving rise to an erroneous distance scale is small for several reasons. First, for a stream or warp to undermine the method, the correlations it introduces must vary on the sky in a similar way to the correlations associated with distance errors. Consequently, the impact of a stream or warp is likely to be suppressed given sufficient sky coverage. Second, a warp could be accounted for in much the same way we have accounted for Galactic rotation. Third, the footprints of streams or a warp will show up in conflicting values for f obtained from the two possible target velocities, W and U. Finally, a stream or warp would induce identical correlations in the velocities of stars in the broad colour and gravity range that made up the physical feature, whereas distance mis-estimates will usually vary with spectral type.

In Section 9.4.1 we showed that the estimators given in Section 9.3 are mildly biased in the sense that when there is a scatter in the distribution of distance errors, the estimated value of f will be larger than it should be by an expression quadratic in the width of the distribution. Equation (9.50) can be used to correct for this effect. As we discussed in Section 9.4.2, the method can be extended to probe the full probability distribution of f values rather than just determining the mean value of f. Details of this extension will be given in a later paper.

In Section 9.5 we applied the method to samples of stars from the SEGUE survey. We concluded that the distances to stars used by Carollo et al. (2010) are on average significantly over-estimated among stars deemed to be counter-rotating, and tend to be under-estimated by ~ 10 per cent near solar velocity. This is also a nice example on how a spread in the distance errors within a sample can be directly seen by eye, when we dissect the sample in velocity: the distance over-estimates assemble at velocities remote from the solar value (i.e. mostly the retrograde tail of the halo velocity distribution), while in our all-star sample, which is contaminated by numerous giants, the giants are dragged towards the solar motion, so a trough forms in a plot of the correction factor f versus azimuthal velocity.

In Section 9.5.3 we demonstrated the use of the method to assess the reliability of the Ivezic (2008) A7 distance scale for dwarfs and to assess the degree of contamination by non-dwarfs that arises as the lower limit on $\log g$ for entering the sample is varied. For low contamination the lower limit on $\log g$ should increase with metallicity. We conclude that using only the DR8 grav-

ities it is not possible to achieve a satisfying selection of subgiants. The level of contamination by dwarf stars becomes large once the upper limit on $\log g$ exceeds ~ 3.5. Since any dwarf that is misidentified as a subgiant has a seriously over-estimated distance, studies of stellar kinematics that are based on DR8 gravities should rigorously exclude subgiants.

We are currently applying the method to recent distances to stars in the RAVE survey (Zwitter et al., 2010; Burnett et al., 2011). A wide variety of applications to this method will follow as it offers a standard tool to identify groups of stars with problematic parameters, to check the reliability of selection schemes and distance assignments and finally to correct for any biases in these distances, e.g. by deviations in reddening with distance from the Sun.

Our study has also illuminated the kinematic patterns that distance errors can generate. These are not limited to the production of spurious counter-rotating components, but include tilts of the velocity ellipsoids, and by allowing rotational velocity to masquerade as motion in either the radial or vertical direction, can extend to patterns of mean motion that, in a sample that is anisotropically distributed on the sky, can imply a wrong motion of the local standard of rest.

Acknowledgements

Chapter 10

Galactic rotation and solar motion from stellar kinematics[1]

10.1 abstract

I examine the imprint of Galactic rotation and Solar motion in the stellar kinematics from the Sloan Digital Sky Survey. Apart from the azimuthal velocities of stars the rotational streaming invokes a strong dependence of the observed heliocentric radial velocities (U) on Galactic position that allows for a direct measurement of rotation in a component that does not depend on the assumed velocity of the Sun. Neglect of this dependence can cause a bias in the estimate of the solar radial motion $U_\odot$ in excess of $10\,\mathrm{km\,s}^{-1}$. Accounting for this effect I find a solar radial motion $U_\odot \sim 12.7\,\mathrm{km\,s}^{-1}$ in concordance with results from the Geneva-Copenhagen Survey, albeit slightly larger. More important comparing the two rotation estimates from U and V_g velocities, I directly obtain the total azimuthal velocity $v_{\phi,\odot}$ of the Sun in the Galactic rest frame and hence the local circular speed of the Milky Way. The dependence of this value on the assumed Galactocentric radius of the Sun can be broken by either using the proper motion of Sgr A^* or by measuring R_0 directly from the stars in comparing slow and fast rotating populations. I find that my values are consistent with results from different strategies and can by combination of these independent approaches reduce formal errors. From this work alone I estimate $R_0 = (8.11 \pm 0.29)\,\mathrm{kpc}$ and $v_{\phi,\odot} = (245 \pm 9)\,\mathrm{km\,s}^{-1}$ and by combination with other data $R_0 = (8.25 \pm 0.14)\,\mathrm{kpc}$ and $v_{\phi,\odot} = (249.5 \pm 4.2)\,\mathrm{km\,s}^{-1}$. The measurements carry an additional systematic uncertainty of about $5 - 10\,\mathrm{km\,s}^{-1}$ and parallel correction in R_0.

---

[1] The work in this chapter is being submitted to MNRAS as Schönrich (2011b). The content and text are identical apart from minor changes during the refereeing process and from language editing or adaptions to this work.

10.2 Introduction

Among the central questions in Galactic structure and parameters are the Solar motion, Solar Galactocentric radius R_0 and the local circular velocity V_c of our Galaxy. Galactic rotation curves are found to be generally quite flat over a vast range of Galactocentric radii (Krumm & Salpeter, 1979). As common for Galaxies with exponential discs (Freeman, 1970) there is some evidence for a radial trend of the Galactic circular velocity near the Sun, but it is very moderate (Feast & Whitelock, 1997; McMillan & Binney, 2010), so that the circular velocity at solar Galactocentric radius R_0 characterises well the entire potential.

Initially stellar samples were the main source of information on Galactic parameters. Since the invention of the Oort constants (Oort, 1927) local kinematic data were used to constrain Galactic parameters including the local circular velocity. While studies determining the Local Standard of Rest (LSR) are still primarily based on stellar samples, the accuracy of geometric parallaxes and the magnitude requirements of stellar spectroscopy limited the spatial extent of available data sets and hence their importance in finding Galactic parameters. The significant kinematic heat of the stellar populations requires large sample sizes. Hence some classical strategies like the position determination of the Galactic centre by Shapley (1918) reached their limits by the number of available luminous standard candles and a lack of stellar observations far from the solar neighbourhood.

To date a few attempts have been made to use luminous stars for structure determination (e.g. Burton & Bania, 1974). Yet most evidence on these Galactic parameters derives from modelling streams in the Galactic halo (see e.g. Ibata et al., 2001; Majewski et al., 2006) and from radio observations of the *HI* terminal velocity (see the discussion in McMillan, 2011), of the Galactic centre, molecular clouds and MASERs (e.g. Reid & Brunthaler, 2004; Broderick et al., 2011). While the first line of determinations depends strongly on underlying assumptions like distance scale and on the shape of the Galactic potential (cf. the discussion in Majewski et al., 2006), there are further complications like the fact that the apparent structure of tidal streams does not exactly delineate the involved stellar orbits (Eyre & Binney, 2009). Radio observations (Reid & Brunthaler, 2004) have provided us with very accurate proper motion of the radio source Sgr A^*, which is identified with the central black hole of the Milky Way. This sets narrow limits to the ratio of the solar speed in the azimuthal direction to the solar Galactocentric radius. Yet it is not only desirable to have more than one approach in measuring such an important quantity, but we need further information to get the actual circular velocity. Recently parallaxes to objects in the central Galactic regions have become available (see the discussion in Reid et al., 2009a), and values for the Galactic circular speed have been derived from *HI* motions and from MASERs (Rygl et al., 2010). Despite the high accuracy in the determined kinematics of MASERs, these objects are rare leading to statistical and systematic uncertainties, particularly as they are first not on pure circular orbits and second intimately connected to the intense star formation in spiral arms, where the kinematic distortions are largest. Hence the exact values for Galactic parameters remain under debate.

These uncertainties make an independent determination of Galactic parameters desirable, which

is facilitated by the new large spectroscopic surveys like RAVE (Steinmetz et al., 2005) and SEGUE (Yanny et al., 2009). Of course we can not attain yet the accuracy achievable with Gaia astrometry and sample sizes. Yet I will show that already now the stellar samples, which have been so far primarily used for the exploration of substructure, be it for halo streas (Kepley et al., 2007; Belokurov et al., 2007) or tidal streams in the disc (Hahn et al., 2011) give results for V_c competitive with radio observations.

Knowing the LSR velocity of the Sun to reasonable accuracy we need to measure either the total azimuthal velocity of the Sun $v_{\phi,\odot}$ or the circular velocity V_c to know the other quantity. In this work I suggest some basic techniques to measure the rotation of a component under study and to fix the Galactocentric radius of the Sun as well as the Galactic circular speed from stellar kinematics.

In Section 10.3 I lay out the general method before describing the sample selection and treatment in Section 10.4. This contains especially a discussion of proper motion issues and in subsection 10.4.3 a description of the distance corrections via the method of Schönrich et al. (2011b). In Section 10.5 I shortly lay out the radial velocity based rotation measurement on SEGUE data, discuss the local standard of rest values in radial and vertical motion in subsection 10.5.1 and then dissect the sample in metallicity to get estimates on Galactic parameters in 10.5.3 presenting three methods to get the Galactocentric radius and the circular speed from stellar samples. In Section 10.6 I summarize the results.

10.3 General Idea

Before I start the dirty work of data analysis it seems appropriate to concisely lay out the general definitions and ideas.

10.3.1 Definitions

This paper is based on comparisons between velocities in the heliocentric frame and galactocentric velocities. In the heliocentric frame I define the velocities U, V, W in a cartesian coordinate system as the components pointing at the Sun towards the Galactic centre, in the direction of rotation and vertically towards the Galactic North pole. The galactocentric velocities are defined in cylindrical coordinates around the Galactic centre with U_g, V_g, W_g pointing again towards the Galactic central axis, in the direction of rotation and vertically out of the plane, as illustrated in Fig. 10.1. $U_\odot, V_\odot, W_\odot$ are the three components of the Solar motion relative to the Local Standard of Rest (i.e. the circular orbit at the local galactocentric radius R_0), for which I assume the values from Schönrich, Binney & Dehnen (2010) if not stated otherwise. The total azimuthal velocity of the Sun in the Galactic frame is written $v_{\phi,\odot} = V_\odot + V_c$ where V_c denotes the circular velocity in the disc plane of the Milky Way at R_0.
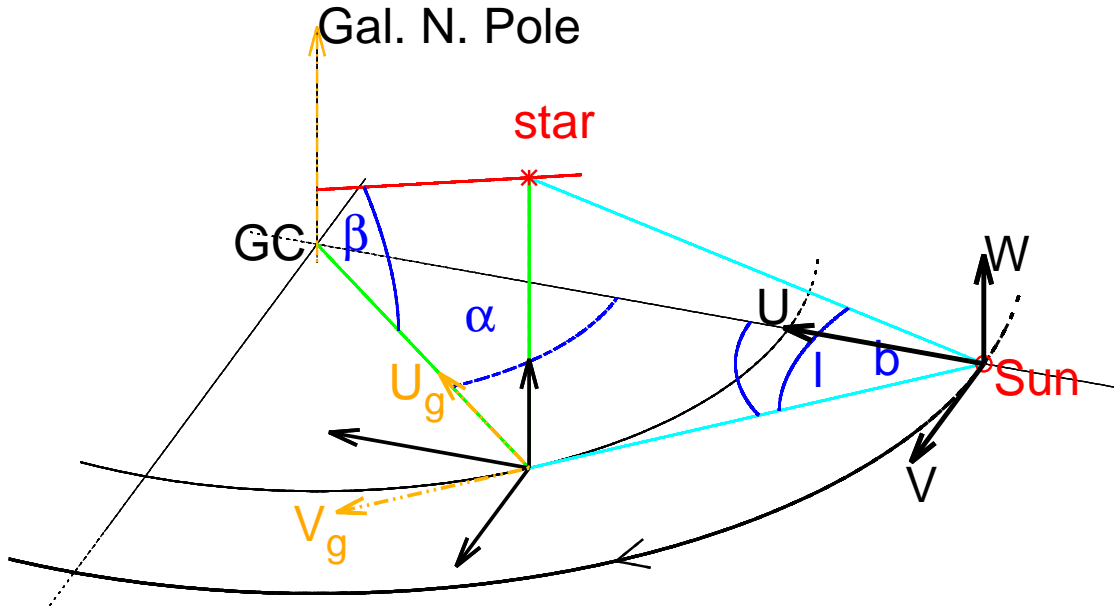
Figure 10.1: Definition of kinematic quantities. On the connection line between Sun and Galactic centre the heliocentric and "galactocentric velocities", i.e. velocities in the galactocentric cylindrical coordinate system are identical, while they differ in general. This gives rise to systematic streaming motion in the heliocentric frame.

10.3.2   An absolute measure of rotation

Usually studies on the rotation of Galactic components suffer from the uncertainty in the solar azimuthal velocity that directly translates into a systematic uncertainty of stellar azimuthal velocities. In a sufficiently extended sample this can be cured: As already discussed in Schönrich et al. (2011b) and evident from Fig. 10.1 Galactic rotation leaves its imprint in both the heliocentric U and V velocities: As the direction of the rotational component of motion turns through with the angle α between the lines Galactic centre – Sun and Galactic centre – star, it gets partly aligned with the radial component of the local cartesian frame. Hence from the heliocentric U velocities we can directly infer the Galactic rotation as a global streaming motion. In parallel the observed heliocentric azimuthal velocity shrinks for larger $|\sin\alpha|$. Accounting for rotation the mean motions of stars in the heliocentric frame are:

$$\overline{U} = -U_\odot + \theta \sin\alpha$$
$$\overline{V} = -v_{\phi,\odot} + \theta(1 - \cos\alpha) \qquad (10.1)$$
$$\overline{W} = -W_\odot,$$

where $(U_\odot, v_{\phi,\odot}, W_\odot)$ are the velocity components of the Solar motion in the Galactic rest frame radially towards the Galactic centre, azimuthally in the direction of disc rotation and vertically out of the plane. θ is the rotation speed of the population. Observing the change of heliocentric U velocity in a sufficiently extended sample hence estimates the rotation of a component θ, once we know the angle α.

Prima facie it might be tempting to use the azimuthal velocity term. Yet, all it expresses is a slowing of heliocentric azimuthal velocities. However, θ is in general not a real constant, but a function of altitude z, galactocentric radius R, metallicities, etc. In particular it is a known fact that the kinematically hotter disc populations at higher altitudes above the plane have a larger asymmetric drift (see e.g. Binney, 2010), or vice versa a slower rotation rate, while the fraction of halo stars with nearly no rotation increases as well. As I do not hold an exact model describing this behaviour, no trustable statistics can be drawn from the azimuthal component. A similar uncertainty derives from the possibility for variations of θ in R even at the same altitude.

For the radial component the situation is different: Setting aside the problem of distance errors the worst concern for a rotation measurement are streams with significant radial motion (which would have to make up a significant part of the sample to yield an effect) and disturbances from the Galactic potential itself. Especially the bar region with its pronouncedly non-circular motions can hamper this estimator. One important warning is that one needs sufficient spatial coverage in the sample to avoid a bias like in the azimuthal velocities: If e.g. populations with larger $|\sin\alpha|$ have a slower θ, a naive linear fit on a sample with meagre extension in α can deliver a wrongly shallow slope or respectively low rotation rate. This problem diminishes when one can either assume a sane $U_\odot$ or have sufficient coverage of stars on both sides of the Galactic centre and/or low $|\sin\alpha|$ so that a linear fit gives a reliable anchoring on $U_\odot$. In addition one may test for the presence of higher order terms of U in α. These criteria fulfilled the radial motion $\overline{U(\alpha)}$ gives a weighted, but reliable estimate of the mean $\overline{\theta}$ in a sample.

In contrast to the use of V_g, a population's rotation θ derived from heliocentric radial motions is independent from the assumed Solar motion. This different dependence can be exploited to measure the solar azimuthal velocity $v_{\phi,\odot}$ from stellar samples without having to involve any modelling: The Galactic parameters $v_{\phi,\odot}$ and R_0 can be varied until the rotation estimates from V_g and θ agree. As we will see this results in a relation between $v_{\phi,\odot}$ and R_0 that can be combined with an additional datum like the proper motion of Sgr A^* to get definitive values for both parameters. An independent estimate for R_0 of similar accuracy can be generated by the demand that different populations with different values of θ must give the same value for $v_{\phi,\odot}$. This is possible because the parameter θ is roughly proportional to R_0. Hence the estimates for $v_{\phi,\odot}$ get sheared between populations with small θ and populations with large θ when a wrong R_0 is assumed. To complete the series of model-independent measurements I will estimate R_0 from the direction of stellar motions with Galactocentric radius. Though this estimate is roughly consistent with the other results, it does not give any additional useful constraint compared to the other strategies and is more vulnerable to assumptions on Solar motion.

10.4   Sample selection and distances

10.4.1   Data selection

Any reader not interested into the details of sample selection, distance analysis and the proper motions may skip this section and turn directly towards Section 10.5.1.

All data used in this study were taken from the seventh and eighth data release (hereafter DR7 and DR8 Abazajan et al., 2009; Aihara et al., 2011) of the Sloan Digital Sky Survey (SDSS Eisenstein et al., 2011). The stellar spectra have been taken by the Sloan Extension for Galactic Understanding and Exploration (SEGUE, Yanny et al., 2009). An evaluation of the performance of their parameter pipeline (SSPP) can be found in Lee et al. (2008a,b). In this work there is no interest in specific metallicity distributions, but in having kinematically unbiased samples that include as many stars as possible. Hence the sample drawn from DR8 consists of a raw dataset of 224 019 stars from all SEGUE target categories and the photometric and reddening standard stars that do not include any proper motion cuts and have clean photometry. In particular I use the categories of F turnoff/subdwarf, Low Metallicity, F/G, G dwarf, K dwarf, M subdwarf stars from SEGUE1, MS turnoff, Low Metallicity and the reddening and photometric standard stars from all samples. The older DR7 forms a subset of 182627 stars among these.

To ensure sufficient quality of the involved proper motions, I select only stars with a match in the proper motion identifications ($match = 1$) and a good position determination with $\sigma_{RA}, \sigma_{DEC} < 350\,\mathrm{mas}$ as suggested by Munn et al. (2004). I furthe require the formal errors on the proper motions to fulfil $\sigma_{\mu_b}, \sigma_{\mu_l} < 4\,\mathrm{mas\,yr^{-1}}$, skimming the tail of uncertain proper motion determinations and cut for line-of-sight velocity errors below $20\,\mathrm{km\,s^{-1}}$.

Sample homogeneity is not a concern in this study, but to avoid issues with reliability of the used isochrones in colour regions with insufficient coverage to check them by statistics, I select $0 < (g-i)_0 < 1$, tossing out a handful of stars especially on the red side. I tested that narrower colour cuts would have no significant effect on the presented results.

For our purpose it is most important to have a good discrimination between dwarf stars and other categories and to dispose of as many evolved stars above the main sequence as possible. Hence only stars are used that have values for gravity and metallicity determined by the pipeline, otherwise distances could not be properly assigned. The sample must be restricted to dwarf stars, as Schönrich et al. (2011b) showed that stars with especially intermediate gravities in the pipeline are an indeterminable blend of dwarf, subgiant and giant stars, hence exhibiting huge distance errors making their use detrimental to any kinematic study.

Following Schönrich et al. (2011b) I adopt a sloping gravity cut generally tighter than the usually applied $\log(g) > 4.0$, demanding $\log(g) > 4.3 + 0.2[\mathrm{Fe/H}]$ and setting a constant limit of $\log(g) > 3.9$ for $[\mathrm{Fe/H}] < -2$ and $\log(g) > 4.3$ for $[\mathrm{Fe/H}] > 0$.

Quite commonly it is expected that a cut for spectra with signal to noise ratio $S/N > 10$ ensures reasonable parameters in the SEGUE pipeline. Still the accurate determination of parameters is more difficult in those noisy spectra. There is a mild drift in the derived quantities pointing to a decreasing giant contamination towards higher S/N, motivating a cut at $S/N > 15$ where the

derived quantities become more stable.

Reddening is accounted for by subtracting the reddening vectors estimated in the DR8 catalogues from the observed magnitudes. To avoid problems with complicated three dimensional behaviour of the reddening and to limit uncertainties in the dataset, I remove all objects with an estimated g magnitude extinction $A_g > 0.75$ mag. This strips all stars in the low latitude fields from the sample. I tested that the exclusion does not have a significant impact on my results due to the low number of concerned objects (apart from increasing the derived formal errors), but keep this cut for the sake of sample purity. I exclude all stars flagged for spectral aberrations apart from suspected carbon enhancement. In all cases we cut all stars beyond 4 kpc distance after applying the distance corrections to limit the impact of proper motion errors.

10.4.2 Proper motions

For a precise measurement of Galactic rotation I am reliant on high accuracy of proper motions and a decent control of systematic aberrations on those proper motion terms. Aihara et al. (2011erratum) reported significant problems with the DR8 astrometry implying also problems with proper motions. From that perspective it seems appropriate to use DR7 proper motion values. A less well-known problem in Sloan astrometry is the the possibility for stars contaminating the galaxy sample used to set the astrometric frame. Those objects can give rise to some "frame-dragging". The largests aberrations were found for about 15% of the DR7 objects in *rerun* 648, which have to excluded from the data when using DR7. Despite constituting a minority in the sample their inclusion would distort estimates for the Galactic circular speed by as much as $14\,\mathrm{km\,s^{-1}}$ consistent with the idea that the astrometry frames were dragged into the Galactic rotation direction underestimating the real motion. Still there remain additional aberrations also in DR8: (Bond et al., 2009) et al. reported significant net proper motions on quasars. They traced the declination dependent systematic components of their quasar proper motions back to chromatic aberration by Earth's atmosphere (Kaczmarczik et al., 2009): the angle at which the stellar light passes through Earth's atmosphere strongly depends on the declination and this should give rise to colour dependent offsets. While this appears plausible, I tested proper motion on the cleaner Schneider et al. (2010) quasar sample. For this I fitted a simple linear function in right ascension and declination to the proper motions from DR7 (and found it quite consistent with DR8):

$$\frac{\mu_i}{\mathrm{mas\,yr^{-1}}} = f_{i,\mathrm{RA}} \cdot \frac{\mathrm{RA}}{deg} + f_{i,\mathrm{DEC}} \cdot \frac{\mathrm{DEC}}{deg} + c_i \qquad (10.2)$$

where $i = \mathrm{RA, DEC}$ denotes the two possible proper motion components in right ascension (RA) and declination (DEC), f are the coefficients, c are free fitting constants. Using the combined fit diminishes the impact from omitted variable bias that might arise from the particular sample geometry (the explaining variables are mildly correlated). For μ_{DEC} I obtain $f_{\mathrm{DEC,RA}} = 0.00015 \pm 0.00015$, $f_{\mathrm{DEC,DEC}} = 0.00706 \pm 0.00047$ and $c_l = -0.192 \pm 0.031$. So, despite a marginally significant dependence on right ascension, for μ_{DEC} indeed most of the

bias originates from the declination of the objects, which is consistent with the interpretation as chromatic aberration. Targeting μ_{RA} the picture reverses: $f_{\mathrm{RA,RA}} = 0.00045 \pm 0.00015$, $f_{\mathrm{RA,DEC}} = -0.00052 \pm 0.00047$ and $c_b = 0.078 \pm 0.031$ most of the bias originates from the right ascension itself. This is not implausible as errors should be aligned with the corresponding coordinates, but on the right ascension (unless some information was missed in this crude analysis) it is seems only viable to reason this outcome with chromatic aberrations, if the observations were made at a specific nighttime in a short period of the year or in a very particular manner that correlates the airmass of a stellar observation significantly to right ascension.

Consequently another source of systematic proper motion bias should be tested for: Astrometric "frame" dragging by stellar contamination in the Galaxy sample used for Sloan astrometry: These misclassified stars will follow the general Galactic streaming by rotation and the relative motion of the Sun. In the following I develop a very crude analytic term approximating the proper motion bias depending on (l,b) as it could arise from Galactic streaming: Candidates for contamination of the galaxy sample should preferentially populate a certain magnitude range and also have preferred colours resembling the used galaxies. It seems hence appropriate to assume for simplification a dominant distance for stars contaminating the sample, placed at $s = 1\,\mathrm{kpc}$. The outcomes will anyway not be critically affected by this distance (that will alter the shape of the systematic bias once the stars are sufficiently remote for the small angle approximation to break down). On this shell I assume the stars to rotate dependent on their altitude z around the Galactic centre with $\theta(z) = (215 - 10z/kpc)\,\mathrm{km\,s}^{-1}$. The proper motion can be written down from the heliocentric velocities from equation (10.1) subtracting the reflex motions of the solar Local Standard of Rest (LSR) values from Schönrich, Binney & Dehnen (2010) and assuming a total solar azimuthal velocity according to the IAU recommendations at $v_{\phi,\odot} = 232\,\mathrm{km\,s}^{-1}$. Using this the simple Galactc streamig terms are:

$$\mu_l = \left(f_l \chi_l + a_l \cos l \cos b v_{\phi,\odot}\right)/(sk) + c_l \mathrm{mas\,yr}^{-1} \tag{10.3}$$
$$\mu_b = \left(f_b \chi_b + a_b \sin b \sin l v_{\phi,\odot}\right)/(sk) + c_b \mathrm{mas\,yr}^{-1}$$

with

$$\chi_l = -\sin l U + \cos l V \tag{10.4}$$
$$\chi_b = \sin b(\cos l U - \sin l V) - \cos b W_\odot$$

where $k \sim 4.74\,\mathrm{pc/mas\,yr}^{-1}$ does the unit conversion, U and V are the heliocentric velocities from streaming minus the assumed motion of the Sun and $f_l, a_l, c_l, f_b, a_b, c_b$ are the fit parameters. The terms connected to a_i give a crude estimate for the effects from halo streaming.

The derived values for DR7 and DR8 are presented in Table 10.4.2. The errors for DR8 proper motions are slightly larger because of the increased random scatter. Cutting out the about 10% of the objects with the largest proper motions does not significantly alter these results. The coefficients f_i and a_i may be understood roughly as contamination fraction. Especially they are very rough estimates as by the distance dependence of proper motions, the reqired fraction varies with the assumed distance. A priori the expected trends are not obvious as the Schneider

name	DR7	σ_{DR7}	DR8
f_l	-0.0641	0.0057	-0.0644
c_l	-0.016	0.011	-0.009
a_l	0.00521	0.00064	0.00447
f_b	-0.0702	0.0061	-0.0670
c_b	-0.151	0.012	-0.147
a_b	0.00533	0.00081	0.00371

Table 10.1: Fit parameters for systematic streaming in the quasar proper motions as described in the text.

et al. (2010) sample might have some residual stellar contamination that competes with possible astrometry problems. In both cases the main rotation term f_i is significantly negative hinting to some misclassified stars affecting astrometry. On the other hand the coefficients a_i that resemble terms expected for the Galactic halo are positive, which might be interpreted as a tiny fraction of halo stars hiding in the quasar sample. I rather understand it as an omitted variable bias: Neither do I know the exact functional shapes and distance distributions of the contamination, nor do I have precise terms at hand to cope with the possible chromatic aberrations. Exact terms for contamination would demand a complete modelling of the entire measurement process including a reasonable model to the Milky Way, other galaxies and the exact Sloan selection function. If I fit alone either a_i or f_i, both variables turn out negative and still their counterparts are negative when I fit them with this naively derived value. So one could argue that f_i is getting excessively negative being balanced by a slightly positive a_i to cope with these uncertainties.

In the end I cannot achieve more than a rather phenomenological correction without being able to determine the true cause for the observed trends. The main information is, however, the influence on Galactic rotation measurements and this is well controlled by the derived naive approximation. I will use these terms for correction of stellar proper motions. As it is unknown which of the named effects prevails in our case and how much residual contamination there is in the sample I use the terms from equation. (10.3) multiplied by a factor ζ_μ of 0.5 on the red end rising to 1.5 on the blue end of the sample:

$$\zeta_\mu = \begin{cases} 1.5 & \text{for } (g-i) < 0.45 \\ (0.9 - (g-i))/0.3 & \text{for } 0.45 < (g-i) < 0.75 \\ 0.5 & \text{for } 0.75 < (g-i) \end{cases} \qquad (10.5)$$

where $(g-i)$ is the observed colour without reddening correction.

As can be seen from Table 10.4.2 the fit coefficients on DR8 data are not very different from the DR7 values, indicating that DR8 proper motion systematics should not be more troublesome than those in DR7. Since I cannot exclude further catastrophic errors in DR7 apart from the problem with *rerun* 648 I use the significantly larger DR8 sample as standard throughout this work, showing DR7 results for comparison where appropriate.

For proper motion errors, which influence the distance determinations, I use the values from Dong et al. (2011) for DR7 and multiply those by 1.22 for DR8 to account for the 22% larger

rms scatter of my fit residuals. I checked that use of the Munn et al. (2004) values does not significantly affect the presented analysis.

10.4.3   Distances

In this work I make use of the statistical distance correction method developed by Schönrich et al. (2011b). This approach relies on the velocity correlations over Galactic angles that are induced by systematic distance errors and promises a better precision and robustness than classical methods. The method can find the average distance in any sample of a couple of hundred stars. So the only thing required as first input is a smooth distance or respectively absolute magnitude calibration that has a roughly correct shape. The shape has some importance as erroneous assumptions would result in an increased distance scatter on the sample bins resulting in residual systematic trends for different subpopulations. The use of statistical distance corrections is important as there are in all cases expected offsets by reddening uncertainties, mild differences by evolutionary differences on the main sequence, systematic metallicity offsets and by the helium enhancement problem, where the isochrones appear to be to faint at a fixed colour.

To derive a correction field I bin the sample in metallicity and $(g-i)_0$ colour. I also attempted binning the sample simulateneously in distance as well, but found no additional benefits, probably because the bulk of the sample is further away than $0.5\,\mathrm{kpc}$ and I excluded high reddening regions so that variations of reddening with distance are comparatively small.

Primary stellar distances are derived from a dense grid of BASTI isochrones (Pietrinferni et al., 2004, 2006) that was kindly computed by S. Cassisi for the purpose of our age determinations in Casagrande et al. (2011). For a first distance estimate I use the $11.6\,\mathrm{Gyr}$ isochrones which seems an appropriate compromise between the suspected age of the first significant disc populations (see e.g. Aumer & Binney, 2009; Schönrich & Binney, 2009a; Bensby et al., 2004) and the age of halo stars. For metal-poor stars with [Fe/H] < -0.6 I account for alpha enhancement by raising the effective [Fe/H] by $0.2\,\mathrm{dex}$ as suggested by Chieffi et al. (1991) or Chaboyer et al. (1992). In analogy to the observations of Bensby et al. (2007); Meléndez et al. (2008) I let the alpha enhancement go linearly to zero towards solar metallicity:

$$[\mathrm{Me/H}] = \begin{cases} [\mathrm{Fe/H}] + 0.2 & \text{for } [\mathrm{Fe/H}] < -0.6 \\ [\mathrm{Fe/H}] - \frac{1}{3}[\mathrm{Fe/H}] & \text{for } -0.6 \leq [\mathrm{Fe/H}] \leq 0 \\ [\mathrm{Fe/H}] & \text{for } 0 < [\mathrm{Fe/H}] \end{cases} \tag{10.6}$$

Some of the stars are located bluewards of the turn-off point at this age. To cope with these objects I search the point at which the old isochrone is $0.5\,\mathrm{mag}$ brighter than the corresponding $50\,\mathrm{Myr}$ isochrone and extrapolate bluewards parallel to the main sequence defined by the $50\,\mathrm{Myr}$ isochrones. I also experimented with using the turnoff point, i.e. the blue-most point of the old isochrone, but this introduces larger shot noise in distances that would hamper the distance corrections via the method of Schönrich et al. (2011b). Comparing the expected r-band absolute magnitude of each star to the measured reddening corrected r_0 I then infer its expected distance modulus and hence distance s_0.
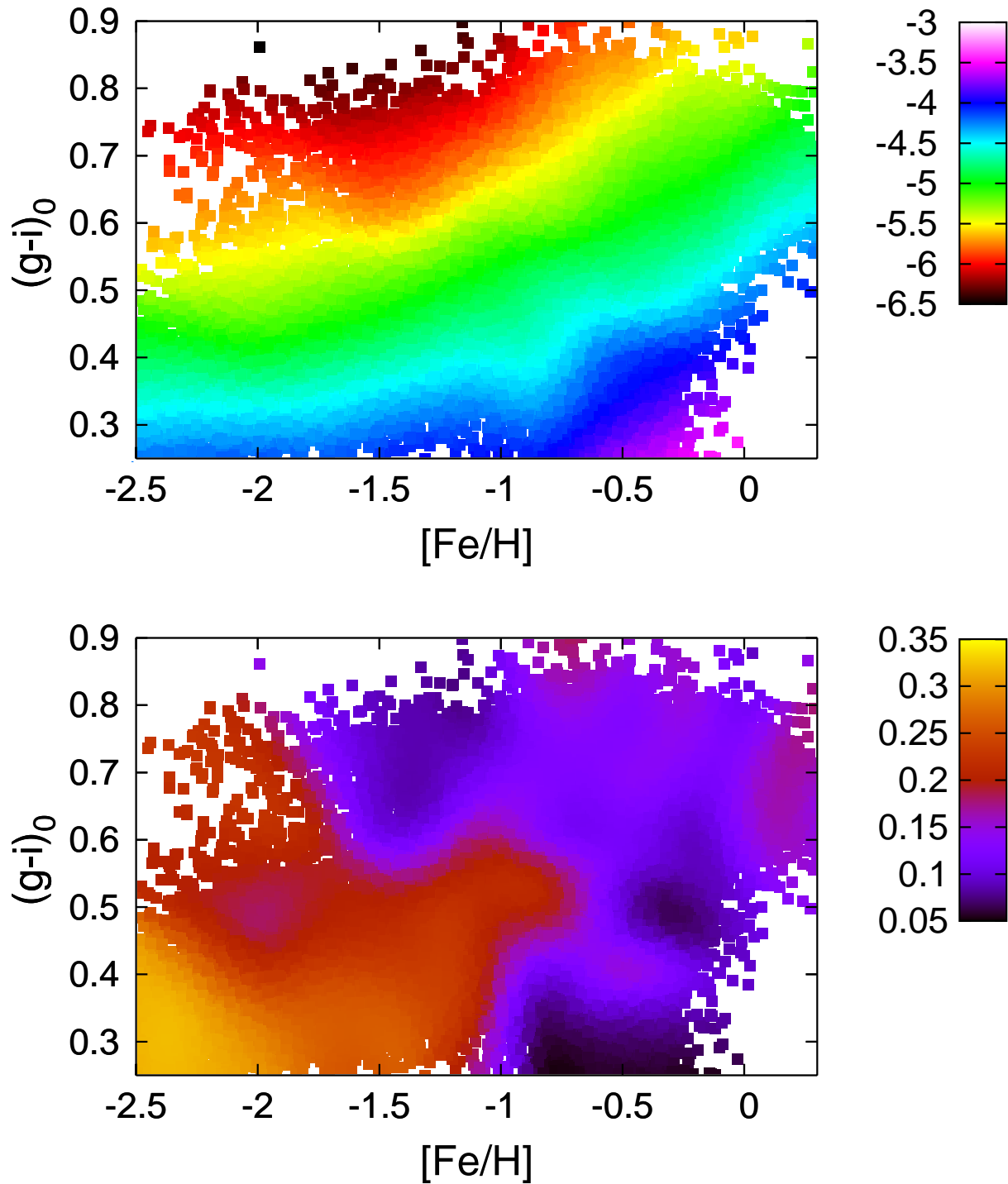
Figure 10.2: Upper panel: Assumed absolute *r*-band magnitudes from isochrone interpolation in the metallicity-colour plane after statistical distance correction. Lower panel: Distance correction factors in the metallicity-colour plane with the smoothing from equation (10.8).

To correct those distances I cut the sample in metallicity, colour and distance to derive the systematic aberrations. There is a trade-off between resolution of the smallest possible structures in the aberration field and the introduction of Poisson noise the effective numbers of stars contributing to the estimate at a certain point in the observed space. The strategy is to select every 50th star in the sample and estimate the distance aberrations for its 800 closest neighbours (I checked that the bin size has no significant effect) using an euclidean metric on the parameter space:

$$d^2_{\text{param}} = 2\Delta^2_{(g-i)_0} + \Delta^2_{[\text{Fe/H}]} \tag{10.7}$$

For non-halo or respectively metal-rich stars that offer less accurate statistics by the smaller heliocentric velocities this results in some significant scatter, which is reduced by smoothing the distance corrections:

$$s = s_0 \left(1 + \frac{\sum_i x_{\text{est},i} \exp\left(-\sum_j \frac{\Delta^2_{i,j}}{2\sigma_j^2} \right)}{\sum_i \exp\left(-\sum_j \frac{\Delta^2_{i,j}}{2\sigma_j^2} \right)} \right), \tag{10.8}$$

where s_0 is the first naive distance estimate from isochrone interpolation. The first sum runs over all stellar parameter sets i around which the best-fit distance correction $x = 1 - 1/(1+f)$ or respectively the distance misestimate factor f has been evaluated. The second sum j runs over used parameters (here metallicity and colour), to evaluate the parameter differences $\Delta_{i,j}$ between the star in question and the mean values of all evaluation subsets and smooth via the exponential kernel with the smoothing lengths σ_j. I chose $\sigma_{[\text{Fe/H}]} = 0.12\,\text{dex}$ and $\sigma_{(g-i)_0} = 0.04\,\text{mag}$. When binning the sample a second time for measuring Galactic parameters I fit the distance for a second time, to diminish the danger of remaining systematic biases. Anyway there is no evident trend e.g. with distance in the second step and the remaining corrections are on the noise level. Schönrich et al. (2011b) reported that their method gives a slight mean distance underestimate in the presence of significant intrinsic distance scatter, which is caused by stars with distance overestimates populating the edges of the fitting baseline and hence acquiring larger weight. This bias was found at $\delta_f \sim 0.5\sigma_f^2$, where f denotes the relative distance aberration and σ_f its dispersion. I confirmed the validity of the prefactor 0.5 for the sample in use by applying a range of Gaussian broadenings to our isochrone distances. Yet it is not straight forward to estimate the values of σ_f dependent on metallicity and colour. On the red side the stars are relatively firmly placed on the main sequence, the reddening vector runs quite parallel to the main sequence, and hence the colour and metallicity errors dominate justifying a moderate error estimate $\sigma_f \sim 15\%$. On the blue end the placement of the stars on the turn-off becomes increasingly uncertain and especially on the metal-rich side one must expect significant spread in ages and hence absolute magnitudes as well. I hence adopt a mild increase in distance depending on colour

$$\frac{\delta_s}{s} = 0.01 + 0.08\left((g-i)_0 - 0.8\right)^2 \left(1 + \frac{1}{4}\left([\text{Fe/H}] + 2.3\right)^2 \right), \tag{10.9}$$

which is larger on the blue side and increases mildly with metallicity. I limit the relative distance increase to a maximum of 4.5%, which corresponds to a distance scatter $\sigma_f = 30\%$.

Fig. 10.2 shows the adopted absolute magnitudes (upper panel) and the correction field for the isochrone distances (lower panel) in the colour-metallicity plane. Along the metal-poor stars Ii require moderate distance stretching. This is the turn–off region, where the 11.6 Gyr isochrones might be a little bit too young and get shifted upwards and on the other hand a bit of contamination by subgiants is more likely because of the reduced physical differences. In principle this contains information on the structure around the turn–off and the dominant ages among these populations, but such an investigation is beyond the scope of this work and so I store it for a later paper. At higher metallicities the turn–off line evidently shifts upwards, i.e. to redder colours as expected from stellar models. On the other hand there is some evidence for a younger metal-rich population at blue colours, indicated by the absence of distance under-estimates that are seen on the metal-poor side. Some vertically aligned features might point to minor systematics in the pipeline metallicities (i.e. under-estimating a star's metallicity makes us underestimate its distance), but their discussion is beyond the scope of this work. Throughout the range of G and K dwarfs there is a quite constant need for mildly larger distances than envisaged by naive use of the isochrone distances.

10.5 Detecting global rotation in SEGUE

Fig. 10.3 shows the streaming motion for the sample projected into and binned in the Galactic plane. At each bin I evaluate the mean motion in the heliocentric frame (left panel) and the mean motion in the Galactocentric frame (right). While I would expect some minor systematic motion even in the Galactocentric frame by spiral structure and maybe influence by the bar, such contributions will be relatively small as most of this sample is at high altitudes where the stars with large random motion experience less important changes of motion by the relatively shallow potential troughs of the spiral pattern. Some of the residual structure will likely be blurred out by Poisson noise and distance uncertainties, so that it is no surprise not to see any appreciable signal. As a good sign there are no significant aberrations, which would be expected under systematic distance errors, where especially the azimuthal velocity component could cross over into the radial velocity determinations. In the left panel, however, we see the very prominent rotational streaming of the Galactic disc, which is central to the following investigations.

10.5.1 The standard of rest

The strong influence of rotational streaming on the observed radial motion makes any determination unreliable that does not explicitly deal with this problem. In the literature varying offsets of the solar radial motion of up to more than $10\,\mathrm{km\,s^{-1}}$ from the value derived from local samples have been claimed. One possible reason are the velocity cross-overs invoked by systematic distance errors (Schönrich et al., 2011b). However, irrespective of the use of proper motions one
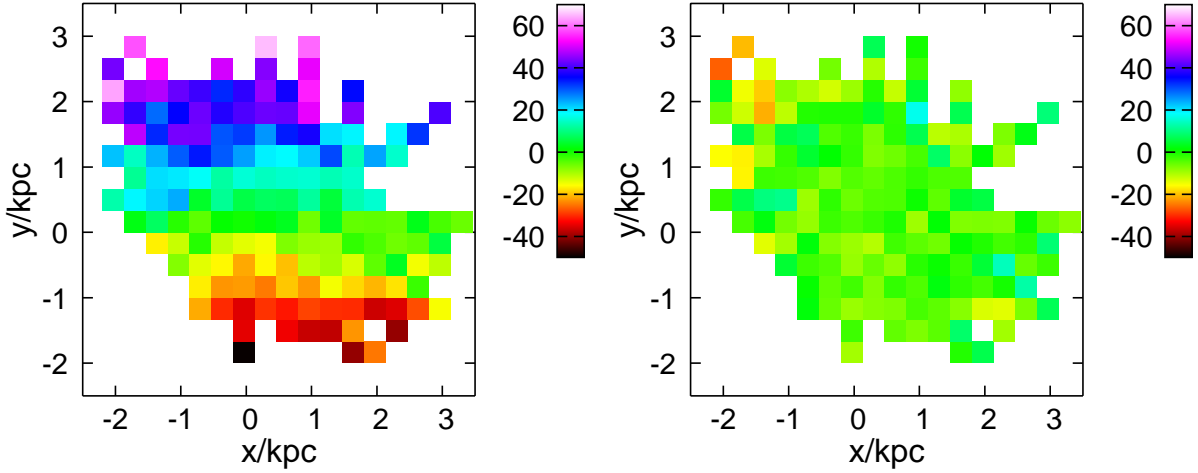
Figure 10.3: Systematic streaming in the SEGUE sample. The left hand panel shows the heliocentric U velocity, while the right hand panel gives the galactocentric U_g, i.e. the real radial motion at the position of the star assuming a solar galactocentric radius $R_0 = 8.2$ kpc and $v_{\phi,\odot}$ set accordingly to the proper motion of Sgr A^*. The sample was binned in separate boxes a third of a kpc wide, plotted when they contain more than 50 stars. The sample thins out towards the remote stars, which causes the increased scatter seen particularly in the galactocentric velocities. For both panels I restrict the sample to stars with [Fe/H] > -1.

must not neglect rotation. In any sample that is not demonstrably rotation-free and is not symmetric in Galactic longitude the streaming motion offsets the mean heliocentric radial motion and hence the inferred Solar motion with the error growing the more remote the observed stars are.

Fig. 10.4 shows the heliocentric U velocities for all stars (red crosses) from DR8 and stars with [Fe/H] > -0.5 (light blue points) against $\sin\alpha$. I set $R_0 = 8.2$ kpc, the value for $v_{\phi,\odot}$ is set accordingly via the Reid & Brunthaler (2004) relation. The metal-rich subsample displays a nearly linear relationship of the mean U velocity in $\sin\alpha$ as expected for rotational streaming from equation (10.1). This streaming motion is far larger than the expected offset caused by the solar LSR motion $U_\odot \sim 11.1\,\mathrm{km\,s}^{-1}$ (Schönrich, Binney & Dehnen, 2010). Thus even a mild asymmetry like in the SEGUE sample will give a wrong estimate in a naive fit without rotation. Consistently one would infer from those data a solar motion of $U_\odot = (3.92 \pm 0.45)\,\mathrm{km\,s}^{-1}$ using the metal-rich objects and $U_\odot = (6.54 \pm 0.44)\,\mathrm{km\,s}^{-1}$ for the entire sample. As expected for a rotational bias the aberration from the standard LSR value is significantly larger for the disc sample. To rid my results from this bias, I use the estimator

$$\overline{U_{\mathrm{rot}}(\alpha)} = \theta_g \sin\alpha - U_\odot' \tag{10.10}$$

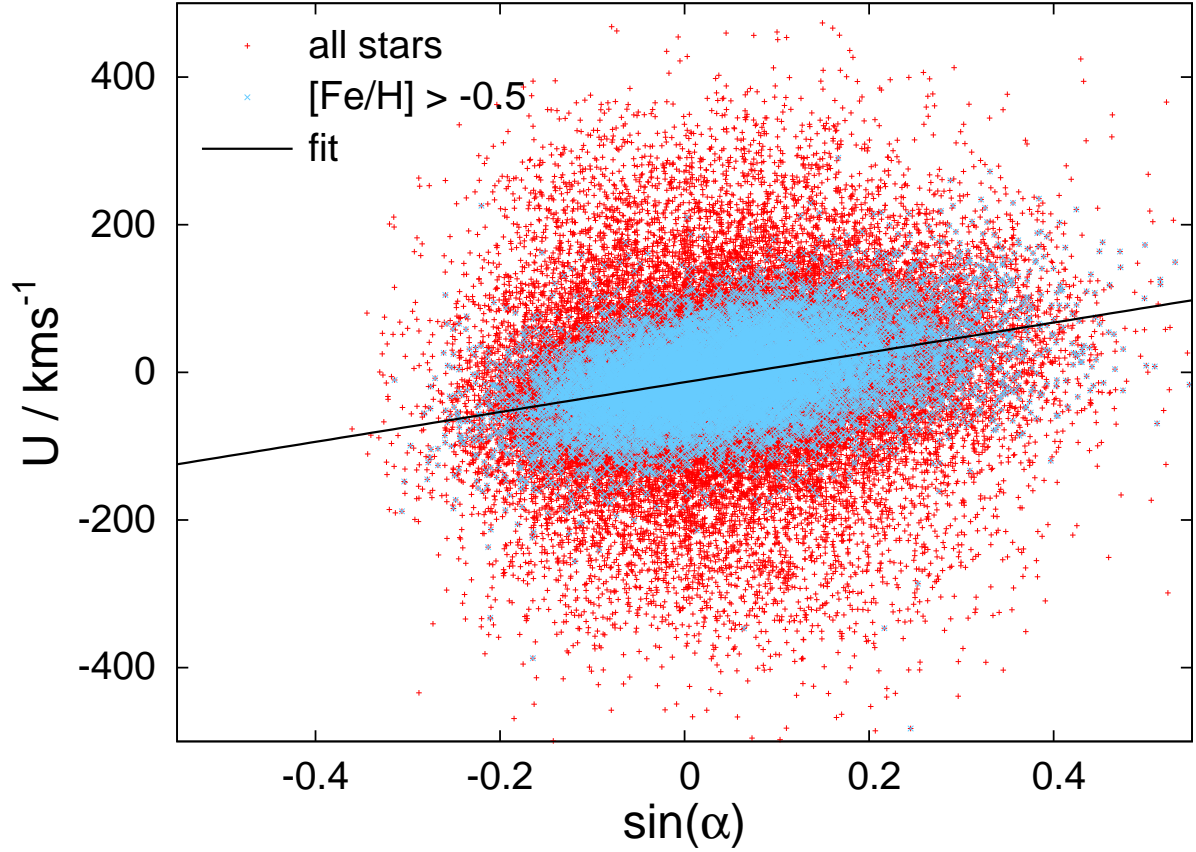where the free parameters θ_g and $-U_\odot'$ are the effective rotation in the sample and the reflex

Figure 10.4: U velocities versus $\sin \alpha$ for all stars in the SEGUE sample (red crosses) and objects at disc metallicities ([Fe/H] > -0.5, blue points). The line represents the linear fit for the metal-rich subsample.

of the solar motion. I obtain $(\theta_g, U_\odot') = (202.0 \pm 3.5, 13.39 \pm 0.44)\,\mathrm{km\,s^{-1}}$ for the metal-rich subsample and $(\theta_g, U_\odot') = (139.8 \pm 3.5, 13.14 \pm 0.47)\,\mathrm{km\,s^{-1}}$ for all stars. Formally this is different from the Schönrich, Binney & Dehnen (2010) estimate at the 1σ-level. Yet there are larger uncontrolled systematic biases: This fit implies that the effective rotation term carries all the observed bias. While the detailed rotation pattern is not of interest here, the measurement will be biased if one encounters a larger fraction of slow rotators on one side than on the other. E.g. a different number of halo stars or unmatched differences of rotation with galactocentric radius could bias the estimate of θ_g which correlates with $U_\odot'$. The systematic uncertainty can be quantified by the uncertainty in θ_g. In the sample $U_\odot'$ shrinks by $0.5\,\mathrm{km\,s^{-1}}$ for every $10\,\mathrm{km\,s^{-1}}$ decrease in θ_g.

Despite all efforts put into the SEGUE parameter pipeline, it cannot be granted that we can trust the radial velocities to be free of any systematic aberrations of order $1\,\mathrm{km\,s^{-1}}$. To shed light on this problem let us examine the vertical velocity component. Replacing U by W in

equation (10.10) gives interestingly a marginally significant $\theta_g \sim (3.1 \pm 2.1)\,\mathrm{km\,s^{-1}}$ and an estimate of $W_\odot = (5.13 \pm 0.28)\,\mathrm{km\,s^{-1}}$ that is surprisingly different from the local values derived from Hipparcos and GCS. The vertical velocity component should not carry and rotational signature, so that θ_g could be identified with a warp of the Galactic disc (cf. Dehnen, 1998), but accounting for the fact that without statistical correction of the isochrone distances I would have obtained a baffling estimate of around $20\,\mathrm{km\,s^{-1}}$, this may well be a residual distance bias. $W_\odot$ can, however, be probed without significant systematic uncertainties directly on the cones around the Galactic poles, where proper motions and distances play hardly any role. This reveals $W_\odot = (4.97 \pm 0.78)\,\mathrm{km\,s^{-1}}$ for the 6740 stars with $\sin b > 0.9$ versus $W_\odot = (10.03 \pm 1.34)\,\mathrm{km\,s^{-1}}$ for their southern counterpart of 1446 stars with $\sin b < -0.9$. Allowing for the projection of a radial velocity offset as a free fit parameter:

$$W = \delta v_{\mathrm{los}} \sin b - W_\odot \tag{10.11}$$

the final result is on the chosen poleward cones $\delta v_{\mathrm{los}} = (2.79 \pm 0.95)\,\mathrm{km\,s^{-1}}$ and $W_\odot = (7.58 \pm 0.90)\,\mathrm{km\,s^{-1}}$. Testing for streams by cuts in metallicities I obtain $\delta v_{\mathrm{los}} = (2.67 \pm 0.75)\,\mathrm{km\,s^{-1}}$ for [Fe/H] > -1.0 (4762 stars) and $\delta v_{\mathrm{los}} = (1.35 \pm 0.93)\,\mathrm{km\,s^{-1}}$ for 1624 objects with [Fe/H] > -0.5. If I am not very unlucky in this sample, either the stars in the solar cylinder are currently expanding vertically or far more likely the stellar line-of sight velocities velocities are redshifted by $\sim 2\,\mathrm{km\,s^{-1}}$. In this light I control the estimate for $U_\odot$ for a line-of-sight velocity bias by expanding equation (10.10) to:

$$U(\alpha) = \theta_g \sin \alpha + \delta v_{\mathrm{los}} \cos l \cos b + c \tag{10.12}$$

Assuming $\delta v_{\mathrm{los}} = 2\,\mathrm{km\,s^{-1}}$ reduces the estimate for $U_\odot$ to $(12.65 \pm 0.47)\,\mathrm{km\,s^{-1}}$ for all stars and $12.67\,\mathrm{km\,s^{-1}}$ for the metal-rich subsample. This result does also not change significantly when I choose distances $s > 2\,\mathrm{kpc}$.

After all, when accounting for the systematic uncertainties in the data, no hint for a motion of the solar neighbourhood against some Galactic standard of rest can be detected in this sample. In the light of this result and the following sections I recommend a value of $U_\odot = 12.7 \pm 0.5\,\mathrm{km\,s^{-1}}$ with a systematic uncertainty of about $1.5\,\mathrm{km\,s^{-1}}$.

10.5.2   Divide and conquer: The rotation of components

So far I exclusively looked at the global rotation pattern, yet the new rotation indicator can do more: Any measurement relying on observed azimuthal velocities does not provide the real rotation of the component in question, but only a value relative to the Sun, from which we conclude its rotation speed by discounting for the Galactic circular velocity plus the solar azimuthal LSR motion. On the contrary the radial velocity part of (10.1) relates to the velocity differences at a range of Galactic longitudes gives the real rotation of the component without significant influence by assumptions on the motion of the Sun. Similarly, azimuthal velocity measurements can be influenced by streams and so it is desirable to have an independent source of information: In
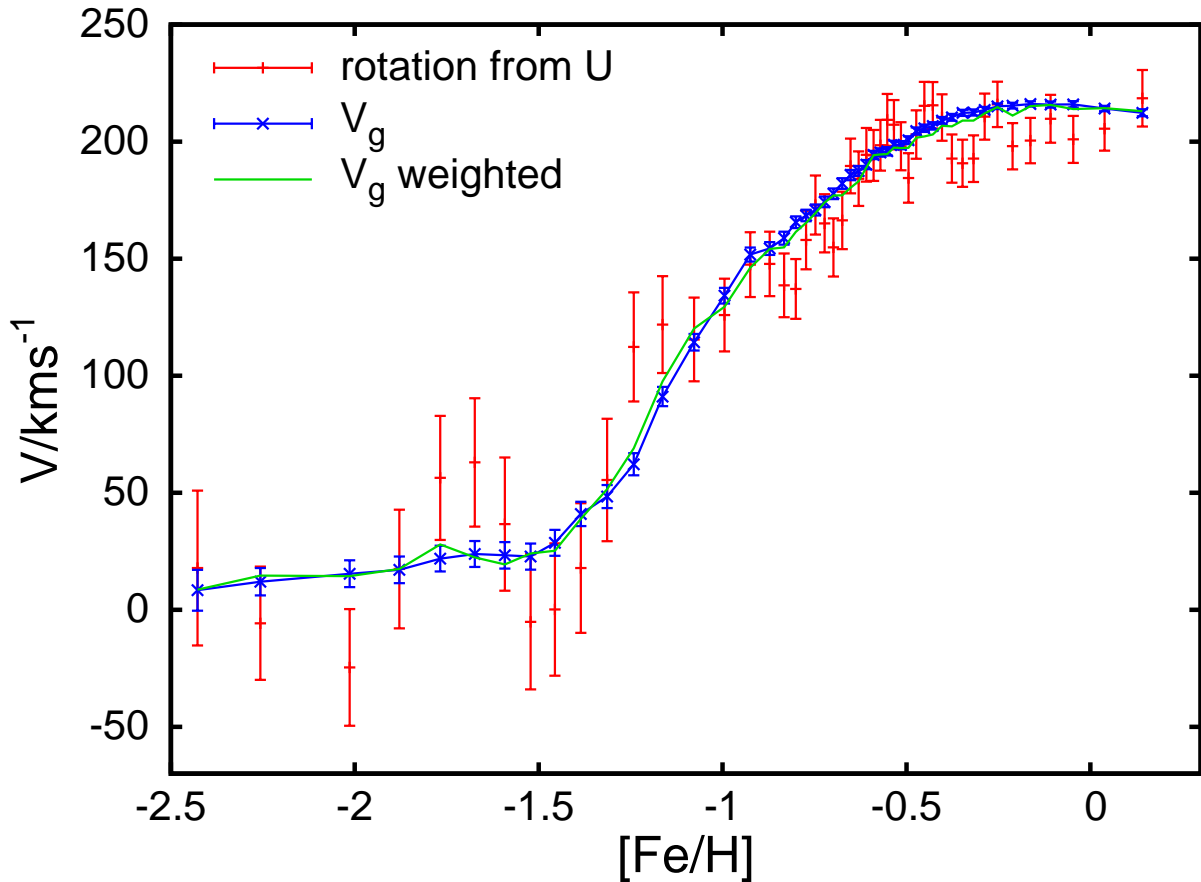
Figure 10.5: Measuring the intrinsic rotation of the populations. I assume $R_0 = 8.2\,\text{kpc}$ and $v_{\phi,\odot} = 245\,\text{km}\,\text{s}^{-1}$. After sorting the sample in [Fe/H] I move a 2000 stars wide mask in steps of 1000 so that every second data point is independent. The red data points show the measured rotation speed in each subsample, while the blue data points with small errors give the mean azimuthal velocity V_g in each bin. The green line shows the same, but weighted with $(\sin\alpha - \overline{\sin\alpha})^2$.

general a stream will then show up in highly different values for the two rotational velocity indicators. The price one has to pay for the radial velocity estimator is a larger formal error, the need for extended samples, a different dependence on the assumed R_0 and some stronger vulnerability to distortions from axisymmetry, e.g. influence by the Galactic bar. As discussed by Schönrich et al. (2011b) dissecting a sample by kinematics is detrimental for this kind of kinematic analysis, but one can divide the Galaxy into its components by a selection in metallicity.

Fig. 10.5 shows the rotation measurement from the radial velocity estimator when I dissect the sample into bins of 2000 objects in metallicity and move half a bin in each step (large red errorbars). The two plateaus of disc and halo rotation with the transition region in between show up nicely. Clearly there is no significant average net rotation in the Galactic halo. Despite the far

smaller formal error, this would be more difficult to state on firm grounds by using the average azimuthal velocity alone (blue error bars), which does depend strongly on the solar Galactocentric motion. In fact the azimuthal velocity estimator has been shifted onto the curve by matching $v_{\phi,\odot} = 245\,\mathrm{km\,s^{-1}}$, which turns us to the topic of the next subsection.

10.5.3 Deriving Galactic parameters

More important than mutual confirmation of results one can play off the two measurements against each other. Matching their absolute scales gives a quantity that has up to now largely eluded stellar dynamics: the azimuthal velocity of the Sun in the Galactic rest frame $v_{\phi,\odot}$. Subtracting the solar LSR motion this grants an estimate for the circular speed V_c near the solar radius without any need to invoke complicated models.

To bring the two measurements on common ground we have to apply weights to our estimate of the mean azimuthal velocity $\overline{V_g}$ for each subpopulation: In a least squares estimate on the rotation speed θ each star gets assigned a weight proportional to its distance from the population mean on the baseline $d = |\sin\alpha - \overline{\sin\alpha}|$. As the value U_h invoked by rotation varies linearly on this baseline, each star in the fit attains the weight $w = (\sin\alpha - \overline{\sin\alpha})^2$. Now all stars have equal weights in both types of measurement diminishing impact from inhomogeneities in the sample. Those weighted averages on the azimuthal velocities are drawn with the green line in Fig. 10.5. Generally the weighted values in the disc regime are a bit lower, because the extreme ends on $\sin\alpha$ are populated by remote stars at higher altitudes and at larger asymmetric drift.

Via the Galactic angle α the assumed solar galactocentric radius enters the derivation. The larger R_0 the smaller the derived $|\alpha|$ will be for stars on our side of the Galaxy. This results in a larger rotation speed required for the same pattern and so increases the estimate of the circular velocity. Fortunately the rotation speed of Galactic components is lower than the solar value and further – in contrast to the linear Oort constants – the dependence on α is not linear in the distance, which helps towards a flatter relationship than a mere proportionality between V_c and $V_\odot$. This is shown with the red error bars in Fig. 10.6. For the practical calculation I assume a first guess solar velocity vector $(U_\odot, v'_{\phi,\odot}, W_\odot)$ and calculate in each bin of 2000 stars the difference between θ and the weighted galactocentric azimuthal velocity. As the estimate for $v'_{\phi,\odot}$ hardly matters for the derived $v_{\phi,\odot}$ I set $v'_{\phi,\odot}$ according to the Reid & Brunthaler (2004) relationship for Sgr A^*. The weighted average of the single values gives then the sample datapoint at each assumed R_0. By using the proper motion of Sgr A^* (determined as $6.379 \pm 0.026\,\mathrm{mas\,yr^{-1}}$ by Reid & Brunthaler, 2004) as a second constraint the Galactocentric radius can be fixed to to $R_0 = 7.97^{+0.36}_{-0.33}\,\mathrm{kpc}$ for DR8 and hence the total velocity of the Sun to about $v_{\phi,\odot} = 241^{+11}_{-10}\,\mathrm{km\,s^{-1}}$. For the resulting circular speed one has to subtract about $12\,\mathrm{km\,s^{-1}}$. By coincidence this result hits almost exactly the value determined by Eisenhauer et al. (2003) on the orbit of $S2$ around the black hole of our Galaxy.

One can even gain an estimate for the Galactocentric radius that is fully independent of any other results. For this we have to recapitulate the impact of R_0 on the derived $v_{\phi,\odot}$ for different populations: The measurement compares the mean azimuthal velocity in any population to the
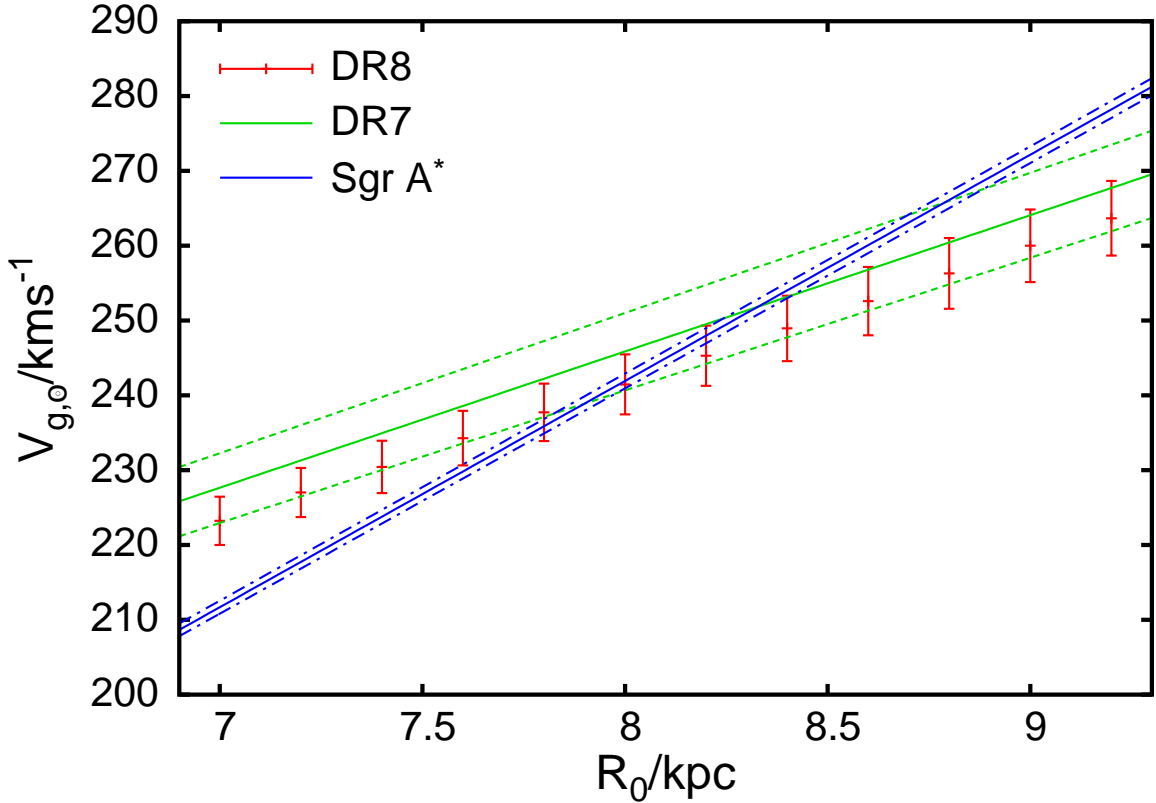
Figure 10.6: Measuring the total azimuthal velocity $v_{\phi,\odot} = V_c + V_\odot$ of the Sun. The sample was binned in distance at bins of a bit more than 2000 stars and then a weighted average taken. The red errorbars show the results from DR8 proper motions, while the green lines show the values from DR7. The significantly lower number of objects results in larger error bars. For comparison I plot the constraint from the proper motion of Sgr A^*.

derived absolute rotation θ. Changing the Galactocentric radius R_0 makes the coordinate system bend differently and hence gives mild changes to V_g, but more important it changes $\sin\alpha$ and so almost proportionally affects θ. As a weakly rotating population has a far smaller value of θ this relative change will be considerably smaller than the change experienced for fast rotating disc stars. However, for all populations one measures the same quantity, i.e. the azimuthal speed of the Sun, and so they must give fully consistent results. Aberrations caused by a wrong R_0 are hence easily detected by dissecting the sample in metallicity, which is (as can be seen from Figure 10.5) a very good proxy for rotation. I cut the sample again into bins of 2000 stars – now in metallicity instead of distance – and evaluate the trend of $v_{\phi,\odot}$ against the mean azimuthal speed in each bin. From the red error bars in Fig. 10.7 one can see that already on the quite modest sample size and extension of the 47790 stars in DR8 I get an independent and competitive estimate of the solar Galactocentric radius $R_0 = 8.43^{+0.63}_{-0.54}$ kpc.
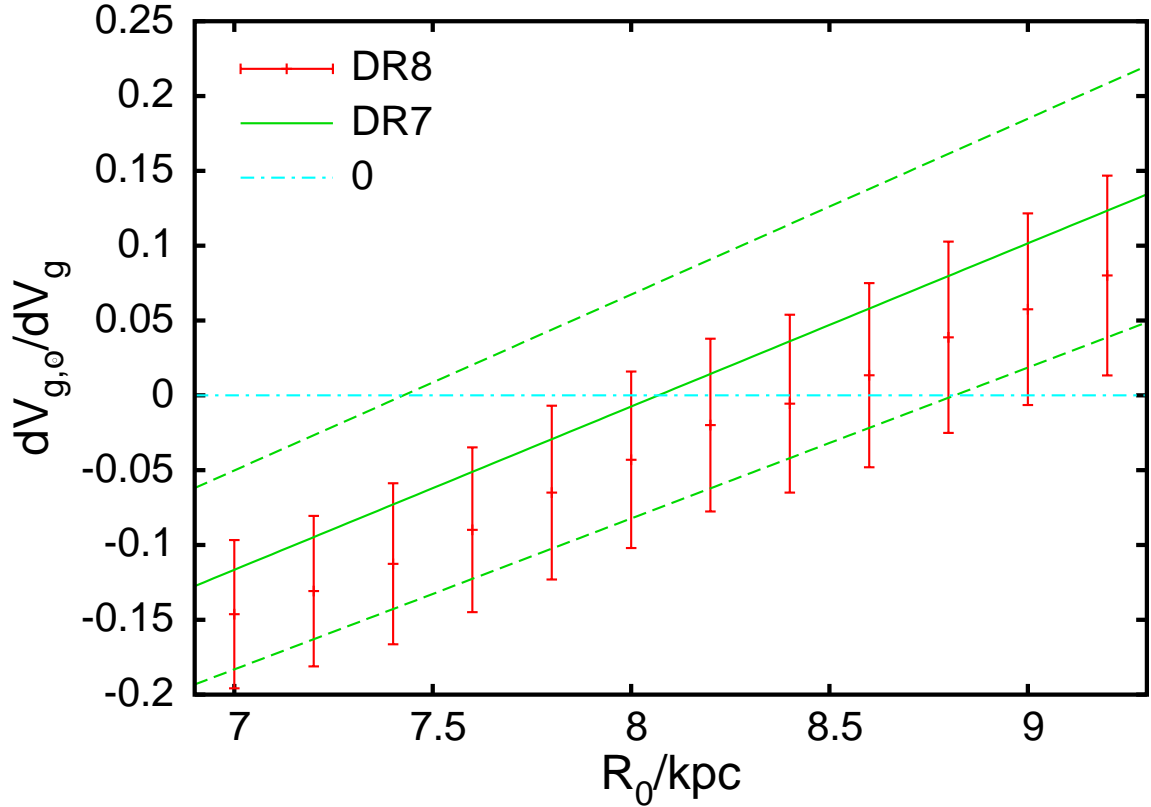
Figure 10.7: Using the trend in determined rotation speed versus mean azimuthal velocity to get another constraint to the galactocentric radius. For this purpose I sorted the sample by metallicity into bins of 2000 stars and estimated $dv_{\phi,\odot}/dV_g$ (vertical axis in the plot, a dimensionless quantity) while varying R_0.

As in the first measurement I used the absolute value of rotation while here the unit-less slope $dv_{\phi,\odot}/V_g$ is employed, the two results are formally independent and can be combined to $R_0 = (8.11 \pm 0.29)\,$kpc. Blending this result with the higher estimate of McMillan (2011) gives $R_0 = (8.25 \pm 0.14)\,$kpc. This translates to $v_{\phi,\odot} = (245 \pm 9)\,$km s^{-1} from this work alone and $v_{\phi,\odot} = (249.5 \pm 4.2)\,$km s^{-1} when blending with the values of McMillan (2011). Working in the LSR values of Schönrich, Binney & Dehnen (2010) I hence obtain $V_c = (233 \pm 7)\,$km s^{-1} for the presented analysis only and $V_c = 237 \pm 5\,$km s^{-1} for the blended result.

10.5.4　Assessment of systematic errors

To assess the systematic uncertainties I vary some of the assumptions. First I checked that the choice of bin size does not change the results more than the general noise induced by bin changes as long as the bins are not unreasonably small. I tested that neither of the measurements depends

on the initial assumption of $v'_{\phi,\odot}$, when varying this value by of order $20\,\mathrm{km\,s^{-1}}$. Galactic rotation at fixed R_0 is increased by $4\,\mathrm{km\,s^{-1}}$ when I globally increase distances by 10% and would be about $7\,\mathrm{km\,s^{-1}}$ lower without the Schönrich et al. (2011b) distance correction. It is not affected to more than $1\,\mathrm{km\,s^{-1}}$ by increased distance scatter of $10-30\%$. It is obvious that such a scatter has a minor effect, as the relation between U_h and $\sin\alpha$ is linear and hence at small changes the mean of U_h is only mildly affected. This is a benefit from operating remote from the Galactic centre where the changes in Galactic angle become more rapid. The mean azimuthal velocity is mostly affected by distance scatter via the bias on average distance derived from our statistical method. Tests reveal an expected systematic bias of order $1\,\mathrm{km\,s^{-1}}$.

Similarly the slope of the derived rotation speed $dv_{\phi,\odot}/dV_g$ depends mostly on distance. Here the dependence is larger: It reacts by 0.08, i.e. about 1.5 standard deviations to a forced increase of 10% in distance and by -0.05 to a forced decrease of 10%. Removing the statistical distance correction would lift values by about 0.2 and increased distance scatter without distance correction increases the value by 0.018 for an additional scatter of 10% and lowers it by 0.021 for a scatter of 30%. Gravity cuts have minor influence on my results: The mean rotation rate is affected to less than $0.5\,\mathrm{km\,s^{-1}}$ when I instead apply a constant gravity cut at $\log(g) > 4.0$ and at the same time the trend in azimuthal velocity drops by 0.019. Using a minimum gravity value of $\log(g) > 4.1$ in addition to the cut sloping in metallicity the rotation measurement does not change significatly either, but the second approach for determination of R_0 deviates by -0.03. While there are strong hints to a lower degree of contamination from the distance estimator, the observed deviation in R_0 is still not significant and likely results partly from random scatter as many metal-poor objects are lost by this tighter cut. The robustness of the result against changes in the gravity selection points to the statistical distance estimator being able to cope with the different contamination by adjusting the mean distances. The largest uncertainty appears to arise from the proper motion determinations. The correction I apply raises rotational velocities by about $3\,\mathrm{km\,s^{-1}}$ and in light of the unsatisfactory physical reasoning as discussed in Section 10.4.2 I have no clue how well this correction works. Further I find that a change of $U_\odot$ by $3\,\mathrm{km\,s^{-1}}$, which acts mainly by biasing the average azimuthal velocities in the lopsided sample, affects the rotation value by less than $0.2\,\mathrm{km\,s^{-1}}$ and the dimensionless slope by 0.0004.

10.5.5   Using the direction of motion

As a third possibility for fixing Galactic parameters I suggest use of the direction of motion. All that needs to be done is to compare the expected Galactic angle α to the angle that the Galactocentric mean motion in the subsamples has against the local azimuth. The upper panel in Fig. 10.8 shows the angle

$$\alpha_v = \arctan\left((\overline{U} + U_\odot)/(\overline{V} + v_{\phi,\odot})\right) \qquad (10.13)$$

of the mean velocity for a binned sample of all stars with [Fe/H] > -0.7 (above that value I expect sufficient rotation) assuming a solar azimuthal velocity $v_{\phi,\odot} = 242\,\mathrm{km\,s^{-1}}$ and plotting only bins with more than 10 stars. To make use of this angle I note that the ratio $\overline{U}/\overline{V}$ behaves
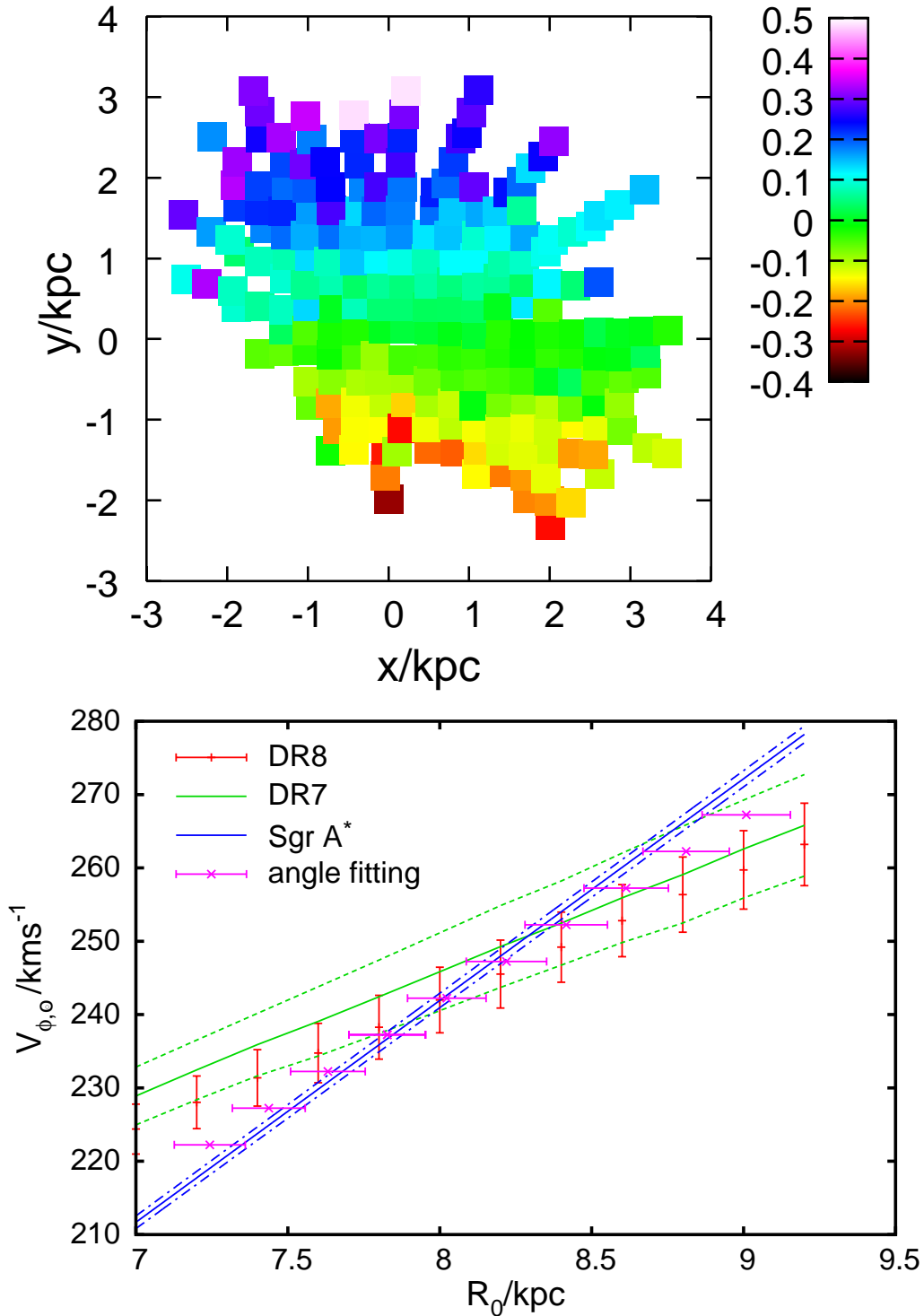
Figure 10.8: The upper panel shows the angle of the mean motion vector in the plane for bins with more than 10 stars. The distribution of bins is irregular because the mean values in *x* and *y* were used in contrast to Fig. 10.3 where bin boundaries were used. The lower panel shows the resulting estimates for R_0 varying $v_{\phi,\odot}$ and allowing for $U_\odot$ as free parameter.

as $y/(x+R_0)$. This relationship is more direct to the observables and allows for a simpler fit (that does not have to account for the bending of the arcustangens). It is obvious that this kind of statistics critically depends on the choice of $U_\odot$ and the total azimuthal velocity of the Sun. While I can fit $U_\odot$ directly to these data, this is not possible for $V_{\rm tot}$ as the fit would then converge to the wrong global minimum: Let $V_{\rm tot}$ and R_0 go to infinity and the fit becomes perfect with all ratios/angles zeroed. In this light I vary $V_{\rm tot}$ externally and allow for $U_\odot$ and R_0 as free fit parameters. All bins were weighted by the inverse number of stars they contain and I only accepted bins with more than 10 objects. The result is shown in the lower panel of Fig. 10.8, where I plot the new result in addition to the previously discussed data. On the first glance this looks good, the formal error margins are competitive making this most probably be a useful tool in larger samples with better precision, but in the present case does not provide a lot of new information: The dependence between R_0 and $v_{\phi,\odot}$ largely resembles that of Sgr A^* and I would need a larger sample extension and more stars to be able to compete with that. In addition tests reveal that different sample selections in metallicity can yield R_0 larger by 1σ at the same $v_{\phi,\odot}$ and at the same time I get about 0.2 kpc smaller results when I restrict the sample to in-plane distances below 2 kpc. This may just be bad luck, alternatively it may either point to Galactic substructure, or to problems with proper motions and radial velocities. Also the assumed radial motion of the Sun has a significant impact on the result. For this reason I used it as a free fit parameter, but the derived values either imply that the rotation frame must be turned by about 0.8 degrees or that $U_\odot$ is about $2-3\,{\rm km\,s^{-1}}$ larger then the GCS value. The fit works out very well, but due to the arising systematic uncertainty (plus the uncertain status of proper motions and radial velocities) and the fact that for the current rather small sample we cannot compete with the accuracy of the Sgr A^* proper motion, I do not use the results for the presented determination of Galactic parameters.

10.6   Conclusions

In this work I developed the idea that in a spatially extended sample the absolute rotation of stellar components can be measured from systematic streaming in the heliocentric radial direction. The stars on one side of the Galactic center show an opposite U velocity to those on the other side. This value has a lower formal accuracy than the classically used azimuthal velocity, but in contrast to the commonly used galactocentric azimuthal velocities does not require assumptions about the velocity of the Sun. The systematic radial motion in any extended sample severely affects determinations of the Local Standard of Rest: $U_\odot$ and $W_\odot$ are generally determined by simply taking the sample average in each velocity component with the reasoning that what flies inwards/downwards has to be balanced by the flow outwards/upwards. All presently available surveys are, however, lopsided, i.e. they are not symmetric in Galactic longitude making the $U_\odot$ measurements biased by disc rotation. For SEGUE I find this systematic error to be $\sim 10\,{\rm km\,s^{-1}}$ getting worse the more remote the used objects are. Accounting for rotation the otherwise observed difference to halo stars disappears and I find $U_\odot = (13.14 \pm 0.47)\,{\rm km\,s^{-1}}$. While there

could of course be some interesting physics involved, a systematic difference of $\sim 5\,\mathrm{km\,s^{-1}}$ in the average W motion between narrow cones towards the Galactic North and South Poles points to a systematic error in the line-of-sight velocities by $\sim 2\,\mathrm{km\,s^{-1}}$ towards us. This does not seem implausible considering that the pipeline radial velocities had to be corrected by an adhoc shift of $7.3\,\mathrm{km\,s^{-1}}$ (Adelman-McCarthy et al., 2008; Aihara et al., 2011). The correction reconciles $W_\odot$ to perfect agreement with Hipparcos and the Geneva-Copenhagen Survey (Holmberg et al., 2009; Aumer & Binney, 2009) and $W_\odot = 7.25\,\mathrm{km\,s^{-1}}$ from Schönrich, Binney & Dehnen (2010). The correction leads to a recommended value for the radial component of $U_\odot = (12.7 \pm 0.5\,\mathrm{km\,s^{-1}}$ with an additional systematic uncertainty of about $1.5\,\mathrm{km\,s^{-1}}$, a bit higher than the GCS value, but still within the error margin.

Comparing the absolute rotation measure based on heliocentric U velocities to the mean V_g velocities in a sample delivers the solar azimuthal velocity $v_{\phi,\odot}$. This measurement is correlated with the assumed Galactocentric radius R_0. Combining the fitting line with another datum like the proper motion of Sgr A^* one can determine both R_0 and $v_{\phi,\odot}$. For DR8 I obtain $R_0 = 7.97^{+0.36}_{-0.33}\,\mathrm{kpc}$ and $v_{\phi,\odot} = 241^{+11}_{-10}\,\mathrm{km\,s^{-1}}$. By dissecting the sample into slow and fast rotating subgroups I can independently infer the Galactocentric radius from their comparison: As fast rotators experience a larger absolute change in the rotation speed θ_g the value of $v_{\phi,\odot}$ derived from them differs from the slow rotators, when R_0 is wrong. Enforcing consistency between the subgroups this effect provides $R_0 = 8.43^{+0.63}_{-0.54}\,\mathrm{kpc}$ and in combination with the simple rotation measure and the proper motion of Sgr A^* I get $R_0 = (8.11 \pm 0.29)\,\mathrm{kpc}$ and $v_{\phi,\odot} = (245 \pm 9)\,\mathrm{km\,s^{-1}}$. Combining those estimates with the values from McMillan (2011) improves the estimate to $R_0 = (8.25 \pm 0.14)\,\mathrm{kpc}$ and $v_{\phi,\odot} = (249.5 \pm 4.2)\,\mathrm{km\,s^{-1}}$. From this I obtain the circular speed $V_c = v_{\phi,\odot} - V_\odot$ by the LSR value of $V_\odot = (12.24 \pm 0.47 \pm 2)\,\mathrm{km\,s^{-1}}$ from Schönrich, Binney & Dehnen (2010). With the LSR value of $V_\odot = 12.24\,\mathrm{km\,s^{-1}}$ from Schönrich, Binney & Dehnen (2010) this translates into $V_c = (233 \pm 7)\,\mathrm{km\,s^{-1}}$ for the presented analysis only and $V_c = 237 \pm 5\,\mathrm{km\,s^{-1}}$ for the blended result.

Another strategy would be to use only the direction of motion in the Galaxy to estimate R_0. In contrast to the previously described measurement this bears, however, a strong dependence on the solar radial motion apart from the dependence on $v_{\phi,\odot}$ I also encountered with the rotation statistics. As the resulting relationship is only weakly inclined against the result from Sgr A^*, but for this sample size is still significantly less accurate, this approach will be more relevant for larger samples and here far just provides some reassurance. It also points to a slightly larger $U_\odot$ (or that our coordinate system should be turned by around 0.8 degrees in longitude) consistent with the previous finding.

There are a couple of systematic uncertainties in this approach that demand our caution. The worst uncertainty comes from the proper motions: I tested both DR7 and DR8 proper motions on the Schneider et al. quasar sample and it is not entirely clear how much of the observed trends can be attributed to chromatic aberration in the Earth's atmosphere and which part may be caused by Galactic frame dragging, i.e. contamination of the galaxy sample used for astrometry with Galactic stars. In any case the systematics are strongly correlated with Galactic rotation and force me to apply a correction of questionable amplitude and colour dependence. The correction alters

the derived Galactic rotation rate at fixed solar position by about $3 \, \mathrm{km \, s^{-1}}$, the systematic error is unknown and must be suspected to be a considerable fraction of this number. The fact that an entire rerun in DR7 proper motions (*rerun* 648) has been found distorted and would lower the Galactic rotation estimate by more than $10 \, \mathrm{km \, s^{-1}}$ does not increase trust in *DR*7 proper motions, while the problem with *DR*8 seems to have largely the effect of an increased scatter that does not noticeably affect the accuracy of the results. I hence decided in favour of the significantly larger sample size available in DR8 and provide DR7 results as a consistency check where it seems necessary. The radial velocity uncertainty mostly affects the measurements of $U_\odot$ and $W_\odot$ and I explicitly correct for the possible shift only in those places. The effect on rotation should (dependent on if the correction is constant) be small.

I made extensive use of the distance corrections developped by Schönrich et al. (2011b). Besides that this project would have been futile without the accuracy achieved by the statistical corrections we are of course prone to all the weaknesses of that method. Especially streams and wrong assumptions about the velocity ellipsoid can induce systematic distance errors of order 5%. Further the distortions caused by the bar or spiral pattern can induce both a distance bias and bias especially the rotation estimates from U. I could not detect significant structures connected to this, so the consequences should be rather small, particularly as we stay out of the region dominated by the bar and as the sample is at the same time large enough not to sample just over one side of a spiral arm. The accuracy could be far better could I use more stars and had I better control of the systematic errors by another dataset. To resolve that problem we will cope with the RAVE sample in an upcoming paper.

If the reader should take only one point from this note then let it be this: With the advent of the large surveys stellar samples are regaining their place as a primary source to obtain not only the Local Standard of Rest, but global Galactic parameters. Already a sample of ~ 50000 stars from SEGUE can deliver formal accuracies for the galactocentric radius and the solar azimuthal velocity that is competitive with any other known approach. Stellar samples will quickly rise in significance with their rapidly growing stellar numbers and spatial extension. Even if stars did not reach this precision, stars provide in extremely valuable source of information, as their systematic errors are highly different from the other sources.

Acknowledgements

Chapter 11

Concluding remarks

The main points the reader should take from this work are: Radial migration as described by Sellwood & Binney (2002) is the only known way to explain the observed local metallicity distribution. There is no way around immigration if one accepts that the age determinations in Casagrande et al. (2011) are at least approximately correct, that imply a quite flat age-metallicity relation.

Radial migration can also describe the full wealth of links between chemistry and kinematics that are observed in the Solar Neighbourhood without having to tune any further parameter. By explaining all features of the Galactic thick disc it has made a Galactic merger or other cosmic catastrophes in the past obsolete. This does not mean that such a merger has not taken place, it simply means that from the current data Ockham's razor tells us to use the simplest possible picture that does not require such a merger. In the near future it will be our task to look for real and significant deviations of model predictions from the data to learn more about the history of our Galaxy. Apart from that we do not expect such a simple model to really describe a complicated thing like the Galactic disc, it would be sad and boring, if all the model predictions were really fulfilled.

The links between chemistry and kinematics give rise to an until now neglected error in the determination of the Local Standard of Rest, or respectively the Solar motion in relation to a local circular orbit. Our Galactic model makes a firm prediction about the distortion in the asymmetric drift relaton classically used for the determination of the Local Standard of Rest that agrees very well with the independent result obtained by fitting the local azimuthal velocity disribution and hence we increased the estimate for the solar motion in the rotational direction at good confidence by about $7\,\mathrm{km\,s^{-1}}$.

The predictions of the model for detailed kinematic structure on the colour-magnitude diagram that led to the error in the LSR determination remained untested in observations so far in the literature, but we have demonstrated that we can see the predicted trends both in the metallicity plane of the new Geneva-Copenhagen Survey and in the colour-magnitude diagram of the Hipparcos data.

Further it was shown that recent claims of a dual structure of the Galactic halo lack any sub-

stance and can be traced back to distance errors and inappropriate Gaussian analysis of velocity components that neglects the fact that neither the underlying velocity distributions nor the error of the data are even remotely Gaussian. This does not exclude differences between the inner and outer halo of our Galaxy, but if those exist (and we expect them to exist) they must be far more subtle than claimed.

To cope with the problem of Gaussian analysis we have put forward an analytic formula that captures the assymetric shape of the disc's azimuthal velocity distribution perfectly, while its parameters are physically motivated. Of course this is not a full kinematic model of our Galaxy, but a useful little formula that can be used to characterize the azimuthal velocity distribution very well.

We also developed a novel statistical approach that can be used to determine distances with an accuracy that could not be attained by classical strategies of statistical astronomy. This approach opened the way to determine the local circular speed in our Galaxy to high accuracy and for the first time reinstitutes stellar samples as a competitive source of information on Galactic parameters. The new method presents an easy way to obtain the intrinsic rotation of a population from heliocentric radial velocities. Once we hold this value the circular speed of our Galaxy is obtained by matching of the absolute rotation of a component with its azimuthal velocities in the Galactic frame. The dependence on the assumed Galactocentric radius can be resolved by the condition that slow and fast rotating populations must yield the same value for the velocity of the Sun or by comparison to the proper motion of Sgr A^*.

Despite all those successes this work has not come to its end, nor did it achieve in time what it was planned for. For quite a long time now it was attempted to replace the simple isothermal approximation in our chemo-dynamic model by adiabatic models. Yet, it had to be noticed that by using simple adiabatic modelling the asymmetric drift at higher altitudes and the vertical extent of the thick disc component at intermediate and large Galactocentric radii would be severely underestimated. Consequently it was not obvious why adiabatic models should be to any extent superior to the isothermal approximation, as they explicitly violated energy conservation. We have solved this problem by the introduction of the adiabatic potential that corrects for the energy transfer from and to the vertical component of motion. With those new inputs we have finally started a recalibration of the model to the new Geneva-Copenhagen Survey that is not finished yet.

A lot needs to be done with the new model: The possibility of pronounced inside-out formation has to be re-investigated as well as different scenarios for the formation of the thick disc. The formation and impacts of bulge and bar are still an open issue and will demand separate modelling. The model also requires recipees for a proper implementation of the halo. In addition my student and I have run a new algorithm that describes the inflow in an angular momentum conserving way. While not explicitly shown in this work, the new algorithm confirms that the inflows in the Schönrich & Binney (2009a) model were on firm physical grounds and will demonstrate that the Galactic gradients measured by Luck & Lambert (2011) are consistent with the accretion from the Galactic corona as put forward by Fraternali & Binney (2008). Among those necessary advances many works are waiting that apply the model for detailed chemical abundance studies

or other studies. So far we have also hardly made use of the fact that we do hold a full Galactic model that can be used for making detailed predictions and exploration of Galactic structure. This latter point will also be of great importance for further modelling. So far we have developed an axisymmetric model that works in the dynamic consequences of the spiral pattern, but does not incorporate the present day spiral pattern with all its consequences. From the current perspective this will best be done by coupling the model to the torus machinery that is being built by Binney & McMillan (2011).

On the side of distances our new method requires further tests that need better models of our Galaxy. Further the kinematics with their changes evoked by the new distance assessment have been hardly explored.

Bibliography

Abazajan K. et al., 2009, ApJS, 182, 543

Adelman-McCarthy J.K. et al., 2006, ApJS, 172, 634

Aihara H. et al., 2011, ApJS, 193, 29

Aihara H. et al., 2011erratum, ApJS, 195, 26

Allende Prieto C. et al., 2008, AJ, 136, 2070

An D. et al., 2008, ApJS, 179, 326

Antoja T., Valenzuela O., Pichardo B., Moreno E., Figueras F., Fernández D., 2009, ApJL, 700, L78

Árnadóttir A. S., Feltzing S., Lundström I., 2010, arxiv:1008.3848

Asensio Ramos A., Allende Prieto C., 2010, ApJ, 719, 1759

Asplund M., 2005, HiA, 13, 542A

Asplund M., 2005, ARA&A, 43, 481

Asplund M., Grevesse N., Sauval A.J., Scott P., 2009, ARA&A, 47, 481

Aumer M., Binney J., 2009, MNRAS, 397, 1286

Aumer M., Burkert A., Johansson P.H., Genzel R., 2010, ApJ, 719, 1230

Bacon R. et al., 2001, MNRAS, 326, 23

Bedin L.R., Piotto G., Anderson J., Cassisi S., King I.R., Momany Y., Carraro G., 2004, ApJ, 605, 125

Beers T.C. et al., 2000, AJ, 119, 2866

Beers T.C. et al., 2011, arXiv:1104.2513

Bekki K., Freeman K.C., 2003, MNRAS, 346, 11

Belokurov V. et al., 2007, ApJ, 654, 897

Benjamin R.A., Danly L., 1997, ApJ, 481, 764

Bensby T., Feltzing S., Lundström I., 2003, A&A, 410, 527

Bensby T., Feltzing S., Lundström I., 2004, A&A, 421, 969

Bensby T., Feltzing S., Lundström I., Ilyin I., 2005, A&A, 433, 185

Bensby T., Zenn A.R., Oey M.S., Feltzing S., 2007, ApJL, 663, 13

Bensby T., Alves-Brito A., Oey M.S., Yong D., Meléndez J., 2011, ApJ, 735, 46

Bensby T. et al., 2011, A&A, 533, 134

Bertelli G., Girardi L., Marigo P., Nasi E., 2008, A&A, 484, 815

Bertelli G., Nasi E., Girardi L., Marigo P., 2009, A&A, 508, 355

van den Bergh S., 1962, AJ, 67, 486

van den Bergh, 1967, AJ, 72, 70

Bessel M.S.,2005, ARA&A, 43, 293

Bethe H.A., 1939, PhRv, 55, 434

Binney J., Dehnen W., Bertelli G., 2000, MNRAS, 318, 658

Binney J., Lacey C., 1988, MNRAS, 230, 597

Binney J., 2010, MNRAS, 401, 2318

Binney J., McMillan P., 2011, MNRAS, 413, 1889 (BM11)

Binney J., Merrifield M., 1998, "Galactic Astronomy", Princeton: Princeton University Press

Binney J., Tremaine, S., 2008, *Galactic Dynamics*, 2nd ed., (Princeton: PUP)

Bird J.C., Kazantzidis S., Weinberg D.H., 2011, MNRAS accepted, arXiv:1104.0933

Blackwell D.E., Shallis M.J., 1977, MNRAS, 180, 177

Bland-Hawthorn J., Cohen M., 2003, ApJ, 582, 246

Bond J. et al., 2009, ApJ, 716, 1

Borkova T.V., Marsakov V.A., 2005, ARep, 49, 405

Bournaud F., Elmegreen B.G., Martig M., 2009, ApJL, 707, 1

Broderick A.E., Loeb A., Reid M.J., 2011, ApJ, 735, 57

Brook C., Richard S., Kawata D., Martel H., Gibson B.K., 2007, ApJ, 658, 60

Burnett B., Binney J., 2010, MNRAS, 407, 339

Burnett B., and the RAVE collaboration, A&A, 523, 113

Burton W.B., Bania T.M., 1974, A&A, 33, 425

Byrd G.G., Saarinen S., Valtonen M.J., 1986, MNRAS, 220, 619

Caretta E. et al., 2009, A&A, 505, 117

Carollo D. et al., 2007, Nature, 450, 1020 (C07)

Carollo D. et al., 2010, ApJ, 712, 692 (C10)

Carollo D., Beers T.C., Sivaran T., Norris J.E., Freeman K.C., Aoki W., Lee Y.S., 2011, arXiv:1103.3067

Casagrande L., Flynn C., Portinari L., Girardi L., Jimenez R., 2007, MNRAS, 382, 1516

Casagrande L., Ramírez I., Meléndez J., Bessell M., Asplund M., 2010, A&A, 512, 54

Casagrande L., Schönrich R., Asplund M., Cassisi S., Ramírez I., Meléndez J., Bensby T., Feltzing S., 2011, A&A, accepted, arXiv:1103.4651

Cassisi, S.; Pietrinferni, A.; Salaris, M.; Castelli, F.; Cordier, D.; Castellani, M.

Cescutti G., Matteucci F., François P., Chiappini C., 2007, A&A, 462, 943

Chaboyer B., Sarajedini A., Demarque P., 1992, ApJ, 394, 515

Chaboyer B., Demarque P., Sarajedini A., 1996, ApJ, 459, 558

Charlot S., Worthey G., Bressan A., 1996, ApJ, 457, 625

Chiappinin C., Matteucci F., Gratton R., 1997, ApJ, 477, 765

Chiappini C., Matteucci F., Romano D., 2001, ApJ, 554, 1044

Chiba M., Beers T.C., 2000, AJ, 119, 2843

Chieffi A., Straniero O., Salaris M., 1991, ASPC, 13, 219

Chieffi A., Limongi M., 2004, ApJ, 608, 405

Colavitti E., Matteucci F., Murante G., 2008, A&A, 483, 401

McConnachie A.W., Chapman S.C., Ibata R.A., Ferguson A.M.N., Irwin M.J., Lewis G.F., Tanvir N.R., Martin N., 2006, ApJL, 647, 25

Cooper A.P. et al., 2010, MNRAS, 406, 744

Curtis H.D., 1920, JRASC, 14, 317

Daflon S., Cunha K., ApJ, 617, 1115

Deason A. J., Belokurov V., Evans N. W., 2010, MNRAS, tmp.1761D

Dehnen W., 1998, AJ, 115, 2384

Dehnen W., 1999, AJ, 118, 1201

Dehnen W., 1999, ApJL, 524, L35

Dehnen W., Binney J., 1998, MNRAS, 294, 429

Dehnen, W. & Binney, J., 1998, MNRAS, 298, 387

Delhaye J., 1965, in Blaauw A., Schmidt M., eds, Stars and Stellar Systems, Vol. 5. Univ. Chicago Press, Chicago, p. 61

De Simone R., Wu X., Tremaine S., 2004, MNRAS, 350, 627

Dong R., Gunn J., Knapp G., Rockosi C., Blanton M., 2011, arXiv1107.5314

Dotter A. et al., 2010, ApJ, 708, 698

Edvardsson B., Andersen J., Gustafsson B., Lambert DL., Nissen P.E., Tomkin J., 1993, A&A, 275 101

Eggen O.J., Lynden-Bell D., Sandage A.R., 1962, ApJ, 136, 748

Eisenhauer F., Schödel R., Genzel R., Ott T., Tecza M., Abuter R., Eckart A., Alexander T., 2003, ApJ, 597, 121

Eisenstein D. et al., 2011, arXiv:1101.1529

Eyre A., Binney J., 2009, MNRAS, 400, 548

Feast M., Whitelock P., 1997, MNRAS, 291, 683

Fink M., Röpke F.K., Hiollebrandt W., Seitenzahl I.R., Sim S.A., Kromer M., 2010, A&A, 514, 53

Flynn, C., Holmberg, J., Portinari, L., Fuchs, B., & Jahreiss, H. 2006, MNRAS, 372 1149

Förster F., Wolf C., Podsiadlowski Ph., Han Z., 2006, MNRAS, 368, 1893

Francois P., Matteucci F., Cayrel R., Spite M., Spite F., Chiappini C., 2004, A&A, 421, 613

Fraternali F., Binney J., 2008, MNRAS, 386, 935

Freeman K.C., 1970, ApJ, 160, 811

Fuhrmann K., 1998, A&A, 338, 161

Fuhrmann K., 2004, AN, 325, 3

Fukugita M., Peebles P.J.E., Hogan C.J., 1998, ApJ, 503, 518

Gerssen J., Kuijken K., Merrifield M.R., 1997, MNRAS, 288, 618

Gilli G., Israelian G., Ecuvillon A., Santos N.C., Mayor M., 2006, A&A, 449, 723

Gilmore G., Reid N., 1983, MNRAS, 202, 1025

Goetz M., Koeppen J., 1992, A&A, 262, 455

Gounelle M., Meibom A., 2008, ApJ, 680, 781

Gradsteyn I.S., Ryzhik J.M., *Table of Integrals, Series, and Products*, 4th ed., (London: AP)

Grevesse N., Noels A., 1993, p.15-25 in Origin and Evolution of th Elements, eds. Prantzos N., Vangioni-Flam E., M. Casse

Grevesse N., Sauval A.J., 1998, Space Science Reviews, 85, 161

Grevesse N., Asplund M., Sauval A.J., 2007, S.S.Rv., 130, 105

de Grijs R., Peletier R.F., van der Kruit P.C., 1997, A&A, 327, 966

Hahn C.H., Sellwood J., Pryor C., 2011, arXiv:1102.4626

Halliday C. et al., 2006, MNRAS, 369, 97

Haywood M., 2002, MNRAS. 337, 151

Haywood M., 2006, MNRAS, 371, 1760

Haywood M., 2008, MNRAS, 388, 1175

Helmi A., White S.D.M., de Zeeuw P.T., Zhao H., 1999, Nature, 402, 53

Herschel W., 1785, Philosophical Transactions of the Royal Society of London, 75, 213

Hill V. et al., 2011, A&A, 534, 80

Holmberg J., Nordström B., Andersen J., 2007, A&A, 475, 519

Holmberg J., Nordström B., Andersen J., 2009, A&A, 501, 941

Ibata R.A., Gilmore G., Irwin M.J., 1995, MNRAS, 277, 781

Ibata R., Lewis G.F., Irwin M., Totten E., Quinn T., 2001, ApJ, 551, 294

Ivezić Ž., et al., 2008, ApJ, 684, 287

Iwamoto K., Brachwitz F., Nomoto K., Kishimoto N., Umeda H., Hix W., Thielemann F.-K., 1999, ApJS, 125, 439

Janka H.-Th., Langanke K., Marek A., Martínez-Pinedo G., Müller B., 2007, PhR, 442, 38

Jenkins A., 1992, MNRAS, 257, 620

de Jong R.S., 1996, A&A, 313, 377

Jørgensen B.R., Lindegren L., 2005, A&A, 436, 127

Jurić, M., Ivezić, Ž., Brooks, A., et al., 2008, ApJ, 673, 864

Just A, Jahreiss H., 2007, arXiv0706.3850

Just A., Jahreiß H., 2010, MNRAS, 402, 461

Kaczmarczik M. C., Richards G.T., Mehta S.S., Schlegel D.J., 2009, AJ, 138, 19

Kaib N.A., Roškar R., Quinn T., 2011, Icar, 215, 491

Kalberla P.M.W., Dedes L., 2008, A&A, 487, 951

Kant I., 1755, *Allgemeine Naturlehre und Theorie des Himmels*, Akademie-Ausgabe, BBAW

Kepley A. et al., 2007, AJ, 134, 1579

Kharchenko N.V., Piskunov A.E., Röser S., Schilbach E., Scholz R.-D., 2005, A&A, 438, 1163

Kennicutt R.C., 1998, ApJ, 498, 541

Klement R. et al., 2006, ApJ, 698, 865

Koposov S.E., Rix H.-W., Hogg D.W., 2010, ApJ, 712, 260

Kregel M., van der Kruit P.C., 2005, MNRAS, 358, 481

van der Kruit P.C., Searle L., 1982, A&A, 110, 79

van der Kruit P.C. & de Grijs R., 1999, A&A, 352, 129

Krumm N., Salpeter E.E., 1979, AJ, 84, 1138

Lacey C.G., Fall S.M., 1985, ApJ, 290, 154

Lai D.K., Bolte M., Johnson J.A., Lucatello S., Heger A., Woosley S.E., 2008, ApJ, 681, 1524

Lee Y.S. et al., 2008, AJ, 136, 2022

Lee Y.S. et al., 2008, AJ, 136, 2050

Lee Y.S. et al., 2011, ApJ, 738, 187

van Leeuwen F., 2007, Hipparcos, the New Reduction of the Raw Data. Springer

Lewis J.R., Freeman K.C., 1989, AJ, 97, 139L

Limongi M., Chieffi A., 2008, http://orfeo.iasf-roma.inaf.it/

Lind K., Charbonnel C., Decressin T., Primas F., Grundahl F., Asplund M., 2011, A&A, 527, 148

Linsky J.L. et al., 2006, ApJ, 647, 1106

Loebman S.R., Roškar R., Debattista V.P., Ivezić Ž., Quinn T.R., Wadsley J., 2011, ApJ, 737, 8

Loktin A.V., Beshenov G.V., 2003, Astronomy Reports, 47, 6

Luck R.E., Lambert D.L., 2011, AJ, 142, 136

Lutz T.E., Kelker D.H., 1973, PASP, 85, 573

Maeder, A., 1992, A&A, 264, 105

Magic Z., Serenelli A., Weiss A., Chaboyer B., 2010, ApJ, 718, 1378

Majewski S.R., 1992, ApJS, 78, 87

Majewski S.R., Law D.R., Polak A.A., Patterson R.J., 2006, ApJL, 637, 25

Mannucci F., Della Valle M., Panagia N., 2006, MNRAS, 370, 773

Marconi M., Cignoni M., Di Criscienzo M., Ripepi V., Castelli F., Musella I. Ruoppo A., 2006, MNRAS, 371, 1503

Marigo, P., 2001, A&A, 370, 194

Marinacci F., Fraternali F., Nipoti C., Binney J., Ciotti L., Londrillo P., 2011, MNRAS, 415, 1534

Marino A.F. et al., 2011, ApJ, 731, 64

Martell S.L., Grebel E.K., 2010, A&A, 519, 14

McMillan P. & Binney J., 2008, MNRAS, 390, 429

McMillan P. & Binney J., 2010, MNRAS, 402, 934

McMillan P., 2011, MNRAS, 414, 2446

Meléndez J. et al., 2008, A&A, 484, L21

Minchev I., Boily C., Siebert A., Bienayme O., 2009, MNRAS, 407, 2122

Munn J.A et al., 2004, AJ, 127, 3034

Murante G., Poglio E., Curir A., Villalobos A., 2010, ApJL, 716, 115

Naab T., Ostriker J.P., 2006, MNRAS, 366, 899

Navarro J.F., Abadi M.G., Venn K.A., Freeman K.C., Anguiano B., 2011, MNRAS, 412, 1203

Nieva M.F., Przybilla N., 2008, A&A, 481, 199

Nordström B., Mayor M., Andersen J., Holmberg J., Pont F., Jørgensen B.R., Olsen E.H., Udry S., Mowlavi N., 2004, A&A, 418, 989

Norris J.E., Ryan S.G., 1989, ApJL, 336, 17

Olling R.P., Dehnen W., 2003, ApJ, 599, 275

Oosterloo T., Fraternali F., Sancisi R., 2008, AJ, 134, 1019

Oort J.H., 1926, Publications of the Kapteyn Astronomical Laboratory Groningen, 40, 1

Oort J.H., 1927, BAN, 3, 275

Pagel B.E.J., 1997, *Nucleosynthesis and Chemical Evolution of Galaxies* (Cambridge: CUP)

Parenago P.P., 1950, Astron. Zh., 27, 150

Persic M., Salucci P., 1992, MNRAS, 258, 14

Percival S., Salaris M., 2009, ApJ, 703, 1123

Pettini M., Madau P., Bolte M., Prochaska J.X., Ellison S.L., Fan X., 2003, ApJ, 594, 695

Pietrinferni A., Cassisi S., Salaris M., Castelli F., ApJ, 612, 168

Pietrinferni A., Cassisi S., Salaris M., Castelli F., ApJ, 642, 797

Pietrinferni A., Cassisi S., Salaris M., Percival S, Ferguson J.W., 2009, ApJ, 697, 275

Pizagno J., Prada F., Weinberg D.H., Rix H.-W., Harbeck D., Grebel E.K., Bell E.F., Brinkmann J., Holtzman J., West A., 2005, ApJ, 633, 844

Pont F., Eyer L., 2004, MNRAS, 351, 487

Popowski P., Gould A., 1998, ApJ, 506, 259

Portinari L., Chiosi C., Bressan A., 1998, A&A, 334, 505

Portinari L., Chiosi C., 2000, A&A, 355, 929

Preston G.W., Shectman S.A., Beers T.C., 1991, ApJ, 375, 121

Quinn P.J., Goodman J., 1986, ApJ, 309, 472

Reddy B.E., Tomkin J., Lambert D.L., Allende Prieto C., 2003, MNRAS, 340, 304

Reddy B.E., Lambert D.L., Allende Prieto C., 2006, MNRAS, 367, 1329

Reid M.J., Brunthaler A., 2004, ApJ, 616, 872

Reid M.J., Menten K.M., Trippe S., Ott T., Genzel R., 2007, ApJ, 659, 378

Reid M.J. et al., 2009, ApJ, 700, 137

Reid M.J., Menten K.M., Zheng X.W., Brunthaler A., Xu Y., 2009, ApJ, 705, 1548

Rich R.M, Howard C., Reitzel D.B., Zhao H.-S., de Propris R., 2007, IAUS, 245, 333

Robin, A.C., Reylé, C., Derrière, S. & Picaud, S., 2003, A&A, 409, 523

Rocha-Pinto H.J., Maciel W.J., 1996, MNRAS, 279, 447

Rolleston W.R.J., Smartt S.J., Dufton P.L., Ryans R.S.I., 2000, A&A, 363, 537

Roman N.G, 1950, ApJ, 112, 554

Roman N.G, 1954, AJ, 59, 307

Roskar R., Debattista, V.P., Stinson G.S., Quinn T.R., Kaufmann T., Wadsley J., 2008, 675, L65

Roskar R., Debattista, V.P., Quinn T.R., Stinson G.S., Wadsley J., 2008, 684, L79

Ryan S.G., Norris J., 1991, AJ, 101, 1865

Ryan S.G., 1992, AJ, 104, 1145

Rygl K.L.J., Brunthaler A., Reid M.J., Menten K.M., van Langevelde H.J., Xu Y., 2010, A&A, 511, 2

Saha A., 1985, ApJ, 289, 310

Sales L.V., 2009, MNRAS, 400, 61

Salpeter E.E., 1955, ApJ, 121, 161

Samland M., Gerhard O.E., 2003, A&A, 399, 961

Sancisi R., Fraternali F., Oosterloo T., van der Hulst T., 2008, A&ARv, 15, 189

Sandage A., 1970, ApJ, 162, 841

Schmidt M., 1963, ApJ, 137, 758

Schneider D.P. et al., 2010, AJ, 139, 2360

Schönrich R., Binney J., 2009a, MNRAS, 396, 203

Schönrich R., Binney J., 2009b, MNRAS, 399, 1145

Schönrich R., Binney J., Dehnen W., 2010, MNRAS, 403, 1829

Schönrich R., 2010, Sterne und Weltraum, Aug 2010

Schönrich R., Asplund M., Casagrande L., 2011, MNRAS, 415, 3807

Schönrich R., Binney J., 2011, MNRAS, accepted, arXiv: 1109.4417

Schönrich R., Binney J., Asplund M., 2011, MNRAS, submitted

Schönrich R., 2011, Jahrbuch der Max-Planck-Gesellschaft 2011, Forschungsberichte

Schönrich R., 2011, MNRAS, submitted

Schörck T. et al., 2009, A&A, 507, 817

Schwarzschild K., 1907, Göttingen Nachr., 614

Schwarzschild M., 1952, AJ, 57, 57

Sellwood J.A. & Binney J., 2001, MNRAS, 336, 785

Sesar B., Jurić M., Ivezić Ž., 2011, ApJ, 731, 4

Siebert A. et al., 2011, AJ, 141, 187

Schuster W.J., Nissen P.E., 1989, A&A, 221, 65

Searle L., Zinn R., 1978, ApJ, 225, 357

Shaver P.A., McGee R.X., Newton L.M., Danlks A.C., Pottasch S.R., 1983, MNRAS, 204,53

Shapley H., 1918, PASP, 30, 42

Shu F.H., 1969, ApJ, 158, 505

Siebert A., et al., 2011, RAVE DR3

Sim S.A., Röpke F.K., Hillebrandt W., Kromer M., Pakmor R., Fink M., Ruiter A.J., Seitenzahl I.R., 2010, ApJL, 714, 52

Smith M.C. et al., 2009, MNRAS, 399, 1223

Sommer-Larsen J., & Zhen C., 1990, MNRAS, 242, 10

Sommer-Larsen J., 1991, MNRAS 249, 368

Steigman G., 2010, J. Cosmology Astropart. Phys., 4, 29

Steinmetz M. et al., 2006, AJ, 132, 1645

Strömberg G., 1927, 65, 238

Strömberg G., 1946, ApJ, 104, 12

Thomas D., Greggio L., Bender R., 1998, MNRAS, 296, 119

Trumpler R.J., Weaver H.F., 1962, *Statistical Astronomy*, New York, Dover Publications

Twarog B.A., Anthony-Twarog B.J., Tanner D., 2002, AJ, 123, 2715

VandenBerg D., 2000, ApJ, 129, 315

VandenBerg D., Casagrande L., Stetson P., 2010, AJ, 140, 1020

Veltz L., Bienaymé O., and the RAVE collaboration, 2008, A&A, 480, 753

Venn K.A., Irwin M., Shetrone M.D., Tout C.A., Hill V., Tolstoy E., 2004, AJ, 128, 1177

Vila-Costas M.B., Edmunds M.G., 1992, MNRAS, 259, 121

Vilchez J.M., Esteban C., 1996, MNRAS, 280, 720

Vorobyov E. I. & Theis Ch., 2008, MNRAS, 383, 817

von Weizsäcker C.F., 1937, Phys. Zeitschr., 38, 176

von Weizsäcker C.F., 1938, Phys. Zeitschr., 39, 633

Wielen R., Fuchs B., Dettbarn C., 1996, A&A, 314, 438

Williams B.F., 2003, AJ, 126, 1312

White H., 1980, Econometrica, 48, 817

Mo H., van den Bosch F., White S., 2010, *Galaxy Formation and Evolution*, Cambridge, CUP

van Woerden H., Wakker B. P. 2004, in "High Velocity Clouds", ed. H. van Woerden, B. P.Wakker, U. J. Schwarz, & K. S. de Boer (Dordrecht: Kluwer), 195

Yanny B. et al., 2009, ApJ, 137, 4377

Yoachim P., Dalcanton J.J., 2006, AJ, 131, 226

York, D. G., et al. 2000, AJ, 120, 1579

Zinn R., 1993, The Globular Cluster-Galaxy Connection, 48, 38

Zwitter T., & the RAVE collaboration, 2008, AJ, 136, 421

Zwitter T., & the RAVE collaboration, 2010, A&A, 522, 54

Curriculum Vitae

Name:	Ralph Alexander Schönrich
Born:	30th March 1982 in München
Marital Status:	single/ledig
Citizenship:	German/Deutsch
Home:	Max-Planck-Str. 1, 81675 München

Education		
	1988 – 1992	St.Anna primary school Munich
	1992/93	Wilhelmsgymnasium Munich
	1993 – 2001	Gymnasium Christian Ernestinum Bayreuth
	2001	Abitur (A-levels) with grade 1.0
	Oct. 2001	Start of studies in physics at LMU Munich
	March 2003	Vordiplom (corresponds to a bachelor) in physics, grade very good
	April 2003	Start of Economics studies at LMU Munich
	Sept. 2004	Vordiplom (corresponds to a bachelor) in economics, grade very good
	2004/2005	Merton College, University of Oxford
	Oct 2008	Diploma (equals a master) in physics, grade 1.0 with distinction (highest possible grade)
	March 2009	Diploma (equals a master) in economics, grade 1.28, 3rd out of 67 students
	April 2009	Start of PhD studies at LMU/MPA with IMPRS scholarship of the Max-Planck-Gesellschaft

Awards and stipends:

Maximilianeum Scholarship (granted 2001)

Bavarian State Scholarship for especially gifted students (2001)

Stipend of the Studienstiftung des Deutschen Volkes (2003)

Max-Weber stipend for excellent students (2006)

IMPRS scholarship of the Max-Planck-Gesellschaft for PhD studies (2008)

prize for excellent studies in economics (2009)

Hubble fellowship (2011)

Danksagungen

Mein besonderer Dank gilt Prof. Dr. James Binney, ohne den ich nicht zur Astrophysik gekommen und Prof. Dr. Martin Asplund, ohne den ich vermutlich nicht in diesem Fach geblieben wäre. Dank an Martin Asplund, der mir nicht nur ein großartiger Lehrer in Fragen der Spektroskopie und Sternphysik, sondern auch in der Galaktischen wie zwischenmenschlichen Chemie ist, der mich zur rechten Zeit in seine Arbeitsgruppe holte und der sich als Idealfall eines Dissertationsbetreuers erwies, geduldig meine wöchentlichen Interessenwechsel begleitete, nie etwas einforderte, mir stets die nötige Ruhe und Freiräume gewährte, wenn Projekte kaum Fortschritt machten, aber immer half, wo Hilfe nötig war. Dank an James Binney, der mich einst mit seiner Vorlesung begeisterte, den Anstoß zu unserer ersten gemeinsamen Publikation gab, und - obwohl nicht mein Betreuer - sich immer Zeit nahm für alle Fragen und Probleme, so wie er geduldig meine ersten Schritte auf dem Feld der Galaxiendynamik begleitete und mir ein phantastischer Lehrer und Vorbild in wissenschaftlicher Schärfe und auch Ethik ist.

Mein aufrichtger Dank gilt Prof. Dr. Simon White für die Betreuung meiner Doktorarbeit, für den Sieg in einer wichtigen Wette gegen mich und die großartige Unterstützung auf meinem Weg. Besonderer Dank auch an Luca Casagrande, den ich nicht nur als Kollegen, sondern auch als Freund schätze, von dem ich viel lernen durfte und mit dem mich eine hoffentlich lange und fruchtbare Zusammenarbeit verbinden wird. Besonders danke ich auch Jan-Uwe Ness für seinen freundlichen und offenen Rat in vielen Fragen und viele anregende Diskussionen. Großer Dank an Fernanda Nieva und Michael Aumer mit denen ich das Büro und viele wundervolle Diskussionen über Astrophysik und das Tagesgeschäft teilen dufte. Ich danke auch Prof. Dr. Heather Morrison für ihre hilfreichen Ratschläge und Erklärungen astrophysikalischer Probleme. Dank auch an Prof. Dr. Walter Dehnen, der mir den richtigen Umgang in wissenschaftlichen Auseinandersetzungen demonstrierte und der eine wichtige Publikation kritisch und hilfreich mitgestaltete.

Erklärung

Hiermit erkläre ich, dass ich diese Doktorarbeit ohne fremde Hilfe angefertigt habe. Außer den im Literaturverzeichnis angegebenen Quellen habe ich keine weiteren Hilfsmittel verwendet.

München, den 21. Oktober 2011